Nanotechnology Applications in Coatings

ACS SYMPOSIUM SERIES **1008**

Nanotechnology Applications in Coatings

Raymond H. Fernando, Editor
California Polytechnic State University

Li-Piin Sung, Editor
National Institute of Standards and Technology

American Chemical Society, Washington, DC

The paper used in this publication meets the minimum requirements of American National Standard for Information Sciences—Permanence of Paper for Printed Library Materials, ANSI Z39.48–1984.

Distributed by Oxford University Press

PRINTED IN THE UNITED STATES OF AMERICA

Foreword

The ACS Symposium Series was first published in 1974 to provide a mechanism for publishing symposia quickly in book form. The purpose of the series is to publish timely, comprehensive books developed from ACS sponsored symposia based on current scientific research. Occasionally, books are developed from symposia sponsored by other organizations when the topic is of keen interest to the chemistry audience.

Before agreeing to publish a book, the proposed table of contents is reviewed for appropriate and comprehensive coverage and for interest to the audience. Some papers may be excluded to better focus the book; others may be added to provide comprehensiveness. When appropriate, overview or introductory chapters are added. Drafts of chapters are peer-reviewed prior to final acceptance or rejection, and manuscripts are prepared in camera-ready format.

As a rule, only original research papers and original review papers are included in the volumes. Verbatim reproductions of previously published papers are not accepted.

ACS Books Department

Preface

Nanotechnology applications in coatings have shown remarkable growth in recent years. This book highlights scientific advancements and recent applications of nanotechnology in polymeric coatings. Key focus areas are nanocomposite coatings, nanostructured specialty coatings, and advanced characterization techniques. The book begins with an overview chapter on recent scientific and technological advancements in nanotechnology applications in this field. Subsequent chapters cover, in detail, a number of key applications of nanotechnology in coatings, along with the related fundamental science. Some contributions focus on issues related to inorganic/organic nanocomposite coating films, including dispersion of inorganic nanoparticles and nanoclays. Surface Functionalized nanoparticles, predispersed inorganic nanoparticles that can be mixed with existing organic coating formulations and organic/inorganic hybrid latexes are approaches discussed for preparation of nanocomposite coatings having improved scratch, corrosion, and UV resistance.

Several chapters address nanostructure development approaches to impart specialized functionality and performance to coatings. Nanoporous adhesive microbial ink-jet ink for miniature biosensors and biocatalysts and nanostructured conjugated polymer networks are discussed. Characterization of nanostructure and nanoparticle dispersion in coatings is a difficult challenge, and this challenge is addressed in several chapters. Assessment of phopocatalytic activity of nanoparticles, use of atomic force microscopy, applications of Nano-Indentation for mechanical property measurements, and nano-thermal analysis are discussed. Size determination techniques suitable for nanoparticles are also reviewed. The highly multidisciplinary nature of the field is evident throughout the book.

Raymond Fernando
California Polytechnic State University
San Luis Obispo, CA, USA

LiPiin Sung
National Institute of Standards and Technology
Gaithersburg, MD, USA

Nanotechnology Applications in Coatings

Chapter 1

Nanocomposite and Nanostructured Coatings: Recent Advancements

Raymond H. Fernando

Department of Chemistry and Biochemistry, California Polytechnic State University, San Luis Obispo, CA 93407

Scientific concepts regarding the benefits of controlling materials at nano-scale have been around for at least half a century. However, technological breakthroughs leading to commercially viable products began only about twenty-five years ago. Intense research and development efforts in this period have resulted in a tremendous growth of products based on nanomaterials. As coatings are integral to virtually any imaginable product or structure, nanomaterials are having a great impact in this field. Today, there are many approaches to make nanocomposite and nanostructured coatings for a wide range of applications. This chapter focuses on the advancements in nanotechnology applications in liquid based coatings. Following a brief historic review of the development of nanomaterial concepts and key technological breakthroughs, a wide range of today's nanotechnology coatings are discussed. They include polymer-nanoparticle and sol-gel composite coatings for improving scratch and UV resistance, IR reflection, anti-microbial and self-cleaning activity, corrosion resistance, and gas barrier properties. Nano-structured coatings for applications such as superhydrophobic surfaces are also reviewed. Current challenges facing further growth of the use of nanomaterials in coatings -- nano-scale dispersion, nano-scale characterization, and concerns over the health and safety of new naomaterials -- are also discussed.

Introduction

Nanotechnology applications in coatings have shown remarkable growth in recent years. This is a result of two main factors: 1) increased availability of nano-scale materials such as various types of nanoparticles, and 2) advancements in processes that can control coating structure at the nano-scale. Another important reason for this growth is the potential of nanotechnology to address many performance challenges presented by the vast range of products and structures that coatings are an integral part of. Applications of coatings include interior and exterior house paints, interior furnishings, glass and façade coatings for high-rise buildings, all types of transportation vehicles and structures (automobiles, airplanes, bridges, road markings, marine vessels, spacecrafts, etc.), and a wide variety of industrial and non-industrial maintenance coatings. At a much smaller scale, coatings are used in numerous electronic products (both consumer and industrial electronics) and biomedical products. Coating layer thicknesses can vary from hundreds of micrometers (e.g., anti-skid coating on the deck of an aircraft carrier) to less than 100 nm (e.g., insulating coatings in microchips). Coatings play one or more of three key roles in these applications: 1) improve product's esthetic appeal, 2) protect the substrate from a wide range of abuses (e.g., damage due to scratches or impact, corrosion, long term weathering, and bio-fouling), and 3) provide specialized functionality to the product (e.g., conductivity, insulation, water repellency, and heat reflection). It is in the latter two roles where nanotechnology has opened up exciting possibilities to improve performance attributes of coatings and the associated products.

It is generally accepted that a material or device having at least one of its dimensions within less than 100 nm length belongs in the nanotechnology domain *(1)*. This definition is not based on an arbitrary choice; rather, it is grounded on well established principles that govern material behavior, as documented by Feynman over a half a century ago *(2)*. Feynman in his 1959 landmark lecture stated that *"Atoms on a small scale behave like nothing on a large scale, for they satisfy the laws of quantum mechanics. So, as we go down and fiddle around with the atoms down there, we are working with different laws, and we can expect to do different things."* In other words, as the size scale of matter becomes smaller, down to the nano-scale, the principles which govern macroscopic materials become non-scalable. A more recent review *(3)* discussed nanotechnology's promise towards enhancing coating functionality in ways that are not attainable with bulk materials or extension of bulk material properties.

The non-scalable nature of bulk properties down to the nano-scale can be understood on the basis of intermolecular forces (Van der Waals and hydrogen bonding attractions, electrostatic attractions and repulsions, and steric repulsions) that govern material behavior. All of these intermolecular forces

4

have a limited distance of influence, ranging from a few Angstroms to a few nanometers.

Figure 1 schematically illustrates a two-dimensional, ideal arrangement of molecules in a material, represented by the small circles. The radius of the larger circles represents the effective distance of intermolecular forces, with respect to molecules A, B, C, and D in Figure 1(a) and molecule E in Figure 1(b). Molecules A and B [Figure 1(a)] are in the interior of the material, and as a result have sufficient molecules surrounding them to balance the intermolecular forces acting on them in various directions. However, the circles around molecules C and D are not filled with molecules, and as a result, their intermolecular forces are unbalanced. These molecules represent a different state of matter and would be considered surface molecules. In a material with large dimensions, the number of surface molecules would be insignificant compared to the bulk molecules. Consequently, their influence on the behavior of the overall material is insignificant. However, as the size decreases to the same order of magnitude of intermolecular force distances (i.e. nano-scale), the surface molecule content increases dramatically. As shown in Figure 1(b), if the size is small enough, all molecules would be under unbalanced intermolecular forces. Consequently, their properties are un-scalable from bulk properties, and they could exhibit very unique and different behaviors. Same analysis can be applied with respect to atoms of metals or inorganic oxides that will be discussed later on in this chapter. In addition, the same analysis can be extended to an interface between two materials. Molecules of one material near the
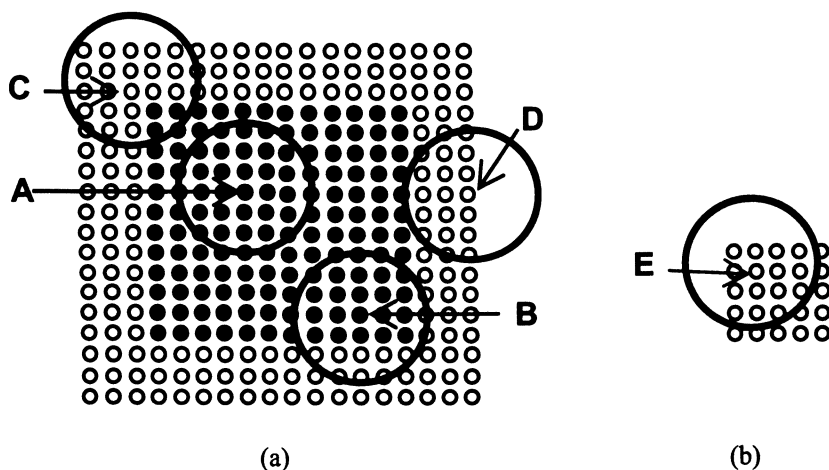

(a)   (b)

Figure 1. Schematic representation of inter-molecular interactions among molecules in, (a) macroscopic, and (b) nano-scale materials

interface with another material would have molecules of the other material within its sphere of intermolecular forces. This will cause the interfacial molecules to be in a different state than the bulk molecules of either material. The interfacial material content would be dramatically enhanced in a nanocomposite, as compared to a macroscopic composite.

An extensive discussion of nanotechnology principles as they apply to nano-scale devices and such quantum properties as electron-hole formation, photovoltaics, and non-linear optics is not the focus of this chapter. Detailed treatments of the underlying nanotechnology principles related to these phenomena can be found in textbooks and other sources *(4-6)*. Utilization of nanotechnology in diverse areas such as defense applications *(7)* and cosmetics *(8)* are also discussed in other treatments of the topic. The two fold objective of this chapter is to review nanocomposite approaches to improving coating properties through the use of nanoparticulate materials and nanostructure development approaches to impart highly specialized functionality to surface coatings.

Nanocomposite Coatings

Incorporation of nano-scale inorganic materials to organic coatings has become one of the most prevalent approaches leading to nanocomposite coating products. As indicated above, a nanocomposite made out of two different materials would have a very high interfacial contact. Consider an example where an inorganic material made up of uniform, spherical particles is incorporated into an organic coating [Figure 2]. In one case, the particles are large, and in the other, they are small. In each case, there is an interfacial region where several molecular or atomic layers of the two phases behave differently from bulk. Dispersing nano-particles, instead of larger particles allows a coating formulator to increase the "interfacial material" content significantly *(9)*. For example, at 30% (by volume) loading, at a particle size of 300 nm and interfacial layer thickness of 10 nm, the interfacial material content is 3%, whereas it increases to 22% when the particle size is decreased to 50 nm. Thus, the interfacial material becomes a major portion of the composite coating. As discussed above, the properties of interfacial material at the interface between two materials are different from the bulk properties of each material. If the interfacial material has better properties that are not offered by individual materials of the composite, this approach would maximize such benefits.

Whether the interfacial material has dramatically different properties compared to the properties of the materials that make up individual phases depend on the difference between intermolecular forces between the two phases. This will be discussed in more detail with respect to the glass transition temperature of polymers in the next section. The actual interfacial material
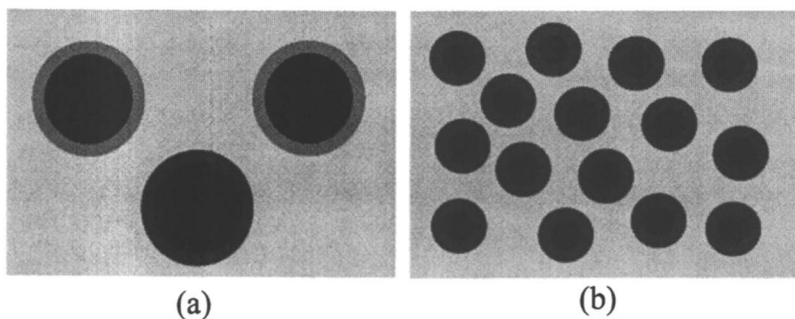
Figure 2. Schematic representation of polymeric composite containing (a) micron size particles and (b) nanoparticles

content having altered properties depends on the thickness of the interfacial layer. The true interfacial layer thickness will depend on the chemistry of the two phases that make up the interface and the specific property of interest.

Optical clarity is an essential property of a number of classes of coatings such as automobile clear coats, floor wear layers, and optical lens coatings. Unless the refractive index can be matched to that of the coating resin, adding inorganic particles cause light scattering that leads to reduction or elimination of film clarity. Since nanoparticles are much smaller in size compared to the wavelength range of visible light (400 – 800 nm), they scatter very little light. Therefore, they can be added to a clear coating formulation with little or no adverse impact on visual characteristics. This feature of nanoparticles has been extremely important in expanding nanoparticle applications in coatings.

Interfacial Effects on Polymer Glass Transition in Nanocomposites

Glass transition temperature (T_g) is one of the most critical parameters that governs the behavior of polymers. A polymer's ability to achieve sufficient molecular mobility to transition from glassy to rubbery behavior can be significantly impacted by an adjacent second phase. Several theoretical and experimental studies have shown that the T_g of a given polymer in the form of ultra-thin films can be very different from its T_g in the bulk form *(10-15)*. One study predicted that near the polymer/air interface, a glassy polymer would exhibit a significant depression in T_g due to chain end enrichment *(10)*. Another theoretical study *(13)* predicted that T_g of low-dimensional polystyrene would depend on the size scale and the interface conditions and found good agreement with available experimental results. Fryer et al. measured *(11)* T_g of polystyrene and poly(methyl methacrylate) (PMMA) films, on polar and nonpolar substrates,

as a function of thickness and found that T_g of polystyrene on silicon oxide decreased by as much as 25°C below the bulk value for films 13 nm thick. For PMMA T_g increased by 7°C above the bulk value for films 18 nm thick. Similar results have been reported by Tsui et al. *(12)*. The implications of film thickness dependence of T_g is very significant in coatings for microelectronic applications where film thicknesses of the order of 100 nm is common. Influence of substrate chemistry on T_g and other properties of ultrathin polymer films in microelectronics has been reported *(15)*.

In an organic/inorganic composite, T_g of the polymer would change due to the steric and enthalpic effects that alter the segmental mobility of the polymer molecule at a polymer/filler interface *(16-21)*. Studies on alumina/PMMA *(16)*, polyurethane/silica *(17)*, polyurethane/organoclay *(18)*, polyurethane/ montmorillonite *(19)*, and polyethylene/silica *(20)* have all shown that the polymer T_g can increase, decrease, or show no change depending on the nature of interfacial interactions between the polymer and inorganic phase. In the work reported by Clarke et al. in Chapter 11 of this book, alumina and silica nanoparticles did not alter the T_g of a polyurethane film. One of the previous studies *(21)*, based on calorimetric data, determined that the immobilized polymer layer thickness in a PMMA/SiO_2 nanocomposite due to interfacial interactions is approximately 2 nm thick. These interactions can dramatically affect the performance of the composite as compared to the pristine polymer. It should be noted that the effect of interfacial interactions on T_g of nanostructured materials (e.g., styrene-butadien-styrene (SBS) block copolymers) has been demonstrated over four decades ago *(22)*. Later on Bares *(23)* reported that T_g of finely dispersed (~12 nm in diameter) phases of a SBS block copolymer was 20°C lower than the analogous bulk phase and proposed the first equation (an extension of the Fox-Flory equation *(24)*) relating the T_g to the enhanced surface-to-volume ratio of the two phases. As Jackson and McKenna demonstrated through their studies of controlled pore size glasses, even smaller molecules such as benzyl alcohol can show significant T_g reduction when there is high surface area contact *(25)*.

Advancements in Nanocomposite Coatings

Nanoclay-Based Composite Coatings

Since Feynman's time *(2)* to the 1980's most of the developments that belong within today's definition of nanotechnology field occurred in computers and other electronic applications. The major developments that led to the excitement about nanomaterials stem from Unichika Company's work on nylon montmorillonite composites and Toyota Motor Company's work on nylon/nano-clay composites. In 1976 Unichika filed a patent application for such com-

posites having unusually high resistance to fire. In the mid 1980's Toyota reported that Nylon/nano-clay composites are not only flame resistant, but, in addition, had vastly improved mechanical properties compared to nylon-6 itself *(26)*. These developments led to extensive research efforts around the world in the field of polymer-clay nanocomposites, including commercialization of a number of automotive parts *(27-29)*. Preparation of nanocomposites with clays involves delamination and random distribution of clay platelets (exfoliation) within a polymer or placement of polymer molecules between clay platelets (intercalation). Chemical and mechanical aspects of the processing conditions required to achieve nano-scale dispersion of these material are not friendly to the typical coating mixing operations. Organically-modified clays that are easier to disperse in appropriate host polymers are commercially available today. However, even these modified clays still have dispersion problems sufficient to limit their applications in *clear* coatings. A synthetic, lithium aluminum silicate clay that can be dispersed into nano-size primary particles (e.g., Laponite) in waterborne coatings has been in the market for a long time. Although its primary use is as a rheology modifier, its use as an additive to improve performance of clear floor wear layer coatings has been reported *(30)*. Recent attempts to disperse organo-clays in UV curable resins (urethane acrylate, polyester acrlate, and cycloalephatic epoxy) have been successful in preparing nanocomposite materials. However, the gloss and film clarity of the resultant films were considerably lower than those of the pristine polymeric films *(31)*.

The most successful applications nano-clays in coatings are in corrosion resistance improvements *(32)* and other barrier property improvements. This is partly due to the increased path length for molecular diffusion caused by the platy nature of the clay materials. The same attribute of nano-clay materials make them good candidates for improving gas barrier properties of coatings.

Nanoparticle-Based Composite Coatings

Incorporation of preformed nanoparticles into organic coating formulations is one of the most straightforward approaches to preparing nanocomposite coatings. Increased availability of inorganic oxide nanoparticles targeted for various property improvements of organic coatings has tremendously helped coating formulating companies to introduce nanotechnology products. A list of properties that can be improved and the types of nanoparticles suitable for the specific property improvements are shown in Table 1. A list of commercial suppliers of these nanomaterials is shown in Table 2. Effective dispersion of nanoparticle powders in an organic resin system is a major challenge. As a result, the majority of successful products in the market are based on nanoparticles predispersed in various solvents, and in some cases, coating resins themselves. Specific examples of nanoparticle based nanocomposite coatings are discussed in more detail later on in this chapter.

Table 1. Nanoparticulate materials candidates for coating property improvements

Coating Property	Nanomaterial
Anti-microbial	CuO ; TiO_2 ; ZnO
Gas Barrier	Nanoclays
Corrosion	Nanoclays, boehmite
Electrical Conductivity, Static Charge Dissipation	ITO, ATO, SnO_2
Fire Retardant	Nanoclays
IR-Absorption/Reflection	ITO, ATO, TiO_2, In_2O_3
Magnetic	Fe_2O_3
Mechanical, Scratch Resistance	Al_2O_3; SiO_2; ZrO_2
Photocatalysis, self-cleaning	TiO_2 ; ZnO
UV stability	TiO_2 ; ZnO; $BaSO_4$; CeO_2

Nanocomposite Latex Emulsions

As mentioned above, pre-dispersion of inorganic nanoparticles in coating resins by nanoparticle suppliers or resin suppliers have made the critical challenge of nano-scale dispersion more manageable for formulated coating manufacturers. This approach works well for solvent based coatings in which the binder resin is dissolved in the continuous liquid phase. In these coatings, when the solvents are removed during the drying step, the resin can form a film with well dispersed nanoparticles. Making predispersed resins for waterborne latex paints (including waterborne UV) is a more difficult challenge. In latex paints, the resin particles need to coalesce properly during the drying step. Incorporation of another dispersed phase (i.e. nanoparticle) can interfere with the coalescence of polymer latex particles. To address this challenge, a number of raw material suppliers and other academic groups have been developing ways to pre-disperse inorganic nanoparticles inside the polymer latex particles. Use of colloidal silica to prepare inorganic-organic hybrid polymer latexes with a variety of monomers, including styrene, butyl acrylate, and methyl methacrylate has been reported *(33,34)*. The hybrid morphology was varied by changing the reaction conditions and the choice of surfactants. BASF's Col.9 latex product is a good example for this type of a product currently in the market. Companies such as Akzo Nobel have introduced low dirt-pick up, improved block-resistance coatings based on this product *(35)*. Another class of hybrid latex products is based on the nano-clay material Laponite *(36)* and sodium exchanged montmorillonite *(37)*. The next chapter of this book by Ming et al.

Table 2. Nanoparticle Suppliers

Supplier	Nanomaterial
Altair Nano	TiO_2; anti-corrosive pigment
BYK Additives	Al_2O_3; SiO_2; ZrO_2,
Clariant	SiO_2
Elementis Specialties	ZnO
Evonik (DeGussa)	ZnO, CeO_2, ITO
Fuso Chemical	SiO_2
Hybrid Plastics	POSS
Ishihara (ISK)	TiO_2, SnO_2
Nanocor	Nanoclay
Nanophase	Al_2O_3, ATO, ITO, ZnO, Bi_2O_3, CeO_2, CuO, Fe_2O_3
Nano Resins AG	SiO_2
Nanoscale	Al_2O_3, ZnO, CeO_2, CaO, MgO, TiO_2
Ningxia Orient Tantalum Industry	ITO
Nissan Chemical	SiO_2, antimony pentoxide, Al_2O_3, ZrO_2
Sasol	Boehmite
Sachtleben	$BaSO_4$, TiO_2
Silco International	SiO_2
Solvey	$CaCO_3$
Southern Clay	Nanoclay
Sukgyung A.-T.	TiO_2, ATO, ITO, ZnO
Sumitomo Osaka Cement	ZnO, ZrO_2
TiPE	TiO_2

contains a more detailed discussion of the preparation of clay encapsulated inorganic/organic hybrid latex polymers. Post-blending of nanoparticles with latex resins is also practiced with some success *(38)*.

Sol-Gel Chemistry Based Nanocomposites

A well known approach to generating inorganic nanophases within an organic matrix is to utilize sol-gel chemistry *(39)*. Typically, Silicon, titanium, aluminum, and zirconium metal alkoxides are used as inorganic sol–gel precursors. A wide range of oligomers as well as low molecular weight organic compounds are used as organic phase precursors. Among many variables that control the hydrolysis and condensation reactions are the pH, solvent, water to alkoxide ratio, concentration of the reactants, type of catalyst, temperature, and reaction time.

Under controlled conditions, silanes and organic molecules can form coatings containing silica nanoparticles or nanophases. In the presence of a coupling agent, the organic and inorganic phases can be covalently linked. This approach has been in practice, including in commercial products, for nearly two decades *(40,41)*. Feasibility of sol-gel derived organic/inorganic hybrid coatings as a replacement for aircraft aluminum alloy primers containing chromate corrosion inhibitors has been an active area of research *(42-45)*. A very recent, comprehensive review of sol-gel technology applications in anti-corrosion coatings is available *(46)*. Other studies have shown improved photostability in aircraft and exterior architectural coatings, and improved scratch resistance of steel and soft substrates such as polycarbonate and plastics *(39,44-46)*. Properties and the nanostructure of the final coating in these applications depend on the selection of the silane, coupling agent (if present) and the chemistry of the organic phase. To a large degree, the same attributes depend on the pH and aging conditions of the sol-gel mix and precursors. The hydrolysis/condensation reaction of the alkoxide is generally reversible. This reversibility is a significant issue in developing hybrid coatings for applications where long term durability under very high or very low pH is essential. Results of sol-gel derived silica-organic hybrid coatings indicate that the morphology is typically an interpenetrating network with the organic phase containing silica clusters of few nano-meters in size. Silica nanofiber formation in a system containing TEOS, methacryloxypropyl-trimethoxysilane (MAPTMS), a urethane acrylate resin, and an acrylated phenylphosphine oxide oligomer (APPO) has been reported *(47)*. The nanofibers were shown to improve the mechanical properties of the organic matrix.

Nanocomposite Coating Performance

Scratch Resistant, Nanocomposite Clear Coatings

Until the recent advancements that led to the availability of a wide range of inorganic nanoparticles, silica has been the choice material for reinforcing clear coatings for applications such as automotive top-coats, floor wear layers, acrylic eye-glass lenses, and scratch resistant polycarbonate sheets for various applications. Colloidal silica has been available for decades from at least a dozen companies around the world in the particle sizes range from about 2 to 100 nm, in aqueous and non-aqueous media. The refractive index (RI) of silica which is 1.46 closely matches the refractive index of common organic binders in coatings, and therefore, high silica loading levels can be achieved without causing haziness problems in coatings. In 1976, Dow Chemical has claimed use of colloidal silica in abrasion resistant coatings for acrylic lenses *(48)*. A few years later, General Electric claimed their use in polycarbonate materials *(49)*.

Highly concentrated, nano-size, colloidal silica dispersed in UV curable monomers has been available for some time. Their use for preparing UV cured coatings with improved abrasion, scratch, and chemical resistance while maintaining a high gloss and film clarity has been reported (50-53). PPG Industries patented and claimed the use of aluminum silicate nanoparticles in automotive coatings (54,55). PPG's CeramiClear coating system for Mercedes automobiles, introduced in 2002 is claimed to be world's first automotive clear coat that incorporates silica nanoparticles to achieve scratch resistance enhancements. Another example of nanotechnology in automotive applications is Ecology Coatings' UV curable clear coating system (licensed to DuPont) containing nano-size silica particles (56).

Sol-gel derived inorganic-organic hybrid coatings for scratch resistance improvements often employ a combination of UV and thermal cure (i.e. dual-cure) (40,57). Recent work by Amerio et al. (57) has shown that linking the inorganic nano-phase with the organic matrix through covalent bonds is important in achieving improved scratch resistance.

The use of higher refractive index inorganic oxides such as alumina, zinc oxide, and titanium dioxide (RI = 1.76, 2.00, 2.50-2.70, respectively) in clear coatings has grown in recent years with the advancements of nanoparticle manufacturing processes. As the refractive index difference between the inorganic material and the resin matrix increases, particle size must be reduced to prevent scattering of light that leads to haze in the composite clear coating. Controlling the average size alone is not sufficient; small amounts of larger particles can cause significant haze problems (58).

Many products with tight particle control suitable for clear coatings are available from suppliers listed in Table 2. SiO_2, ZrO_2, and Al_2O_3 (Mohs hardness 7, 8, and 9, respectively) are mostly used in scratch resistance improvements. Although the hardness of nanoparticle material is an important factor, attempts to relate scratch resistance improvements by nanoparticles to bulk composite mechanical properties and thermal properties have not been completely successful (see reference (59) and Chapter 11 of this book). Further research is needed in this area.

Anticorrosion and Barrier Coatings

The role of nanocomposites in barrier films for packaging applications has been reviewed along with a comprehensive list of other approaches (60). Products in the market today include polyamide, PET, and PP composite films containing nanoclays. An elastomeric barrier coating introduced in 2001 for Wilson's Double Core tennis balls was claimed to be the first nanocomposite coating for such a product. One to two micron thick coating of this nanocomposite is claimed to be as effective as a 12 micron thick layer of ethylene vinyl alcohol (EVOH) copolymer as an oxygen barrier for PET.

Because of the very low thickness, the PET material's clarity can be retained *(61)*. Other examples of thin nanocomposite layers on PET to achieve similar performance are also reported *(62)*. Improvements of gas barrier properties of PET by the treatment of very thin (50 nm), sol-gel derived silica has been the topic of a recent PhD thesis *(63)*.

Use of surface modified boehmite nanoparticles to achieve pH triggered anti-corrosion functionality is discussed in Chapter 5 of this book by Cook and Myers. As indicated earlier, sol-gel approaches to anticorrosion coatings have been reviewed very recently *(46)*.

Nanocomposite Coatings for Controlling UV, IR, and Other Radiation

Coatings play a critical role in controlling the effects of electromagnetic radiation (UV, Visible, IR, other) on many surfaces. The specific electromagnetic frequency range of interest is a factor that determines the coating formulation ingredient selection. Controlling the interactions with the visible light to affect the color and appearance through the right choice of ingredients is the best example of this. Various organic and inorganic pigments are selected for this purpose. TiO_2 (RI=2.5-2.7) is the most effective white pigment; its hiding power is highest at about 250 nm particle size *(64)*.

Prolonged exposure to UV radiation causes degradation of coating films, and special additives are needed to minimize coating damage. In the case of clear coatings, UV stabilizers that do not compromise the film clarity are needed. UV degradation is a critical issue for automobile and aircraft coatings. Protection of wood substrates from UV degradation is also very important. Prior to the development of nanoparticle options discussed below, the most common approach to minimizing damage caused by UV has been the use of additives such as hindered-amine light stabilizers (HALS). In recent years, nano-size oxides such as TiO_2, ZnO, and CeO_2 have been shown to be good UV absorbers that can provide long term protection for various substrates. In coatings, nano titania is being studied as a replacement for organic UV stabilizers such as hindered amines. In one such study *(65)*, the behavior of nano-size TiO_2 (6-92 nm rutile and anatase titania) as a UV absorber in water based acrylic and isocyanate based acrylic coatings was investigated. Results indicate comparable or better performance compared to HALS in the system studied. ZnO is a good broad-band UV absorber whereas CeO_2 is more efficient in UV-B region. These materials are used in both waterborne and solvent based systems *(66,67)*. Inorganic oxides are not consumed in the UV protection mechanism, whereas organic molecules like HALS do, and become depleted over a period of time. However, inorganic oxides are not as efficient as organic compounds. Therefore, the use of a combination of both organics and inorganics is the best approach. A number of suppliers listed in Table 2 provide nanoparticles effective in improving the UV stability of clear coatings. A study

based on sol-gel approach reported both scratch resistance improvement and UV-protection of polycarbonate with the use of polysiloxane coating containing sol-gel derived nano-titanium dioxide *(68)*. The TiO$_2$ nano-particle surface was modified with methyltrimethoxysilane.

Controlling the effects of IR waves is another highly desired characteristic of coatings in a number of applications (e.g. thermal insulation of window glasses and camouflaging military equipment or vehicles from IR detection). IR blocking coatings for window glasses are called low emissivity coatings, and the standard practice is to deposit a very thin (10 – 25 nm) IR-reflective layer of silver or gold metal through physical vapor deposition (PVD). To prevent the oxidation of the metal, the film is sandwiched between two dielectric layers (SiO$_2$, TiO$_2$, or CeO$_2$). The dielectric layers are also of nano-scale thickness (less than 50 nm) to minimize the loss of transmission of visible light *(69,70)*. Recently, there have been attempts to develop liquid coatings for these applications through the use of nanoparticles *(71,72)*. Indium-tin oxide, In$_2$O$_3$, and antimony-tin oxide nanoparticles are used for this purpose.

Halloysite nanotubes (100 nmx500 nm) containing copper nanoparticles are claimed to be used in cell phone blocking (i.e. radio wave) coatings *(35)*.

Photocatalytic, Self-Cleaning and Superhydrofilic Coatings

Photochemical activity of TiO$_2$ and other white pigments such as ZnO plays an important role in the applications of these pigments in coatings. The well known photocatalysis mechanism of TiO$_2$ is described in Chapter 10 of this book by Immoos et al. and in studies reported by Allen et al. *(73)*. Pure TiO$_2$ surface can catalyze degradation of organic compounds in the presence of UV radiation and oxygen or moisture. This phenomenon was exploited in old "chalking paints" sold for exterior decorative applications. Upon exposure to UV and moisture, the top layer of such paints would degrade and become "chalky". During a rain storm this layer would wash off with any dirt collected, thus maintaining a clean appearance. Since photocatalytic degradation is undesirable in other, more typical coatings, hiding grades of TiO$_2$ are supplied with a thin layer of silica, alumina or other surface treatment *(64,74)*. There is a great deal of interest in utilizing the photocatalytic activity of TiO$_2$ to create germicidal, and self-cleaning surfaces *(75,76)*. An early application of this phenomenon includes clear coatings for light fixtures installed in difficult to clean locations such as traffic tunnels. In order to maintain film clarity, nano-size TiO$_2$ must be used in this type of applications. Recent introduction of "self-cleaning" technology include exterior windows coated with nano titania. ZnO use as an antibacterial agent *(77)* and as a light stabilizer has been reported. A number of commercial applications of this technology for self-cleaning and anti-microbial surfaces are discussed by Immoos et al. in Chapter 10 of this book.

Quantifying the photocatlytic effect of TiO_2, ZnO and other oxides is the focus of Chapter 17 of this book by Watson et al. and the work by others *(73,78)*.

Another utility of titanium dioxide's photocatalytic activity is in preparation of anti-fogging surfaces. Application of a thin layer of nano tiatnia on a surface such as glass can make that surface highly polar in the presence of UV and a small amount of moisture. On such a glass surface trace amounts of water would spontaneously spread to form a thin layer rather than forming tiny water droplets that make the glass foggy. This phenomenon is utilized to fabricate anti-fog glass for such applications as automobile windows *(79)*.

Conductive Coatings

Controlling the electrical and magnetic conductivity of coatings is important in a number of applications including displays, solar cells, optoelectronic devices, and gas sensors. Electrostatic charge dissipation is another desirable coating property. A common approach utilized to create such coatings is to deposit a material such as indium-tin oxide (ITO) using PVD, CVD, or sol-gel techniques. In a recent study of polyester polyol, urethane diacrylate UV cure coatings, 20 nm size ITO was dispersed in butyl acetate using a series of dispersants *(80)*. Also, ball milling was employed to reduce the ITO size down to about 35 nm and achieve rather high nanoparticles loadings (10-50%). Improvements in electrical conductivity and UV absorption were demonstrated. A similar study with ITO nanoparticles dispersed with high-shear mixing in ethanol and stabilizing with poly(vinylpyrrolidone) has also been reported *(81)*.

Other Nanoparticle Materials

The utility of a wide range of commercially available nanoparticle materials in coatings were reviewed so far in this chapter. It should be noted that there are other nanoparticle materials such as $BaSo_4$, $CaCo_3$, talc, polyhedral oligomeric silsesquioxanes (POSS) that are also utilized in coatings. Chapters 3 and 6 of this book by Madbouly et al. discuss the mixing and rheological aspects of commercially available POSS in coatings.

Nano-scale carbon materials such as carbon nano-tubes (CNTs) represent another important class of nanomaterials. Since the initial synthesis of multi-wall CNTs by Iijima *(82)* in 1991, these materials have received a tremendous amount of attention *(83, 84)*. There are more than fifty companies around the world today who supply CNTs for commercial products. Although some of the applications are in coatings, much work remains to be done, especially in the area of single-walled nanotubes before more widespread applications in coatings can be realized. Graphenes, two-dimensional carbon nano-sheets, are the newest materials in this class *(85)*.

Nanostructured Coatings

Defined in the broadest sense, all of the coatings discussed in this chapter contain nano-scale structural features, and as such, they are nanostructured. However in this section, coatings prepared under controlled mechanisms to incorporate nano-scale structure will be discussed. Use of nanoparticles under controlled processing methods is an approach for fabricating electronic data storage devices and other uses. Nanoparticle size uniformity and careful control of the application shear forces are critical factors in these processes. A treatment on CVD- and PVD-based nanostructured coating preparations is available elsewhere *(86)*. Controlled nanostructure formation is the topic of several chapters of this book. See Chapter 4 (Advincula), Chapter 8 (Taylor, et al.), and Chapter 9 (Flickinger et al.). Use of polymeric templates to build ordered nanoparticle structures have been reviewed *(87)*. An interesting example of formation of ordered, one-dimensional alumina nanoparticles in a polyurethane coating is the subject of Chapter 7 by Sapper et al.

Leaves of the lotus plant (*nelumbo nucifera*) represent a fascinating example of nanostructure in nature. Barthlott and Neinhuis, two botanists, in 1975 discovered *(88)* that a dual texture in nano- and micro-scale is responsible in making the waxy, hydrophobic surface of the lotus leave superhydrophobic (i.e. the contact angle with water is greater than 150°). This superhydrophobicity makes water droplets roll on the surface, thereby cleaning dirt particles that might be collected. This phenomenon helps keep clean the lotus flowers, sacred in several Asian religions and considered a symbol of purity. Barthlott and Neinhuis called the phenomenon lotus effect, and there are many studies related to advancing its understanding and commercializing products based on it *(89-91)*. An example of preparing a synthetic nanostructured surface involves developing nano-scale roughness on polypropylene *(92,93)*. In this approach, carefully selected solvents are applied on the polypropylene substrate and dried under controlled conditions to create the nano-scale roughness. The result is a super-hydrophobic surface having a water contact angle as high as 160°. Such surfaces are attractive for a wide range of applications including antennas, self-cleaning traffic signals, etc. because of the reduced affinity to water and snow.

Challenges

The major challenges facing continued growth of nanotechnology based coatings can be divided into four main categories: 1) Dispersion, 2) Characterization, 3) Health and Safety, and 4) Material Cost. The material cost has come down in recent years with increasing number of nanoparticle suppliers, improved manufacturing methods, and increased sales volumes. Dispersion,

Characterization, and Health and Safety challenges are discussed in more detail below.

Dispersion

Nano-scale dispersion is critical for realizing the potential benefits of incorporating nanoparticles in coatings. Early attempts to commercialize nano TiO_2 *(94)* were unsuccessful because of the high degree of agglomeration of the powder and subsequent difficulties in re-dispersing the particles in coatings. A recent review of the challenge of dispersion of nanoparticles in polymeric systems *(95)* concluded that virtually all systems reviewed, regardless of the nanoparticle chemistry or the shape (spherical, rod-like, platy etc.), larger scale poorly dispersed material were present.

One approach to achieving nano-scale dispersion is to use effective grinding methods such as ball milling *(96,97)*. Effective dispersing requires grinding media that is much smaller than those used for dispersing conventional particles. The high surface area of dispersed nanoparticles can significantly increase the dispersant demand. High viscosity caused by finely dispersed nanoparticles is another problem that needs to be addressed. The large surface area can increase viscosities due to the increase in interfacial forces (e.g., electroviscous forces) and limit the amount of nanoparticles that can be incorporated. Adding the right surface functionality to address dispersibility and viscosity rise is another approach to address dispersion issue. In addition to promoting dispersion, functionlizing the particle surface enables the nanoparticle to be covalently linked to the organic resin matrix. Thermodynamic aspects of nanoparticle dispersion stabilization have been addressed in a recent study *(98)*. In the work discussed by Cook and Myers in Chapter 5 of this book, the challenge of dispersion of boehmite nanoparticles is addressed by functionalizing the particle surface with attached carboxyl groups.

Characterization

Characterization of nano-scale particle dispersion and nanostructure requires techniques that are not common in a small to mid-size coating manufacturer's research and development laboratory. Surface characterization requires techniques such as Scanning Probe Microscopy (SPM) (e.g. Atomic Force Microscopy) and Scanning Electron Microscopy (SEM). Film cross-sectional analysis requires techniques such as Transmission Electron Microscopy (TEM), SEM, X-ray and neutron scattering. These techniques have been employed in the work described throughout this book. Nano-scale characterization is the specific focus of Chapters 14-18 of this book by

18

Germinario et al., Gu et al., Watson, et al., and Williams, et al., respectively. Application of SPM to characterization has been reviewed by Greene at al. *(99)*.

Health & Safety

Although certain nanomaterials have been commercially used for many decades (e.g. colloidal silica and carbon black), commercialization of new nanomaterials has outpaced development of their safe handling methods. The awareness of the need to understand both short- and long-term effects of nanomaterials heightened in recent years. In 2006, the European Center for Ecotoxicology of Chemicals (ECETOC) published the results of a review of the potential risks of nanomaterials *(100)*. The US Environmental Protection Agency (EPA) in early 2008 launched the registry of TSCA inventory status of nanoscale substances *(101)*. An on-demand video on the topic is available at the Woodrow Wilson Center's Project on Emerging Nanotechnology website *(102)*.

References

1. ASTM Subcommittee E56.01, *"Standard Terminology Relating to Nanotechnology"*, **2008**, http://www.astm.org/Standards/E2456.htm
2. Feynman, R.P., *"There is Plenty at the Bottom: An invitation to join a new field of physics"* **1959**, http://www.zyvex.com/nanotech/feynman.html
3. Baer, D.R.; Burrows, P.E.; El-Azab, A.A., *Prog. Org. Coat.*, **2003**, 47(3-4), 342-356.
4. Chow, G.-M., Gonsalves, K.E., eds. *"Nanotechnology: Molecularly Designed Materials"*, **1998**, Oxford University Press.
5. Poole, C.P. and Owens, F.J., *"Introduction to Nanotechnology"*, **2003**, Wiley Interscience.
6. Taniguchi, N., ed. *"Nanotechnology: Integrated Processing Systems for Ultra-precision and Ultra-fine products"* **1996**, Oxford University Press.
7. Miziolek, A.W., Karna, S.P., Mauro, J.M., Vaia, R.A., *"Defense Applications of Nanomaterials"*, ACS Symposium Series, 891, **2005**, American Chemical Society.
8. Morgan, S.E., Havelka, K.O., Lochhead, R.Y., *"Cosmetic Nanotechnology: Polymers and Colloids in Personal Care"*, ACS Symposium Series, 961, **2007**, American Chemical Society.
9. Fernando, R.H., *JCT CoatingsTech*, **2004**, 1(5), 32-38.
10. Mayes, A.M., *Macromol.*, **1994**, 27, 3114.
11. Fryer, D.S.; Nealy, P.F.; and Pablo, J.J., *Macromol.*, **2000**, 33, 6439.
12. Tsui, O.K.C.; Russell, T.P., *Macromol.*, **2001**, 34, 5535.
13. Jiang, Q. and Lang, X.Y., *Macromol. Rapid Commun.*, **2004**, 25, 825.

14. Lang, X.Y.; Zhang, G. H.; Lian, J. S.; Jiang, Q., *Thin Solid Films*, **2006**, 497, 333.
15. D'Amour, J.N., Okoroanyanwu, U., Frank, C.W., *Microelectron. Eng.*, **2004**, 73-74, 209.
16. Ash, B.J., Siegel, R.W., Schadler, *J. Polym. Sci.: Part B: Polym. Phys.*, **2004**, 42, 4371.
17. Rodriguez, J.G.-I. and e. al., J. Thermal Anal. Calorimetry, 2007. **87**(1): p. 45.
18. Jin, J., Song, M., Yao, K., *Thermochim. Acta*, **2006**, 447, 202.
19. Tien, Y.I., Wei, K.H., *J. Appl. Polym. Sci.*, **2002**, 86, 1741.
20. Kontou, E. and Niaounsikis, M., *Polymer*, **2006**, 47, 1267.
21. Sargsyan, A., Tonoyan, A., Davtyan, S., Schick, C., *Eur. Polym. J.*, **2007**, 43(8), 3113-3127.
22. Hendus, H., Illers, K.H., and Ropte, E., *Kolloid-Z. Z. Polym.*, **1967**, 216-217, 110.
23. Bares, J., *Macromol.*, **1975**. 8, 244.
24. Fox, T.G., Flory, P.J., *J. Appl. Phys.*, **1950**, 21, 581.
25. Jackson, C.L., McKenna, G.B., *J. Non-Cryst. Solids*, **1991**. 131-133(Part 1), 221-224.
26. Lawton, G., *"It's a small world"*, in *Chemistry and Industry*, **2001**, March
27. Pinnavaia, T.J., Beall, G.W., eds. *"Polymer-Clay Nanocomposites"*, **2001**, Wiley Interscience
28. Gao, F., *Mater. Today*, **2004**, 7(11), 50-55.
29. Anonymous, *"Auto applications drive commercialization of nanocomposites"*, in *Plastic Additives & Compounding*, **2002**, 30-33.
30. Fernando, R.H. and Bohrn, W.J., **1992**, US Patent #5,124,202
31. Decker, C., Keller, L., Zahouily, K., Benfarhi, S., *Polymer*, **2005**, 46(17), 6640-6648.
32. Zaarei, D., Sarabi, A.A., Sharif, F., Kassiriha, S.M., *J. Coat. Technol. Res.*, **2008**, 5(2), 241-249.
33. Tiarks, F., Landfester, K., Antonietti, M., *Langmuir*, **2001**, 17(19), 5775-5780.
34. He, Q., Wu, L., Gu, G., You, B., *High Perform. Polym.*, **2002**, 14(4), 383-396.
35. *Nanotechnology Product Directory*, www.nanoshop.com
36. Negrete-Herrera, N., Putaux, J., David, L., Bourgeat-Lami, E., *Macromol.*, **2006**, 39(26), 9177-9184.
37. Noh, M.H., Jang, L.W. Lee, D.C., *J. Appl. Polym. Sci.*, **1999**, 74(1), 179-188.
38. Greenwood, P., *JCT CoatingsTech.* **2008**, February, 44-51.
39. Brinker, C.J., Scherer, G.W, *"Sol-Gel Science"*, **1990**, Academic Press.
40. Glotfelter, C.A., Ryan, R.P., **1992**, US Patent #5,102,811
41. Schmidt, H. and Mennig, M., in *The Sol-Gel Gateway*, http://www.solgel.com/articles/Nov00/mennig.htm

42. Du, Y.J., et al., *Prog. Org. Coat.*, **2001**, 41(4), 226-232.
43. Vreugdenhil, A.J., Balbyshev, V.N., Donley, M.S., *J. Coat. Technol.*, **2001**, 73(915), 35-43.
44. Dworak, D.P., Soucek, M.D., *Prog. Org. Coat.*, **2003**, 47(3-4), 448-457.
45. Pirhady Tavandashti, N., S. Sanjabi, and T. Shahrabi, *Prog. Org. Coat.,*. **In Press, Corrected Proof.**
46. Wang, D., Bierwagen, G.P., *Prog. Org. Coat.*, **In Press, Corrected Proof.**
47. Apohan, N., Karataş, S., Bilen, B., Güngör, A., J. Sol-Gel Sci. Technol., **2008**, 46(1), 87-97.
48. Clarke, H.A., **1976**, US Patent #3,986,997
49. Olson, D.R., **1983**, US Patent #4,410,594
50. Adebahr, T., Roscher, C., Adam, J., *Eur. Coat. J.*, **2001**, 4, 144-147.
51. Lewis, L.N., Katsamberis, D., *J. Appl. Polym. Sci.*, **1991**, 42, 1551.
52. Vu, C., La Ferte, O., Eranian, A., *Proceedings of RadTech Europe 2005 Conference,* **2005**.
53. Bauer, F., et al., Prog. Org. Coat., **2007**, 60(2), 121-126.
54. Vanier, N.R., Munro, C. H., Clarr, J. A., Jennings, R. E., 2005, US Patent #6,916,368 B2
55. Vanier, N.R., et al. **2004**, US Patent #6,770,705 B2
56. Ramsey, S.J.W., **2007**, US Patent #7,238,731 B2
57. Amerio, E., et al., *Prog. Org. Coat.*, **2008**, 62(2), 129-133.
58. Vanier, N.R., Munro, C.H., **2007**, US Patent #7,720,793 B2
59. Sung, L.-P., et al., J. Coat. Technol. Res., **2008**, 5(4), 419-430.
60. J. Lange, Wyser, Y., *Packag. Technol. Sci.*, **2003**. 16(4), 149-158.
61. Sherman, L.M., in *Plastics Technology*, **2007**, May
62. Harrison, A.G., Meredith, W.N.E., Higgins, D.E., **1996**, US Patent #5,571,614
63. Singh, B., *"Hybrid nanocomposite gas-barrier coatings on polymers"*, **2007**, PhD Thesis, Ecole Polytechnique Federale de Lausanne: Lausanne, Switzerland.
64. Diebold, M., *JCT CoatingsTech*, **2004**, 1(1), 36-44.
65. Allen, N.S., et al., *Polym. Degrad. Stab.*, **2002**, 78, 467-478.
66. van den Bosch, J., Verbiest, P., *Proceedings of Nanotechnology in Coatings: Emerging Applications Conference*, FSCT, **2008**. Orlando, Florida, USA.
67. Sawitoski, T., *Proceedings of Nanotechnology in Coatings: Emerging Applications Conference*, FSCT, **2008**. Orlando, Florida, USA.
68. Hwang, D.K., et al., *J. Sol-Gel Sci. Technol.*, **2003**, 26, 783-787.
69. Grosse, P., Hertling, R., Müggenburg, T., *J. Non-Cryst. Solids*, **1997**, 218, 38-43.
70. Mohelnikova, J., Construct. Build. Mater. **In Press, Corrected Proof.**
71. Shan, Y., et al., *Mater. Lett.*, **2004**, 58(10), 1655-1660.
72. Chen, J., et al., *Appl. Surf. Sci.*, **2007**, 253(23), 9154-9158.
73. Allen, N.S., et al., *Polym. Degrad. Stab.*, **2004**, 85(3), 927-946.

74. Diebold, M.P., Bettler, C.R., Mukoda, D.M., *J. Coat. Technol.*, **2003**, 75(942), 29-36.
75. Jang, H.D., Kim, S.-K., Kim, S.-J., *J. Nanopart. Res.*, **2001**, 3(2-3), 141-147.
76. Fujishima, A., Rao, T.N., Tryk,D.A., *Electrochim. Acta*, **2000**, 45(28), 4683-4690.
77. Ammala, A., et al., *J. Nanopart. Res.*, **2002**, 4(1-2), 167-174.
78. Diebold, M., Kwoka, R., Mehr, S., Vargas, R., *J. Coat. Technol. Res.*, **2004**, 1(3), 239-241.
79. Watanabe, T., et al., *Thin Solid Films*, **1999**, 351(1-2), 260-263.
80. Yin, Y., Zhou, S., Gu, G., Wu, L., *J. Mater. Sci.*, **2007**, 42, 5959-63.
81. Carotenuto, G., et al., *J. Mater. Sci.*, **2006**, 41, 5587-92.
82. Iijima, S., *Nature*, **1991**, 354, 56-58.
83. Harris, P.J.F., *Int. Mater. Rev.*, **2004**, 49(1), 31-43.
84. Bredeau, S., et al., *Polym. Int.*, **2008**, 57(4), 547-553.
85. Ruoff, R., *Nat. Nanotechnol.*, **2008**, 3(January), 10-11.
86. Cavaleiro, A., De Hosson, J.T. eds. *"Nanostructured Coatings"*, **2006**, Springer.
87. Arumugam, P., Xu, H., Srivastava, S., Rotello, M., *Polym. Int.*, **2007**, 56, 461-466.
88. Barthlott, W., Neinhius, C., *Planta*, **1997**, 202, 1-8.
89. Dodiuk, H., Rios, P.F., Dotan, A., Kenig, S., *Polym. Adv. Technol.*, **2007**, 18(9), 746-750.
90. Larmour, I. A., Bell, S.E.J., Saunders, G.C., *Angew. Chem. Int. Ed.*, **2007**, 46(10), 1710-1712.
91. Feng, L., et al., *Adv. Mater.*, **2002**, 14(24), 1857-1860.
92. Erbil, H.Y., Demerel, A.L., Avci, Y., Mert, O., *Science*, **2003**, 299(56), 1377-1380.
93. Shang, H.M., et al., *J. Mater. Sci.*, **2005**, 40, 3587-3591.
94. Balfour, J.G., *J. Oil Colour Chem. Assoc.*, **1992**, 75(1), 21-23.
95. Schaefer, D.W., Justice, R.S., *Macromol.*, **2007**, 40(24), 8501-8517.
96. Baer, D.R., Burrows, P.E., El-Azab, A.A., *Prog. Org. Coat.*, **2003**. 47, 342-356.
97. Mende, S., Kolb, G., Udo, E., in *Ceramic Industry*. **2006**, 18-20.
98. Mackay, M.E., et al., *Science*, **2006**, 311(5768), 1740-1743.
99. Greene, M.E., et al., *Microsc. Res. Tech.*, **2004**, 64(5-6), 415-434.
100. Borm, P., et al., *Part. Fibre Toxicol.*, **2006**, 3(1), 11.
101. *"TSCA Inventory Status of Nanoscale Substances - General Approach"*, **2008**, US Environmental Protection Agency, http://www.epa.gov/oppt/nano/nmsp-inventorypaper.pdf
102. *"Nanotechnology: A Progress Report on Understanding Occupational Safety and Health Issues"* **2007**, Woodrow Wilson Center, http://www.wilsoncenter.org/index.cfm?topic_id=166192&fuseaction=topics.event_summary&event_id=224735#

Chapter 2

Encapsulation of Clay Platelets inside Latex Particles

D. J. Voorn[1-3], W. Ming[2,4,*], and A. M. van Herk[1,*]

Laboratories of [1]Polymer Chemistry and [2]Materials and Interface
Chemistry, Eindhoven University of Technology, P.O. Box 513, 5600 MB
Eindhoven, The Netherlands
[3]Dutch Polymer Institute (DPI), P.O. Box 902, 5600 AX Eindhoven,
The Netherlands
[4]Nanostructured Polymers Research Center, Materials Science Program,
University of New Hampshire, Durham, NH 03824

We present our recent attempts in encapsulating clay platelets
inside latex particles by emulsion polymerization. Face
modification of clay platelets by cationic exchange has been
shown to be insufficient for clay encapsulation, leading to
armored latex particles. Successful encapsulation of covalently
edge-modified clay platelets was achieved via surfactant-free,
starved-feed emulsion polymerization. With cryo-TEM and
SEM we showed that small Laponite platelets were
encapsulated inside spherical latex particles, whereas larger
montmorillonite platelets were encapsulated inside dumbbell-
like or snowman-like non-spherical latex particles. Covalent
bonding of polymerizable groups to the clay platelets proves
to be essential for the successful clay encapsulation.

24   © 2009 American Chemical Society

Introduction

There has been increasing interest for encapsulation of fine inorganic powders with organic molecules or polymers to afford various desired physical properties including mechanical and barrier properties. Inorganic platelets such as layered silicates have been extensively investigated as polymer-clay nanocomposites over the past decade (*1*). To make clay organophilic and compatible with polymers, one often employed strategy is to modify inorganic clay by replacing stabilizing alkali with organic cations (*2*). Emulsion polymerization in the presence of clays was employed to prepare polymer/clay hybrid particles, (*3-5*) but only armored particles (clay being located at the particle surface) were obtained. Encapsulation of clays by polymer may render better dispersability and orientation of clay platelets in a polymer matrix, and has appeared to be very challenging and not straightforward. We previously reported a physical approach, heterocoagulation (*6a,b*), to encapsulate synthetic gibbsite (much thicker than individual clay) platelets by polymer (*6c*).

Here we report our recent attempts on the encapsulation of clay platelets, which have been physically and/or chemically modified, inside polymer latex particles via emulsion polymerization. Two approaches are employed to modify clay platelets: (1) physical face modification using cationic exchange of functional groups at the clay surface; and (2) chemical edge modification using coupling agents such as titanates or silanes. A schematic representation of the clay platelet modification is depicted in Figure 1. The face modification uses the
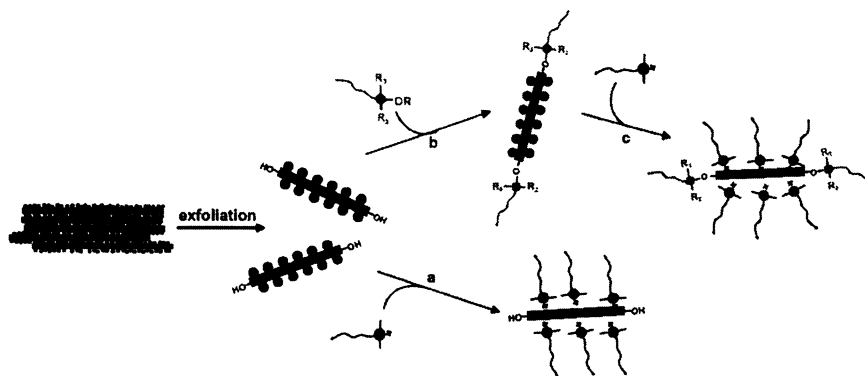
Figure 1. Modification scheme of clay platelets by: (a) cationic exchange of Na⁺ by quaternary ammonium cations at the face of the clay platelets; (b) covalent edge modification of OH-groups using silanes or titanates, and subsequently the covalently modified platelets can also undergo cationic exchanges with quaternary ammonium cations (c), leading to dual-functionalized clay platelets.

exchange of clay cations in an exfoliated clay dispersion with different reactive cations (initiator and monomers). The edge modification of clay platelets with different silanes and titanates was performed in water or aprotic solvents, resulting in covalently modified clay platelets. A combination of face and edge modification of clay was also performed, leading to dual-functionalized clay particles. Emulsion polymerizations in the presence of these face-, edge- and dual-functionalized clay platelets have been investigated.

Experimental Materials

Materials

Laponite RD (LRD) and Cloisite Na^+ (MMT) were received from Districhem B.V. and Southern Clay Products Inc., respectively. Methyl methacrylate (MMA, 99%, Aldrich) was purified by distillation under reduced pressure and stored in a freezer prior to use. A cationic monomer, methacrylatoethyl trimethyl ammonium chloride (MATMAC) was received from Degussa. Water-soluble initiators, 2,2'-azobis (2-methylpropionamide) dihydrochloride (V-50) [recrystallized from water-acetone (50/50 w/w)] and 2,2'-azobis[2-methyl-N-(2-hydroxyethyl) propionamide] (VA-086, 99%) were kindly provided by Wako Chemicals GmbH. Titanium IV, tris(2-propenoato), 2-(2-methoxy-ethoxy)ethanolato (Ken-React® KR39DS) and 3-methacryloxy-propyl trimethoxysilane (MPS, >98%, ABCR) were used as received.

Face Modification of Clay Platelets

Face modification of clay was performed by exchanging the stabilizing cations with either a cationic initiator (V-50) or a cationic monomer (MATMAC). For V-50-modified LRD platelets, at V-50 concentrations up to 1.7 times the CEC, the total weight loss from thermogravimetric analysis (TGA) was 19.7 wt% (data obtained after three centrifugation cycles to remove any excess of organic modifier), indicating a significant amount of cationic initiator has been incorporated into the clay galleries.

Covalent Modification of Clay Platelets

Covalent modifications of LRD and MMT were performed in dichloromethane with silane or titanate. A typical modification procedure is

described as follows. An amount of 2 g of clay was dispersed in 100 mL of dichloromethane and ultrasonically mixed for 10 min. To the clay dispersion 3 g of KR39DS was introduced at a constant feed of 0.1 mL/min. The reaction temperature was kept constant at 45 °C under continuous mixing for 3 days. The modified clay platelets were collected via vacuum filtration on a Buchner funnel and washed with 300 mL of dichloromethane. The solid clay was redispersed and the procedure was repeated twice to remove the excess modifier followed by vacuum drying for 20 h at 80 °C. The modified clay platelets were then dispersed in water by ultrasonification.

Encapsulation via Emulsion Polymerization

Hybrid latexes were synthesized by starved-feed, surfactant-free emulsion polymerization (for recipes containing covalently modified clay platelets, see Table 1). A typical polymerization procedure is described as follows. A 100 mL 3-neck flask was charged with 55 mL of doubly deionized water. About 0.25 g of modified clay platelets was added and ultrasonically dispersed (10 min). Then, the system was flushed with argon for 30 min under continuous stirring using a magnetic stirrer bar at 800 rpm. The reactor was heated to 50 ± 1 °C with an oil bath, followed by the addition of 0.1 g of initiator (VA-086). After 5 min, 4.5 mL of MMA was added at a rate of 0.01 mL/min using a Metrohm Dosimat 776 autotitrator. Upon completion of the addition, the reactor was kept at 50 °C for another 2 h to ensure complete conversion of MMA.

Characterization

Particle size and particle size distribution were determined by dynamic light scattering (DLS) on a Malvern 4700 light scattering instrument at 23 °C. Cryo-TEM samples were prepared using a vitrification robot (Vitrobot). A 3-μL drop of the dispersion was placed on a carbon coated lacy substrate supported by a TEM 300 mesh copper grid (Quantifoil R2/2). Excess of sample was removed by automatic blotting with filter paper. Afterwards, the grid was rapidly plunged into liquid ethane at its melting temperature, resulting in a vitrified film. The vitrified specimen was then transferred into the electron microscope, Tecnai G^2 Sphera (FEI), operating at 200 kV. The working temperature was kept below -170 °C. Morphological investigations of latex particles were also performed using an environmental scanning electron microscope (ESEM) XL30 ESEM-FEG (FEI), operated in low-voltage mode. Thermogravimetric analysis (TGA) was performed with a PerkinElmer Pyris 6 apparatus under nitrogen at a flow rate of 25 cm^3/min. A scanning rate of 10 °C/min was used.

Results and Discussion

Attempts to encapsulate face-modified clay platelets

Emulsion polymerizations of MMA in the presence of unmodified clay platelets did not result in encapsulation of the clay platelets by latex particles (*4*). Starved-feed emulsion polymerizations of MMA in the presence of cationically exchanged, face-modified clay platelets and a nonionic surfactant (Emulan® NP3070 from BASF) were performed. In the presence of V-50-modified platelets (no extra initiator was added), latex particles were obtained with an average size of 67 nm and a PDI of 0.22, but from the cryo-TEM observation it is obvious that the latex particles were covered by LRD platelets (Figure 2a). A surfactant-free MMA polymerization in the presence of V-50-modified LRD platelets led to latex particles with an average diameter of 236 nm; however, armored particles appeared to be formed again.

(a) (b)
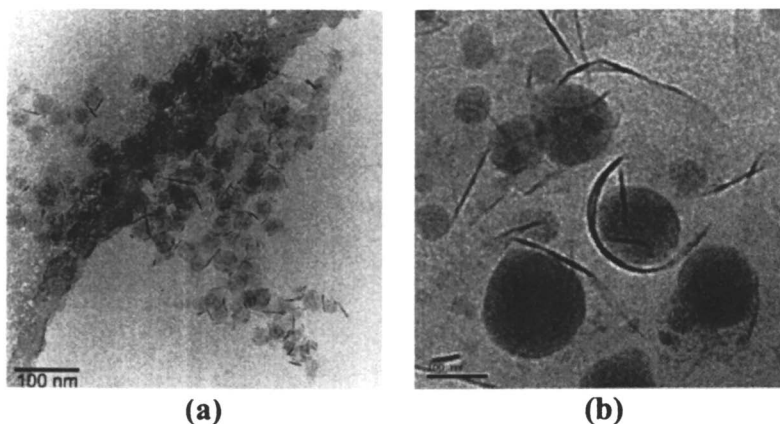
Figure 2. Cryo-TEM micrographs of PMMA latexes in the presence of cationically modified clay platelets: (a) LRD modified by V-50; (b) MMT modified by MATMAC.

MMA emulsion polymerization was also performed in the presence of clay (LRD and MMT) platelets modified by cationic monomers. MMA was starve-fed to the reaction medium to allow the chain growth from the clay surface (polymerizable moiety from MATMAC). However, to our disappointment, no evidence of clay encapsulation was observed. Figure 2b shows a typical cryo-TEM image of PMMA latex particles with surface covered by MATMAC-modified MMT. Even the bending of the MMT platelet was observed.

It has been shown that the encapsulation of clay platelets that are face-modified with either cationic initiator or cationic monomer was unsuccessful. This is likely due to the relocation of the polymer chain during the polymerization, even though the polymer chain might have grown from the clay surface. The polymer relocation would allow the clay platelet (which is intrinsically hydrophilic) to migrate to the surface of the latex particles, resulting in the observed armored particles. The polymer relocation may be attributed to the fact that the electrostatic interaction between the cationic groups of a polymer chain (from either the initiator or the monomer) and the clay surface is not strong enough to prevent the clay migration.

Encapsulation of Covalently Edge-Modified Clay Platelets

Covalent clay modification

Clay platelets, including LRD ($D = \sim 25$ nm) and MMT ($D = \sim 150$ nm, large particles were removed by centrifugation), were covalently modified in dichloromethane by using silane or titanate containing polymerizable (meth)acrylic moiety, which led primarily to edge modification of the platelets (7). Both silane and titanate modification led to slightly turbid dispersions for both MMT and LRD with particle size slightly larger than the unmodified clay platelets. For the silane modification, it was shown from thermogravimetric analysis (Figure 3) that about 4.9 and 8.1 wt% of silane was grafted to MMT (MMT-Si) and LDR (LDR-Si), respectively, in agreement with values reported in literature (5,7a). The titanate modification yielded about 6.9 and 11.3 wt% increase for MMT (MMT-Ti) and LRD (LRD-Ti), respectively. After drying, the modified platelets could be well dispersed in water (Figure 4 shows a TEM image of LRD-Si aqueous dispersion), but the dispersions were more turbid than the unmodified clay dispersions, likely due to the edge hydrophobization of clay platelets.

Encapsulation of Covalently Modified Clay Platelets Inside Latex Particles

Batch emulsion polymerizations in the presence of covalently modified platelets and surfactants were attempted by Herrera et al. (5) but the platelets were observed to cover the latex particles. In this study, covalently modified clay platelets were successfully encapsulated inside latex particles via **surfactant-free, starved-feed** emulsion polymerization (10). Table 1 lists the polymerization recipes and some characteristics of clay-encapsulated PMMA latex particles.

Figure 5b shows the unique, dumbbell-like shape of a PMMA/MMT-Ti hybrid latex particle (Entry DV05). The black line in Figure 5b corresponds to a
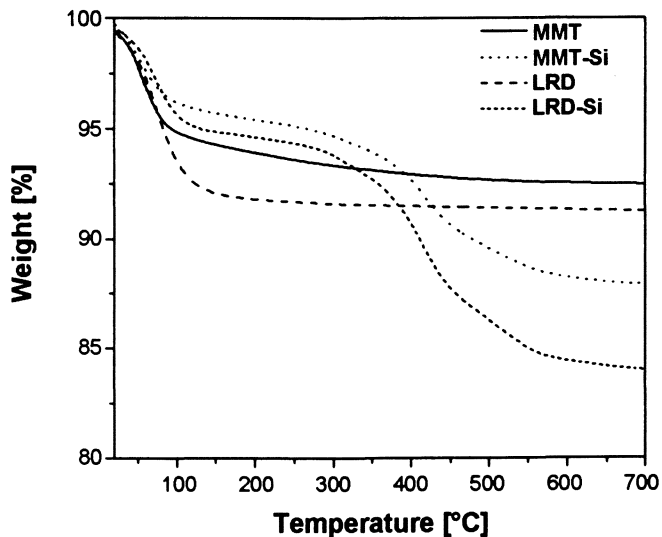
*Figure 3. Thermogravimetric analysis of unmodified MMT and LRD,
and silane-modified MMT-Si and LRD-Si.*
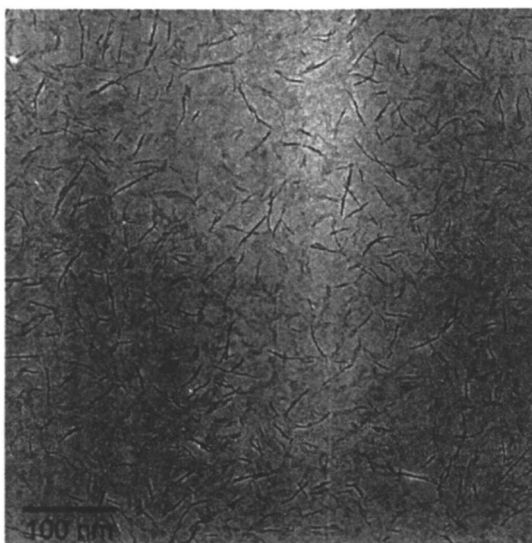
Figure 4. Cryo-TEM micrograph of LRD-Si platelets dispersed in water.

Table 1. Recipes for Emulsion Polymerizations in the Presence of Covalently Modified Clay and Characteristics of Clay-Encapsulated Latex Particles[a]

Entry	Modified clay		MMA	D_n[c]	D_z[d]	PDI[d]
	type	v/v%[b]	[wt%]	[nm]	[nm]	
DV01	LRD-Ti	2.3	7.08	67 ± 15	96.2	0.18
DV02	LRD-Si	2.3	6.89	59 ± 14	93.7	0.21
DV05	MMT-Ti	1.9	7.04	285 ± 87	351	0.32
DV06	MMT-Si	2.0	6.98	327 ± 69	298	0.27

[a] The VA-086 concentration was 0.15 wt% for all polymerizations. [b]Clay volume content based on monomer; [c]Particle sizes determined by TEM; the longest length was measured in the case of non-spherical particles; [d]Z-average particle diameter and polydispersity index (PDI) obtained by DLS measurements.

MMT-Ti platelet with its basal plane orientated parallel to the electron beam. The dumbbell-like shape is due to the presence of a clay platelet (about 130 nm in length) inside. The unique dumbbell-like shape of the latex particles cannot be obtained via emulsion homopolymerizations *in one step* (8); batch emulsion polymerization in the presence of unmodified (4) or covalently modified (5) clays led to latex particles with surface covered by clays. The starved-feed, surfactant-free emulsion polymerization conditions, combined with covalent clay modification, appear to be the key to obtaining clay encapsulation. During the starved-feed, surfactant-free emulsion polymerization, the PMMA chain would likely start growing from the methacrylic moiety at the edge of modified MMT, and then grow along both sides of the platelet. When the clay platelet is large enough, like in the case of MMT-Ti, the presence of the platelet would prevent the uniform growth of the latex particle, resulting in non-spherical particles. For the much smaller LRD-Ti, the effect of the platelet on the particle growth appeared to be less significant, leading to spherical particles (Figure 5a). In both cases, complete encapsulation of clay platelets in latex particles was successfully obtained.

It was found from cryo-TEM analysis that not all non-spherical particles "appeared" to contain clay platelets inside. To clarify the presence of the clay platelets inside latex particles, micrographs at several tilt angles of the cryo-stage between -45° and +45° were obtained. The MMT-Ti platelet, clearly visible in Figure 5b, appeared to "disappear" completely at a tilt angle of -25°. The tilting of the stage made the basal plane orientation of MMT-Ti more perpendicular to the electron beam and reduced the diffraction contrast of the platelet, effectively making it invisible. We checked a number of dumbbell-like particles in the tilt angle range from -45° and +45°; the "sticking-out" of the platelet from the
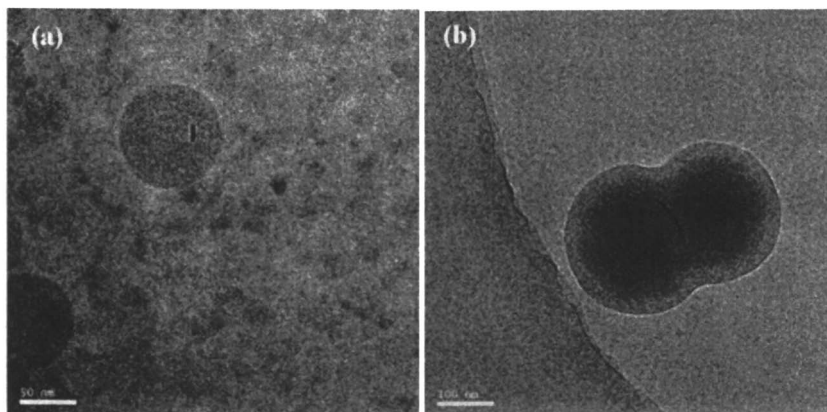
Figure 5. Cryo-TEM micrographs of PMMA latex particles by emulsion polymerization containing (a) LRD-Ti and (b) MMT-Ti. (Reproduced from reference 10. Copyright 2006 American Chemical Society.)

particle surface was never observed. The dumbbell-like or snowman-like shape of the latex particles, irrespective of the "visibility" of clay inside the particle by TEM, further corroborates the encapsulation of clay platelets insides latex particles.

ESEM analysis of latex particles provides additional information on the location of the clay platelets. At first glance, Figure 6 shows "normal" spherical particles with a minor portion of non-spherical latex particles. However, a close examination of the micrograph reveals that more than 50% of the particles depicted in Figure 6 are dumbbell-like/snowman-like in shape, or at least non-spherical. The surface of the latex particles is perfectly smooth, which differs with the rugged surface observed for clay-covered particles (4,9). This confirms that the clay platelets are completely encapsulated inside the latex particles.

MMT-Si platelets were also successfully encapsulated inside snowman-like PMMA latex particles, and it was possible to obtain latex particles with more than one clay platelet inside.

Encapsulation of Dual-Functionalized Clay Platelets

We also adopted a dual functionalization strategy (11) to modify clay platelets, in hope for better control of clay encapsulation. Our dual functionalization procedure started with covalently modified clays (LRD-Si and MMT-Si), followed by the cationic exchange with a hydrophilic quaternary ammonium containing a polymerizable group (PEO-V$^+$, Figure 7). Excess PEO-V$^+$ was removed by centrifugation of the modified platelets.
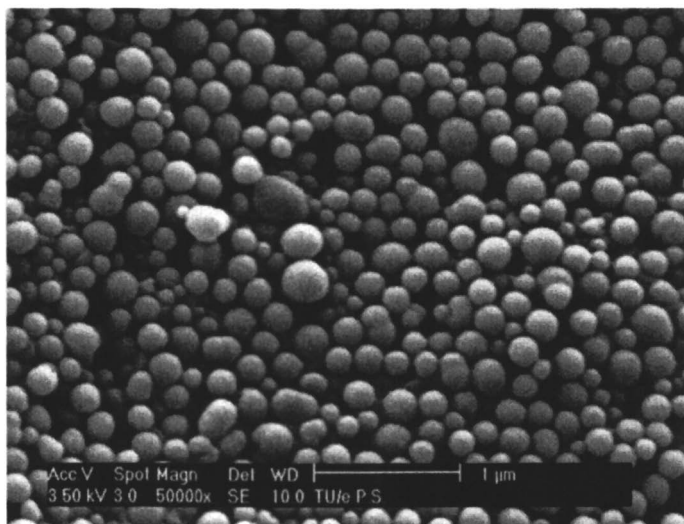
Figure 6. ESEM image of MMT-Ti-encapsulated PMMA latex particles (DV05).

Starved-feed emulsion polymerizations of MMA were performed in the presence of the dual-functionalized clay. For dual-functionalized LRD platelets, it appears from cryo-TEM analyses that the PEO-V$^+$ modification had no significant influence on the encapsulation for LRD platelets, as compared to the case of edge covalent modification only (3.2.2). In some cases, partial encapsulation (part of the clay sticking out of the latex particle; image not shown) was observed. But a more drastic change in the encapsulation behavior was observed for the dual-functionalized MMT platelets: although non-spherical particles (which contain encapsulated clay, as discussed in 3.2.2) were observed, a large amount of MMT platelets appeared to be located at the particle surface, even bending around the latex spheres. The PEO-V$^+$ modification of the MMT platelets did not show additional advantageous effect on the clay encapsulation via emulsion polymerization. Although the MMA polymerization with the edge-modified platelets will produce chemically bonded polymer, the presence of PEO-V$^+$ molecules would enhance the possibility of the clays to be present at the water/particle interface, instead of being encapsulated by less polar polymers. Copolymerization with PEO-V$^+$ increased the hydrophilicity of the polymer, and the PEO-V$^+$ may even behave as a polymerizable surfactant, giving the latex increased stability.

A hydrophobic cation, hexadecyltrimethylammonium bromide (CTAB) was also used for dual functionalization. However, starved-feed emulsion polymerizations in the presence of these hydrophobic platelets did not produce (single) platelet-encapsulated latex particles, and only large aggregates with a
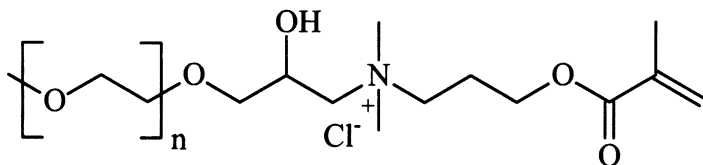
Figure 7. Chemical structure of PEO-V⁺, a hydrophilic quaternary ammonium containing a polymerizable group.

diameter > 1 µm were formed. A different route was also explored by first dispersing the hydrophobic clay platelets in MMA, followed by emulsion polymerization. The dispersion showed significant sedimentation, indicating the incomplete exfoliation of both platelets. The subsequent batch and starved-feed emulsion polymerizations were not successful.

In summary, the dual functionalization did not prove to be a successful extension to the covalent edge modification of clay platelets for the encapsulation purpose. Emulsion polymerizations in the presence of dual-functionalized LRD platelets resulted in clay encapsulation, but did not show any improvement. For larger MMT platelets, the dual functionalization even seemed to be counter productive.

Conclusions

In conclusion, we have demonstrated the encapsulation of covalently modified clay platelets inside latex particles via surfactant-free, starved-feed emulsion polymerization. With cryo-TEM and SEM we showed that small LRD-platelets were encapsulated inside spherical latex particles, whereas larger MMT-platelets were encapsulated inside dumbbell-like or snowman-like non-spherical latex particles. Covalent bonding of polymerizable groups to the clay platelets proves to be essential for the successful clay encapsulation.

Acknowledgements

References

1. (a) Giannelis, E. P. *Adv. Mater.* **1996**, *8*, 29. (b) Usuki, A.; Hasegawa, N.; Kato, M. *Adv. Polym. Sci.* **2005**, *179*, 138. (c) Pinnavaia, T. J.; Beall, G. W.; Eds. Polymer-Clay Nanocomposites; Wiley: Chichester, 2000.
2. (a) Huang, X.; Brittain, W. J. *Macromolecules* **2001**, *34*, 3255. (b) Beyer, F. L.; Tan, N. C. B.; Dasgupta, A.; Galvin, M. E. *Chem. Mater.* **2002**, *14*, 2983.
3. zu Putlitz, B.; Landfester, K.; Fischer, H.; Antonietti, M. *Adv. Mater.* **2001**, *13*, 500.
4. Cauvin, S.; Colver, P. J.; Bon, S. A. F. *Macromolecules* **2005**, *38*, 7887.
5. Herrera, N. N.; Letoffe, J. M.; Putaux, J. L.; David, L.; Bourgeat-Lami, E. *Langmuir* **2004**, *20*, 1564.
6. (a) Xu, Y.; Brittain, W. J.; Xue, C.; Eby, R. K. *Polymer* **2004**, *45*, 3735-3746. (b) Ji, Y.-Q.; Black, L.; Weidler, P. G.; Janek, M. *Langmuir* **2004**, *20*, 9796-9806. (c) Voorn, D. J.; Ming, W.; van Herk, A. M.; Bomans, P. H. H.; Frederik, P. M.; Gasemjite, P.; Johannsmann, D. *Langmuir* **2005**, *21*, 6950.
7. (a) Wheeler, P. A.; Wang, J.; Baker, J.; Mathias, L. J. *Chem. Mater.* **2005**, *17*, 3012. (b) Carrado, K. A.; Xu, L.; Csencsits, R.; Muntean, J. V. *Chem. Mater.* **2001**, *13*, 3766.
8. Gilbert, R. G. *Emulsion Polymerization: A Mechanistic Approach*; Academic Press: New York, 1995.
9. Voorn, D. J.; Ming, W.; van Herk, A. M. *Macromolecules* **2006**, *39*, 2137.
10. Voorn, D. J.; Ming, W.; van Herk, A. M. *Macromolecules* **2006**, *39*, 4654.
11. (a) Wheeler, P. A.; Wang, J.; Mathias, L. J. *Polym. Mater. Sci. Eng.* **2006**, *94*, 55. (b) Wang, J.; Wheeler, P. A.; Mathias, L. J. *Polym. Mater. Sci. Eng.* **2006**, *94*, 284.

Chapter 3

Polyurethane–Polyhedral Oligomeric Silsesquioxanes Nanostructured Hybrid Dispersions by the Prepolymer Mixing Process

Samy A. Madbouly, Joshua U. Otaigbe, Ajaya K. Nanda, and Douglas A. Wicks*

School of Polymers and High Performance Materials, The University of Southern Mississippi, Hattiesburg, MS 39406

Waterborne nanostructured polyurethane with reactive polyhedral oligomeric silsesquioxanes (POSS) hybrid dispersions were synthesized via environmentally-friendly aqueous dispersion through the prepolymer mixing process. To improve the distribution of the POSS monomer in the polyurethane aminoethylaminopropylisobutyl polyhedral oligomeric silsesquioxane was first prereacted with excess isophorone diisocyanate in N-methylpyrrolidone. After this reaction the process was continued by reaction with poly(hexylene adipate - isophthalate) diol, dimethylol propionic acid, and hexamethylene diamine. Dispersion of the polymer was accomplished with triethyl amine as the neutralizing base. The particle size and viscosity of the dispersions were not affected by POSS loading. The resulting polyurethane dispersions did show evidence of some phase inhomogeneity as evidenced by wide angle X-ray diffraction patterns of cast films. Although the incorporation of the POSS monomers did not have a significant effect on the dispersion's properties; the physical properties of the isolated polymers films did display significant changes, with notable increases in storage modulus, T_g, and complex viscosity. POSS was found to react strongly with only the hard segments of PU (urethane segments), while the soft segment was not affected by the presence of POSS. This experimental fact was confirmed by the increase in the T_g of the hard segments with increasing concentration of POSS as measured by DMA.

36

Polyhedral oligomeric silsesquioxane or POSS are materials with general chemical formula $(RSiO_{1.5})n$ where R is hydrogen or an organic group (alkyl, aryl or any of their derivatives), and are characterized by a size in the range 1–3 nm and by high chemical versatility and capability to form nanostructures with tailored dimensionality (*1*). These nanoscale compounds (POSS) are attracting increased attention in nanostructured organic–inorganic hybrid materials (*1–5*). The dispersion of POSS nanoparticles in polymeric matrices, such as, polyacrylates, polyesters, polyimides, polystyrene and its copolymers allows to obtain advanced composite materials. The incorporation of POSS into polymeric materials often results in dramatic improvements in polymeric properties which include, but are not limited to in use temperature, oxidation resistance, surface hardening, and improved mechanical properties as well as reduction in flammability and heat evolution (*6-16*) .

The compatibility of POSS with polymeric materials is expected to be markedly enhanced due to the possibility of modifying the chemical/physical interactions at polymer-filler interface through introduction of functional groups on the POSS molecules. The organic substituents attached to each cage Si atom can improve compatibility with the polymer matrix. Polymerizable substituents on the cages allow the formation of copolymers where POSS becomes part of the polymer chemical structure (*17,18*). Generally POSS can be incorporated into polymer matrix by two different methods: mechanically melt blending as nano-filler particles or chemically by introducing one or more functional groups to the corner of the POSS chemical structure. This functional group can react chemically (via covalent bonds) with the polymer matrix to produce polymer-graft-POSS composite with improved mechanical properties and higher thermal stability which is determined by POSS/POSS and POSS/polymer interactions (*19*).

In recent years, significant emphasis has been placed on the use of waterborne coating systems such as polyurethane dispersions (PUD) due to their health and environmental safety (*20-26*). Design and control of these systems has been traditionally undertaken by trial and error methods due to their inherent complexity. These environmentally friendly products are used to reduce the VOC (volatile organic compounds) released into the atmosphere by solventborne systems and are expected to exhibit the same performance as that of conventional solventborne systems. Typically a waterborne PUD is formed by preparing an isocyanate-terminated prepolymer and a modifying polyol is used to incorporate carboxylic functionality in the prepolymer backbone. The prepolymer is then dispersed in water using a tertiary amine to produce ionic centers thus stabilizing the polymer particle. The resulting chemical species is then chain-extended using a polyamine as described later (*26*). Polyurethane dispersions can be tailored to various applications by varying the preparation method and chemical structures of the polyurethane. Waterborne PUD dispersions are widely used in the coatings and adhesives applications because

of their excellent performance, demands of environmental regulations, abetment costs and safety (27-29). In recent years, there has been a growing interest on the preparation of PU-POSS hybrids to enhance the thermal, mechanical and surface properties of the final polymers. Turi and Levi recently reported on the preparation of PU dispersions incorporating a diol functionalized POSS into the prepolymer reaction before the dispersion step (30). In their work, it was found that the thermal and mechanical properties of PU-POSS hybrid films did not improve compared to the unmodified control. X Ray analysis of the films revealed that much of the crystalline structure of the starting POSS diol was maintained.

Recently, we have prepared PU-POSS hybrid dispersion using the acetone process. A homogenous dispersion with functionalized diamino-POSS has been obtained by modifying the method of addition (31). Films prepared from these acetone process dispersions showed a large change in thermal, mechanical, rheological and surface properties resulting from the POSS incorporation compared to unmodified control. In our preparation method, POSS was reacted initially with isophorone diisocyanate (IPDI) and the homogeneity of POSS in PU matrix was observed by WAXD and gel permeation chromatography (GPC).

Beyond the base chemical compositions, there are several differences in the 2 methods used to get the hybrids discussed above that could lead to the contrary results obtained. First it could be the differences between the prepolymer and acetone process or secondly it could arise from the order of addition. In the work by Turi and Levi (30) the functional POSS was added towards the end of the prepolymer formation, while in our previous work the POSS monomer was prereacted with the diisocyanate. This current work tries to address the impact of process on POSS hybrids prepared by the prepolymer mixing process.

Experimentals

Materials

Poly(hexylene adipate-isophthalate) diol having OH# 55 and max acid #2 (Desmophen 1019-55), and isophorone diisocyanate (Desmodur-I) (IPDI) were supplied by Bayer MaterialScience. Dimethylolpropionic acid (DMPA), dibutyltin dilaurate (DBTDL), triethylamine (TEA), hexamethylene diamine (HDA) and N-methylpyrrolidone (NMP) were purchased from Aldrich Chemical Co. Aminoethylaminopropylisobutyl polyhedral oligomeric silsesquioxane (amino-POSS) was donated by Hybrid Plastics.

Films used for dynamic mechanical analysis (DMA), wide angle x-ray diffraction (WAXD), and small amplitude oscillatory shear measurements were prepared by casting the dispersions with different POSS concentrations onto a

polypropylene plate and drying in a vacuum oven at 90 °C for three days or until constant weight.

Samples for contact angle measurements were prepared using a 5 ml drawdown bar on well-cleaned glass substrates, followed by air-drying for 20 h at ambient temperature and oven drying at 50 °C for 4 h. The wt% solids was determined by heating 1 g of dispersion in a glass vial in a vacuum oven at 120 °C for 6 h and measuring the retained mass.

Measurements

Particle sizes (PS) of the PU dispersions were determined by a Microtrac UPA 250 light scattering ultrafine particle analyzer. WAXD experiments were carried out on POSS powder and on 500 μm thick PU films with a Rigaku rotating anode X-ray generator operating at 40 kV and 250 mA with a Cu target and graphite monochromator. The scanning was performed at $2\theta = 2°$ to $40°$ with step size of $0.02°$ and four seconds per step.

Tan δ (for T_g) and storage modulus of the PU/POSS nanocomposite films as a function of POSS concentration were measured using a TA Instruments 2980 dynamic mechanical analyzer (DMA) in the tensile mode. The temperature response was calibrated with indium while the force and compliance calibrations were performed using standard weight and a clamped steel bar, respectively. Films of $0.80 \times 4.80 \times 12.8$ mm were used for the DMA measurements under nitrogen atmosphere at a heating rate of 2 °C/min from -100 to 150 °C. A minimum of three measurements were performed on each sample.

Viscosities of PU/POSS dispersions of different POSS concentrations were measured at 25 °C using a Brookfield DV-I viscometer (#2 spindle, shear rate of 100 s^{-1}).

Contact angles were determined using a Dataphysics OCA 20 instrument with distilled deionized water. At least 3 independent measurements were carried out and the average reported.

Viscoelastic measurements on the films were performed using an Advanced Rheometrics Expansion System (ARES, Rheometrics Inc.) equipped with 25 mm parallel plates diameter. Strain sweep was carried out at a constant temperature (145 °C) and frequency to evaluate the linear viscoelastic range of the samples. Frequency sweeps (0.1-100 rad/s) are performed at a constant temperature (145 °C) in the linear viscoelastic region (i.e., strain amplitude $\leq$ 10% strain) to obtain the dynamic shear viscosity, η^*, and the storage elastic modulus G' as a function of shear frequency for PU/POSS nanocomposites of different POSS compositions.

The thermal stability of PU/POSS nanocomposites was investigated using thermal gravimetric analysis (Pyris Diamond TGA, PerkinElmer). The heating

rate was 10 °C/min for all measured samples. The measurements were carried out under nitrogen atmosphere.

Base PU Dispersion Synthesis

A 250 mL round-bottom, four-necked flask with a mechanical stirrer, thermometer, condenser with nitrogen in/outlet, and a pipette outlet was used as a reactor. The polymerization was carried out in a constant temperature oil bath. Desmophen 1019-55 and DMPA were charged into the dried flask at 70 °C. While stirring, NMP (10 wt % based on total feed) was added and stirring was continued until a homogenized mixture was obtained. Desmodur-I and DBTL were added and stirring was continued for 30 min. at this temperature. The mixture was heated to 80 °C for about 3 h to afford an NCO terminated prepolymer. The NCO content during the reaction was determined using a standard dibutylamine back titration method (32). Upon obtaining a theoretical NCO value, the prepolymers were cooled to 60 °C, and the neutralizing solution, i.e., TEA (DMPA equiv.) dissolved in NMP (2 wt %) was added and stirred for 30 min while maintaining the temperature at 60 °C.

Dispersion was accomplished by adding the prepolymer to the mixture of water and surfactant (4 wt% based on total solid). Agitation was maintained at 750 rpm. After 20 min, 20 wt % solution of HMDA in water was added over a period of 30 min, and chain extension was carried out for the next 1 h. Subsequently, a defoamer (Foamstar-I) was added, and stirring was continued for 5 min at a speed of 250 rpm. The solids content of the PU dispersion was kept constant at 32 wt% PU. For experiments requiring control of the polymer molecular weight, diethyl amine was included in the chain extension step.

In the preparation of all polymers the ratio of isocyanate groups/amine groups (from chain extension/termination) was 1.1/1. The synthesis of PUD is presented in Scheme 1. The role of the ionic groups is to provide a stable PU dispersion in water. Additional details of the synthesis and chemistry of the process are given elsewhere (33).

Representative Hybrid Dispersion Preparation (PU10)

35 g of NMP was charged into a 250 ml round bottom flask. Amino-POSS (7.5 g, 0.016 amine equiv.) was added, and the content was stirred for 5 min. IPDI (19.3 g, 0.174 isocyanate equiv.) was added drop wise with constant stirring at 20 °C. After 20 min DBTDL added and stirring was continued at the same temperature for another 40 min. The flask was attached to a mechanical stirrer, thermometer, condenser with nitrogen inlet and outlet, and a pipette outlet. The polyester diol (37 g, 0.036 hydroxyl equiv) and DMPA (3.7 g, 0.056

$$\text{HO}\sim\sim\sim\text{OH} + \text{HOCH}_2\underset{\underset{\text{COOH}}{|}}{\overset{\overset{\text{CH}_3}{|}}{\text{C}}}\text{CH}_2\text{OH} + \text{OCN-R-NCO}$$

80 °C ↓

$$\sim\sim\sim\text{O}\overset{O}{\overset{||}{\text{C}}}\text{NH-R-NH}\overset{O}{\overset{||}{\text{C}}}\text{OCH}_2\underset{\underset{\text{COOH}}{|}}{\overset{\overset{\text{CH}_3}{|}}{\text{C}}}\text{CH}_2\text{O}\overset{O}{\overset{||}{\text{C}}}\text{NH-R-NH}\overset{O}{\overset{||}{\text{C}}}\text{O}\sim\sim\sim$$

$(C_2H_5)_3N$ ↓

H_2O ↓ HMDA

$$\sim\sim\sim\text{O}\overset{O}{\overset{||}{\text{C}}}\text{NH-R-NH}\overset{O}{\overset{||}{\text{C}}}\text{OCH}_2\underset{\underset{\text{COO}^\ominus\text{HN}^\oplus(C_2H_5)_3}{|}}{\overset{\overset{\text{CH}_3}{|}}{\text{C}}}\text{CH}_2\text{O}\overset{O}{\overset{||}{\text{C}}}\text{NH-R-NH}\overset{O}{\overset{||}{\text{C}}}\text{O}\sim\sim\sim$$
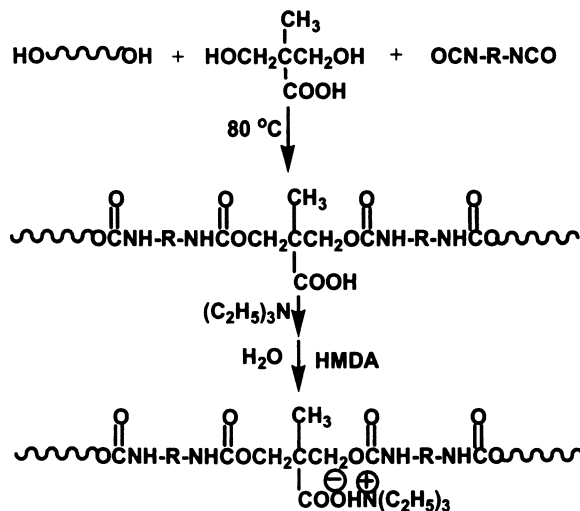
Scheme 1. Elementary steps for the synthesis of pure PUD Dispersion and Chain Extension

hydroxyl equiv, 0.028 acid equiv) were charged and stirring was continued until a homogeneous mixture was obtained. The temperature was raised to 80 °C using a temperature controller. The isocyanate content during the reaction was monitored using a standard dibutylamine back titration method (*32*).

Upon reaching the theoretical isocyanate value, the prepolymer was neutralized by triethyl amine (2.9 g, 0.028 equiv.) by stirring for 30 min. The prepolymer was dispersed into water at an agitation speed of 750 rpm. After 20 min, a 20 wt% solution of HMDA in water was added for a period of 30 min, and chain extension was carried out for the next 30 min. The solids content of the dispersion was 32 wt%. The elementary steps for the preparation of nanostructured PU/POSS hybrid dispersions through prepolymer mixing process is presented in Scheme 2. A series of PU/POSS hybrid dispersions, were synthesized with 0, 4, 6 and 10 wt % of the amino functional-POSS (PU0, PU4, PU6 and PU10 Table 1). The particle sizes of the 3 modified dispersions and the control at ~40 nm were in line with expectations indicating no impact by the addition of POSS.

Results and Discussion

The prepolymer process for the preparation of PU dispersions was evaluated for the formation of PU/POSS hybrids. To this end a series of PU dispersions
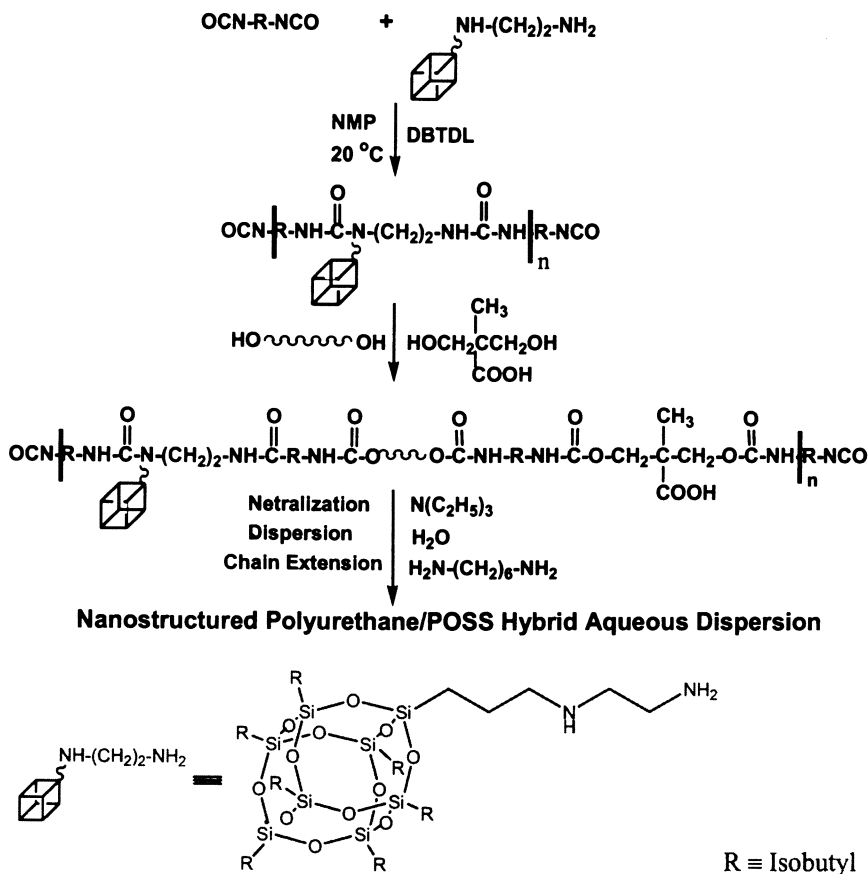
Scheme 2. Elementary steps for hybrid dispersion by prepolymer mixing process

were made using various amounts of POSS (Table 1). For each of these systems the DMPA concentration was held at 5.5 wt % based on total concentration of polymer, polymer concentration at 32 wt % and chain extension at 90%. As a result of compensating for the inclusion of the POSS comonomers, the polyester diol content reduced from 73 to 62 wt% of the total polymer solids. The inclusion of the POSS monomers did not have a major impact on the solution properties of the dispersions relative to the control (**PU0**). The minor differences in particle size and viscosity with increasing POSS content are within the limits of reproducibility and indicate that the POSS monomers do not affect the dispersion step. As clearly seen in Table 1 the viscosities of PU/POSS dispersions are almost constant ($\eta = 55\pm2$ mPa-s) regardless of the increase in the POSS concentration at 20 °C and 100 s^{-1} shear rate. This constant value of

viscosity is attributed to the fact that the inclusion of POSS to PUD does not change the particle sizes of the dispersions for different POSS concentrations as presented in Table 1. Therefore the addition of POSS does not play any role for controlling the particle-particle interactions or the hydrodynamic interactions and consequently all the PU/POSS dispersions have same viscosity. In addition the PU/POSS dispersions are very stable and the dispersion particle sizes for all samples were unimodal and remained constant over six months of storage at room temperature.

Table 1. Particle size and viscosity of PU/POSS dispersions as a function of POSS concentration

Sample	POSS wt%	Particle size (nm)	η (mPa-s)
PU0	0	37	54
PU4	4	39	54
PU6	6	40	57
PU10	10	42	56

Films prepared from the dispersions were clear and defect free. The physical properties changed systematically with the incorporation of POSS monomers and are indicative of homogeneous incorporation (Table 2). The results of our WAXD evaluation of the polyurethane films are shown in Figure 1, along with a powder pattern for the POSS monomer. The main reflections of the amino-POSS monomer found at $2\theta=8.1$, 10.8, 12.1 and $18.8°$ are similar to those reported by Turi et al. for a diol-POSS (30). **PU0** (control) shows only an amorphous halo indicating that the base polymer does not have a crystalline component. With the addition of POSS even at the lowest result, a WAXD reflection at $2\theta = 8.6°$ indicating that at least some of the POSS is forming a crystalline domain. Although the amino-POSS was reacted in the beginning with IPDI to avoid the inhomogeneity of POSS and PU, the WAXD data is probably due to the presence of some unreacted POSS in the PU matrix. Perhaps the reaction mixture was not as homogeneous in presence of NMP as it was in the acetone process we described earlier or crystalline oligomers may have been formed (31).

The surface behavior was investigated through measurements of contact angles against water (Table 2). The incorporation of POSS macromer increases the contact angles of the coated surface against water. This implies that the POSS residues are preferentially oriented toward the air-film interface. Incorporating 4 wt % POSS (**PU4**) results in an increase the contact angle from 64 to $76.1°$, and higher loadings slowly increase the contact angle to $78.6°$. This phenomenon is quite commonly observed for POSS modified polymers with as surface tension preferentially drives the lower energy POSS residues to the air

interface (*34,35*). The 15° increase in contact angle found in this study is slightly lower than the 23° increase found for the acetone process hybrids (*31*).
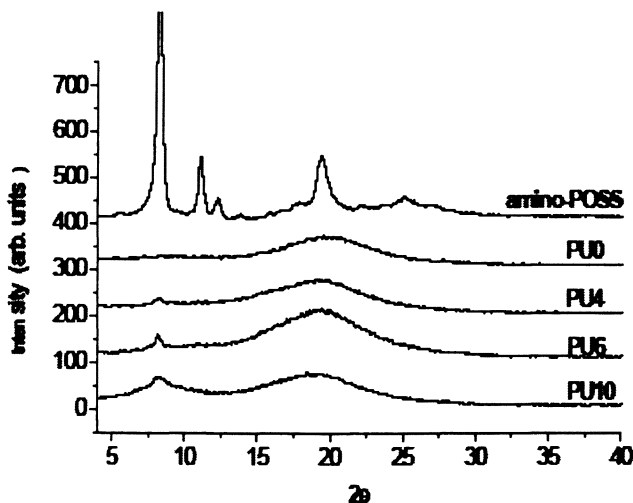
Figure 1. WAXD patterns of amino-POSS PU0, 4, 6 and 10 films

Table 2. Physical Properties of PU/POSS hybrid films

Sample	Contact angle/°	Tg/°C (hard segment)	E'/MPa (T= 20 °C)	E'/MPa (T= 100 °C)
PU0	64.0	80	51.4	4.7
PU4	76.1	81	123.5	11.9
PU6	77.2	84	151.4	12.0
PU10	78.6	123	263.5	38.4

The storage moduli (E') versus temperature response of the PU/POSS nanocomposite films are presented in Figure 2 and Table 2. The storage modulus increases with POSS content in the polyurethane. However, the storage moduli for 4 and 6 wt% of POSS loading were nearly similar. There is a dramatic increase in modulus at 10 wt % of POSS. The increase in modulus was not systematic as seen for the acetone process hybrid materials (31). The E' at 20 and 100 °C is presented in Table 2. There is an increase in modulus at these two temperatures with the addition of POSS. As with the control (**PU0**) the hybrid films also showed two maxima for tanδ (Figure 3) due to the soft and hard segments T_gs at high and low temperature ranges, respectively. When POSS is
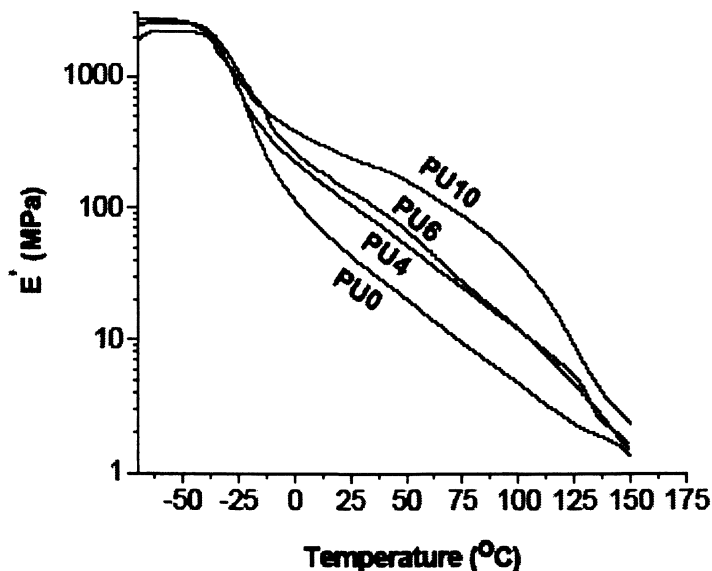
Figure 2. Storage modulus of PU/POSS nanocomposite films for different POSS concentrations

incorporated there is little or no change in the soft segments, while, the hard segments are considerably affected by adding POSS , i.e.; the peak maxima of the hard segment shifted to higher temperatures with increasing POSS concentration in the composites.

Viscoelastic and TGA Measurements

Incorporating of POSS to the PU polymeric chains would be expected to have a dramatic effect on the rheological behavior of PU film. Figure 4 shows the storage modulus of PU/POSS nanocomposite films as a function of shear frequency at 145 °C for different POSS concentrations. Obviously, POSS can significantly increase the storage modulus of PU, i.e.; the value of G' increases by more than two orders of magnitude at the low frequency region (terminal zone) by adding 10 wt% POSS. In addition the slope of G' at the terminal zone decreases significantly with increasing the concentration of POSS. This behavior shows very clearly how the inclusion of small amounts of POSS can produce a dramatic change in the viscoelastic properties of PU film.

The dependence of dynamic shear viscosity on the variation of POSS content for different shear frequencies is shown in Figure 5. The incorporation
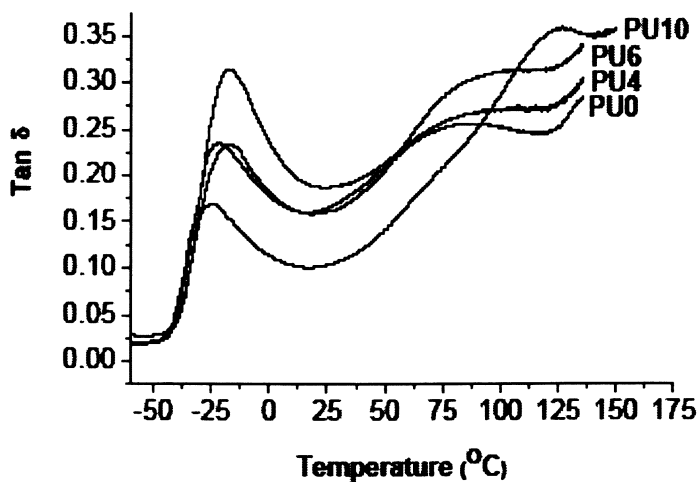
Figure 3. Tanδ of PU/POSS nanocomposite films for different POSS concentrations
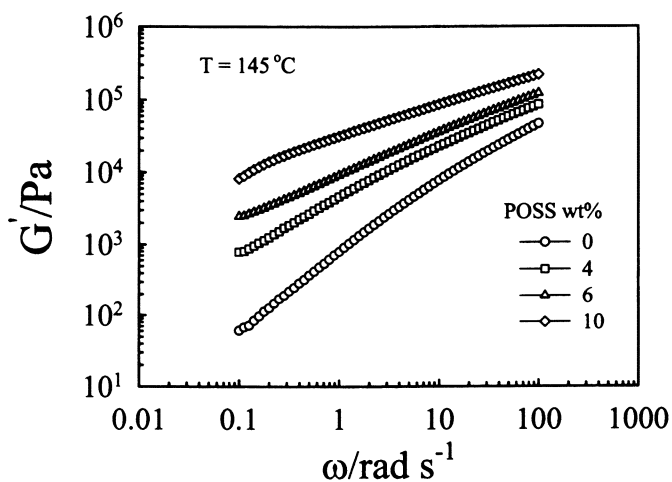
Figure 4. Shear frequency dependence of storage modulus of PU/POSS nanocomposite films as a function of POSS concentrations at 145 °C.
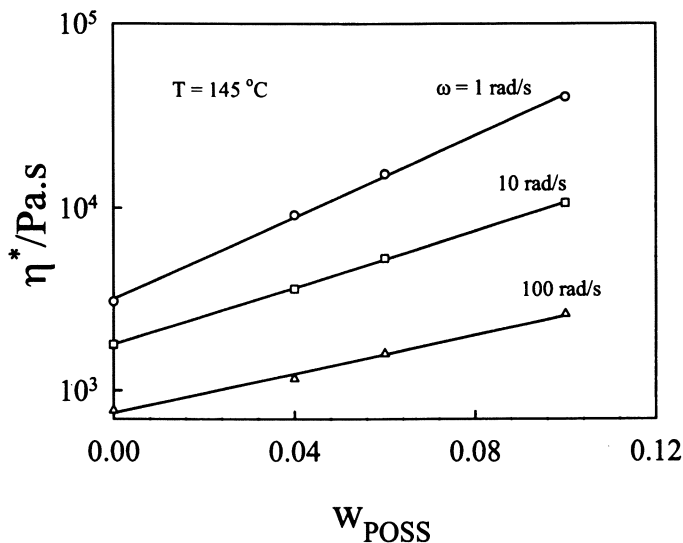
*Figure 5. Weight fraction dependence of complex viscosity for PU/POSS
nanocomposite films at 145 °C and different shear frequencies*

of small amount of POSS into the PU polymer backbone produced a significant change in the dynamic viscosity at 145 °C. The complex viscosity increases linearly with increasing the POSS composition for all shear frequency values. This increase in viscosity corroborates the reinforcement of POSS in the PU backbone. In addition, the dynamic viscosity strongly depends on frequency (Figure 6) revealing the non-Newtonian behavior of PU-POSS composites with the dynamic viscosity at the whole rage of shear frequency (1, 10, and 100 rad/s).

Our results stand in contrast to those reported by Turi and Levi (*30*) and suggested that any small variations in process and composition of this system must be carefully considered. Within this work our own results showed that the sequencing of the reaction steps at the outset of polymer preparation dictate whether or not the POSS was homogenously incorporates, and that morphology can be dramatically altered by sample fabrication.

The TGA measurements for base PU and PU/POSS = 90/10 composites are shown in Figure 6. This Figure demonstrates the percent mass as a function of temperature at 10 °C/min heating rate under nitrogen atmosphere. Obviously the PU and composite undergo thermal degradation beginning at 270 °C regardless of the presence of POSS. It is also clear that the soft segments of PU start to degrade first at 270 °C and the hard segments degrades later on at 350 °C. This data suggests that the incorporation of POSS to the hard segments of PU does not enhance the thermal stability of PU significantly under nitrogen atmosphere.
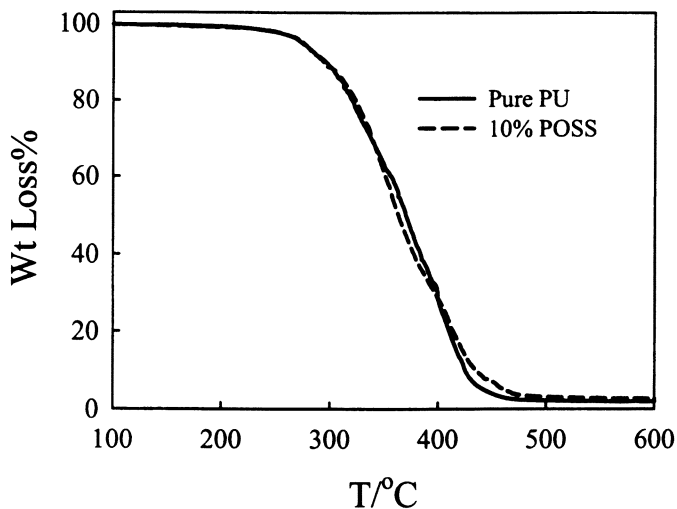
*Figure 6. TGA measurements for PU0 and PU10 nanocomposite films
at 10 °C/min heating rate under nitrogen atmosphere.*

Conclusions

The waterborne polyurethane hybrid dispersions have been successfully synthesized through the incorporation of diamino functionalized POSS (NH$_2$-POSS) monomers in the polyurethane ionomeric backbone through the prepolymer process. The inclusion of the POSS monomers did not have a major impact on the solution properties of the dispersions relative to the control polyurethane dispersion. The minor differences in particle size and viscosity with increasing POSS content are within the limits of reproducibility and indicate that the POSS monomers do not affect the dispersion step. It has also been found that the addition of POSS does not play any role for controlling the particle-particle interactions or the hydrodynamic interactions in the PU/POSS dispersions. The POSS macromers appear to be included in the PU hard segments as evidenced by the increase in hard segment T$_g$ with increased POSS content. Storage modulus, complex viscosity and T$_g$ of the hard segments of PU film increased with increased POSS content. The films remained transparent with up to 10 wt % incorporation of the POSS monomers. Interestingly, films prepared from the POSS containing dispersions showed lower surface wettability. This effect may be due to either a stratification of the non-polar components of the coating close to polymer-air interface or a topographical change of the surface due to formation of nanostructures.

Acknowledgements

References

1. POSS is a registered trademark of Hybrid Plastics, www.hybridplastics.com.
2. Li, G.; Wang, L.; Ni, H.; Pittmann, C. U. *J. Inorg. Organomet. Polym.* **2001**, *11*, 123.
3. Baney, R. H.; Itoh, M.; Sakakibara, A.; Suzuki, T. Chem. Rev. **1995**, *95*, 1409.
4. Pittmann, C. U., Li, G.; Ni, H. *Macromol. Symp.* **2003**, *196*, 301.
5. Phillips, S. H.; Haddad, T. S.; Tomczak S. J. *Current Opinion in Solid State and Material Science.* **2004**, *8*, 21.
6. Gao, F.; Tong, Y.; Schricker, S. R.; Culbertson, B. M. *Polym. Adv. Technol.* **2001**, *12*, 355.
7. Tegou, E.; Bellas, V.; Gogolides, E.; Argitis, P. *Microelectr. Eng.* **2004**, *73-74*, 238.
8. Kickelbick, G. *Prog. Polym. Sci.* **2003**, *28*, 83.
9. Lichtenhan, J. D.; Otonari, Y. A.; Carr, M. J. *Macromolecules* **1995**, *28*, 8435.
10. Haddad, T. S.; Lichtenhan, J. D. *Macromolecules* **1996**, *29*, 7302.
11. Romo-Uribe, A.; Mather, P. T.; Haddad, T. S.; Lichtenhan, J. D. *J. Polym. Sci., Part B: Polym. Phys.* **1998**, *36*, 1857.
12. Mather, P. T.; Jeon, H. G.; Romo-Uribe, A. *Macromolecules* **1999**, *32*, 1194.
13. Bharadwaj, B. K.; Berry, R. J.; Farmer, B. L. *Polymer* 2000, *41*, 7209.
14. Tsuchida, A.; Bolln, C.; Sernetz, F. G.; Frey, H.; Mulhaupt, R. *Macromolecules* **1997**, *30*, 2818.
15. Lee, A.; Lichtenhan, J. D. *Macromolecules* **1998**, *31*, 4970.
16. Lin, E. K.; Snyder, C. R.; Mopsik, F. I.; Wallace, W. E.; Zhang, Laine, R. M. In *Organic/Inorganic Hybrid Materials*; Laine, R. M., Sanchez, C., Brinker, C. J., Giannelis, E., Eds.; Mater. Res. Soc. Symp. Ser. Vol. 519; Materials Research Society: Warrendale, PA, 1998; pp 15-20.

17. Lichtenhan, J. D.; Schwab, J. J.; Reinerth, W. A., Sr. *Chem. Innovation* **2001**, *1*, 3.
18. Haddad, T. S.; Stapleton, R.; Jeon, H. G.; Mather, P. T.; Lichtenhan, J. D.; Plillips, S. *Polym. Prepr.* **1999**, *40*, 496.
19. Lichtenhan, J. D.;Vu, N. Q.; Carter, J. A.; Gilman, J. W.; Feher, F. J. *Macromolecules* **1993**, *36*, 2141.
20. Markusch, P. H.; Tirpak R. E. Symposium New Orleans, LA, **1990**.
21. Kim, B. Y.; Kim, T. K. *J. Appl. Polym. Sci.* **1991**, *43*, 393.
22. Kim, C. K.; Kim, B. K. *J. Appl. Polym. Sci.* **1991**, *43*, 2295.
23. Chan, W. C.; Chen, S. A. *Polymer* **1993**, *43*, 1265.
24. Dreja, M.; Heine, B.; Tieke, B.; Junkers, G. *J. Colloid. Interf. Sci.* **1997**, *181*, 131.
25. Wicks, Z. W.; Wicks D. A.; Rosthauser, J. W. *Progr. Org. Coat.* **2002**, *44*, 161.
26. Howarth, G.A. "Polyurethanes, polyurethane dispersions and polyureas: Past, present and future," Surface Coatings International Part B: Coatings Transactions, **2003**, *86 (B2)*, 111.
27. Kim, B. K.; Lee, J. C.; *J. Polym. Sci. Polym. Chem.* **1996**, *34*, 1095.
28. Wicks, D. A.; Wicks, Z. W. *Pro. Org. Coatings* **1999**, *36*, 148.
29. Hourston, D. J.; Williams, G. D.; Satguru, R.; Padget, J. C.; Pears, D. *J. Appl. Polym. Sci.* **1999**, *74*, 556.
30. Turri, S. ; Levi, M. *Macromolecules* **2005**, *38*, 5569.
31. Nanda, A. K.; Wicks, D. A.; Madbouly, S. A.; Otaigbe, J. U. *Macromolecules* **2006**, *39*, 7037.
32. Nanda, A.K.; Wicks, D. A. *Polymer* **2006**, *47*, 1805.
33. Nanda. A. K.; Wicks, D. A.; Madbouly, S. A.; Otaigbe, J. U. *J. Appl. Polym. Sci.* **2005**, *98*, 2514.
34. Marby, J. M.; Marchant, D.; Viers, B.; Ruth, N. P. ; Barker, S. ; Schaefler, C. E.; *SAMPE* **2004**, *49*, 1316.
35. Suresh, S.; Zhou, W.; Spraul, B.; Laine, R. M. ; Ballato, J. ; Smith, D. W. *J. Nanosci. Nanotechnol.* **2004**, *4*, 250.

Chapter 4

Nanostructured Conjugated Polymer Network Ultrathin Films and Coatings Using the Precursor Polymer Approach

Rigoberto Advincula

Department of Chemistry and Department of Chemical Engineering, University of Houston, Houston, TX 77204

This work focuses on describing the precursor approach to conjugated polymer network thin films: synthesis, electrodeposition, patterning, and applications. The preparation of "smart coatings" involves the use of new materials and mechanism towards common applications. By targeting the preparation and deposition of nanostructured ultrathin and optically homogeneous conjugated and electrically conducting polymer materials, it should be possible to develop new and smart coating applications. This includes anti-static, anti-corrosion, electrochromic, and display applications. The use of precursor-polymers is described based on the synthesis of a passive or active polymer backbone bearing electro-active monomer groups. These in turn can be electrodeposited or cross-linked by oxidative chemical methods to form ultrathin film coatings. A number of approaches will be described in this chapter including the use of surface sensitive spectroscopic and microscopic methods for analysis and patterning of these films.

The coatings industry has had a fascination for "smart coatings" for some time. Smart coatings are not new in the sense that they take into account everyday applications using new materials and mechanisms to improve the performance of existing coatings. On the other hand, because of fundamental discoveries made in the field of polymeric and inorganic materials there is a

51

potential to generate new and "smart applications". The use of so-called macromolecular assemblies in ultrathin films provides new ways of assembly of ultrathin film coatings even through a layer-by-layer approach. This includes self-assembly, langmuir-blodgett films, layer-by-layer deposition of polyelectrolytes, and polymer brushes by surface initiated polymerization. On the other hand, while electropolymerization has been utilized for some time, current approaches using the direct deposition of monomers to form conjugated polymers is not ideal for depositing homogeneous and optically uniform coatings.

In the area of polymer materials, organic π-conjugated polymers and intrinsically conducting polymers (ICPs) have shown very promising behavior as alternative electrical conducting, nonlinear optical, and electroluminescent materials.(1) Other applications includes: energy storage, electrochromic displays, sensors, charge-dissipation, and anti-corrosion coatings. Both the doped and undoped forms are being investigated for these applications with the idea of replacing their inorganic material counterparts. A wealth of synthetic techniques leading to novel molecular, macromolecular, and microstructural design has been reported. This primarily involves the use of metal-mediated coupling reactions or condensation polymerizations. The addition polymerization of acetylene monomers to form substituted polyacetylenes have been reported widely but they have been generally unstable towards oxidation.(1) Electrochemical methods have been utilized to control the oxidation potential for polymerization and investigate the resulting electronic properties of these polymers. In this case, the conjugated polymers are formed *in situ* as the monomers are polymerized (radical cation mechanism) and deposited on a conductive electrode. Recently, the importance of optical film qualities of these materials has been emphasized for electrochromic applications.(2) For non-doped film applications such as polymer light emitting diode (PLED) and field effect transistor (FET) devices, the optical dielectric constants, charge carrier properties, thickness, morphology (crystallinity or aggregation), and layer order of the films are deemed to be important.

We have demonstrated previously in many occasions the deposition of high optical quality ultrathin film coatings of conjugated polymers through the *precursor polymer approach* (Figure 1).(3) This has been a perennial problem with respect to the application of conjugated polymers as coatings because of the poor morphology and processing conditions for the direct deposition of heteroaromatic or electroactive monomers for thin film coatings. We have reported the synthesis and electrochemical deposition of "passive" polysiloxane–precursor derivatives (by cyclic voltammetry or potentiostatic methods) of thiophene and pyrrole to form crosslinked polythiophene and polypyrrole respectively.(4) On the other hand, it is also possible to synthesize "active" precursor polymers in which the polymer backbone itself is conjugated and has electro-optical activity.(5) *These polymers can be directly deposited from an*

electrolyte solution or spin-coated to the electrode substrate first and electrochemically oxidized. We have also reported the electrodeposition and electrochemical grafting to indium tin oxide (ITO) substrates of a precursor polymer (copolymer) with an "active" conjugated polyfluorene backbone.(*5*) The electro-active carbazole side group facilitated electrodeposition forming oligocarbazole links. Recently, we have also investigated the use of poly(vinyl carbazole) or PVK as precursor polymer materials for polycarbazole thin films that can be used for modifying PLED device properties.(*6*)

Flexible Polymer Backbone (Passive)

Active Conjugated Polymer Backbone

[O]

[O]

Formation of Cross-links via inter- and intra-molecular reaction

⬤ = Electropolymerizable Monomer
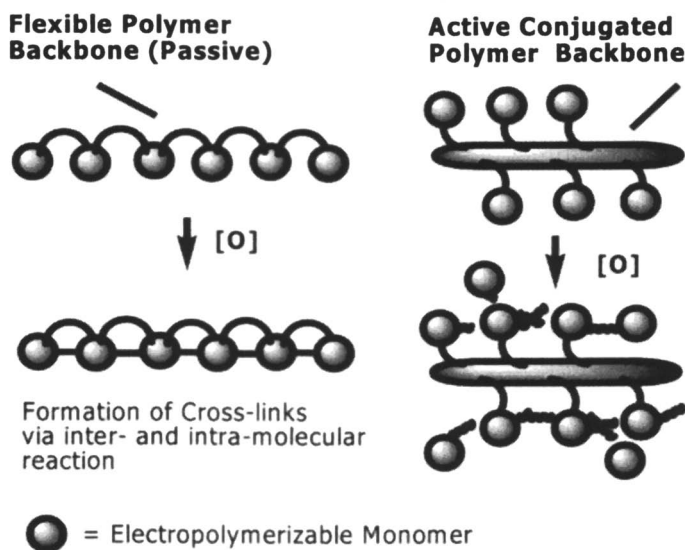
Figure 1. The Precursor Polymer approach to conjugated polymers with different polymeric backbones.

In all these cases, the coating film formation was accomplished by electrochemically cross-linking and polymerizing the precursor polymers through the electro-active monomer side group as they deposited to the surface of the electrode. We believe that the reason the films were of such good quality is because the mechanical strength is "built in" at the precursor stage. The films are held together by the entanglements between chains due to the inter- and intra-molecular polymerization pathways resulting in crosslinks. It is also possible to increase the amount of linear conjugated polymer chains simply by introducing non-polymer bound electro-active monomers as we have demonstrated in the case of precursor polypyrroles with polysiloxane and polymethacrylate backbones.(*3*)

In this paper we report various methods of coating and patterning of precursor polymers electrochemically. We will also present several strategies for the synthesis, fabrication, and characterization of these unique conjugated polymer ultrathin films. The application of these cross-linked materials is towards electro-optical devices, for example, polymer light emitting diode (PLED) devices will also be described. Micro-contact printing (μCP) is a soft-lithographic approach that has been used for creating micron sized patterns on flat surfaces. By controlling the deposition site using micro-contact printing, patterns on the electrode surface can be formed prior to electropolymerization. This resulted in light emitting regions from the selectively deposited sites containing carbazole modified polyfluorenes. Furthermore, we will also demonstrate the possibility of sequential electrochemical deposition of two different precursor polymers based on precursor polycarbazole and polythiophene derivatives. Electrochemical Nanolithography (ECN) is a technique in which a pattern is created by applying a potential between the AFM tip and the substrate (conducting AFM set-up) during "writing".(7)

Results and Discussion

Precursor Polymers

The synthesis of the polymers containing conducting segments can be done either by polymer analogous reactions or through direct polymerization of vinyl monomers containing electropolymerizable side-groups. Several synthesis strategies have been reported.(3,4) One such copolymer is shown in Figure 2, where the presence of carbazole and thiophene side groups provided a cross-linking unit for electrochemical deposition.(3b) We have also utilized extensively polyvinylcarbazole (PVK) which function as very good hole-transport layers and can be cross-linked to form polycarbazole thin films. All of these polymers have the common design feature that they have tethered electropolymerizable monomers which can be varied in composition. The synthesis of polyfluorenes bearing carbazole monomer side groups has been previously accomplished by Suzuki and Yamamoto coupling reaction. The copolymer can be prepared by either incorporating carbazole containing fluorenes or by the incorporation of carbazole monomer units in the backbone (Figure 3).

The precursor polymer were then cross-linked by electropolymerization and monitored by cyclic voltammetry at various solvents, substrates, solution concentrations, and counter electrolytes. The cross-linking can also be done by potentiostatic methods. Crosslinking occurs to form very uniform and optically
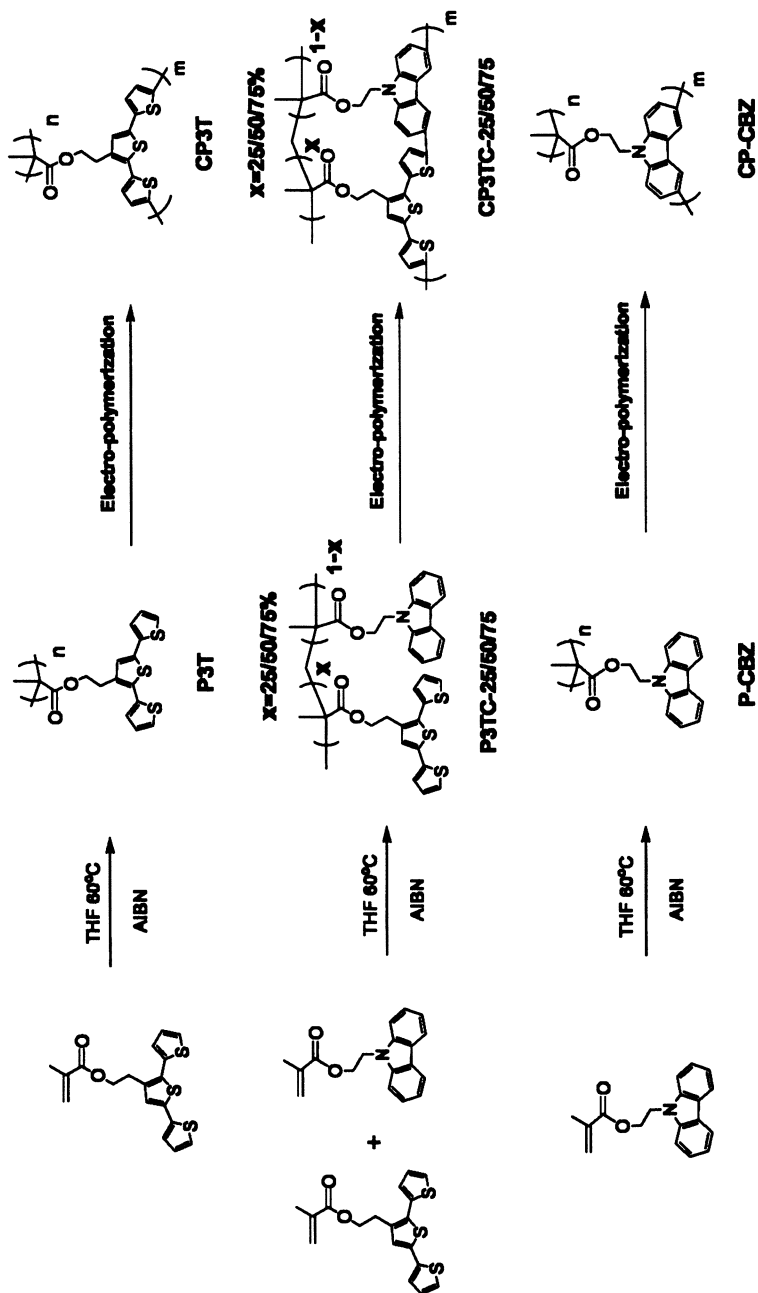
Figure 2. Synthesis of precursor homopolymers/copolymers and their electro-polymerization.

56

clear films and are essentially *insoluble* once formed. Most of the films investigated showed reversible color changes (electrochromism) during the redox process and CV cycling. This property should be very useful for the development of smart electrochromic windows and mirrors.(*2*) The use of surface plasmon spectroscopy (SPS) electrochemical quartz crystal microbalance (E-QCM), X-ray photoelectron spectroscopy (XPS), and FT-IR spectroscopy and AFM revealed interesting deposition, doping, morphology, and cross-linking chemistry for these conjugated polymer films.
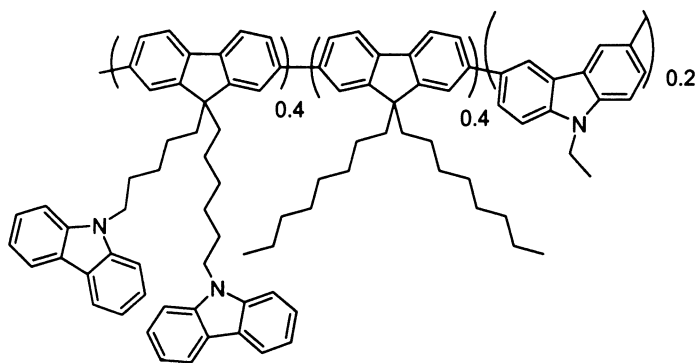
Figure 3. Chemical structure of an electrochemically cross-linkable Polyfluorene precursor polymer, P4F4C2E. This polymer was synthesized by a nickel mediated Yamamoto coupling reaction

Patterning by microcontact printing

To investigate in-situ the growth of conjugated polymers on patterned conducting surfaces, we have employed an electrochemical surface plasmon microscopy (EC-SPM) technique (Figure 4). The patterns on the electrode surface were first defined by micro-contact printing (Figure 5). Upon electro-deposition of the electroactive monomer or precursor polymer (as in Figure 3) on the surface by cyclic-voltammetry (or potentiostatically), the polymer was observed to grow only on the bare Au surfaces which have not been insulated by the ODT layers used under a particular potential. We observed that the contrast of the images where the conjugated polymer has grown varied with the "height" of the deposited polymer, the refractive index contrast, and the angle of observation for microscopy. These changes were also correlated with the specific redox stages of the potential on the CV. The in-situ EC-SPM technique emphasizes the sensitivity of these patterns to optical reflectivity changes, which can have possible applications in micro-displays and sensors.

Grafting of Carbazole-modified Polyfluorenes on Electrode Surfaces

We have previously reported the grafting of carbazole-modified polyfluorenes. Using the precursor polymer shown in Figure 3, we grafted the polymers directly to an ODT microcontact printed surface. The grafting was done electrochemically by CV or by potentiostatic methods from solution. Different morphologies and deposition behavior were observed. Interestingly, the polymer preferentially deposited on the hydrophobic SAM modified surfaces. This underscores the importance of matching the particular surface
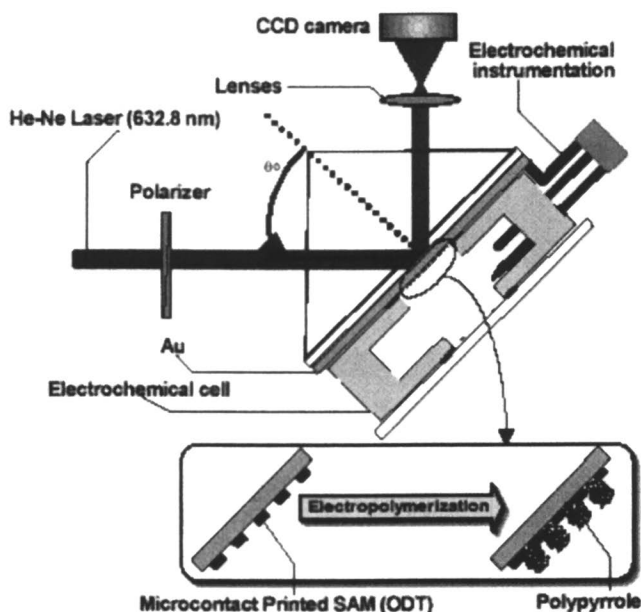
Figure 4. Electrochemical surface plasmon microscopy (EC-SPM) set-up to monitor the electrodeposition of the precursor polymer on the bare Au surface.

energies of the electrodeposited organic polymer materials to the substrate surface. Since, the electrochemical activity was limited to the carbazole side groups, the absorption and fluorescence properties of the polyfluorene backbone remained intact. That is why patterned fluorescence was observed on these dots using fluorescence microscopy (Figure 5). This selective electropolymerization and electrodeposition is an interesting method for preparing thermally stable and mechanically robust conjugated polymer patterns and should be useful for a number of electro-optical applications including PLEDs.
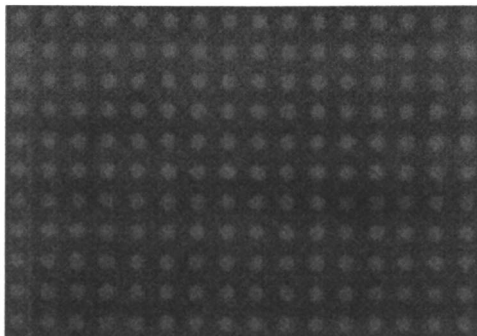
*Figure 5. Micro-contact printed patterns of electrochemically grafted
polyfluorene on Au substrates by AFM.*

Electrochemical Nanolithography (ECN)

A negative voltage bias can be applied to the AFM tip (anode) and electrochemical oxidation occurs on a dielectric material coated on a conducting electrode (cathode). This voltage bias (constant potential) in the presence of the right condition for an electrochemical reaction will result in cross-linking of the precursor.(*7,8*) *The patterns are formed and the conductivity will differ, i.e. direct electropolymerization of patterns by the AFM tip.* Control of patterning involves varying the potential, writing speed, film thickness, and specific sites. While previous work has described ECN based on direct introduction of electroactive monomers from the AFM tip to the substrate, here we emphasize the preparation of nanopatterns on polymer films through electrochemical polymerization/ cross linking of a precursor polymer film.(*8*) The method has been demonstrated recently on polyvinylcarbazole (PVK), spin-coated on a conducting substrate.(*7*) In our experiment, the application of a biased potential from the AFM tip resulted in the oxidation of carbazole followed by polymerization or cross- linking under ambient conditions (23 °C, in air with 75 % humidity). A pattern "NUS-UH" was written on the spin-coated PVK film (Figure 6). This electropolymerization-crosslinking was facilitated by the bias voltage inducing an electrochemical redox reaction, in which humidity is a key component. Test lines showed that the pattern varied in thickness and resolution as a function of voltage and writing speed. The control of thickness was not explored at that time. Recently, we have demonstrated electrochemical nanolithography on polyelectrolyte layer-by-layer films of polycarbazole precursors with controlled nm thicknesses and will be reported in a future publication. The layer-by-layer films were deposited based on electrostatic interaction between oppositely charged polyelectrolytes deposited on a conducting substrate. The ordering and controlled layer thickness makes these interesting substrates for models in controlled electropolymerization conditions.
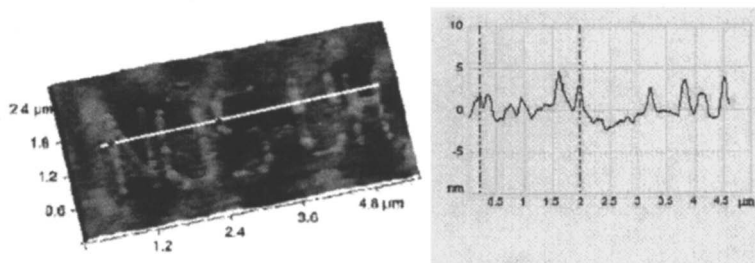
Figure 6. Nanopatterning process demonstrated by the ECN method with "NUS-UH" written on a spin-coated PVK precursor film.
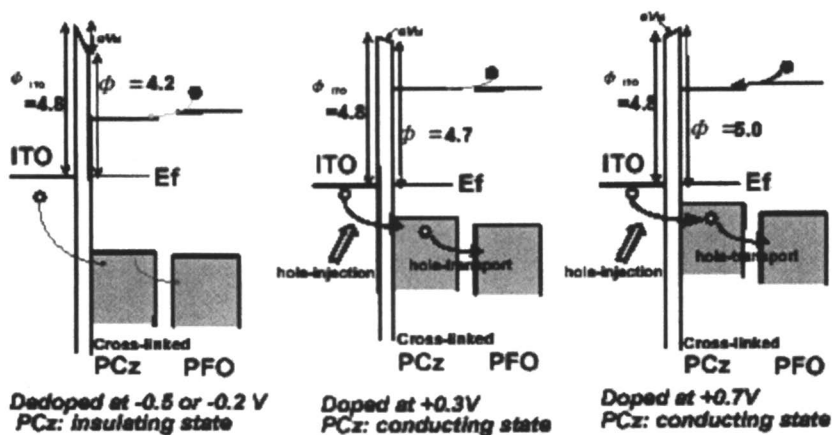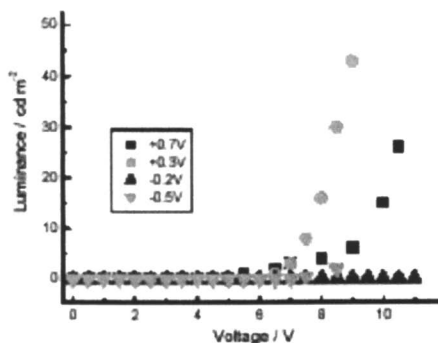
Figure 7. Variable turn-on voltage based on the electrochemical doping of crosslinked PVK thin films on ITO and their energy-band-gap matching conditions with the work-function of ITO and the electroluminescent polymer PFO.

PLED Devices

Our recent investigations on the application of these cross-linked films to the fabrication polymer light emitting diode (PLED) devices showed dramatic improvements towards lower turn-on-voltages and greater efficiencies (Figure 7).(9) For example, the application of cross-linked polyvinylcarbazole (PVK) as a hole transport material for a heterojunction bilayer PLED device with polyfluorene (PFO) or aluminum-tri-quinoline (Alq$_3$) showed significant improvements and tenability with doping. The fact that the voltage varies with doping indicated that the presence of a hole-transport layer like PVK is tunable towards low or high turn-on voltages. Low turn-on voltage means that the devices can operate in relative lower power requirements and perhaps better efficiency. These interesting results show that cross-linked conjugated polymer films play an important role in the development of these display devices and their application to other types of semiconductor devices. In principle, electrical or band gap tuning is possible with the right choice of a conjugated or non-conjugated polymer backbone. The difference is that these films are very robust both thermally and mechanically because of thermoset nature of a crosslinked polymer film. Other applications of these films to sensors, dielectric materials, non-lithographic patterning, etc. are currently being investigated by our group.

Future Applications

The previous methods and applications have shown the potential for ultrathin film applications based on the precursor approach for conjugated polymer networks. Most of this has been applications involving the electrodeposition of thin films ranging from a few to a hundred nm in thickness. It is obvious that bulk or thick film coatings applications have yet to be demonstrated. The cross-linking and electropolymerization leads to the formation of conjugated/conducting and electrochromic or even fluorescent coatings. It is possible that applications involving anti-corrosion, electrochromic windows, anti-static, and even "sensing" coatings will be fully exploited in the near future.

Acknowledgements

References

1. *Handbook of Conducting Polymers*, 2nd ed.; Skotheim, T. A., Elsenbaumer, R. L., Reynolds, L. R., Eds.; Marcel Dekker: New York, 1998.
2. *Electrochromism Fundamentals and Applications*; Monk, P. M. S.; Mortimer, R. J.; Rosseinsky, D. R.; VCH: New York, 1995.
3. (a) Deng, S.; Advincula, R. *Chem. Mater.* **2002**, *14*, 4073-4080. (b) Taranekar, P.; Fulghum, T.; Baba, A.; Patton, D.; Advincula, R. *Langmuir* **2007**, *23*, 908-917 (c) Taranekar, P.; Park, J.; Patton, D.; Fulghum, T.; Ramon, G.; Advincula, R. *Adv. Mater.* **2006**, *18*, 2461-2465. (d) Ravindranath, R.; Ajikumar, P.; Advincula, R.; Knoll, W.; Valiyaveettil, S. *Langmuir* **2006**, *22*, 9002-9008. (e) Fulghum, T.; Karim, S.; Baba, A.; Taranekar, P.; Nakai, T.; Masuda, T.; Advincula, R. *Macromolecules* **2006**, *39*, 1467-1473.
4. (a) Xia, C.; Fan, X.; Park, M.-K.; Advincula, R. *Langmuir* **2001**, *17*, 7893-7898. (b) Taranekar, P.; Fan, X.; Advincula, R. *Langmuir* **2002**, *18*, 7943-7952.
5. Xia, C.; Advincula, R. *Chem. Mater.* **2001**, *13*, 1682-1691.
6. Inaoka, S.; Roitman, D. B.; Advincula, R. *Chem. Mater.* **2005**, *17*, 6781-6789. 7. Jagadesan, S.; Advincula, R.; Valiyaveettil, S. *Adv. Mat.* **2005**, *17*, 1282.
8. (a) Jegadesan, S.; Sindhu, S.; Advincula, R.; Valiyaveettil, S. *Langmuir* **2006**, *22*, 780-786. (b) Jegadesan, S.; Sindhu, S.; Advincula, R.; Valiyaveettil, S. *Langmuir* **2006**, *22*, 3807-3811.
9. Baba, A.; Onishi, K.; Knoll, W.; Advincula, R. *J. Phys. Chem. B.* **2004**, *108*, 18949-18955.

Chapter 5

Nanoparticle Surface Modification for Advanced Corrosion Inhibiting Coatings

Ronald L. Cook and Andrew W. Myers

TDA Research, Inc., 12345 West 52nd Avenue, Wheat Ridge, CO 80033

In the last decade, surface engineering of inorganic nanoparticles has advanced to the point that it has become possible to fabricate and tune the functional properties of nanoparticles. The final properties of a nanocomposite are related to the nanoparticle itself (aspect ratio), the degree of dispersion, and the identity of the surface groups (surface density, oligomer length, etc.). Additionally, surface engineering can produce functional nanoparticles and by extension functional nanocomposites. At the most basic level, functional nanoparticles are surface engineered to both disperse into a host phase (e.g. a coating) and to carry a functional agent. Protective coatings are the most effective weapon in the battle to prevent corrosion, and soluble chromate additives have historically been used for corrosion protection for both steel and aluminum. Chromates released from pigments "heal" the corrosion sites thereby stopping corrosion. Unfortunately, chromates are toxic and OSHA regulations have reduced workplace Cr(VI) levels to 5 ppm. Nanoparticle additives with triggered release mechanisms have been developed as chromate replacements in protective coatings. Nanoparticle additives are attractive materials for corrosion protection because their high surface areas allow them to function as carriers for molecular corrosion inhibitors and their small particle sizes often generate novel chemistries not observed in bulk materials that permit the design of triggered release mechanisms.

© 2009 American Chemical Society

Introduction

Polymer nanocomposite coatings offer tremendous improvements in physical, mechanical and chemical properties over the neat coatings at low filler loadings. Nanocomposite coatings are a combination of a polymeric host matrix (e.g. an epoxy, acrylic or polyurethane) and filler particles that are in the order of 100 nm or smaller. The nanosized particles have a very high surface area that leads to high levels of interaction between the polymer and the nanoparticles. The properties of nanocomposites reflect the properties of all three phases (i.e. inorganic core, bulk polymer and interphase). By creating *well-dispersed* nanoparticle coatings, the bulk properties of the coating can be altered leading to the development of coatings that have very different properties than can be achieved by the addition of traditional macroscopic-sized fillers. Coatings can be made to be tougher, harder (or more flexible), lubricious (or skid-resistant), or heat and fire resistant by the careful addition of nanoparticles. "Smart Coatings" – coatings that have either multiple functionality or that respond in an orchestrated manner to changes in the coating environment – have been created from nanocomposites that are self-cleaning, ultra-hydrophobic, or resistant to corrosion and microbial attack.

The preparation of nanocomposites is actually centuries old; for example, nanoparticle impurities give stained glass its vivid and varied colors (*1*). However, the specific manipulation and preparation of nanoparticles with the express purpose of creating a nanocomposite – and measuring its properties – is a much more recent practice. Toyota first prepared a commercial nylon nanocomposite with nanosized clay with improved thermal resistance in the 1980's (*2-7*). Unfortunately, despite the widespread research on nanoparticles and nanocomposite formulation, few additional commercial products have resulted. One area that is showing significant potential for nanocomposite commercialization is coating applications. This is a result of several key technological advancements, the devotion of significant resources by large (and small!) coatings companies, and the innovation required for the introduction of new technology.

Perhaps the most significant scientific advancement in the development of nanocomposite coatings has been the understanding of the surface properties of nanoparticles and how those surfaces can be made to be compatible with various coating environments. In the last decade, surface engineering of inorganic nanoparticles has advanced to the point that it has become possible to tune the functional properties of nanoparticles – and in turn, modify the final bulk coating properties. Intermediate in size between molecules and bulk solids, inorganic nanoparticles offer the convenience of carrying out chemical modifications in solution while retaining the properties of the inorganic core. As such, surface modified inorganic nanoparticles are ideal materials for the production of nanostructured materials and nanocomposites. When the surfaces

of the inorganic nanoparticles are correctly designed, they can be fully dispersed into polymers and coatings, resulting in the formation of polymer nano-composites having exceptional thermal, mechanical and barrier properties. Finite Element Analysis shows that these properties are intimately tied to the degree of dispersion and the aspect ratios of the inorganic nanoparticles (8). Self-Consistent Field Theory modeling of surface engineered inorganic nanoparticles suggests that the surface density, oligomer length and the cohesive energy density of the organics attached to the surface of the inorganic nanoparticle are important factors to consider when seeking to improve the dispersibility of nanoparticles (9).

Surface modified nanoparticles can improve the mechanical and barrier properties of polymers and coatings. In addition, the nanoparticle surface can be tailored to impart specific property enhancements. At the most basic level, functional nanoparticles can be surface engineered both to facilitate dispersion into a host phase (e.g. a coating) and to carry the functional agent. Additional functions such as controlled or triggered release can also be designed into the surface modification. In this paper, we discuss the importance of engineering the surface of nanoparticles for the successful development of a nanocomposite coating. We will describe several tools to design surface engineered inorganic nanoparticles and the development of several types of functional nanoparticles. A specific example will be the use of surface engineered inorganic nanoparticles for corrosion inhibition.

Nanoparticle Surface Effects

One of the key features of nanoparticles is their large surface effects. Not only do nanoparticles have large surface areas, but their surface to volume ratios are large compared to conventional, macroscopic materials. For example, a 10 nm particle has approximately 20% of the atoms at the surface. In a 2nm particle, however, 80% of its atoms are surface atoms (10). The high percentage of surface atoms gives large surface energies to nanoparticles. Van der Waals forces dominate the small particle interactions, and lead to the aggregation of nanoparticles. These surface effects greatly influence the behavior of nanoparticles with a polymer host and with each other.

The attraction between nanoparticles is a major hurdle toward complete dispersion of nanoparticles and is one of the more significant barriers towards nanocomposite formation, reproducible properties and commercialization. Most nanoparticles require severe forces to disperse the particles down to the nanometer scale – and to keep them from re-aggregating. In the case of nanoclays, the layers of clay must be separated (exfoliated) by solvent swelling, in situ polymerization, and/or extensive mixing with high shear in a coating formulation or polymer melt (11). While current methods such as horizontal

bead mills and mixing media for coatings and batch mixers or twin-screw extruders for polymers can introduce enough shear to break down aggregates of nanoparticles (*12*), these methods have several drawbacks. This physical mixing is usually not sufficient to achieve full dispersion of nanoparticles. If the system is relatively mobile (i.e., an uncured coating or a polymer melt), there is nothing to prevent the nanoparticles from re-aggregating.

In order to prepare and benefit from a nanocomposite, the individual nanoparticles need to be fully dispersed and kept segregated down to the nanoparticle scale. This can be accomplished either physically (by "locking in" nanoparticles in a coating by fast application and rapid cure after high shear mixing) or chemically (by modifying the surface of the nanoparticles to prevent them from being attracted to each other). The chemical method offers a wide variety of chemistries and techniques, and can be incorporated into the nanoparticle preparation. Chemical modification of nanoparticles typically refers to the attachment, either by a covalent chemical bond or by the electrostatic or hydrogen bonding forces of surfactants, of organic groups to an inorganic nanoparticle core.

These surface groups prevent the nanoparticles from grouping together by reducing the effect of the nanoparticle surface energies, by providing a steric "bumper" to keep distances between nanoparticles, and by making the nanoparticles more compatible with the host polymer. All of these effects help to increase the attraction between the polymer and the nanoparticles and to stabilize the nanoparticles as discrete particles. The dispersion of nanoparticles in the coating is necessary to achieve a nanocomposite.

The Interphase

Without the separation and dispersion of nanoparticles, the result is larger aggregates of nanoparticles to create larger particles. Larger particles have much lower surface energies, and are similar to the dispersion of standard filler additives. It has been proposed that nanoparticles give their novel property improvements by modifying a host resin in the area directly in contact with the nanoparticle (*13*). Called the "interphase", this area of influence is greater for large surface energy nanoparticles – as long as the nanoparticles are well dispersed. Most nanocomposite properties depend on the full dispersion of nanoparticles and the maximization of the interphase region. When the interphase region comprises a significant portion of the final coating, the bulk properties of that coating can be altered.

Large, macroscopic fillers and coating additives actually produce smaller interphase regions. The overall effect is an additive one, with the final coating properties a combination of the host resin, the interphase and the additives themselves. Examples of standard coating fillers in this area are pigments, reinforcing agents, and flatting agents. Even nanoscale materials like TiO_2 and
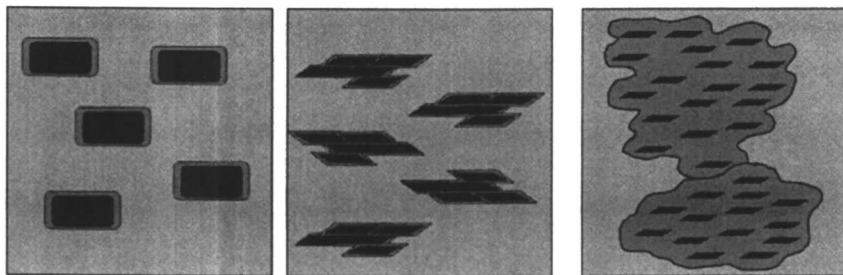
Figure 1. The interphase region of a nanocomposite is formed when nanoparticles are well dispersed. The first image represents large particles and small interphase regions. The middle image represents poorly dispersed nanoparticles, also with small interphase regions. The last image displays well dispersed nanoparticles and large interphase regions.

$CaCO_3$ behave like larger particles if they are used at high loadings. As the concentration of particles increases – even in the case of nanoparticles – the aggregation and collection of particles increases as well. These aggregates then act as larger fillers, and any nanoscale effects become negligible.

Technical Design Factors

As the number and type of commercially manufactured and available nanoparticles increases, so do the various design factors for nanoparticle surface modification. Nanoparticles are available in several morphologies, most commonly spheres and platelets. Elliptical and rod-shaped nanoparticles are also available. Nanoparticles can be made with metals or metal oxides, inorganic compounds of group V and VI (oxides, nitrides, sulfides, selenides, etc.), and carbon-based materials like nanotubes and fullerenes. Organic nanoparticles are also well known, including polymers and biomaterials. These nanoparticles have inherent chemistries related to their composition and surface and/or edge effects. Suitable surface modifications are those that match the nanoparticle surface chemistries with appropriate organic surface modifying groups.

The influence of the aspect ratio of nanoparticles has received much attention as well (*14*). Spherical nanoparticles, while plentiful, don't often add significant barrier or structural properties to a nanocomposite from their small aspect ratio alone. However, these nanoparticles are easier to disperse, and are often used to improve hardness or scratch resistance. More interesting results have been found from platelet or rod-shaped nanoparticles. Barrier properties are commonly investigated in nanocomposites, and improved barrier materials

can be prepared by well-dispersed, high aspect ratio (analogous to individual playing cards instead of a deck of cards) nanoparticles which slow down the permeation of small molecule permeants such as O_2, CO_2, N_2, and water vapor. The best properties have been achieved with platelet-shaped nanoparticles (*2, 14, 15*). While many have predicted that larger aspect ratios are necessary for significant barrier improvements, some evidence exists for a trade-off between aspect ratio and a maximization of the interphase area due to careful control of the nanoparticle surface (*16, 17*). This doesn't *have* to be a trade-off if careful control of the surface chemistries of nanoparticles is achieved.

Predictive modeling research from the Balazs group has studied the interaction of nanoparticles and polymer domains at surfaces (*18, 19*). Recently, the group found that nanoparticles in polymer melts should aggregate selectively in nanoscale scratches or other surface defects when a polymer nanocomposite is placed over a more brittle, crack-prone surface. This migration of nanoparticles was suggested to occur by entropic depletion of the nanoparticles from the polymer phase. This concept could lead to the development of "self healing" coatings or nanocomposites that repair scratches and cracks by pushing nanoparticles into them. Nanoparticle morphology and aspect ratio were also examined, and rod-shaped nanoparticles were predicted to show better packing in defect sites because of their greater attraction to the scratch surfaces.

The range of surface modification strategies is often limited only by the researcher's imagination. A wealth of surface chemistry is available from the surfactant literature, which can be supplemented by ion exchange methods, self-assembled materials (polyelectrolyte layering, for example), and the addition of small molecules to the particles by covalent or ionic bonding. Many of these groups can be added during nanoparticle manufacturing, but numerous techniques are available for surface modification after nanoparticle production.

Nanoparticle modification should also consider the desired final outcomes for the nanocomposites in preparation. The size, shape, and chemical properties (i.e., solubility parameters, additional reactive groups) of the surface groups all produce different results (Figure 2). The addition of short and long organic chains has the capacity to alter the physical nature of a coating or polymer by altering glass transition temperatures (T_g), storage and loss moduli, flexibility, and load transfer. High and low surface densities can be critical for dispersion in organic materials. The dispersibility and solubility of nanoparticles can be intelligently adjusted by choice of surface groups. Additionally, the presence of additional reactive groups can allow the nanoparticles to be crosslinked into an appropriately curing coating for increased stability or durability.

Surface Modified Nanoparticle Components

Numerous types of nanoparticles are available, and many of them are inorganic and hydrophilic. Unfortunately, many thermoset coatings resins and
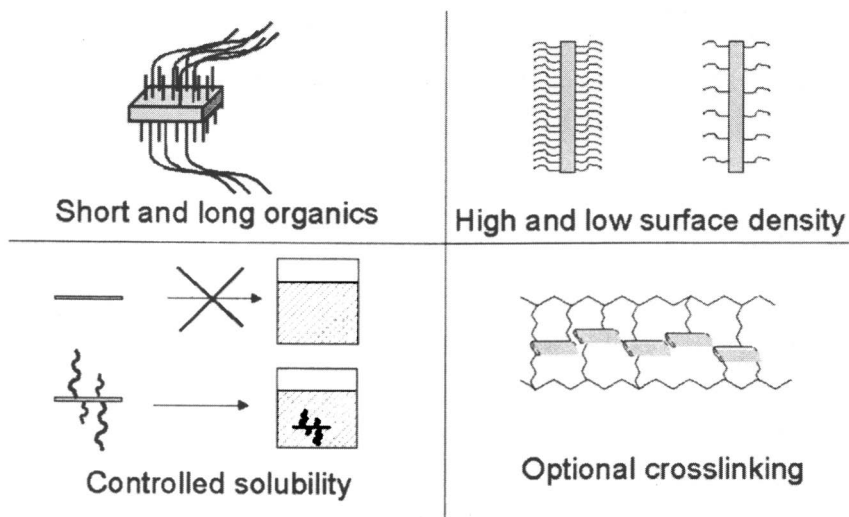
Figure 2. Various ways to modify a nanoparticle.

thermoplastic polymers are hydrophobic, leading to an inherent incompatibility between nanoparticle and host polymer. "Like dissolves like" says the old chemistry adage, and careful design of the surface groups can make an incompatible, hydrophilic nanoparticle compatible with a hydrophobic polymer.

As mentioned previously, the chemical nature of these nanoparticles needs to be paired with the surface groups that are to be added to the nanoparticle surface. To borrow from surfactant terminology, the "head" or primary reactive group responsible for attaching to the nanoparticle needs to have the right chemical properties in order to attach selectively to the nanoparticle surface (Figure 3) The head is the linkage between the inorganic nanoparticle core and the organic surface groups. Many different types of reactive groups are available for bonding to nanoparticles, including alcohols, acids (including carboxylic, phosphonic, and sulfonic acids), amines, thiols, anhydrides, and quaternary ammonium cations to name only a few.

The "body" is the primary feature of a surface modifying group that gives the new surface modified nanoparticle its new solubility and dispersibility features. The body has to be connected to the head for attachment to the nanoparticle. This can be accomplished by selecting a single compound that can contain both the head and the body (like stearic acid, a compound used as a surface modifying agent for many particles, nanoscale and larger). Additional modification can be carried out if the head portion contains a second reactive group (*20, 21*). This second reactive group can be the basis for the addition of a

"second generation" of surface modifying groups. Additional layers of surface groups can be added that were (a) incompatible with the nanoparticle core (b) did not contain a suitable reactive group to attach to the nanoparticle or (c) contain additional functional groups for further reactions (like crosslinking). The body protects the nanoparticles from agglomerations, and can shield the nanoparticles from reacting or separating from a host resin or extreme environment (i.e., in a polymer melt).
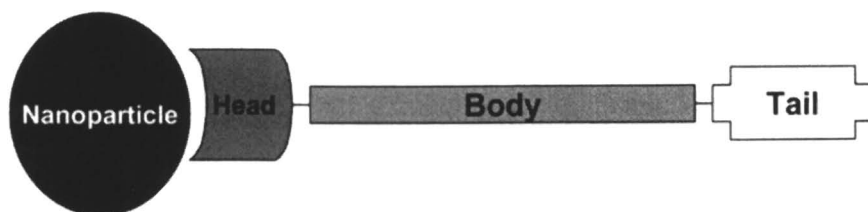
Figure 3. Representation of the various parts of a surface-modified nanoparticle (not to scale).

The "body" is the primary feature of a surface modifying group that gives the new surface modified nanoparticle its new solubility and dispersibility features. The body has to be connected to the head for attachment to the nanoparticle. This can be accomplished by selecting a single compound that can contain both the head and the body (like stearic acid, a compound used as a surface modifying agent for many particles, nanoscale and larger). Additional modification can be carried out if the head portion contains a second reactive group (20, 21). This second reactive group can be the basis for the addition of a "second generation" of surface modifying groups. Additional layers of surface groups can be added that are (a) incompatible with the nanoparticle core (b) did not contain a suitable reactive group to attach to the nanoparticle or (c) contain additional functional groups for further reactions (like crosslinking). The body protects the nanoparticles from agglomerations, and can shield the nanoparticles from reacting or separating from a host resin or extreme environment (i.e., in a polymer melt).

Finally, a "tail" can add a final functionality to the surface groups. Many times, this tail can be a reactive group or a traditional polymer additive. By attaching these compounds to a nanoparticle (through the head-body-tail connection), one can achieve interesting properties like permanence and stability. Corrosion inhibitors, biocides, and colorants have all been added to nanoparticles as the "tail" portion, with greater retention of those additives in a coating (22).

Applications of Surface Modified Nanoparticles in Corrosion Protective Coatings

The future direction of protective coatings includes the development of responsive coatings (also called smart or intelligent coatings). Responsive corrosion inhibiting coatings with smart corrosion inhibitors that incorporate the corrosion inhibitor into a delivery system whose release is triggered by some aspect of the corrosion phenomena or by the formation of coating defects. Triggers can be mechanical (e.g. impact damage or microcracks formed by mechanical or thermal stress), electrochemical (e.g. the potentials developed by the corrosion cells at the metal surface) or chemical (the presence of corrosion products such as hydrogen, hydroxide or metal salts).

Chromate conversion coatings are excellent models for a chemically triggered smart corrosion inhibiting system. Detailed experimental studies of chromate conversion coatings show that they are comprised of a porous chromium (III) hydroxide sol-gel onto which chromium (VI) anions (CrO_4^{2-}) are chemically bound. At low pH (the conditions under which the chromate conversion coating is formed) the chromate anion is bound to the porous Cr(III) hydroxide matrix.(Figure 4) At higher pH the chromium (VI) anion is released. Thus the chromate conversion coating is an example of a chemically triggered release of a corrosion inhibitor.

Over the last decade a number of new responsive corrosion inhibiting coatings have been developed that fit either in the chemically triggered or the electrochemically triggered categories. In addition, a number of new responsive corrosion inhibiting coatings have also been designed around microcapsules filled with corrosion inhibitors that release their contents when the capsules are damaged by mechanical damage to the coating. These coatings are part of a trend towards stimulus-response coatings. By stimulus-response coatings we mean coatings that release corrosion inhibitors in response to a specific stimulus.
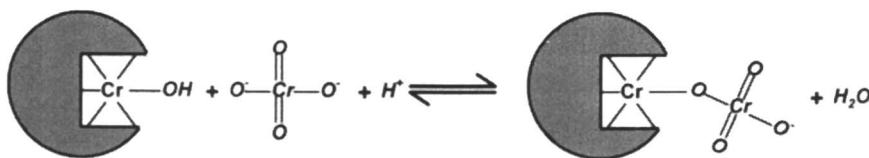
Figure 4. Model of storage and release of CrO_4^{2-} from chromate conversion coatings (23)

Thus, these coatings do not include materials that have been designed to change the rate of release of the corrosion inhibitor (e.g. plasma treated triazole (*24*), anion embedded sol gel films (*25*), cation embedded sol-gel films (*26*) or hybrid sol-gel films (*27*). Most of the developments in new stimulus-response

corrosion inhibiting coatings use one of the following three triggering mechanisms; galvanic de-doping of intrinsically conducting polymers (*28-30*), mechanical damage of microcapsules (*31, 32*) and pH change. The latter materials are discussed below.

Coatings Operating by pH Triggered Release

Corrosion of metals is electrochemically driven by two half-cells. The anodic half-cell is oxidation of the metal. The cathodic half cell is either reduction of oxygen

$$O_2 + 2H_2O + 4e^- \rightarrow 4OH^- \qquad (1)$$

or the reduction of water

$$2H_2O + 2e^- \rightarrow H_2 + 4OH^- \qquad (2)$$

Either cathodic half cell reaction involves the formation of hydroxide that raises the pH around the cathode. This increase in pH has been widely used as a triggering mechanism for the release of corrosion inhibitors. Kelly and coworkers (*33*) studied inhibitor storage, release, transport, and corrosion inhibition using a computational Finite Element Analysis framework whose goal was to identify parameters that would provide assistance in the design and development of triggered release corrosion inhibiting coating systems. The pH-dependence of the inhibitor release rate was found to be the most important parameter controlling system performance. Thus, it is not surprising that a common thread (i.e. pH triggered release of corrosion inhibitors) underlies the development of many new corrosion-inhibiting systems. Systems for triggered release of corrosion inhibitors range from anion- and cation-exchanged clays, polyelectrolyte coated silica nanoparticles, organically modified sol-gels, and nanoparticles surface-modified using covalently bonded organic corrosion inhibitors (*33*). Most of the pH-triggered corrosion inhibitor delivery systems are based on nano-sized materials or materials having nanosized features. Examples of these materials are described below.

Hydrotalcite and Related Materials

Hydrotalcite and montmorillonite are both sheet-like clays having layered crystal structures. It has long been known that these materials could undergo ion exchange, forming nanosized galleries. More recently these materials have been exchanged with corrosion inhibiting anions and cations (hydrotalcite is anion-exchangeable and montmorillonite is cation-exchangeable). Hydrotalcites have

a general composition of $MII_{1-x}MIII_x(OH)_2An^-_{x/n} \bullet yH_2O$ where MII and MIII are divalent and trivalent metal cations and An⁻ is an n-valent anion, respectively. At temperatures of approximately 300°C to 500°C, hydrotalcite-like compounds are decomposed to form mixed oxides of MII and MIII metals. In aqueous solutions, a rehydration of these mixed oxides takes place, which is accompanied by recovery of the layered hydrotalcite structure and incorporation of the anions from solution into the interlayers. Worsley and McMurray (*34*) showed that hydrotalcites anion-exchanged with chromate anions (CrO_4^{2-}) and incorporated into a poly(vinylbutyral) coating applied to Al2024-T3 panels provided excellent resistance to filliform corrosion.

The presence of chloride or hydroxide anions triggers the release the corrosion inhibiting anions that are intentionally exchanged into the interlayer galleries of hydrotalcite. Removal of chloride ions from the salts percolating through the coating is expected to improve the corrosion resistance of the coatings since chloride ions promote anodic dissolution by allowing the formation of highly soluble metal salts. In addition to CrO_4^{2-} anions other corrosion inhibiting anions such as molybdate (MoO_4^{2-}), vanadate (VO_3^-) and permanganate (MnO_4^-) have been exchanged into hydrotalcites and have shown good corrosion inhibiting performance. Finally, organic anions (e.g. the anion of 2,5-dimercapto-1,3,4-thiadiazole, DMcT) have also been exchanged into the hydrotalcite galleries (35). 2,5-Dimercapto-1,3,4-thiadiazole is a strong inhibitor of the oxygen reduction reaction on the copper cathode sites in Al/Cu alloys such as Al-2024-T3. Thus when DMcT-hydrotalcite is incorporated into a primer and anion release is triggered by high pH, the DMcT shuts down the cathodic half cell thereby stopping corrosion. Hydrotalcites ion-exchanged with corrosion inhibiting anions have been evaluated as both pigments and as conversion coatings grown on the metal substrates.

Hybrid Sol-Gels

Organically doped/organically modified sol-gel materials have seen wide application as carriers, encapsulants and delivery systems for a wide range of inorganic and organic molecules over the last 30 years (*36*). Organic modification of sol-gel materials is a convenient way of controlling/modifying the material properties of the sol-gel materials. Thus it is not surprising that numerous applications of organically doped/organically modified sol-gel materials have been developed for corrosion control. Vreugdenhil and Woods (*37*) have recently demonstrated pH release in hybrid silica sol-gel that could have potential as a triggered release corrosion inhibiting pigment. Tetramethoxysilane, 3-glycidoxypropyltrimethoxysilane and methyltrimethoxy-silane were hydrolyzed in the presence of diethylenetriamine (a cross-linker) and methyl orange. The latter material was a molecular probe to demonstrate pH triggered release. Studies over a pH range of 2-12 showed pH triggered release

at high and low pH, and minimal release at intermediate pH. It determined that electrostatic interactions between the dye and the matrix, and not decompostion of the sol-gel, were the mechanism for the pH triggered release. Thus, this organically modified sol-gel approach could easily be extended to the release of corrosion inhibitors.

Supported Polyelectrolyte Layers

Layer-by-layer (LbL) deposition of oppositely charged species (e.g. polyelectrolytes, nanoparticles, enzymes, dendrimers, etc.) from solutions onto solid substrates represents an interesting approach to prepare reservoirs with regulated storage/release properties. LbL-assembled polyelectrolyte multi-layers have been shown to have controllable permeabilities that can be modified by changing pH, ionic strength or temperature. Shchukin and coworkers (38) have modified silica nanoparticles using a LbL deposition of poly(ethyleneimine) and poly(styrenesulfonate). Silica nanoparticles have a negative surface charge so the surface is first decorated by deposition of the positively charged poly(ethyleneimine). Deposition of poly(styrenesulfonate) follows and the procedure is repeated to build up the surface coating. Benzotriazole (a well known corrosion inhibitor) is incorporated with the poly(styrenesulfonate) layers. The resulting nanoparticles are mixed with zirconia/silica sol-gels and applied to the surface of Al-2024-T3 panels. Defects were introduced into the coated panels using a sharp needle and both electrochemical impedance spectroscopy and scanning vibrating electrode techniques showed evidence of self-healing. The coatings exhibited self-healing (e.g. reduction in corrosion currents) that was triggered by pH increase in the vicinity of the defects. The increase in pH leads to distortion in the polyelectrolyte layers, destabilizing the poly(styrenesulfonate)/benzotriazole complex and thereby releasing the benzotriazole corrosion inhibitor.

Surface-Modified Boehmite Nanoparticles

As mentioned previously, the standard method of providing active corrosion protection to a protective coating is the use of sparingly soluble corrosion inhibiting pigments. Upon migration of water through the coating, the corrosion inhibiting pigment dissolves reaching a limiting concentration defined by its solubility product. The preceding overview of stimulus-response coatings indicates that development of stimulus-response corrosion inhibitors combines a reactive structure (e.g. conducting polymers, microcapsules, sol-gels, clays, etc.) with an inorganic/organic corrosion inhibitor that can be released by external triggering agents/forces acting on the reactive structure. We have been following a similar path to development of smart corrosion inhibiting additives. In our

approach, nanoparticle surfaces are modified with covalently bound organic corrosion inhibitors. The bonding between the organic corrosion inhibitor and the nanoparticle surface is accomplished through a carboxylate bond. At high pH (above pH 9) the bond between the nanoparticle surface and the organic corrosion inhibitor is broken releasing the corrosion inhibitor

Nanoparticles (materials having at least one dimension between 1 nm and 100 nm), because of their high surface areas and high surface to volume (S/V) ratios, are attractive materials for the storage and release of corrosion inhibitors. One distinguishing characteristic of nanometer-scale structures is that, unlike macroscopic materials, they typically have a high percentage of their constituent atoms at the surface. The volume of an object ($V \propto l^3$, where l is the characteristic length) decreases more quickly than its surface area ($S \propto l^2$). Thus as particle size diminishes the surface to volume ratio scales as $S/V \propto l^{-1}$. This scaling behavior means that for nanomaterials at the smaller length scales most of the atoms are surface atoms. While the structure and chemical composition within macroscopic materials determine most of their physical properties (e.g., thermal and electrical conductivity, hardness, and plasticity) the physical properties of nanostructures depend to a much greater extent on their surface and interfacial environment.

Thus the surface plays an important role in the properties of nanoparticles, including the solubility, reactivity, stability, melting point, and electronic structure. The surface of the nanoparticle is also its interface with the external world. Surface modification of nanomaterials can influence not only the physical/chemical properties of the nanoparticle but, in addition, the surface modifications can mediate the interaction of the nanoparticle with the environment.

Economic and Chemical Aspects of Boehmite Nanoparticles

The design of smart corrosion inhibiting additives involves satisfaction of multiple criteria often with conflicting constraints. Among these criteria are the composition, size shape and surface chemistry of the nanoparticles. These properties influence interaction of the additives with the coating from the manufacturing/formulation of the coating to its final properties. Affected properties include thixotropic rheology, pot life, barrier properties, adhesion to the metal surface and long term coating stability. In addition, raw materials costs, synthesis costs, and the labor/equipment costs for applying the coating to the metal surface will have a strong impact on the successful development of smart corrosion inhibiting additives. For example, coatings for Navel ships cost $15 to $25 per gallon and are applied with coating thicknesses up to 5 mils thick. Aerospace coatings are much thinner (~1-2 mils) and cost up to $80 per gallon. Thus, smart corrosion inhibiting coatings for large steel surfaces are more constrained by price than aerospace coatings for Al/Cu alloys.
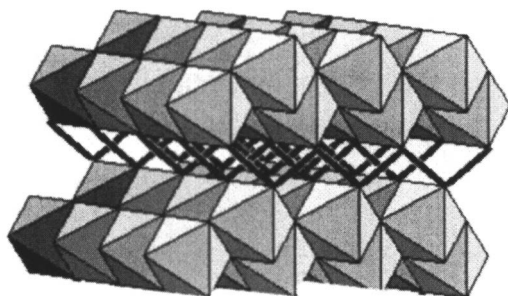
Figure 5. Crystal structure of boehmite

Thus, in the process of designing a smart corrosion inhibiting nanoparticle additive we looked at a number of criteria. First, we looked at materials that were available in large quantities at relatively low costs. Then we looked at availability in various shapes. Nanomaterials with high aspect ratios (e.g. platelets) offer the possibility of improving the barrier properties of coatings by increasing the path tortuosity of water and salt migration through the coating. Finally, we also looked at the potential for a wide range of surface chemistries to modify the nanoparticle surface. To keep costs low, it must be possible to modify the nanoparticle surface with commodity chemicals and in addition use existing organic/inorganic corrosion inhibitors in their available forms to avoid additional costs associated with chemical modification of the corrosion inhibitors. One material that met the above criteria was an oxyhydroxide of aluminum known as boehmite.

Boehmite (Al(O)OH) crystallizes in a hexagonal close packed arrangement of hydrogen bonded oxides built up of edge sharing $AlO_4(OH)_2$ or $AlO_3(OH)_3$ units. In boehmite the Al^{3+} ions exist in a distorted edge-sharing octahedral array of oxide ions that forms a double layer with the layers being connected by zig-zag chains of hydrogen bonds (Figure 5)(*39*).

Boehmite is produced in commercial quantities by one of two processes. So-called on-demand syntheses react aluminum metal (scrap or otherwise) with an alcohol (e.g. hexanol) to form the aluminum alkoxide and hydrogen. Subsequent reaction of the aluminum alkoxide with water forms boehmite and the alcohol is recovered. The largest quantity of commercial boehmite is, however, produced as a co-product of surfactant synthesis. An alloy of aluminum with titanium is reacted with ethylene and hydrogen forming an aluminum alkyl ($Al(CH_2)_xCH_3$, x = 12-18). Subsequent reaction of the aluminum alkyl with water and oxygen forms the linear alkyl alcohols (e.g. $CH_3(CH_2)_xOH$, x = 12-18) plus boehmite. Boehmite production volume by this process is approximately forty million pounds per year. Boehmite sols are widely used to prepare high surface area supports for catalyst applications. The

availability of boehmite and its numerous market applications means that its cost is relatively low ($1-$2/lb). Thus from a cost viewpoint boehmite is cheap enough to be used in a wide range of coating applications.

Boehmite Nanoparticles as a Smart Delivery System for Corrosion Inhibitors

The next question we addressed was whether surface-modification of boehmite could be carried out, and if so, could it be done in a cost effective manner. Literature surveys identified that boehmite could be surface-modified by heating with carboxylic acids. Barron and co-workers (40) reported that heating the boehmite agglomerates with an organic acid in xylenes over a period of several days to a week followed by multiple ether washes of the resulting materials resulted in the formation of surface modified boehmite nanoparticles. Similarly, heating the boehmite in a pure (liquid) acid could also be used to prepare the surface modified boehmite. Unfortunately, both of these methods involved considerable time and generated significant waste streams.

One of the primary uses of boehmite is as a catalyst support in automotive catalytic converters. A boehmite sol is prepared and the sol is used to coat the honeycombed surface of the catalytic converter. Calcination above 500°C results in conversion of the boehmite to a high surface area γ-alumina support. The commercial boehmite used in this process is available as 50-100 μm agglomerates. The preparation of catalyst support coatings involves formation of boehmite sols by dispersing boehmite in water with a strong acid (e.g. nitric acid) (41). This suggested that it may be possible to disperse boehmite in water using sub-stoichiometric amounts of organic acids. Acrylic acid was a natural choice as a dispersing/functionalizing acid. Many corrosion inhibitors possess amines or carboxylic acids as functional groups. Both primary and secondary amines undergo Michael Addition with conjugated double bonds. In addition, the pKa of acrylic acid (pKa = 4.26) is between those of acetic acid (pKa = 4.76) and formic acid (pKa 3.75); both could be used to disperse boehmite agglomerates to a stable aqueous sol. Thus we anticipated that we could surface modify boehmite in water using acrylic acid.

A commercial form of boehmite (Catapal, supplied by Sasol, NA) was therefore added to water with stirring to make a thick slurry and then acrylic acid was added to the aqueous slurry. More water was then added to the thick slurry to reduce the solids content to ~15-20% and the mixture heated to 80°C. The mixture was maintained at this temperature overnight and then cooled to room temperature. Using many physical and instrumental characterization methods we showed that the resulting material was a boehmite nanoparticle (approximately 40nmx40nmx2.5nm) whose surface was covered with covalently bonded acrylic acid (Figure 6). Both solid state multi-nuclear NMR studies and Density Functional Theory calculations support the bonding mode shown in

Figure 6 (*42*). The surface areas of the organically modified boehmite nanoparticles are in the range of 250 to 300 m^2/g and are thus excellent carriers for surface anchored organics to be incorporated into paints.

Figure 6. Covalent bond between boehmite and acrylic acid.

Many other carboxylate surface modified boehmite nanoparticles have been prepared after we demonstrated that mild conditions (e.g. atmospheric pressure, low temperatures (80°C) and water or water/alcohol solutions) could be used to prepare the surface modified boehmite particles (*20,21*). Since many organic corrosion inhibitors are carboxylates, this allowed us to prepare a nanoparticle carrier for corrosion inhibitors. However, there are a number of effective organic corrosion inhibitors that are based on amines and thiols. Therefore, to expand the number of corrosion inhibitors that could be carried by the boehmite nanoparticles it was necessary to identify additional surface modification techniques for the carboxylate-surface modified boehmite nanoparticles.

An important reaction in organic chemistry is the Michael-type addition, e.g.

(3)

(where Z = CHO, COR (including quinones) COOR, CONH$_2$ CN, NO$_2$ SOR, SO$_2$R). Under basic conditions a proton is removed (e.g. Z-CH$_2$-Z' → (Z-CH-Z')-) and the resulting nucleophile adds to the activated double bond. Michael-type reactions are not limited to carbon-type nucleophiles but can also be carried out with amine (-NH-) and thiol (-S-) nucleophiles.

Initial experiments thus involved dispersing the acrylate-surface modified boehmite into water and then increasing the pH using base. Unexpectedly, the boehmite precipitated out of solution. Centrifugation and subsequent thermal

gravimetric analysis showed that the acrylic acid had been stripped from the boehmite under basic conditions. The experiment was then retried using neutral to acidic conditions with an organic amine. To our initial surprise, the amine underwent Michael Addition to the surface-anchored acrylic acid. Calculations carried out at TDA Research, Inc. using Density Functional Theory show that attaching the acrylic acid to the boehmite surface removes electron density from the double bond thereby activating the anchored double bond to nucleophilic attack. Later experiments showed that thiols could also be added to the surface anchored acrylate. Since most organic corrosion inhibitors are weak acids (carboxylates, amines or thiols), weak bases (aromatic amines) or their derivatives, surface chemistry allowing to be anchored to the boehmite surface opened up the use of boehmite nanoparticles as carriers for a wide range of corrosion inhibitors.

The effectiveness of organic corrosion inhibitors can be correlated to the extent of their hydrophobic surface area and the placement of their electron rich centers. Organic corrosion inhibitors are generally most effective if they can form tenacious films on sites that drive either the anodic or cathodic corrosion half cells, thereby suppressing the cathodic reaction (e.g. oxygen reduction or hydrogen evolution) or the anodic reaction (metal dissolution). Because film formation is an adsorption process, the effectiveness inhibitors depends on their chemical composition, their molecular structure, their affinity for the metal surface along with inhibitor concentration and temperature. However, the strength of the adsorption bond formed between the organic corrosion inhibitor and the metal is the dominant factor determining the performance of soluble organic inhibitors. This generally means those chemical structures that form strong and/or multiple bonds with the metal will be the most effective organic corrosion inhibitors.

Unfortunately, the types of functional groups that form strong bonds to the metal surfaces (e.g. carboxylates, amines thiols, etc.) are also the types of functional groups that react with the functional groups (e.g. epoxies and isocyanates) that are commonly used to form corrosion protective coatings. This means that the most effective organic corrosion inhibitors can be trapped in the thermoset polymer by reaction with the coating resins and therefore would not be available for corrosion protection.

By "hiding" the functional groups temporarily through attachment to a nanoparticle surface, carboxylates, amines and thiols can be incorporated into a thermoset coating. In this form the reactive groups are protected from reaction with the curing paint. However, such materials would not be of much use if the organic corrosion inhibitors were not free to migrate through the coating, adsorb on the active corrosion site and thus stop corrosion. For surface modified boehmite nanoparticles the bond between the boehmite nanoparticle and the carboxylate anchoring group is broken under basic conditions (pH >9). If the carboxylate anchored group is a corrosion inhibitor then basic conditions trigger the release of the corrosion inhibitor from the boehmite surface (Figure 7). This

pH triggered release is the basis of the stimuli-response corrosion inhibitor technology.
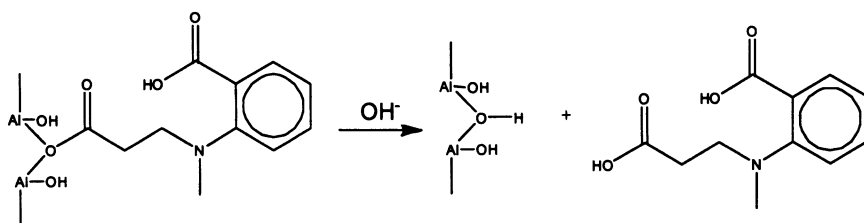
Figure 7. Release of a corrosion inhibitor from a boehmite nanoparticle surface.

For most organic polymer coated (e.g. epoxy) metals in an air/water vapor environment, the corrosion cell consists of the oxidation of the metal (anode) and reduction of oxygen (in the presence of water) to form hydroxide anions (cathode). Hydrogen evolution at the cathodic half cell also generates hydroxide. In either case the cathodic corrosion cell generates highly basic conditions thereby promoting the base-triggered release of the attached corrosion inhibitor from the boehmite surface.

Corrosion Inhibiting Boehmite Nanoparticles for Al/Cu Alloys.

The core material of the releasable corrosion inhibitor technology discussed in this paper is commercially available boehmite (Catapal) produced by Sasol North America (formerly Condea Vista). The initial chemical modification of the boehmite surface is carried out by heating acrylic acid (8:1, Al:Acid) with boehmite in water at 80°C. The resulting material was then spray-dried to form a free flowing white powder. The acrylate-modified boehmite nanoparticles were then dispersed into a 50:50 mixture of water and ethanol and heated to 80°C. In one example of attaching a corrosion inhibitor to the surface modified boehmite nanoparticles, a heated ethanol solution of 6-amino-benzothiazole is added drop wise to the dispersion of the acrylate-modified boehmite nanoparticles. Benzothiazoles are well known corrosion inhibitors for copper and bond strongly to copper surfaces forming insoluble films. The resulting surface-modified-boehmite corrosion inhibitors are then spray-dried to form a powder that could be added to the epoxy side of a two-component epoxy primer.

To test the surface modified boehmite nanoparticles for corrosion protection, Al-2024-T3 panels with an Alodine 1200S conversion coating were used as substrates. For one set of coatings the amino-benzothiazole/acrylate

surface modified boehmite nanoparticles were incorporated at 10 wt% into the epoxy side of a two-part epoxy primer using zirconium oxide mini-media and a Cowles blade and then mixed with a polyamide curative. The resulting paint was applied to the cleaned and degreased panels using a HVLP spray gun. A second set of panels was coated with an $SrCrO_4$ loaded (10 wt%) epoxy primer that was also applied using a HVLP spray gun. The coatings were evaluated using the ASTM- B117 salt fog test.

The ASTM- B117 salt fog test is an aggressive, accelerated corrosion test that involves attacking the coatings with a high-humidity, high-temperature (95°F) fog containing sodium chloride. Chloride ions are especially aggressive corrosion agents since they form soluble complexes with most metals, allowing the corrosion products to be removed from the corrosion site thus promoting new metal sites for corrosion. This provides a 'fresh site' for corrosion to continue. The salt fog tests were carried in an Atotech salt fog chamber. Figure 8 shows the comparison of the 10 wt% nanoparticle-inhibited epoxy coating against the 10-wt% chromated inhibited epoxy (both on Al-2024 panels) for a 2000-hour salt fog test. The benzothiazole modified nanoparticle additives performed exceptionally well in epoxy coating during the 2000-hour salt fog tests. The corrosion inhibiting nanoparticle additives did not have any underfilm corrosion or blistering, although we did see some darkening in the scribe. The control coating (Alodine 1200 conversion coating but no chromate pigment in the epoxy) showed significant corrosion in the scribe as did a commercial non-chromate corrosion inhibiting pigment.

Corrosion Inhibiting Boehmite Nanoparticles for Cold-rolled Steel

The corrosion of steel has widespread economic and environmental effects. About 40% of U.S. steel production goes to replace corroded metal parts and consumer goods. Corrosion of steel also has a significant impact on the environment. Structures such as storage tanks, pipelines, ships, railcars, and tanker trucks, which store and/or transport hazardous materials are frequently damaged by corrosion and leak their contents into the environment. The temporary shutdown of oil transport from BP's Prudhoe Bay terminal is a recent example of the effect corrosion on the economy (42).

Chromates have been effective corrosion inhibitors for steel and are often used to seal zinc-phosphate coated cold rolled steel. For environmental reasons (as previously discussed) zinc phosphate inhibitors are used instead of chromates in epoxy primers for steel. However, zinc phosphates perform nowhere near as well as chromates. With zinc phosphate inhibitors, primers are replaced more frequently and thicker coatings are often applied. Both options have their own environmental impacts, including increased emissions of volatile organic compounds (VOCs) and generation of more solid waste. Further, frequent repainting uses more paint and additional labor is involved in surface

preparation and repainting. Thus improved corrosion inhibiting additives for steel structures are also desired.

A survey of the corrosion inhibitor literature for steel showed that anthranilic acid is a very good corrosion inhibitor. Therefore we use the Michael Addition reaction to adduct the anthranilic acid to the acrylate-surface modified boehmite. The nanoparticles were incorporated into a Sherwin Williams commercial two-component epoxy coating (V93V227/E90H226). Currently, zinc phosphates are used as the corrosion inhibitor in this coating. At thin coating thicknesses (1.5 mil of less), with only the zinc phosphate corrosion inhibitor, this coatings has poor long-term corrosion protection efficiency.

Thus we evaluated enhancing the corrosion performance of a zinc-phosphate based epoxy primer with a releasable corrosion inhibitor. The nanoparticle corrosion inhibitor was incorporated at 2.4 wt% loading (based on total formula weight of Part A (epoxy component)). The zinc phosphate was used at its current loading in the commercial paint, 4.4 wt%. All samples were compared to the commercial formulation that contained only the zinc phosphate corrosion inhibitor (as a positive control) and a formula with no corrosion inhibitors (as a negative control). Additional talc pigment was added to the negative control to maintain the same total pigment volume concentration (PVC). Coatings were applied to Bonderite 952-P60 steel panels with chrome seal and DI rinse. The nanoparticles were dispersed in the epoxy component of the two-part epoxy primer. Using a Cowles blade and mini-media (1-2 micron zirconia pellets) during the grind allowed us to disperse the nanoparticles into the epoxy component to a Hegman Fineness of grind of 5-7.

The coatings were sprayed out according to the manufacturer's instructions using a high-volume low-pressure (HVLP) paint sprayer and allowed to cure for 24 hr at room temperature and 50% relative humidity. The samples were then cured in a 140°F convection oven overnight. Before being loaded into the salt fog chamber the samples were scribed per ASTM method B-117. Scribe thickness was a generous 0.075 mm (3 mil) and coating thicknesses were around 1.5 mil.

As with the Al-2024 panes, the coatings were screened for corrosion resistance using ASTM method B-117. Improvement in the corrosion protection was provided by using anthranilic acid with zinc phosphate. This combination was significantly better than the zinc phosphate alone, or with the nanoparticle anchored anthranilic acid inhibitor alone. At 500 hours the combination showed significantly less rusting and blistering in the scribe. There are also no blisters under the coating. The control panels show a large amount of corrosion in the scribe and undercoating of the scribe.

Future directions in this area will involve evaluations of release of multiple organic corrosion inhibitors to take advantage of potential synergies when combinations of corrosion inhibitors are used together (44).

In summary, surface-modified boehmite nanoparticle whose surfaces are decorated with releasable organics are attractive delivery systems for organic
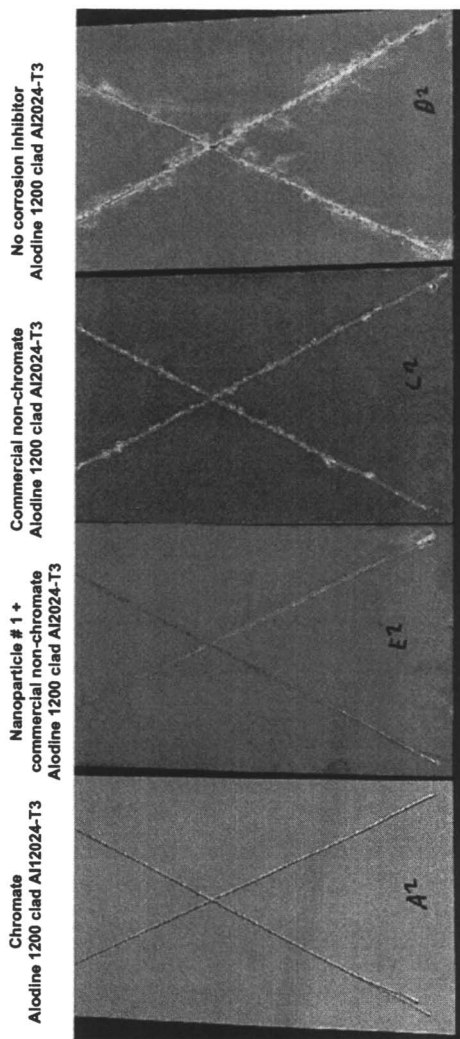
Figure 8. Comparison of chromated and nanoparticle inhibited epoxy primers
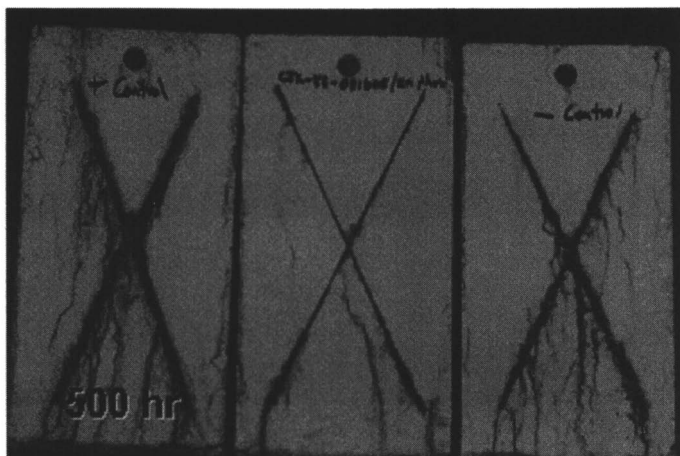
Figure 9. Left to right: commercial formula (zinc phosphate); anthranilic acid nanoparticle + Zn phosphate; and no corrosion inhibitor after 500 hr of salt fog testing.

corrosion inhibitors. The organic corrosion inhibitors are tethered to the surface of the boehmite nanoparticles through a carboxylate bond that is broken at high pH, thereby providing a pH dependent release mechanism. The platy nature of the boehmite nanoparticles also provide for enhanced barrier properties and chemical resistance for the coatings into which they are incorporated.

References

1. Smith, D. In *Managing nanohype: navigating through the boom and bust cycle of nanotechnology's promise* Tire Technology Expo, Cologne, Germany, March 21-23, 2005.
2. Kojima Y., A. Usuki, M. Kawasumi, A. Okada, Y. Fukushima, T. Kurauchi, and O. Kamigaito "Mechanical properties of nylon 6-clay hybrid", *J. Mater. Res.* **1993**, *8*, 1185-1189.
3. Kojima, Y; Usuki, A; Kawasumi, M; Okada, A; Kurauchi, T; Kamigato, O *J. Appl. Poly. Sci.* **1993**, *49*, 1259-1264.
4. Kojima, Y., A. Usuki, M. Kawasumi, A. Okada, T. Kurauchi, O. Kamigaito, and K. Kaji "Novel preferred orientation in injection-molded nylon 6-clay hybrid", *J. Polym. Sci. Part B* **1995**, *33*, 1039-1045.
5. Yano K., A. Usuki, A. Okada, T Kurauchi, and O. Kamigaito "Synthesis and properties of polyimide-clay hybrid", *J. Polym. Sci. Part A* **1993**, *31*, 2493-2498.

6. Usuki, A., M. Kawasumi, Y. Kojima, A. Okada, T. Kurauchi, and O. Kamigaito "Swelling behaviour of montmorillonite cation-exchanged for ω-amino acids by e-caprolactam", *J. Mater. Res.* **1993**, *8*, 1174-1178.

7. Usuki, A., M. Kawasumi, Y. Kojima, A. Okada, T. Kurauchi, and O. Kamigaito "Synthesis of nylon 6-clay hybrid", *J. Mater. Res.* **1993**, *8*, 1179-1184

8. Gusev, A.A. and HR Lusti "Rational Design of Nanocomposites for Barrier Applications", *Advanced Materials* **2001**, *13*(21), 1641-1643.

9. Thompson, R.B., V.V Ginzburg, M.W. Matsen, and A.C. Balazs "Block Copolymer-Directed Assembly of Nanoparticles: Forming Mesoscopically Ordered Hybrid Materials" *Macromolecules* **2002**, *35*(3), 1060-1071.

10. Fernando, R. In *Nanotechnology in Coatings: Realizing the Potential*" Nanotechnology Applications in Coatings Conference, Seattle, WA; June 8-10, 2005.

11. Rhoney, I., S. Brown, N.E. Hudson and R.A. Pethrick "Influence of processing method on the exfoliation process for organically modified clay systems I. Polyurethanes", *J. of Applied Polymer Science* **2003**, *91*(2), 1335-1343.

12. Ray S.S. and M. Okamoto "Polymer/Layered Silicate Nanocomposites: A Review from Preparation to Processing," *Prog. Polymer Science* **2003**, *28*, 1539-1641.

13. Ploehn, H.J. and C. Liu "Quantitative Analysis of Montmorillonite Platelet Size by Atomic Force Microscopy" *Ind. Eng. Chem. Res.* **2006**, *45*(21), 7025-7034.

14. Gusev, A.A. "Numerical Identification of the Potential of Whisker and Platelet Filled Polymers", *Macromolecules* **2001**, *34*(9), 3081-3093.

15. Yano, K; Usuki, A; Okada, A *J. Polym. Sci.; Part A* **1997**, *35*, 2289-2294.

16. Beall, G. W. In *Polymer-clay Nanocomposites*, Pinnavaia, T. J.; Beall, G.W., Eds., John Wiley & Sons Ltd. **2000**, 267-279.

17. Beall, G.W. In *Annual Technical Conference, Society of Plastics Engineers* (ANTEC) New York, NY, May 2-6, 1999.

18. Lee, J. Y., Buxton, G. and Balazs, A. C. "Using Nanoparticles to Create Self-Healing Composites", *J. Chem. Phys.* **2004**, *121*, 5531.

19. Smith, K. A.; Tyagi, S.; Balazs, A. C. "Healing Surface Defects with Nanoparticle-Filled Polymer Coatings: Effect of Particle Geometry", *Macromolecules* **2005**, *38*, 10138.

20. Cook, R.L., B.J. Elliott, S. DeVito-Luebben, A.W. Myers, B.M. Smith "Surface Modified Particles by Multi-Step Michael-Type Addition and Process for the Preparation Thereof," U.S. Patent # 6,887,517, May 3, 2005.

21. Cook, R.L., B.J. Elliott, S. DeVito-Luebben, A.W. Myers, B.M. Smith "Surface Modified Particles by Multi-Step Addition and Process for the Preparation Thereof," U.S. Patent # 6,986,943, Jan. 17, 2006

22. Cook, R.L. "Designing nanoparticles for functional materials and coatings", In *Particles 2005, Surface Modification in Particle Technology* 13-16 August, 2005.

23. Xia, L., E. Akiyama, G. Frankel, R.L. McCreery "Storage and Release of Soluble Hexavalent Chromium from Chromate Conversion Coatings," *J. Electrochem. Soc.* **2000**, *147*, 2556-2562.

24. Yang, H. and W.J. van Ooij "Plasma-treated triazole as a novel organic slow-release paint pigment for corrosion control of AA2024-T3," *Prog. in Organic Coatings* **2004**, *50*(3), 149-161.

25. Sheffer, M., A. Groysman, D. Starosvetsky, N. Savchenko and D. Mandler "Anion embedded sol-gel films on Al for corrosion protection" *Corrosion Science* **2004**, *46*(12), 2975-2985.

26. Montemor, M.F., W. Trabelsi, M. Zheludevich, M.G.S. Ferreira and P. Cecílio "Modification of bis-silane solutions with rare-earth cations for improved corrosion protection of galvanized steel substrates", *Prog. in Organic Coatings* **2006**, *57*, 67-77.

27. Khramov, A. N., V. N. Balbyshev and R. A. Mantz "Protection of Aluminum Alloys via Hybrid Sol-Gel Coatings with Encapsulated Organic Corrosion Inhibitors," *Materials Science Forum* **2006**, *519/521,* 661-666.

28. Kinlen, P.J. D.C. Silverman and C.R. Jeffreys "Corrosion protection using polyaniline coating formulations", *Synthetic Metals* **1997**, *85*(1/3), 1327-1332.

29. de Souza, S., J. Pereira, S. Cordoba de Torres, M. Temperini, R. Torresi, "Polyaniline Based Acrylic Blends for Iron Corrosion Protection", *Electrochemical and Solid State Letters* **2001**, *4*(8), B27.

30. Rammelt, U., L. M. Duc and W. Plieth. "Improvement of protection performance of polypyrrole by dopant anions", *J. of Appl. Electrochemistry* **2005**, *35*(12), 1225-1230.

31. Kumar, A., L.D. Stephenson and J.N. Murray "Self-healing coatings for steel", *Prog. Organic Coatings* **2006**, *55*(3), 244-253.

32. Guilbert; C. R., Enos, D. G., and Boyer, C.E. "Latent Coating For Metal Surface Repair", U.S. Patent 3 6,075,072, June 13, 2000.

33. Wang, H., F. Presuel and R.G. Kelly "Computational modeling of inhibitor release and transport from multifunctional organic coatings" *Electrochimica Acta* **2004**, *49*, 239-255.

34. Williams, G. and H. N. McMurray "Chromate Inhibition of Corrosion-Driven Organic Coating Delamination Studied Using a Scanning Kelvin Probe Technique", *J. Electrochem. Soc.* **2001**, *148*(10), B377-B385.

35. Kendig M. and Hon, M. "A Hydrotalcite-Like Pigment Containing an Organic Anion Corrosion Inhibitor" Electrochem', *Solid-State Lett.* **2005**, *8*(3), B10-B11.

36. Blum, J and Avnir, D. "Catalysis and Reactivity with Sol-Gel Entrapped Organic and Organometallic Chemicals" In *Handbook of Sol-Gel Science and Technology*, S. Sakka, Ed., Kluwer, 2004, Ch. 33

37. Vreugdenhil, A.J. and M. E. Woods "Triggered release of molecular additives from epoxy-amine sol-gel coatings", *Progress in Organic Coatings* **2005**, *53*(2), 119-125.

38. Shchukin, D. G., M. Zheludkevich, K. Yasakau, S. Lamaka, M. G. S. Ferreira, and H. Möhwald "Layer-by-Layer Assembled Nanocontainers for Self-Healing Corrosion Protection", *Advanced Materials* **2006**, *18*, 1672-1678.

39. Wefers K. and C. Misra 'Oxides and Hydroxides of Aluminum", Technical Paper No. 19, **1987** Aluminum Company of America, Pittsburgh, Pa.

40. Landry, C.C., Pappe, N., Mason, M.R., Apblett, A.W., Tyler, A.N. Macinnes, A.N. and Baron., A.R. "From Minerals to materials: Synthesis of Alumoxanes from the Reaction of Boehmite with Carboxylic Acids". *J. Mater. Chem.* **1995**, *5*, 331

41. Morgado E., Y.-L. Lama, S.M.C. Menezes and L.F. Nazar "Characterization of Peptized Boehmite Systems: An ^{27}Al Nuclear Magnetic Resonance Study," *J. Colloid and Interface Science* **1995**, *176*(2), 432-441.

42. a) Peterson, B. Air Products and Chemicals, Personal communication, 1998; b), Maciel, G. Colorado State University, Personal communication, 2001.

43. Krauss C. and Peters, J.W. "Biggest Oil Field in U.S. Is Forced to Stop Pumping" New York Times, August 8, 2006.

44. Tavakoli, H., Shahrabi, T. and Hosseini, M.G. "Synergistic effect on corrosion inhibition of copper by sodiumdodecylbenzenesulphonate (SDBS) and 2-mercaptobenzoxazole", *Materials Chemistry and Physics* **2008**, *109*(2/3/), 281-286.

Chapter 6

Effect of Method of Preparation on the Rheological Behavior of Polyurethane–Polyhedral Oligomeric Silsesquioxanes Nanostructured Hybrid Films

Samy A. Madbouly, Joshua U. Otaigbe[*], Ajaya K. Nanda, and Douglas A. Wicks

School of Polymers and High Performance Materials, The University of Southern Mississippi, Hattiesburg, MS 39406

Two series of nanostructured polyurethane with reactive diamino-polyhedral oligomeric silsesquioxanes (POSS) hybrid were synthesized via environmentally-friendly aqueous dispersions through two different methods, namely, acetone and prepolymer processes. The resulting PU/POSS nano-composites prepared via acetone process did show more phase homogeneity compared with that of prepolymer process as confirmed by wide angle X-ray diffraction patterns of the cast films. Rheological behavior of these important classes of materials has been investigated as a function of POSS concentration and preparation method over a wide range of shear frequency and temperature. The complex viscosity and the elastic storage modulus of PU and PU/POSS nanocomposites prepared via prepolymer process were much higher than that of acetone process at a constant temperature due to the difference in the molecular weight and percentage of internal surfactant. For the PU/POSS nanocomposites prepared by the two different methods, the rheological behavior in the melt confirmed the existence of microphase separation of the hard and soft segments. The value of the microphase separation temperature (T_{MPS}) was found to be concentration independent when the POSS concentration is ≤ 6wt%. For 10 wt% POSS the T_{MPS} shifted by 20 °C to a higher temperature. The effect of POSS on the value of T_{MPS} for prepolymer

© 2009 American Chemical Society

89

samples is considerably different. The value of T_{MPS} of pure PU shifted from 165 °C to 178 °C for all PU/POSS samples regardless of the concentration of POSS as measured from the dynamic heating ramps (2 °C/min heating rate at $\omega = 1$ rad/s) of G'. The shift of T_{MPS} to high temperature in both cases (acetone and prepolymer processes) is attributed to the large surface areas of POSS that produces relatively large interaction zones with the PU hard and soft segments.

Introduction

Polyhedral oligomeric silsesquioxanes (POSS) molecules can be thought of as the smallest particles of silica possible (*1*). However unlike silica or modified clays, each POSS molecule contains covalently bonded reactive functionalities suitable for polymerization or grafting to polymer chains. Each POSS molecule contains nonreactive organic functionalities for solubility and compatibility of the POSS segments with the various polymer systems. Enhancements in the physical properties of polymers incorporating POSS segments result from POSS's ability to control the motions of the chains while still maintaining the processability and mechanical properties of the base polymer. This is a direct result of POSS's nanoscopic size and its relationship to polymer dimensions. The size of the pendant POSS cage is comparable to the dimensions of the linear polymer, enabling POSS to control the motions of the chains at the molecular level (*1-3*). Therefore an enhancement in the physical properties would be expected, while the processability and mechanical properties of the base polymer are retained. Despite the growing number of scientific and patent literature, there are few reported examples of practical and optimal exploitation of POSS (*4-6*). Such nano-reinforced polymers lead to significant thermomechanical property enhancements, while simultaneously improving or retaining the material's other physical properties (e.g., optical clarity, mechanicals) as well as its processability. Other property enhancements such as gas permeability may also be realized. Generally, a higher thermal stability, a better environmental durability in special conditions (i.e., exposure to atomic oxygen and fire resistance), and, in some cases, an improvement in mechanical properties (reinforcement) are expected for POSS-modified polymers (*7-9*).

Recently, POSS has been shown to stratify at the surfaces of polymers and is expected to provide unique properties with novel applications. A special field represented by POSS-modified polyurethanes (*10,11*), (PU/POSS) because these

polymers encompass a huge number of specialized applications such as tissue engineering, textile and plastic coatings, leather finishing, adhesives, sealants, wood finishes, glass fiber sizing, biological fluids, drilling muds, cosmetics, and pharmaceuticals. Widespread use of PU/POSS hybrids is limited by the needs and conditions under which these products are used. Solid thermoplastic polyurethanes are limited to use as hot melt adhesives, and the organic solvent based polyurethanes are increasingly restricted in their traditional applications by environmental legislation (12,13). These regulations along with abatement costs and safety are shifting the base technologies towards aqueous polyurethane dispersions prepared with low levels of organic solvent to gain in commercial use. Recently, significant emphasis has been placed on the use of waterborne coating and adhesive systems such as polyurethane dispersions (PUDs) due to their health and environmental safety (14,15). These environmentally friendly products are used to reduce the VOC (volatile organic compounds) released into the atmosphere by solventborne systems and exhibited the same performance as that of conventional solventborne systems. PUDs can be tailored to various applications by varying the preparation method and chemical structures of the polyurethane. PUDs can be prepared in industry by several methods such as acetone process, prepolymer emulsification process, melt dispersion and cetimine-cetazine process. The first two methods are the most widely used in industry. Acetone process is used to prepare PUDs for adhesives applications, while prepolymer emulsification process is used to prepare PUDs for coatings industry.

The current chapter focuses on preparing polyurethane/polyhedral oligomeric silsesquioxane (PU/POSS) hybrid dispersions from homogeneous solution polymerization (or the so-called 'acetone process') and prepolymer emulsification process (or the so-called 'NMP-process'). The PU/POSS nanocomposite films are obtained from solvent casting of their dispersions without the use of processing aids or modifiers (lubricants) that can negatively impact surface properties such as bond strength, biological activity and antibacterial surface action of the films. Functionalized diamino-POSS is used to obtain nanostructured PU/POSS hybrids. Another objective is to understand the relationships amongst the polymer structure, rheological properties, and performance of the nanocomposite dispersion films under conditions that they are likely to encounter during use. It is expected that incorporation of small amounts of POSS to PU films can significantly enhance the rheological properties, and present a new class of materials for special industrial applications. It is also essential to understand the rheological behavior of these important classes of materials so that they can be rationally engineered during processing to yield new materials with enhanced properties for a number of applications.

Experimentals

Materials

Isophorone diisocyanate (Desmodur-I) and poly (butylene adipate-isophthalate) diol (Desmophen 1019-55) were donated by Bayer MaterialScience, Pittsburgh, PA. Dimethylol propionic acid (DMPA), dibutytin dilaurate (DBTDL), triethyl amine (TEA), and 1,4-butane diol (BD) were purchased from Aldrich Chemical Co. Acetone (99.5 %) was received from Fluka. Hexamethylene diamine (HDA) and N-methylpyrolidone (NMP) were purchased from Aldrich Chemical Co. Aminoethylaminopropylisobutyl polyhedral oligomeric silsesquioxane (amino-POSS) was donated by Hybrid Plastics.

Synthesis and Dispersion of PU/POSS (10 wt% POSS)

Preparation steps of PUDs and PU/POSS naocomposite via prepolymer emulsification process were described in detail in our accompanying chapter in this book. Here, the synthesis of PU/POSS nanocomposites with 10 wt% POSS via acetone process will be described in detail.

In a 500 mL round bottom flask equipped with a nitrogen bubbler, 10.0 g diamino-POSS (0.021 amine equiv.) was dissolved into 125 g of acetone. To this solution 23.0 g of IPDI (0.207 isocyanate equiv.) was added dropwise while stirring using a magnetic stirrer at 20 °C. After 20 min. 3 drops of DBTDL were added. After 10 min the flask was fitted with a mechanical stirrer, a thermocouple controlled heating mantle, a condenser with nitrogen bubbler and a pipette outlet. The polyester polyol (61.1 g, 0.06 hydroxyl equiv.) and DMPA (3.1 g, 0.046 hydroxyl equiv., and 0.023 acid equiv.) were charged into the flask and stirring was continued while the temperature was raised to 60 °C. The isocyanate (NCO) content was monitored during the reaction using the standard dibutylamine back titration method (16). Upon reaching the theoretical NCO value, the prepolymer was chain extended with BD (2.6 g, 0.057 hydroxyl equiv.) and the reaction continued for 2 h to complete polymerization, yielding the desired polyurethane/POSS copolymer. Lastly, the polymer was neutralized by the addition of 2.3 grams of triethyl amine (0.023 equiv.) and stirred for 30 min while maintaining the temperature at 55 °C. Formation of the dispersion was accomplished by slowly adding water to the neutralized acetone solution of the polyurethane polymers at 45-50 °C over 30 min with agitation speed of 600 rpm. After stirring for 30 min the reaction mixture was transferred to a rotary evaporator and the acetone was removed at 35 °C and a partial vacuum of 70 mm Hg to afford organic solvent free dispersions with 32 wt% solids. The reaction
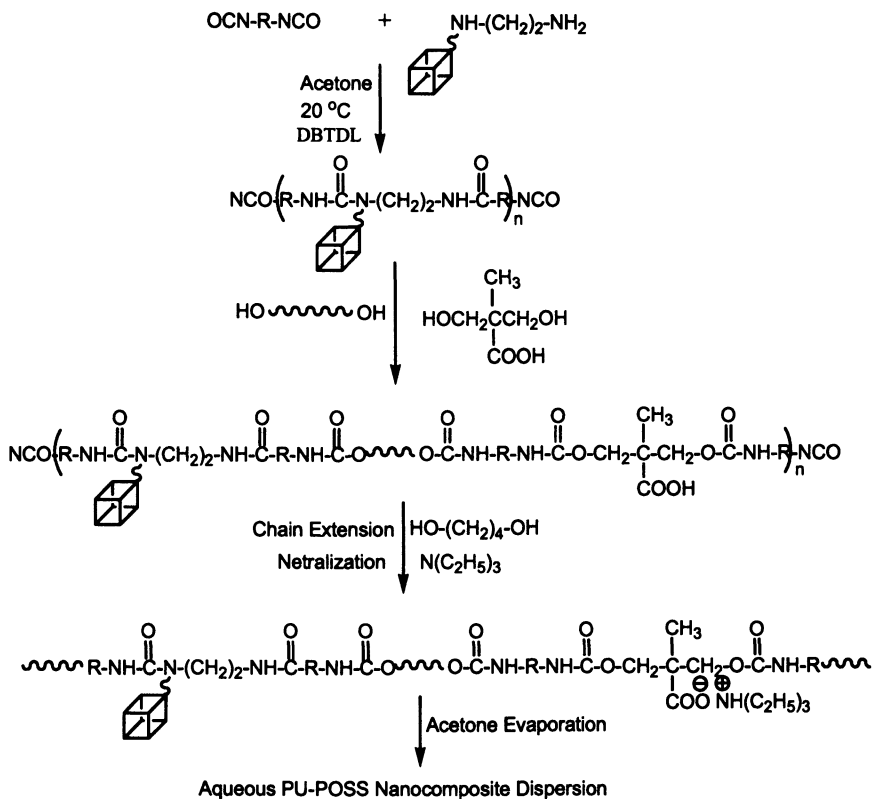
Scheme 1. Elementary steps for hybrid dispersion by acetone process

Scheme 1 shows the elementary steps for the synthesis of PU/POSS nanocomposite with 10 wt% POSS.

Measurements

The films of pure PU and PU/POSS nanocomposites obtained from acetone and prepolymer processes with different concentrations (0, 4, 6, and 10 wt% POSS) were obtained by casting the dispersions onto a polypropylene plate and drying to constant weight in a vacuum oven at 90 °C for three days. The viscoelastic measurements were done on the dried films using an advanced Rheometerics Expansion System (ARES, TA Instruments) equipped with 25 mm diameter parallel plates. In this study, the following rheological experiments were performed:

- Strain sweep at a constant temperature and frequency range of 0.1-100 rad/s to obtain the linear viscoelastic range of the films.
- A time sweep at a constant temperature and frequency to obtain steady state and thus ensure that the measurements were carried out under equilibrium condition.
- Frequency sweep at a given temperature ($100°$-$230°$C) in the linear viscoelastic region (strain amplitude $\leq 10\%$ strain) to obtain the complex viscosity, $|\eta^*|$, and the dynamic shear moduli, i.e. storage shear modulus, G', and loss modulus, G''. Master curves were obtained by horizontal shifts of the experimental data. The zero shear viscosities (η_0) of the blends were calculated by fitting the complex viscosity versus ω data to the Carreau-Yasuda model (*17*).
- The rheological microphase separation (T_{MPS}) of the hard and soft segments of PU/POSS nanocomposites will be evaluated from the temperature ramp of G' at 1 rad/s shear frequency and 2 °C/min heating rate.

Results and Discussion

The complex viscosity of pure PU and PU/POSS nanocomposites (acetone process) as a function of angular frequency for different concentrations of POSS at 110 °C is shown in Figure 1a. We selected $T = 110$ °C for this comparison because it is lower than the microphase separation temperature (T_{MPS}) of all samples as will be discussed later. The viscosity of PU changed greatly with increasing concentration of POSS (i.e., the higher the concentration of POSS the larger the increase in the complex viscosity). The viscosity increased by more than one and half order of magnitudes for PU/POSS with 10 wt% POSS and exhibits more non-Newtonian behavior over the entire range of shear frequency compared to that of pure PU at the same temperature (see Fig. 1a).

The dependence of the viscosity of the PU/POSS on angular frequency can be expressed through the Carreau-Yasuda model according to the following Equation (*17*):

$$\eta^* = \eta_0 \left[1 + \left(\frac{\eta_0 \omega}{\tau^*} \right)^a \right]^{(n-1)/a} \tag{1}$$

where η_0 is the zero-shear viscosity and n, a and τ^* are material constants. Using the above model one can calculate η_0 as a fitting parameter to the experimental results using non-linear regression technique. An excellent description of the

data was obtained as shown in Figure 1a for all compositions, where the lines passing through the experimental data were calculated using Equation 1.

The systematic increase in the elastic modulus with increasing POSS concentration at high temperature (Figure 1a) is attributed to the reinforcement of PU film by the POSS nanostructures.
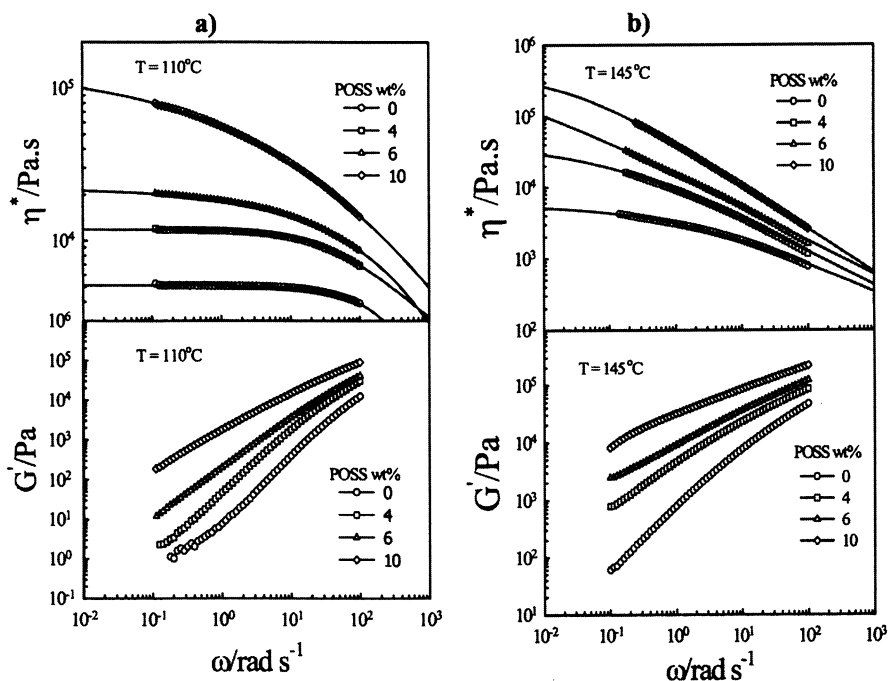
Figure 1. Shear frequency dependence of the complex viscosity, η^*, and elastic modulus, G', for different PU/POSS nanocomposite concentrations, a) acetone process, b) prepolymer process. The solid lines passing through the experimental data are calculated from Eq. 1.

Similar behavior has been detected for the PU/POSS naocomposites obtained from the prepolymer process as shown in Figure 1b at 145 °C. The viscosity and elastic modulus of PU and PU/POSS nanocposites are much higher for the samples prepared by prepolymer process than that of acetone process at a constant temperature. Here we can not measure the samples prepared via prepolymer process at temperatures lower than 140 °C due to the high molecular

weight of these materials (for example pure PU has M_n = 32,000 g/mol) compared with that of acetone process (M_n = 23,000 g/mol for pure PU). Another very important reason for this difference is the percentage of the internal surfactant, DMPA, was 5 wt% for the prepolymer process, while it was only 3 wt% in the acetone process to get stable dispersions (18). The high percentage of DMPA leads to a very strong interaction or hydrogen bonding between the polymeric chains which in turn lead to a physical crosslinkage structure preventing the samples to flow at low temperature. Furthermore, we can not make comparison for viscosity and elastic modulus at 145 °C because the samples obtained from acetone process undergo microphase separation at temperature higher than 130 °C as will be discussed later. The incorporation of dimaino POSS significantly increases the complex viscosity and elastic modulus for the samples obtained from both acetone and prepolymer processes.

Figure 2a illustrates the volume fraction (ϕ) dependence of the dimensionless complex viscosity of the PU/POSS composites, η_r (reduced by the viscosity of pure PU) for the samples prepared via acetone process. The critical volume fraction of POSS (ϕ_c) at which the viscosity of the composite increased strongly was determined using Krieger-Dougherty Equation (19).

$$\eta_r = \left(1 - \frac{\phi}{\phi_c}\right)^{-k\phi_c} \tag{2}$$

With

$$\eta_r = \frac{\eta_0(\phi)}{\eta_0(0)} \tag{3}$$

where k is a shape parameter, $\eta_0(\phi)$ is the zero shear viscosity of the composites, and $\eta_0(0)$ is the zero shear viscosity of pure PU. The experimental data can be described using the above equation, where the symbols are experimental data while the line is the calculated line using k and ϕ_c as fitting parameters. The value of ϕ_c obtained from this regression analysis was found to be 0.14. The Krieger-Dougherty Equation works well for hard spheres dispersions with volume fraction less than 0.55. It is well known that the value of ϕ_c strongly depends on the specific system under consideration. For example small, mono-dispersed particles show lower value of ϕ_c than large ones, and ϕ_c increases with polydispersity (20). Clearly, Figure 2a shows an excellent description of the experimental data using the above two Equations. The Einstein or the modified Einstein-Batchelor Equation (Equation 4) (21) for hard-sphere suspensions shown by the dotted line in Figure 2a is clearly deviated from the experimental data. Normally the Einstein-Batchelor Equation predicts a slight increase in the zero shear viscosity for suspensions of hard-sphere particles in a polymer matrix (21).

$$\eta_0(\phi) = \eta_0(0)\{1 + 2.5\phi + 6.2\phi^2 + ...\} \qquad (4)$$

Clearly, the magnitude of the elevation in the reduced zero shear viscosity caused by the hard-sphere particles given by Equation 4 (dashed line in Figure 2a) is very small compared to the actual increase in viscosity in the present system (PU/POSS, acetone process).
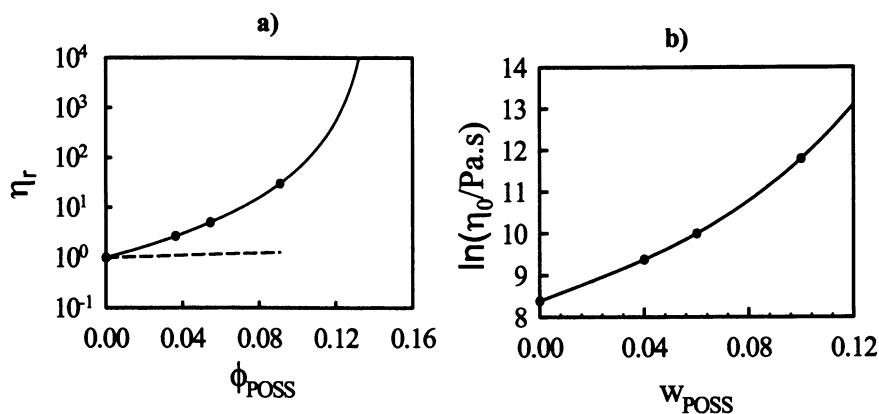
Figure 2. a) POSS volume fraction dependence of reduced viscosity at 110 °C for PU/POSS nanocomposites prepared via acetone process. The solid line calculated from Equations 2 and 3, while the dashed line calculated from equation 4. b) POSS weight fraction dependence of zero shear viscosity at 110 °C for PU/POSS nanocomposites prepared via acetone process. The solid line calculated from Equation 5.

In the current system of this study the POSS is completely reacted with the hard segments of PU and there is no unreacted dispersed phase in this composite. Therefore, the current system is a homogeneous composite containing POSS that is completely reacted with the hard segments (urethane segments) to form part of the PU main chain. Therefore, it is reasonable to examine the composition dependence of zero shear viscosity of this composite using another model for miscible polymer mixtures, such as, the Lecyar model described by the following Equation (22).

$$\ln \eta_b^* = Aw_1^3 + Bw_2^3 + Cw_1^2 w_2 + Dw_1 w_2^2 \qquad (5)$$

Where w_1 and w_2 are the weight fractions of PU and POSS, respectively. The constants A, B, C and D are material parameters that are both functions of shear frequency and temperature. A slightly negative deviation from the linear

mixing rule ($\ln \eta_b^* = w_1 \ln \eta_1^* + w_2 \ln \eta_2^*$ where η_1^* and η_2^* are the zero shear viscosity of PU and POSS, respectively) was detected for this composite, as clearly seen in Figure 2b. The line is computed from Eq. (5) using a non-linear regression method, while the symbols are experimental data; a good description of the data was obtained using this model. This Equation is normally used to describe the composition dependence of η_b^* of miscible polymer blends. Recently, we reported a negative deviation from the additivity rule in miscible polymer blend of poly(methyl methacrylate)/poly(methyl styrene-co-acrylonitrile), and the data was well described by Lecyar model (23). It is noteworthy that this is not a general behavior for all miscible polymer mixtures. To our knowledge, there is no generally acceptable and universally valid mixing rule for the viscosity of polymer mixtures (24).

The behavior of PU/POSS nanocomposites obtained via prepolymer process is different as shown in Figures 3. There is a clear deviation from the Krieger-Dougherty Equation (solid like) and Einstein-Batchelor Equation (dashed line) as clearly seen in Figure 3a. In addition, the zero shear viscosity shows a negative deviation followed by a positive deviation with increasing POSS concentration from the linear mixing rule (see Figure 3b).

This behavior is attributed to the fact that some of PU/POSS nanocomposites prepared via prepolymer process can make a crystalline structure particularly when the POSS concentration is higher than 4 wt% as illustrated in the WAXD pattern of Figure 4b. The materials prepared by acetone process are totally amorphous without any crystalline structure (Figure 4a). On the other hand there is a distinct sharp reflection peaks at about $2\theta = 8.6°$ for the samples prepared by prepolymer when POSS concentration higher than 4 wt%. Although the amino-POSS was reacted in the beginning with IPDI to avoid the inhomogenity of POSS and PU, the WAXD data is probably due to the presence of some unreacted POSS in the PU matrix. Perhaps the reaction mixture was not as homogeneous in presence of NMP as it was in acetone.

The master curves of the dynamic shear moduli, G' and G'' can be constructed based on the concept of thermorheological simplicity. For example, the storage modulus can be superimposed by horizontal shifts along the x-axis (frequency axis), according to the following equation;

$$G'(\omega\, a_T, T_0) = G'(\omega, T) \qquad (6)$$

where ω is the magnitude of the shear frequency, a_T is the horizontal shift factor and T_0 is the reference temperature. The time-temperature superposition increases the accessible frequency window of the linear viscoelastic experiments. This principle applies to stable materials without any thermal-induced physical
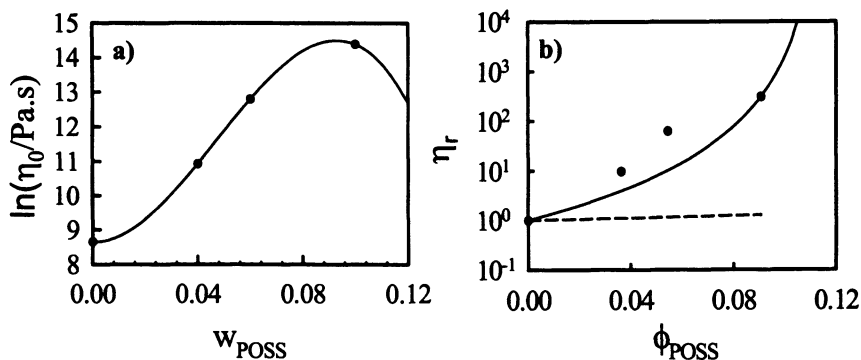
Figure 3. a) POSS volume fraction dependence of reduced viscosity at 145 °C for PU/POSS nanocomposites prepared via prepolymer process. The solid line calculated from Equations 2 and 3, while the dashed line calculated from equation 4. b) POSS weight fraction dependence of zero shear viscosity at 145 °C for PU/POSS nanocomposites prepared via prepolymer process. The solid line calculated from Equation 5.

or chemical reactions or transitions during the dynamic measurements, and only the effect of temperature on the relaxation process is considered. Therefore, the principle works well when the stress-sustaining structure in the system does not change with temperature, and when the relaxation times of all modes of this structure change with temperature by the same factor. Figure 5a shows the master curves of the dynamic shear moduli, G' and G'' for PU/POSS = 90/10 nanocomposite (acetone process) at $T_0 = 120$ °C. Clearly there is strong deviation in the terminal zone of the master curve of G' starting at about 160 °C. This deviation means that the WLF (Williams-Landel-Ferry) Equation is no longer valid at high temperature range. This behavior is attributed to the fact that the PU chemical structure is a multiblock copolymer comprised of alternating soft polyester and hard polyurethane-urea segments. These two segments undergo microphase separation into hard and soft phases, respectively, below and above their glass transition temperatures. This microphase separation is responsible for the excellent elastomeric properties of PU. The G'' does not show any deviation in the terminal zone of the master curve indicating that the stress induced in the system by the concentration fluctuations accompanying the microphase separation transition is mostly elastic in origin. It is apparent from this figure that the WLF principle is only valid for temperatures lower than 160 °C; the WLF principle failed for $T \geq 160\,°C$. The existence of microphase
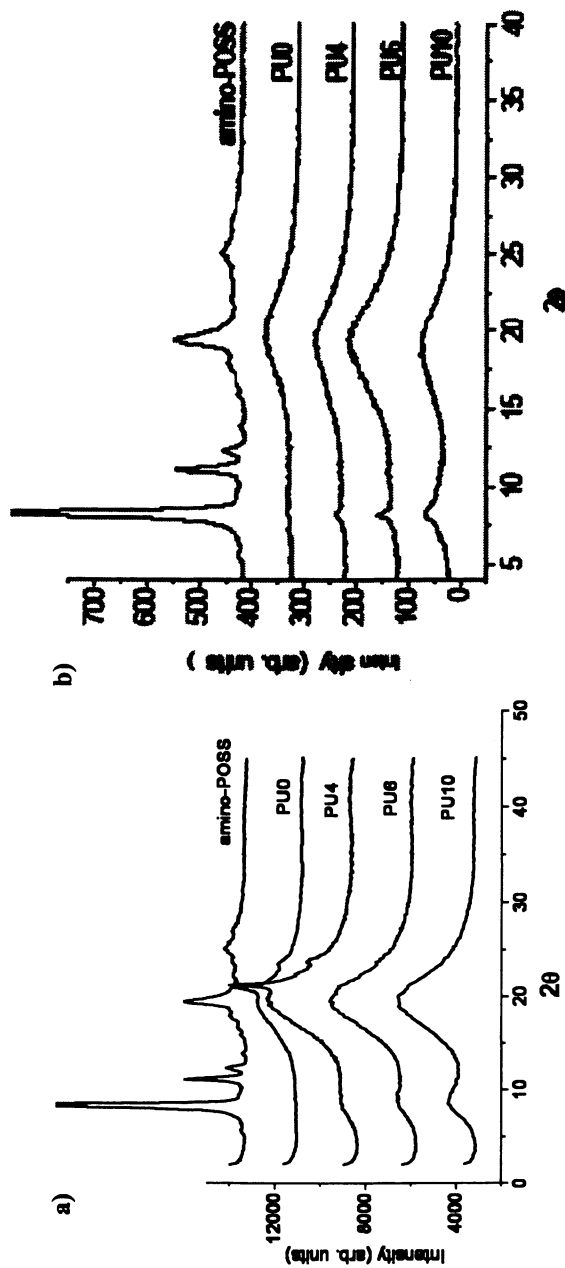
Figure 4. WAXD patterns of amino-POSS PU0, 4, 6 and 10 films, a) acetone process and b) prepolymer process.
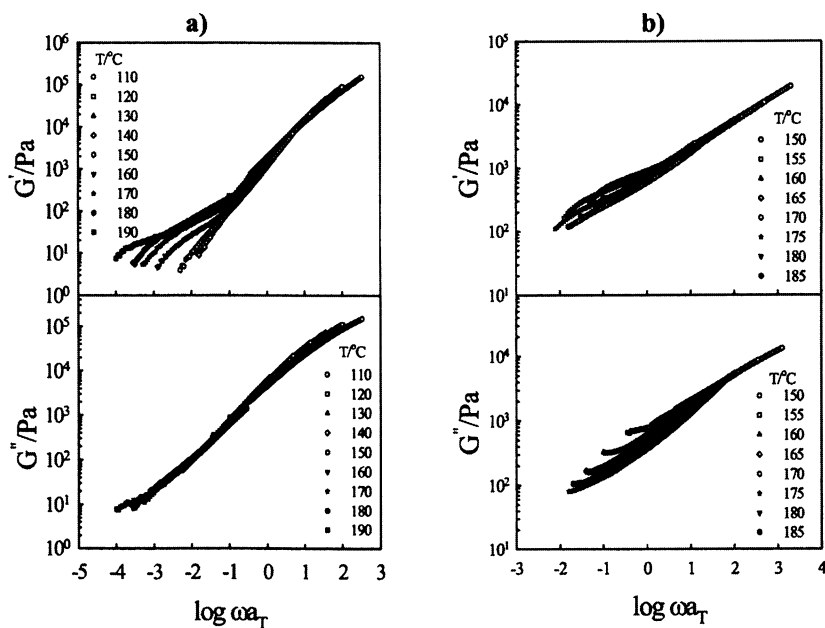
Figure 5. a) Master curves of the dynamic shear moduli, G' and G" for PU/POSS = 90/10 (acetone process) at T_0 = 120. b) Master curves of the dynamic shear moduli, G' and G" for PU/POSS = 90/10 (prepolymer process) at T_0 = 160.

separation transition in PU elastomers has been clearly demonstrated (beyond any doubt) in the literature using different techniques (25-28). Similar breakdown in the WLF principle has been observed in several diblock and triblock copolymers, and polymer blends with lower and upper critical solution temperatures phase diagrams (LCST and UCST, respectively). For a number of diblock and triblock copolymers reported in the literature, this breakdown of WLF principle has been shown to be related to a microphase separation transition. The microphase separation of PU based on soft segments of polycaprolactone as a function of block length has been investigated rheologically and by using small angel X-ray scattering (SAXS) measurements by Velankar et al. (28). They showed, for the systems studied, that the WLF principle failed at high temperatures to an extent that depends on the multiblock lengths.

For the samples prepared via prepolymer process, the failing of WLF-superposition principle is very clear for both G' and G'' as shown in Figure 5b. This experimental fact suggests that the contribution of concentration fluctuations to the viscoelastic material functions due to the microphase separation is higher for the samples prepared via prepolymer process than that of acetone process.

The temperature dependence of the shift factor (a_T) can be studied using the Arrhenius (Equation 7) and the WLF (Williams-Landel-Ferry) (Equation 8) expressions (29):

$$\log a_T = \frac{E_A}{2.303R}\left(\frac{1}{T} - \frac{1}{T_0}\right) \quad (7)$$

$$\log a_T = \frac{-c_1(T - T_0)}{c_2 + (T - T_0)} \quad (8)$$

where R is the universal gas constant, E_A is the activation energy of flow, and c_1 and c_2 are the WLF parameters. Figure 6a shows the temperature dependence of the shift factor a_T for the data of Figure 5a (acetone process). The experimental points are fitted by the WLF Equation using c_1 and c_2 as fitting parameters. The inset-figure shows the Arrhenius type plot for the same data. Although, there is a considerable deviation from the master curve of G' at high temperatures in the terminal zone, the temperature dependence of the shift factor is well described by the above two Equations over the entire temperature range (for only samples obtained by acetone process).

However, a large deviation of the temperature dependence of shift factor from the WLF-superposition principle for the samples prepared via prepolymer process is very obvious at high temperatures as shown in Figure 6b. The inset plot of this figure shows the Arrhenius type plot for the same experimental data. As clearly seen in this Figure there are two straight lines that intersect at the T_{MPS}.

The rheological value of the microphase separation temperature (T_{MPS}) can be obtained from the dynamic heating ramps (2 °C/min heating rate at $\omega = 1$ rad/s) of the viscoelastic material functions such as G' as shown in Figure 7 for pure PU and PU/POSS nanocomposites of different POSS concentrations. The value of G' is observed to be very sensitive to the microphase separation temperatures. It is very clear from these figures that the value of T_{MPS} is relatively unaffected by POSS concentration up to 6 wt% POSS. At 10 wt% POSS the T_{MPS} increased by about 20 °C as shown in Figures 7a for the samples prepared via acetone process. Clearly, this figure shows that G' decreases with temperature in the low temperature range due to the increase in mobility of the polymer chains caused by Brownian motion. At the microphase separation temperature, a considerable change in the slope of G' was observed. It is apparent that the change of G' at the phase separation temperature might be attributed to a competition between two opposing factors. One factor that tends to decrease G' with increasing temperature is the Brownian motion and the other factor is the concentration fluctuations at the microphase separation temperature that gives rise to an additional contribution to G' (30-33). The value of the microphase separation temperature (T_{MPS}) can be obtained from the onset temperature at which the slope of G' versus T starts to deviate. Based on this
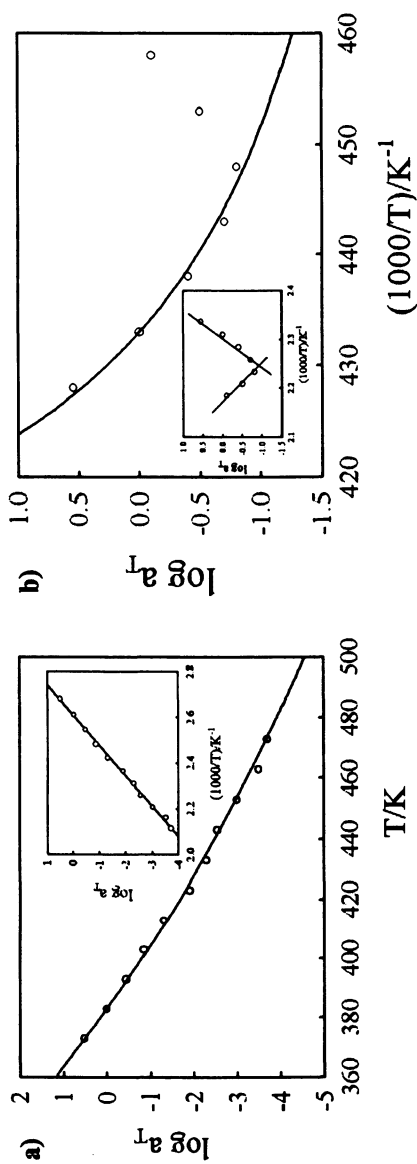
Figure 6. Shift factor a_T as a function of temperature for PU/POSS = 90/10. The inset plot demonstrates the Arrhenius-type plot for the temperature dependence of a_T. a) Acetone process and b) prepolymer process.

method the T_{MPS} of pure PU and PU/POSS composite (10 wt% POSS) are approximately 140° and 160°C, respectively for the samples prepared via acetone process. This observation supports our suggestion that POSS can enhance the miscibility of the hard and soft segments of PU to produce relatively more homogenous nanostructures (34).

The effect of POSS on the value of T_{MPS} for prepolymer samples is considerably different. For example the T_{MPS} of pure PU shifted from 165 °C to 178 °C for all PU/POSS samples regardless of the concentration of POSS as clearly seen in Figure 7b. The high value of T_{MPS} of pure PU prepared via prepolymer process compared to that of acetone process is attributed to the different molecular weight and internal surfactant percentage and consequently different phase behavior and interaction between hard and soft segments as discussed earlier. In addition all samples of PU/POSS nanocomposites with POSS concentration higher than or equal to 4 wt% have the same value of T_{MPS} might be attributed to the inhomogeneity of the samples with high load of POSS as we confirmed by the WAXD measurements (Figure 4b). The shift of T_{MPS} to high temperature in both cases (acetone and prepolymer processes) is attributed to the large surface areas of POSS that produces relatively large interaction zones with the PU hard and soft segments and consequently enhances the phase homogeneity of the two segments.

Conclusions

Chemical incorporation of a well-defined nanostructured inorganic cluster of polyhedral oligomeric silsesquioxanes (POSS) into the polyurethane matrix to form special organic/inorganic hybrids has been successfully achieved in aqueous dispersions using the acetone and prepolymer processes. The viscoelastic behavior of polyurethane film changed greatly due to addition of small amounts (up to 10 wt%) of functionalized diamino-POSS to the isophorone diisocyanate before the polymerization steps. A significant increase in the melt viscosity and zero shear viscosity was observed. This increase in the viscosity is attributed to the reaction between the hard segments of PU (urethane segments) and diamino POSS. It has been found that PU/POSS nanocomposites prepared via the acetone process were more homogenous than that obtained from the prepolymer process as confirmed by WAXS patterns of the cast films. The values of the microphase separation temperature (T_{MPS}) of the hard and soft segments were evaluated rheologically from the onset temperature at which the slope of G' versus T starts to deviate. For acetone process, the T_{MPS} of pure PU and PU/POSS composite (10 wt% POSS) were 140° and 160°C, respectively. The T_{MPS} of pure PU shifted from 165 °C to 178 °C for all PU/POSS samples regardless of the concentration of POSS for prepolymer process. This shift in
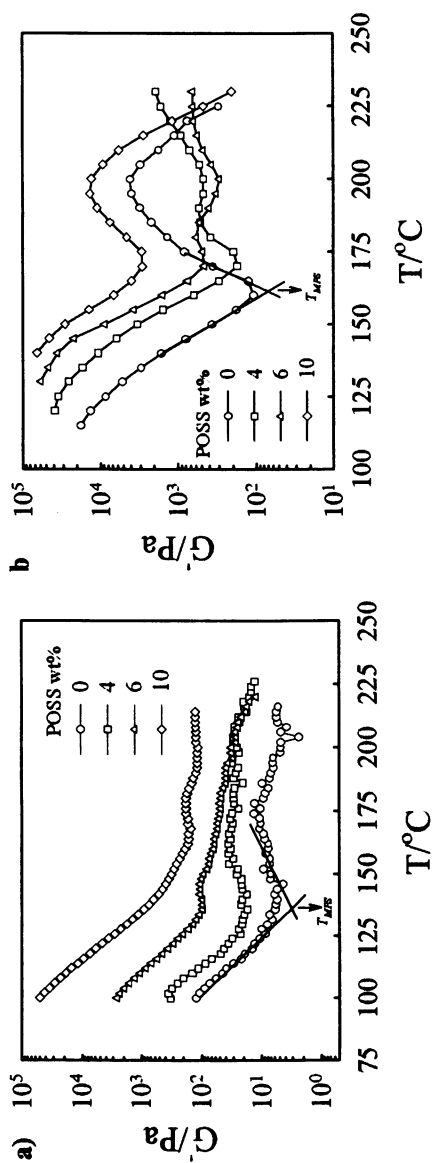
Figure 7. Temperature dependence of the storage modulus of PU/POSS nanocomposites for different POSS concentrations at 1 rad/s shear frequency and 2 °C/min heating rate. a) Acetone process, b) prepolymer process.

T_{MPS} to higher temperaturedue to the addition of POSS supports our suggestion that POSS can enhance the miscibility of the hard and soft segments due to the large surface areas of POSS that produces relatively large interaction zones with the PU hard and soft segments and consequently enhances the phase homogeneity. It is hoped that this work may stimulate a better understanding of the processing/structure/property relations for the innovative POSS/PU system and other related nano structured hybrid materials.

Acknowledgements

References

1. Baney, R. H.; Itoh, M.; Sakakibara, A.; Suzuki, T. Chem. Rev. **1995**, *95*, 1409.
2. POSS is a registered trademark of Hybrid Plastics, www.hybridplastics.com.
3. Li, G.; Wang, L.; Ni, H.; Pittmann, C. U. J. Inorg. Organomet. Polym. **2001**, *11*, 123.
4. Gilman, J. W.; Schlitzer, D. S.; Lichtenhan, J. D. J. Appl. Polym. Sci. **1996**, *60*, 591.
5. Phillips, S.; Haddad, T. S.; Tomczak, S, J. Curr. Opin. Solis State Mater. Sci. **2004**, *8*, 21.
6. Gonzalez, R. I.; Phillips, S.; Hoflund, G. B. J. Spacecraft Rockets **2000**, *37*, 463.
7. Gao, F.; Tong, Y.; Schricker, S. R.; Culbertson, B. M. Polym. Adv. Technol. **2001**, *12*, 355.
8. Tegou, E.; Bellas, V.; Gogolides, E.; Argitis, P. Microelectr. Eng. **2004**, 73-*74*, 238.
9. Kickelbick, G. Prog. Polym. Sci. **2003**, *28*, 83.
10. Neumann, D.; Fisher, M.; Tran, L.; Matisons, J. G. J. Am. Chem. Soc. **2002**, *124*, 13998.
11. Turri, S.; Levi, M. Macromolecules **1999**, *32*, 1194.
12. Neumann, D.; Fisher, M.; Tran, L.; Matisons, J. G. "J. Am. Chem. Soc. **2002**, *124*, 13998-13999.

13. Turri, S.; Levi, M. Macromolecular Rapid Communications **2005**, *26*, 1233-1236.
14. Wicks, Z. W.; Wicks D. A.; Rosthauser, J. W. Progr. Org. Coat. **2002**, *44*, 161-183.
15. Howarth, G.A. Surface Coatings International Part B: Coatings Transactions, **2003**, *86* (B2), 111.
16. Nanda, A. K.; Wicks, D. A. Polymer **2006**, *47*, 1805.
17. Carreau, P. J.; De Kee, D.; Chhabra, R. P. Rheology of Polymeric Systems: Principles and Applications, Hanser, Munich 1997.
18. Madbouly, S. A.; Otaigbe, J. U. Nanda, A. K.; Wicks, D. A.; Antec **2006**, 2366-2370.
19. Krieger, I. M.; Dougherty, T. J. Trans. Soc. Rheol III **1959**, 137.
20. Farris, R. J. Trans. Soc. Rheol III **1968**, *2*, 281.
21. Batchelor, G. K.J. Fluid Mech. **1977**, *83*, 97.
22. Carley, J. F. Polym. Eng. Sci. **1985**, *25*, 1017.
23. Madbouly, S. A. J. Macro. Sci. part B-Phys. **2003**, *B42*, 1209.
24. Utracki, L. A.; Kamal, M. R. Polym. Eng. Sci. **1982**, *22*, 63.
25. Koberstein, J. T.; Russell, T. P. Macromolecules **1986**, *19*, 714.
26. Ryan, A. J.; Macosko, C. W.; Bras, W. Macromolecules **1992**, *25*, 6277.
27. Wilkes, G. L.; Emerson, J. A. J. Appl Phys. **1976**, *47*, 4261.
28. Velankar, S.; Cooper, S. L.; Macromolecules **1998**, *31*, 9181.
29. Eckstein, A.; Suhm, J.; Friedrich, C.; Maier, R. D.; Sassmannshausen, J.; Bochmann, M.; Mulhaupt, R. Macromolecules **1998**, *31*, 1335.
30. Bates, F. S. Macromolecules **1984**, *17*, 2607.
31. Rosedale, J. H.; Bates, F. S. Macromolecules **1990**, *23*, 2329.
32. Fredrickson, G. H.; Larson, R. G. Macromolecules **1987**, *20*, 1897.
33. Fredrickson, G. H. J. Chem. Phys. **1986**, *85*, 5306.
34. Madbouly, S. A.; Otaigbe, J. U. Nanda, A. K.; Wicks, D. A. Macromolecules **2007** (in press).

Chapter 7

Shear-Induced One-Dimensional Alignment of Alumina and Silica Nanoparticles in Coatings

Erik D. Sapper, Lucas J. Brickweg, Bryce R. Floryancic, and Raymond H. Fernando*

Department of Chemistry and Biochemistry, California Polytechnic State University, 1 Grand Avenue, San Luis Obispo, CA 93407

One-dimensional (1-D) strings of alumina and silica nanoparticles, formed in an extended pearl-necklace fashion were observed near the surface of cured polyurethane films. The nanoparticles have been shown to arrange in perfectly straight lines in the direction of shear. As shear increases, the abundance and length of the arrangements increases. The mechanism of alignment is hypothesized to be a combination of shear-induced patterning and oriented attachment. The alignments have been imaged with atomic force microscopy as well as scanning electron microscopy. Energy dispersive x-ray spectroscopy elemental analysis has confirmed the presence of colloidal nanoparticles in arrangements of smaller particles, while similar arrangements of larger particles that can be seen with an optical microscope have been shown to contain mostly silicon element, presumably a phase-separated polysiloxane containing additive present in all formulations. These findings help advance the knowledge on preparing 1-D aligned particles through template-free approaches.

108   © 2009 American Chemical Society

Introduction

Controlled formation of colloidal particle assemblies has received a great deal of attention in recent years (*1-9*). Applications such as electronics, optics, and medical science could benefit from the unique properties of such highly ordered materials. Some of the previous studies have addressed shear-induced alignment of concentrated colloidal suspensions. Particle size uniformity is an important factor in forming ordered structures under shear flows, and shear-induced particle structure formation has been correlated with shear-thinning at high rates (*1*). The majority of prior research in this area concerns 2-D and 3-D ordered structures formed from highly crowded dispersions.

Literature on 1-D particle arrangements is limited; however, interested readers will find the review by Tang and Kotov (*10*) immensely helpful. 1-D nanoparticle arrangements have been found in nature; for example, the anisotropic structure of maghemite particles in magnetotactic bacteria produces a permanent magnetic dipole, which serves as a critical orientation system (*11*). Particle arrangements of the 1-D type have been prepared by employing numerous methods. Dielectrophoresis and other electrostatic techniques (*6,7,9*) as well as various template-assisted methods (*12*) that make use of entropic force fields to "push" particles in place (*13*) have been reported. While template-assisted methods may yield straight, single nanoparticle wires, a self-assembly method would be favored due to simplicity and compatibility with various integration processes. Previously reported self-assembly methods such as vertical deposition assisted by dewetting have produced well-aligned particle stripe patterns (*14*). Transient particle string formations under shear flows have been reported for highly concentrated dispersions. The transient string formations have been shown to occur as 3-D ordered structures of particles begin to break up, leaving strings of particles aligned parallel to the direction of shear flow (*1*).

This chapter presents an even simpler self-assembly method for producing stable 1-D nanoparticle arrangements. Shear-induced assembly orders nanoparticles into nearly perfect straight and parallel lines produced by simple application methods.

Experimental

Polyurethane coating films containing either alumina or silica nanoparticles were prepared according to the same methods described in Chapter 11 of this book and elsewhere(*15-17*). Commercially available nanoparticle dispersions (Table 1) were incorporated into the 2K polyurethane clear coat formulation at and below levels of 1.0 wt % (approx. 0.25% by volume) of the cured film.

Coating samples were prepared on glass microscope slides using various application methods and cured at 70°C for 30 minutes. Application methods represent various levels of application shear rates and included spray, drawdown, and minimal-shear deposition of liquid coating drops onto the substrate. Final coating thicknesses ranged from 0.25 to 1.5 mils (6-38 μm).

Table 1. Predispersed Nanoparticles Used in the Study

Particle Type	Dispersion Medium	Solids (Wt.%)	Average Particle Size
Alumina C	Methoxypropyl acetate	34.0	20 nm
Alumina D	Methoxypropyl acetate	33.0	20 nm
Silica A	Methoxypropyl acetate/ Methoxypropanol (6:1)	32.0	20 nm

Samples were analyzed with a Pacific Nanotechnology Nano-R atomic force microscope using an Ultrasharp silicon cantilever. Close-contact mode was used for all AFM imaging. A JEOL S-890 scanning electron microscope and a Hitachi S4700 (with Oxford Instruments energy dispersive x-ray spectroscopy (EDS) Detector) scanning electron microscope were used to record electron micrographs and perform elemental analysis.

Results and Discussion

AFM and cross-sectional SEM analysis as well as visual appearance of all the coatings used in this study indicated that, in general, the nanoparticles are well dispersed throughout the film (Chapter 11). However, in some occasions, what appeared to be nanoparticles aligned in straight lines were detected. Careful examination of experimental conditions of the occurrences of these 1-D alignments indicated that their formation depends on the coating film application method.

Application by Drop Deposition Method

Four drops of coating were placed on a glass slide and allowed to flow and spread out for 10 minutes before being cured under the same conditions as stated above (70°C for 30 min.). No linear formations were found by AFM analysis.

c:\program files\pacific nanotechnology\pscan2002\scandata\luke and bryce nanoparticles\new stuff\36
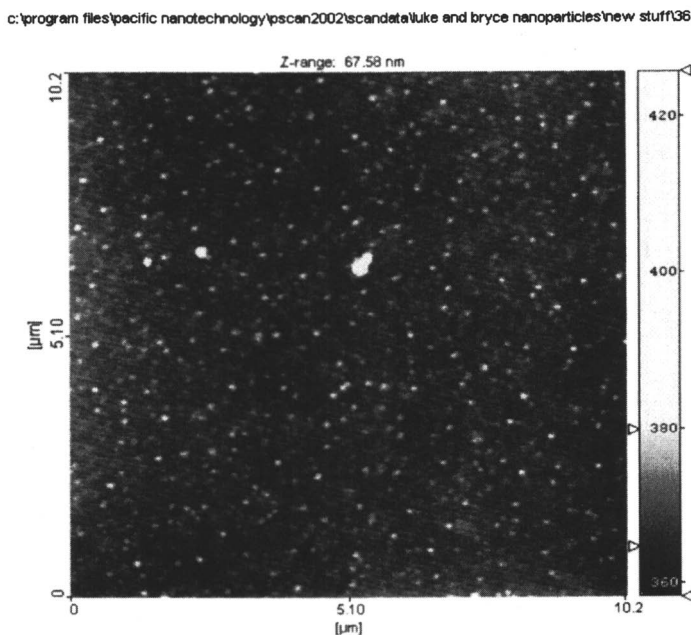
Figure 1. AFM height image (10x10 μm area) of a polyurethane coating containing 1.0 wt.% Alumina C nanoparticles. Application method: drop deposition.

Very few aggregates of large particles were visible under optical microscope, and aggregates that were present did not display any evidence of linear nanoparticle arrangements when observed with AFM (Figure 1).

Application by Drawdown Method

Drawdown application method using a 75μm-gap drawdown cube produced very straight particle strings in all three of the systems. The alignments are continuous for a few hundred micrometers in many cases. AFM height images of coatings containing Alumina C (0.67 wt.%) and Alumina D (1.0 wt.%) are shown in Figure 2. These samples were prepared at an approximate application speed of 5 cm s^{-1}. Stable, multiple straight-line formations of what was suspected to be alumina and silica nanoparticles were observed. As application speed increased from 1 to 10 cm/sec, the abundance and length of particle strings increased.

Application by Spray Method

Application by spray method produced large strings covering the entire microscope slide surface. The AFM images of these samples show many parallel arrangements in the direction of spray (Figure 3). The AFM line profile shows that most of the smaller particles have heights between 20 and 40 nm, while the larger features have heights over one hundred nanometer range. SEM micrographs of spray-produced alignments were also recorded, and SEM images obtained at two random locations on a film containing 1.0Wt.% Silica A are shown in Figure 4. Although the modes of deformations in spray applications are complex (*18*), it is a process that involves very high shear rates.
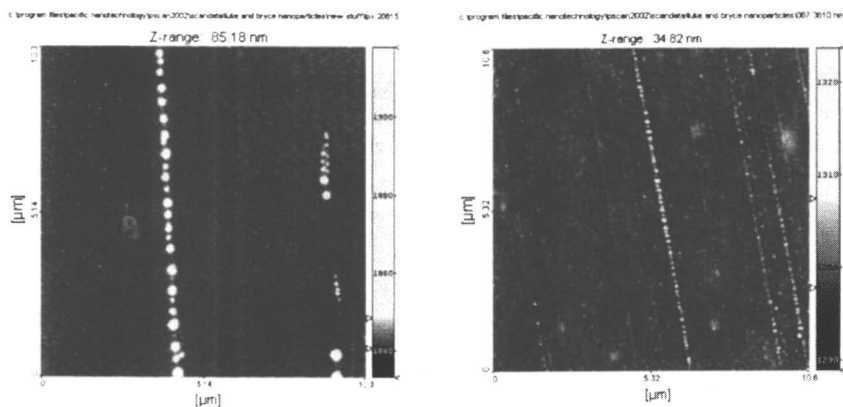
Figure 2. AFM height images (10 x 10 μm) of coatings containing nanoparticles: (left) Alumina-D (1.0 wt.%) and (right)Alumina-C (0.67 wt.%)
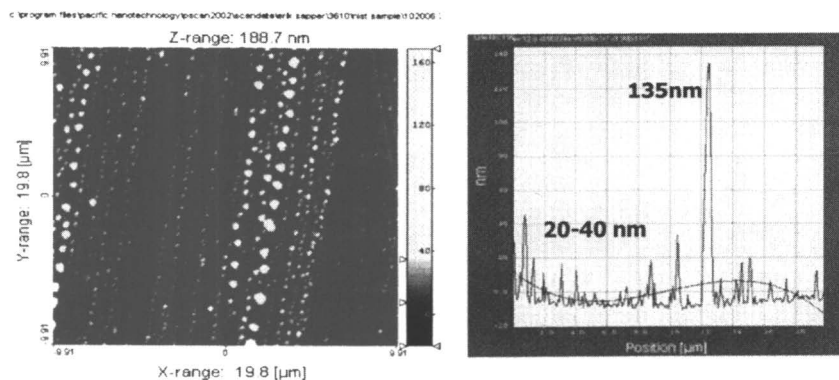
Figure 3. AFM height image (20 x 20 μm) and line profile of Alumina C (1.0 wt.%) arrangements produced by spray application.

Results presented so far establish the formation of a highly ordered phase when coatings are applied at shear rates exceeding a minimum threshold value. Although the exact threshold shear rate was not determined in this study, estimated shear rates as low as 13 s^{-1} (0.05 cm s^{-1} at 75 μm wet coating thickness) produced strings of particles. However, the apparent sizes of some of the circular features in the images are much too large compared to the known sizes of individual alumina or silica nanoparticles used in the study. In some cases, the 1-D alignments can be seen by an optical microscope at 100X magnification (Figure 5). Surprisingly, we were able to detect few, but definitive 1-D aligned features in films containing no nanoparticles. Contamination was suspected; however, repeated experiments confirmed these patterns are present even when the films were prepared under conditions that eliminated the possibility of contamination by alumina or silica nanoparticles (Figure 6).
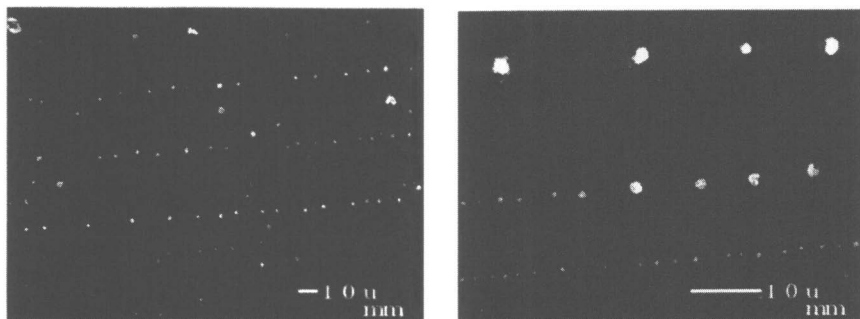
Figure 4. Electron micrographs of Silica A (1.0 wt%) arrangements produced by spray application. The scale bar in each micrograph is 10 μm.
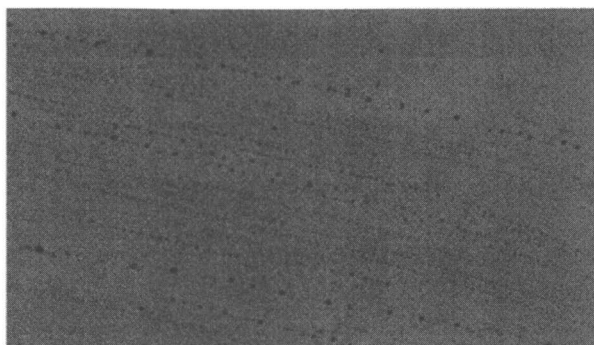
Figure 5. Optical microscopy image of 1-D alignments at 100x magnification. The image represents an approximately 20x12 μm area.
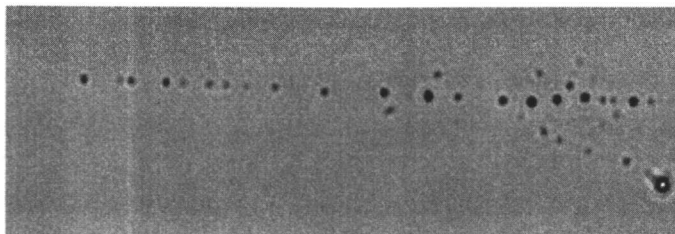
Figure 6. Optical microscope image (400x mag.) of micrometer-scale arrangements produced by spray application of a 2K PU containing no nanoparticles.

SEM Elemental Analysis

As evident from the AFM and SEM images presented so far, many of the features that make up the 1-D strings are much larger than the sizes of alumina and silica nanoparticles. Elemental analysis of the coating film was performed with an SEM equipped with EDS which provided valuable insight into the composition of these features. Electron microscopes operate by firing a beam of electrons or photons at the surfaces of materials. This beam causes inner-shell atomic electrons to dislodge, which eventually create the TEM or SEM micrograph. When the inner-shell electron is emitted a "positive" hole is created, which is quickly occupied by a higher-energy, outer-shell electron. The excess energy from the outer shell electron is given off in the form of an x-ray, which can be measured with an EDS spectrometer. Because every element has a unique atomic and electronic structure, each element emits a different x-ray wavelength when excited by an electron or photon beam. Since the biggest 1-D aligned feature size discrepancy was with spray applied samples, all samples analyzed in this manner were prepared by spray applications on glass substrates. Nanoparticle loading in each case was 1.0 wt.%.

Figure 7 shows EDS analysis results for a spray applied coating sample containing 1.0 wt.% Silica A nanoparticles. The EDS spectrum on the right represents the elemental abundance of a 1 μm diameter area marked "Spectrum 1" in the left image. Presence of Si element is detected. However, when a film containing Alumina D nanoparticles was tested ("Spectrum 1" location in Figure 8, SEM image) not only Al but also Si was detected. When a sample containing Alumina C was analyzed, only Si was detected within a relatively large feature that makes up a 1-D string (see "Spectrum 3" location in Figure 9).

These observations indicate that the shear-induced, 1-D alignments made up of not only the nanoparticles, but also a silicon containing ingredient in the coating formulation. Indeed, siloxane oligomers are commonly used as additives
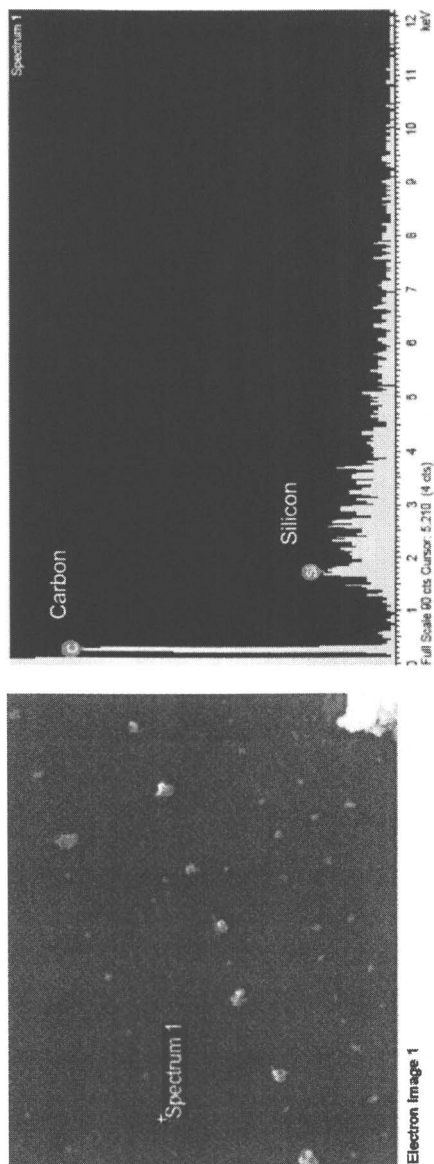
Figure 7. EDS analysis results of a nano-scale aligned feature of a coating containing Silica A nanoparticles.
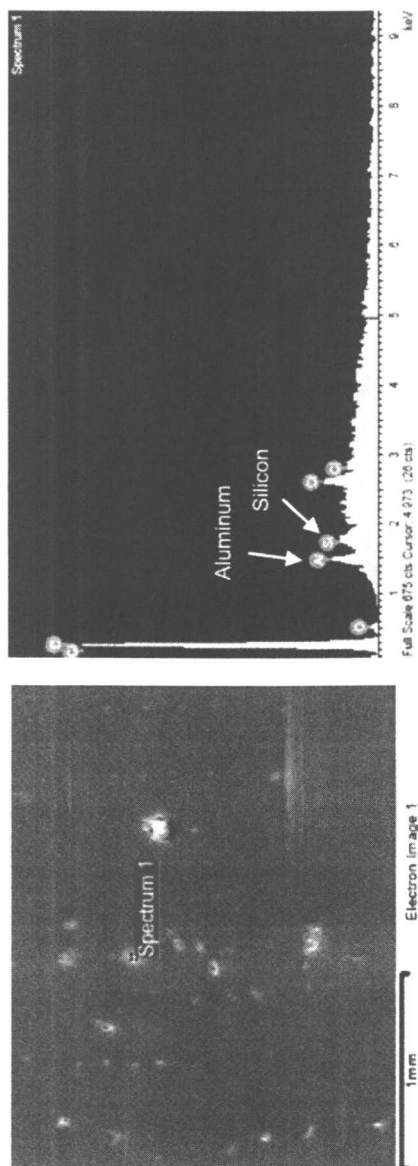
Figure 8. EDS analysis results of aligned particles in a coating containing Alumina D sample shows both Al and Si elements.
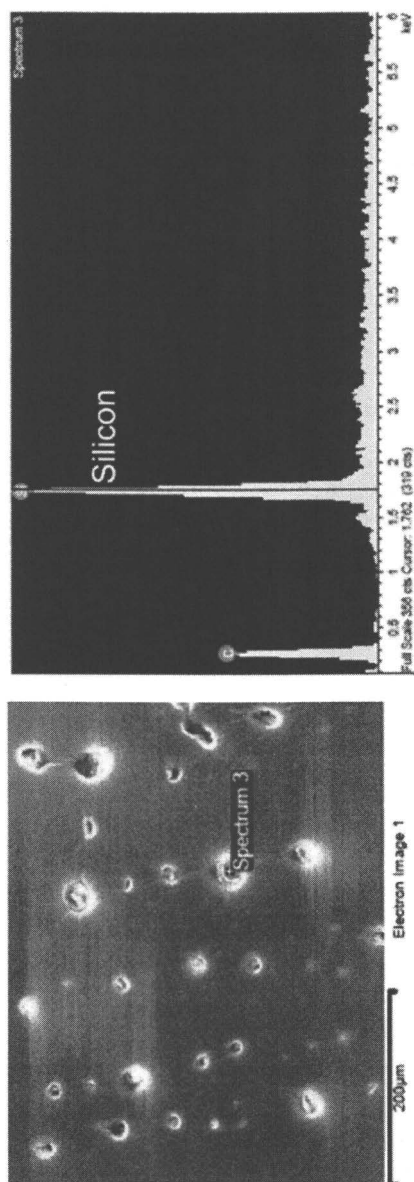
Figure 9. EDS analysis results of larger aligned feature in Alumina C containing coating shows mostly silicon element, believed to be phase-separated siloxane additive in the formulation.

in these types of coatings (See Chapter 11, Table 1). When the region of a coating containing 1-D aligned features was subjected to multiple scans within the SEM, craters began to develop (Figure 10). We believe that the emergence of craters in the micrograph is caused by the evaporation of phase-separated
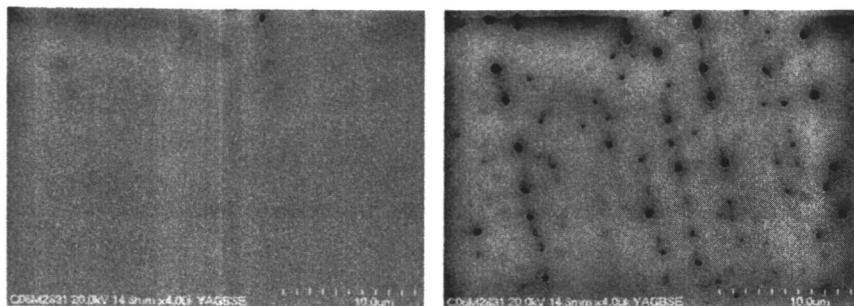
Figure 10. Heat from electron beam of the SEM evaporated large deposits on the coating surface, leaving behind craters on the films surface. The micrograph on the left is after one scan, while the micrograph on the right is the same region after four scans.

silicone due to the heat from the electron beam of the SEM apparatus (Figure 10). Figure 11 contains the SEM image and EDS spectrum of a very small feature after a film containing Alumina C has been subjected to multiple SEM scans. Aluminum element is detected. Similar experiments conducted on films prepared with the formulation containing no nanoparticles showed silicon element within the features that makes up the 1-D strings. In addition, there were other phase separated regions that contained silicon element (Figure 12).

Proposed Mechanism of Alignment

Results presented above establish shear-induced alignment as a template-free method for preparing 1-D strings of alumina and silica nanoparticles. Although their formation mechanism remains somewhat elusive, the siloxane additives in the coating formulations appear to play a critical role. It should be pointed out that, in addition to the siloxane additives incorporated into the formulations, the pre-dispersed nanoparticles (Table 1) contain other siloxane based additives used for stabilizing the dispersions. These surface active materials have marginal compatibility with relatively polar polyurethane phase. It appears that the shear forces are sufficient to cause separation of the siloxane phase and align in the direction of shear flow. To visualize this on the
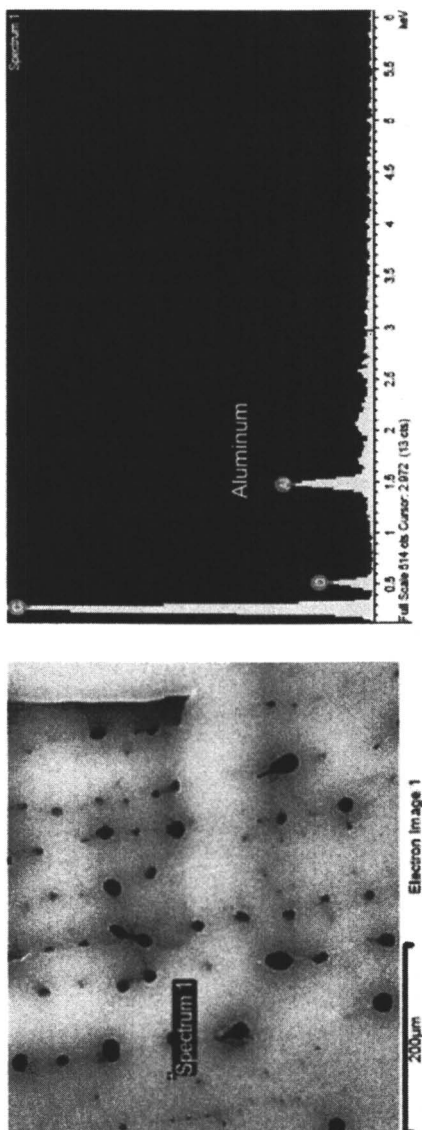
Figure 11. EDS analysis results of Alumina C containing coating shows that smaller aligned particles contain aluminum element, as expected. XRF scans are 1 micron in diameter and are taken in the upper-left area of the SEM image, after four scans
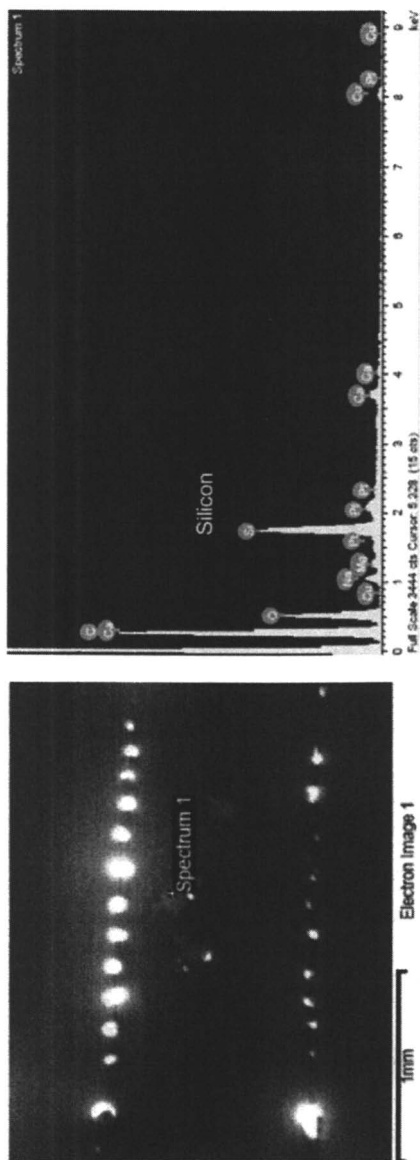
Figure 12. EDS analysis of 1-D arrangements in the control coating system contain primarily carbon and silicon element.

macroscale, consider a bathroom mirror that has condensed water on it (like a "foggy mirror" after a shower is taken); the water droplets are evenly, yet randomly, distributed on the mirror surface. If a hand is used to wipe away portions of the condensation in a horizontal direction, larger water droplets will align horizontally. This combination of shear and directional application may be the most important factor in forming these nanoparticle alignments. String formation in a sheared polymer blend through a similar mechanism has been reported (19).

Also, many properties of the nanomaterials may help provide an intrinsic anisotropy, such as dipole moments of unique axes, anisotropic crystal lattices, and non-uniform stabilizer and surface treatment distributions (20). These qualities contribute to Penn and Banfield's crystal growth theory that they have named "oriented attachment". In a typical example of oriented attachment, primary particles align perfectly along one axis, dock, and fuse together under thermal conditions to yield oriented nanocrystal or nanoparticle chains. There is a strong thermodynamic driving force for oriented attachment, as surface energy is reduced substantially when interfaces are eliminated (20).

We propose the arrangements presented here arise from a combination of high rates of shear flow, combined with early stages of oriented attachment, possibly aided by uneven distribution of surface treatment on the particle surface. This is similar to ligand-directed assembly of titania nanoparticles with partially removed organic stabilizers (21). Furthermore, it is has been shown that oxide nanoparticles are favorably suited for oriented attachment (22). Organic ligands, which impede close contact of crystal surfaces, are usually not needed for stabilization.

Conclusions

Atomic force microscopy and scanning electron microscopy equipped with energy dispersive x-ray analysis capability were used to study shear-induced alignment of alumina and silica nanoparticles in two-component polyurethane clear coatings. One-dimensional strings of nanoparticles, formed in an extended pearl-necklace fashion, were observed on both interfaces of the cured films with nanoparticle volume fractions less than 0.05. This alignment is affected by the shear conditions of the application method. When applied by spraying, linear nanoparticle strings as long as 5 centimeters were observed in the direction of shear and application. Linear arrangements of larger, micron-sized particles were present in all coating systems studied, including the control coatings with no added nanoparticle. EDS elemental analysis revealed that these large-particle alignments contain mostly silicon element, believed to be from phase-separated siloxane additive used in all of the formulations. Nanoparticle strings were also found, to a lesser extent, when coatings were applied by a drawdown method.

The phenomenon was not observed in coatings applied with minimal shear, such as drop-wise deposition of liquid coating. These nanoparticle alignments, in addition to affecting the performance of coatings, may have broader implications in the field of nanomaterials. Our literature searches have not uncovered reports of stable, 1-D nanoparticle arrangements with equal degree of linearity produced under simple shear with compositions having very low particle loadings.

Acknowledgements

References

1. Ackerson, B. *J. Rheol.* **1990**, *34*(4) 553-590.
2. Ackerson, B.; Clark, N.A. *Phys. Rev. Lett.* **1981**, *46*(2), 123-126.
3. Cohan, I.; Mason, T. G.; Weitz, D. A. *Phys. Rev. Lett.* **2004**, *93*(4), 4600-4601.
4. Haw, M. D.; Poon, W.C.; Pusey, P. N. *Phys. Rev. E.* **1998**, *57*(6) 6859-6864.
5. Pham, H. H.; Gourevich, I.; Oh, J. K.; Jonkman, J. E. A.; Kumacheva, E. *Adv. Mater.* **2004**, *16*(9), 516-520.
6. Kretschmer, R.; Fritzsche, W. *Langmuir.* **2004**, *20*, 11797-11801.
7. Winkleman, A.; Gates, B.; McCarty, L. S.; Whitesides, G.M. *Adv. Mater.* **2005**, *17*, 1507-1511.
8. Shenhar, R.; Norsten, T. B.; Rotello, V. M. *Adv. Mater.* **2005**, *17*(6), 657-669.
9. Bhatt, K. H.; Velev, O. D. *Langmuir,* **2004**, *20*, 467-476.
10. Tang, Z.; Kotov, N. *Adv. Mater.* **2005**, *17*(8), 951-962.
11. Dunin-Borkowski, R.E.; McCartney, M.R.; Posfai, M.; Frankel, R.B.; Bazylinski, D.A.; Buseck, P.R. *Eur. J. Mineral.* **2001**, *13*, 671-684.
12. Hutchinson, T.O; Liu, Y.-P.; Kiely, C.; Kiely, C.J.; Brust, M. *Adv. Mater.* **2001**, *13*(23), 1800-1803.
13. Dinsmore, A.D.; Yodh, A.G. *Langmuir,* **1999**, *15*(2), 314-316.
14. Huang, J.; Kim, F.; Tao, A.R.; Connor, S.; Yang, P. *Nature Materials,* **2005**, *4*, 896-900.
15. Brickweg, L.J.; Floryancic, B.R.; Fernando, R.H. *Polymer Materials: Science and Engineering,* **2006**, *51*, 124-125.

16. Floryancic, B.R.; Brickweg, L.J.; Comer, J.B.; Sung, L.-P.; Forster, A.M.; Fernando, R.H. *Polymer Materials: Science and Engineering,* **2006**, *51*, 251.
17. Brickweg, L.J.; Floryancic, B.R.; Sapper, E.D.; Fernando, R.H. *J. Coat. Tecnhol. Res.* **2007**, *4*(1), 107-110.
18. Xing, L.-L.; Glass, J. E.; Fernando, R. H. *J. Coat. Tech.*,**1999**, *71*(890), 37.
19. Migler, K. B., *Phys. Rev. Lett.*, **2001**, *86*(6), 1023.
20. Alivisatos, A.P., *Science,* **2000**, *289*(5480), 736-737.
21. Polleux, J.; Pinna, N.; Antonietti, M.; Niederberger, M. *Adv. Mater.* **2004**, *16*(5), 436-439.
22. Pacholski, C.; Kornowski, A.; Weller, H. *Ang. Chem. Int. Ed.*, **2002**, *41*(7), 1188-1191.

Chapter 8

Increasing Coating Functionality Using Nanodimensioned Materials

S. R. Taylor[1], G. J. Shiflet[1], J. R. Scully[2], R. G. Buchheit[3],
W. J. van Ooij[4], K. Sieradzki[5], R. E. Diaz[5], C. J. Brinker[6],
and A. L. Moran[7]

[1]University of Texas Health Science Center, 6516 M.D. Anderson Boulevard, Houston, TX, 77030
[2]Department of Materials Science and Engineering, University of Virginia, P.O. Box 400745, 395 McCormick Road, Charlottesville, VA 22904
[3]Department of Material Science and Engineering, Ohio State University, 2041 College Road, Columbus, OH 43210
[4]Department of Chemical and Materials Engineering, University of Cincinnati, Cincinnati, OH 45221
[5]School of Materials Engineering, Arizona State University, Mailcode 8706, Tempe, AZ 85287
[6]Department of Chemical and Nuclear Engineering, University of New Mexico, 1001 University Boulevard SE, Albuquerque, NM 87106
[7]Mechanical Engineering Department, U.S. Naval Academy, 590 Holloway Road, Annapolis, MD 21402

The coating system presently used on military aircraft is constrained in function and limited to the use of chromate-based compounds for the mitigation of corrosion. The objective of this program was to expand the functionality of the military aerospace coating using recent advances in the materials sciences. By implementing gains in molecular and nano-engineered materials, the scientific and technological foundations will be laid for a coating that: (1) provides corrosion protection and adhesion using environmentally compliant materials, (2) senses corrosion and mechanical damage, (3) initiates mitigating responses to the sensed damage (chemical and mechanical), (4) improves fatigue resistance, (5) has the ability to change color-on-demand, and (6) provide water rejection and self-cleaning capability. The enhanced functionality of this advanced coating system will be achieved

© 2009 American Chemical Society

through the incorporation of: (1) a field-replaceable, nano-engineered metallic cladding, (2) the use of molecular-engineering and self-assembled colloidal crystals for packaging, sensing, color-on-demand, and super-hydro-phobicity, (3) the development of new approaches for the identification, encapsulation, and delivery of environmentally compliant corrosion inhibitors, and (4) the optimization of organic coating adhesion through the use of environmentally compatible surface treatments. A summary of program achievements will be presented.

Introduction

The skin of military aircraft when received from the original equipment manufacturer (OEM) consists of AA2024-T3 sheet having a multi-layer coating system that provides corrosion protection and mission function. This coating system is comprised of: (1) an aluminum cladding (*e.g.*,AA1100), (2) a chromate-based conversion coating or chromate-sealed anodized oxide layer, (3) an epoxy-based or polyurethane-based primer coat containing chromate-containing inhibitive pigments, and (4) a single color, low-gloss mission topcoat. Each of these material layers provides a specific function and collectively interacts to provide corrosion protection, both real-time and active, as well as some level of mission capability (e.g. low glint, ground camouflage). However, many of the materials most critical to the function of this current military aerospace coating system are either: (1) hazardous to worker health and safety, (2) hazardous to the environment, (3) removed and not replaced during the maintenance cycle, or (4) are extremely limited with regards to mission function. These limitations result in constrained mission safety and impose substantial costs in the management of worker safety and hazardous waste disposal.

The majority of corrosion protection of OEM military aerospace coating systems is determined by the cladding. The cladding provides a homogenous, passive substrate that has excellent barrier properties and inherently low corrosion susceptibility(*1*). This cladding is an excellent substrate for subsequent organic coatings(*2-4*). However, its surface is routinely augmented by a chromate conversion coating (CCC) to facilitate the corrosion protection provided by subsequent organic layers. The facility of CCC within the coating system appears not to be related to its stand alone corrosion properties(*5-9*), but more to its ability to enhance adhesion(*10*), especially as-applied in the maintenance cycle(*11*).

The second-most important contributor to corrosion protection of OEM military aerospace coatings is from chromate-based inhibitive pigments contained within the primer layer. These inhibitive compounds (*e.g.*, strontium chromate, zinc tetraoxychromate, and zinc/potassium chromate(*12*)) have an optimum balance of solubility and inhibitor efficiency so that chromate is leached out of the primer coating at a rate sufficient to achieve a concentration at

the metal/coating interface needed to mitigate corrosion, but does not solvate to the extent that osmosis or porosity occurs in the primer(13). The hexavalent chromium species (Cr^{6+}) within the primer and to a lesser extent within the CCC layer, through a combination of mobility and inhibitor efficiency can mitigate corrosion within physical breaches of the coating system and provide a self-healing character(10,14). However, chromate-based materials are highly toxic and carcinogenic(15) and pose significant risks to workers and the environment. There are significant costs now in the management of this hazardous material during both its application and removal in the maintenance cycle.

This functional primer is then coated with a single color, low gloss topcoat. The topcoat provides very little, if any, benefit from the standpoint of corrosion protection[10]. Its primary function is to minimize glint during combat and provide some level of ground camouflage. In the context of emerging coating capabilities, current topcoats are very limited and static in nature, and are ultimately constraining with respect to mission capability.

The limitations of the OEM coating system described above are perpetuated in the course of depot maintenance, where the aircraft coating will be stripped so that the skin can be inspected for corrosion and mechanical damage. Depainting eventually results in the removal of the cladding, thus exposing the underlying AA2024-T3 skin material. The localized corrosion susceptibility of AA2024-T3 and other current generation age-hardenable aerospace alloys is high due to the micro-galvanic couples created by inherent micro-structural and micro-chemical hetero-geneities(16-19). This increased susceptibility can eventually affect structural integrity through the loss of load-bearing cross-section, increased stress intensity at pits, or increased frame stress due to corrosion product buildup within lap splice joints. Exposure of AA2024-T3 substrate material for subsequent painting presently mandates the use of chromate conversion coatings and chromate-bearing primers to ensure adequate adhesion and corrosion protection.

The methods and materials used in present military aerospace coating systems present significant concerns with regards to worker and environmental safety, maintenance costs, asset availability, and mission safety. An expansion of these functional and material limitations is needed. This study seeks to identify a new coating system that will significantly advance coating function.

The new coating system will:

- provide on-demand corrosion protection using environmentally safe materials
- sense corrosion and mechanical damage of the aircraft skin
- initiate coating repair responses to sensed chemical and physical damage
- achieve optimal adhesion using environmentally compliant materials
- improve the fatigue resistance and mechanical integrity of the skin

- provide changes in color on-demand
- provide water rejection and self-cleaning capability.

This advancement will be accomplished through the:
- development of a field-replaceable, multi-functional, nano-engineered metallic cladding
- use of molecular engineering and micro-electro-mechanical approaches to develop mechanical and chemical sensing capability of the coating/substrate interface
- identification, encapsulation, and delivery of environmentally compliant inhibitor compounds with optimum solubility and resin compatibility
- optimization of organic coating adhesion through the use of environmentally compatible surface treatments
- development of biomimetic surface structures through self-assembly methods

Results and Discussion

Nano-Engineered Cladding

The OEM cladding on military aircraft is a dilute, non-heat treatable alloy that has a much lower corrosion rate than the underlying substrate (AA2024-T3(*1*)). This quality minimizes organic coating debonding and filiform corrosion(*2-4*) and provides superior field-corrosion resistance in lap/splice joints when compared to the bare substrate in the presence of chromates. However, current cladding compositions provide limited sacrificial cathodic protection of crevices, rivet holes, exfoliated regions, and cracks(*1*). More importantly, this first line of corrosion protection is removed during the maintenance cycle, and presently cannot be replaced.

Thermal spray methods have been advanced to the point that rapidly quenched aluminum-based materials (*e.g.*, Al-Mg, Al-Zn, and Al-In-Sn) can now be applied to ferrous and precipitation age-hardenable aluminum alloys(*20,21*). Thermal spraying allows the production of cladding compositions (*e.g.*, Al-In-Sn) that can attain the significant anodic potentials needed for suppression of localized corrosion and stress corrosion in high strength aluminum alloys(*22*). The high cooling rates developed in this process (up to 10^7 degrees/s) also impart: partitionless phase transformation, solute trapping, extended solid solubility limits(*23*), and the capacity to produce amorphous alloys(*24*). Amorphicity in metals has the advantage of establishing micro-structural homogeneity (*i.e.*, elimination of second phase particles), thus reducing

corrosion rates. This loss in crystalline structure also inhibits dislocation motion, which dramatically increases tensile strength while maintaining modulus. Thus, thermally-sprayed, amorphous aluminum claddings could provide significant electrochemical and mechanical advantage relative to current Alclad™.

Advances in thermal spray technology are paralleled by achievements in the science of aluminum-based metallic glasses where compositions can now be vitrified at reduced quench rates(*26-29*). Aluminum-based amorphous alloy chemistries can be produced to provide improved barrier protection (*e.g.*, inclusion of transition metal (TM), Fe, Ni, Co, Cr), as well as improved localized corrosion(*30*) and active corrosion protection (*e.g.*, inclusion of lanthanides). Several amorphous Al-TM-Ce alloys have been produced (*e.g.*, $Al_{85}Ni_{10}Ce_5$, $Al_{87}Co_{8.7}Ce_{4.3}$, and $Al_{90}Fe_xCe_{10-x}$). Since Ce is in supersaturated solid solution, oxidized layers of Al_2O_3 that contain CeO_2(*31*) can be produced. In the presence of moisture, soluble Ce^{4+} in the form of $Ce(OH)_2^{2+}$, could then migrate to cathodic sites, precipitate the less soluble trivalent form upon reduction, and block further cathodic activity, and hence corrosion(*32*).

To date, amorphous aluminum-based alloys have been made using the following systems: Al-Co-Ce, Al-Co-Ce-Mo, and Al-Cu-Mg-Ni. One facet of this research effort, alloy design, utilizes computational thermodynamics to develop predictive models for the glass forming region (GFR) for an alloy system. Since there is no fundamental thermodynamic information for these amorphous materials, a database was generated using x-ray diffraction, differential scanning calorimetry, differential thermal analysis, transmission electron microscopy, analytical scanning electron microscopy, and other methods.

Alloy design was conducted in concert with corrosion property characterization of these materials. The alloying elements for a particular alloy, e.g., Co and Ce, can be released from the surface depending on the environment, and attenuate the corrosion process by either reducing the anodic (e.g., by Co ions) or cathodic (e.g., by Ce ions) process. As mentioned, alloys can also be designed such that the barrier properties are optimized.

Finally, the third component needed for this technology is the ability to spray apply the material onto AA2024-T3 and maintain amorphicity without compromising the metallurgy or performance of the substrate alloy. A variety of thermal (plasma, HVOF) and athermal (cold spray) methods were examined to determine the effects of annealing, cold work, porosity, and oxide content, on cladding performance.

The GFR for an Al-Ce-Co system is shown in Figure 1. The outlined area demarks the alloy compositions that form amorphous metal upon cooling as determined by numerous researchers.

The physical state of amorphicity is not thermodynamically stable for a metal. There is a driving force for an amorphous metal to become crystalline. If crystallites grow to full contiguity, *i.e.* touching crystal faces, then all advantages
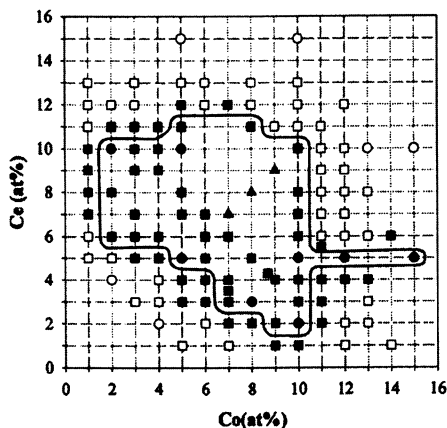
Figure 1. Schematic of the GFR for the Al-Ce-Co system. This data was acquired for a fixed rotational speed (Cu cooling mandrel) of 4600 rpm.

of the amorphous state are lost, and the disadvantages of defect structures (*e.g.*, grain boundaries, intermetallic particles) on corrosion and mechanical properties are introduced. Thus, it is of interest to determine the kinetics and activation energy for the amorphous to crystalline transition as a function of temperature. Figure 2 shows the transformation of an Al-Gd-Co alloy system as a function of time. The amorphous aluminum-based systems developed in this program are unique in that the rare earth additions create a concentration boundary around crystals when in the nano-dimension that limits further growth. The presence of nano-crystallites within a continuous amorphous phase creates a material that retains the mechanical and corrosion characteristics of the fully amorphous alloy. The development of a contiguous crystalline structure takes many hundreds of hours at high temperature and is not viewed as a hindrance to the use of these materials in aircraft.

Modeling is now able to predict the GFR for specific amorphous aluminum alloys. Figure 3 shows an example of the experimentally determined GFR for the Al-Fe-Gd system (dark region in lower left) which is overlaid onto a calculated graph showing regions that are kinetically favored for the formation of crystalline material.

Corrosion characterization has optimized the TM and RE content of Al-Co-Ce and Al-Co-Ce-Mo(*33*) shown in Figure 1. Three distinct corrosion functions of this family of alloys have been investigated: corrosion barrier properties associated with halide induced pitting and dissolution at low and high pH, sacrificial anode behavior, and active corrosion inhibition based on the idea that the Al-Co-Ce layer acts in a similar manner as pigmented paint. Inhibitive ions (Co^{2+} and Ce^{3+}) are stored and released on-demand, and attain a critical inhibitor

200°C – 10 min.   200°C – 1 hour   200°C – 3 hours
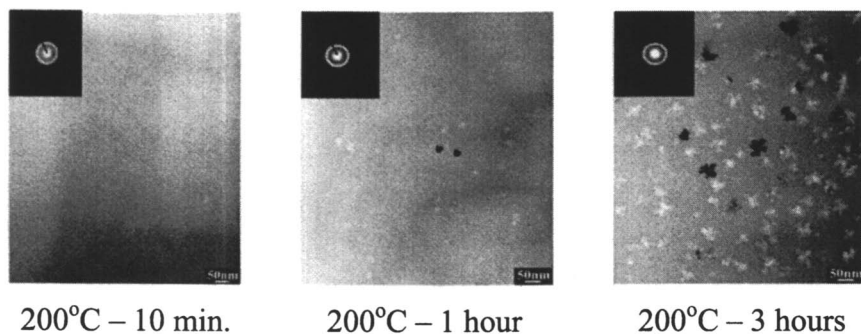
Figure 2. TEM bright field micrographs of $Al_{90}Co_3Ce_7$ (atomic percent) at 200° C.
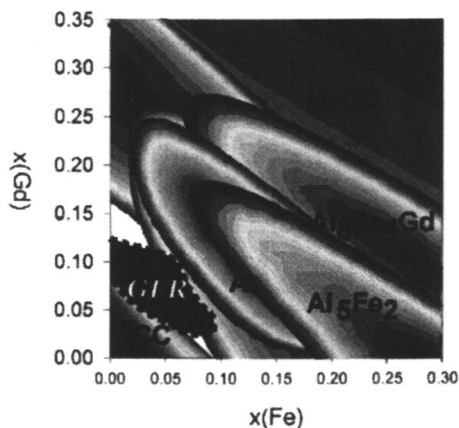
Figure 3. The experimental GFR for Al-Fe-Gd superimposed on calculated plot for crystallinity. Note the overlap of GFR with region predicted not to be kinetically favored for crystallization.
(See page 1 of color insert.)

concentration at a physical breach in the coating system(*34,35*). With respect to all three corrosion functions, the Al-Co-Ce alloy system has the ability to select a performance behavior based on composition(*33*). For example, the OCP can be lowered by minimizing the Co content which influences the oxygen reduction reaction on the alloy(36). Figures 4 and 5 show the open circuit and repassivation potential as a function of elemental content for the Al-Co-Ce system. The highest pit repassivation potentials of these amorphous alloys are obtained in alloys that maximize Co content, with a secondary influence brought about by a reduction of Ce.

Initial experimentation on the application of amorphous cladding onto AA2024-T3 employed pure aluminum and demonstrated that a coated material with improved corrosion and fatigue properties was achievable. A 99.0-99.8 % Al coating/AA2024-T3 skin substrate system was used to evaluate the corrosion/fatigue performance as a function of the thermal spray coating process (i.e., powder flame spray, atmospheric plasma spray, and HVOF spray) and cold spray processes). Comparison of the microstructures, mechanical properties, fatigue, and pre-corroded fatigue properties of samples with the three types of thermal spray coating, as well as samples of bare AA2024-T3 and Alclad^{TM} AA2024-T3, revealed that HVOF is the most promising thermal spray process for the deposition of aluminum coatings. In particular, HVOF coatings greatly increase the fatigue and pre-corroded fatigue lifetimes of the AA2024-T3 substrate.

Coatings of Al-18Co-9Ce and Al-13Co-26Ce (wt. %) were deposited from powders by thermal spray and cold spray processes. Feedstock powders and processed coatings were characterized by X-ray diffraction and Scanning Electron Microscopy (SEM). X-ray diffraction patterns, as shown in Figures 6 for the HVOF process, indicate that feedstock powders were nanocrystalline and the deposited coatings demonstrate reduced crystallinity. A modified form of HVOF, pulsed thermal spray (PTS) has been used to deposit an amorphous or nano-crystalline coating using traditional crystalline feedstock. PTS coatings tend to demonstrate a higher degree of amorphicity as shown in the x-ray diffraction pattern given in Figure 6c. Coating hardness values were higher and fatigue lifetimes were lower than expected, most likely due to high Co and Ce content and processing effects.

An evaluation of available, commercially developed cold spray methods such as Kinetic Metallization was also conducted. The resulting coating demonstrated the high strength and reduced ductility associated with cold working so that fatigue properties were limited. Preliminary fatigue results for cold spray coatings using an alternative technique developed at the University of Ottowa are very promising (Figure 7).
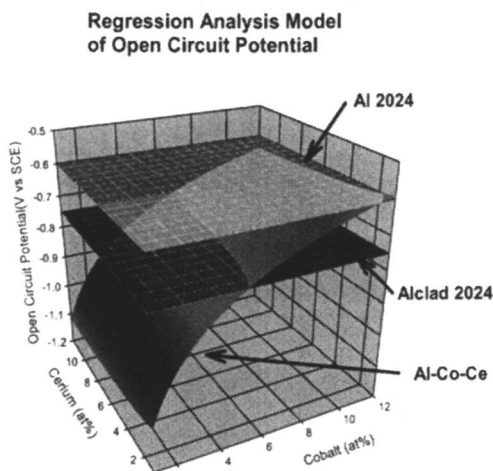
Figure 4. The open circuit potential of the Al-Co-Ce system as compared to AA2024 and Alclad™ 2024. (See page 1 of color insert.)
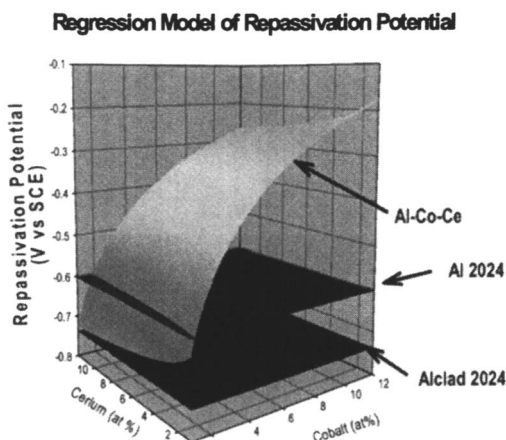
Figure 5. The repassivation potential of the same Al-Co-Ce system shown in Figure 4. (See page 1 of color insert.)

Rapid Identification of Non-chromate Corrosion Inhibitors

Corrosion protection by current military aerospace coatings is provided primarily by the chromate-based inhibitive pigments present within the primer layer(*10*). Chromate pigments are unique within the current repertoire of inhibitors in that they have very high inhibitive power (*i.e.*, high efficiency at extremely low concentrations) even when used on the more susceptible Cu-bearing aluminum alloys(*13*). This inhibitive power allows certain chromate compounds to be incorporated into primer resins because they dissolve at a sufficient rate to deliver an effective inhibitor dose to the metal substrate, yet not dissolve so fast so as to produce porosity or blistering. The effective water solubility for chromate pigments appears to be in the range of 5×10^{-3} moles CrO_4^{2-} L^{-1} (strontium chromate ($SrCrO_4$)) to 1.1×10^{-2} moles CrO_4^{2-} L^{-1} at $25°$ C (zinc yellow ($K_2CrO_4 \cdot 4ZnCrO_3 \cdot$ $Zn(OH)_2 \cdot 2H_2O$))^{12}. Other chromate compounds, *e.g.*, zinc tetraoxychromate ($ZnCrO_4 \cdot 4Zn(OH)_2$), require an acidic environment to achieve the proper solubility (used in acidified wash primers), while others, *e.g.*, zinc chromate, are too insoluble under any condition and can actually promote corrosion. Thus, the proper balance of inhibitive power and pigment solubility are requisite for total system performance.

Numerous compounds have been examined with the hope of providing a chromate replacement. These compounds include molybdates(*37*), vanadium-based compounds(*38*), boron-based compounds(*39-41*), and rare earth salts(*41*), among others, and have recently been examined for inhibitor efficacy on aerospace alloys(*42,43*). To date, <u>no</u> <u>single</u> environmentally compliant compound has demonstrated an effective inhibitive power (efficiency at specified concentration) comparable to chromate, much less with appropriate pigment solubility.

A promising alternative to the use of a single inhibitive species is that of using synergistic combinations of two or more compounds. Synergy occurs when the inhibitive property of the combination exceeds the sum of the individual compounds. Synergistic combinations of inhibitors have been examined extensively for steel in acidified(*44-51*) and neutral(*52-55*) aqueous environments, as well as for copper in neutral aqueous environments(*56-57*). Numerous theories for synergy have emerged depending on whether active anions(*45,49,56,59,60*), cations(*44,48,50,53,55*), or organic species(*54-55*) are employed.

Recent studies have examined synergistic combinations of the previously described rare earth and transition metal salts(*42,63,64-66*). These preliminary experiments have only examined 1:1 ratios of the components at a single concentration; however synergistic effects have been observed using both electrochemical and pit morphology analyses.

There are a large number of relevant experimental variables that must be examined in the proper identification of potential corrosion inhibitors, *e.g.*,
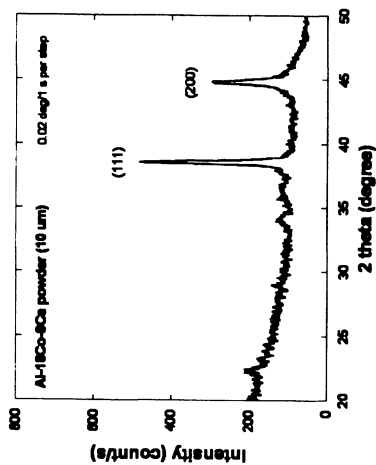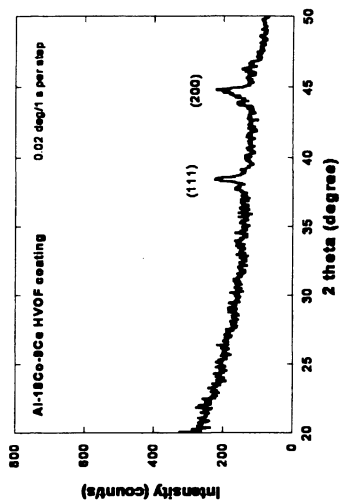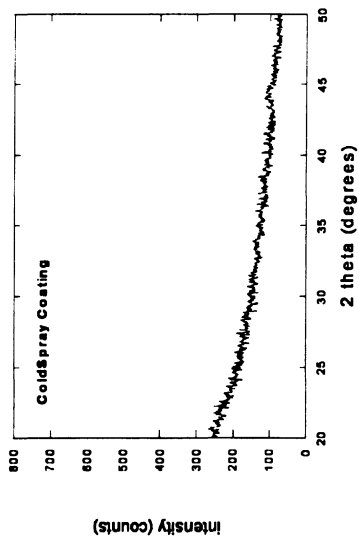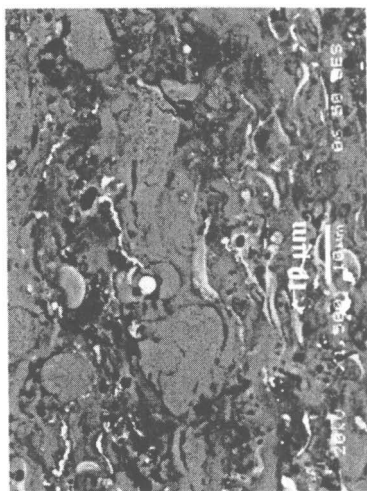
(d)
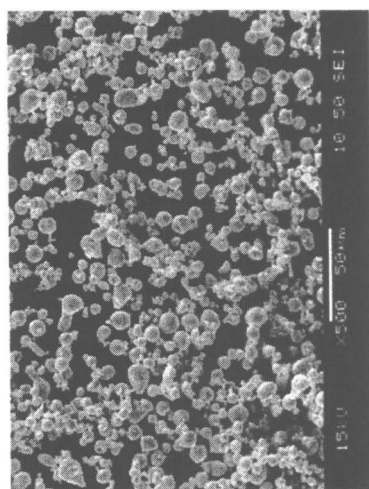
(e)

Figure 6. X-ray diffraction patterns of Al-18Co-9Ce feedstock powders, HVOF coating, and PTS coating (a, b, c) and SEM images for the powders versus the resulting HVOF coating (d, e).
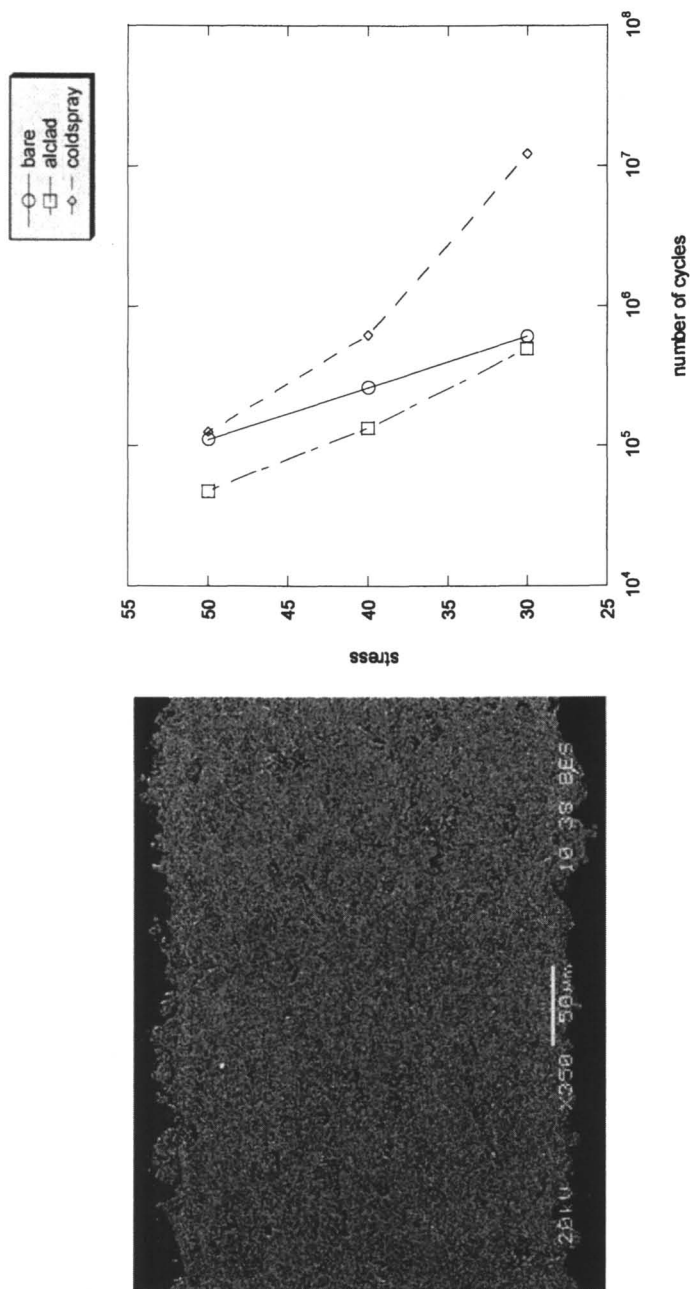
Figure 7. SEM images of Al-13Co-26Ce coatings and coating fatigue properties as compared to bare AA2024 and Alclad (b).

concentration, pH, temperature, etc. This creates an expansive number of experiments for the discovery of synergy. This exploding matrix and the long test times (days or weeks) needed to gather data create the need for high throughput screening (HTS) methods. This program has developed three HTS assays for the rapid identification of corrosion inhibitors and inhibitor synergies for AA2024-T3: DC polarization(65), measurement of surface copper(67), and fluorometric assessment of Al^{3+} (68).

In the DC method, two AA2024-T3 wires (with the same metallurgical structure as sheet) are polarized with a low amplitude (100 mV), DC bias(65). The resulting current is measured for 9 hours and the steady state current (7-9 hours) is used as a measure of performance. This method has been scaled up in number through the use of a multi-channel potentiostatic device (Multiple Micro-Electrode Array (MMA), Scribner Assoc.) which can allow 50 simultaneous DC polarization tests of the two-electrode combination as described. Through the use of the MMA and a traditional 96-well reaction frame fitted with the appropriate top, large number of experiments can now be performed in parallel.

The surface copper method is based on the de-alloying mechanism of copper-bearing aluminum alloys and the subsequent re-deposition of copper(69-72). Measurement of the amount of surface copper via cyclic voltammetry has been used to assess the degree of corrosion damage on AA2024-T3(71,73-75). This study has used this same method for the HTS of corrosion inhibitors for AA2024-T3. Using the same reaction frame concept, 96 AA2024-T3 wire segments are immersed in the individual cells of the reaction frame and left at open circuit in the respective test solutions. After 24 hours the samples are removed, rinsed, and inserted into a separate cell for electrochemical detection of surface copper on the AA2024-T3 samples.

The chemical assay uses the same exposure procedure as above, but rather than test the electrodes, the amount of Al^{3+} in solution is accessed via a fluorometric technique(68). This fluorometric technique is highly automated and can easily assess 10^5 experiments per day. The electrochemical methods are presently able to perform 10^3 experiments per day.

Figure 8 shows a matrix of experiments which examined the inhibitor performance of a particular combination of inhibitor compounds as a function of A:B ratio (total concentration always maintained at 3.4 mM) and pH using the three methods described. This number of experiments would have taken several months to perform using conventional methods, but was conducted easily in 8 hours using the methods described above. These results clearly show unpredicted synergistic behavior. It is believed that variations between the methods may be indicative of the inhibitor mechanism specific to the compound(s) tested since the corrosion of complex alloys such as AA2024 involves many events.

These HTS methods were used to screen large numbers of single compounds and their binary and ternary combinations. Figure 9 shows a summary of the inhibitor efficiencies of some of the materials compared to a

chromate-based inhibitor (top). Interestingly, some of the best performers are the synergistic combinations.

Packaging and Delivery of Inhibitor Compounds

It is unlikely that the optimum non-chromate inhibitor compound(s) identified in the effort above will also have the optimum solubility characteristics needed for inclusion into a paint. Fortunately, numerous molecular and nano-engineering packaging schemes are presently available to control compound solubility and deliver inhibitors in an intelligent manner.

This program has shown hydrotalcites (HT) as a means to contain and deliver inhibitive species on-demand(76-79). In this approach an inhibitive anion is incorporated into the gallery space of the HT structure. The inhibitive anion exchanges for an anion in the local environment (e.g., ingressed Cl⁻) which changes the lattice spacing of the HT. Thus, the inhibitor is released on demand, getters an aggressive anion(80) (chloride), and also changes the lattice spacing thus providing a sensing scheme. This delivery, scavenging, and sensing capability is now well documented(81). The protective capabilities of an epoxy resin loaded with 25% HT containing vanadate (VO_3), a corrosion inhibitor, is shown in Figure 10. An AA2024-T3 substrate was pretreated with a single coating consisting of a silane-containing polymer-wrapped cerium and HT containing vanadates. This coating system was capable of providing scratch protection for over 1500 hours of salt spray (ASTM B117).

More recent research has examined the use of bentonite clays as a means to contain inhibitive cations such as Ce^{3+}. These materials behave similarly to the HT's, except the gallery-contained cation exchanges for local cation in the environment. Neutron activation analysis (NAA) has shown exchange of Ce^{3+} for Na+ in solution (NaCl).

Nanoporous silica is a mechanically and thermally stable, cheap, and environmentally benign ceramic. The well controlled pore size, narrow pore size distribution, and controllable pore surface chemistries of self-assembled mesoporous silica materials are also being explored as an encapsulating material for controlled release of corrosion inhibitors. Spherical mesoporous silica particles have been prepared by aerosol assisted self-assembly. In this method, amphiphilic molecules (surfactants or block copolymers) are used as nanostructure directing agents.

The surfactant-directed assembly of nanoporous particles starts with a homogeneous solution of corrosion inhibitors, soluble silica plus surfactant prepared in an ethanol/water solvent with initial surfactant concentration much less than critical micelle concentration. Aerosol droplets generated by

atomization are passed through an aerosol reactor and collected on a filter. In this process, preferential alcohol evaporation enriches the particles in surfactant, water, inhibitor, and silica, inducing micelle formation and successive co-assembly of silica-surfactant micellar species into liquid-crystalline mesophases in a radially-directed self-assembly process. Accompanying condensation of the silica species solidifies the droplets, resulting in spherical particles with highly ordered hexagonal, cubic or vesicular mesostructures. During self-assembly, the water soluble corrosion inhibitor salts are concentrated and diffuse inward with the moving evaporating interface. This results in a core-shell structure with the corrosion inhibitor compartmentalized at the center. Removal of the surfactant by calcination leaves solid spherical mesoporous particles of uniform network of mono-sized nanopores as shown in Figure 11).

The nanostructured core-shell cerium/silica particles with high loading of corrosion inhibitors have been tested for protection of aluminum alloy AA2024-T3 during 100 hour exposure to 0.05M NaCl solution. Preliminary results demonstrated that these core-shell nanostructured particles are effective for corrosion inhibition of AA2024-T3.

Another method of inhibitor containment for solubility control and improved resin miscibility is that plasma polymer-wrapping of inhibitor materials. The efficacy of this approach has been demonstrated and offers yet another method of inhibitor containment and delivery. The successful application of this method can be seen in the 'super-primer' coated sample shown in Figure 10. This is a primer consisting of water-borne resins, organofunctional silanes and anti-corrosion pigments. The particular system shown in Figure 10 consisted of an epoxy and an acrylate resins. The system was engineered such that the epoxy component phase separated to the surface and the acrylate to the metal interface during drying and curing. Since acrylate is more hydrophilic, water-soluble anti-corrosion pigments disperse within the acrylate only and not in the epoxy. This prevents inhibitors from washing out of the coating, so that they are available at scribes and other defects. With inhibitive pigments like zinc phosphate, cerium vanadate, cerium silicate and cerium-exchanged silica, 4000 hours (6 months) of effective on-demand corrosion protection was provided to AA2024-T3 in the B-117 salt spray and in salt immersion tests.

The simultaneous use of all of the delivery approaches described above may be needed, particularly if a synergistic inhibitor system is required. While the ideal scenario would be to implement an inhibitor system that demonstrates synergy at all concentrations, it is quite possible that synergy is optimized at a specific ratio. In this case delivery systems will be needed such that the appropriate ratio of compounds is delivered.

142
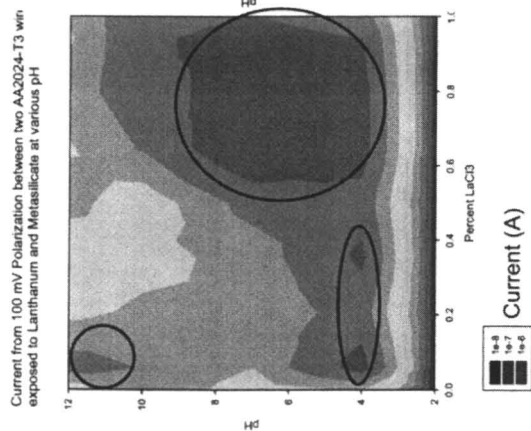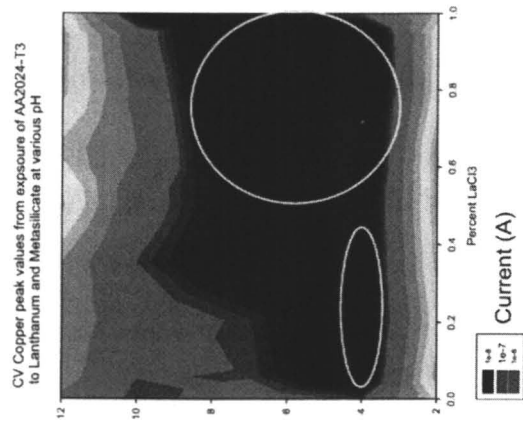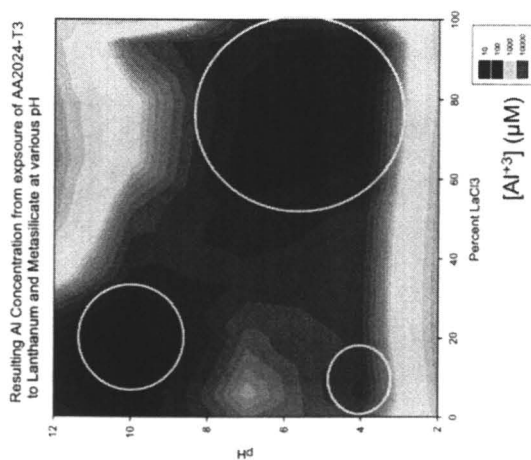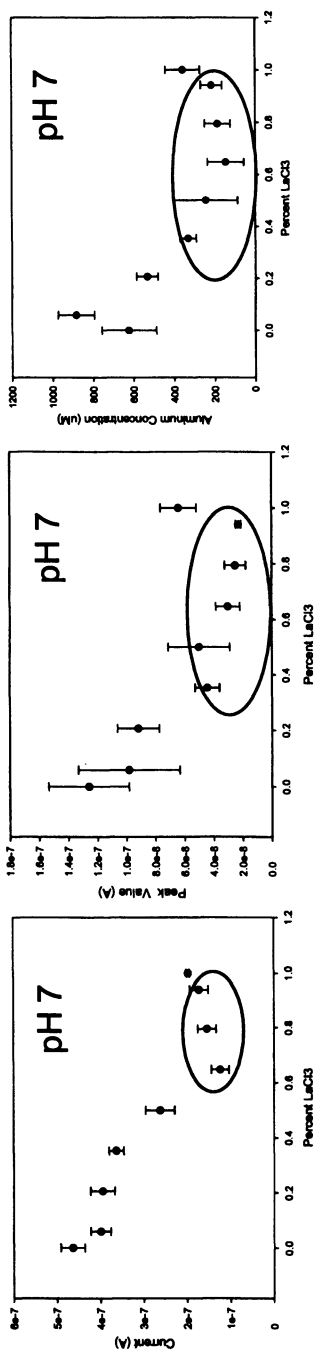
Figure 8. Inhibitor performance results for lanthanum chloride and sodium metasilicate using DC polarization (left), Cu redeposition (center) and fluorometric detection of Al³⁺The regions showing synergy have been circled 66. (See page 2 of color insert.)
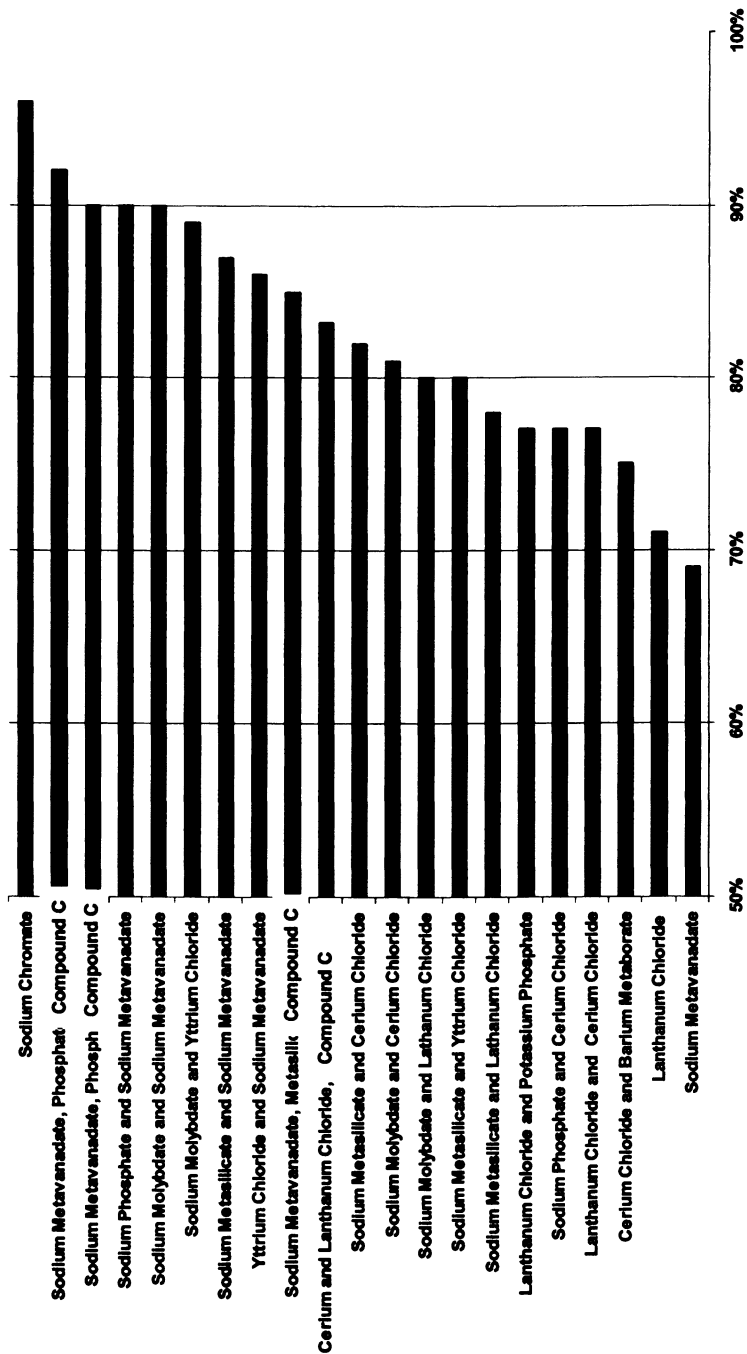
Figure 9. Summary of inhibitor efficiencies for a variety of materials and combinations at pH 7. All inhibitors were tested at 3.4 mM (total for combinations) on AA2024-T3[66] .
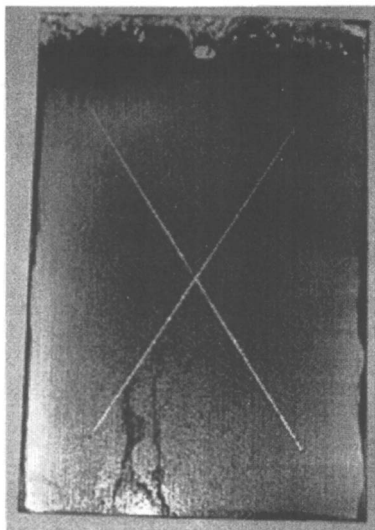
Figure 10. Scribe protection after 1008 hours of salt spray (ASTM B117) by a neat epoxy resin loaded with 25% HT-V and applied to silane treated AA2024-T3.
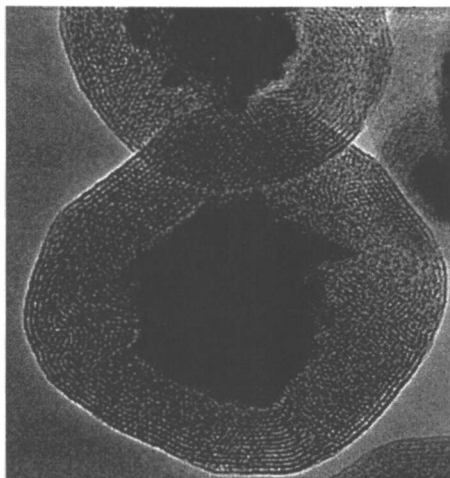
Figure 11. TEM image of core-shell CeCl$_3$/SiO$_2$ particles.

Water Rejection and Self-cleaning

Another technical outcome from this program is a method that creates a super-hydrophobic surface finish. A sol gel-based solution can be spray applied to the surface of the aircraft (or any other surface), and. through self-assembly processes establishes a fractal surface that mimics the lotus effect. The super-hydrophobic character of the surface causes water to be rejected in such a way that not only does it not wet, but the water rolls off and picks up any debris that may be sitting on the surface. Thus, the surface is now self-cleaning. Figure 12 shows an SEM comparison of the sol gel based surface and the lotus leaf.
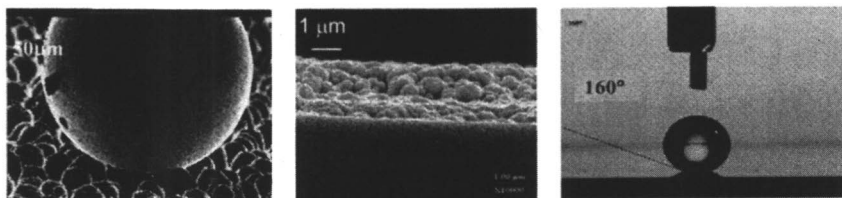
Figure 12. Left image shows the surface of a lotus leaf. Center image is that of self-assembled sol gel coating. Right image shows contact angle of 160° for water on super-hydrophobic sol gel surface.

Augmented Adhesion with Non-chromate Materials

In an effort to eliminate chromate conversion coatings, this program has shown that bis-silane coupling agents can very effectively augment the adhesion of organic coatings to metal substrates. This silane-based material can be spray applied and replaces the conventional chromate conversion coating system. Inhibitors can be incorporated into the silane layer such that it possesses some degree of active corrosion protection. It should be remembered that the chromate conversion coating applied in the depot, has little if any active healing capabilities, and simply provides adhesion promotion. Thus, the silane-based conversion coating is improved in attributes and performance to field-applied chromate conversion coatings.

Methods for Sensing and Self-Repair

The ability of an aircraft coating to sense damage, whether it be mechanical or chemical, and then initiate a protective measure is an extremely desirable

characteristic. One approach to achieve this objective has involved the use self-assembly techniques that incorporate mono-disperse polymeric or ceramic (*e.g.*, polystyrene, silica) colloidal spheres that are on the order of 100's of nanometers in diameter to construct photonic crystal coatings. With these dimensions, these photonic crystals can be easily interrogated with visible light for damage using simple optical techniques. As shown in Figure 13, a two-dimensional colloidal crystal made by evaporative techniques was used as a mechanical strain sensor.
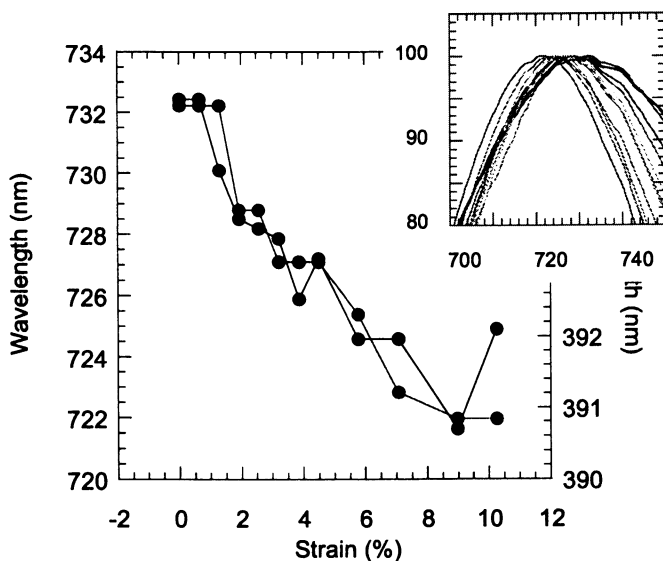
Figure 13. Summary of shifts in the position of the Bragg diffraction peak as a function of applied strain for a 2-D face-centered cubic colloidal crystal array (CCA) grown on a nylon tensile sample. The CCA had a (111) surface texture and the inset shows the scattering peaks shifting to lower wavelength with imposed positive tensile strain as the (111) crystal interplanar spacing decreases.

Other approaches have been examined as briefly summarized below. Ordered monolayers of monodisperse polystyrene spheres were grown on to a substrate and the monolayers were subsequently infiltrated by an elastomer as shown in Figure 14. Subsequently the particles were removed from the elastomer creating a so-called inverse opal. The inset to Figure 14 shows an optical diffraction pattern from the opal. This laboratory has demonstrated the ability of inverse opals to serve as strain sensors, a component that will ultimately provide the function of mechanical damage sensing in a multi-functional coating system.

Another approach that is being investigated involves the use of colloidal gold particles that are encased in polymer structures such as silica spheres. These structures are subsequently self-assembled into ordered synthetic crystals. The plasmon adsorption band in these structures is a function of the separation between nearest-neighbor colloidal gold particles in the crystal. Figure 15 shows some recent results.

A final method that is being examined involves the use of ordered, self-assembled monolayers of polystyrene spheres with tailored interstitial sizes using appropriate thermal treatment. This is shown in Figure 16. These monolayer structures can be grown on electrically conductive substrates (e.g., aluminum). After appropriate heat treatment, a noble metal such as gold or copper is deposited through the interstitial holes onto the substrate. Subsequent thermal treatment will close-up the interstitials so that the latex completely covers the substrate as a continuous film. Underneath this latex coating, there will be an ordered array of noble metal particles that will diffract light and have a plasmon absorption wave. These structures are anticipated to be able to serve as strain sensors.
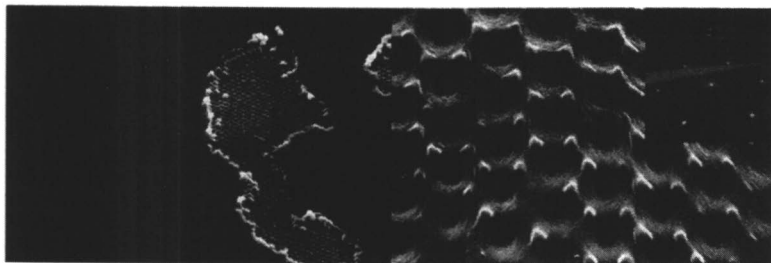
Figure 14. Stages in the construction of the inverse opal. (A) Elastomer which has infiltrated the ordered monolayer array of polystyrene spheres. (B) Close-up view of void lattice (inverse opal) after the spheres have been removed. The inset shows optical diffraction from the inverse opal.

Color-on demand

Another objective of this program was the development of a color-on-demand functionality. The ultimate goal of this project is the creation of intelligent flakes of paint able to change color when commanded by an onboard microwave signal. To accomplish this the system must include: (1) a metachromatic element that is: self-powered during transition, but thereafter passive, and amplified, (2) an actuator that: responds to a microwave signal, causes a latching trigger to evoke the color change, is self-powered during transition, but thereafter passive, and is all implementable in mass-producible MEMS/semiconductor technology.
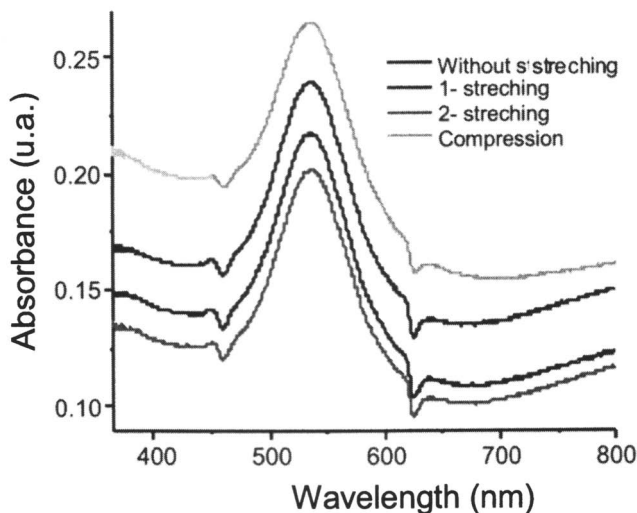
*Figure 15. Plasmon adsorption spectra from a colloidal gold lattice as discussed in the text. The different curves demonstrate the strain sensitivity of the structure. Zero deformation: black, Compression: blue, tension: red and green. The film used to obtain the spectra is shown on the right.
(See page 3 of color insert.)*
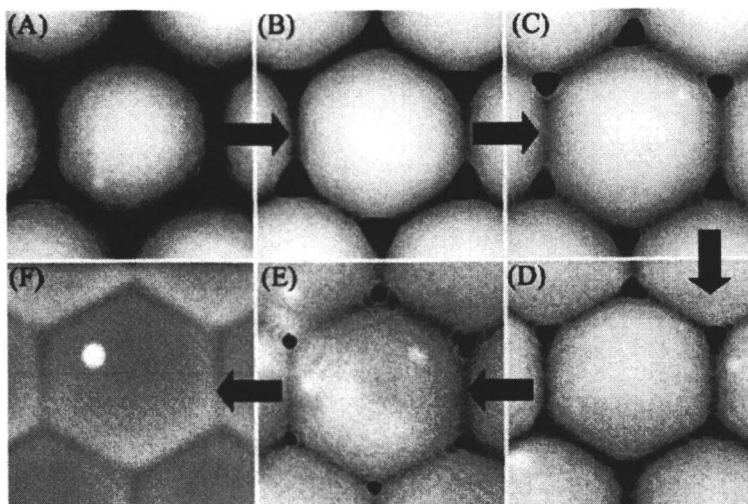
Figure 16. A sequence of images starting with the as-assembled polystyrene array (A), and showing how appropriate heat treatment (B)-(F) can be used to tailor the interstitial size for subsequent noble metal deposition and continuous latex film formation.

Two parallel paths are being explored toward meeting the objective. These constitute a proof of feasibility step before proceeding with the complete paint flake system design: **Path 1** is a self-assembling crystal version of a solid state electrochromic cell, amplified with surface plasmon nanoparticles. **Path 2** is a MEMS/NEMS mechanically tuned photonic antenna. The development of this intelligent paint flake requires a combination of disciplines including electromagnetics, chemistry of polymers and viologens, materials engineering, and microfabrication.

To date this study has demonstrated: (1) an electro-chromic cell based on nano-sphere components and (2) the mechanical tuning of photonic antennae via computation. An example of a constructed "bowtie" photonic antennae is shown in Figure 17. It can be tuned to different λ's by insertion of an actuator in the middle of the bow tie shape.
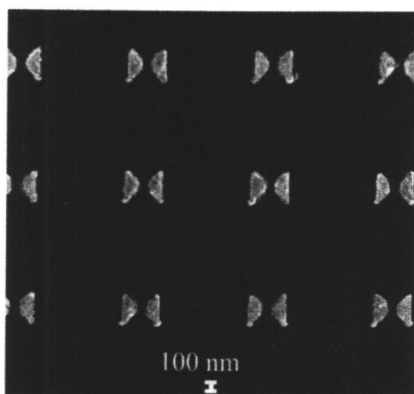
Figure 17. A MEMS constructed photonic antennae that emits amplified light based on the surface plasmon effect.

Summary

This paper has provided an overview of some of the significant strides made towards the development of a multi-functional aerospace coating. A coating is envisioned that will:

- provide on-demand corrosion protection using environmentally safe materials
- sense corrosion and mechanical damage of the aircraft skin

- initiate coating repair responses to sensed chemical and physical damage
- achieve optimal adhesion using environmentally compliant materials
- improve the fatigue resistance and mechanical integrity of the skin.
- provide changes in color on demand
- provide water rejection and self-cleaning capability

This is being accomplished through the:

- development of a field-replaceable, multi-functional, nano-engineered metallic cladding
- use of molecular engineering, self-assembly, and MEM approaches to develop sensing capability of mechanical and environmental conditions at the surface of the aircraft.
- development of new approaches for the identification, encapsulation, and delivery of environmentally compatible inhibitor compounds that will optimize solubility and compatibility with the paint resins when used as inhibitive pigments.
- optimization of organic coating adhesion through the use of environmentally compatible surface treatments
- development of biomimetic surface structures through self-assembly methods

An amorphous aluminum-based alloy system has been identified for the formation of a nano-engineered cladding that will have tunable corrosion protection properties. The micro-structural and functional stability of this material as a function of time and temperature is excellent. The sprayability of this material is now being explored. In addition, the experimental throughput for screening non-chromate corrosion inhibitors has been increased by over 1000-fold. This has allowed the discovery of synergistic combinations of inhibitors with performance that surpass chromate-based inhibitors in the tests performed. This now provides a means to produce environmentally compliant coatings. Nano and meso-dimensioned packaging and delivery systems for these new inhibitors can control inhibitor solubility and establish compatibility with the coating resin. In addition, adhesion augmentation using non-chromate materials (bis-silanes) are promising replacements for chromate conversion coatings. Meso-dimensioned self-assembled materials have been developed to produce super-hydrophobic surfaces with the ability to reject water and self-clean. Mechanical sensing capability has been demonstrated in colloidal crystalline arrays formed via evaporative methods. Finally, two approaches for color-on-demand have also been demonstrated.

Acknowledgements

References

1. *ASM Handbook* **13**:587-589 (1987).
2. G.M. Hoch, A Review of Filiform Corrosion, R.W. Staehle, J. Kruger, A. Agrawal, Ed., Localized Corrosion (NACE Houston, TX, 1974).
3. K. Nisancioglu, H. Let-Olsen, and O. Lunder, Electron Microscopic Investigation of Filiform Corrosion Morphologies on Aluminum, D. S. Scantlebury and M. W. Kendig, Ed., Advances in Corrosion Protection by Organic Coatings II (The Electrochemical Society, Pennington NJ, 1990).
4. L.F. Vega, F. Bovard, T. Nakayama, K. Ikeda, H. Sige, E.L. Colvin, Filiform Corrosion of Aluminum Alloys: Influence of Alloy Composition, R.G. Buchheit, M.R. Jaworski, and P.D. Chalmer, Ed., Surface Conversions of Al and Ferrous Alloys for Corrosion Resistance (CORROSION 2000 Research Topical Symposium, 2000).
5. P.L. Hagans and C.M. Haas, *Surf. Interface Anal.* **21**:65 (1994).
6. M.W. Kendig, A.J. Davenport and H.S. Isaacs, *Corr. Sci.* **34**:41 (1993).
7. F.W. Little, G.L. Bibbins, K.Y. Blohowiak, R.E. Smith, and G.D. Tuss,, *Corr. Sci.* **37**:349 (1995).
8. A.E. Hughes, R.J. Taylor and B.R. Hinton, *Surf. Interface Anal.*, **25**:223 (1997).
9. G.O. Ilevbare, J.R. Scully, J. Yuan, and R.G. Kelly, *Corrosion* **56**:227-242 (2000).
10. C.N. Hunter, J.H. Osborne, and S.R. Taylor, *Corrosion* **56**:1059-1070 (2000).
11. R.B. Leggat, S.R. Taylor, R.G. Buchheit, and W. Zhang, 197th Meeting of The Electrochemical Society, Toronto, Ontario CAN (2000).
12. Z.W. Wicks, F.N. Jones, and S.P. Pappas, in *Organic Coatings, Science and Technology, Vol.2: Applications, Properties, and Performance* . (John Wiley and Sons, Inc., New York, 1994), vol. 2, pp. 183.
13. J. Sinko, Considerations on the Chem. and Action Mech. of Corr. Inh. Pigm. in Org. Ctgs, 6th Bien. Conf. on Sci. and Techn. of Org. Ctgs, Hilton Head, SC (Institute of Materials Science, 2000).
14. M.M. Madani, R.M. Simmons, K.M. Mann, Y.M. Sigonney, and R.D. Granata, Chromate Inhibition of Polymer-Coated AA2024-T3, 198th Meeting of the Electrochemistry Society, Phoenix, AZ (2000).

15. P. L. Hagans and C. N. Haas, in *ASM Handbook, Vol.5: Surface Finsihing* J. A. S. C.M. Cotell, and F.A. Smith, Ed. (ASM International, Metals Park, OH, 1994), vol. 5, pp. 405-411.
16. E.A. Starke, Jr. and J.T. Staley, *Prog. Aerospace Alloys* **32:**131-172 (1995).
17. J.R. Scully, T.O. Knight, R.G. Buchheit, and D.E. Peebles, *Corrosion Science* **35:**185 (1993).
18. G.S. Chen, M. Goa, and R.P. Wei, *Corrosion* **52:**8 (1996).
19. R.G. Buchheit, *J. Electrochem. Soc.* **142:**3994 (1995).
20. M.J. Bayley and C. D. S. Tuck, *Industrial Corrosion* **10**, 5-12 (1992).
21. S.S. Birley, W. Hepples, N.J.H. Holroyd, The Corrosion Protection of Weldable 7XXX Aluminum Alloys by Al-based Arc Spray Coatings, E. A. Starke, Ed., 3rd Intl. Conference on Al Alloys, Charlottesville, VA .
22. H.H. Holroyd, NACE 10, R.P.G. and B. Ives, Ed. (NACE, Houston, TX).
23. K. D. Krishnanand, R.W. Cahn, in *Rapidly Quenched Metals,* N.J.Grant, B.C. Giessen, Ed. (MIT Press, Cambridge, MA, 1976) pp. 67-75.
24. T. Shymyreva and A. Ivanov, Characterization of the Thermal Spray Coatings Having Amorphous and Nanocrystalline Structures, United Thermal Spray Conference 99 (1999).
25. O. Kelser, J. Matejicek, S. Sampath, and S. Suresh, *Materials Science Forum* **308-31:**389-395 (1999).
26. Y. He, G.J. Shiflet and S.J. Poon, *J. of Alloys and Compounds,* **207/208:**349-354 (1993).
27. A. Inoue, K. Ohtera, and T. Masumoto, *Japanese Journal of Applied Physics* **27:**L736-L739 (1988).
28. T. Masumoto, *Materials Science and Engineering* **A179/A180:**8-16 (1994).
29. Y. He, S.J. Poon, and G.J. Shiflet, *Science* **241:**1640-1642 (1988).
30. J.E. Sweitzer, J.R. Scully, R.A, Bley, and J.W.P. Hsu, *J. Electroche. Soc. - Solid State Letters* **2:**267-270 (1999).
31. A.N. Mansour, S.J. Poon, Y. He, and G.J. Shiflet, *Surface Science Spectra* **2**, 31-44 (1993).
32. R.G. Buchheit, S.B. Mamidpally, P. Schmutz, and H. Guan, Ed., *Active Corrosion Protection in Chromate and Chromate-free Conversion Coatings* (NACE, Houston, TX, 2000).
33. M.E. Goldman, N. Unlu, G.J. Shiflet, and J.R. Scully, *J. Electrochem. Sol. St. Letters,* **8**(2):B1-B5 (2005).
34. M.A. Goldman, F. Presuel, J.R. Scully, *Corrosion,* **61**(3):246-263 (2005).
35. F.J. Presuel-Moreno, M.E. Goldman, R.G. Kelly, J.R. Scully, J. Electrochem. Soc., (in press).
36. M.E. Goldman, N. Unlu, G.J. Shiflet, and J.R. Scully, Paper No 04276, CORROSION/2004, New Orleans, LA, March (2004).
37. M. Stern, *J. Electrochem. Soc.* **24:**787-806 (1958).
38. D. Bienstock and H. Field, *Corrosion,* **17:**87-90 (1961).

39. N. R. Whitehouse, *Polymer Paint and Colour J.* **178**:239 (1984).
40. J. Boxall, *Polymers, Paints and Colour J.* **174**:382-384 (1984).
41. B.R.W. Hinton, *Metal Finsihing* **Sept. '91, Oct. '91**, 55-61, 15-20 (1991).
42. H.E. Hager, C.J. Johnson, K.Y. Blohowiak, C.M. Wong, J.H. Jones, R.R. Taylor, R.L. Cook, Jr., *U.S.Patent 5,866,652* (The Boeing Company, U.S.A., 1999).
43. R.L. Cook and S.R. Taylor, *Corrosion* **56**:321-333 (2000).
44. Y. Feng, K.S. Siow, K.T. Teo, and A.K. Hsieh, *Corr. Sci.* **41**:829-852 (1999).
45. S. Sayed Azim, S. Muralidharan S. V. Iyer, B. Muralidharan, and T. Vasudevan, *Br. Corr. J.* **33**:297 (1998).
46. M.Mustafa. S.M. Shahinoor, amd I. Dulal, *Br. Corrosion J.* **32**:133-137 (1997).
47. S. Sayed Azim, S. Muralidharan, S. Venkatkrishna Iyer, *J. of Appl. Electrochem.* **25**:495-500 (1995).
48. D.D.N. Singh and A.K. Dey, *Corrosion* **49**:594-600 (1993).
49. M.A. Quraishi, J. Rawat, and M. Ajmal, *Corrosion* **55**:919-923 (1999).
50. G.N. Mu, T.P. Zhao, and T. Gu, *Corrosion* **52**:853-856 (1996).
51. M.A. Quraishi, S. Ahmed, and M. Ansari, *Br. Corrosion J.* **32**, 297-300 (1997).
52. J.M. Abd El Kader, A.A. Warraky, and A.M. Abd El Aziz, *Br. Corr. J.* **33**:152-157 (1998).
53. S. Rajendran, B.V. Apparao, and N. Palaniswamy, *Electrochem. Acta* **44**:533-537 (1998).
54. T. Suzuki, H. Nishihara, and K. Aramaki, *Corr. Sci.* **38**:1223-1234 (1996).
55. Y. Gonzalez, M.C. LaFont, N. Pebere, and F. Moran, *J. of Appl. Electrochem.* **26**:1259-1265 (1996).
56. Y. Feng, K.S. Siow, W.K. Teo, K.L. Tan, and A.K. Hsieh, *Corrosion* **53**:546-555 (1997).
57. S. Gonzalez, M.M. Laz, R.M. Souto, R.C. Salvarezza, and A.J. Arvia, *Corrosion* **49**:450-456 (1993).
58. K.T. Carron, M.L. Lewis, J. Dong, J. Ding, G. Xue, and Y. Chen, *J. Matl. Sci.* **28**:409-4103 (1993).
59. K. Aramaki and N. Hackerman, *J. Electrochem. Soc.* **116**:558 (1969).
60. N. Shikai and L. Yefen, Study of the Synergy Mech. of Acidic Inh., 8th Europ. Symp. on Corr. Inh. (1995).
61. S.A. Hodges,, W.A. Uphues, and M.T. Tran, *Surf. Coatings Australia* **34**:24-30 (1997).
62. A.T. Evans, J.D. Scantlebury, and L.M. Callow, The Adh. and Corr. of Chromate Cont. Ctgs on Al, J. D. Scantlebury and M. W. Kendig, Ed., Adv. in Corr. Prot. by Org. Ctgs II (ECS, Pennington, NJ, 1995).
63. R.L. Cook, Jr. M.S., University of Virginia (1995).

64. S. R. Taylor, An Examination of Possible Synergy Between Paired Combinations of Transition and Rare Earth Metal Salts, 197th Meeting of the ECS, Toronto, CAN (ECS, Pennington NJ, 2000).

65. B.D. Chamber, S.R. Taylor. M.W. Kendig, *Corrosion*, **61**(5):480-489 (2005).

66. S.R. Taylor and B.D. Chambers, "Novel Synergistic Combinations of Chromate-Free Corrosion Inhibitors and Methods for Discovery Using High Throughput Screening", U.S. Provisional Patent No. 60/657,298.

67. B.D. Chambers and S.R. Taylor, "Multiple Electrode Methods to Massively Parallel Test Corrosion Inhibitors for AA2024-T3", NACE 2006 - San Diego, CA, Paper No.06678, National Association of Corrosion Engineers, Houston, TX (2006).

68. B.D. Chambers, S.R. Taylor, *Corrosion Science*, 49(3):1584-1596, 49(3):1597-1609 (2007).

69. G.S. Chen, M. Gao, R.P. Weir, *Corrosion*, **52**(1):8-15 (1996).

70. R.G. Buchheit, R.P. Grant, P.F. Hlava, B. Mckenzie, and G.L. Zender, *J. Electrochem. Soc.* **144**(8): (1997).

71. N. Dimitrov, J.A. Mann, and K. Sieradski, *J. Electrochem. Soc.* **146**, (1) 98-102 (1999).

72. R.G. Buchheit, M.A. Martinez, and L.P. Montes, *J. Electrochem. Soc.* **147**, (1) 119-124 (2000).

73. Alison J. Davenport and Bin Liu, "Copper Accumulation during Cleaning of Al-Cu Alloys," Electrochemical Society Proceedings, Vol. 2000-23, p.41-46

74. D.A. Little, J.R. Ferrell, and J.R. Scully, "The Effect of Pretreatment and Temper on the Under-Paint Corrosion of AA2024", Corrosion/2004, paper no. 04277, NACE, Houston, TX (2004)

75. D.A. Little and J.R. Scully, "The Effect of Alloy Composition and Pretreatment on the Under-Paint Corrosion of Copper Bearing Aluminum Alloys," in Proceedings of the 2003 Tri-Service Corrosion Conference, Organized by AFOSR/AFRL (Tri-Services Committee on Corrosion, U.S. Department of Defense), Las Vegas, NV, Nov 17 -21, 2003.

76. R.G. Buchheit, M.D. Bode and G.E. Stoner, *Corrosion* **50**:205 (1994).

77. I. Sissoko, E.T. Iyagba, R. Sahai, and P. Biloen, *J. of Solid State Chem.* **60**:283 (1985).

78. M. A. Drezdzon, *Inorg. Chem.* **27**:4628 (1988).

79. E. T. Iyagba, Ph.D., University of Pittsburgh (1986).

80. J.K.G. Panitz and D.J. Sharp, "Th Use of HT as a Chloride Ion Getter for a Barrier Al Anodization Process" *Sandia Report CAND95-2300* (SNL, 1995).

81. R.G. Buchheit, H. Guan, S. Mahajanam, F. Wong, "Active Corrosion Protection and Corrosion Sensing in Organic Coatings," *Prog. Org. Coat.*, August (2003)

Chapter 9

Formulation of Reactive Nanostructured Adhesive Microbial Ink-Jet Inks for Miniature Biosensors and Biocatalysis

M. C. Flickinger[1,2,7,*], O. K. Lyngberg[1,3,4], E. A. Freeman[1], C. R. Anderson[1,5], and M. C. Laudon[1,6]

[1]BioTechnology Institute, University of Minnesota, St. Paul, MN 55108
[2]Department of Biochemistry, Molecular Biology and Biophysics, University of Minnesota, St. Paul, MN 55108
[3]Current address: Bristol-Myers Squibb, New Brunswick, NJ 08903
[4]Department of Chemical Engineering and Materials Science, University of Minnesota, Minneapolis, MN 55455
[5]Current address: GrainValue LLC, St. Paul, MN 55118
[6]Current address: Department of Plant Biology, University of Minnesota, St. Paul, MN 55108
[7]Current address: Department of Microbiology; Chemical and Biomolecular Engineering, North Carolina State University, Raleigh, NC 27695
*Corresponding author: Michael_Flickinger@ncsu.edu

Reactive adhesive microbial inks can be formulated from aqueous latex emulsions for drop on demand (DOD) piezoelectric deposition. Ink-jet printing of a high density of living microorganisms many be useful to generate microstructures for micro-biosensors, as biocatalytic coatings in micro-fluidic devices, or micro-channel bioreactors. Microbial inks are viable wet cell paste mixed with aqueous (organic solvent-free) emulsions of adhesive polymer particles

NOTE: Portions of this work were presented at the Bio-Printing and Bio-Patterning Workshop, Manchester Conference Centre, UMIST, the University of Manchester, Manchester, UK, September 27-28, 2004 and the European Coating Conference "Power of Ink Jet Materials III", Berlin, Germany, December 1-2, 2005.

156 © 2009 American Chemical Society

that dry rapidly with arrested coalescence as thin, adhesive, nanoporous coatings. Latex ink viscosity (~1.5 to 3 cP) is semi-shear rate dependent. Nanoporosity is essential for the embedded microorganisms to retain viability and reactivity. The nanoporous latex inks in this study contain glycerol and sucrose added to a low T_g acrylate/vinyl acetate latex emulsion (particle dia. ~280nm, T_g ~10°C). The glycerol and sucrose arrest polymer particle coalescence during film formation (porogens) and also act as osmoprotectants. Viability and reactivity is measured by bioluminescence following deposition, drying, and rehydration in nitrogen-limited (nongrowth) media. As a model system, the reactivity of *Escherichia coli* (<1 μm by ~2 μm, 5 x 10^4 cfu/nl ink) containing a mercury (Hg^{+2})-inducible promoter-*lux* fusion was studied by printing patches, microwells and multi-layer dot arrays onto polyester using office ink-jet printers and a piezoelectric nano-plotter. *E. coli* can be printed at a density of ~1.5 cells/μm^2. Reactivity (luminescence resulting from *luxCDABE* expression) is a function of drying conditions (temperature, relative humidity), nanoporosity following rehydration, Hg^{+2} concentration, and volume printed. Print resolution is determined by piezo tip aperture diameter (25 μm, ~0.2 nl/droplet; 50 μm, ~0.5 nl/droplet) and drying rate. Profilometry of dry latex microstructures indicated significant surface-tension driven flow prior to ink drying. Viable *Kluyveromyces fragilis* (~12 μm diameter) have also been printed as a larger model microbe for developing ink-jet methods for bio-patterning of surfaces with microcolonies.

Tissue engineers and molecular biologists are rapidly developing direct writing ink-jet deposition methods to generate periodic arrays, three-dimensional nano-particle microstructures or microfluidic systems containing living eukaryotic cells (*1-5*). Surprisingly, few studies have appeared on how to formulate adhesive ink-jet inks for deposition of a high concentration of much smaller (~1 μm to ~10 μm) viable microorganisms (bacteria, yeast, fungi) as thin coatings on surfaces or as reactive components of nano-structured bioelectronic or microfluidic devices. Critical to development of microbial inks is fundamental knowledge of how to generate aqueous formulations which are adhesive but non-toxic to the microbes, nanoporous when dried at ambient temperature, and which preserve microbial viability and reactivity. Ink reactivity is the ability of the embedded microbes to respond to their chemical environment following the

stress of piezoelectric deposition, rapid ink drying, storage and rehydration. The most important criteria are the density and viability of the microbes deposited, the nanoporosity of the surrounding adhesive matrix following rehydration which allows the microbes access to nutrients, and microbe specific reactivity.

Nanoporous microbial biocatalytic coating technology is emerging as a method to preserve and concentrate microbes on surfaces at ambient temperature to increase whole-cell biocatalyst reactivity (process intensity) (6-10). Coating nanoporosity is measured by tracer diffusivity and visualized by cryogenic scanning electron microscopy (cryo-SEM) methods (6). Microbial biocatalytic coatings are ~10 μm to 75 μm thick and can be generated in the laboratory with simple draw down coating methods on a variety of substrates. However, these coating methods cannot generate uniform coatings of <10 μm thickness. Development of latex formulations for coating of a high concentration of living microbes in a <5 μm to ~10 μm thick adhesive nanoporous coating using the precision of piezoelectric droplet deposition would extend latex biocatalytic coating technology for applications of microbes as miniature biosensors in bioelectronic devices for environmental monitoring, intensification of biocatalytic reaction zones in microfluidic devices, or for generating highly structured perfusive coatings for microchannel bioreactors (7).

Approaches for Formulating Reactive Latex Microbial Inks

Microbial latex biocatalytic coating formulations are generated from non-toxic low glass transition temperature (T_g) latex emulsions adjusted to neutral pH combined with ~50% (v/v) of wet viable cell paste resulting in high suspended solids emulsions which are used immediately after mixing for generating single or multi-layer coatings at ambient temperature (6-10). In contrast, aqueous latex microbial ink-jet ink formulations must be low viscosity (~ 4cP) and may also need to be stabilized to preserve microbial viability during ambient temperature storage in ink reservoirs prior to printing. As the reactive component in microbial inks, the microbes can be genetically manipulated before mixing with latex by molecular biology methods to contain optimal levels of the enzymes needed for a specific response to their chemical environment (oxidations, reductions, multi-step reactions, photo reactivity). The microbial ink emulsion then is immediately reactive when formulated and may lose reactivity during storage if not stored under special conditions (such as refrigeration) to sustain the viability of the microbes. However, refrigerated storage may not be compatible with low T_g adhesive latex polymer emulsions.

An alternative approach is to genetically manipulate the microbes' enzyme content with an inducible promoter (region of DNA recognized by RNA polymerase) that responds to an external chemical or environmental signal after

the ink is printed, dried and rehydrated by up-regulation of gene transcription. This response results in expression of new genes and gene products (proteins, enzymes) thus "activating" the ink after printing.   In this case, ink reactivity following rehydration is a function not only of the number of viable cells which survive printing but also the "strength" of the transcriptional and translational machinery used for gene expression (the promoter, the forms of RNA polymerase, stability of mRNA, ribosome stability, availability of charged tRNAs for translation, etc.) present in the microbes under nongrowth conditions. Using this approach, microbial inks may be formulated that are stable but not reactive at ambient temperature (do not require refrigeration) and if some cell viability is lost during storage, printing and ink drying, it will be compensated by the inducible activation following printing and rehydration. For example, the specific reactivity of nitrogen-starved *E. coli* can be increased up to 100,000-fold by inducible genetic regulation which can be manipulated at the level of transcription using appropriate promoters actively transcribed under nongrowth conditions (*9*).

The rate and maximum reactivity of microbial inks is related to the number of viable microbes preserved in the ink formulation prior to printing and the number of cells that survive osmotic stress and desiccation during rapid ink drying, preferably at ambient temperature. Preservation of microbial viability during drying is accomplished by including preservative osmoprotectants (carbohydrates, polymers, salts) in the formulation. It is well established that microorganisms can withstand very significant changes in external osmotic conditions and partial desiccation without loss of viability when dried with preservative biomolecules (*11-13*). Viability following rehydration is related to the composition and structure of osmo-protectant biomolecules (glycerol, sugars, salts), bound water surrounding the microbes in the desiccated state, changes in intracellular biomolecular composition and cytoplasmic water content (*11-13*). The *in vivo* microbial response to osmotic and desiccation stress is altered gene regulation resulting from changing cytoplasmic water content and biomolecular crowding. Expression of new genes can result in significant changes in intracellular composition to preserve cell viability (*14*).

Altered *in vivo* gene expression in microorganisms is often detected by using recombinant DNA methods to construct reporter genes (encoding luminescent or fluorescent proteins) transcriptionally-fused to stress-induced promoters activated by chemicals or environmental signals (temperature, osmotic stress, salinity, nutrient starvation). The selectivity and sensitivity of these stress-induced gene fusion reporters has been exploited as whole cell biosensors and for environmental monitoring (*9, 15-17*). Fusion of a stress-inducible promoter to the *luxCDABE* bioluminescence reporter genes is an often used microbial whole cell biosensor system (see for example *18*).

Microbial Inks for Micro-Biosensors and Bioelectronic Devices

Integrated circuits which function as micro-biosensors have been constructed containing bioreporter microorganisms (microbes engineered to respond to chemicals in the environment by expression of bioluminescence) coated onto micro-luminometers in a light-tight enclosure. These bioelectronic sensors may be useful for remote environmental monitoring of liquids or gases, or for use as logic gates in biocomputing (*19-23*). Encapsulation or entrapment of reactive bioreporter microorganisms adjacent to the photo or electrochemical sensing elements of biosensors has been investigated using millimeter-thick hydrogels. Gels that have been evaluated for viable cell immobilization include: agar, carrageenan, alginate, polyurethane-polycarbomyl sulfonate (PCS), polyacrylamide, polyvinyl alcohol, or sol-gel silicates (*15, 24*). For example, 280 μm to ~950 μm thick-film microbial waste treatment biological oxygen demand sensors have been developed with viable microorganisms immobilized in PCS directly onto the transducer surface to increase the signal response time (*25*). Because of the thickness of these hydrogel layers, analyte diffusion distance is long, reactive microorganisms are often leached from the large gel pores, and the microorganisms entrapped in the gel lose viability when the sensor is stored dry. In addition, dried hydrogel whole cell biosensors often require hydration for several days for activation in order to swell the gel and for microbial resuscitation by growth (*25*). These severe mass transfer, dry storage and mechanical stability limitations reduce the usefulness of thick-film gel entrapment and screen printing methods for micro-scale biosensors, and result in slow biosensor reactivity. Hydrogels are also not adhesive.

In order to reduce the size of biosensors to a single integrated circuit chip, new adhesive polymer coatings are needed to permanently entrap a high density of viable bioreporter microorganisms directly onto the surface of electronic sensors in a much thinner (<10 μm) nanoporous layer. These materials must be adhesive, maintain entrapped microbial viability as a dry coating, and require minimal rehydration time for sensor activation. Layers of porous polymer less than 10 μm thick will reduce the diffusion distance of the molecules being detected, allow the cells to be supplied with sufficient nutrients and oxygen to retain viability, and should dramatically improve micro-biosensor sensitivity and reactivity.

Several methods have recently been reported to deposit arrays of individual living cells which encode engineered reporter genes such as green fluorescent protein (gfp) for automated screening of drug candidates (*26-29*), but these single cell methods are not suitable for deposition of a high density of bacteria or yeast with an adhesive polymer in a small surface area. Microbial direct write deposition using ambient laser transfer has also been reported for *E. coli*, but no direct evidence about the viability as a function of time, the density of

deposition, the adherence of the cells following hydration, or the reactivity (inducible gene expression) of the deposited *E. coli* was reported (*30*).

Characteristics of Polymer and Solvent-Dye Based Ink-Jet Inks

It is well established that precise polymer or nano-particle deposition can be achieved using drop on demand (DOD) ink-jet printing which is considered to be one of the best technologies for fabrication of micro-scale polymer devices (*31*). Ink-jet printing of solvent-based formulations of polymers and polymer blends in dots and arrays has been exploited for the manufacture of polymer light emitting diodes (pLEDs), organic transistors (polytronics), ceramic micro-structures, and combinatorial polymer arrays using a variety of deposition devices (*31-35*). However neither desk top ink-jet printers (where the ink supply comes from a reservoir) nor aspirating (pipette mode) ink-jet deposition devices reported for deposition of polymers have been used to deposit aqueous suspensions of film-forming polymer particles and living microorganisms. Fundamental knowledge is lacking on how to formulate an aqueous ink-jet ink containing adhesive polymer particles to preserve viability and reactivity with printing characteristics similar to solvent-dye based ink-jet inks (Table I.) (*36*). For micro-biosensor and device applications, aqueous ink formulations need to have engineered flow and adhesive properties on non-porous substrates whose surface energy and hydrophobicity will be significantly different from paper.

Microbial inks must be formulated without organic solvent, dyes, additives or salts that may be toxic on contact (kill the reactive microorganisms) or may become toxic when concentrated around the microbes during ink drying. For optimal reactivity, microbial ink-jet inks should also not contain toxic surfactants, or residual toxic monomers from the polymer synthesis. Optimal ink formulations should preserve the activity of a very high volume fraction of cells, just below the maximum critical limit for film formation (~50% v/v dry solids basis), and when dried and rehydrated be <10 μm thick for minimal analyte diffusion distance. Rehydrated inks should have the same characteristics as biocatalytic coatings: stable pores with sufficient nanoporosity for diffusion of nutrients and oxygen to the cells to maintain cell viability, be adhesive to nonporous substrates (metals, polyester), and be stable (insoluble, resistant to delamination following rehydration, abrasion resistant) (*6, 7*).

We have previously developed thin (30 μm to 80 μm thick) nanoporous, adhesive, low T_g latex multilayer coating methods to entrap a high density of viable, nongrowing (nitrogen starved) but reactive *E. coli* and other microorganisms at ambient temperature on nonporous substrates (polyester, metals) (*6-10*). When these coatings are rehydrated, the microbes are viable, enzymatically reactive and capable of gene expression for use as biosensors and high intensity biocatalysts (*9, 10, 37-40*). Microbial viability is retained in these

coatings under nitrogen-source limited conditions (9, 10, 41-44) and nanopores are generated during coat drying by the addition of osmo-protectants such as glycerol and carbohydrates (sucrose, trehalose) (41-44). These biomolecules also function as porogens by reducing capillary pressure-driven polymer particle coalescence by formation of a glassy vitrified state when dried at ambient temperature which blocks polymer particle coalescence (6). A bimodal blend approach to block wet coalescence following coating rehydration for high temperature polystyrene/acrylate coating has recently been reported (40).

Table I. Characteristics of Solvent-Dye Based Ink-Jet Inks Which May be Unsuitable for Aqueous Microbial Latex Inks

Solvent-Dye Ink	Aqueous Microbial Latex Emulsions Used for Biocatalytic Coatings
Maximum viscosity ~4cp	Latex viscosity is shear rate dependent
Particle size <1 μm	Bacteria are >1 μm in their long dimension, fungi >10 μm in diameter
Solids content <0.02%	Latex emulsions have high dry solids content. High microbial dry solids content needed for maximum reactivity
Surface tension ~30N/m	
Conductivity >1000 μS/cm	
Carrier solvents: ketones, glycol ether, alcohols	Must be organic solvent-free. Organic solvents toxic to microbes on contact.
Other components: dyes, pigments, cellulose binders, plasticizers, flow, adhesion control and viscosity modifiers, anti-oxidants, conductive salts	May be toxic when concentrated in pore space surrounding microbes during ink drying

Adapted from Reference 36.

Adaptation of Latex Biocatalytic Coating Formulations as Microbial Ink-Jet Inks

In this study, we modify a biocatalytic coating formulation to reduce viscosity to print very thin nanoporous latex ink microstructures: patches, micro-wells, and dot arrays (<5 μm thick) using several DOD ink-jet deposition methods with two tip aperture sizes. Because it is difficult to disrupt the adhesive partially coalesced latex surrounding the microbes in very small

microstructures in order to accurately determine the number of cells that survived printing using standard microbiological methods, an indirect approach of measuring cell viability in larger "macrodots" and measurement of biological reactivity by the bioluminescence of printed micro-wells and dot arrays is used. In this method, the cell's ability to bioluminesce is used as an estimate of the number of microbes that survived printing, rapid drying and rehydration. Only viable microbes are capable of *lux* operon gene expression leading to synthesis of the bioluminescent protein. Therefore the level of bioluminescence is proportional to the number of viable and metabolically active microbes in the printed and rehydrated ink.

We use the mercury-inducible bioluminescence reactivity of *E. coli* pRB28 (Figure 1) (*9, 45*) as a model inducible reactive microbe to investigate formulations of adhesive microbial latex inks. Printed *E. coli* must be viable, capable of *lux*CDABE operon expression and able to synthesize reducing equivalents and ATP in order to bioluminesce. Therefore Hg^{+2}-inducible bioluminescence measured by a liquid scintillation counter is a sensitive measure of cell viability following printing. The latex formulations investigated are derived from ~280 nm diameter acrylate/vinyl acetate copolymer latex polymer emulsion (Rovace™ SF091, T_g ~10°C, Rohm and Haas). Prior to this study, no aqueous ink-jet ink formulations have been reported to deposit a high density of microorganisms preserved in a thin, adhesive, nanoporous latex coating to retain microbial viability and reactivity at ambient temperature.
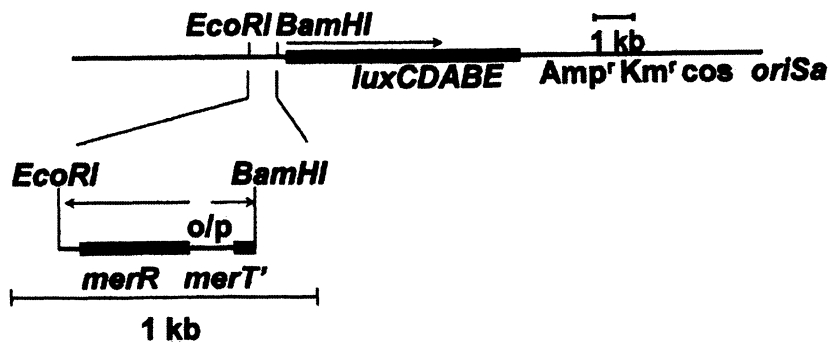
Figure 1. The mercury-inducible merRo/pmerT'-lux plasmid pRB28 is used to measure the reactivity of E. coli HB101 by the ability to induce luciferase expression following ink-jet deposition, drying, rehydration and induction by Hg^{+2}. (Reproduced with permission from reference 45. Copyright 1993 American Society for Microbiology)

Materials and Methods

Bacterial Growth and Determination of Viability

E. coli strain HB101 [F⁻*hsdR520* (r$_k$⁻, m$_B$⁻), *recA13, ara-14, proA2, lacY1, galK2, rpsL20* (Sm^r), *xyl-5, mtl-1, supE44*] containing a pRB28 plasmid was previously reported *(9, 45)*. Cells were grown in Luria-Bertani (LB) medium (10 g/l tryptone (Difco), 5 g/l yeast extract (Difco), 5 g/l NaCl (analytical grade), pH 7.2) containing 30 μg/ml kanamycin (Sigma Chemical Company, St. Louis, MO) at 30°C. HgCl$_2$ was purchased from J.T. Baker Chemical Company (Phillipsburg, NJ). All other chemicals purchased were of the highest analytic quality available. Five hundred ml of *E. coli* cultures grown to an OD$_{600}$ of 1.0 for blending into latex ink formulations were cultivated in 2 liter baffled Erlenmeyer flasks on a rotary shaker (Model 3525C, Lab-Line Instruments, Melrose Park, IL) at 30°C in LB media. The cells were centrifuged at 4,424 x g for 10 min, washed with 550 ml of phosphate buffered saline (PBS), and resuspended in 40 ml of PBS, centrifuged at 3500 x g for 10 min, the supernatant decanted and the wet cell pellet weighed. Cell viability was determined by diluting the cell pellet in PBS for determination of colony forming units (cfu) on LB agar petri plates incubated at 30°C for 24 hours. The recovery of viable *E. coli* from "macrodots" was determined by LB plate counting following three cycles of sonication for 5 min (in bursts) followed by 30 s vortex mixing at 4°C.

As a control for loss of cell viability and reactivity due to shear stress during piezo deposition, *E. coli* pRB28 latex ink formulations were also deposited manually deposited as "macrodots" on polyester sheet substrate (DuPont Merlinex 454, Tekra Corp., NJ) using a manual pipetting device (Pipetteman, Gilson Instruments). Drying temperature and relative humidity (RH) were monitored by a calibrated digital relative humidity indicator (model TM125, Dickson, Addison, IL). *Kluyveromyces fragilis* was grown on ATCC culture medium 1245 YEPD (10 g/l yeast extract, 20 g/l Bacto-peptone, Difco, 0118 Detroit, MI, 20 g/l glucose) in an overnight culture, harvested by centrifugation and prepared for ink-jet printing by mixing yeast cell pellet with YEPD medium.

Determination of Reactivity after Ink-Jet Printing by Bioluminescence

The reactivity of *E. coli* pRB28 deposited with polymer on polyester sheet in micro-wells or dot arrays was assayed for Hg^{+2}-inducible bioluminescence activity (*lux*CDABE) by soaking the microstructures in 10 ml of 5 mM pyruvate in PBS buffer containing HgCl$_2$ (from 0 to 1,000 nM) in sterile glass scintillation vials *(9, 44)*. Samples were incubated in duplicate at ambient temperature, and

luciferase activity was detected as luminescence counts per minute (CPM) of ATP-dependent photon emission in liquid scintillation counters (Beckman, LS 7000, or Beckman LS 3801, Beckman Coulter, Fullerton, CA). The rate of luciferase induction and the maximum induction were calculated from the slope and maximum of the CPM versus time data respectively. All measurements were averages of triplicate determinations unless otherwise indicated.

Piezoelectric Deposition Devices

Two DOD piezoelectric office printers (reservoir dispense deposition) with different nozzle aperture sizes and an ink-jet nano-plotter (aspirate pipette deposition) with two interchangeable piezo tip aperture sizes were used to investigate reactive *E. coli* pRB28 ink formulations. The specifications for these deposition devices are summarized in Table II.

Table II. Piezoelectric Deposition Devices

Device Type	Nozzle Aperture (μm)	Droplet Size	
		volume (nl)	diameter (μm)
Reservoir Dispense (moving substrate)			
Epson 640	26	0.1	~27
Canon 1080A	64	0.3	~125
Aspirate Pipet (stationary substrate)			
GeSIM Model 1.2	25	0.1 - 0.2	~60
GeSIM Model 1.2	50	0.25 - 0.5	~90

Ink-Jet Office Printers - Reservoir Dispense Deposition

Latex ink formulations containing glycerol as the biopreservative were initially evaluated using an Epson 640 office printer with 26 μm diameter nozzles (Epson America, Long Beach, CA). The foam-filled ink cartridges were cleaned of printing ink by flushing with distilled water, and the chambers were filled with 10 ml of *E. coli* latex ink emulsion (see below) using a syringe until drops formed through the bottom opening in the cartridge. The cartridge was then blotted on a paper towel before loading into the printer. Five to 10 cleaning cycles were performed until print quality checks showed that all nozzles were firing. All printing was performed with at least 25 of the 32 nozzles firing.

Irreversible nozzle clogging occurred when latex inks were allowed to dry (hours to days) between printings. Nozzles were cleaned by washing under running distilled water, filling with water and performing 20-50 cleaning cycles. The format for printing 12.7 mm diameter patches was generated in Paint software (Microsoft Windows 3.11).

Formation of latex micro-wells was investigated using a modified Canon JP1080A color ink-jet office printer with 64 μm diameter nozzles and J1-20C ink cartridges (Canon, Inc., Tokyo, Japan). SF091 latex (see below) used to form the nonporous micro-well walls and *E. coli* latex ink formulations used to fill the micro-wells (see below) were loaded into custom made 5 cm by 5 cm square polyethylene bag reservoirs with a 5 cm long 3 mm OD and 1 mm ID PVC tube connecting the bag to the JI-20C ink cartridge septum. The printer was modified by relocating the printer ink reservoir needles from a horizontal position within the printer to an aluminum plate outside of the printer. The needles were located in a vertical position so that the polyethylene reservoir bags and ink cartridges were vertical when the JI-20C cartridge mouthpiece septa were mounted onto the needles. The ink reservoir bags were filled with a 10 ml syringe. Once the cartridge was loaded, 5 to 10 manual cleaning cycles were performed until the ink lines were filled. Ink jet printing with this modified office printer was performed with all four nozzles firing. Unused nozzles were filled with colored liquid. The Canon JP1080A was operated by programs written in visual basic (Windows 3.11). Cleaning of the piezoelectric head after printing was performed by removing microbial ink from the ink bags and washing each reservoir with distilled water. The cartridge was then reloaded with water and the print head cleaned by manually pumping water through the piezo head nozzles.

Ink-Jet Nano-Plotter - Aspirate Pipette Deposition

In order to improve nozzle cleaning, print layer by layer (LBL) on stationary substrate, and to be able to switch piezo nozzle aperture size without changing printers, a four print head robotic nano-plotter (model NP1.2 *Gesellschaft für Silizium-Mikrosysteme*, GeSIM mbH, Großerkmannsdorf, Germany) was used for ink-jet deposition of dot arrays of ink formulations containing *E. coli* pRB28 or *K. fragilis*. The nano-plotter was located in an acrylic chamber with humidity monitoring and control. Two interchangeable piezo-heads similar in aperture size to the office printers were used (25 μm and 50 μm) to vary droplet size and deposition rate (Table II). Cameras monitored drop formation and impact on polyester sheet substrate attached to the 260 x 270 mm X-Y workspace. Ink formulations and piezo tip cleaning fluids were aspirated from wells of a 384 well microtiter plate mounted on the workspace. An automated tip cleaning protocol was developed using a tip flushing, surface cleaning and blotting workstation mounted adjacent to the workspace. Latex emulsion drying rate in

the microtiter plate wells was not significant during the time needed for dot array printing. Aspiration volume, droplet deposition density and the pitch (spacing) of dot arrays were programmed using NP12 software (GeSIM). Array deposition was evaluated first using water on water sensitive paper (WSP, Novartis) followed by aspiration and deposition of latex ink formulations onto 124 μm thick polyester sheet cleaned with 70% ethanol or for *K. fragilis* directly onto YEPD agar plates. Piezo tips were cleaned with 70% isopropanol in filtered water, flushed with filtered water to remove isopropanol and blotted.

Latex Ink Formulations, Determination of Microbial Toxicity, Formulation Rheology and Dry Ink Thickness

Latex Ink Formulations

A monodispersed acrylate/vinyl acetate copolymer latex, Rovace™ SF091 emulsion (Rohm and Haas, Spring House, PA) 55% solids, average particle size of ~280 nm, T_g~10°C, was used after adjusting the pH to 7 with sodium hydroxide (Table III). For formulations *I – IV* and *VI*, glycerol or glycerol and sucrose were added to generate nanopores as described previously (*9, 10, 41, 44*). Ink-jet inks were prepared by diluting the previously reported latex coating formulation (*9, 10, 39, 43*) with water to reduce viscosity to <4 cP. Ink for forming non-porous micro-well walls (*V*, Table III) was diluted Rovace™ SF091 without glycerol or sucrose. A re-dispersible formulation without latex was also used to print *E. coli* (*VI*, Table III) to evaluate viability and reduction in bioluminescence by the nanoporosity of the polymer matrix surrounding the printed cells. In order to formulate the ink, room temperature *E. coli* pRB28 wet cell paste was first gently mixed with a small spatula with glycerol and sucrose in a 50 ml tube until homogeneous. The appropriate amount of latex was added and the mixture blended with a spatula without generating air bubbles. All latex inks were used immediately after preparation without refrigeration. The composition of all of the ink formulations is shown in Table III.

Determination of Latex Ink Toxicity to Microorganisms

Because commercially available SF091 latex contains ~15 ppm of a mixture of isothiazalone biocides to extend its shelf-life (5-chloro-2-methyl-4-isothiazolin-3-one, 2-methyl-4-isothiazolin-3-one, Kathon® XL, Rohm and Haas) as well as residues for the copolymer synthesis (acetaldehyde, vinyl acetate, methyl propionate, butyl ether, butyl propionate), a contact toxicity assay was performed to determine how many *E. coli* and *K. fragilis* cells were killed on

contact with this emulsion. The complete latex ink formulations (*III, IV,* Table III) were incubated in a 50 ml tube without shaking for 30 min at 28°C to 30°C. Following incubation, the ink formulation was diluted to 50 ml with PBS, and serially diluted to determine the number of viable cells by colony forming units (cfu). *E. coli* and yeast suspended in the same volume of PBS, without glycerol, sucrose or latex, and incubated for 30 min at 28°C to 30°C was used as the control.

Table III. Latex ink formulations

Formulation Component	I	II	III	IV	V	VI
Wet cell paste	1.2g	1.2g	1.2g	1.2g	-----	1.2g
SF091 latex (pH 7)*	1.0 ml	1.0 ml	1.0 ml	1.0 ml	1.0 ml	-----
Sucrose (0.58 g/ml)	------	------	350μl	350μl	-----	350μl
Glycerol (100%)	------	------	-----	150μl	-----	150μl
Glycerol (50%)	300μl	300μl	650μl	-----	-----	-----
Distilled water (μl) or total volume	8 x	4 x	7,850	3 x	4,000	3 x

* Adjusted to pH 7 prior to use, contains Kathon™ biocide, ~15 ppm.

Determination of Latex Ink Rheology and Dry Coating Thickness

Ink viscosity as a function of shear rate was determined at room temperature using a Model ARES-LS1 rheometer (TA Instruments, New Castle, DE). Dry ink thickness was determined using either a foot-pad constant load micrometer (Model 691B-R2, 284g load, Federal Products, Providence, RI) or a foot-pad digital micrometer (Model ID-C112GEB, Mitutoyo Corp., Japan).

Microscopy, Image Analysis and Profilometry

The size of printed micro-wells and dot arrays were visualized and measured using a profilometer (Model P10, KLA Tencor, San Jose, CA). Dot arrays and individual dots were also visualized using light microscopy with a GIF filter, BF condenser with -65° polarizer, DIC analyzer (Nikon E800, 1x Optivar Magnifier) and the images measured using Image Pro Plus software. Measurement of latex polymer coating diffusivity and cryogenic field emission scanning electron microscopy methods (cryo-FESEM) to visualize nanopores generated by arrested polymer particle coalescence have previously been described (*4, 7, 10, 41-44*).

Results

Toxicity of Acrylate/Vinyl Acetate Latex Emulsions to *E. coli* pRB28 and Yeast

To measure latex contact toxicity, the average number of cfu was determined from four plates of *E. coli* pRB28 (plated on LB agar at 37°C overnight) from a contact toxicity assay (7). The assay mixture initially contained 1.35 x 10^{10} cfu/ml of viable cells. Following incubation for 30 min in SF091 latex emulsion without Kathon™ biocide and with 15 ppm or 30 ppm Kathon™ a 10% gain in cfu was measured without biocide and a 11% to 17% loss in cfu was measured for biocide levels of 15 ppm and 30 ppm respectively. The effect of Kathon™ biocide was therefore insignificant at the very high levels of *E. coli* used since the concentration of *E. coli* in the ink formulations shown in Table III which was 10-fold higher, ~1 – 3 x 10^{11} cfu/ml.

Contact toxicity of Kathon™ to yeast was previously determined using *Saccharomyces cerevisciae* 204508 and found to be reduced by 27% to 30% (average of 5 petri plates) for latex without biocide which was the same as for latex containing 15 ppm biocide. Dialyzed latex resulted in the same level of toxicity, ~20% reduction in cfu following 30 min incubation indicating that the latex particles themselves and not biocide or dialyzable residues from polymer synthesis were toxic (7). Because of the level of toxicity determined using *S. cerevisiae*, in this study *K. fragilis* was printed in YEPD growth media without latex.

Effect of Ink Drying on Mercury-Inducible *E. coli* Bioluminescence Reactivity

Manually Deposited "Macrodots"

The effect of ink drying conditions (temperature, RH) on bioluminescence reactivity was investigated by manually pipetting ~0.1 µl (100 nl containing 9.6 x 10^6 cfu following sonication) and ~0.25 µl (250 nl containing 2.2 x 10^7 cfu following sonication) of latex coating formulation (formulation *IV*, Table III) onto polyester sheet in ~6 mm diameter "macrodots" of <30 µm thickness (Table IV). These "macrodots" could be disrupted by sonication at 4°C for deter-mination of the number of cells that survived ink formulation and manual deposition. Refrigerated temperature and increased humidity were both evaluated to determine the effect of reducing ink drying rate on the number of viable *E. coli* recovered by sonicating the "macrodots" to disrupt the structure

for viable plate counting. The recovery of viable *E. coli* by plate counting from sonicated and disrupted "macrodots" was $1.9 \pm 0.52 \times 10^6$ cfu which is ~87% recovered as viable compared to suspended *E. coli* sonicated by the same method prior to plating.

The reactivity of dried "macrodots" was compared to the reactivity of the same volume of latex emulsion that was not dried on polyester. These volumes were chosen to correspond to the total volumes printed by the nano-plotter in 10 x 10 dot arrays (5 droplets/dot) using the 25 μm or 50 μm piezo tips (see below). Bioluminescence was induced with 100 nM Hg^{+2}, incubated in 2 ml PBS + 5 mM pyruvate, and light measured as counts per minute (CPM) using a scintillation counter. The initial rate of bioluminescence was determined from five consecutive points starting where the CPM was >20% of the previous determination. All determinations were done in triplicate.

Table IV. Effect of Drying Temperature, Relative Humidity on *E. coli* Bioluminescence Reactivity in Latex Ink Formulations Manually Deposited "Macrodots"

Volume (nl)	RH (%)	T (°C)	*lux* Response (Δ log cpm)	Initial Rate ($\times 10^{-3}$)	r^2
100 (liquid)*	-----	22	2.31	12.2*	0.9925
100	8.9	22^1	2.94	18.3	0.9738
100	45.7	22^1	2.85	14.9	0.9965
100	46.2	3^2	3.22	22.8	0.9814
250 (liquid)	-----	22	1.99	9.7	0.9948
250	20.1	23^1	0.86	4.6	0.9967
250	64.2	24^1	0.86	4.7	0.9952
250	88.7	3^2	1.07	2.4	0.9952

Formulation *IV*, Table III, n = 3.
* Volume too low to accurately measure luminescence
[1] Evaporation rate 27 nl/s at 22°C
[2] Evaporation rate 17 nl/s at 3°C

Table IV shows that ink drying as manually deposited "macrodots" at low relative humidity (<50% RH) reduced total bioluminescence reactivity compared to the reactivity of the same volume of formulation that was dried at >50% RH and the initial rate was reduced. High humidity and low temperature reduced "macrodot" drying rate (from ~ 6 s to ~10 s) and increased both the total bioluminescence response as well as the initial rate. Manual deposition of 100 nl

produced "macrodots" that were more reactive than deposition of 250 nl. The differences in reactivity upon drying were more evident with manual deposition of 250 nl of ink formulation because of the difficulty of accurately manually pipetting 0.1 µl. However because neither the office printers nor the nano-plotter could be easily operated at refrigerated temperature (~3°C), ink reactivity was investigated at ambient temperature, ~22°C, initially without humidity control using the office printers and with humidity control at >50% RH using the nano-plotter enclosed in a humidified chamber.

E. coli Bioluminescence in Ink-Jet Printed Patches, Micro-Wells, and Dot Arrays

Bioluminescence Response of Ink-Jet Printed Patches

The Hg^{+2}-inducible reactivity of ink-jet deposited latex inks containing *E. coli* pRB28 was initially demonstrated by duplicating the previously reported mercury-inducible bioluminescence in 12.7 mm diameter patches of 30 µm layers of the same *E. coli* strain prepared in SF091 latex and coated onto polyester using a manual Mayer rod drawdown coating method (*9*). In order to duplicate these results using an office printer, a 9 x 11 array of 12.7 mm diameter and 2 µm thick patches spaced 17 mm on center was printed on an 21.6 cm x 27.9 cm sheet of polyester with ink formulation *I* (Table III) using the Epson 640 printer (Figure 2). Total printed patch volume was 240 nl. Figure 3 shows the induction kinetics for these patches which is 1.5 logs less than the bioluminescence of the same diameter but much thicker 30µm thick, ~6 µl SF091 latex patches previously reported (*9*). The maximum luciferase induction kinetics was similar to that previously reported, but bioluminescence was maintained for a shorter period of time (5 hours versus 24 hours) because of the reduced volume printed. The minimum concentration of Hg^{+2} detected was 10n M. At 1,000 nM Hg^{+2} the maximum induction was less than at 100 nM Hg^{+2} indicating mercury is toxic at >100 nM as previously reported (*9*). This demonstrated that *E. coli* remained viable and reactive (inducible) following ink-jet deposition in a SF091 latex ink formulation deposited through a 26 µm diameter ink-jet aperture.

Bioluminescence Response of Latex Micro-Wells Filled with Nanoporous Latex Ink using Reservoir Dispense Deposition

Latex emulsion inks can be formulated to retain nanopores when dried by the addition of glycerol or sucrose to arrest polymer particle coalescence (*10*,
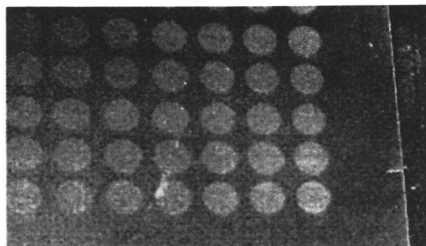
Figure 2. 12.7 mm diameter, 2 μm thick E. coli latex ink patches printed on polyester sheet. Epson 640 printer, 26μm aperture (44).
(See page 3 of color insert.)

(A)   (B)
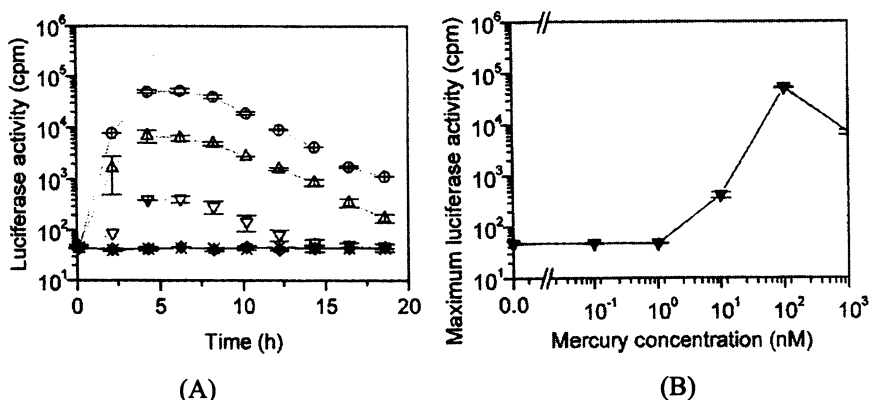
Figure 3. Bioluminescence kinetics of 12.7 mm diameter, ~2 μm thick patches of E. coli pRB28 printed using latex ink Formulation I (Table III.) on polyester using an Epson 640 printer. A. HgCl₂ concentration: △, 1,000 nM; ○, 100 nM; ▼, 10 nM; ◇, 1 nM; +, 0.1 nM; ✕, 0.01 nM. B. ▼, Maximum lux expression (sensitivity, dynamic range) (44).

41-43) (formulations *I-IV*, Table III).   Without these additives, SF091 latex polymer particles completely coalesce during ink drying to create very low permeability polymer coatings. These nonporous coatings can be used for printing walls, ceilings, and channels creating micro-fluidic structures containing whole-cell microbial reaction zones (*44, 46*).

In order to demonstrate this concept, the Canon JP 1080A printer was used to print SF091 latex (formulation *V*, Table III) to form the walls of square microwells of decreasing volume on polyester sheet. Two rows of droplets were deposited around a center of 4 x 3 droplet spaces wide. Each row or column of droplets was 0.3 mm wide. The ink-jet printer head moved in the y direction (0-2000 μm) delivering a line of droplets and then advanced one row in the x

direction (0-3000 μm) and delivered a second row of drops. This was repeated until all 7 rows were deposited. The entire well was created by printing 10 consecutive layers (10 LBL) with a 60 s to 120 s drying step between deposition of each layer. Figure 4A shows a profilometer image of an empty micro-well and 4B a well filled by printing *E. coli* in ink formulation *II*. Individual droplet deposits are visible as craters. The micro-well wall height was composed of two lines of droplets (Figure 4A). The average wall height at the ridges was ~10 μm. In B the well is filled with formulation *II* (Table III) and the height of the center is lower than the wall material because of the higher water content of the ink containing *E. coli* compared to the walls (formulation *V*) formed by only SF091 latex. The minimum micro-well that could be constructed using the Canon 1080A printer and SF091 latex was 1 row of droplets deposited 10 LBL.

The Hg^{+2}-inducible bioluminescence of *E. coli* pRB28 printed in micro-wells was investigated for square micro-well sizes of the following number of droplets (10 LBL) on each side: 28 x 28, 14 x 14, 4 x 3, and 2 x 2 (generating 8.4 mm x 8.4 mm, 4.2 mm x 4.2 mm, 1.2 mm x 0.9 mm and 0.6 mm x 0.6 mm micro-wells respectively) which corresponded to micro-well volumes of 141 nl, 35 nl, 2.2 nl, and 0.72 nl well arrays. The *E. coli* filled micro-wells were induced with 100 nM Hg^{+2} and the luciferase activity measured by excising individual microwells and placing them in a liquid scintillation vial. Figure 5A shows the induction kinetics for different sizes of micro-wells. Wells of 28 x 28, 14 x 14 and 4 x 3 droplets were induced by Hg^{+2} within 2 hours and maintained activity for 12 hours or longer. Micro-wells of 2 x 2 droplets (<1 nl volume) showed a short peak of reactivity above background at 10 hours following induction. 28 x 28, 14 x 14, and 4 x 3 wells showed induction similar to that of the 12.7 mm diameter, 240 nl patches printed with the Epson 640 printer, where maximum induction occurred after approximately 5 hours. 28 x 28 droplet wells showed a maximum induction plateau after 5 hours, which remained constant for 15 hours.

Figure 5B shows the luciferase activity related to well size for *E. coli* deposited in micro-wells using ink formulation *II* as a function of well diameter and coating thickness. Well sizes ranged from dot squares of 8.4 x 8.4 mm, 4.2 x 4.2 mm, 1.2 x 0.9 mm, and 0.6 x 0.6 mm. Printing thickness varied between ~2, ~6, and ~10 μm. The total micro-well volumes ranged from 705 nl (28 x 28, 10μm wall height) to 0.72 nl (2 x 2, ~2 μm wall height).

As well volume decreased the reactivity was expected to decrease linearly based on the assumption that the specific bioluminescence activity would be constant per volume of *E. coli* latex ink deposited. However, the specific *lux* activity decreased dramatically as the well size and printed thickness decreased. The activity ranged from 150 CPM/nl for 6 μm to 10 μm thick wells down to ~25 CPM/nl for 2 μm thick wells This indicated that ink formulation *II* which contained only glycerol could not block polymer particle coalescence creating a sufficiently nanoporous structure and that glycerol alone was not sufficient to preserve *E. coli* viability and specific reactivity in very small micro-wells <5 μm
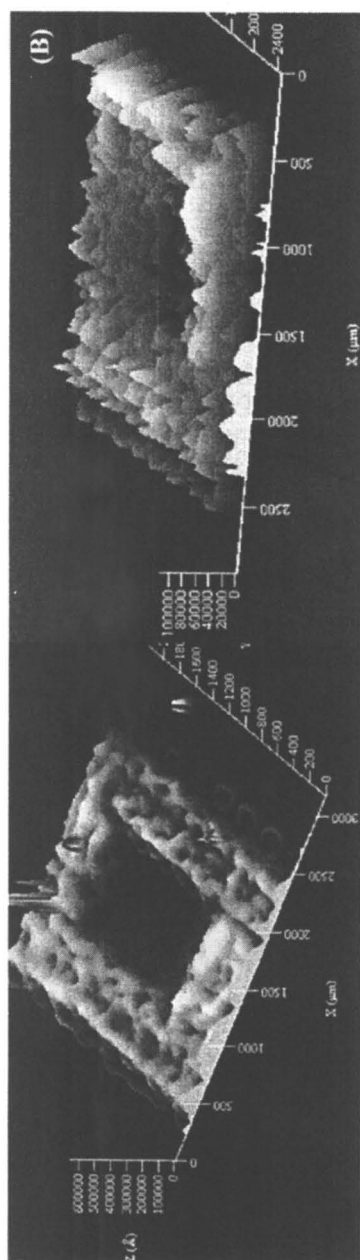
Figure 4. Profilometer images of latex micro-well printed using a Canon 1080A printer.
A. Nonporous wells formed on polyester sheet by completely coalesced SF091 latex (formulation V).
B. Well filled with ink formulation II containing E. coli pRB28 (44).
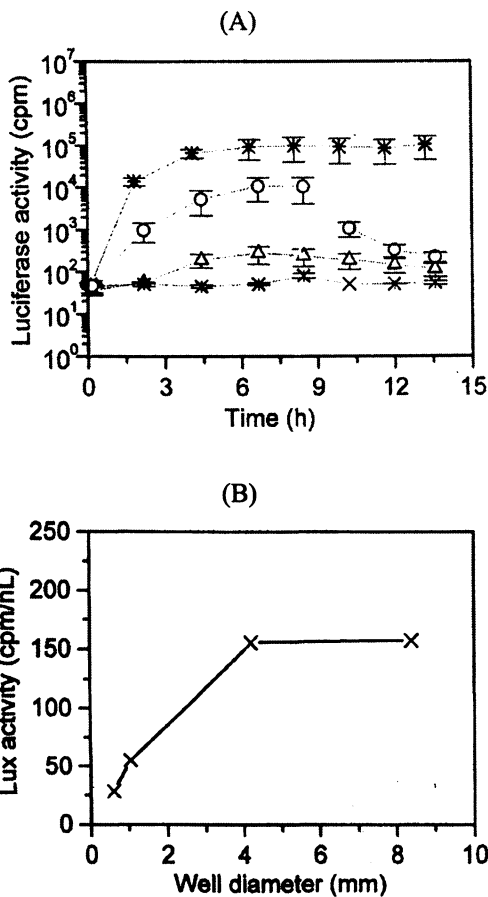
Figure 5. Bioluminescence of E. coli pRB28 in latex micro-wells ink-jet printed using a Canon 1080A printer. A. ✳, 28 x 28 dot micro-wells; ○, 14 x 14 dot micro-wells; △, 4 x 3 dot micro-wells; ✕, 2 x 2 dot micro-wells. B. Lux reactivity per micro-well volume (CPM/nl) at different micro-well diameters (44).

thick following rapid ink drying (*41-43*). It also indicated that a better piezoelectric deposition method was needed to more accurately control droplet size, printed volume and humidity to optimize reactivity.

Printing E. coli pRB28 Using a Nano-plotter for Aspirate Pipette Deposition

Preliminary ink-jet data using office printers indicated that *E. coli* pRB28 could survive the shear stress in 26 μm diameter and 64 μm diameter piezoelectric aperture tips and was capable of induction with Hg^{+2} when printed in SF091 latex + glycerol, however there were numerous disadvantages to this experimental system to further improve ink formulations such as: office ink-jet printers were not originally designed to deposit latex polymer particles, reservoirs had to be manually emptied and cleaned to change inks, inability to clean nozzles with organic solvents followed by water, a moving substrate resulting in poor LBL (manual) alignment, poor monitoring of droplet size and volume printed, poor control of drying rate (humidity, temperature). These disadvantages resulted in a low bioluminescence reactivity (maximum $<10^5$ cpm) even though the volume printed into micro-wells was >700 nl.

For these reasons, a 250 μl tip volume, 4-head aspirate pipette drop on demand (DOD) piezoelectric deposition robotic X-Y nano-plotter (GeSIM model 1.2) with Z-plane control was used for further ink formulation studies enclosed in an acrylic chamber for humidity control. This nano-plotter was equipped with interchangeable 25 μm diameter (~60 μm dia. droplet) and 50 μm diameter aperture tips (~90 μm dia. droplet). GeSIM software was used for printing 10 x 10 dot arrays of 1 to 5 droplets per dot (LBL) and 0.1 mm to 0.5 mm pitch (dot spacing) on polyester sheet or directly onto nutrient agar contained in Petri dishes. Microbial ink emulsions which contain glycerol and sucrose to generate nano-porosity (formulations *III, IV*, Table III.) and tip cleaning solutions (70% isopropanol in water) were pipetted into supply wells of a 384 well plate mounted on the nano-plotter. *E. coli* microbial ink viscosity was found to be >1.5 to ~3cP and semi-shear rate dependent over a shear rate range of 1 to 30,000 s^{-1} (data not shown). The maximum shear rate of the 25 μm tip was calculated to be ~28,000 s^{-1}.

An automated washing station was provided with the nano-plotter including an optical system to adjust droplet size and eliminate satellite droplets. Print quality and LBL alignment of droplets was evaluated first using WSP (Novartis) and also by light microscopy. Microbial ink arrays containing 5 x 10^4 cfu *E. coli* per nl ink formulation were printed onto 95% ethanol-cleaned polyester sheet taped to the plotter X-Y workspace. Droplet (0.2 nl or 0.5 nl) drying time was <0.1 s at ~22°C (>50% RH). The bioluminescence reactivity of 10 x 10 dot arrays was determined by excising the entire printed array, placing the polyester patch containing the array upright in the bottom of a scintillation vial,

.

submerging the array in PBS + 5 mM pyruvate and measuring array luminescence in a liquid scintillation counter in response to induction with 1 nM to 10,000 nM Hg^{+2} (Figure 6). The bioluminescence of an individual multi-droplet latex dot could be determined by dividing the array CPM by 100.

(A) (B)
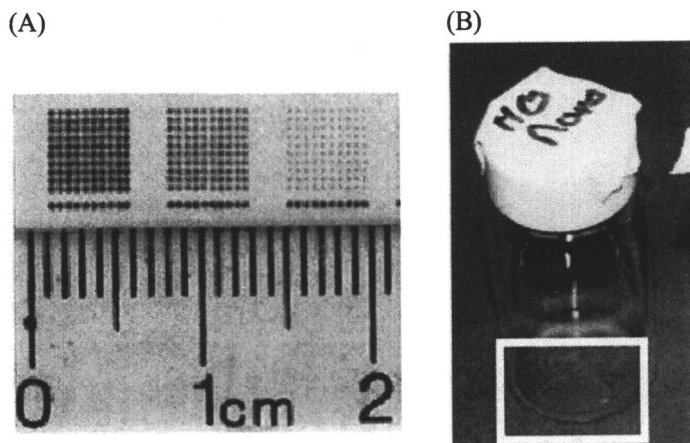
Figure 6. Latex microbial ink dot arrays. A. Printed on WSP using a 50 μm aperture tip, 0.5 mm pitch, ~0.5 nl droplets; 10 x 10 arrays of 5, 3, and 1 droplet per dot respectively left to right. B. E. coli dot array printed on polyester, excised and placed in a scintillation vial for measurement of bioluminescence reactivity by mercury induction.
(See page 4 of color insert.)

Nano-Plotter Printing of E. coli Without Adhesive Latex

Preliminary printing studies with the nano-plotter were carried out by evaluating Hg^{+2}-inducible reactivity of *E. coli* pRB28 printed with glycerol and sucrose but without SF091 latex using the 50 μm tip (Formulation *VI*, Table III). Without the adhesive SF091 latex to entrap the printed cells, dot arrays of *E. coli* ($\sim 5 \times 10^4$ cfu/nl) printed onto polyester and dried immediately re-dispersed and responded (maximum luminescence in suspension in 2.5h) to as low as 5 nM Hg^{+2} ($5.7 - 7 \times 10^6$ CPM per 10 x 10 dot array, 5 droplets per dot, 0.5 mm pitch) indicating minimal loss of reactivity by the shear stress of the tip aperture. However, as reported previously for latex patches of *E. coli* pRB28 used as a mercury biosensor (*9*), without the "protection" of the nano-porous latex surrounding the cells, *E. coli* was very sensitive to Hg^{+2} and dots printed without latex were completely killed by exposure to 50 nM $HgCl_2$.

Structure of E. coli Latex Ink Dot Arrays Printed using a Nano-Plotter

Figure 7A shows a light microscopic image of a section of a 10 x 10 dot array printed on polyester (shown in Figure 6) of 5 droplets/dot of SF091 latex containing glycerol, sucrose and *E. coli* pRB28; 7B is a higher magnification image of a single dot showing that the dots have a raised edge structure. The

(A) (B)
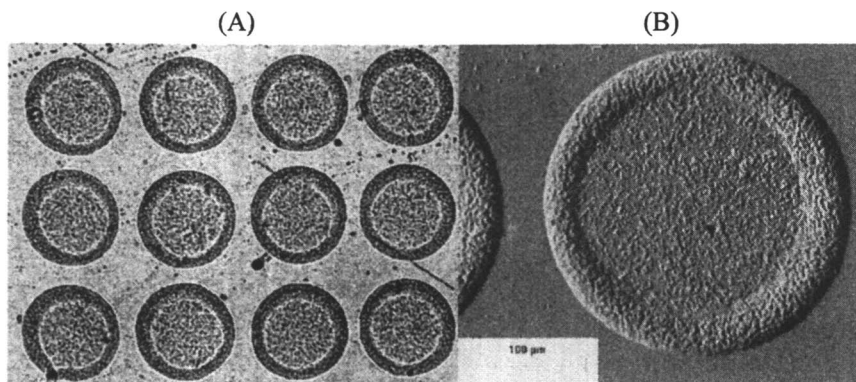
Figure 7. Light microscopic image of a section of an E. coli pRB28 dot array printed with SF091 latex ink formulation IV on polyester with a 55.65 μm tip aperture. A. Portion of 10 x 10 dot array. B. Single dot, bar equals 113 μm.

mean dot diameter of dry or hydrated dots was ~180 μm for dots printed with the 25 μm aperture and ~244 μm for the 50 μm aperture. Analysis of these structures using profilometery revealed dot edges higher in relation to the center of the dots (Figure 8). This indicates that surface tension driven convective flow of ink during rapid drying likely generates significant concentration gradients and mechanical stresses prior to film formation. (Similar structures are visible in Figure 4A for formulation *V* used to print micro-well walls which did not contain *E. coli*). Average *E. coli* dot thickness (5 LBL) determined by profilometry with 1 mg force was <2 μm with a maximum edge thickness of ~6 μm. *E. coli* density per dot and printing density are summarized in Table V. The dimensions of *E. coli* in suspension and entrapped in latex coatings is <1 μm by ~ 2 μm and therefore the calculated microbial ink printing density is close to the maximum for an average printed coating thickness over the entire dot of 1 to 2 cells thick. However the microscopic and profilometer images clearly indicate very non-uniform cell distribution over the surface of the dots with the majority of the printed *E. coli* likely being entrapped in the raised edges.

Table V. Nano-Plotter Printing Density for *E. coli* Latex Ink

Tip Aperture	*E. coli* Density/dot	Dot Area	Roundness	Printing Density
50 μm	~9.4 x 10^4	4.7 x 10^4 μm^2	1.17	~2 cells/μm^2
25 μm	~3.8 x 10^4	2.6 x 10^4 μm^2	1.14 – 1.26	~1.5 cells/μm^2

Formulation *IV* printed as 10 x 10 dot arrays (5 LBL, 0.5 mm pitch). Dot area and roundness determined using Image Pro Plus software.

Bioluminescence Reactivity of E. coli Latex Dot Arrays

The bioluminescence reactivity of *E. coli* pRB28 latex dot arrays printed using the nano-plotter at >50% RH through either size piezo tip was over 10-fold higher (>10^6 cpm) than for the preliminary studies printing much larger latex micro-wells using office printers (Figure 9) but slightly less than *E. coli* printed without latex which indicated the effect of diffusion resistance of the nanopores. The reactivity of 100 nl and 250 nl of *E. coli* ink printed as latex arrays on polyester was higher than that for the same volume manually deposited as a "macrodot" or induced as a latex emulsion. The addition of glycerol and sucrose to SF091 to generate nanoporosity and to preserve the viability of *E. coli* during ink drying was essential to retain a high level of mercury-inducible bioluminescence. The reactivity of dot arrays printed without glycerol and sucrose was less than one third that of arrays printed with these preservative porogens (not shown).

Ink-Jet Surface Patterning with Living Microbes: Printing micro-colony arrays of *Kluyveromyces fragilis*

Surface bio-patterning is an emerging application of ink-jet deposition. Deposition of uniformly spaced viable micro-colonies could be used to generate large numbers of identical growing bacterial, yeast or fungal colonies on a nutrient surface for drug screening or in combination with adhesive latex to quickly cover a surface with a uniform "synthetic biofilm" with engineered adhesion. In order to investigate surface patterning onto nutrient surfaces and the shear stress of printing larger microorganisms than *E. coli* through piezoelectric tips, deposition of *Kluyveromyces fragilis* which is ~12 μm in length was investigated. Because of the previously determined contact toxicity of SF091 latex to *S. cerevisiae* (7), *K. fragilis* was printed in micro-colony arrays using the nano-plotter with a 50 μm tip in YEPD growth medium (containing carbohydrates, salts and yeast extract) without latex directly onto agar plates containing the same growth media. This direct method was used to determine whether the much larger yeast survived

A.
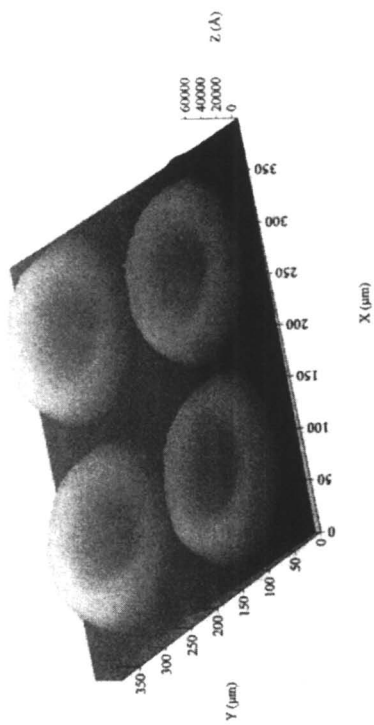
B.
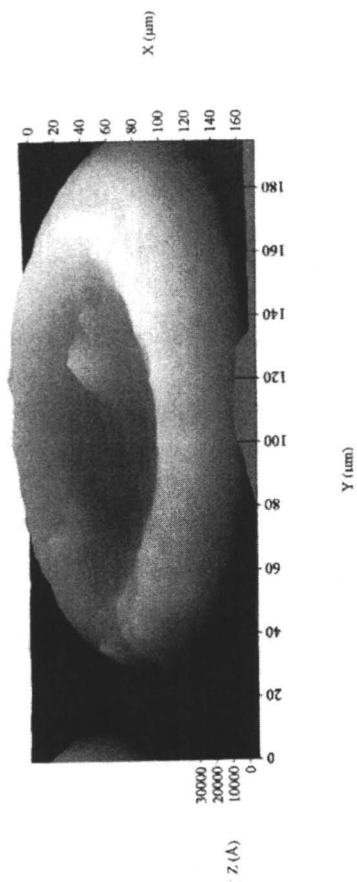
C.
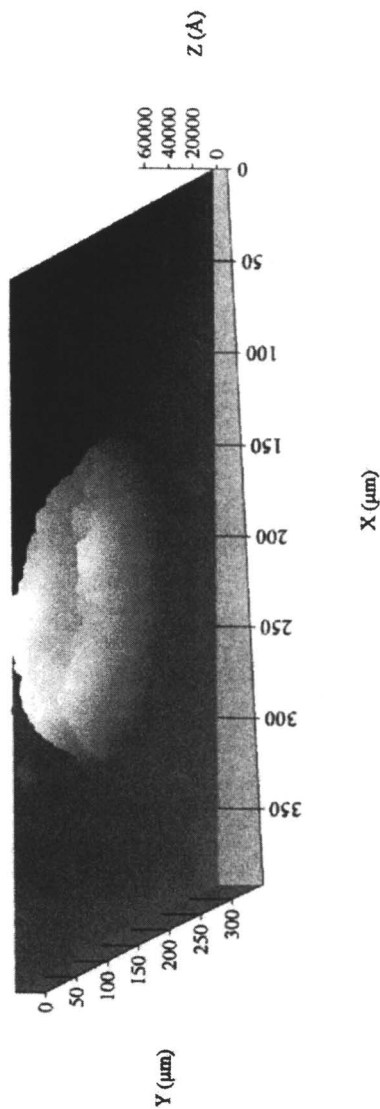
Figure 8. Profilometer images of E. coli pRB28 latex ink dots printed using formulation IV with a piezoelectric DOD nano-plotter. A. 50 μm aperture tip. B. Higher magnification, 50 μm aperture tip. C. 25 μm aperture tip. (See page 5 of color insert.)
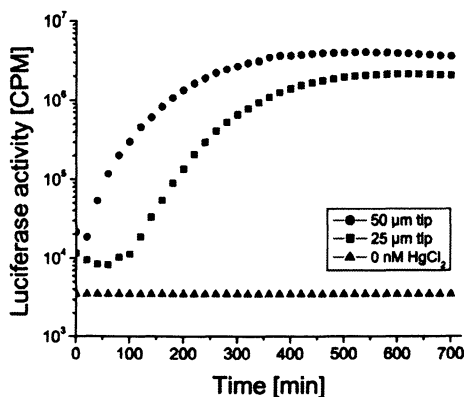
Figure 9. Bioluminescence kinetics of nano-plotter printed dot arrays of E. coli pRB28 induced with 100 nM Hg^{+2}. Total printed array volume: ■, ~100 nl (25 μm aperture tip); ●, ~250 nl (50 μm aperture tip).

the shear stress of the tip by measuring the growth of the micro-colonies. 21 x 20 dot micro-colony arrays (2 mm pitch) consisting of 4.4 nl dots (10 LBL droplets of 0.44 nl) were printed and the plates incubated at 30°C. After 24 hours, very uniform micro-colonies were visible on the YEPD plates which increased in size with further incubation for 48 hours (Figure 10).

Discussion

Two microbial systems were used to investigate ink-jet DOD deposition for printing viable, reactive microbes as thin coatings (<10 μm thick) onto polyester or nutrient agar surfaces. *E. coli* (~1 μm x 2 μm) and *K. fragilis* (~12 μm diameter) can be ink-jet printed using glycerol and sucrose to preserve their viability and reactivity using piezoelectric deposition devices with 50 μm and 64 μm tip apertures. Viable, reactive *E. coli* could also be printed using a 25 μm tip aperture. Both cell types survived printing and drying on polyester without latex. However without SF091 latex, dried cells were not adhesive and immediately dispersed when rehydrated.

Two ink-jet deposition devices were used to print diluted low viscosity emulsions (< 3cP) of a very high concentration of *E. coli* (1 – 3 x 10^{11} cfu/ml) with a low T$_g$ acrylate/vinyl acetate latex (SF091) resulting in adhesive nano-porous microbial inks capable of generating coatings of ~2 μm to ~6 μm thick with a printing density of ~1.5 *E. coli* /μm^2. The number of microorganisms that survived ink formulation (mixing with sucrose and glycerol, latex biocides), the shear stress of printing and drying as small microstructures could not be
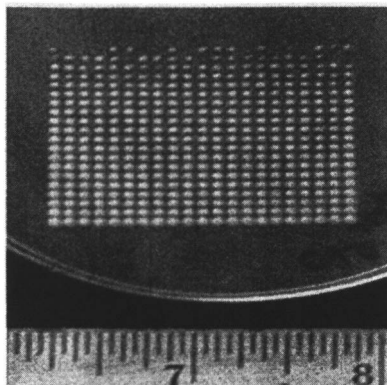
*Figure 10. Ink-jet printed K. fragilis micro colony array printed onto YEPD
agar plate to determine the viability following piezoelectric deposition through a
50 μm diameter aperture tip. Plate incubated for 48 hours, 30°C. Array printed
from left to right starting at the lower left hand corner and then upward.
(See page 4 of color insert.)*

measured directly by viable plate counting due to the difficulty of disruption of
the microstructures by sonication. Disruption by sonication and viable plate
counting was successful on 250 nl manually deposited "macrodots" and this
indirect method indicated that ~87% of *E. coli* survived manual deposition and
drying at >50% RH at ambient temperature when glycerol + sucrose were added
to the ink formulation. A more rapid, sensitive and non-destructive measure of
printed microbial viability in microstructures is needed. A *pmer-gfp* construct
has recently been made in *E. coli* HB101 for this purpose (*47*).

Instead of direct plating, the reactivity of ink-jet printed *E. coli* entrapped in
patches, micro-wells and dot arrays was determined by nitrogen-starved Hg^{+2}-
inducible bioluminescence (expression of *lux*CDABE). Reducing ink drying rate
by reducing the temperature and increasing the RH increased bioluminescence.
In addition to control of ink drying rate, the addition of glycerol <u>and</u> sucrose to
preserve cell viability and generate nanoporosity resulted in an increase in
maximum bioluminescence 2 – 3 fold compared to using glycerol alone (Table
VI). This indicates that further optimization of ink formulation is needed and that
other preservative biomolecules (osmoprotectant sugars, carbohydrate polymers,
salts) should be evaluated. In addition, printing *E. coli* pRB28 without latex
resulted in dispersible microcolonies what were ~1.5 fold more reactive than
printed with SF091 suggesting that further optimization of ink nanoporosity is
needed to reduce the diffusion resistance and increase porosity.

Microscopic and profilometer images of the dried printed latex dots
indicated <2 μm thickness in the middle with raised edges suggesting significant
movement of ink formulation during drying. These non-uniform dot structures

Table VI. Effect of Glycerol and Sucrose on Ink-Jet Printed *E. coli* Bioluminescence.

Preservative (formulation)	Device	Tip (µm)	Microstructure	Vol. Printed (nl)	RH (%)	Max. response (CPM/nl)
Glycerol (I)	Epson	26	12.7 mm patches	240	nd	~400
Glycerol (II)	Canon	64	8.4 mm microwells	160	nd	~625
Glycerol (II)	Canon	64	4.2 mm microwells	40	nd	~250
Glycerol + sucrose (III,IV)	GeSIM	25	10 x10 dot arrays	100	>50	~1,200
Glycerol + sucrose (III,IV)	GeSIM	50	10 x 10 dot arrays	250	>50	~1,600
None	GeSIM	50	10 x 10 dot arrays	250	>50	~600

nd, not determined (<50% RH)
Bioluminescence induced with 100 nm $HgCl_2$, 22°C.

indicate that gradients occur during ink drying likely resulting in osmotic stresses which may decrease cell viability. Similar height profile structures have been reported for aqueous nanoparticle emulsions printed on solid surfaces known as the "ring stain effect" (44-48). For example, the raised edges of conductive silver nanoparticle dots and lines printed with ink-jet methods could be eliminated by the addition of wetting agents (49). The mechanism of nanoparticle ring formation following ink-jet deposition of aqueous emulsions on solid surfaces has been correlated with surface wetting, surface tension, evaporation-driven convective flows and pinned contact lines (49)

Microscopic and profilometer methods developed in this preliminary study of microbial latex dot array printing could be used in the future to monitor generation of more uniform ink-jet printed structures as a function of non-toxic surfactants or viscosity modifiers to reduce surface tension and evaporation-driven convective flow during drying. However, choice of suitable "wetting" agents depends on fundamental knowledge of surfactant toxicity, substrate surface energy, the molecular interaction between the latex polymer particles, the surfactants during vitrification of the biomolecules trapped in the pore space to arrest polymer particle coalescence and preserve microbial viability, and the latex polymer surface-microbial cell surface interaction. Unfortunately none of these phenomena are well characterized at the molecular level.

A major limitation of the model *E. coli* system investigated in this study is the very slow bioluminescence response in the PBS + pyruvate nongrowth medium, and the fact that Hg^{+2} is toxic at high levels. The rate and level of

bioluminescence was affected by the physical and chemical environment of the latex-entrapped cells. In some experiments with minimal diffusion resistance (for example printing without latex) bioluminescence was very high, however it did not react maximum levels for over 400 min. Screening of additional promoters fused with stress-inducible *luxCDABE* (*6, 15*) or green fluorescent protein (*gfp*) reporters may identify more rapidly responding promoters under nongrowth conditions. Of particular interest are the response of promoters known to regulate genes affected by DNA damage, osmotic stress, low-water-stress, and desiccation stress which would provide information about the response of *E. coli* to printing and rapid ink drying and could lead to approaches to genetically optimize microbes for higher survival and bioreactivity when printed, dried and rehydrated in non-toxic latex inks.

Acknowledgements

References

1. Alper, J. Science (Washington, D. C.) **2004**, *305*, 1895.
2. Gratson, G. M.; Xu, M.; Lewis, J. A. Nature (London) **2004**, *428*, 386.
3. Li, Q.; Lewis, J. A. Adv. Mater. **2003**, *15*, 1634-1641.
4. Thomas, G.; El-Giar, E. M.; Locascio, L. E.; Tarlov, M. J. In Microfluidic Techniques, Minter, S. D. Ed.; Methods Molecular Biol., Humana Press, Totowa, NJ, 2006; Vol. 321, pp 83-96.
5. Bartos, H.; Goetz, F.; Peters, R-P. In Nanobiotechnology: Concepts, Applications and Perspectives, Niemeyer, C. M.; Mirkin, C. A. Eds.; Wiley-VCH, Weinheim, Germany, 2004; pp 13-30.
6. Flickinger, M. C.; Schottel, J. L.; Bond, D. R.; Aksan, A.; Scriven, L. E. Biotechnol. Prog. **2007**, *23*, 2-7.
7. Flickinger, M. C.; Fidaleo, M.; Gosse, J.; Polzin, K.; Charaniya, S.; Solheid, C.; Lyngberg, O. K.; Laudon, M.; Ge, H.; Schottel, J. L.; Bond, D. R.;

Aksan, A.; Scriven, L. E. In Smart Coatings; T. Provder, Ed.; ACS Symp. Series; American Chemical Society, Washington, D.C., 2008 (in press).

8. Gosse, J. L.; Engel, B. J.; Rey, F. E.; Harwood, C. S.; Scriven, L. E.; Flickinger, M. C. Biotechnol. Prog. **2007**, *23*, 124-130.

9. Lyngberg, O. K.; Stemke, D. J.; Schottel, J. L.; Flickinger, M. C. J. Ind. Microbiol. Biotechnol. **1999**, *23*, 668-676.

10. Fidaleo, M.; Charaniya, C.; Solheid, C.; Diel, U.; Laudon, M.; Ge, H.; Scriven, L. E.; Flickinger, M. C. Biotechnol. Bioeng. **2006**, *95*, 446-458.

11. Bremer, E.; Krämer, R. In Bacterial Stress Response; Storz, G.; Hengge-Aronis, R., Eds.; ASM Press, Washington, D. C., 2000; pp 79-97.

12. Webb, S. J.; Bound Water in Biological Integrity; Thomas, Springfield, IL, 1956.

13. Cayley, S.; Record, T. M. J. Molec. Recogn. **2004**, *17*, 488-496.

14. Potts, M. Microbiol. Rev. **1994**, *58*, 755-805.

15. Van Dyk, T. K.; Smulski, D. R.; Elsemore, D. A.; LaRossa, R.A.; Morgan, R. W. In Recent Advances in Environmental Chemical Sensors and Biosensors, Mulchandani, A.; Sadik, O. A., Eds.; ACS Symp. Ser., American Chemical Society, Washington, D. C., 2000; Vol 762, p 167.

16. Segi, E.; Hever, N.; Rosen, R.; Bartolome, A. J.; Pemkumar, J. R.; Ulber, R.; Lev, O.; Scheper, T.; Belkin, S. Sensors Actuators B **2003**, *90*, 2-8.

17. Belkin, S. Curr. Opinion Microbiol. **2003**, *6*, 206-212.

18. Neufeld, T.; Biran, D.; Popovtzer, R.; Erez, T.; Ron, E. Z.; Rishpon, J. Anal. Chem. **2006**, *78*, 4952-4956.

19. Simpson, M. L.; Saylor, G. S.; Applegate, B. M.; Ripp, S.; Nivens, D. E.; Paulus, M. J.; Jellison, G. E. TIBTECH **1998**, *16*, 332-338.

20. Ripp, S.; Daumer, K. A.; McKnight, T.; Levine, L. H.; Garland, J. L.; Simpson, M. L.; Saylor, G. S. J. Ind. Microbiol. Biotechnol. **2003**, *30*, 636-642.

21. Nivens, D. E.; McKnight, T. E.; Moser, S. A.; Osbourn, S. J.; Simpson, M. L.; Saylor, G. D. J. Applied Microbiol. **2004**, *96*, 33-46.

22. Simpson, M. L.; Saylor, G. S.; Fleming, J. T.; Applegate, B. TIBTECH **2001**, *19*, 317-323.

23. Willner, I.; Willner, B. TIBTECH **2001**, *19*, 222-230.

24. Premkumar, J. R.; Lev, O.; Rosen, R.; Belkin, S. Adv. Mater. **2001**, *13*, 1773-1775.

25. Chan, C.; Lehmann, M.; Chan, K.; Chan, P.; Chan, C.; Gruendig, B.; Kunze G.; Renneberg, R. Biosen. Bioelectron. **2000**, *15*, 343-353.

26. Chia, S.; Urano, J.; Tamanoi, F.; Dunn, B.; Zink, J. I. J. Am. Chem. Soc. **2000**, *122*, 6488-6489.

27. Biran, I.; Walt, D. R. Anal. Chem. **2002**, *74*, 3046-3054.

28. Thompson, D. M.; King, K. R.; Wieder, K. J.; Toner, M.; Yarmush, M. L.; Jayaraman, A. Anal. Chem. **2004**, *76*, 4098-4103.

29. Kuang, Y.; Biran, I.; Walt, D. R. Anal. Chem. **2004**, *76*, 2902-2909.

30. Ringeisen, B. R.; Chrisey, D. B.; Piqué, A.; Young, H. D.; Modi, R.; Bucaro, M.; Jones-Meehan, J.; Spargo, B. J. Biomaterial **2002**, *23*, 161-166.

31. de Gans, B-J.; Schubert, U. S. Macromol. Rapid Comm. **2003**, *24*, 659-666.

32. de Gans, B-J.; Duineveld, P. C.; Schubert, U. S. Adv. Mater. **2004**, *16*, 203-213.

33. de Gans, B-J.; Schubert, U. S. Langmuir **2004**, *20*, 7789-7793.

34. Tekin, E.; de Gans, B-J.; Schubert, U. S. J. Mater. Chem. **2004**, *14*, 2627-2632.

35. Percin, G.; Khuri-Yakub, B. T. Rev. Sci. Instrum. **2003**, *74*, 1120-1127.

36. Leach, R. H.; Pierce, R. J. The Printing Ink Manual, 5th ed.; Kluwer Scientific Publishers, Drodrecht, The Netherlands, 1999.

37. Swope, K. L.; Flickinger, M. C. Biotechnol. Bioeng. **1996**, *51*, 360-370.

38. Swope, K. L.; Flickinger, M. C. Biotechnol. Bioeng. **1996**, *52*, 340-356.

39. Lyngberg, O. K.; Thiagarajan, V.; Stemke, D. J.; Schottel, J. L.; Scriven, L. E.; Flickinger, M. C. Biotechnol. Bioeng. **1999**, *62*, 44-55.

40. Lyngberg, O. K.; Solheid, C.; Charaniya, S.; Ma, Y.; Thiagarajan, V.; Scriven, L. E.; Flickinger, M. C. Extremophiles **2005**, *9*, 197-207.

41. Thiagarajan, V. S.; Huang, Z.; Scriven, L. E.; Schottel, J. L.; Flickinger, M. C. J. Coll. Interfac Sci. **1999**, *215*, 244-257.

42. Huang, Z.; Thiagarajan, V. S.; Lyngberg, O. K.; Scriven, L. E.; Flickinger, M. C. J. Coll. Interfac Sci. **1999**, *215*, 226-243.

43. Lyngberg, O. K.; Ng, C. P.; Thiagarajan, V.; Scriven, L. E.; Flickinger, M. C. Biotechnol. Prog. **2001**, *17*, 1169-1179.

44. Lyngberg, O. K. Ph. D. Thesis, University of Minnesota, Minneapolis, MN, 2000.

45. Selifoniva, O.; Burlage, R.; Barkay, T. Appl. Environ. Microbiol. **1993**, *59*, 3083-3090.

46. Lyngberg, O. K.; Flickinger, M. C.; Scriven, L. E.; Anderson, C. R.; U. S. Patent 7,132,247, 2006.

47. Schottel, J. L.; Orwin, P. M.; Anderson, C. R.; Flickinger, M. C. J. Ind. Microbiol. Biotechnol. **2008**, *35*, 283-290.

48. Magdassi, S.; Moshe, M. B. Langmuir **2003**, *19*, 939-942.

49. Magdassi, S.; Grouchko, M.; Toker, D.; Kamyshny, A. Balbreg, I.; Millo, O. Langmuir **2005**, *21*, 10264-10267.

Chapter 10

Reactive Nanoparticles in Coatings

Chad E. Immoos, Matthew D. Jaoudi, Feng K. Gu, and Deborah L. Wang

Department of Chemistry and Biochemistry, California Polytechnic State University, San Luis Obispo, CA 93407

This chapter provides a short review of the use of nanoparticles in the creation of reactive coatings. We will focus upon the use of reactive nanoparticles in the following three applications: self-cleaning surfaces, antimicrobial coatings, and surfaces capable of neutralizing chemical hazards. In the first section we will outline the use of photoactive TiO_2 nanoparticles to create self-cleaning and self-sterilizing surfaces. Photocatalytic titanium dioxide is the most commonly used material in the production of reactive coatings. In particular, we will discuss the commercial application of TiO_2 nanoparticle thin films in the formation of self-cleaning glass. The second section will focus on the applicaiton of reactive nanoparticles in the development of effective antimicrobial coatings. Although TiO_2 nanoparticle thin films have some utility as antimicrobial surfaces, the majority of antimicrobial surfaces utilize silver nanoparticles. In the third section we will discuss recent work in our laboratory to create nanoparticle-containing coatings capable of degrading chemical warfare agent simulants. Chemical warfare agents are extremely toxic. Hence, there is considerable interest in developing methods to protect military personnel from fatal exposures. Our laboratory has developed a metal oxide-containing polyelectrolyte thin film capable of degrading simulants of toxic chemical warfare agents.

188   © 2009 American Chemical Society

Introduction

Most studies of metal and metal oxide nanoparticles immobilized in polymers have been limited to their use as fillers in the formation of polymer nanocomposites.(1-8) For example, aluminum and silicon oxide nanoparticles have been used widely as additives in industrial coatings. Fillers (particulates) are added into a polymer matrix for a multitude of reasons, ranging from synergistic effects between particle and polymer, to reduction of costs, to improvement of polymer properties. The majority of recent reports have focused on determining the effects nanoparticle fillers have on the physical and mechanical properties of the polymers. Although individual results have varied, it has been shown that the mechanical properties of filled polymers are affected by the size, shape, and adhesive strength between the polymer and filler.(8) Moustafa and coworkers investigated the effect of various filler types on the mechanical hardness of poly(methyl methacrylate) (PMMA). PMMA composites were prepared with Cu_2O, MgO, copper biphthalocyanine, $FeCl_2$, and iron metal fillers. It was found that mechanical hardness increased the greatest for copper biphthalocyanine. This was attributed to the lipophilic part of the filler, which allowed for the best compatibility with PMMA. The iron-PMMA composite had the least increase of hardness, which was explained by the minimal compatibility between filler and polymer.(8)

Zhu and coworkers reported the improved mechanical properties of poly(vinyl chloride) (PVC) with SiO_2 nanocomposites.(9) The tensile yield strength of PVC nanocomposites increased as a function of filler content until the maximum load of 3% was reached. SEM observations of enhanced interfacial adhesion between nanosilica and polymeric matrix also showed an increasing relationship to tensile strength of nanocomposites. Thus, tensile strength of a polymer is dependent on the interfacial interaction between filler and polymer, in addition to filler content.(9)

Self-cleaning surfaces

The most common technology used in commercially available self-cleaning coatings takes advantage of the photocatalytic activity of titanium dioxide (titania). Titanium dioxide is a semiconductor metal oxide capable of photocatalytic degradation of organic matter. This process is commonly referred to as "cold combustion" because the ultimate products of this degradation process are carbon dioxide and water.(10)

Titanium dioxide is capable of absorbing energy equal to or greater than its band gap energy. The absorbed energy can generate charge-separated states such as excitons in the material.(11) Although most excitons rapidly recombine, a small portion migrates to the surface to form hydroxyl radicals (HO·). These

reactive hydroxyl radicals are well known to degrade organic molecules.(12,13) It has also been suggested that the holes cause oxidation of adsorbed organic molecules while the electrons reduce adsorbed molecules, as shown in Figure 1.
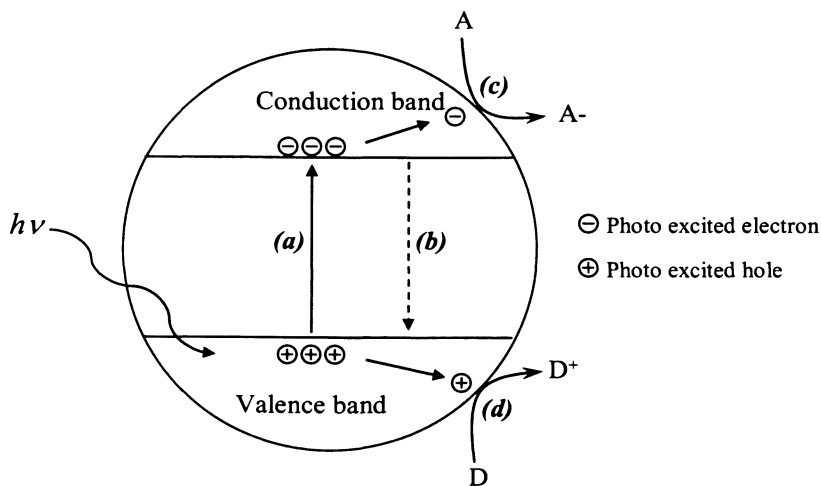
Figure 1. (a) Upon irradiation of the TiO₂ with UV light, the semiconductor undergoes photoexcitation. The resulting electron and hole can follow several pathways: (b) recombination of the electron and the hole; (c) reduction of an electron acceptor, A, by the excited electron, (d) oxidation of the electron donor, D, by the photogenerated hole.

Alternatively, the electrons can eventually combine with atmospheric oxygen to give superoxide radicals, which are also capable of degrading organic compounds. In these processes, the organic contaminants are ultimately converted to carbon dioxide and water through a series of successive oxidation steps. The destruction of organic molecules by irradiated TiO₂ particles is surprisingly effective, in most cases resulting in very little partially oxidized organic material on the surface. In this manner, a variety of organic pollutants and contaminants from liquids and gases can be degraded on titania at ambient temperatures in the presence of UV irradiation. Several methods have been developed to test the photocatalytic effectiveness of TiO₂ surfaces. Photocatalysis, or photoactivity, can be tested by monitoring the destruction of a model pollutant such as methyl viologen, oxygen uptake experiments, or using electron spin resonance (ESR) to look for photogenerated Ti^{3+} ions. A thorough discussion of these methods is beyond the scope of this chapter, but more detailed information can be found in the associated references.(11,14-16)

In addition to degrading organic pollutants by photocatalysis, TiO_2-containing films also self-clean by generation of a super-hydrophilic surface.(17) The super-hydrophilicity is a result of the photocatalytic properties of TiO_2. Holes produced in the semi-conductor upon UV irradiation oxidize lattice oxygen atoms located at the surface of the material, ultimately resulting in the generation of hydroxyl groups. These hydroxyl groups at the surface of the TiO_2 make the material more hydrophilic and therefore favorable for wetting with water. Irradiation of TiO_2 significantly decreases the static contact angle of deposited water causing it to spread on the surface. The spreading of water over the surface allows it to run off, carrying away deposited contaminant material.

For decades, titanium dioxide has been used in the coatings industry as a pigment in paints. It is non-toxic, chemically inert in the absence of sunlight, relatively inexpensive, and easy to handle and deposit into thin films. The primary use of titanium dioxide in the coatings industry is as an opacifier, but recent studies have proven its utility in the development of self-cleaning surfaces. It is generally accepted that the incorporation of "untreated" TiO_2 in polymers and coatings greatly decreases the durability and lifetime of the materials. Titanium dioxide materials exhibit a wide range of photoreactivities, all of which depend on the crystal phase, particle size, and post-processing treatment. Several polymorphs of TiO_2 are known, but the most commonly used forms are the anatase and rutile crystal phases of the material. Pure anatase pigments are generally more photoactive than the rutile forms. For example, in studies of the photocatalytic reduction of phenol by anatase and rutile titanium dioxide, the anatase nanoparticles showed significant photoreactivity while the rutile form was essentially inactive.(18,19)

The mechanisms ascribed to the self-cleaning processes in TiO_2-containing surfaces have been studied extensively. Although research continues to elucidate the finer details regarding the mechanisms, a few basic models for the reactions have been widely accepted. In one proposed mechanism, irradiated TiO_2 reacts with water via electron transfer to form a highly reactive hydroxyl radical (Equation 1). The Ti^{3+} ions generated during the process are reoxidized by molecular oxygen to regenerate Ti^{4+}.

$$TiO_2 + H_2O \xrightarrow{\ h\nu\ } H^+ + e^- (aqueous) + OH\bullet \qquad (1)$$

$$Ti^{4+} + e^- \longrightarrow Ti^{3+} \qquad (2)$$

$$Ti^{3+} + O_2 \longrightarrow Ti^{4+} \qquad (3)$$
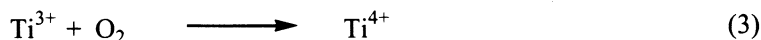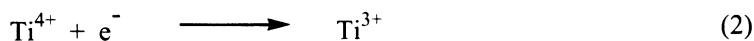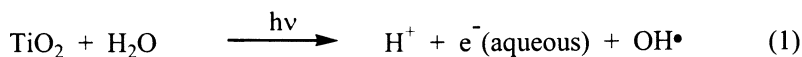
Another mechanism suggests that the photoreactivity of TiO_2 is due to the formation of excitons upon irradiation (Equation 4). An exciton is a separated electron (e^-) and hole (h^+) pair.

$$TiO_2 \xrightarrow{h\nu} e^- + h^+ \tag{4}$$

$$OH^- + h^+ \longrightarrow HO^\bullet \tag{5}$$

$$Ti^{4+} + e^- \longrightarrow Ti^{3+} \tag{6}$$

$$Ti^{3+} + O_2 \longrightarrow [Ti^{4+}...O_2^-] \text{ adsorbed} \tag{7}$$

$$[Ti^{4+}...O_2^-] \text{ adsorbed} + H_2O \longrightarrow Ti^{4+} + OH^- + HO_2 \tag{8}$$
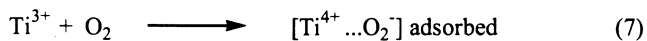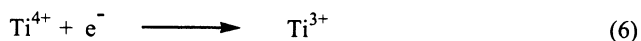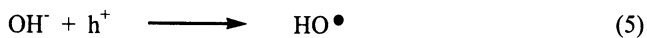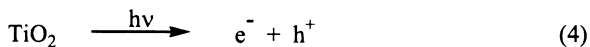
As one would expect, particle size strongly influences the photoreactivity of immobilized TiO_2 particles. Theoretically, nanoparticle titanium dioxide should show greater photoreactivity than macroscale particles due to significantly higher surface area and a larger band gap. However, some studies have shown that thin films of immobilized TiO_2 nanoparticles have markedly lower photoreactivity than larger immobilized TiO_2 particles.[10,20,21] Heller and coworkers compared immobilized nano-titania thin films to immobilized macro-sized TiO_2 particles.[22,23] They found that stearic acid, the model contaminant used in these studies, was stripped off of a surface at a rate of 20 nm of liquid stearic acid film per hour when irradiated with 2.4 mW/cm^2 at 365 nm.[22] This is 3 times slower than the comparable macro-sized TiO_2 film. Several theories have been proposed to explain this observation.[24,25] One proposal suggests the increased band gap in nanoparticulate TiO_2 increases the energy of the radiation required to generate excitons in the material. The increased energy requirement decreases the occurrence of excited species capable of chemical reactivity. Another possible explanation is increased rates of electron-hole recombination, therefore increasing the intensity of light required for efficient photocatalysis. Regardless of their lower photoreactivity, nanoparticulate TiO_2 is used in commercially available self-cleaning surfaces where transparency is important.

The most popular, and commercially successful, application of photoactive TiO_2 coatings has been the development of "self-cleaning" windows. Pilkington Glass announced the first self-cleaning windows in 2001, with its Pilkington Activ[TM] line of windows.[10] Similar products soon followed, but to date, three major commercial products have gained widespread acceptance, including Pilkington's Pilkington Activ[TM], PPG's SunClean[TM], and SGG's Bioclean[TM] products. For Pilkington's self-cleaning glass surfaces, a 20-30 nm layer of nanocrystalline TiO_2 is deposited on the surface of soda-lime float glass by chemical vapor deposition (CVD) at atmospheric pressure. The optical transparency of these products is paramount to their performance, and to this end, the size of the TiO_2 particles is critical. To ensure the photocatalytic particles do not scatter visible light, the size of TiO_2 particles must be much smaller than the shortest (400 nm) visible wavelength. Therefore, the TiO_2

particle size in these thin films is kept between 2-50 nm. Even after application of the TiO_2 thin film, the optical quality of these products remains comparable to untreated soda-lime float glass. Mills and coworkers(10) reported that the Pilkington Activ^{TM} treated surfaces had a visible reflectance of ~7% and a visible haze of less than 1%. The surfaces were also reported to absorb ~20% of solar UV light for self-cleaning purposes. Although the photocatalytic surfaces of the glass are relatively thin (20-30 nm), they are remarkably durable, capable of withstanding most common window cleaning methods.(10) Moderate mechanical abrasion with dry paper and application of adhesive tape do not greatly affect the performance of the photocatalytic surfaces.

Other self-cleaning materials based on the same or similar technology have also been introduced by a number of different companies. The largest among these is the Japanese company TOTO Ltd. and its subsidiary company Japan Hydrotect Coatings Co. TOTO has been developing a wide variety of applications utilizing the photocatalysis of titanium dioxide. In 1994, TOTO released to market ceramic tiles coated with titanium dioxide. The tiles were initially used in hospitals and public restrooms because of their antibacterial properties. The low-level UV irradiation from common fluorescent lamps was found to be sufficient to prevent the growth of microorganisms. TOTO later applied the technology to exterior architectures where self-cleaning properties would be beneficial. Their Hydrotect^{TM} outdoor tiles have been used in numerous buildings throughout Japan, including the Marunouchi Building in Tokyo. The Marunouchi Building faces a road with heavy traffic. Under these conditions, a normal exterior wall would tend to blacken over time from the particulate matter released in automobile exhaust. Hydrotect claims that by applying Hydrotect^{TM} tiles and coatings to the exterior, the building is made "self-cleaning." On sunny days, the tiles work to break down dirt and stains from environmental contaminants, while their hydrophilic properties allow these substances to be washed away on rainy days. Through these processes the outside of the building remains clean. The most impressive application of Hydrotect^{TM} coatings is perhaps the "Tower of Earth" Nagoya City Pavilion, shown in Figure 2. This 47 meter high structure is coated with a water-based Hydrotect^{TM} Color Coat, allowing water to flow continuously over the surface of the structure. The super-hydrophilic properties of the TiO_2–containing coating makes the water flow in a more natural manner and prevents the surface from becoming stained by dirt and pollution in the air.

Several companies are now marketing solutions that can be applied to form self-cleaning surfaces on any desired substrate. For example, Green Millennium offers a peroxotitanium sol for creation of self-cleaning coatings. Their TPXsol product is a neutral aqueous solution of peroxotitanium hydrates that can be spray- or dip-coated onto surfaces and does not require a high temperature curing step to form the photocatalyst. Green Millennium claims that following
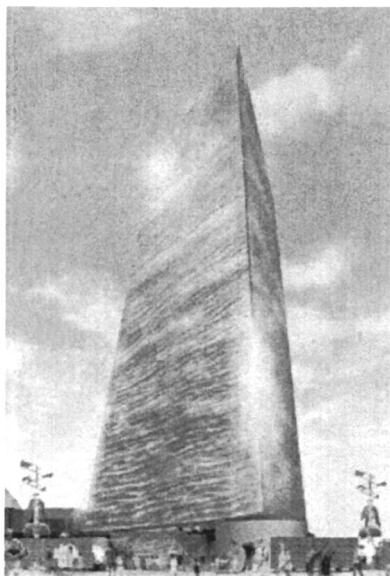
*Figure 2. The Tower of Earth in Nagoya City Pavilion.
(Nagoya City, Aichi, Japan)*

curing the coating contains anatase TiO_2 nanoparticles approximately 10 nm in diameter. They claim to have tested the coatings on a variety of substrates including ceramic, glass, paper, and textiles. Both chemical and biological contaminants are effectively degraded under UV irradiation on these substrates.[26]

Antimicrobial surfaces

The ability of titanium dioxide nanoparticles to destroy a wide spectrum of organisms including viruses, bacteria, fungi, algae, and cancer cells has also been demonstrated. As a result, immobilized titanium dioxide nanoparticles have been incorporated in the formation of antimicrobial surfaces. The hydroxyl radicals and superoxides formed during UV irradiation of TiO_2 particles have been proven to be effective in killing microorganisms such as bacteria.(27,28) Kikuchi and coworkers showed that the survival ratio for a liquid film of *E. coli* in contact with a 0.4 μm TiO_2 thin film on glass under illumination decreased to a negligible level within 1 hour. (Figure 3).

In a related study, Huang proposed that irradiation of the titanium dioxide nanoparticles leads to cell wall damage of bacteria followed by direct intracellular attack. It was shown that treatment of *E. coli* with TiO_2 and near-

UV light resulted in an immediate increase in permeability to small molecules such as *o*-nitrophenol β-D-galactopyranoside, and the leakage of large molecules such as the enzyme β-D-galactosidase after 20 min. In fact, total oxidation of *E. coli* in the presence of TiO_2 particles has been demonstrated.(29,30) Extensive studies of the photocatalytic antimicrobial properties of TiO_2 have revealed that the sensitivity of microorganisms to TiO_2 photocatalysis is likely in the following order: virus > bacterial cells > bacterial spores. This suggests that microorganisms respond differently to TiO_2 photocatalysis due to their structural differences, particularly in the complexity and thickness of the cell envelope.
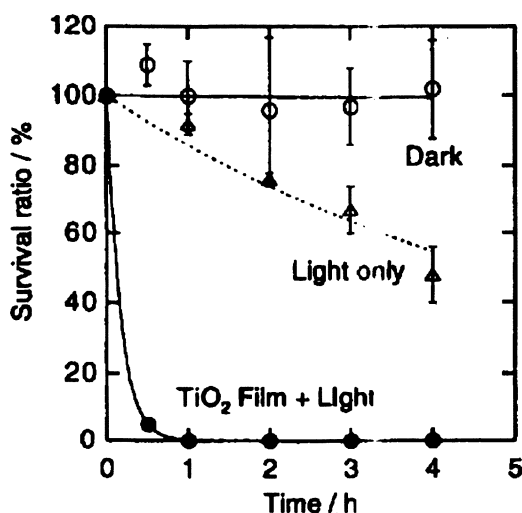
Figure 3. Survival ratio of E. coli in a liquid film with and without TiO_2 thin film under black light illumination (1.0 mW cm^{-2}) and with a TiO_2 thin film in the dark.(27)

Although titanium dioxide coated surfaces are highly effective at providing long-term antimicrobial protection, the reliance upon UV irradiation has limited their use in many applications. The relatively slow rates of reaction under ambient lighting conditions have also proved to be problematic. Alternatively, an antimicrobial surface capable of killing pathogenic bacteria upon contact can be created by incorporation of heavy metal ions or nanoparticles into polymers and coatings. Silver is the most commonly used metal nanoparticle in the creation of antimicrobial surfaces and coatings, and known to have extraordinary bactericidal properties.(31-33) In comparison to other heavy metal ions, silver is among the most useful in coatings due to its high antimicrobial activity and

remarkably low human toxicity. Various medical devices such as sutures and urinary catheters contain silver as an antiseptic component.[34-36]

It is generally accepted that the biocidal activity of silver is related to silver ions (Ag$^+$) released from inorganic silver salts or silver metal. The silver ions bind strongly to electron donor groups such as sulfur, oxygen, and nitrogen on important biological molecules. Important functional groups in proteins, enzymes, and lipids are thus affected. Binding of silver to thiols, amines, imidazoles, carboxylates, and phosphate groups have been reported in literature and are suggested to contribute to the antimicrobial effects of silver additives.(36) For example, binding of silver ions to thiols in bacterial membranes is suggested to alter the membrane permeability and ultimately lead to cell death.(37,38)

The effectiveness of silver nanoparticles as antimicrobial agents has been demonstrated in bacteria. Son and coworkers showed the percentage of gram-positive and gram-negative bacteria reduced by 99.9% when in contact with silver containing cellulose acetate nanofibers.(39,40) In this study, the cellulose acetate nanofibers were electrospun with silver ions and subsequently irradiated with UV light to create silver nanoparticles within the fibers. TEM imaging of the nanofibers showed silver particles with an average size of 21 nm following irradiation for 240 min. Son et al. proposed that the high antimicrobial activity of the silver nanoparticle can be attributed to its small particle size. Although there is little agreement on the identities of the intracellular targets, it is generally accepted that bacterial cell death occurs because the cell membranes, DNA, or enzymes of the bacteria lose important functions upon silver ion binding.

A large number of antimicrobial polymers have been reported to date. A detailed discussion of antimicrobial polymers can be found in the review article by Kenawy.(41) Multifunctional antimicrobial coatings have also been created by incorporation of silver nanoparticles into polymers containing reactive organic functionalities. Sambhy and coworkers reported the formation of dual-action antimicrobial coatings through spin coating two-component composites of poly(4-vinyl-*N*-hexylpyridinium bromide) and embedded silver bromide nanoparticles on surfaces, as shown in Figure 4.(42) Quaternary ammonium groups, such as 4-vinyl-*N*-hexylpyridinium bromide, are believed to kill bacteria on contact by penetration and disruption of the bacterial cell membrane.(42) Silver halides are an effective choice for antimicrobial surfaces because of their well-known low solubility of these compounds in aqueous conditions ($K_{sp} = 10^{-14} - 10^{-16}$). This method provided surfaces capable of killing both gram-negative and gram-positive bacteria. The kill rates for the composites were comparable to that of highly active soluble silver salts and gave sustained release of biocidal silver ions without loss of activity. It was also found that by varying the size of the polymer-embedded nanoparticles, the release rates of the silver component could be tailored.

Li and coworkers also reported an antibacterial coating with both release-killing and contact-killing capabilities.(43) A thin film coating containing two distinct functional regions was created using a combination of layer-by-layer

STEP 1

poly(4-vinylpyridine)

NPVP

STEP 2

Silver *para*-toluene sulphonate (AgPTS)

ON SITE PRECIPITATION
$Ag^+ + Br^- \rightarrow AgBr_{(s)}$

NPVP

AgBr/NPVP composite
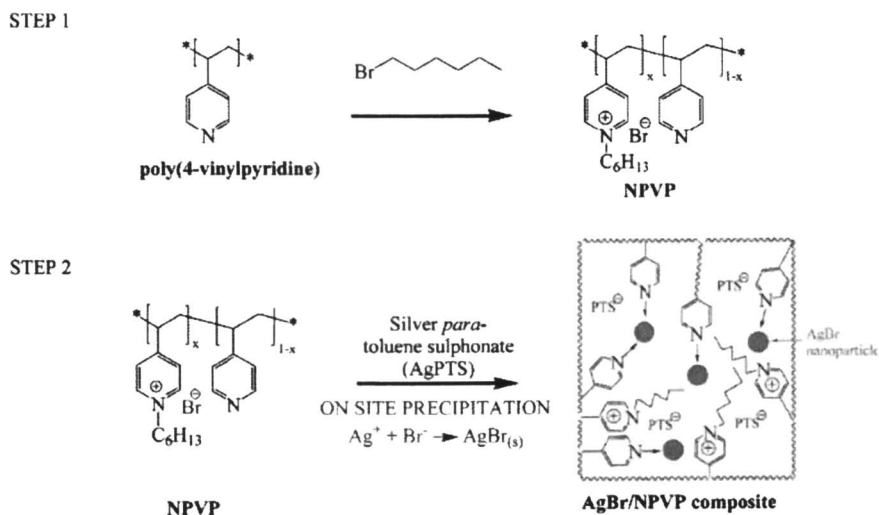
Figure 4. Schematic of on-site precipitation method for the synthesis of dual action antibacterial composite material, AgBr/NPVP (NPVP) poly(4-vinylpyridine)-co-poly(4-vinyl-N-hexylpyridinium bromide).[42]

deposition, nanoparticle surface modification, and in-situ silver nanoparticle formation. The topmost layer of the coating contained quaternary ammonium groups in the form of [3-(trimethoxysilyl)propyl]octadecyl-di-methylammonium chloride (OQAS) modified SiO_2 nanoparticles and the internal portion served as a reservoir for silver ions, Figure 5. It was shown that the embedded Ag (in the form of Ag^+ or Ag nanoparticles) was releasable through the OQAS-modified cap region of the thin film. These surface coatings were shown to kill bacteria not only through release of the imbedded silver ions, but also via the immobilized quaternary ammonium salts.(44-46) Having a coating with two bactericidal mechanisms offers the opportunity to overcome the limitations of each individual component. For example, the constant leaching of silver ions from the surface will eventually lead to depletion.   The presence of the ammonium groups then provides a constant source of antimicrobial activity even after the silver ions have been fully utilized. In addition, the method of silver incorporation offers the opportunity to "reload" the system with silver following depletion of the silver reservoir.
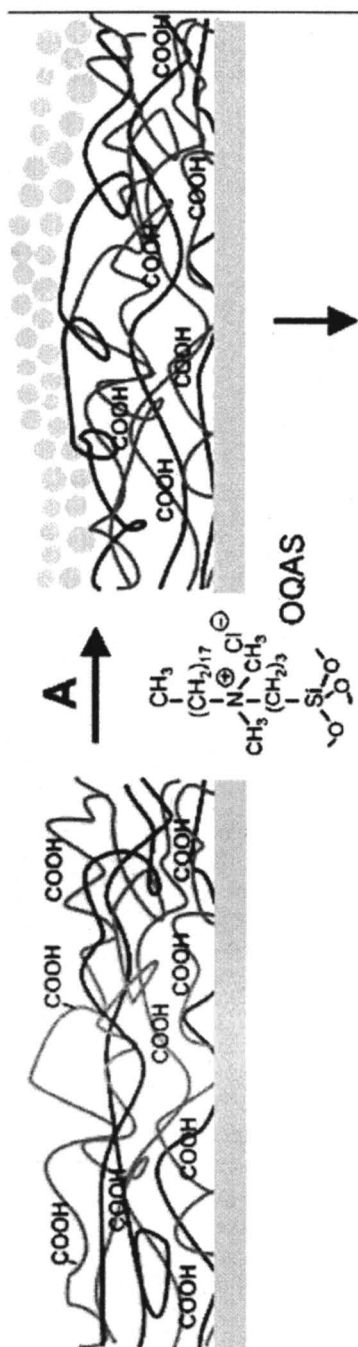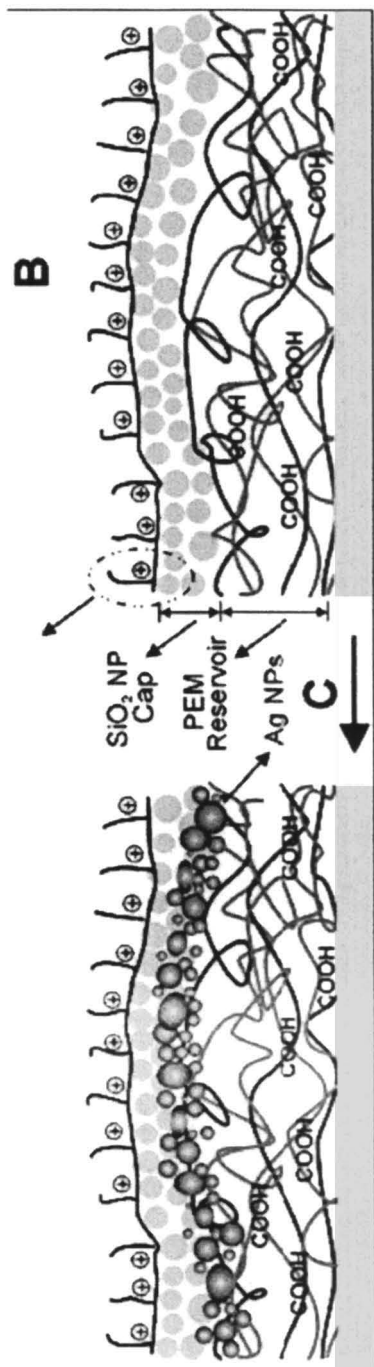
Figure 5. Scheme showing the design of a two-level dual-functional antibacterial coating with both quaternary ammonium salts and silver. The coating process begins with LbL deposition of a reservoir made of bilayers of PAH and PAA. (A) A cap region made of bilayers of PAH and SiO$_2$ NPs is added to the top. (B) The SiO$_2$ NP cap is modified with a quaternary ammonium silane, OQAS. (C) Ag$^+$ can be loaded inside the coating using the available unreacted carboxylic acid groups in the LbL multilayers. Ag NPs are created in situ by reduction of the Ag$^+$ ions.

A two-level coating offers separate control of the surface chemistry and chemical impregnation of the coating. This coating scheme is not limited only to silver and quaternary ammonium groups and it should be possible to incorporate other components. The combination of other functional groups such as antibiotics or nanoparticles is likely to create unique coatings with widely different applications.

Hazard Protection

Another area of interest is the creation of coatings for protection against chemical and biological hazards, such as pesticides, chemical weapons, and pathogenic bacteria. In this section, we will focus on protective coatings designed to react with and degrade chemical warfare agents. Chemical warfare (CW) agents are extremely hazardous materials that are toxic in both their liquid and vapor states. Effective at very low concentrations, these agents can cause death within minutes of exposure. Among these compounds are certain organophosphate, phosphinate, and phosphonate esters such as VX, Sarin, and Soman, shown in Figure 6.(47,48) In addition to their acute ability to incapacitate, they are also easily dispersed, making chemical warfare agents a significant threat to civilian populations and the military personnel assigned to interact with these compounds. As such, considerable effort has been directed toward finding methods to facilitate the decomposition of organophosphorous materials, particularly through hydrolysis or oxidation.(49)

Several systems have been developed for the degradation of chemical warfare agents; however, few have been adapted for use as surface coatings.[47,48] Reactive coatings capable of chemical warfare agent degradation offer a unique
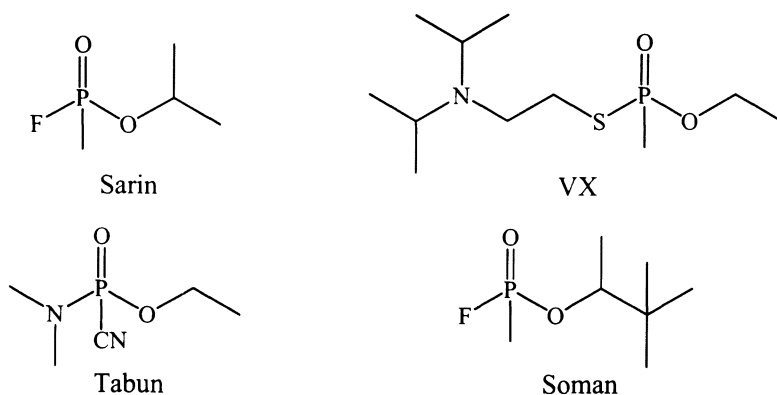
Figure 6. Chemical structures of representative chemical warfare agents.

opportunity to decontaminate equipment/vehicles without intervention from personnel. In addition, reactive coatings on protective equipment and garments provide an additional layer of protection for personnel assigned to decontaminate affected areas.

The chemical degradation of organophosphorous compounds has been reported using several different methods.(49) Among these, the use of inorganic oxides have shown promise as reactive adsorbents for the decontamination of chemical warfare agents.(50-52) Although conventional inorganic oxides such as alumina show some activity toward CW agents, this reactivity is markedly enhanced in nanosize particles. Nanoparticles of metal oxides have also been shown to be reactive adsorbents for CW agent degradation, with reactivity greatly enhanced over common commercial forms of the oxide powders. The increased reactivity of nanosize inorganic oxides is proposed to be due to the larger relative surface areas (typically >700 m^2/g) and greater number of highly reactive edge and corner "defect" sites in the nanoparticles.

Klabunde and coworkers have championed the use of nanoparticles for the adsorption and decomposition of chemical warfare agents.(51,53-57) They have reported the use of nanoparticles such as Al_2O_3, TiO_2, CaO, and MgO for the adsorption and neutralization of chemical hazards.(51) It has been shown that in addition to adsorbing chemical warfare agents, these nanoparticle metal oxides also effectively and nonselectively decompose the chemical agents. Furthermore, the degradation products are found to be nontoxic. For example, Al_2O_3 nanoparticles carry out the room temperature degradation of a number of chemical warfare agents such as VX, GB, and GD to form nontoxic phosphonate products.(58) The mechanism of degradation of several chemical agents has been investigated and reported to involve adsorption of the agents onto the surface of the metal oxide nanoparticle to form surface-bound phosphonates. The reactive capacity of Al_2O_3 nanoparticles is exceedingly large for the nerve agents as their surface-bound phophonic acid hydrolysis products effect facile erosion of the alumina surface to form bulk aluminophosphonate complexes.(58) Reactivity studies have shown that MgO nanoparticles are the most effective room temperature adsorbents for the neutralization of chemical warfare agents. In a similar report of the reactions with nanosize MgO, the degradation of nerve agents VX and GD were demonstrated, as shown in Scheme 1.(50) These reactions are analogous to their solution chemistry with two exceptions: the phosphonate products reside as surface-bound complexes and the toxic EA-2192 byproduct, which is formed during basic hydrolysis, is not observed on MgO nanoparticles.

Although nanoparticle systems exist for the degradation of chemical warfare agents, there have been few reports of these systems being adapted to create reactive surfaces. Sundarrajan reported the incorporation of MgO nanoparticles into poly(vinyl chloride) (PVC), poly(vinylidene fluoride-co-hexafluoro-propylene) (PVDF), and polysulfone (PSU) to produce nanocomposite mem-

VX

MgO →

ethyl methylphosphonic acid (EMPA)

MgO

"EA-2192"

methylphosphonic acid (MPA)
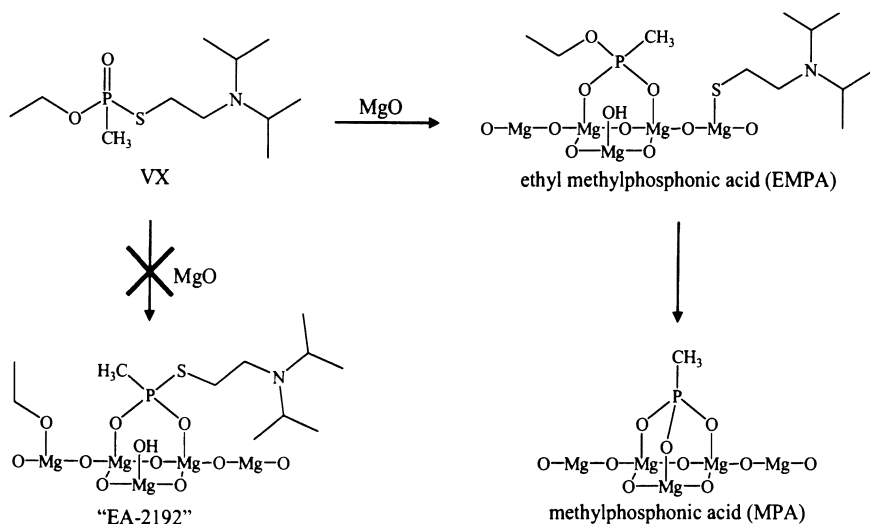
Scheme 1. Reaction of MgO nanoparticles with VX. [50]

branes.(59) Metal oxide nanoparticles were synthesized by the aerogel method and incorporated into the candidate polymers by electrospinning (Figure 7). The fibers were loaded with varying amounts of MgO nanoparticles and tested for reactivity against a nerve agent simulant. Scanning electron microscopy (SEM) and energy dispersive X-ray (EDX) analysis demonstrated the presence of MgO nanoparticles on the surface of the electrospun fibers. The reactivity of the resultant membranes was found to depend on the polymer used as the support. The reactivity of the polymer-nanoparticle composites was found to be PVC-MgO < PVDF < PSU < PVDF-MgO < PSU-MgO. It was suggested that undesirable reactivity of the MgO nanoparticles with functional groups in the polymer scaffold limited the reactivity of the nanoparticles towards chemical warfare agents. Additional experiments with PSU-MgO nanocomposites, the most reactive candidate, showed that the fabricated membranes were twice as reactive as the currently used charcoal adsorbent. The maximum loading percentage of the MgO in PSU was reported to be ~35%. These MgO-polymer fiber membranes are good candidates for the production of textiles for protective clothing or wipes against nerve agents.

Our laboratory is investigating methods for the incorporation/ immobilization of metal oxide nanoparticles on surfaces in a manner that retains reactivity toward chemical warfare agents. The work of Klabunde and others have shown that metal oxide nanoparticles are effective at degrading chemical warfare agents.(47,50,51,54,59,60) We are currently employing a method similar to that reported by Rubner and coworkers(61) for the deposition of metal
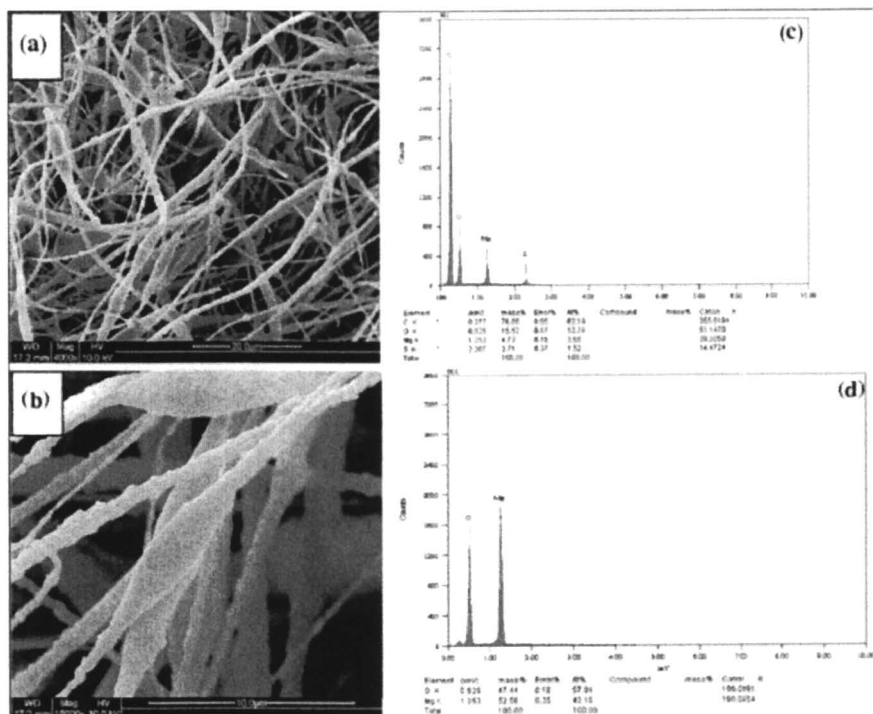
*Figure 7. SEM micrographs of electrospun PSU-MgO (35%) at 12.4 KV (a);
spindle like structure formation (b); EDX data for PSU-MgO (35%) (c);
and EDX data for MgO nanoparticles (d)(59)*

oxide (SiO_2) nanoparticles onto the surface of porous polyelectrolyte multilayer films. Porous multilayer films of polyacrylic acid (PAA) and poly(allylamine hydrochloride) (PAH) have been generated and MgO nanoparticles immobilized onto the surface. Multilayer polyelectrolyte thin films were created by electrostatic layer-by-layer deposition of PAA, a negative polyelectrolyte, and PAH, a positive polyelectrolyte. Deposition times were optimized to create stable films of 100 bilayers of PAH/PAA. After deposition, the polyelectrolyte multilayers were treated with acid to create a porous surface (Figure 8) as demonstrated by atomic force microscopy (AFM). This porosity increases the surface area available for both nanoparticle adsorption and hydrolysis of chemical warfare agents. The average pore size of the surfaces is estimated to be 0.8 μm. Rubner has shown that the porosity of the thin films can be tuned by varying the duration of the acid treatment step, with pore sizes ranging from 0.5 - 2 μm.(61) Following acid treatment, the multilayer films were heated at 180 °C
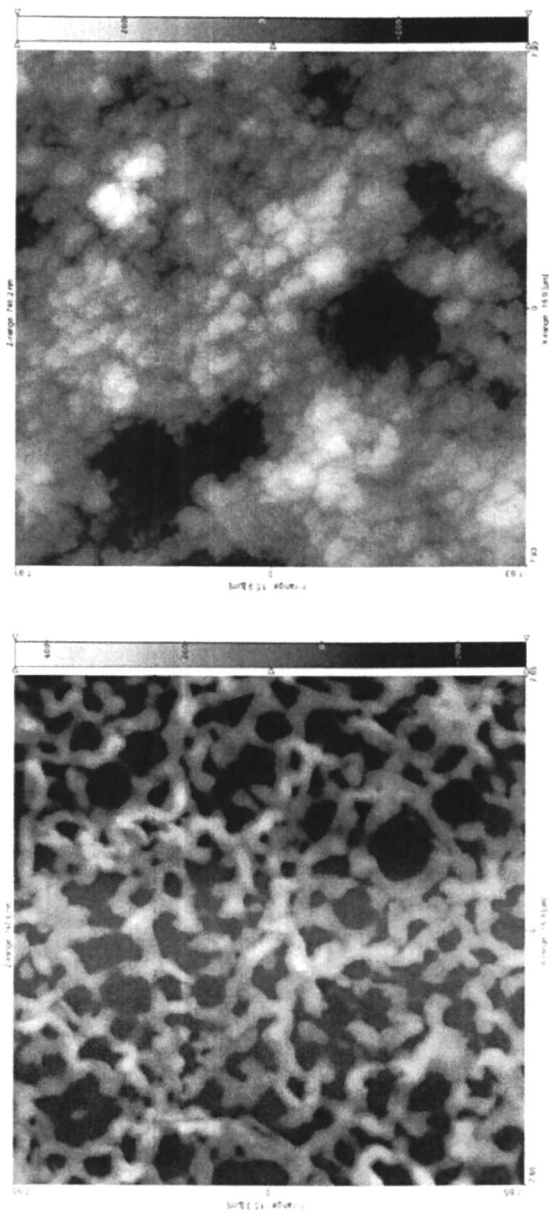
Figure 8. Atomic Force Microscopy images of a) a porous PAH/PAA multilayer film after acid treatment and b) a porous PAH/PAA multilayer film following acid treatment and MgO nanoparticle deposition.

for 2 hours to crosslink the polyelectrolyte layers, thus providing a more durable surface. Nanoparticles were deposited onto the resulting surface by treatment of the porous multilayer film with ~0.1 wt% aqueous suspension of MgO nanoparticles (~50 nm). The pH of the nanoparticle solution was made basic to ensure a negative surface charge for the MgO nanoparticles. The resulting MgO surfaces were then treated with PAH solution followed by a second layer of MgO nanoparticles. Atomic force microscopy of the nanoparticle-multilayer films (Figure 8) shows that the porosity has decreased and the surface features suggest that the MgO nanoparticles have deposited onto the surface.

The polyelectrolyte thin films containing magnesium oxide nanoparticles were tested for reactivity against Paraoxon, a chemical warfare agent simulant. Paraoxon can be used as a spectroscopic probe for investigation of reactivity against chemical warfare agents because hydrolysis of Paraoxon releases *para*-nitrophenolate, Scheme 2. Para-nitrophenolate absorbs strongly at 400 nm, giving it a distinct, bright yellow color. Monitoring the increase in absorbance at 400 nm, we are able to determine the reactivity of our multilayer films. The polyelectrolyte-nanoparticle surfaces show modest reactivity toward Paraoxon.
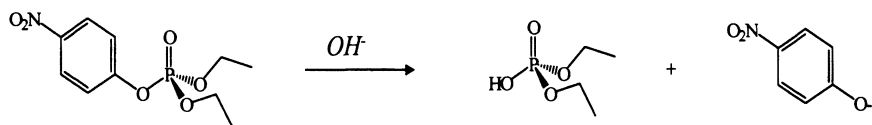
Scheme 2. Hydrolysis of paraoxon, a chemical warfare agent simulant.

This is not unexpected given that MgO reacts with chemical agents in a stoichiometric fashion. Additionally, the very small amount (two layers) of MgO nanoparticles present in the thin film severely limits the capacity of the surfaces. A surface loading of ca. 37 μg MgO/cm^2 is estimated for the reactive nanoparticle-polyelectrolyte thin films. Future work will investigate the effect of increasing the number of MgO nanoparticle layers to determine if higher loadings of MgO will improve the reactivity of the coatings.

Conclusion

A myriad of applications exist for coatings that contain reactive nanoparticles, of which this chapter has examined just a handful. The most popular use for reactive nanoparticles in coatings is in self-cleaning surfaces, where photocatalytic titanium dioxide nanoparticles are most commonly employed. UV irradiation of TiO_2 nanoparticles embedded in the coating

produces a super-hydrophilic surface and generates reactive species capable of degrading organic and biological contaminants. Reactive nanoparticles have also been utilized in antimicrobial surfaces to destroy a wide range of organisms, including bacteria, viruses, spores, and cancer cells. Silver nanoparticles are chiefly used in antimicrobial surfaces and coatings, due to their exceptional biocidal activity and minimal human toxicity. More recently, reactive nanoparticles have found application in coatings that neutralize chemical hazards. The incorporation of metal oxide nanoparticles onto surfaces results in reactive coatings capable of degrading chemical warfare agents. Our laboratory has successfully produced polyelectrolyte multilayer films containing reactive magnesium oxide nanoparticles. These reactive surfaces have demonstrated a modest response towards the degradation of Paraoxon, a chemical warfare agent simulant. Future work of our lab will optimize the parameters for maximal reactivity of these coatings.

Immobilization of nanoparticles in coatings continues to grow, and the studies discussed in this chapter have only highlighted a select few uses of reactive nanoparticles in the coatings industry. Given the wide range of available applications, the incorporation of reactive nanoparticles will soon become a commonplace tool for the development of coatings and surfaces with specific reaction chemistries.

References

1. Ash, B. J.; Siegel, R. W.; Schadler, L. S., *Macromolecules* **2004**, *37*, 1358-1369.
2. Zhang, Z.; Yang, J. L.; Friedrich, K., *Polymer* **2004**, *45*, 3481-3485.
3. Shi, G.; Zhang, M. Q.; Rong, M. Z.; Wetzel, B.; Friedrich, K., *Wear* **2004**, *256*, 1072-1081.
4. Rong, M. Z.; Zhang, M. Q.; Pan, S. L.; Lehmann, B.; Friedrich, K., *Polymer International* **2004**, *53*, 176-183.
5. Rong, M. Z.; Zhang, M. Q.; Pan, S. L.; Friedrich, K., *Acta Polymerica Sinica* **2004**, 184-190.
6. Lee, Y.-M.; Viswanath, D. S., *Polymer Eng. and Sci.* **2000**, *40*, 2332-2341.
7. Maity, A.; Biswas, M., *J. Applied Polymer Sci.* **2003**, *88*, 2233-2237.
8. Moustafa, A. B.; Faizalla, A.; Abd El Hady, B. M., *J. Applied Polymer Sci.* **1998**, *67*, 637-641.
9. Zhu, A.; Cai, A.; Zhang, J.; Jia, H.; Wang, J., *Journal of Applied Polymer Science* **2008**, *108*, 2189-2196.
10. Mills, A.; Lepre, A.; Elliott, N.; Bhopal, S.; Parkin, I. P.; O'Neill, S. A., *Journal of Photochemistry and Photobiology a-Chemistry* **2003**, *160*, 213-224.

11. Mills, A.; Le Hunte, S., *Journal of Photochemistry and Photobiology A: Chemistry* **1997**, *108*, 1-35.
12. Dong, C. D.; Huang, C. P. In *Aquatic Chemistry*, 1995; Vol. 244.
13. Gray, K. A.; Stafford, U., *Research on Chemical Intermediates* **1994**, *20*, 835-853.
14. Brezova, V.; Dvoranova, D.; Stasko, A., *Research on Chemical Intermediates* **2007**, *33*, 251-268.
15. Mills, A.; Wang, J. S.; McGrady, M., *Journal of Physical Chemistry B* **2006**, *110*, 18324-18331.
16. Evans, P.; Mantke, S.; Mills, A.; Robinson, A.; Sheel, D. W., *Journal of Photochemistry and Photobiology a-Chemistry* **2007**, *188*, 387-391.
17. Wang, R.; Hashimoto, K.; Fujishima, A.; Chikuni, M.; Kojima, E.; Kitamura, A.; Shimohigoshi, M.; Watanabe, T., *Nature* **1997**, *388*, 431-432.
18. Sakanoue, M.; Kinoshita, Y.; Otsuka, Y.; Imai, H., *Journal of the Ceramic Society of Japan* **2007**, *115*, 821-825.
19. Okamoto, K.; Yamamoto, Y.; Tanaka, H.; Tanaka, M.; Itaya, A., *Bulletin of the Chemical Society of Japan* **1985**, *58*, 2015-2022.
20. Sun, B.; Smirniotis, P. G., *Catalysis Today* **2003**, *88*, 49-59.
21. Serpone, N.; Maruthamuthu, P.; Pichat, P.; Pelizzetti, E.; Hidaka, H., *Journal of Photochemistry and Photobiology a-Chemistry* **1995**, *85*, 247-255.
22. Paz, Y.; Luo, Z.; Rabenberg, L.; Heller, A., *Journal of Materials Research* **1995**, *10*, 2842-2848.
23. Paz, Y.; Heller, A., *Journal of Materials Research* **1997**, *12*, 2759-2766.
24. Heller, A., *Accounts of Chemical Research* **1995**, *28*, 503-508.
25. Schwitzgebel, J.; Ekerdt, J. G.; Gerischer, H.; Heller, A., *Journal of Physical Chemistry* **1995**, *99*, 5633-5638.
26. Mori, Y.; Morioki Sangyo Company Ltd, 2001.
27. Kikuchi, Y.; Sunada, K.; Iyoda, T.; Hashimoto, K.; Fujishima, A., *Journal of Photochemistry and Photobiology a-Chemistry* **1997**, *106*, 51-56.
28. Sunada, K.; Kikuchi, Y.; Hashimoto, K.; Fujishima, A., *Environmental Science & Technology* **1998**, *32*, 726-728.
29. Wolfrum, E. J.; Huang, J.; Blake, D. M.; Maness, P. C.; Huang, Z.; Fiest, J.; Jacoby, W. A., *Environmental Science & Technology* **2002**, *36*, 3412-3419.
30. Huang, N. P.; Xiao, Z. D.; Huang, D.; Yuan, C. W., *Supramolecular Science* **1998**, *5*, 559-564.
31. Zhao, G. J.; Stevens, S. E., *Biometals* **1998**, *11*, 27-32.
32. Slawson, R. M.; Lohmeiervogel, E. M.; Lee, H.; Trevors, J. T., *Biometals* **1994**, *7*, 30-40.
33. Slawson, R. M.; Vandyke, M. I.; Lee, H.; Trevors, J. T., *Plasmid* **1992**, *27*, 72-79.
34. Schierholz, J. M.; Beuth, J.; Pulverer, G.; Konig, D. P., *Antimicrobial Agents and Chemotherapy* **1999**, *43*, 2819-2820.
35. Schierholz, J. M.; Beuth, J.; Pulverer, G., *American Journal of Medicine* **1999**, *107*, 101-102.

36. Schierholz, J. M.; Lucas, L. J.; Rump, A.; Pulverer, G., *Journal of Hospital Infection* **1998**, *40*, 257-262.
37. Feng, Q. L.; Wu, J.; Chen, G. Q.; Cui, F. Z.; Kim, T. N.; Kim, J. O., *Journal of Biomedical Materials Research* **2000**, *52*, 662-668.
38. Kim, T. N.; Feng, Q. L.; Kim, J. O.; Wu, J.; Wang, H.; Chen, G. C.; Cui, F. Z., *Journal of Materials Science-Materials in Medicine* **1998**, *9*, 129-134.
39. Son, W. K.; Youk, J. H.; Park, W. H., *Carbohydrate Polymers* **2006**, *65*, 430-434.
40. Son, W. K.; Youk, J. H.; Lee, T. S.; Park, W. H., *Macromolecular Rapid Communications* **2004**, *25*, 1632-1637.
41. Kenawy, E. R.; Worley, S. D.; Broughton, R., *Biomacromolecules* **2007**, *8*, 1359-1384.
42. Sambhy, V.; MacBride, M. M.; Peterson, B. R.; Sen, A., *Journal of the American Chemical Society* **2006**, *128*, 9798-9808.
43. Li, Z.; Lee, D.; Sheng, X. X.; Cohen, R. E.; Rubner, M. F., *Langmuir* **2006**, *22*, 9820-9823.
44. Lin, J.; Tiller, J. C.; Lee, S. B.; Lewis, K.; Klibanov, A. M., *Biotechnology Letters* **2002**, *24*, 801-805.
45. Tiller, J. C.; Lee, S. B.; Lewis, K.; Klibanov, A. M., *Biotechnology and Bioengineering* **2002**, *79*, 465-471.
46. Tiller, J. C.; Liao, C. J.; Lewis, K.; Klibanov, A. M., *Proceedings of the National Academy of Sciences of the United States of America* **2001**, *98*, 5981-5985.
47. Yang, Y. C.; Baker, J. A.; Ward, J. R., *Chemical Reviews* **1992**, *92*, 1729-1743.
48. Yang, Y. C., *Accounts of Chemical Research* **1999**, *32*, 109-115.
49. Morales-Rojas, H.; Moss, R. A., *Chem. Rev.* **2002**, *102*, 2497, and references therein.
50. Wagner, G. W.; Bartram, P. W.; Koper, O.; Klabunde, K. J., *Journal of Physical Chemistry B* **1999**, *103*, 3225-3228.
51. Rajagopalan, S.; Koper, O.; Decker, S.; Klabunde, K. J., *Chemistry-a European Journal* **2002**, *8*, 2602-2607.
52. Carnes, C. L.; Kapoor, P. N.; Klabunde, K. J., *Chem. Mater.* **2002**, *14*, 2922-2929.
53. Decker, S. P.; Klabunde, J. S.; Khaleel, A.; Klabunde, K. J., *Environmental Science & Technology* **2002**, *36*, 762-768.
54. Koper, O.; Lucas, E.; Klabunde, K. J., *Journal of Applied Toxicology* **1999**, *19*, S59-S70.
55. Koper, O. B.; Lagadic, I.; Volodin, A.; Klabunde, K. J., *Chemistry of Materials* **1997**, *9*, 2468-2480.

56. Stark, J. V.; Park, D. G.; Lagadic, I.; Klabunde, K. J., *Chemistry of Materials* **1996**, *8*, 1904-1912.
57. Klabunde, K. J.; Stark, J.; Koper, O.; Mohs, C.; Park, D. G.; Decker, S.; Jiang, Y.; Lagadic, I.; Zhang, D. J., *Journal of Physical Chemistry* **1996**, *100*, 12142-12153.
58. Wagner, G. W.; Procell, L. R.; O'Connor, R. J.; Munavalli, S.; Carnes, C. L.; Kapoor, P. N.; Klabunde, K. J., *Journal of the American Chemical Society* **2001**, *123*, 1636-1644.
59. Sundarrajan, S.; Ramakrishna, S., *Journal of Materials Science* **2007**, *42*, 8400-8407.
60. Wagner, G. W.; Koper, O. B.; Lucas, E.; Decker, S.; Klabunde, K. J., *Journal of Physical Chemistry B* **2000**, *104*, 5118-5123.
61. Zhai, L.; Cebeci, F. C.; Cohen, R. E.; Rubner, M. F., *Nano Letters* **2004**, *4*, 1349-1353.

Chapter 11

Effects of Alumina and Silica Nanoparticles on Polyurethane Clear Coating Properties

Matthew F. Clarke, Adam A. Paiz, Cameron L. Wilson, Lucas J. Brickweg, Bryce R. Floryancic, and Raymond H. Fernando*

Polymers and Coatings Program, Department of Chemistry and Biochemistry, California Polytechnic State University, San Luis Obispo, CA

Understanding effects of inorganic nanoparticles on properties of automotive polyurethane coatings has been a focus of studies within our research group. This chapter presents our most recent results on scratch resistance testing and characterization of thermal and mechanical properties of the coatings with and without nano-alumina and nano-silica. Controlled scratch resistance testing, Differential Scanning Calorimentry (DSC), Thermo-Gravimetric Analysis (TGA), Dynamic Mechanical Analysis (DMA), and microscopy techniques were the primary tools employed. Our results show that alumina and silica nanoparticles significantly improve the scratch resistance of the control polyurethane coating. Coating solvents and nanoparticle dispersion media retained in the films have complicated initial attempts to isolate nanoparticle effects. However, when the results of coatings containing no retained solvents were analyzed, no correlation was found between scratch resistance and thermo-mechanical properties.

210

© 2009 American Chemical Society

Introduction

In the first chapter of this book, potential benefits of incorporating inorganic nanoparticles into organic coatings were reviewed. In addition to hardness enhancement, the small size of nanoparticles offers two additional features -- high surface area contact with a host polymer and optical clarity of the nanocomposite -- both of which are important in clear coating applications. The increased interfacial contact can cause significant shifts in properties of the overall composite compared to the properties of the organic phase alone. An example is the modification of glass transition temperature (T_g) of a polymer at an interface. T_g would change due to the steric and enthalpic effects that alter the segmental mobility of the polymer molecules at a polymer/inorganic filler or polymer/air interface (1-7).

Optical clarity is an essential property for a number of classes of coatings such as automobile clear coats, floor wear layers, wood coatings, and optical lens coatings. Unless the refractive index can be matched to that of the coating resin, adding inorganic particles cause light scattering that leads to reduction or elimination of film clarity. Since nanoparticles are much smaller in size compared to the wavelength range of visible light (400 – 800nm), they scatter very little light. Therefore, they can be added to a clear coating formulation with little or no adverse impact on visual characteristics. This feature of nanoparticles is extremely important in expanding nanoparticle applications in coatings. Silica was a material of choice in reinforcing clear coatings for many years (8-13) due to its low refractive index that matches the refractive index of common polymeric coating binders. With the recent commercialization of alumina and other harder inorganic materials in nano-particulate form, coating formulators today have more choices for reinforcing coatings while retaining film clarity; their use has been reported in several studies (14).

In this chapter, results of a study to determine the effects of alumina and silica nanoparticles on the performance of a polyurethane automotive refinished coating are reported. Some insights into the mechanisms of scratch resistance improvements offered by nanoparticles are also presented. Scratch resistance is an important performance attribute of organic coatings such as those found in automotive, wood, and other products. Understanding scratch mechanisms of these types of coatings has been the focus of many previous studies (15-25). A wide range of test methods have been utilized in these studies, from those representing real-life performance (e.g., simulated car washing) to well controlled laboratory methods (e.g., instrumented nano-indentation scratching).

Understanding the mechanisms of scratch resistance improvements by nanoparticles is important for the advancement of this field. However, there are many complexities that make it a challenging task. Hardness of the film, plastic versus brittle failure, self-healing through plastic reflow, friction, and localized

heat generation during scratching are all contributing factors. Another complicating factor is correlating laboratory test results with practically relevant scratch and mar resistance behavior. For example, abrasion tests, such as Taber Abrasion, are too severe to be correlated with scratch and mar resistance of automotive clear coatings.

Research efforts in our laboratories have been directed towards understanding and quantifying the scratch and mar behavior of coatings under conditions related to those found in car washing and similar conditions. A two-part, polyurethane, automotive refinish coating is used as the control coating. This coating can be cured under ambient conditions or elevated temperatures, with and without nanoparticles, to prepare samples for testing. In this chapter, we will discuss the results of our work on quantifying scratch resistance improvements offered by certain types of predispersed alumina and silica nanoparticles. In addition, it describes results of thermo-mechanical characterization of the coatings and attempts to determine whether there are correlations between thermo-mechanical properties and scratch behavior of the polyurethane coating system.

Experimental Details

The automotive refinish polyurethane coating (Control-L) was prepared according to the formulation in Table 1. The acrylic polyol (Joncryl 910, supplied by BASF) has a hydroxyl number of 94 and equivalent weight of 600. It is supplied at 71.0 Wt.% solids in methyl n-amyl ketone. Hexamethylene diisocyanate (HDI) trimer (Desmodur N3300) is supplied by Bayer. The Control-L formulation was utilized in our early experiments to prepare approximately 25-50μm (dry thickness) coatings. Latter studies involving thicker films (75-100μm) utilized the higher-solids formulation (Control-H) shown in Table 2. The solids content in that formulation is significantly higher (65.26 Wt.%) compared to the Control-L formulation's solids content (44.36 Wt.%). Predispersed alumina and silica nanoparticles were supplied by BYK-Chemie Company, and they are described in Table 3. Alumina C and D dispersions contain the same nanoparticles; however, Alumina C dispersion contains an extra additive, a siloxane-polyether oligomer. Solids contents of nanoparticle dispersions were determined by Thermo-Gravimetric Analysis (TGA). The TGA scans are shown in Figure 1. Average particle sizes were provided by the supplier. To prepare coating films containing a given level of particles (based on dry weight), the required amount of predispersed nanoparticles was added to Part A. After Parts A & B were mixed (2 minutes with a spatula), the mixture was left undisturbed for ten minutes. Control-L coatings were applied with a 3mil (1mil = 25.4μm) Bird-type draw-down

applicator to prepare approximately 25µ thick dry films, whereas a 10 mil applicator was utilized to prepare the thicker films with Control-H formulation.

Coatings for various testing were applied and cured on cold-rolled steel panels, steel panels primed with black and white coatings, and Leneta BK chart paper. Films for Differential Scanning Calorimetry (DSC), Dynamic Mechanical Analysis (DMA), and Thermo-Gravimetric Analysis (TGA) were applied on a polypropylene substrate according to ASTM procedure described elsewhere (26). The films were placed in a laboratory oven and cured for various lengths of time at 70°C. Free films of the coatings were easily peeled off from the polypropylene substrate, after curing.

Table 1. Polyurethane Coating Formulation (Control-L)

PART A	
Acrylic polyol (71 Wt.%)	47.02
Methyl n-amyl ketone	20.72
Xylene	6.48
n-Pentyl propionate	4.72
UV stabilizer 1	0.48
UV stabilizer 2	0.32
Polysiloxane wetting agent	0.24
Total Part A	**80.00**
PART B	
HDI trimer	10.90
Butyl acetate	9.10
Total Part B	**20.00**
Part A + Part B	**100.00**
%NVW = 44.36; %NVV = 39.82; NCO:OH = 1.05:1.00	

Scratch Resistance Testing:

Control-L Formulation:

Scratch resistance of the coatings on black and white primed steel panels were tested with a 325 mesh size grit containing Norton scratch pad (3.8 cm x 3.8 cm) attached to a one-pound (454 g) hammer. The panel was scratched by moving the scratch pad back and forth on a 10.2 cm x 3.8 cm area one time (1-cycle); Average value of three gloss measurements at 20° and 60° was recorded

before and after scratching. Gloss measurements following scratching were made at least one hour after scratching to allow recovery via re-flow commonly observed in polyurethane coatings (27).

Control-H Formulation:

Scratch resistance of the coatings on Leneta BK charts were tested with a 325 grit Norton scratch pad (1.5"x1.5") attached to a one pound hammer. The panel was scratched by moving the scratch pad back and forth on a 4" x 1.5" area two times (2-cycles); gloss at 20° and 60° was recorded before and one-hour after scratching.

Table 2. Polyurethane Coating Formulation (Control-H)

PART A	
Acrylic polyol (71 Wt.%)	79.95
Methyl n-amyl ketone	3.53
Xylene	1.10
n-Pentyl propionate	0.80
UV stabilizer 1	0.82
UV stabilizer 2	0.54
Polysiloxane wetting agent	0.41
Total Part A	**87.15**
PART B	
HDI trimer	11.87
Butyl acetate	0.98
Total Part B	**12.85**
Part A + Part B	**100.00**
%NVW = 65.26; %NVV = 65.16; NCO:OH = 1.05:1.00	

Table 3. Predispersed Nanoparticles Used in the Study

Particle Type	Dispersion Medium	Solids (Wt.%)	Particle Size
Alumina C	Methoxypropyl acetate	34.0	20 nm
Alumina D	Methoxypropyl acetate	33.0	20 nm
Silica A	Methoxypropyl acetate/ Methoxypropanol (6:1)	32.0	20 nm
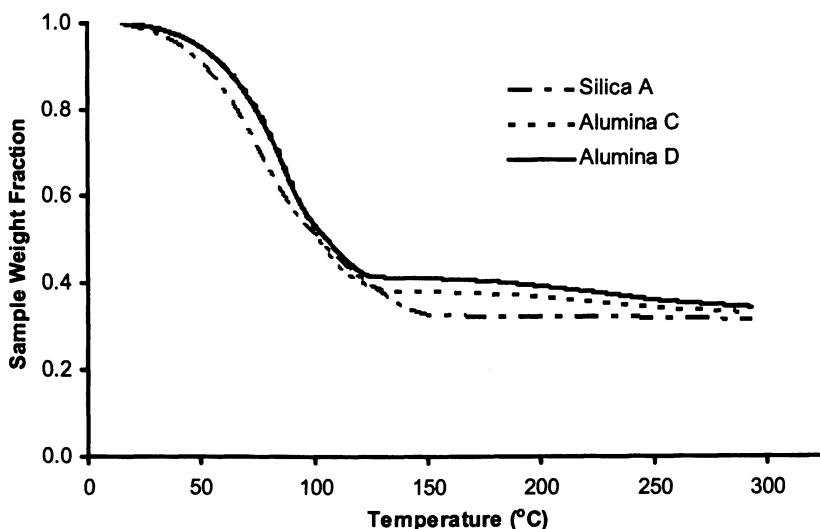
Figure 1. Thermo-Gravimetric Analysis results of nanoparticle dispersions

All scratch tests were conducted at an ambient temperature of 21±1 °C. Gloss measurements were made with a BYK-Gardner Micro-TRI-gloss #4520 gloss-meter.

Thermo-Mechanical Analysis

The glass transition temperatures of the cured films of Control-H formulation were measured with differential scanning calorimetry (DSC) and dynamic mechanical analysis (DMA). For DSC, a clear piece of film was cut and the areas were examined with a Starrett 734XFL micrometer to determine its thickness. A thickness of about 75-100μ was desired. Circular film areas were then cut with a ¼" McGill punch, and were loaded into a TA Instruments DSC Q1000. Each sample was tested with a HEAT/COOL/HEAT cycle from -30°C to 100°C. The samples were heated at 10°C per minute and cooled at 5°C per minute. Coating films for DMA testing (TA Instruments Q800) were prepared with a McGill slot punch (#16500). The length of the film was measured by the DMA instrument; the width of the film was measured by Fowler Pro-Max Calipers, and the thickness of the film was measured by a Starrett 734XFL micrometer. A thickness of about 100 μm was desired. DMA testing parameters are shown in Table 4. Thermo-Gravimetric Analysis (TGA) was run with a TA Instruments TGA Q500. Samples were heated from ambient to 300°C at a heating rate of 10 °C per minute under a nitrogen atmosphere.

Table 4. Test parameters for DMA Scans

Mode	DMA Multi-Frequency Strain
Test	Temp Ramp/Frequency 1 Hz
Strain	0.15%
Preload Force	0.1N
Start Temp	- 40°C
Soak Time	5min
Final Temp	110°C
Ramp Rate	5°C/min

Microscopy

Atomic Force Microscopy (AFM) was conducted using a Pacific Nanotechnology AFM. Samples were drawn down at 75.4 µm wet thickness on glass microscope slides. Testing was conducted in close contact mode with a silicon cantilever. Scanning Electron Microscopy (SEM) images were obtained with a JEOL 890 instrument.

Results and Discussion

Degree of Dispersion of nanoparticles

Proper dispersion of nanoparticles is critical in realizing their potential benefits in a composite. Both indirect and direct evidence discussed below indicated that the particles are well dispersed. However, some agglomerates were observed in SEM cross-sections of the thicker films prepared with Control-H formulation.

Initial Gloss

Gloss data (measured at 20° angle) of coatings containing 1.0 Wt.% and no nanoparticles are shown in Table 5. There is no significant effect on gloss by nanoparticles, indicating good dispersion.

Viscosity

Viscosity of the Control-L formulation without nanoparticles is 43 mPa s, and it did not change significantly as a result of addition of nanoparticles. Control-H formulation had a viscosity of 465 mPa s which did not change significantly when nanoparticles were incorporated. Both formulations exhibited Newtonian behavior.

Table 5. 20° Gloss Values of Coatings before Scratching (Initial gloss)

Coating	Nanoparticle Loading (Wt.%)	Gloss Value at 20°
Control-L	None	88.5
	1% Alumina C	92.5
	1% Alumina D	88.2
	1% Silica A	87.8
Control-H	None	86.4
	1% Alumina C	88.7
	1% Alumina D	86.4
	1% Silica A	86.6

Film Clarity

All three nanoparticle systems were drawn down onto glass plates and their film clarity was observed. A subjective, 0-10 rating scale was used to quantify film clarity, 0 being transparent and 10 being opaque. No reduction of film clarity was detected for films containing up to 3.0 Wt.% Alumina C, Alumina D, or Silica A (*28,29*).

Atomic Force Microscopy

AFM was used to determine the surface morphology of the films containing nanoparticles. The films were shown to contain evenly dispersed nanoparticles near the surface layer as evident in AFM images (Figure 2) for 25μ films prepared with Control-L formulation. Figure 2(a) is an AFM height image (5μx5μ area) of a coating containing 2.67 Wt.% Alumina B, whereas Figure 2(b) is an image (10μx10μ area) of a coating containing 0.67 Wt.% Silica A. It should be noted that the feature sizes of these images do not represent the actual particle sizes because they can be buried in the film at different depths However,

such surface abundance of particles was not observed for 100μ films prepared with Control-H formulation. This is not surprising because of the ten-fold higher viscosity and the low solvent content in the Control-H formulation. Both factors would retard drainage of binder around particles as the coating dries.
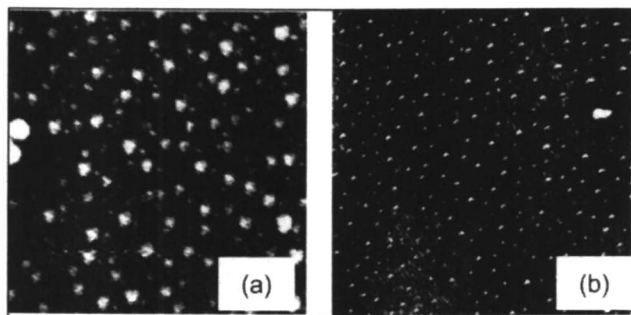
Figure 2. AFM Images of coatings containing nanoparticles: (a) Alumina-B (2.67 Wt.% - 5μx5μ area), (b) Silica-A (0.67 Wt.% - 10μx10μ area)

Scanning Electron Microscopy

SEM images obtained with a JEOL 890 instrument are shown in Figure 3. The cross-sections were prepared by cooling the samples in liquid nitrogen followed by fracturing. Images from near the top surface and center of Control-H, Alumina C, and Silica A coatings are shown. An additional SEM image of a Control-H film containing 1.5 Wt.% Alumina D is shown in Figure 4. Nanoparticles appear to be fairly well dispersed; however, some agglomerates are present. Based on the overall evidence presented above, we conclude that the nanoparticles are rather well dispersed in the coating films.

Scratch Resistance Results

Scratch resistance test results for coatings prepared with Control-L formulation are shown in Figure 5. These results were generated with the scratch test defined in experimental section, by subjecting each film to 1-cycle scratching. Results are expressed in terms of percentage of gloss (measured at 20° angle) retained after scratching. Control-L coating (i.e., the film with 0 Wt.% nanoparticles) retains 45% of its gloss. There are some variations in the performance of coatings containing different types of nanoparticles. However, it is clear that they improve the scratch resistance significantly at very low levels of
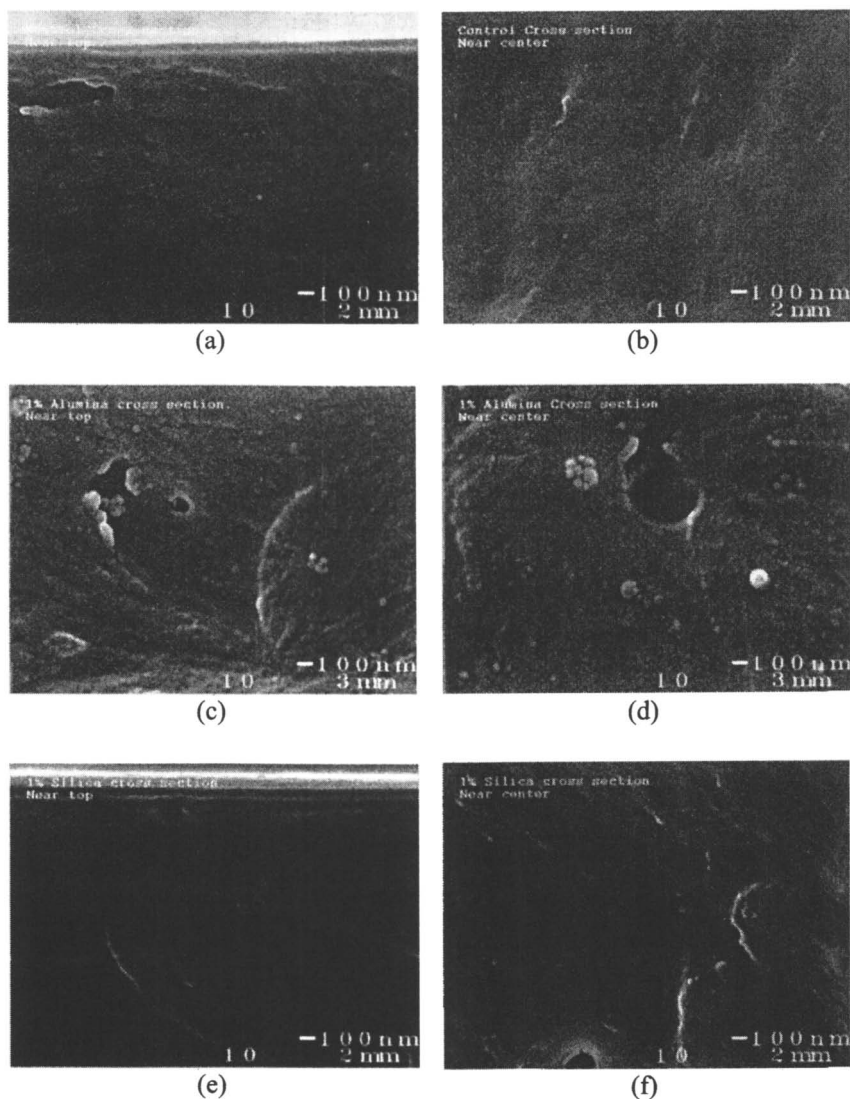
*Figure 3. Cross-Sectional SEM Images of coating samples. Images in the left
column are from near the top surface of films whereas images in the right
column are from near the center: (a), (b) Control-H; (c), (d) Control-H/1.0
Wt.% Alumina C; (e), (f) Control-H/1.0 Wt.% Silica A*
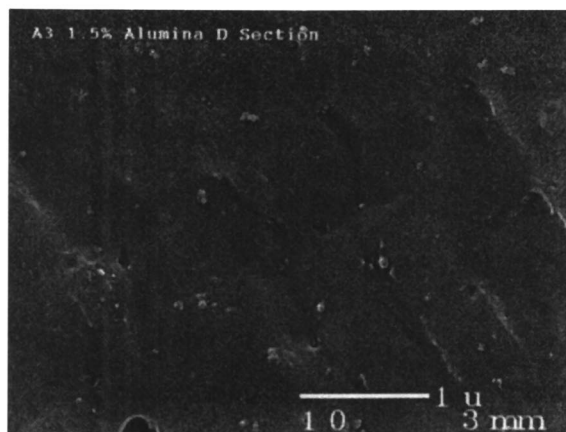
Figure 4. Cross-sectional SEM image of a Control-H film containing 1.5 Wt.% of Alumina D nanoparticles.
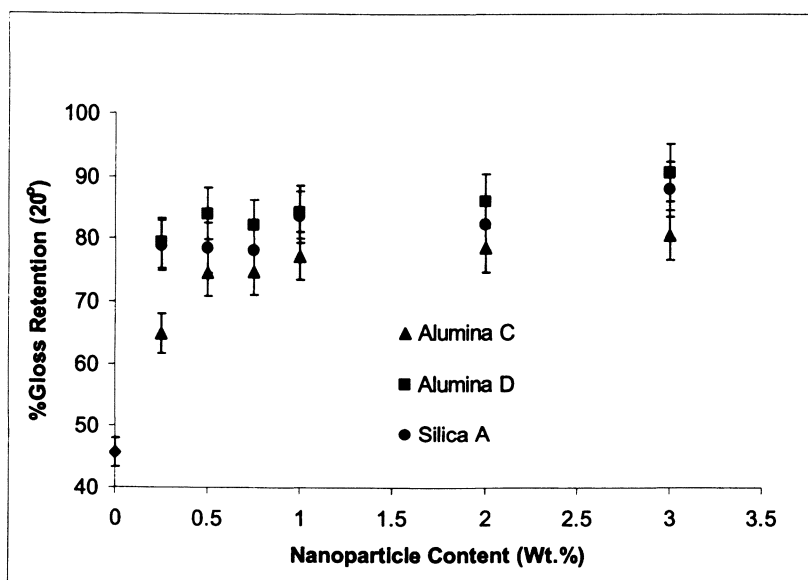
Figure 5. Scratch resistance of coatings as measured by percentage of gloss retained after scratch test (1-cycle). Error bars represent one-standard deviation.

loadings. Their effectiveness appears to reach a plateau at about 1.0Wt.% nanoparticle loadings.

The higher solids Control-H formulation was used in our recent studies in order to prepare thicker films for mechanical property testing. Scratch resistance results of the thicker polyurethane coatings and a coating containing 1.0Wt.% Alumina D, as measured by gloss retention after two cycles of scratching, are shown in Table 6. Our latter studies were conducted with the 2-cycle scratch test. Although it is more severe, it produces results that are more repeatable than does the 1-cycle test. Gloss retention values after two-cycle scratching (13.9 for control versus 23.8 for Alumina D at 20°; 31.8 for control versus 43.1 for Alumina D at 60°) clearly indicate that nanoparticles have improved this property. As shown in Figure 5, gloss retention of the Control-L films after 1-cycle scratch test is 45%. Control-L films were shown to have gloss retention of 20% after 2-cycle scratching.

Table 6. Scratch resistance of Control-H coatings as measured by gloss retention

	Gloss measured at 20°			Gloss measured at 60°		
	Pre-Scratch	Post-Scratch (24hr)	% Gloss Retention	Pre-Scratch	Post-Scratch (24hr)	% Gloss Retention
Control						
Sample 1	84.5	7.2	8.5	93.2	22.4	24.0
Sample 2	83.6	12.8	15.3	93.2	31.5	33.8
Sample 3	82.8	14.9	18.0	92.7	34.8	37.5
Average	**83.6**	**11.6**	**13.9**	**93.0**	**29.6**	**31.8**
Alumina D (1.0 Wt.%)						
Sample 1	86.6	20.6	23.8	91.8	38.8	42.3
Sample 2	86.4	18.9	21.9	91.4	38.0	41.6
Sample 3	86.3	22.1	25.6	92.3	41.8	45.3
Average	**86.4**	**20.5**	**23.8**	**91.8**	**39.5**	**43.1**

Figure 6 shows results of scratch testing of coatings containing all three types of nanoparticles and a Control-H coating, in terms of % Gloss Retention after 2-cycles of scratching as defined in the experimental section. All nanoparticle types improve the scratch resistance. The effect of Alumina C appears to be greater than the effects of Alumina D and Silica A.
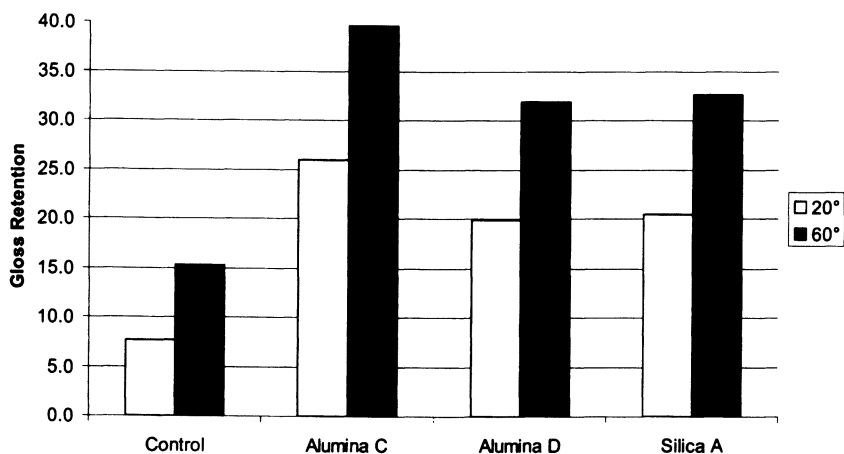
Figure 6. %Gloss retention (2-cycle scratching) of Control-H and Control-H plus 1.0Wt.% nanoparticles: White – 20°; Black – 60°

Thermal Properties

Differencial Scanning Calorimetry was conducted in triplicate, and the Tg values obtained from the reheat cycle of the scans are compared in Table 7. The Tg values of Alumina D film is approximately 8°C lower than the Tg of the control film. It should be noted that the Tg values of the control formulations reported in our previous studies (25,28) were closer to 50°C. Reasons for lower Tg values found in this study will be addressed in a section that follows.

Glass transition temperatures of the coatings, based on the storage moduli from DMA testing, are shown in Figure 7. Tg of the Alumina D film is determined to be 47.5°C which is about 7°C lower than Tg of the control film.

Table 7. Tg values (as determined by DSC) of coatings prepared with Control-H formulation

Coating	Sample	Tg (°C)	Tg (°C)
Control	1	38.0	40.0±1.8
	2	41.4	
	3	40.7	
Alumina D	1	31.6	31.9±0.4
	2	32.4	
	3	31.7	

This result confirms the trend seen in DSC data. Overall, the DMA derived Tg values are higher, but this is typical due to the dynamic nature of the DMA method that shifts glass transition to a higher temperature. If the oscillatory frequency of the DMA is lowered, the resultant Tg values would approach the Tg values determined by DSC. The lowering of Tg by Alumina D is somewhat surprising because alumina is a harder material than the polyurethane. Glass transition of organic-inorganic nanocomposites has been the subject of a number of previous studies (1-4). These studies have shown increases, decreases, and no changes in Tg of polymers containing nano-scale inorganic phases. Typically, an increase in polymer Tg indicates favorable enthalpic interactions between the polymer and inorganic phase, whereas a reduction in Tg indicates lack of such interactions.
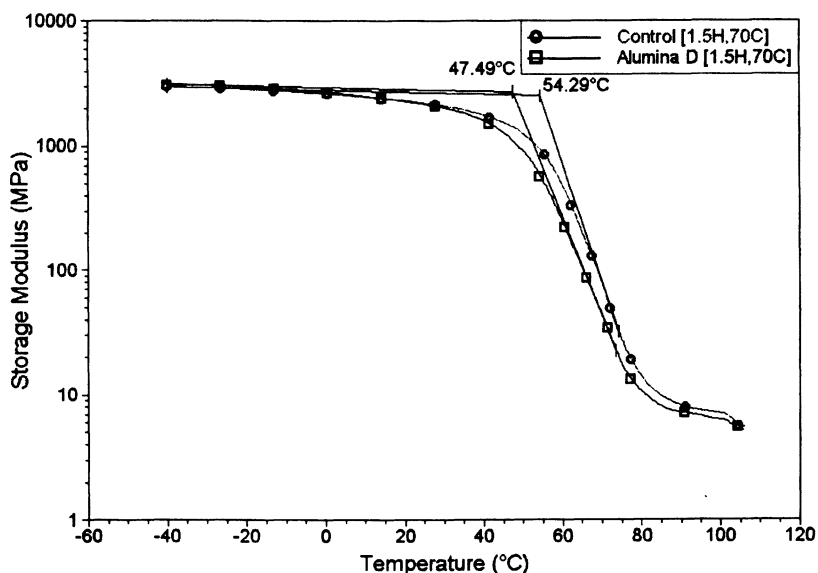
*Figure 7. DMA scans of control and Alumina D coatings
(Heating rate: 10°C per minute)*

Tg values determined by DSC for all four coatings systems in a separate set of experiments are shown in Table 8. The Tg reduction of the control polyurethane coating by Alumina D, observed in the previous experiments, is reproduced in this experiment. The standard deviation for Control-H film is much higher, and Alumina C and Silica A coatings' Tg values are well within the standard deviation of control film's Tg.

**Table 8. Tg values of Control-H coatings and coatings containing
1.0 Wt.% nanoparticles, as determined by DSC**

Coating	Sample	Tg (°C)	Tg (°C)
Control-H	1	35.3	37.9±4.2
	2	35.7	
	3	42.7	
Alumina C	1	34.2	35.7±1.4
	2	36.7	
	3	36.4	
Alumina D	1	32.8	31.5±1.9
	2	29.4	
	3	32.4	
Silica A	1	34.9	35.4±0.4
	2	35.6	
	3	35.6	

Formulation Solvent Effects

The low Tg values and their high degree of variability led us to question whether some of the coating solvents and nanoparticle dispersion media remain in the coating and cause plasticization of the polymeric matrix. A list of all solvents used in the formulation and nanoparticle dispersion media is shown in Table 8. It should be noted that films in this study are much thicker (75-100μ) than the films in previous studies (25-50μ). Although the curing time was longer (90 minutes) in this study, it is possible that some of the solvents remain trapped within the film.

In order to determine whether the solvents are completely removed from the film, samples were subjected to a thermo-gravimetric analysis. The results are shown in Figure 8. These TGA scans clearly indicate loss of volatile material (4.0-5.0Wt.%) within 100-200°C temperature range. It is reasonable to conclude that the volatile material consists of one or more of the solvents listed in Table 9. To determine the optimum drying time for complete removal of solvents at 70°C, Control-H coatings were dried in an oven for increasing lengths of time, and resultant films were subjected to thermo-gravimetric analysis. Their TGA scans shown in Figure 9 indicate presence of solvents even after 24 hours of drying. Only the sample dried for 30 hours appears free of solvents. Glass transition temperatures of the Control-H films as a function of drying time at 70°C are plotted in Figure 10. The Tg value reaches the expected 50°C after 30 hours of drying. Based on these results, 30 hours was selected as the optimum drying time for experiments described in the remainder of this chapter.

Thermo-mechanical Properties of Solvent-Free Coatings

Glass transition temperatures of solvent-free coatings (i.e. coatings dried at 70°C for 30 hours) are shown in Figure 11. These data indicate that incorporation of 1.0 Wt.% of nanoparticles does not alter the Tg of the coating. The Young's modulus (at 20°C) of the Control-H coating is compared with the coatings containing nanoparticles in Figure 12. Coatings containing nanoparticles appear to have slightly lower moduli compared to the modulus of the Control-H coating. However, all values are within the experimental error.

Table 9. Boiling Points of Solvents in the Coatings Studied

Solvent	Boiling Point (°C)	Source of Solvent
PMA (propylene glycol monomethyether acetate)	146	Alumina C; Alumina D; Silica A
n-Pentyl propionate	165	PU-Part A
Methyl n-amyl ketone	151	PU-Part A
Xylenes	138-144	PU-Part A
n-Butyl acetate	126	PU-Part B

Scratch Resistance of Solvent-Free Coatings

Gloss retention results of solvent-free coatings (dried for 30 hors at 70°C) subjected to the 2-cycle scratch test are shown in Figure 13. Although there were no significant differences in thermo-mechanical properties, these results clearly indicate that both silica and alumina nanoparticles cause improvements in scratch resistance.

Scratch Resistance Mechanisms

As discussed in the introductory section, understanding scratch resistance mechanisms is complicated by various factors. In this study, we have demonstrated that although the thermal and mechanical properties of the coatings are not significantly altered by the nanoparticles, they still can cause improvements in scratch resistance. Lack of changes in glass transition temperatures indicates that there are no significant interactions between the nanoparticle surfaces and the polyurethane matrix. This lack of interactions was evident in cross-sectional SEMs of coatings containing nanoparticles. As seen in Figure 14 for a film containing 0.25 Wt.% Alumina D particles, nanoparticles cleanly separate from the polymer matrix upon fracturing in liquid nitrogen. An
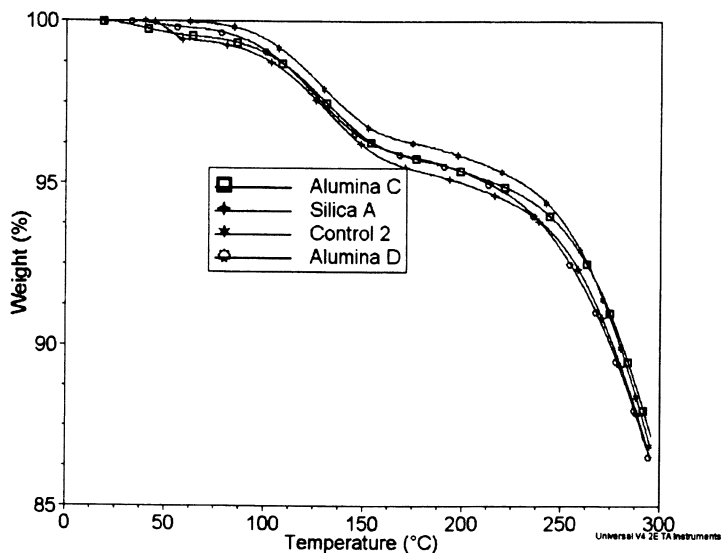
Figure 8. TGA scans of Control-H coating and Control-H coating containing 1.0Wt.% nanoparticles, dried for 90 minutes at 70°C.
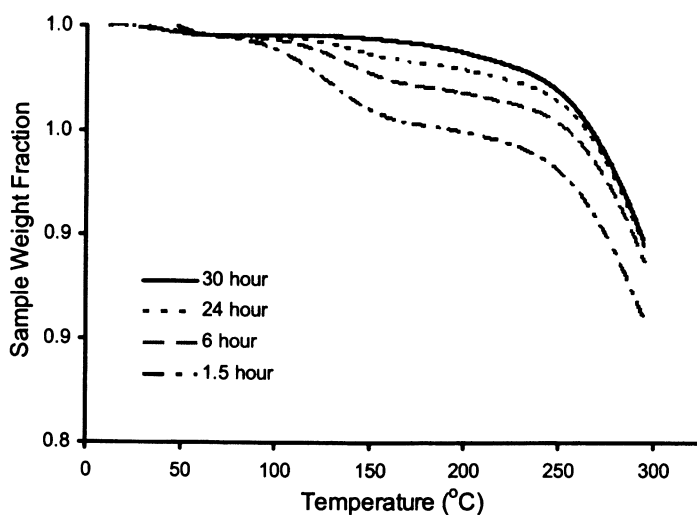
Figure 9. TGA scans of Control-H films dried at 70°C for varying lengths of time.
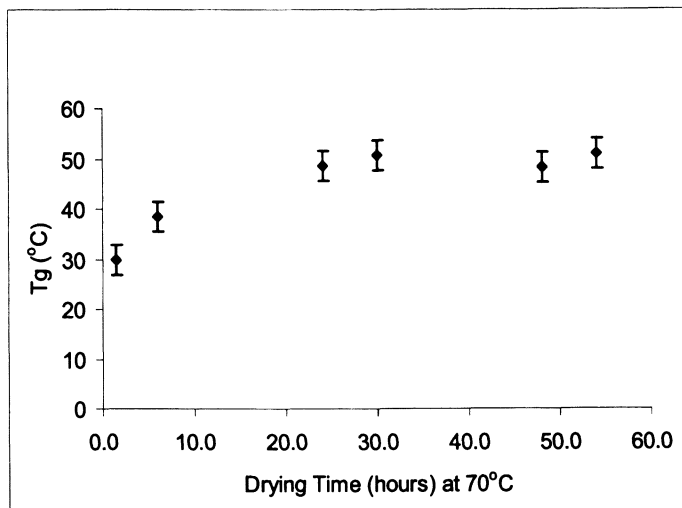
*Figure 10. Tg values as a function of Control-H coating drying time at 70°C
(Tg values were determined by DSC)*
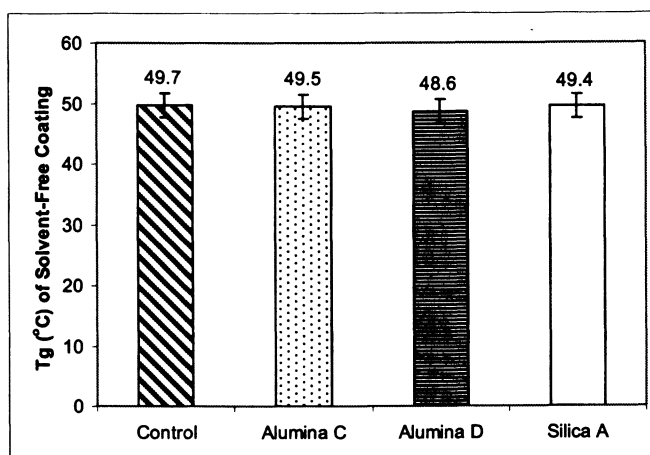
Figure 11. DSC data for samples cured at 70°C for 30 hours.
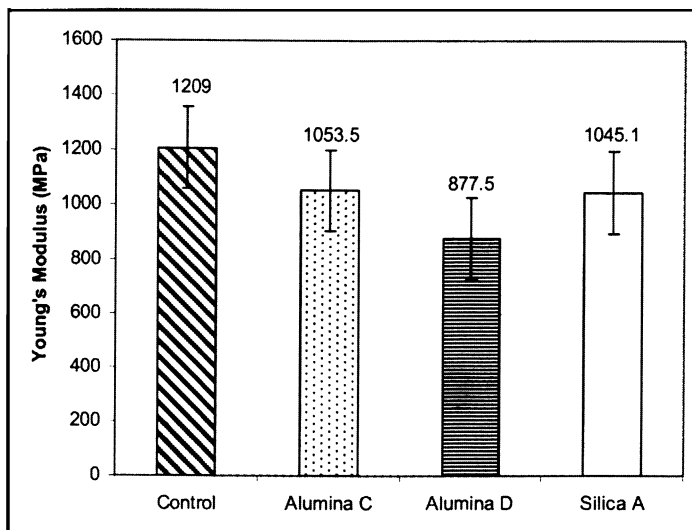
Figure 12. Young's modulus of samples cured at 70 ℃ for 30 hours.
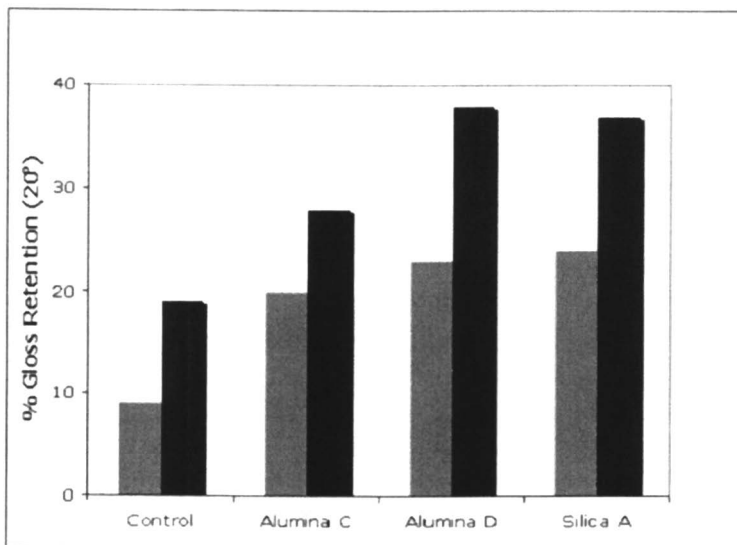
Figure 13. Scratch resistance of Control-H coatings (i.e., % retained gloss after 2-cycle scratching) dried for 30 hours at 70°C. Control contains no nanoparticles, whereas others contain 1.0 Wt.% nanoparticles

isolated particle and dimples, most likely left by removed particles, can be seen in Figure 14.
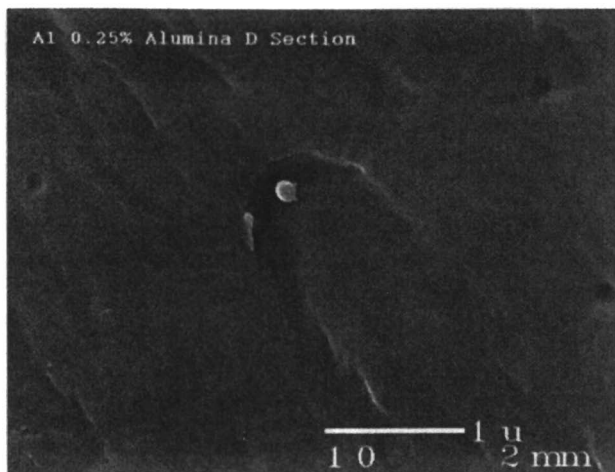
Figure 14.   Cross-sectional SEM-image of a Control-H film containing 0.25 Wt.% Alumina D nanoraticles.

Conclusions

Results presented in this paper clearly established scratch resistance improvements of polyurethane coatings containing alumina and silica nanoparticles. However, the improvements are not dramatic, and no correlation was found between scratch resistance and thermo-mechanical properties tested. The improved performance can be explained in terms of enhanced energy dissipation modes at the nanoparticle-polymer interface. Retention of small but significant levels of formulation solvents severely complicated data analysis. Use of thermo-gravimetric analysis was shown to be a valuable tool in guaranteeing preparation of consistent coating films for testing.

Acknowledgement

References

1. Kontou E. and Niaounsikis, M., *Polymer,* **2006**, *47*, 1267
2. Ash, B. J., Siegel, R. W., and Schadler, L. S., *J. Polym. Sci.: Part B: Polym. Phys.*, **2004**, *42*, 4371.
3. Rodriguez, J. G.-I., et al., *J. Thermal Anal. Calorimetry*, **2007**, *87(1)*, 45.
4. Bares, J., *Macromolecules*, **1975**, *8*, 244.
5. Mayes, A. M., *Macromolecules*, **1994**, *27*, 3114
6. Tsui, O. K. C., and Russell, T. P, *Macromolecules*, **2001**, *34*, 5535.
7. Fryer, D. S., Nealey, P. F., and Pablo, J. J. de, *Macromolecules*, **2000**, *33*, 6439.
8. Lewis, L. N., and Katsamberis, J. Appl. Polym. Sci., **1991**, *42*, 1551
9. Fernando, R. H., and Bohrn, W. J., US 5,124,202, **1992**
10. Zhou, S., Wu, L., Sun, J., and Shen, W., *Prog. Org. Coat.,* **2002**, *45*, 33-42,
11. Barna, E., Bommer, B., Kursteiner, J., Vital, A., Trzebiatowski, O., Koch, W., Schmid, B., and Graule, T., *Composites: Part A,* **2005**, *36*, 473-480,
12. Vanier, N. R., Munro, C. H., Clarr, J. A., and Jennings, R. E., US 30162015:A1, **2003**.
13. Vanier, N. R., Munro, C. H., McCollum, G. J., O'Dwyer, J. B., and Kutchko, C., US 301662876:A1, **2003**.
14. "Nanotechnology in Coatings: Emerging Applications" FSCT Advancements in Coatings Series Symposium, March 26-28, **2008**, Orlando, FL, USA.
15. Shen, W, *JCT Coatings Tech,* **2006**, *March*, 54-60,
16. Jones, F., Shen, W., Smith, S., Huang, Z., and Ryntz, R., *Prog. Org. Coat.,* **1998**, *34*, 119-129.
17. Ryntz, R., Abell, B.D., Pollano, G.M., Nguyen, L.H., and Shen, W.C., *J. Coat. Tech.,* **2000**, *72(904)*, 119-129.
18. Hara, Y., Mori, T., and Fujitani, T., *Progress in Organic Coatings,* **2000**, *40*, 39-47.
19. Wagner, G., and Osterhold, M., *Mat.-wiss. U. Werkstofftech,* **1999**, *30*, 617-622.
20. VanLandingham, M., Villarrubia, J., Guthrie, W., and Myers, G., *Macromol. Symp.,* **2001**, *167*, 15-43
21. Kutschera, M., Sander, R., Herrmann, P., Weckenmann, U., and Poppe, A., *J. Coat. Tech. Res.,* **2006**, *3*(2), 91-97
22. Lin, L., Blackman, G.S., and Matheson, R.R., *Prog. Org. Coat.,* **2000**, *40*, 85-91.
23. Hosseinpour, D., Guthrie, J. T., and Berg, J. C., *Prog. Org. Coat.,* **2008**, *62*, 214-218
24. Groenewolt, M., *Progress in Organic Coatings,* **2008**, *61*, 106-109.
25. Sung, L., Comer, J., Forster, A. M., Hu, H., Floryancic, B., Brickweg, L., and Fernando, R. H., *J. Coat. Tech. Res.,* **2008**, *On-Line First Edition*

26. ASTM D4708-99, **1999**.
27. Yu, D., Floryancic, B. R., Brickweg, and Fernando, R. H., PMSE Proceedings, ACS National Meeting, San Francisco, CA, **2006**.
28. Floryancic, B. R., Brickweg, L. J., Comer, J. B., Sung, L., Forster, A. M., and Fernando, R. H., PMSE Proceedings, ACS National Meeting, San Francisco, CA, **2006**.
29. Floryancic, B. R., Brickweg, L. J., and Fernando, R. H., Smart Coatings II, ACS Symposium Series, T. Provder and J. Baghdachi (Ed), Chapter 11, **2008**.

Chapter 12

Impact of Nanoparticles on the Scratch Behavior of a Polyurethane Coating

Li-Piin Sung[1], Jeffrey Comer[1,2], Aaron M. Forster[1], Haiqing Hu[1],
Bryce Floryancic[2], Lucas Brickweg[2],
and Raymond H. Fernando[2]

[1]Polymeric Materials Group, Building and Fire Research Laboratory,
National Institute of Standards and Technology, 100 Bureau Drive,
Gaithersburg, MD 20899
[2]Polymers and Coatings Program, Department of Chemistry and
Biochemistry, California Polytechnic State University,
San Luis Obispo, CA 93407

In this paper, we report a quantitative study of the effect of
nanoparticles (nano-alumina and nano-silica) on the surface
mechanical properties and scratch behavior of a polyurethane
coating. An instrumented indenter with a conical diamond tip
is used to measure surface mechanical properties (modulus
and hardness) and to perform scratch test over a wide range of
scratch loads. The scratch behavior in terms of the onset of
elastic–plastic transition and scratch morphology were
characterized by laser scanning confocal microscopy. The
scratch results were correlated to the surface mechanical
properties and relevant bulk material properties to understand
the overall scratch behavior of the coatings. The results
indicate that the scratch behavior of the coatings depends
strongly on the concentration and type of nanoparticles.

Introduction

Nano-fillers represent an immense opportunity for the development of innovative products and technologies for virtually all industries. A variety of nanofillers, such as nanoparticles, nanotubes, and nanoclay are being incorporated into polymeric materials to enhance material properties and are increasingly replacing traditional coatings in many commercial applications (1,2). The desired properties include enhancements in stiffness, toughness, UV absorption, flame resistance, ionic conductivity, and biodegradability. For example, incorporating metal-oxide nanoparticles such as nano-alumina and nano-silica into polymer coatings to enhance the mechanical durability has empolyed in the current anti-scratch and mar technologies.

In this paper, we report on a quantitative study of the effect of a nanoparticle (nano-alumina and nano-silica) on the surface mechanical properties and scratch behavior of a polyurethane coating. The key experimental variables investigated in this study are the particle type and concentration. Surface mechanical properties (modulus and hardness) of the coatings were measured using an instrumented indentation system (3), and the results were compared to relvent bulk properties, such as as glass transition temperature, modulus and hardness (Pendulum Hardness Test). A series of scratch tests was conducted over a wide range of scratch loads and particle concentrations to study the scratch behavior of the nanoparticle filled systems using a single-probe scratch test utilizing the same indentation system. Scracth behavior in terms of the onset of the elastic-plastic transition (4) and scratch damage morphology (scratch width, depth, and deformation patterns) were characterized by laser scanning confocal microscopy (LSCM). The scratch data were correlated to the surface mechanical properties and relevant bulk material properties to understand the overall scratch behavior of the coatings. The results show that (1) the addition of nanoparticles affects on surface mechanical properties (surface modulus and hardness) more significantly than on the bulk mechanical properties, and (2) the scratch behavior of the nanoparticle-filled coatings depends strongly on the concentration and types of nanoparticles.

Experimental

Materials

Three types of commercially available nanoparticles were studied: Filler A (nano-alumina), Filler B (nano-alumina), and Filler C (nano-silica). These nanoparticles were supplied predispersed in a solvent medium. The dispersion medium for Filler A, Filler B, and Filler C are tripropylene glycol diacrylate

(TPGDA), methoxypropyl acetate, and methoxypropyl acetate/methoxy propanol, respectively. The avaged particle diameters were: Filler A: (90 ± 15) nm, Filler B: (90 ± 15) nm, and Filler C: (50 ± 10) nm, determined by dynamic light scattering (DLS) measurements in a dilute particle suspension at National Institute of Standards and Technology (NIST). Note that the avaged particle sizes obtained from DLS experiments are larger than the manufacture data (Filler A ≈ 30 nm - 40 nm; both Filler B and Filler C are ≈ 25 nm). This result implies that nanoparticles are not fully dispersed in the solvent medium. A two-part polyurethane (PU) automotive refinish coating was used as the base formulation in all experiments. The unfilled and nanoparticle-filled coatings were prepared in the coating laboratory at California Polytechnic State University using draw-down application with a film thickness of ≈ 75 μm on a black and white painted steel panels (76 mm x 132 mm, designed for measuring the hiding power using ASTM D 6441 test method). The samples were cured in an oven at 70 °C for 30 minutes, and all tests were performed on the cured samples. The final cured samples appear transparent and this outcome indicates the nanoparticles were well dispersed and wetted in the polymer blinder. Additional sample preparation details were reported elsewhere (5).

Mechanical Measurements

Coating surface mechanical properties such as elastic modulus and hardness were measured using a nanoindenter with a 10 μm diameter 45° semi-apical angle diamond cone indenter in a continuous stiffness mode (6-8). The nanoindenter experiments were conducted at a fixed strain rate of 0.05 s^{-1} and indented to a depth of 5 μm. Reported modulus values are the average values obtained between the depths of 1 μm to 3 μm for a minimum of 10 indents. Error bars represent one standard deviation of the measurements. Tests designed to probe the bulk material properties such as glass transition temperature, T_g, and pendulum hardness have been also carried out to investigate the effects of nanoparticles on other coating physical properties. Details on sample preparation and T_g and pendulum hardness measurements were reported elsewhere (5).

Scratch Testing and Scratch Morphology Characterization

The same indenter used to measure the surface mechanical properties was used to scratch the surface of the nanocomposite coatings. A series of progressive-load and constant-load scratch tests were performed over a wide range of applied loads and velocities using a single-probe scratch testing method developed at NIST (9-10). In this study, all scratch tests were performed at a fixed velocity of 10 μm/s with scratch loads progressively increasing from 0 mN to 50 mN over a scratch length of 1000 μm. Penetration depth (initial and

residual), pile-up height, percentage of recovery, and friction coefficient for coating with three different particle types and concentrations were obtained.

A reflection laser scanning confocal microscope (LSCM) was employed to characterize scratch morphology. A detailed description of LSCM measurements can be found elsewhere (11-12). The laser wavelength used in this study was 543 nm. LSCM images presented in this paper are 2D intensity projections (an image formed by summing the stack of images over the z direction, 512 pixel x 512 pixel) of the nanocomposite surface. The 2D intensity projection images are effectively the sum of all the light scattered by different layers of the coating, as far into the coating (approximately 100 μm in the 5x configuration) as light is able to penetrate and reflect back. The pixel intensity level represents the total amount of back-scattered light. Darker areas represent regions scattering less light than lighter colored areas. The scratch width was defined as the peak-to-peak distance perpendicular to the scratch length. Details of the scratch profile characterization have been described elsewhere (10).

Results and Discussion

Surface Mechanical Measurements

Figure 1 shows the surface elastic modulus and hardness of nanocomposite coatings determined from nanoindentation measurements. Here, the surface elastic modulus was calculated from the stiffness of the contact during initial unloading in conjunction with the contact area. Indentation hardness is also the mean stress or pressure in an indentation experiment, i.e., it is the ratio of force, P, to contact area, A, where A is in general related to displacement, h, by the tip geometry. The definition and measurements of the surface elastic modulus and hardness using instrumented nanoindentation were described elsewhere (5,9,10). Both surface modulus and hardness decreased in the presence of three nanoparticle fillers. The decreases in surface modulus and hardness values are more than 50 % in the Filler A system. This result would be due to the decrease in the coating cross-link density, as reflected by a decrease in the glass transition temperature (T_g) determined by differential scanning calorimetry (DSC) shown in Figure 2a.

However, T_g values (Figure 2a) are almost independent of particle concentration for the Filler B and Filler C systems within measurement uncertainties. The obvious difference between Filler A and Filler B systems was the solvent used as the dispersion medium. A parallel study was conducted to investigate the effect of the dispersion medium on the T_g and scratch damage of the coatings. We further confirmed that the reduction in T_g of the Filler A system was due to a plasticizing effect of the tripropyleneglycol diacrylate (TPGDA) in

which the Filler A was supplied (5). This result implies that the addition of nanoparticles has less effect on the bulk materials properties than on the surface mechanical properties of coatings as shown in the Filler B and Filler C systems.

In addition to the T_g measurements, pendulum hardness tests using ISO 1522 test method were performed in the Koenig mode and average dampening times (second) of three trials were recorded. The Koenig hardness values of coatings measured seven days after curing are shown in Figure 2b. It is found that the bulk hardness decreases rapidly with increasing Filler A concentration, while the hardness values decrease slightly as Filler B or Filler C concentration increases. Not surprisingly, the pendulum hardness data closely resemble the glass transition temperature data. This is consistent with the surface hardness measurements as shown in Figure 1b for Filler A system. This result shows that the addition of nanoparticles does not strongly affect the bulk hardness (see Figure 2b) but impacts the surface harness measurements considerably.
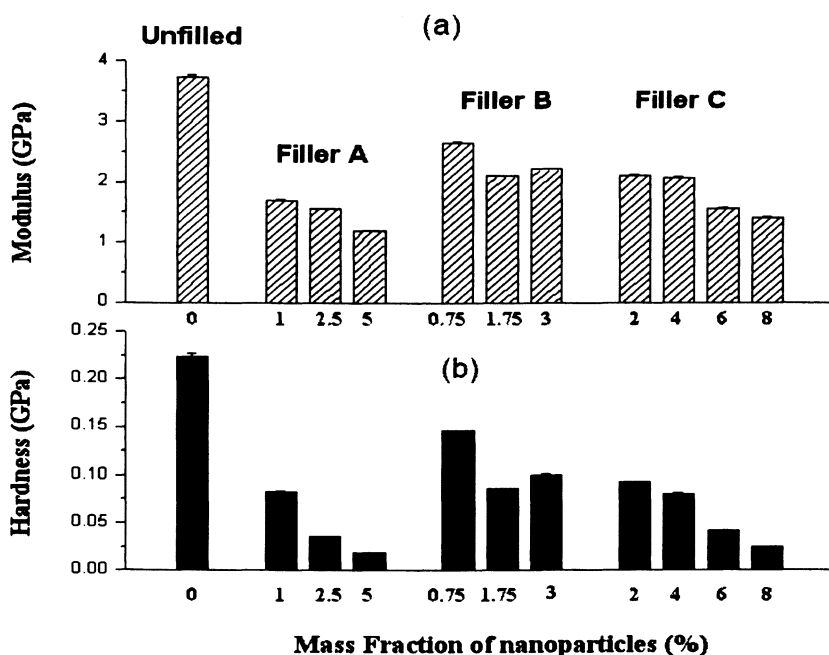
Figure 1. Surface (a) elastic modulus and (b) hardness as a function of nanoparticle concentration for three nanocomposite coatings, consisting of Filler A, Filler B, and Filler C. The error bars represent one standard deviation.

Progressive-load Scratch Testing

The scratch penetration data (initial penetration depth, D_i, and residual penetration depth D_r) as a function of scratch distance during progressive-load scratch (P-scratch) testing for an unfilled PU coating is presented in Figure 3a. The scratch load ranged from 0 mN to 50 mN over a total scratch length of 1000 μm using a scratch velocity of 10μm/s. The percentage of recovery is defined as 100 % x $(D_i - D_r)/D_i$, and the quantity reflects viscoelastic response of the material. In Figure 3b, LSCM is used to characterize the resulting surface deformation and identify the chosen onset of scratch visibility. The corresponding elastic-plastic transition onset point is labeled "onset" in Figure 3a just below 100 % recovery. In addition to penetration depths, the overall scratch morphology including scratch width and pile-up were obtained from LSCM measurements to quantify the severity of surface deformation. Figure 3c illustrates the definition of these quantities: full scratch width, w_f, peak-to peak scratch width, w_p, full depth, D_f, and pile-up height, h_p. In this study, the reported results are the average of a set of three progressive scratch tests.

Scratch Testing Results for Filler A System

Figure 4 shows LSCM images of scratch profiles generated from a progressive-load scratch test on an unfilled PU coating (0 wt %) and the Filler A system for three different particle concentrations: 1 wt %, 2.5 wt %, and 5 wt % (mass fraction), as indicated in the Figure 4. A lower onset is observed for the 2.5 wt % and 5 wt % Filler A systems compared to the unfilled system. Moreover, a change in scratch profile of the 1 wt % Filler A system is also noticeable in Figure 4. It appears that the scratch profile in the 1 wt % Filler A system is similar to that of the unfilled system at lower scratch loads, and the profile becomes wider and shallower shape similar to the profiles of the 2.5 wt % and 5 wt % Filler A systems at higher loads.

There are significant differences between these LSCM scratch images: (1) the optical contrast between a scratch and the glossy PU coating surface is greatly reduced with increasing filler concentration; (2) the shape and width of the scratch pattern changes with the addition of fillers; and (3) the onset of elastic-plastic transitions move to a lower load. Note that the LSCM images are 2D intensity projection images, which are effectively the sum of all the light reflected and scattered by different layers of the coating. The total optical contrast results from both specular and near-specular scattering due to the collected angular range of a laser scanning confocal microscope. Therefore, the optical contrast provides a more robust measurement of the relationship between damage and visibility. From the optical contrast assessment of scratch damage from LSCM images, we may conclude that the onsets of elastic-plastic transition move to a higher scratch load upon the addition of nanoparticles.
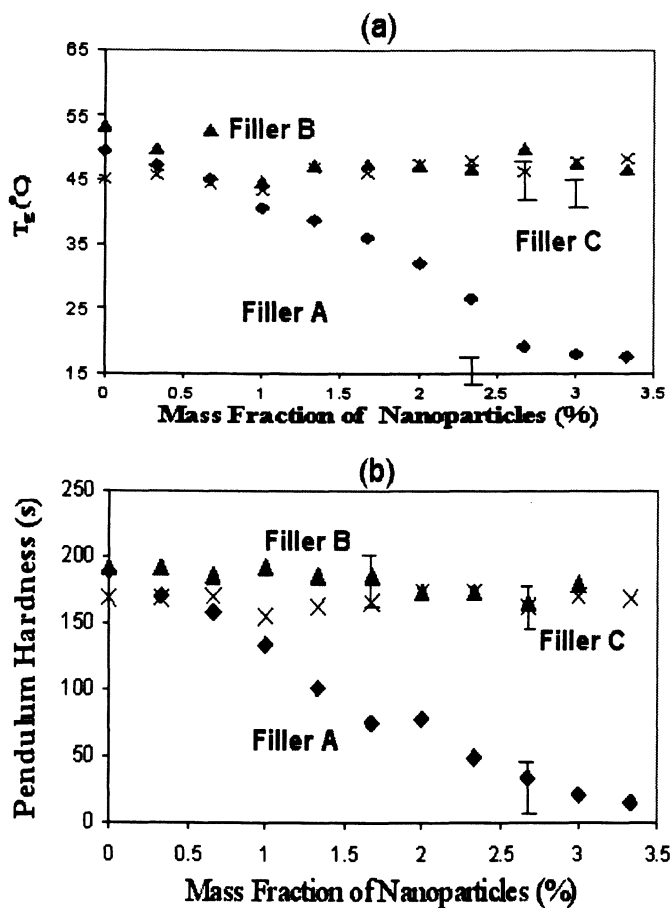
Figure 2.   (a) Glass transition temperature, T_g, and (b) pendulum hardness, as
a function of particle concentration for three nanocomposite coatings consisting
of Filler A, Filler B, and Filler C, respectively. The error bars represent a
single standard deviation.
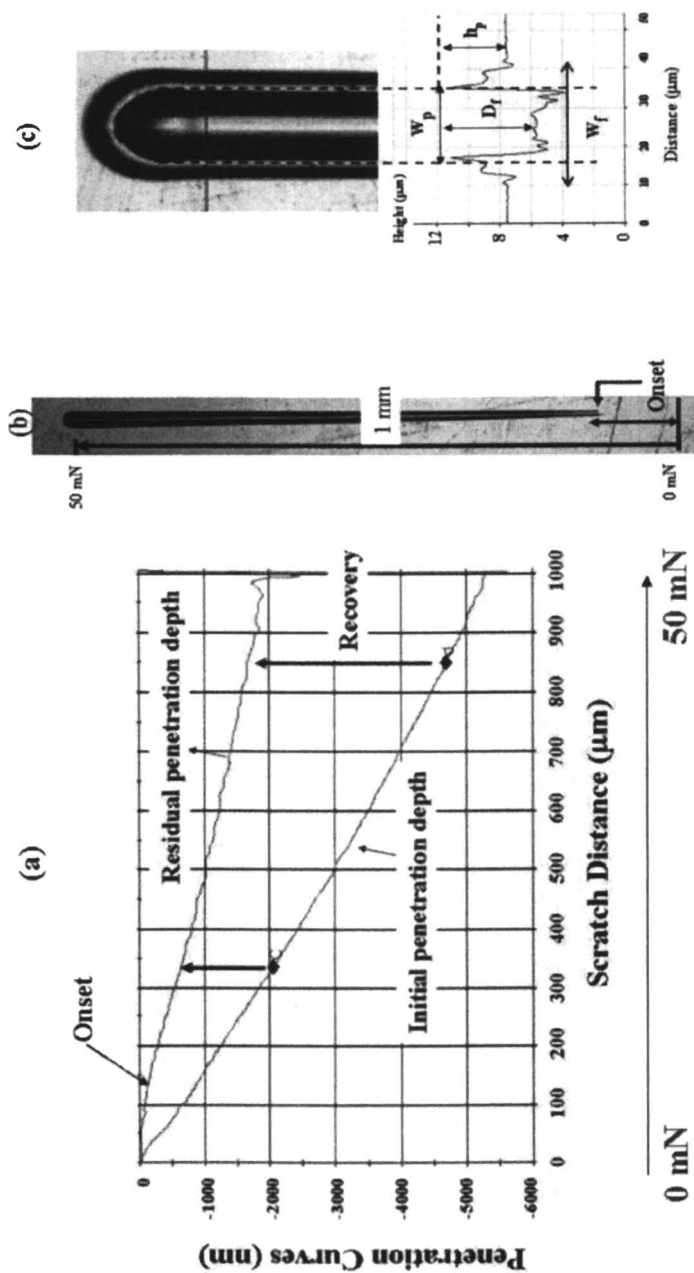
Figure 3. (a) Penetration curves obtained from a P-scratch (progressive scratch) testing on an unfilled PU coating with loads ranging from 0 mN to 50 mN, (b) LSCM image of scratch, and (c) a high magnification LSCM image of the scratch profile near 50 mN. Figure labels are defined in the text.
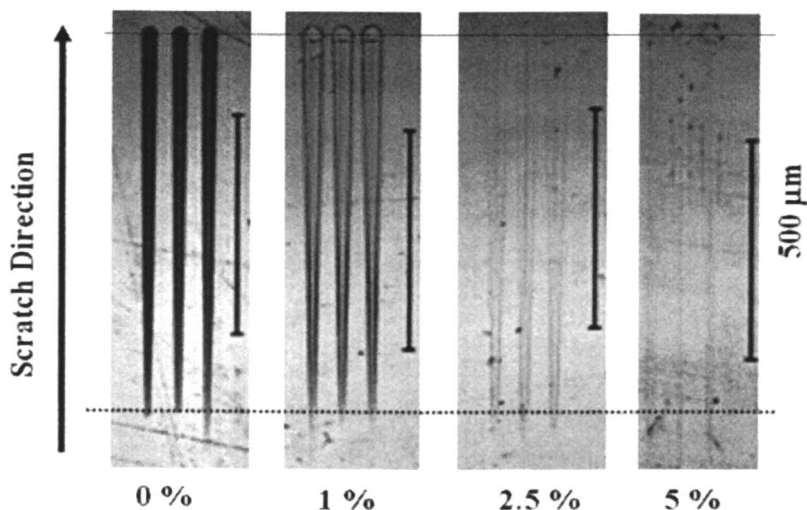
Figure 4. LSCM images of P-scratch profiles from a P-scratch test on an unfilled coating and the nanocomposite coatings containing Filler A at varying particle concentrations. The scale bar represents 500 μm. The dashed lines are for the visual guidelines for the onset force comparison.

The transition observed in LSCM images is more evident in the plot of penetration curves vs. scratch distance (Figure 5). A near linear relationship between initial penetration depth and the applied scratch load (proportional to scratch distance) is observed for the unfilled system. This near linear relationship is common for typical polymer coatings (9-10). Initial scratch penetration depth increases as the particle concentration increases, and no linear relationship between the initial penetration depth and scratch distance (or scratch load) is observed for the Filler A system (Figure 5a). The relationship between the residual penetration depth (Figure 5b) and scratch distance is more complicated. At lower loads (< 20 mN), the residual penetration depth decreases with increasing particle concentration. However, at higher loads (≈ 50 mN), the 1 wt % system has the largest residual penetration depth. Table 1 summarizes the peak-to-peak scratch width and full scratch depth (w_p and D_f) at 49 mN measured by LSCM as well as the aspect ratios of the two values. The aspect ratio increases more than 50 times with an addition of 5 wt % filler compared to the unfilled system. A high aspect ratio of w_p/D_f results in a low visibility of a scratch as expected. Figure 6 shows the scratch profiles of 1 wt % and 2.5 wt % Filler A system. The scratch depths of the scratches in both cases are less than 0.5 μm, which are quite different from the residual depth from nanoindenter output (4 μm to 7 μm). The scratch damage of the 2.5 wt % system at 49 mN is almost invisible.

Table 1. Peak-to-peak scratch width, w_p, full scratch depth D_f, and ratio of w_p/D_f, measured by LSCM at 49 mN for the Filler A system. The error bar represents one standard deviation, and the estimated uncertainties in the w_p/D_f ratio are ±3 %.

Filler A Content (wt %)	w_p (μm)	D_f (μm)	Ratio of w_p/D_f
0	21.3 ± 1.2	5.1 ± 0.7	4.2
1	36.5 ± 2.1	0.4 ± 0.1	91
2.5	41.7 ± 1.5	0.2 ± 0.1	208
5	44.9 ± 2.2	0.2 ± 0.1	224.5

Scratch Testing Results for Filler B System

Figure 7 shows the scratch profiles produced by a progressive-load scratch test for the unfilled PU coating and Filler B system of three different particle concentrations: 0.75 wt %, 1.75 wt %, and 3 wt % fillers. The corresponding initial and residual penetration curves as a function of scratch distance are plotted in Figure 8. The scratch testing protocol is identical to that performed on the Filler A system. The scratch width near 50 mN increases with increasing filler concentrations. Unlike the Filler A system, there is no dramatic change in optical contrast of the scratch with the addition of fillers. However, there is a similar shape transition to that was observed in the case of Filler A system. There is a noticeable transition point (or inflection point) in the plots of penetration curves (see Figure 8). At lower loads (< 10 mN), the results show an increasing penetration depth vs. scratch distance as filler concentration increases. As scratch load increases, there is no clear trend among these systems; however, the position of their inflection point varies. It seems the inflection point moves toward a shorter scratch distance, i.e. a smaller scratch load.

Both the 0.75 wt % and 3 wt % systems begin and end at the same initial and residual penetration depths (see Figure 8). For the 0.75 wt % system, the penetration depth increases gradually with a profile that is similar to that of the unfilled coating up until a scratch length of around 700 μm (at 35 mN scratch load). After this point, the penetration increases rapidly. The penetration depth of the 3 wt % system coating, on the other hand, increases rapidly initially and levels off after a scratch length of around 300 μm (at 15 mN scratch load). For the 1.75 wt % system, the inflection point appears around 300 μm. After the inflection point, the penetration curves decrease rapidly, and level off around 900 μm. It appears that there are three sections in the residual penetration curve of Filler B systems shown in Figure 8: The 1st section: before the inflection point, the system exhibits the same scratch behavior as unfilled coatings. The 2nd section: between the inflection and leveling points, the shape of scratch profile
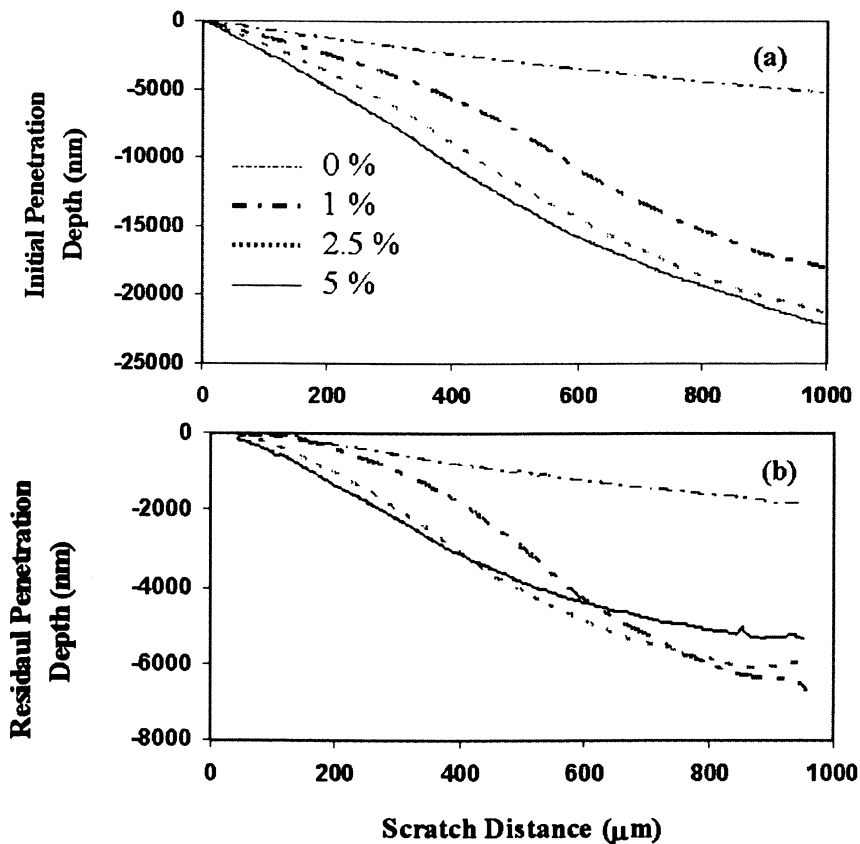
Figure 5. (a) Initial and (b) residual penetration depths obtained from the P-scratch profiles of the Filler A systems as shown in Figure 4. The error bar is smaller than the width of the lines.
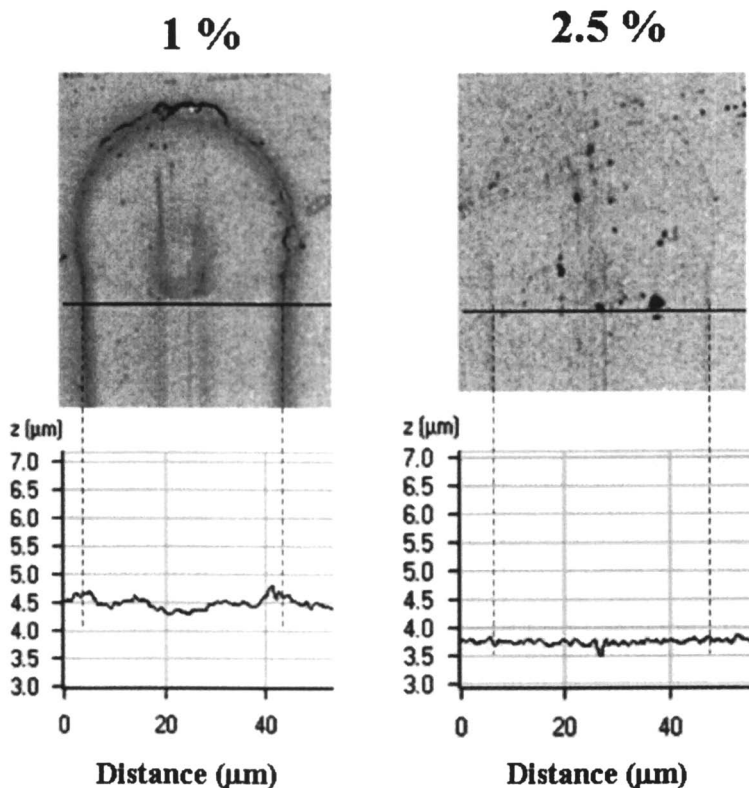
Figure 6. Scratch profiles of 1 wt % and 2.5 wt % Filler A systems near 50 mN load.

changes and the optical contrast decreases as observed in the Filler A system. Finally the 3rd section: beyond the leveling point, a different scratch behavior is observed. The location of the inflection and leveling points strongly depends on the filler concentration.

Figure 9 presents the (a) full (b) and peak-to-peak scratch width as a function of scratch distance. These widths measured by LSCM are defined as in Figure 3c. There is no relationship or trend in curves for the scratch width data among various filler concentrations with increasing scratch load. At lower load (< 25 mN), the 3 wt % system is the worst among all. At higher load (> 35 mN), the 1.75 wt % system has the most severe damage width in both full and peak-to-peak widths. Overall the scratch damage in terms of scratch width increases with the addition of Filler B. It is also noted that scratch shape changes as scratch

500 μm

0 %   0.75 %   1.75 %   3 %
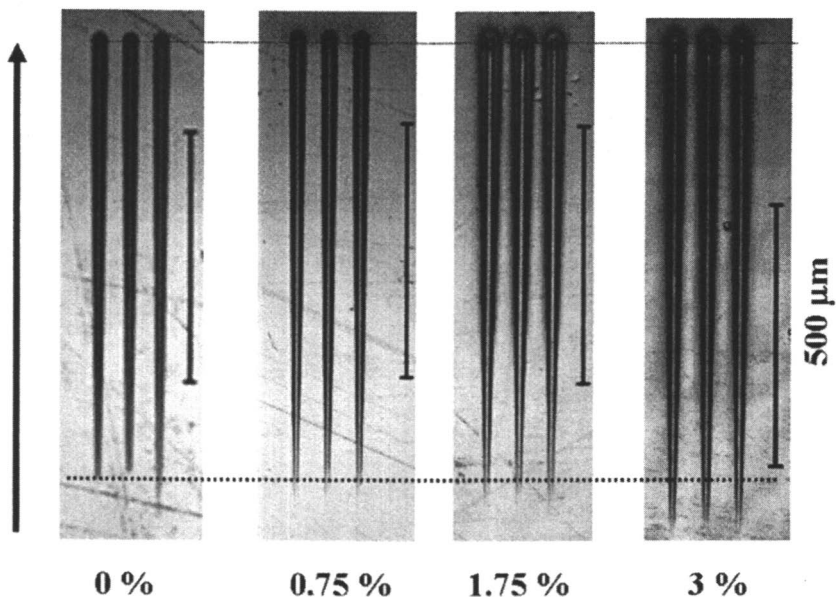
Figure 7. LSCM images of P-scratch profiles from a progressive-load scratch testing on an unfilled coating and nanocomposite coatings containing Filler B with various particle concentrations, as indicated in the graph. The dashed lines are for the visual guidelines for the onset force comparison.

load increases. For example, at lower load (< 25 mN), the 0.75 wt % system has the same scratch width as the unfilled system. For the scratch load > 25 mN, the peak-to-peak width departs from that of the unfilled system while the full width remains similar to that of the unfilled system. This result implies that the overall scratch profile/shape changes with addition of nanofillers.

Figure 10 shows the scratch profiles in LSCM images (2D intensity projection) and the height profiles near 50 mN for the unfilled and three Filler B systems. The profiles are dramatically different, not only in the height profile, but also in the shape of the end of the scratch. This result indicates that the viscoelastic behavior of the system changes with addition of nanoparticles. To quantify how the shape changes, we have measured the scratch width, depths and pile-up height, as listed in Table 2. At 49 mN, the ratios of w_p/D_f and w_p/h_p increase as filler concentration increases. The increase in w_p/D_p ratios are not as large as that was seen in the Filler A system.
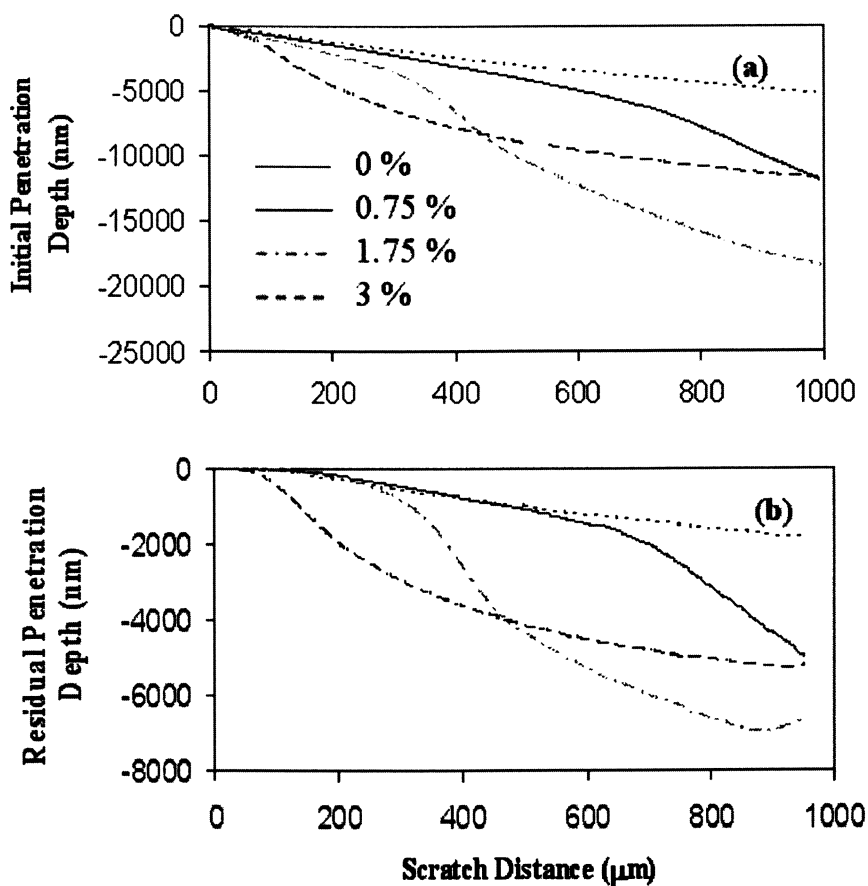
Figure 8. (a) Initial and (b) residual penetration depths from a P-scratch testing on an unfilled coating and the nanocomposite coatings, containing various particle concentrations of Filler B, as indicated in the graph.
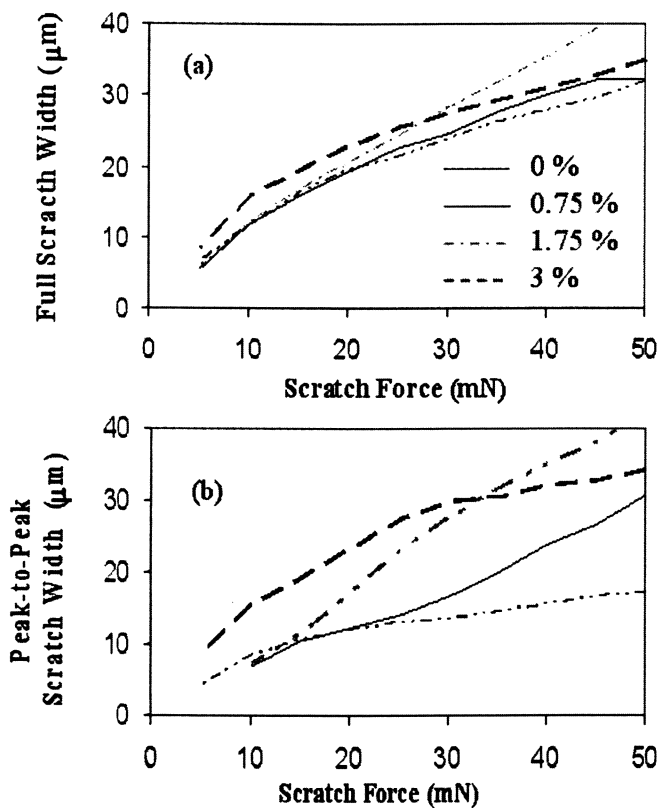
Figure 9. (a) Full scratch width (b) peal-to-peak scratch width as function of scratch force obtained from the P-scratch testing of the unfilled and Filler B systems, containing various particle concentrations of Filler B, as indicated in the graph.
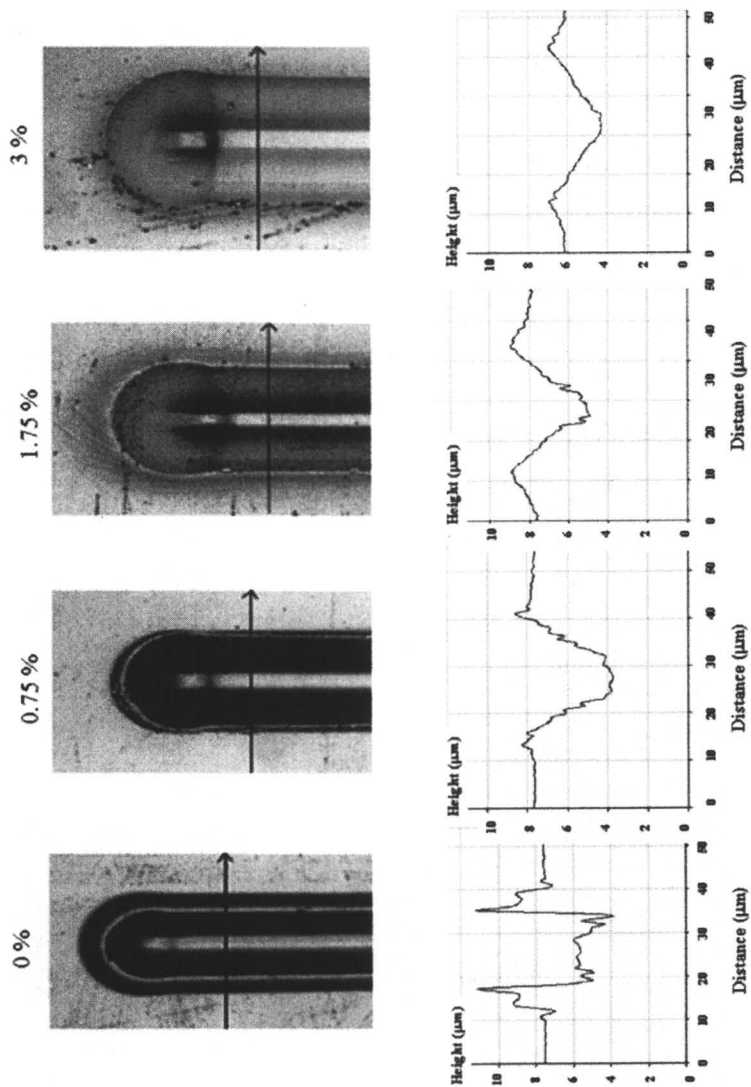
Figure 10. LSCM images of a set of P-scratch (Filler B systems) near the 50 mN force range and the scratch profiles are shown for all four scratches. Each division in height is 2 μm.

Scratch Testing Results for Filler C System

Figure 11 shows LSCM images of (a) scratch profiles and (b) the residual penetration depth generated from a progressive scratch test on Filler C (nano-silica) systems for five different particle concentrations: 0 wt%, 2 wt%, 4 wt%, 6 wt%, and 8 wt%, respectively. It is clear that even with only 2 wt% nanoparticle additives, the scratch damage (vs. scratch depth) decreases significantly. The onset of elastic-plastic transition moves to a lower scratch load but there is no direct relationship between the onset force and the nanoparticle concentration. However, the optical contrast significant decreases (scratch width increases) as nanoparticle concentration increases. The scratch depth increases with increasing particle concentration; however, it is not a linear relationship (see Figure 11b). The relationship between the scratch depth and the applied scratch load as a function of particle concentration appears to be complicated. But the general trend is smilar to the Filler B system. At lower loads (< 10 mN), the results show an increasing penetration depth vs. scratch distance as filler concentration increases. As scratch load increases, there is no clear trend among these systems; however, the position of their inflection point varies. It seems the inflection point moves toward a shorter scratch distance, i.e. a smaller scratch load.

Table 2. Peak-to-peak scratch width, w_p, full scratch depth D_f, pile-up height h_p, ratio of w_p/D_f, and ratio of w_p/D_f, measured by LSCM at 49 mN for the Filler B system. The error bar represents one standard deviation, and the estimated uncertainties in the w_p/D_f ratio are ± 3 %.

Filler B Content (wt %)	w_p (μm)	D_f (μm)	$h_p(\mu m)$	Ratio of w_p/D_f	Ratio of w_p/h_p
0	21.3 ± 1.2	5.1 ± 0.7	3.4 ± 0.7	4.2	6.7
0.75	28. 6 ± 2.0	4.1 ± 0.5	0.6 ± 0.2	6.9	47.7
1.75	40.5 ± 2.5	4.0 ± 0.4	1.3 ± 0.2	10.1	31.1
3	33.3 ± 2.0	2.8 ± 0.2	0.9 ± 0.2	11.9	37

Comparsion of The Three Filled Systems

The scratch behavior of these three filled systems is complicated by filler concentration, and is different in terms of scratch shape, width and depth, pile-up, and the percentage of recovery. Figure 12 shows the LSCM images of scratch profiles generated from a progressive scratch test, with load increasing

from 0 mN to 50 mN at length of 1000 μm, for unfilled coatings and three nanocomposite coatings containing around 2 wt % nanoparticles as indicated in the graph. Clearly, the scratch profiles and patterns of these four systems are dramatically different. Firstly, the Filler A and B (nano-alumina) systems have a lower onset force of the elastic-plastic transition than that of the unfilled and Filler C (nano-silica) systems. This result implies with the addition of nano-alumina changes the elastic or viscoelastic properties of the system at lower scratch loads regardless of the changes in surface modulus. Filler A system has the lowest surface modulus and exhibits less scratch damage (almost invisible in all range of scratch load) in the same scratch test condition. However, the surface modulus of Filler B and C systems are similar (see Figure 1a) but the scratch damage patterns, i.e. scratch behavior, were different in terms of scratch width and depth.

In general, the percentage of recovery is a good indicator for probing/identifying the elastic-plastic transition and understanding the scratch behavior of the materials. Figure 13a shows the relationship between the percentage of recovery and scratch load for these four systems. For scratch loads less than 20 mN, the comparison of the percentage of recovery: Filler B > Filler C > Unfilled > Filler A. And for scratch loads greater than 20 mN, the ranking order is: Filler A > Unfilled > Filler C > Filler B. Therefore, the scratch assessment in terms of recovery depends on the scratch loads.

Alternatively, the scratch width, which usually is the dominant parameter in scratch visibility, can be a good indicator for accessing the scratch resistance. In all filled systems, the scratch width changes as particle concentration increases. The relationship between the scratch width and the applied scratch load as a function of particle concentration is complicated. Figure 13b shows the full scratch width for Unfilled, Filler A, Filler B, and Filler C systems at scratch force of 6 mN and 9 mN. Scratch widths were obtained from a constant force scratch test, and measured by LSCM. At a lower force of 6 mN, only the Filler B (1.75 wt %) and Filler C (2 wt %) systems show less scratch damage than the unfilled system. At a larger force of 9 mN, none of the filled system shows less scratch damage than the unfilled system. Thus, it is not convincing that ranking scratch resistance via scratch width alone is sufficient. In order to accurately and objectively assess scratch resistance, we need to take into account the overall scratch profile and optical contrast of the scratch, which affects the visibility of a scratch.

However, the scratch profiles in terms of shape, i.e. aspect ratio of w_p /D_p changes significantly as shown in Figures 4, 7 and 11. Thus, the characterization of visibility of the scratch damages is extremely complicated. The method of scratch visibility assessment focuses the onset force obtained from Figures 4, 7, 11 at lower scratch loads is not applicable in these nanocomposite systems neither, due to the different optical contrast of the scratch and its neighboring area from different types of plastic deformation patterns at different scratch
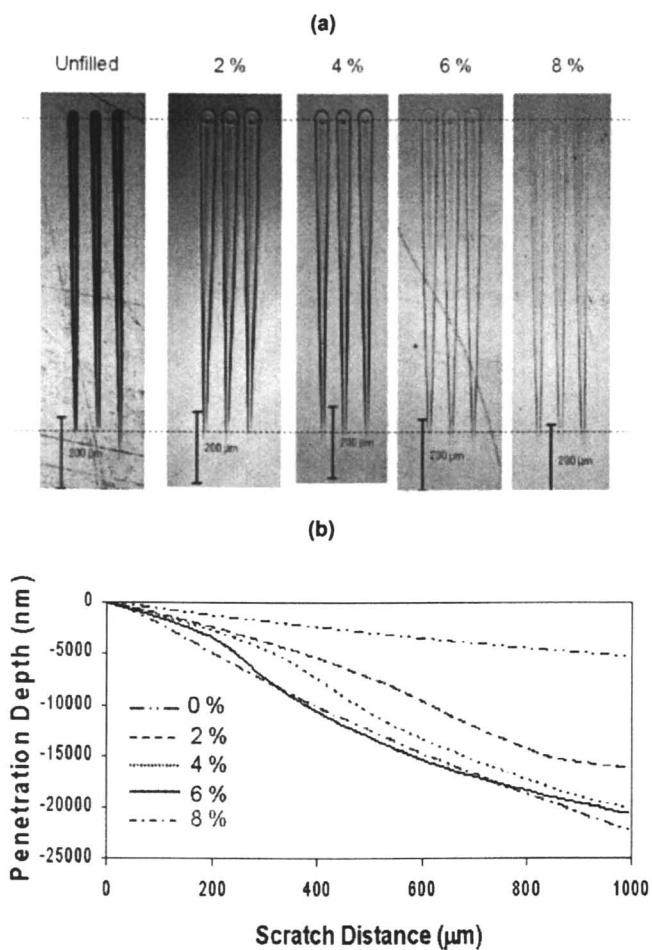
Figure 11. (a) LSCM images of progressive scratch profiles (b) residual scratch depth from a progressive scratch test on an unfilled coating and the nanocomposite coating containingFiller C with various particle concentration, as indicated in the graph.
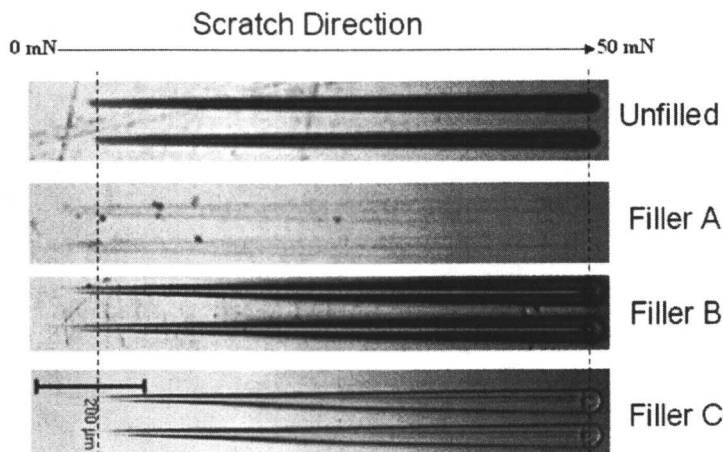
Figure 12. LSCM images of scratch profiles from a progressive scratch test with load increasing from 0 mN to 50 mN for an unfilled coating and three nanocomposite coatings with nanoparticles of Filler A (2.5 wt %), Filler B(1.75 wt %), and Filler C (2 wt %).

loads. Moreover, the visibility of a scratch does not necessarily increase with increasing applied scratch load as we observed earlier, for example, the scratch becomes less visible as the scratch force increases, in the case of the 2.5 wt % Filler A system (also similar in the 1.75 wt % Filler B system). These examples might provide some insight into how inconsistent test results can be within the anti-scratch coating industry when the test conditions (applied scratch load and tip geometry) vary. Truly, the assessment of scratch resistance via scratch visibility depends highly the application of the materials as well as the application environment.

Concluding Remarks

We have investigated the effect of nano-alumina and nano-silica particles on the scratch behavior of a polyurethane coating through single-probe scratch testing via an instrumented indentation system. The addition of nanoparticles affects strongly on surface mechanical properties (surface modulus and hardness) and has a slight impact on the bulk mechanical properties, except the Filler A system due to a plasticizing effect of dispersion medium. The Filler A system has the lowest surface modulus and exhibits less scratch damage (almost invisible at high scratch loads) in the same scratch test conditions. A transition

Figure 13. (a) Percentage of recovery from a P-scratch test with load increasing from 0 mN to 50 mN; and (b) the scratch width obtained from constanct load scratch at a scratch load of 6 mN and 9 mN, for an unfilled coating and three nanocomposite coatings with nanoparticles of Filler A (2.5 wt%), Filler B (1.75 wt %), and Filler C (2 wt%).
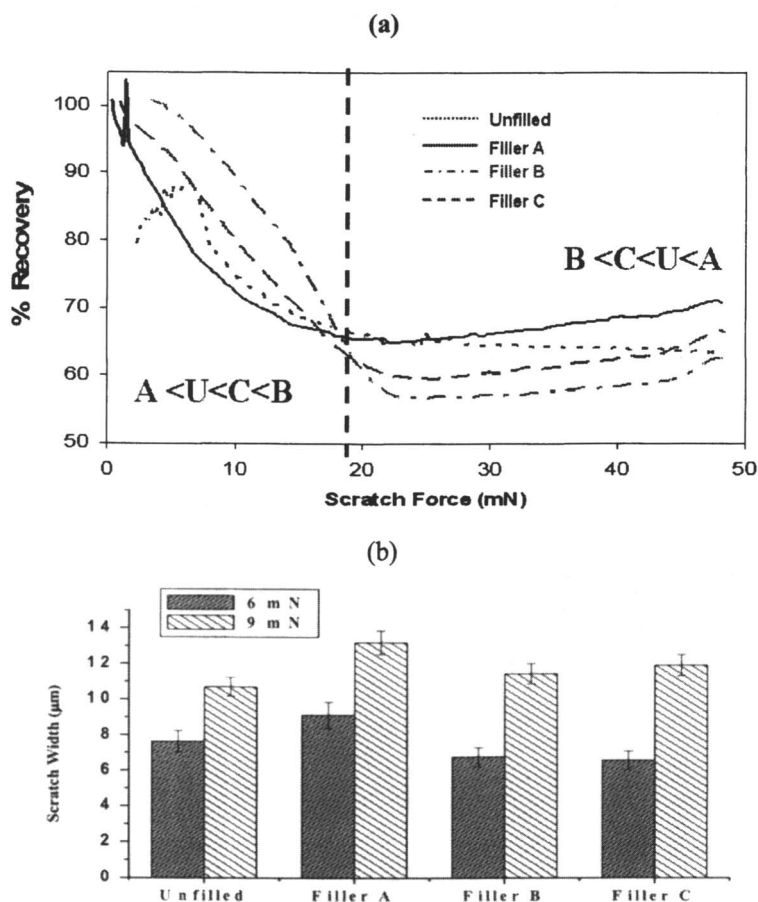
from the unfilled scratch profile to a wider, shallower profile was observed, and the location of this transition point moved to lower scratch load as filler concentration increased. The onset of the elastic-plastic transition decreased with increasing filler concentration; however, scratch visibility at higher scratch loads is dramatically reduced. This suggests that the assessment of scratch resistance depends highly on the force range applied to the filler systems.

The changes in scratch profile (via the penetration depth) of the Filler B and Filler C systems were similar to that of the Filler A system. The scratch profile can be divided into three sections: the 1st section: before the inflection point, the system exhibited the similar scratch behavior to that of the unfilled coatings; the 2nd section: between inflection and leveling points, the shape of scratch profile changed and the optical contrast decreased, and the 3rd section: beyond the leveling point, a different scratch behavior was observed. The location of inflection and leveling points strongly depended on the concentration of the fillers. This result shows that the scratch behavior of the coatings depends strongly on the concentration and types of nanoparticles. Expanded studies on the nanoparticle filled systems of different types of nanoparticles, surface treatments, dispersant with/without particles are ongoing to investigate the role of nanoparticles in the complex scratch behavior of nanoparticle filled systems.

Reference

1. FSCT Symposium on Nanotechnology in Coatings: Realizing the Potential, Seattle, WA (2005).
2. Fernando, R. H., *JCT CoatingsTech*, **2004**, *1*(5), 32-38.
3. VanLandingham M. R., "Sctach and Mar Resistance of Polymeric Materials," in *Service Life Prediction-Challenging the Status Quo*, J.W. Martin, R.A. Ryntz, and R.A. Dickie, Editors, Federation of Societies for Coatings Technology, Chapter 25, 349-363 (2005).
4. Sung, L., Drzal, P. L., VanLandingham, M. R., and Forster, A. M. "Metrology for Characterizing the Scratch resistance of Polymeric Coatings Through Optical scattering ," Chapter 5, PP. 102-123, in *Scratching of Materials & Applications,* edited by Professor Sujeet Kumar Sinha, Elsevier, London (2006)
5. Floryancic, B., Brickweg, L. Comer, J., Sung, L. Forster, A., and Fernando, R.H., "Effects of Alumina and Silica Nanoparticles on Automotive Clear-Coat Properties," *Polymers Preprint, 232nd American Chemical Society Meeting*, Sept. 10-14 (2006).
6. Fisher-Cripps, A.C., *Nanoindentation* (Springer, 2004).
7. VanLandingham, M.R., "A Review of Instrumented Indentation," *Res. Natl. Inst. Stand. Technol.*, **2003**, *108*(4), 249-265.

8. VanLandingham, M.R., Chang, N.K., Drzal, P.L., White, C.C., Chang, S.H., "Viscoelastic characterization of polymers using instrumented indentation. I. Quasi-static testing," *J. of Polymer Sci. Part B-Polymer Physics*, **2005**, *43* (14), 1794-1811.

9. VanLandingham, M. R., Chang, N.K., Wu, T. Y., Sung, L., Jardret, V.D., and Chang S.H., "Measurement Approaches to Develop a Fundamental Understanding of Scratch and Mar Resistance." *JCT Research*, **2004**, *1*(4), 257-266.

10. Sung, L. Drzal, P. L., VanLandingham M. R., Wu, T-Y., and Chang, S.H., "Metrology for Characterizing Scratch Resistance of Polymer Coatings," *JCT Research*, **2005**, *2* (8), 583-589.

11. Corle, T.R. and Kino, G.S., *Confocal Scanning Optical Microscopy and Related Imaging Systems*, 37-39 (Academic Press 1996).

12. Sung, L., Jasmin, J., Gu, X., Nguyen, T., and Martin, J.W., "Use of Laser Scanning Confocal Microscopy for Characterizing Changes in Film Thickness and Local Surface Morphology of UV Exposed Polymer Coatings," *JCT Research*, **2004**, *1*(4), 267-276.

Chapter 13

Effect of Organoclay on the Physical Properties of UV-Curable Coatings

Funda Inceoglu, Cahit Dalgicdir, and Yusuf Z. Menceloglu

Faculty of Engineering and Natural Sciences, Material Science and Engineering Program, Sabanci University, 34956 Orhanli, Tuzla, Istanbul, Turkey

The combination of UV-curing and nanocomposite technology has been studied to produce cost-effective coatings with superior physical and mechanical properties. The clay was modified with dimethyl dihydrogenated-tallow quaternary ammonium salt and made organophilic. The effect of the organoclay(2-10 phr) on curing rate, mechanical, thermal and physical properties of a urethane-acrylate coating has been determined. X-ray diffraction analysis, AFM, SEM and TEM images as well as the tensile properties of different formulations have confirmed the uniform distribution of organoclay in polymer matrix. At 3 phr organoclay addition, the UV-cured film exhibited the best mechanical performance due to the formation of both intercalated and exfoliated morphologies. Curing time was reduced and the initial thermal decomposition temperature shifted 50°C to higher temperature by the incorporation of small amount of organoclay. The nanocomposite coating was also found to be more resistant against scratching compared with clay-free coating.

© 2009 American Chemical Society

255

Introduction

There is a growing interest today in polymeric nanocomposites because of the superior properties of this type of material. The layered smectite clay like montmorillonite is the most common type of inorganic filler for the preparation of such nanocomposites because the starting clay materials are easily available and they usually exhibit remarkable improvements in material properties when compared to virgin polymer or conventional microcomposites. Several studies have indicated that the addition of a few percentage of layered silicates resulted in enhanced mechanical, thermal, and barrier properties of the polymeric matrix material(*1-5*). The main reasons for these improvements are the clay layer thickness, which is on the order of 1 nm and very high aspect ratios (e.g. 10-1000). Therefore, when the clay layers are properly dispersed throughout the matrix with the possible mechanisms of intercalation and/or exfoliation, a few weight percent of clay creates a much higher surface area for polymer-filler interactions than do conventional composites. In order to achieve the good dispersion and thus enhanced properties, molecular structure of the silicate filler should be adjusted for the polymer used; otherwise phase separation may prevent nano-sized dispersion and lead to the formation of micron-sized agglomerates. The effect of adjustment includes the attenuation of adhesive forces between the silicate layers by the addition of alkyl ammonium salts. The resulting clay is known as organoclay(*6*).

The UV-curing process is used commonly for applications in the coating and ink industries because of its many advantageous properties offered. Among these benefits, the ultra-fast, solvent-free, ambient temperature curing are the most important ones which lead to an energy-saving up to 70%. The formulations for UV-curing process have three essential components: photoinitiator, oligomer or prepolymer, and reactive diluents. A photoinitiator is necessary to generate free radicals that will attack the double bond of the oligomer and start the chain reaction. There are several types of oligomers; the most commonly used are epoxy acrylates, urethane acrylates, unsaturated polyesters, polyester acrylates, and polyether acrylates(*7-14*). The wide use of urethane acrylates is due to their versatile chemistry that offers many different possibilities to the formulator. In this work, an aromatic urethane diacrylate was used. Generally, an aromatic urethane diacrylate gives good hardness, toughness, water resistance and gloss retention and it is used in applications like clear coating for paper, screen and metal decorating inks and coatings for rigid and flexible plastics. Reactive diluents are functional monomers that are used to adjust the properties of the solution like the viscosity. They are also added to regulate the volatility, odor, and solubility of the resulting films.

Recently, the UV-curable nanocomposite coating systems have attracted great attention due to their combined advantageous of both superior mechanical

properties and cost effective preparation technique(*15-23*). Decker et al. first demonstrated the preparation of UV curable acrylate-bentonite nanocomposite materials and suggested that an exfoliated structure was formed in the formula containing organoclay as evidenced by the absence of a X-ray diffraction (XRD) peak. They also observed higher transparency in the nanocomposite compared to the microcomposite obtained with the untreated bentonite(*15*). Benfarhi et al. synthesized different types of nanocomposite materials by photo-initiated crosslinking polymerization of epoxy, vinyl ether and acrylate-based resins containing 3 wt % of an organoclay(*16*). They showed that the glass transition temperature (T_g) of nanocomposites was lower and the materials were more flexible than the corresponding microcomposites obtained with untreated clay. The incorporation of silicate nanoparticles was also found to cause a severe drop of the gloss of the UV-cured polymers. Keller et al. examined the preparation and performance of polymer nanocomposites made of organoclay and a UV-cured polyurethane-acrylate(*17*). The nanocomposite materials exhibited superior tensile strength and elongation at break but the addition of clay or organoclay had hardly any effect on Young's Modulus and on T_g values. They also reported a significant reduction on gloss values of UV-cured coatings with the addition of organoclay and attributed this observation to an increase in surface roughness upon the addition of the clay nanoparticles. Shemper et al. investigated the effect of synthetic clay (Laponite) on the photo-polymerization kinetics of methyl α-hydroxymethylacrylate (MHMA) systems and suggested that, in the presence of clay, earlier onset of autoacceleration was observed, higher rates of polymerization were achieved, and high final overall conversions were reached(*18*). Higher rates and increase in conversions were also realized as the clay content increased in the medium. Similar results were also reported by Uhl et al. in their studies related with UV-curable urethane acrylate films containing organoclay(*19*). Decker et al. have developed a novel method to synthesize highly resistant nanocomposite polymers by photo-initiated polymerization of multifunctional acrylate or epoxy monomers containing small amounts (3 wt%) of an organoclay(*20*). The highly crosslinked nanocomposite polymers were found to be quite resistant to organic solvents, moisture and weathering, as well as to scratching. The loss of gloss was attributed to a surface roughness created by the clay nanoparticles. The nanocomposite surface was reported to be less slippery due to the increased roughness. Fogelstrom et al. prepared nanocomposites from the hyperbranched polyester Boltorn H30, acrylated to 30% and 70%, and modified Na^+-montmorilonite(*21*). They revealed that films prepared from 30% acrylated Boltorn H30 with clay added after the acrylation exhibited a harder surface, better scratch resistance, better adhesion to metal substrates and a small increase in flexibility. Uhl, et al. studied the structure and properties of UV curable epoxy acrylate films reinforced with nanoclay(*22*). The intercalated structures were observed and the mechanical

properties were found to be improved for all films containing modified or unmodified clay. It was suggested that property enhancements were not only dependent upon the nanoclay but the structure of the polymer and how the two interact. Tensile strength, Young's Modulus and elongation at break showed increases up to about 50%, 50% and 20%, respectively, due to the addition of various clays. In very recent work of Wang, et al., the preparation of a UV-curable intercalated/exfoliated nanocomposite resin that was applied to an organic light-emitting device (OLED) packaging was demonstrated(23). Better thermal stability, lifetime and moisture properties were observed in nanocomposite samples.

The present work investigates the effect of organoclay on mechanical, thermal, scratch resistance, and flame-retardant properties of UV-curable acrylate films. The structure-property relationship is discussed in a comprehensive manner. This study is also unique in illustrating the highest improvements, especially in mechanical properties of UV-curable acrylate resins, which were achieved up to now by using organically modified clays.

Experimental

Materials

Aromatic urethane diacrylate, supplied from UCB Chemicals (Belgium), was used as the oligomer matrix. 1,6-Hexanediol diacrylate (HDDA) and N-vinyl pyrrolidone (NVP) as reactive diluents were supplied by BASF (Germany). Trimethylol propane triacrylate (TMPTA) from UCB Chemicals was used as a cross-linker. The photoinitiator is 2,4,6 trimethyl benzoyl diphenyl phosphine oxide (TPO) and was supplied by Ciba Specialty Chemicals (Switzerland). Clay was obtained from Karakaya Company and modified with dimethyl dehydrogenated-tallow quaternary ammonium salt supplied by Kalekimya Company. The hydrogenated tallow consists of ~ 65% C18, ~30% C16 and ~5%C14 and the counterion is chloride.

Organoclay Preparation

40 g of bentonite having cation exchange capacity (CEC) of 64 meq/100 g was dispersed in deionized water and kept at room temperature until the red (ferric oxide) and white (calcium bentonite) precipitates have been observed. The upper part of the dispersion, which is rich in sodium bentonite with CEC of 104 meq/100 g (determined by methylene blue test), was then treated with dimethyl dihydrogenated-tallow quaternary ammonium salt for 6 hrs at 80°C.

The weight ratio of clay:quaternary salt was kept at 1:1. The organoclay was then filtered, washed with methanol and dried in an oven.

Coating Preparation

The liquid formulation of resin containing 45 wt % aromatic polyurethane diacrylate, 30 wt% HDDA, 10 wt % TMPTA, 10 wt % NVP and 5 wt % TPO was prepared for clay-free resin. The clay was dried in a vacuum oven at 120°C for 24 hours and then dispersed in the range between 2-10 phr (parts per hundred weight of resin) for preparing nanocomposite coating formulation. The solution was stirred at room temperature for half an hour and then put into ultrasonic bath for an hour in order to disperse the clay particles homogeneously in the resin. The liquid resin was then applied on glass plates and exposed to UV-radiation for 60 min. from a photoreactor consisting of eight TL 6W/08/F6T5 BLB–type UV lamps (6W, Phillips; The Netherlands).

Characterization

The progress of photo-polymerization was determined by gel content measurements. The weight loss after 48 hours of extraction in acetone using soxhlet apparatus was calculated for the determination of gel content. The level of interlayer separation of clay platelets were measured by X-ray diffraction (XRD) analysis conducted using a Bruker AXS-D8 diffractometer operating at 40kV and 40 mA. The mechanical properties of the coating films (at least 5 samples from each formula) were measured via Instron Model No. 5565 at a cross speed of 5 mm/min. A Netzsch DSC 204 was used to determine glass transition temperature(T_g) of the samples. The samples were cyclically heated and cooled from -50 to 200°C, using a heating rate of 5K/min. and cooling rate of 50K/min. For the morphology observations, Leo G34-Supra 35VP scanning electron microscope (SEM) was used. AFM images were taken using Digital Instruments NanoScope IIIa. Samples for TEM analysis was prepared using a Nova ultramicrotome equipped with a diamond knife and the sections were collected on formvar/carbon 300-mesh copper grids. The TEM micrographs were taken at an acceleration voltage of 200kV. The thermal properties of the films were analyzed using Netzsch STA 449C with a heating rate of 20 °C / min. under air atmosphere. The gloss measurements were conducted on a Minolta Multigloss 268. The effect of clay on the flame retardancy of the coatings was determined via home made limiting oxygen index (LOI) apparatus according to ASTM D 2863. Scratch testing was done by performing 50 double rubs using 0000 grade steel wool. The percentage of gloss values maintained after the scratch test was measured for both clay free and nanocomposite coatings. The

surfaces were analyzed by SEM to determine the depth and the number of the scratches formed.

Results and Discussion

In order to achieve layered dispersion of clay in polymeric matrix, the molecular structure of the filler should be adjusted for the polymer used. In the present study, this adjustment was achieved by exchanging alkali cations between the clay layers with alkyl ammonium salt. This treatment leads to the widening of the clay galleries, as shown by the shift of the peak belonging to d_{001} plane toward the smaller angles of x-ray diffraction pattern (Figure 1). The clay galleries were opened up from 1.2 nm to 1.9 and 3.3 nm after the treatment with alkyl ammonium salt. The peak of original clay at $2\theta = 7°$ was still present in organoclay, but the intensity was very low. When organoclay was incorporated into the acrylate resins, the characteristic peaks at $2\theta = 7°$ and $2\theta = 4.5°$ completely disappeared from the spectrum for the samples with 2-7 phr organoclay, while the peak at $2\theta = 4.5°$ was retained in sample with 10 phr filler. In all organoclay containing films, most of the clay galleries were opened up to 4.0 nm, indicating the highly intercalated morphology. The detector peak broadening at around $2\theta = 2.0°$ for the sample containing 3 phr organoclay was attributed to the presence of both intercalated and exfoliated clay layers (Figure 2).
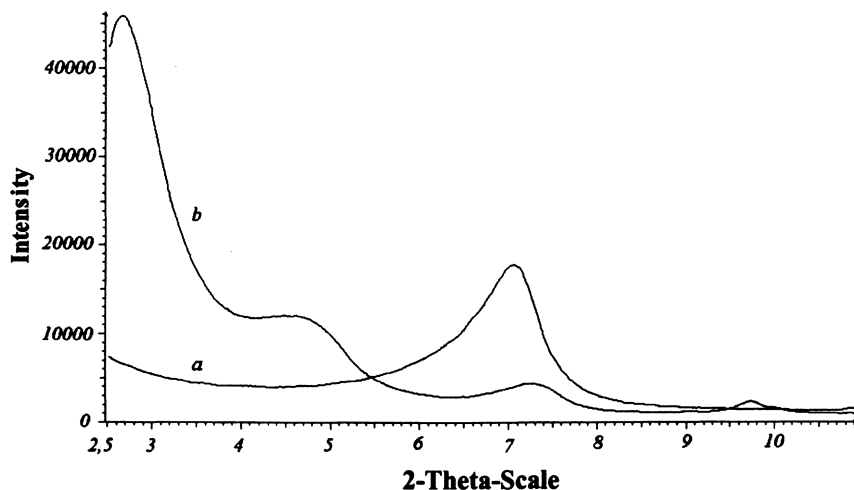
Figure 1. X-ray diffraction profile of (a) pure clay, (b) organoclay.
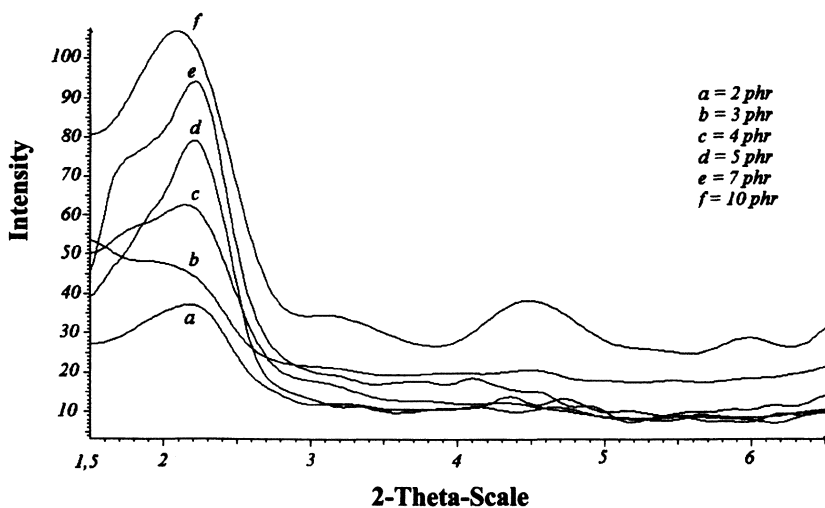
Figure 2. X-ray diffraction profile of nanocomposite films with 2-10 phr organoclay.
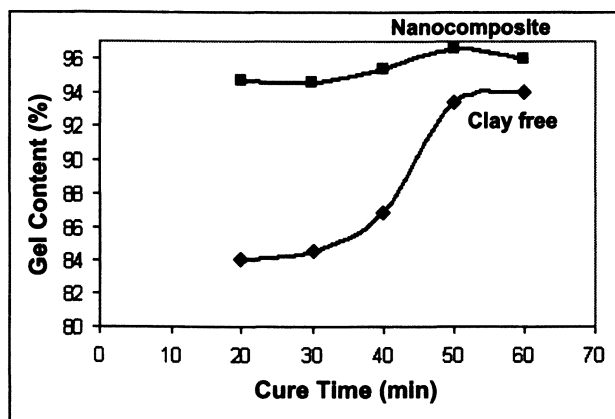
Figure 3. Gel content versus UV-radiation exposure time curves for clay-free and nanocomposite (3 phr organoclay) samples.

The effect of organoclay on the progress of polymerization was determined from the gel content measurements. Figure 3 shows gel content versus time graph for clay-free and nanocomposite films. It was observed that the gel content increased rapidly with the time of UV exposition for clay-free resin and reached a plateau at 50 minutes, after which the change was very little due to the mobility restriction upon gelation. The final gel content is 94% after 60 minutes of radiation. A faster polymerization was observed in nanocomposite films, reaching the same level of crosslink density at a shorter time of UV-radiation. This behavior can be attributed to two different mechanisms. First of all, strong interaction between polymer matrix and silicate layers may occur through the formation of hydrogen bonds which can act as a physical crosslink. Secondly, clay layers may reduce the rate of termination by inhibiting the mobility of polymer chains, resulting in increased rate of polymerization(12). The change in gel content was very low after 20 minutes of radiation in nanocomposite film.

Tensile strength, modulus and strain properties of UV-cured coating films as a function of organoclay content are given in Figure 4. These mechanical properties are closely related to the level of filler dispersion inside the polymer matrix. It can be seen that there is an increase in all the properties with the addition of organoclay. The properties are superior in nanocomposite films, even at 10 phr filler loading. The peak in tensile properties was attained with 3 phr organoclay addition. This observation is related with the layered dispersion and the optimum amount of reinforcing filler in that sample. It is known that each exfoliated layer behaves as single reinforcing filler and affects the tensile properties to a great extent.

In general, the elasticity of most of the thermoplastic materials decreases with the incorporation of inorganic filler. To the contrary, in thermoset films, the flexibility can be enhanced due to the plasticizing effect of long alkyl chains in quaternary ammonium salts(24,25). This effect seems to be much more significant in the nanocomposite film with 3 phr organoclay. We attribute this behavior to the presence of exfoliated clay layers since most of the long alkyl chains are in the polymeric matrix, and as a result, they are freer to move compared to intercalated morphology, in which they reside between the clay layers. This observation is consistent with the glass transition temperatures (T_g) of the films, determined from DSC analysis (Figures 5 and 6). The lowest T_g value belongs to the nanocomposite film with 3 phr organoclay because of the presence of dangling chains with higher degree of freedom that contribute to better flexibility.

Scanning electron microscopy (SEM) and atomic force microscopy (AFM) are the valuable tools to study the dispersion level of fillers in polymer matrix. Figures 7 and 8 illustrate SEM and AFM images of nanocomposite films, respectively. In addition to nano-sized clay particles, small amount of agglomerates were also observed by SEM in the samples containing 5 and 10 phr organoclay. It was not easy to produce a good image from 3 phr organoclay loaded film due to very fine,

layered dispersion. Thus, AFM analysis was conducted to see the dispersion of clay platelets in this sample. The images have confirmed the presence of finely distributed clay platelets in acrylate resin without the formation of any clay agglomerates (Figure 8).

Transmission electron microscopy (TEM) was used to further investigate the nanocomposite structures. Figure 9 shows the TEM micrographs of the sample containing 3 phr organoclay. The micrographs confirmed the homogeneous dispersion of clay layers and the presence of both intercalated and exfoliated morphologies. The d-spacing of clay layers in intercalated structure, which is about 4 nm, corroborates the XRD results given in Figure 2. In the case of nanocomposite sample with 5 phr organoclay, only intercalated morphology was observed with the d-spacing of between 2.8 and 4.2 nm (Figure 10). There were also some clay agglomerates in the sample as they were previously observed in the SEM images (see Figures 7a and 10).

Thermal stability and decomposition behavior of various crosslinked coatings were determined by thermogravimetric analysis (Figure 11). The initial decomposition temperature shifted 50°C to higher temperature with the addition of only 2 phr organoclay. The initial thermal stability is related to the homogeneous distribution of the clay layers throughout the matrix. Each layer in the matrix behaves like a thermal insulation layer and increases the path length of the volatile products. Further addition of filler affected the thermal stability only little compared to that of 2 phr that was attributed to the presence of sufficient barrier layer at this filler content. The decomposition occurred in two steps for neat resin; the main decomposition of the sample took place between 220°C and 400°C and the further decomposition of the macromolecules, formed in the first stage, was observed at temperatures higher than 400 °C. In nanocomposite samples, the decomposition occurred in a single step due to the delayed first decomposition.

The change in char yield with organoclay can be seen in Table 1. The percent change in char yield was larger than the amount of organoclay added, confirming the char promoting effect of the filler. The char yield was not affected much from the organoclay content after 3 phr. This is probably due to the sufficient amount of clay layers acting as thermal insulators at this filler content.

The effect of organoclay on flame retardancy was evaluated by limiting oxygen index (LOI) test method and the results are given in Table 1. It is known that clay cannot stop burning of the polymers by itself, but it decreases the generation of toxic gases, delays the ignition and provides a heat barrier. In our system, the minimum oxygen amount in the mixture of nitrogen and oxygen gases just needed to support the flame of ignition was found to increase from 19% to 20% by the incorporation of 2 phr organoclay. The effect of further addition of filler on flame retardancy was not detectable. This behavior is consistent with the thermal stability results and further indicates the present of sufficient amount of clay layers acting as thermal insulators at this level of filler content.
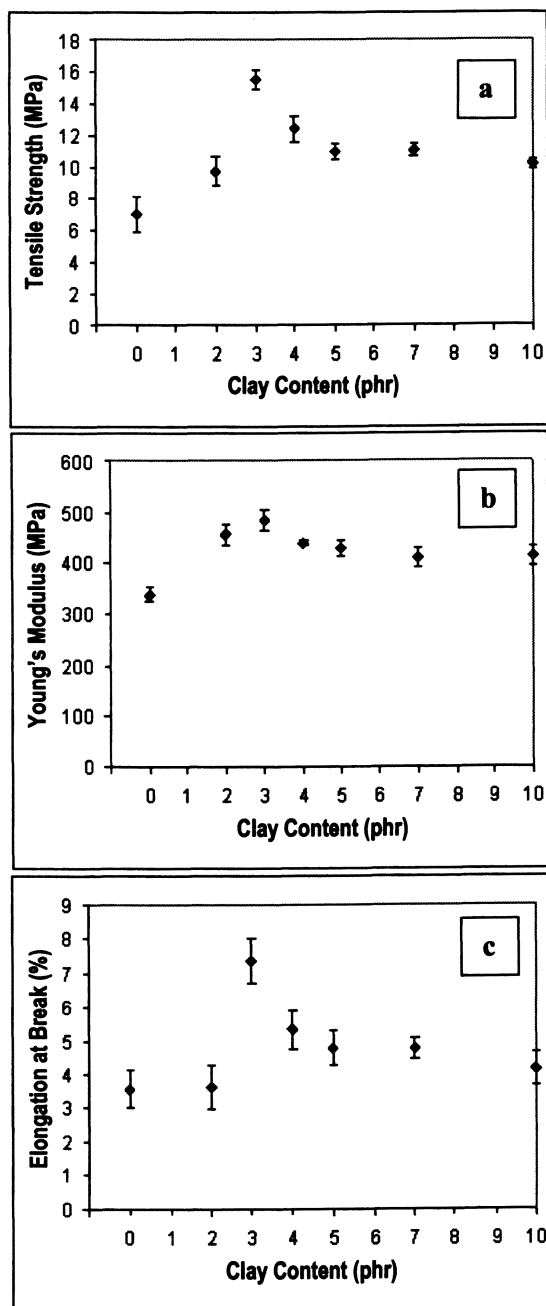
*Figure 4. Tensile properties of acrylate films as a function of organoclay
content: (a) Tensile Strength; (b) Young's Modulus; (c) Elongation at Break.*

DSC /(uV/mg)

↓ exo
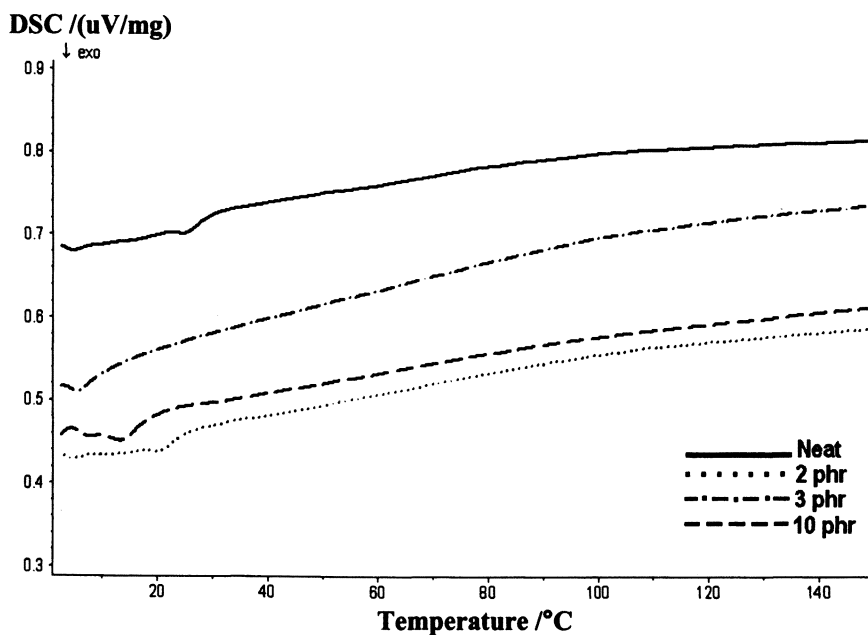
Figure 5. DSC thermograms of neat and organoclay containing acrylate samples.
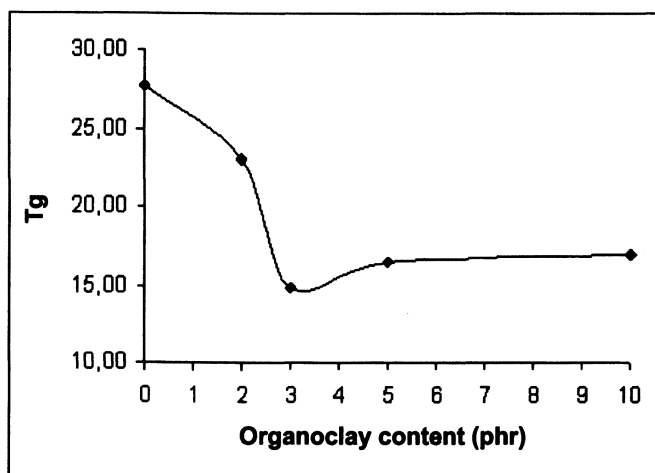
Figure 6. Change in T_g of acrylate samples with organoclay content
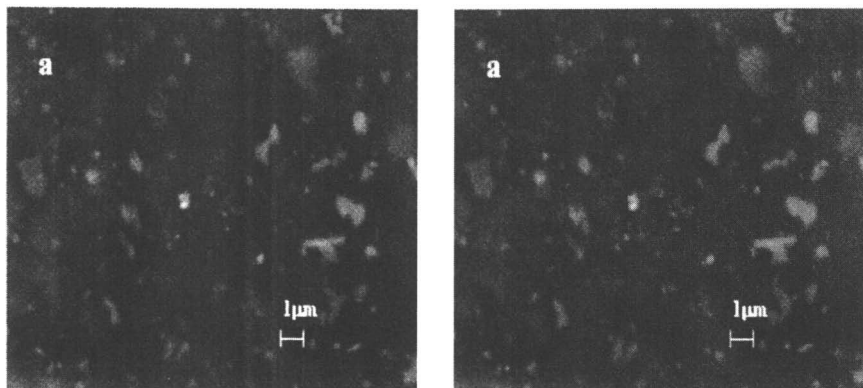
Figure 7. SEM images of acrylate samples having (a) 5 phr, (b) 10 phr, of organoclay.
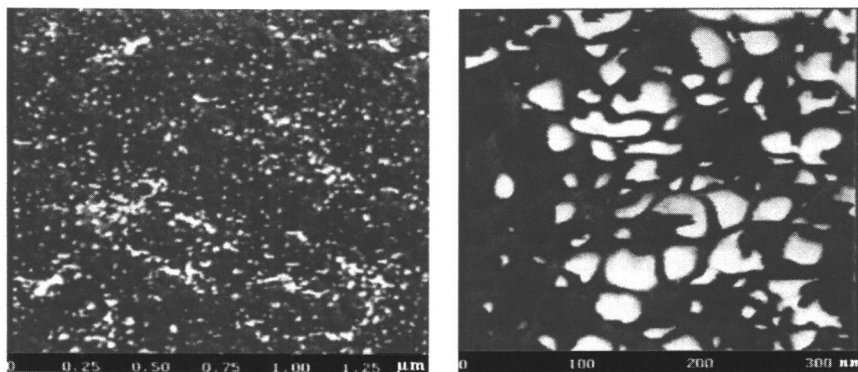
Figure 8. AFM images of nanocomposite sample with 3 phr organoclay
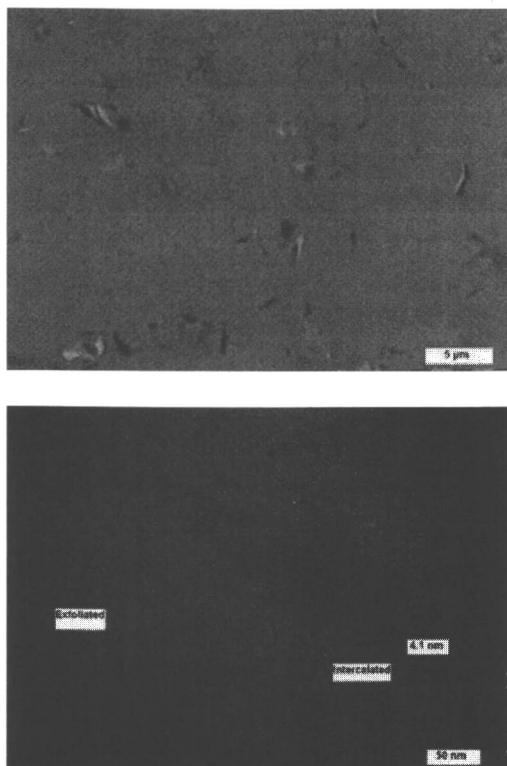
*Figure 9. Transmission electron micrographs of acrylate nanocomposites
with 3 phr organoclay.*

In order to investigate the surface properties of the samples, gloss and abrasion resistance measurements were performed. It can be clearly seen that addition of organoclay as small as 2 phr sharply reduces the gloss of the UV-cured coatings (Table 2). The inorganic fillers usually creates surface roughness and this results in a significant amount of light to be dispersed rather than reflected from the surface. This matting effect of clay is desired for some applications like wood furniture and floor finishes(3). It is advantageous that clay can provide this at a lower level of loading than the conventional matting agents.

Resistance of the coatings to abrasion was determined by taking SEM images and measuring the gloss values after performing 50 cycles of steel wool abrasion test. The number and the width of the scratches are larger in clay-free sample when compared to the nanocomposite sample. To the contrary, the nanocomposite film surface exhibited less scratch damages (Figure 12). This can be related with the surface roughness created by nanofiller which contributes to
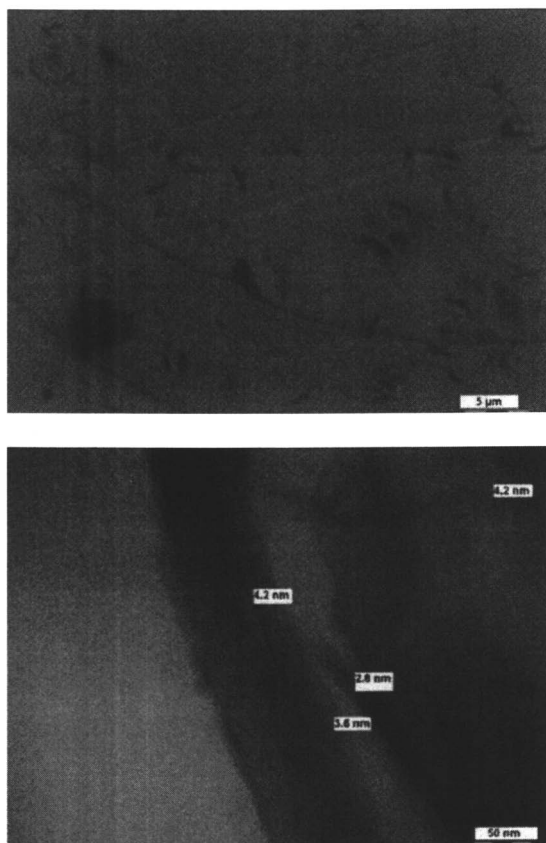
*Figure 10. Transmission electron micrographs of acrylate nanocomposites
with 5 phr organoclay.*

TG /%
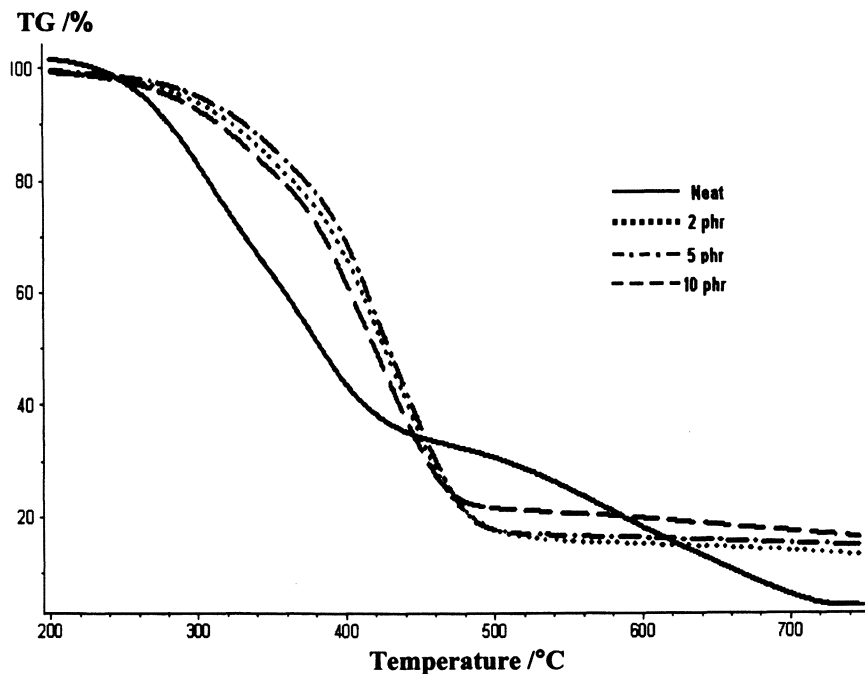
Figure 11. TGA of clay-free acrylate and acrylate nanocomposite coatings.

Table 1. Effect of organoclay content on char yield and limiting oxygen index (LOI).

Organoclay Content (phr)	Char Yield (%)	LOI (%)
0	4.51	19
2	10.66	20
3	12.27	20
4	12.91	20
5	13.74	20
7	14.51	20
10	14.45	20

Table 2. Influence of the clay content on the gloss* of acrylate coating films.

Organoclay Content (phr)	20° Gloss Normalized (%)
0	100
2	52
3	58
4	36
5	27
7	16
10	17

* Gloss measurements were made according to ASTM D523.
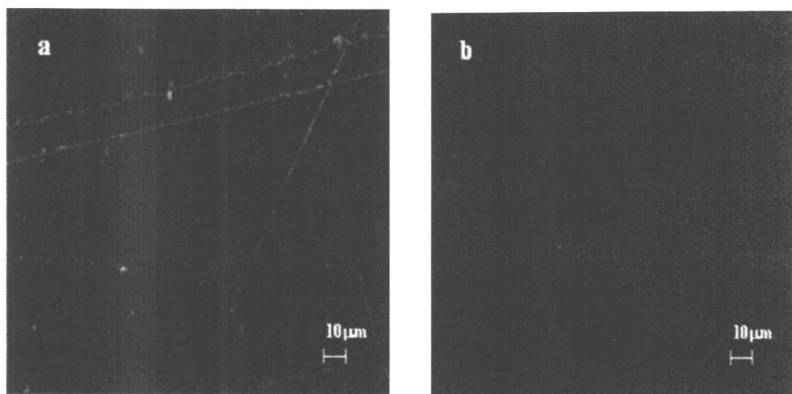
Figure 12. SEM images of (a) clay-free film surface, (b) nanocomposite with 3 phr organoclay film surface, following steel-wool scratch resistance test.

less contact area between the sample surface and the abrasive material. The scratch resistant characteristic of organoclay is also evident from the improvement in gloss retention of acrylate coating following the abrasion test (Figure 13).
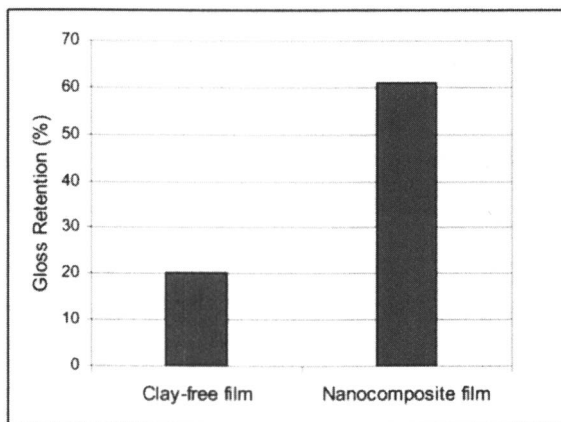
Figure 13. Gloss retention of the sample surfaces after steel-wool scratch resistance test.

Conclusions

The urethane-acrylate based nanocomposite coatings with different amounts of organoclay have been prepared by photoinitiated polymerization technique. Gel content measurements were performed in order to determine the effect of filler on crosslink density. It was found that using organoclay as reinforcing filler shortens the time required for the complete curing. X-ray diffraction studies as well as AFM and TEM images revealed that 3 phr organoclay was uniformly dispersed in the polymer matrix and both intercalated and exfoliated morphologies were present. In the case of acrylate samples with organoclay content higher than 3 phr, intercalated morphology as well as some clay agglomerates were observed. The most significant change in tensile properties and glass transition temperature of urethane-acrylate coating has occurred at 3 phr organoclay loading due to the layered dispersion of clay. The presence of organoclay was found to delay the initial decomposition of the matrix resin by increasing the path of volatile products, while it acted as a heat barrier and lead to the heat build-up at high temperature, thereby increased the char residue. Resistance to scratching was better in nanocomposite sample when compared to

clay-free one. Besides providing good mechanical and physical properties, organoclay appears to be a cost effective matting agent, small amount of which is sufficient to reduce the gloss significantly.

Acknowledgements

References

1. Gopakumar, T.G. Lee, J.A. Kontopoulou, M. Parent, J.S. *Polymer* **2002**, *43*, 5483-5491.
2. Alexandre, M., Dubois, P., *Materials Science and Engineering* **2000**, *28*, 1-63.
3. Decker, C., Keller, L., Zahouily, K., Benfarhi, S., *Polymer* **2005**, *46*, 6640-6648.
4. Nigam, V., Setua, D. K., Mathur, G. N., Kar, K.K, *Journal of Applied Polymer Science* **2004**, *93*, 2201-2210.
5. Zou, K ., Soucek, M.D., *Macromolecular Chemistry and Physics* **2004**, *205*, 2032-2039.
6. Ray, S.S., Okamoto, M., *Progress in Polymer Sience* **2003**, *28*, 1539–1641.
7. Studer, K., Nguyen, P.T., Decker,C., Beck, Schwalm, E. R., *Progress in Organic Coatings* **2005**, *54*, 230-239.
8. Chattopadhyay, D.K., Panda, S.S., Raju, K.V.S.N., *Progress in Organic Coatings* **2005**, *54*, 10-19.
9. Imamoğlu, T, Yağcı, Y, *Journal of Applied Polymer Science* **2002**, *83*, 1181-1189.
10. Ali, M. A., Khan, M.A., Idriss Ali, K. M., *Advances in Polymer Technology* **1998**, *17*, 259-267.
11. Asif, A., Shi, W., *Polymers for Advanced Technologies* **2004**, *15*, 669-675.
12. Inceoglu, A.B., Yilmazer, U., *Polymer Engineering and Science* **2003**, *43*, 661-669.
13. Uhl, F.M., Davuluri, S. P., Wong, S. C., Webster, D. C., *Chemistry of Materials* **2004**, *16*, 1135-1142.
14. Masson, F., Decker, C., Jaworek, T., Schwalm, R., *Progress in Organic Coatings* **2000**, *39*, 115-126.
15. Decker, C., Zahouily, K., Keller, L., Benfarhi, S., Bendaikha, T., Baron, J., *Journal of Materials Science* **2002**, *37*, 4831-4838.
16. Benfarhi, S., Decker, C., Keller, L., Zahouily, K., *European Polymer Journal* **2004**, *40*, 493-501.

17. Keller, L., Decker, C., Zahouily, K., Benfarhi, S., Le Meins, J.M., Miehe-Brendle, J., *Polymer* **2004**, *45*, 7437-7447.
18. Shemper, B.S., Morizur, J.F., Alirol, M., Domenech, A., Hulin, V., Mathias, L.J., *Journal of Applied Polymer Science* **2004**, *93*, 1252-1263.
19. Uhl, F.M., Davuluri, S. P., Wong, S. C., Webster, D. C., *Polymer* **2004**, *45*, 6175-6187.
20. Decker, C., Keller, L., Zahouily, K., Benfarhi, S., *Polymer*, **2005**, *46*, 6640-6648.
21. Fogelstrom, L., Antoni, P., Malmstrom, E., Hult, A., *Progress in Organic Coatings* **2006**, *55*, 284-290.
22. Uhl, F.M., Webster, D. C., Davuluri, S. P., Wong, S. C., *European Polymer Journal* **2006**, *42*, 2596-2605.
23. Wang, Y.Y., Hsieh, T.E., *Journal of Materials Science* **2007**, *42*, 4451-4460.
24. Wang, Z., Pinnavaia, T. J., *Chemistry of Materials* **1998**, *10*, 1820-1826.
25. Wang, Z., Pinnavaia, T. J., *Chemistry of Materials* **1998**, *10*, 3769-3771.

Chapter 14

Elastic Modulus Characterization of Nanocomposite Latex Coatings

Aaron M. Forster, Stephanie Watson, and Jonathan White

Building and Fire Research Laboratory, National Institute of Standards and Technology, 100 Bureau Drive, Gaithersburg, MD 20899

The elastic modulus of a polystyrene-butyl acrylate latex coating was measured using three different techniques: instrumented indentation, dynamic mechanical analysis, and tensile testing. The coating was formulated with 25 nm and 250 nm diameter TiO_2 particles at three different pigment volume concentrations (PVC). Additional coatings were formulated with sol-gel created TiO_2 and ZnO particles at 2.5 % PVC. Indentation consistently measured a higher modulus than DMA or tensile testing. All three metrologies agreed after the elastic modulus was normalized by the unfilled coating modulus. Nanoparticles produced less of an improvement in the elastic modulus than 250 nm particles at higher PVC. Existing theoretical models for normalized modulus were used to indirectly infer the particle dispersion in the samples.

Introduction

Mechanical properties are not the main focus of traditional coating performance measurements. Newer coating technologies and applications have increased the need for accurate mechanical property measurements for coating performance assesment. For example, nanometer sized alumina and silica particles have found use in multifunctional coatings [1-3] because they can increase the modulus and hardness of coatings, while maintaining optical clarity at low pigment volume concentrations [4,5]. Since these coatings are applied to protect the substrate from scratch damage, an accurate, quantitative measure of modulus improvements as a function of particle concentration is needed to properly assess durability. Photoactive nanoparticles, such as titanium dioxide and zinc oxide, are important for ultraviolet light absorption. Unprotected titanium dioxide has been shown to reduce coating performance by local degradation of the surrounding polymer during ultra-violet light exposure [6-10]. A metrology for local surface mechanical property measurements during ultraviolet exposure would improve coating performance assesment. Coating technology is also shifting towards water-borne systems that reduce volatile organic compounds [11]. These new material systems require suppliers to quantify changes in modulus with curing time in order to demonstrate improvements over existing product lines. Each of these examples is relevant for different coating materials such as epoxy, urethane, acrylic, and latex coatings.

Bulk measurement techniques such as dynamic mechanical analysis (DMA) and tensile testing are capable of measuring the coating modulus, but they are not sensitive to the unique properties of nanocomposites such as surface segregation of particles and low particle loadings. In addition, the precision of DMA and tensile testing is susceptible to sample preparation and force resolution for *compliant* coatings such as a latex.

Latex coatings are important because they represent a significant portion of commercial interior and exterior coatings. These coatings are challenging because they require a complicated blend of components to stabilize the aqueous dispersion of polymer and filler [12-14]. If not formulated properly, the particles can aggregate to form a non-uniform coating [15-16]. In addition, the modulus of latex coatings is low compared to glassy thermoset epoxy and urethane coatings. Therefore, latex resins present an excellent material to compare measurement techniques for assessing mechanical properties.

Instrumented indentation (IIT) has an advantage over DMA and tensile testing because it can measure the mechanical properties of polymeric coatings within 100 nm of the coating surface to 3 μm into the bulk of the coating. This

test can be performed using as-prepared coatings on almost any substrate. Research has also shown the capability of IIT to measure viscoelastic properties such as storage and loss modulus [17-20] and creep or stress relaxation [21-24].

The objective of this study is to compare frequently used metrologies for measuring coating mechanical properties to determine if one technique provides any advantage over the other for nanoparticle containing latex coatings. In addition, the impact of nanoparticle concentration on the modulus of a latex coating is measured and compared to that of a model 250 nm diameter particle. Several existing theoretical models for the dependence of modulus on particle volume will be used to provide qualitative information on the particle dispersion.

Experimental[1]

Materials

Latex dispersions were prepared using UCAR 481 (polystyrene-butyl acrylate) latex resin in accordance with the Cary Gloss White Enamel formulation E-2216C (DOW) [25]. The resin is 53 % mass solids with a reported latex particle size of 0.085 µm, and a reported glass transition temperature (T_g) of -3 °C. Latex particles and inorganic particles were dispersed to a fineness of grind of 6 or less (agglomerate size < 25.4 µm) on the Hegman block gauge. The viscosity of the combined grind and letdown was measured with a paddle viscometer (KU-2, Brookfield) and adjusted to 0.956 Pa·s using a 9×10^4 molar mass hydroxyethylcellulose (Natrosol 250 LR PA, Hercules). Filled latex coatings were cast onto release paper using a 150 µm Bird film applicator that produced dry film thicknesses between 100 µm to 115 µm. The coatings were allowed to dry for 7 days at ambient conditions.

Zinc oxide (ZnO) and titanium dioxide (TiO_2) particles were used in the coatings. Both oxide types had different particle size distributions and methods of manufacture. Table 1 lists particle properties, where two diameters listed indicate the 10 % and 90 % limits of the particle diameter distribution. The particles are named according to the oxide and the mean diameter of the particle distribution (50 %) obtained from the manufacturer provided particle distribution data. TiO_2-282 and ZnO-181 had no surface treatment and a bimodal particle

---

[1] Certain instruments or materials are identified in this paper in order to adequately specify experimental details. In no case does this imply endorsement by the National Institute of Standards and Technology or imply that it is necessarily the best product for the experimental procedure.

distribution with a surface weighted mean diameter of 218 nm and 181 nm, respectively. These particles were prepared via a sol-gel process and the tail of the particle distribution shows a small amount of particles have diameters less than 100 nm. TiO_2-21 was prepared via vapor deposition and had no surface treatment. TiO_2-250 was prepared through a grinding process with a mean diameter of 250 nm and an Al_2O_3 and SiO_2 surface treatment.

Table 1. Properties of particles used in the latex coatings

Particle	Material	Diameter	Type	Surface Coating
		nm		
TiO_2-282	TiO_2	100 to 1000	amorphous	none
ZnO-181	ZnO	100 to 1000	-	none
TiO_2-21	TiO_2	21	anatase	none
TiO_2-250	TiO_2	250	rutile	Al_2O_3 + SiO_2

TiO_2-21 (Degussa) and TiO_2-250 (Millenium) were mixed at PVCs of (2.5, 10 and 17.8) %. The calculation of PVC was based on the true density of the pigment, not volume of pigment. There were significant problems encountered in obtaining an ideal coating for TiO_2-282 (Nanoscale Materials, Inc.) and ZnO-181 (Nanoscale Materials, Inc.) at PVC levels above 2.5 %. For these particles, combination of the grind and letdown created a thick paste that could not be drawn into a coating. For ZnO, the poor paste quality is related to the incompatibility of the particle surface chemistry (isoelectric point) with this particular latex formulation. It is believed that the surface chemistry of the sol-gel created TiO_2-282 particles was also not compatible with this latex formulation.

Characterization

Instrumented Indentation Testing (IIT) - Measurements were performed using a commercial nanoindenter (MTS Nanoinstruments, NanoXP). A 10 μm radius, 90° diamond cone indenter was used to indent the latex films and the tip area function was determined using a fused silica standard over the experimental indentation depth. Loading was performed at 0.05 s^{-1} constant strain rate. The stiffness of the tip-sample contact was continuously measured during loading by

imposing a small tip oscillation of 2 nm at a frequency of 45 Hz. The Poisson's ratio of the composite was assumed to be 0.35 and constant. Modulus was determined as the average modulus over an indentation depth from 2000 nm to 3000 nm, without a drift correction, for each indent. The modulus reported here was the average of 15 indents on two films. The indents were spaced 100 μm apart. The films were mounted to aluminum substrates using a fast set cyanoacrylate glue.

Dynamic Mechanical Analysis (DMA) – The storage (E') and loss (E") modulus of unsupported coatings was measured using a dynamic mechanical analyzer (TA Instruments, RSA III). 15 mm x 5 mm rectangular latex films were cut from the master coating using a clean razor blade. These coatings were tested from -30 °C to 100 °C using a strain of 0.04, frequency of 1 Hz and temperature ramp of 5 °C·min^{-1}. The T_g was determined from the maximum in tan δ. Storage modulus at room temperature is reported. The reported values for glass transition temperature and storage modulus are the average from three samples.

Tensile Testing – Coatings were tested using a dynamic mechanical analyzer in tensile testing mode (TA Instruments, RSA III). The sample geometry had to be shortened from the ASTM D638 recommendations, although care was taken to maintain the correct length to width ratios. Samples were 40 mm long and 6 mm wide. A punch was used to create a 2 mm long by 1 mm wide neck in the center of the sample. This served as the gauge length for testing and ensured that breakage occurred in the middle of the sample. This geometry led to a linear engineering stress vs. engineering strain curve that exhibited a yield stress and necking region past the yield point. Strain was measured using grip separation. The apparent Young's modulus was determined from the slope of the linear portion of the engineering stress vs. engineering strain curve. Experiments were conducted at a constant cross-head speed of 0.05 mm·s^{-1}. The reported modulus is the average from four samples. The average yield stress for all of the films was 11.5 ± 0.5 MPa.

Instrumented Indentation Analysis

Instrumented indentation measures load and displacement in a sample as it is indented by an axisymmetric punch. Analysis of indentation load-displacement data was based in Hertzian contact mechanics [26] that was extended to arbitrary punch shapes by Sneddon [27]. The measurement technique was refined by Oliver and Pharr [28] and Doerner and Nix [29]. In

short, the stiffness of the contact, S, (Equation 1) during initial unloading is used in conjunction with the contact area to calculate the relative modulus (Equation 2).

$$S = \frac{dP}{dh} \tag{1}$$

In equation 1, S is determined from a fit to the initial unloading portion of the load vs. displacement curve.

$$E^* = \frac{\sqrt{\pi}}{\beta 2\sqrt{A}} S \tag{2}$$

$$\frac{1}{E^*} = \frac{\left(1 - \upsilon_i^2\right)}{E_i} + \frac{\left(1 - \upsilon_s^2\right)}{E_s} \tag{3}$$

where P is load, h is displacement, E^* reduced modulus, A is contact area, β is a geometric correction, E_x is the modulus of the indenter (i) and substrate (s), ν_x is the Poisson's ratio of indenter (i) and substrate (s). Indentation testing is similar to hardness testing [30], except the contact area between the tip and sample is determined via a tip shape profile calibration into fused silica and not a post-mortem optical microscopy analysis of the indentation. Contact radii are on the order of 1 μm to 2 μm and depths from 100 nm to 1000 nm, depending on tip geometry.

While the above analysis methods work well for elastic-plastic materials, certain challenges arise in measuring viscoelastic materials. Viscoelastic materials may creep during indentation and lead to errors in the determination of S from the unload curve. Contact stiffness information can also be measured by imposing a small oscillation over the loading ramp. This oscillation typically ranges from an amplitude of 2 nm to 5 nm and a frequency of 45 Hz to 75 Hz. A spring and dashpot model is used to determine S of the dynamic contact [13, 31] during loading. The S measured is used with equations (2) and (3) to determine the sample modulus. This was the measurement technique used for these measurements. For indentation, the contact radius at the maximum displacement into the film is ≈ 5 μm. This radius was large compared to the particle filler size and the indentation measurements are expected to represent an average film modulus that could be compared to DMA and tensile measurements.

Results & Discussion

Latex Film Appearance

Digital photography of the coatings was used to provide a qualitative evaluation of pigment dispersion. Figure 1 shows the coatings on a steel panel painted with a black and white background. The unfilled latex coatings were translucent. The refractive index of titanium dioxide, $n_{average} \approx 2.7$, is higher than the polymer, $n \approx 1.5$, or zinc oxide, $n \approx 2.0$. It was expected that, for similar PVC, the titanium dioxide filled coatings would be more opaque compared to the unfilled or zinc oxide filled coatings.

Figure 1a shows the 2.5 % PVC coatings for TiO_2-282, ZnO-181, TiO_2-21, and TiO_2-250 fillers. At this PVC level, the filled samples, TiO_2-282 and TiO_2-21, were more opaque than the unfilled or ZnO-181 coatings. TiO_2-282 and TiO_2-21 coatings exhibited visible agglomerates near the surface of the films. ZnO-181 did not exhibit visible agglomerates. TiO_2-250 was opaque at the 2.5 % pigment volume concentration without visible agglomerates. Figure 1b shows the films containing 2.5 %, 10 % and 17.8 % PVC of filler TiO_2-21 and 2.5 % PVC of filler TiO_2-250. The films were progressively more opaque as the PVC increased. This was expected considering the addition of pigment increases the size of particle agglomerates and decreases the coating transmittance of light. It is interesting to note that TiO_2-21, at 17.8 % PVC, does not achieve the same opacity as TiO_2-250 at the 2.5 % PVC. Optical and electron microscopy was not conducted on these samples. A more detailed analysis of the sample microstructure is currently underway.

Filler Impact on T_g

Dynamic mechanical analysis was used to measure the viscoelastic behavior of the samples. Two glass transition temperatures were observed in the unfilled latex samples as shown in Figure 2. The product literature for this latex formulation lists a single glass transition temperature of -3 °C. The two transition regions were evident at ≈ 5 °C and ≈ 55 °C. The glass transition temperatures are listed in Table 2 for the 2.5 % PVC only, because it was not possible to formulate all particles at higher PVC. The lower T_g of the TiO_2-282 samples was raised ≈ 2 °C, while the lower Tg of the ZnO-181 samples was lowered ≈ 2 °C. The wide particle size distribution in these particles, compared to TiO_2-21 and TiO_2-250, may have caused the slight shift in the coating thermal properties. None of the particles significantly shifted the glass transition region observed at ≈ 55 °C. A slight vertical shift in E' and E" with increasing PVC was measured for TiO_2-21 and TiO_2-250, but this shift was likely caused by sample preparation because
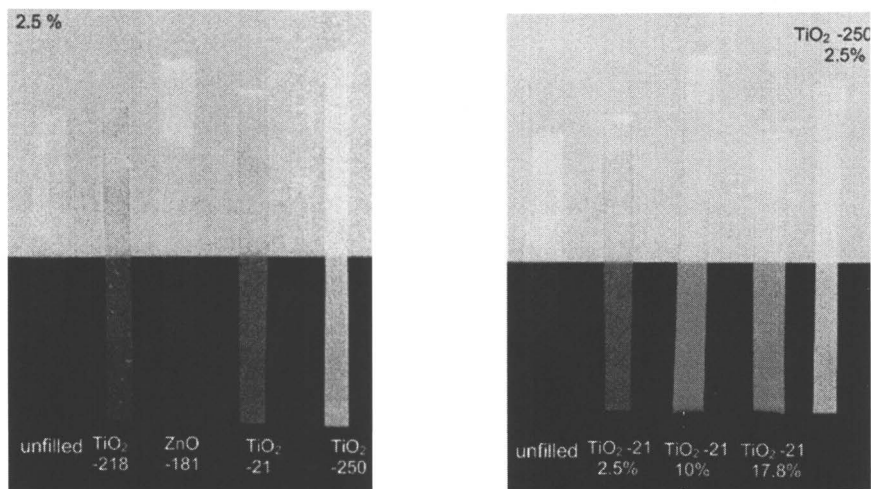
Figure 1. Latex coatings on a steel panel painted with a black and white background. a) Composite films at 2.5 % PVC. b) Composite film with particle TiO$_2$-21 at 2.5 %, 10 % and 17.8 % PVC. The unfilled and 2.5 % PVC particle TiO$_2$-250 films are shown for comparison

the tan δ curves overlapped, within experimental error. The T$_g$ did not change with increasing PVC for TiO$_2$-21 and TiO$_2$-250 (not shown).

Comparison of Measurement Techniques

Normalized Modulus

Three different measurement techniques were used to measure sample mechanical properties. The wide range of oxide type, particle size, and pigment volume concentrations complicated the direct comparison of absolute moduli. In order to better facilitate the comparison between measurement techniques, a normalized modulus was defined as:

$$E_n = \frac{E_{filled}}{E_{unfilled}} \tag{4}$$

where E_n(IIT) is the normalized indentation modulus, E_n(DMA) is the normalized DMA storage modulus and E_n(tensile) is the normalized tensile
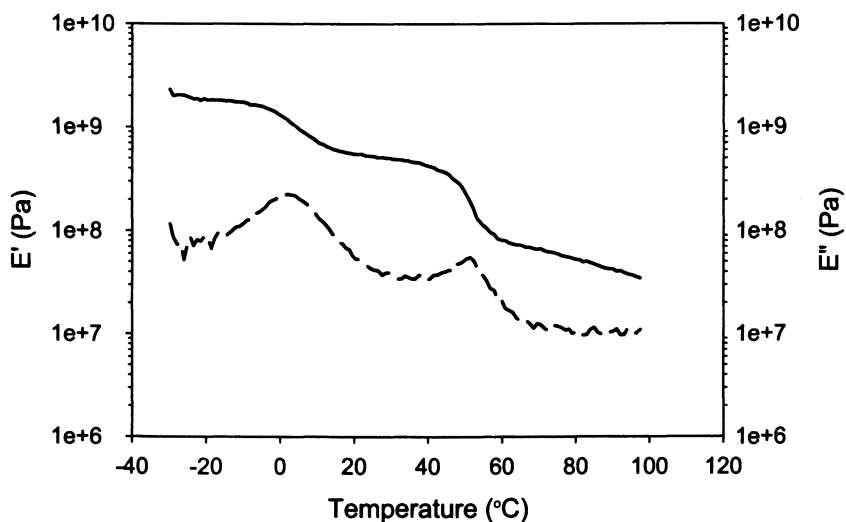
Figure 2. Storage modulus (E', solid line) and loss modulus (E", dash line) as a function of temperature for the unfilled latex coating. The curves indicate two glass transition regions.

Table 2. Glass transition temperatures for the latex films containing inorganic pigments at 2.5 % PVC. The ± indicate one standard deviation

Pigment	Tg_1	Tg_2
	(°C)	(°C)
unfilled	5.7 ± 0.64	54 ± 0.51
TiO_2-282	7.3 ± 0.70	55 ± 0.45
ZnO-181	1.5 ± 2.3	52 ± 0.30
TiO_2-21	5.2 ± 0.67	53 ± 0.35
TiO_2-250	5.7 ± 1.0	55 ± 0.62

testing apparent Young's modulus. E_{filled} is the composite film and $E_{unfilled}$ is the resin only film. Table 3 shows the normalized moduli for the coatings at the 2.5 % PVC level. There is a large standard deviation in the DMA and tensile measurements. For the ZnO-181 nanoparticle containing samples, the normalized modulus, measured with IIT, was lower than the DMA and tensile measurements. Overall, the sol-gel created nanoparticles provided the largest increase in E_n, but the magnitude was dependent on measurement technique. IIT generally measured an $E_n \approx 1$ at the 2.5% PVC for the TiO_2 containing samples. E_n(DMA) and E_n(tensile) had a large standard deviation in the measurements that made it difficult to determine whether the increase was due to the particles or heterogeneity in the coatings.

Table 3. Normalized moduli for the latex coatings at 2.5% PVC. E_n(IIT) is indentation, E_n(DMA) is DMA at ambient temperature and E_n (tensile) is tensile testing. The ± indicate one standard deviation

Pigment	E_n (IIT)	E_n(DMA)	E_n (tensile)
TiO_2-218	1.20 ± 0.04	1.07 ± 0.38	1.29 ± 0.19
TiO_2-21	0.86 ± 0.04	0.97 ± 0.21	0.95 ± 0.14
TiO_2-250	0.98 ± 0.04	1.24 ± 0.29	1.11 ± 0.16
ZnO-181	1.04 ± 0.04	1.43 ± 0.15	1.34 ± 0.19

In 6 of the 7 TiO_2 PVC levels tested, E(IIT) was at least 40 % higher than E(DMA) or E(tensile). Since, the samples were glued to aluminum substrates, the underlying substrate or mounting glue could confine the coating during indentation testing. The modulus of aluminum (E $\approx$ 72 GPa) was much higher than the coating (E $\approx$ 1 GPa), which may result in a higher modulus measured for indentation depths over 10 % of the coating thickness [32, 33]. However, the latex films were at least 100 μm thick and the maximum indentation depth was 3 μm or 3 % of the film thickness. The ratio of contact radius to film thickness, a/h, was between 0.03 and 0.05 and within this range confinement effects are minimized [34]. Therefore, the underlying aluminum substrate or mounting glue (E $\approx$ 4 GPa) was not expected to significantly affect the modulus measurement. Voids, due to insufficient coalescence, or particle agglomeration within the bulk of the film may reduce the value of the modulus measured with DMA or tensile testing. The films were allowed to dry for a week to eliminate voids and the

modulus measurements did not appear influenced by drying time within the two weeks between initial film preparation and testing. In addition, DMA measurements indicate that the viscoelastic properties of the coatings was not affected by dry time. Finally, IIT is a compressive measurement, while the other two techniques are tensile. The strain state within the composite film during DMA and tensile testing is uniaxial within the linear elastic region, but the stress state below the indenter punch is complex [34, 35]. It is compressive and combines simultaneous elastic and plastic deformation. Several authors have reported similar differences in the modulus of the film when comparing indentation of polymers to bulk tensile measurement techniques [36-39].

It was not possible to compare the different particle loadings for TiO_2-282 and ZnO-181, but the comparison was possible for the TiO_2-21 and TiO_2-250 particles. Figure 4 shows E and E_n for these coatings. There was good agreement between E(DMA) and E(tensile), although the standard deviation was large. After E was normalized, the agreement between the three techniques was good. The nanosized titanium dioxide, TiO_2-21, exhibited a relatively flat E_n up to 10 % PVC. The relatively flat E at 2.5 % and 10 % PVC suggests there is a lack of stress transfer between the particles and polymer for the chosen systems. It should be noted that latex coating systems are complicated formulations. Therefore, a different formulation of latex coating may lead to mechanical property behavior not observed here.

At 17.8 % PVC TiO_2-21, E_n(DMA) and E_n(tensile) increased, but E_n(IIT) dropped below the unfilled coating E_n(IIT). The reason for the drop in TiO_2-21 at 17.8 % PVC is unclear. It was expected that the modulus would not drop below the modulus of the unfilled coating with the addition of pigment. DMA measurements showed that TiO_2-21 did not affect viscoelastic properties because the tan δ curves did not shift with increasing PVC. It is possible that particle agglomerates were responsible for weakening the film, but the absolute mechanism is unclear. For the TiO_2-250 particles, the expected stiffening to the coating was observed. E and E_n both increase with PVC above 2.5 % (see Figure 4c and 4d) for all three techniques. The three measurement techniques showed that TiO_2-21 nanoparticles did not provide increases to coating modulus similar to what has been observed for nanoparticles in epoxy and acrylic urethane coatings.

Several theoretical models [40, 41] are available to predict the effect of particulate filler on the E_n. The majority of models have a basis in Einstein's equation to predict the viscosity of a solution containing rigid particles [41-43]. Figure 5 shows the E_n(IIT) for TiO_2-21 and TiO_2-250 along with the predictions of several models. The models are described below.
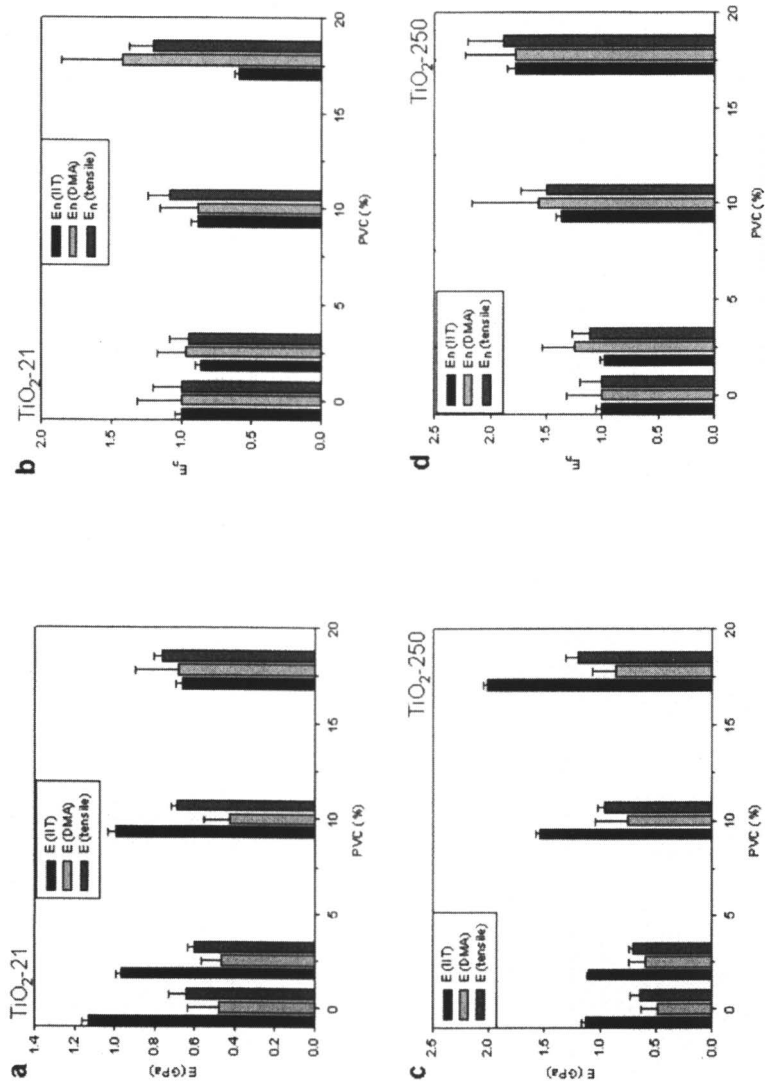
Figure 4. Comparison of moduli as a function of (2.5, 10, and 17.8) % PVC. a) elastic modulus for TiO_2-21 b) E_n for TiO_2-21 c) elastic modulus for TiO_2-250 d) E_n for TiO_2-50. Error bars represent one standard deviation.
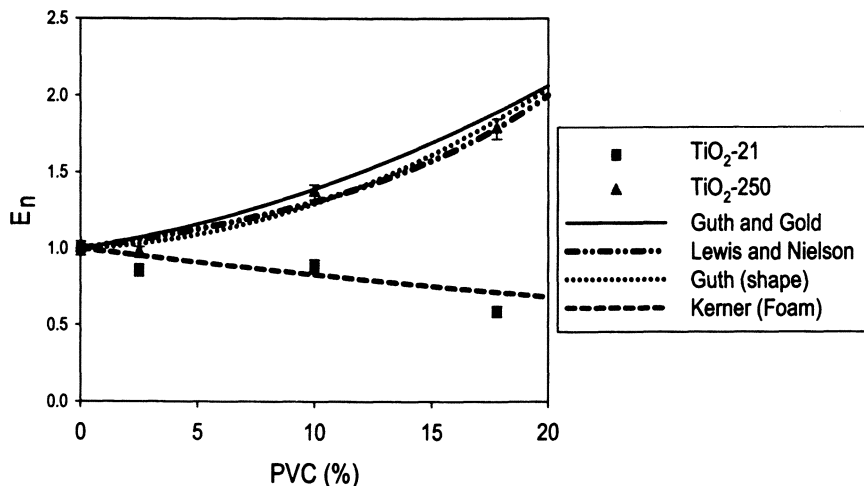
Figure 5. Normalized moduli (E_n) as a function of PVC for two of the inorganic titanium dioxide fillers determined from indentation. The lines represent predicted E_n values and the specific theory is given in the legend. Error bars represent one standard deviation.

The solid line in the graph represents the theoretical prediction [42, 43] expected for spherical particles dispersed in a continuous elastic matrix. Guth and Gold [44, 45] derived (equation 5) by extending Einstein's hydrodynamic analysis to solid materials. The equation is given below:

$$E_n = \frac{E_{filled}}{E_{unfilled}} = 1 + 2.5\phi + 14.1\phi^2 \tag{5}$$

where ϕ is the PVC, the first numerical prefactor represents the impact of the filler itself (length/diameter ratio = 1), the second prefactor represents the interaction between pairs of particles. The theory is valid up to $\phi = 0.1$ and the fit is not good above this PVC. This model slightly overestimated the normalized modulus of TiO_2-250 and does not provide additional information about the dispersion of filler within the film.

The second model shown in Figure 5 was developed by Lewis and Nielson [46] and takes into account the packing of particles within the film. It is a generalized version of the Kerner equation extended to any modulus [41].

$$E_n = \frac{1 + AB\phi}{1 - \psi\phi} \tag{6}$$

where A is a function of particle geometry and Poisson's ratio of the matrix, B is a function of the relative moduli of the two phases and approaches 1 for a large E_{filler}/E_{matrix}, ϕ is the filler PVC, and ψ is a function of the maximum packing fraction. These additional parameters are given by:

$$A = \frac{7 - 5v_{matrix}}{8 - 10v_{matrix}} \tag{7}$$

$$B = \frac{E_{filler}/E_{matrix} - 1}{E_{filler}/E_{matrix} - A} \tag{8}$$

$$\psi = 1 + \frac{1 - \phi_m}{\phi_m^2}\phi \tag{9}$$

where v_{matrix} is the polymer Poisson's ratio (0.35 here) and ϕ_m is the maximum packing fraction. In order to fit the data in Figure 5, the following values were used: A = 1.16, B = 1, and ϕ_m = 0.37. The empirical maximum packing fraction used to fit the data corresponds to random, close packed and agglomerated spheres [41]. The improved fit of this equation to the data suggests there are agglomerates within the composite film for TiO_2-250.

A third equation used to fit the normalized modulus of TiO_2-250 filled coatings was the Guth equation modified with a shape correction factor [45]:

$$E_n = 1 + 0.67\phi + 1.62f^2\phi^2 \tag{10}$$

where f is the length to diameter ratio. The data in Figure 5 was successfully fit using f = 3.75, which indicates an asymmetric distribution in the size of the dispersed particles [41]. The geometry parameters used to fit the experimental data using equations 6 and 10 suggest that even though these coatings appeared visibly uniform, there are asymmetric agglomerations of TiO_2-250 present within the coatings.

The theoretical models described above were not able to properly describe the behavior of TiO_2-21 coatings. In general, these models assume strong adhesion between the particles and the polymer matrix and monodisperse particles. The different functional forms and packing fraction or shape factors are included to account for deviations from the ideal spherical fillers. For TiO_2-21 coatings, the Kerner equation [47], adjusted for foam composites, was able to fit the normalized modulus data for this pigment.

$$E_n = \left(1 + \frac{15(1 - \nu_{filler})}{7 - 5\nu_{filler}} \frac{\phi_{matrix}}{\phi_{filler}}\right)^{-1} \quad (11)$$

where ν_{filler} (TiO_2 = 0.27) is the Poisson's ratio of filler and ϕ_i is the volume fraction of the matrix or filler. Equation 11 describes the particle TiO_2-21 data well. This is not to say TiO_2-21 at 10 % and 17.8 % PVC formed a foamed latex coating, but the dispersion within this film was much different and potentially more agglomerated than the TiO_2-250 latex films. At 17.8 % PVC for this particle, E_n(DMA) and E_n(tensile) measured a slight increase in normalized modulus, although this increase ($E_n \approx 1.4$) does not agree with the predictions for a monodispersed spherical filler ($E_n \approx 2.0$) calculated from Equations 5, 6, or 10. Potential reasons for this behavior include the presence of voids near the surface of the coating or agglomeration of particles within the latex matrix near the surface [41, 48]. A similar decrease in modulus has been observed for SiO_2 nanoparticles in polyvinyl-alcohol coatings [48]. Large agglomerates have been observed for 10 % PVC TiO_2-21 in epoxy and polyurethane films without dispersant. The simple theoretical models discussed here provide insight into the dispersion of particle filler in the matrix, but do not provide the complete details on the coating microstructure. Further measurements such as optical microscopy, TEM, or light scattering are required to understand the impact of particle-latex morphology on mechanical properties.

Summary

The effect of particle size and particle concentration on the mechanical properties of a styrene-butyl acrylate latex coating was investigated. The unfilled coating exhibited two glass transition temperatures, 5 °C and 55 °C, as two peaks in the tan δ. The particles created via a sol-gel process, TiO_2-282 and ZnO-181, shifted the lower glass transition temperature 2 °C higher and 2 °C lower than the unfilled coating, respectively. Instrumented indentation, dynamic mechanical analysis, and tensile testing were utilized to measure the elastic modulus of the coatings. Instrumented indentation measured a higher modulus compared to DMA and tensile techniques for the majority of films tested. Although, the standard deviation in the measurements for indentation was much smaller than DMA or tensile testing. The agreement between the three techniques was good for all particles when the data was presented as a normalized modulus. Overall, the addition of nanoparticles did not significantly increase the modulus of the coatings, but the large standard deviation in DMA and tensile measurements made this difficult to determine absolutely. The normalized modulus of TiO_2-250 was fit to two theoretical models, Lewis and

Nielson and Guth, that have particle geometry corrections to infer the dispersion state within each sample. The geometry corrections within each model indicate that despite the addition of dispersants to the formulation, agglomeration of the particles persists. Normalized moduli for TiO_2-21 containing coatings were fit using a theoretical model for foamed materials. It is believed that the normalized modulus decreases with increasing PVC because of larger than expected agglomerates of TiO_2-21 particles in this coating. The benefit of IIT over the other techniques was a much lower standard deviation between measurements and ease of testing. In addition, a larger number of indentation tests (15 indents per coating) could be conducted in less time than either the DMA and tensile measurements.

References

1. B. Ahmadi, M.Kassiriha, K. Khodabakshi, E.R. Mafi *Prog. Org. Coat* **60**, 99, (2007)
2. B. Bilyeu, W. Brostow, L. Chudej, M. Estevez, H.E.H. Lobland, J.R. Rodriguez, S. Vargas *Mat. Res. Innov.* **11**, 181, (2007)
3. F. Bauer, R. Mehnert *J. Poly. Res.* **12**, 483 (2005)
4. F. Bauer, V. Sauerland, H. J. Glasel, H. Ernst, M. Findeisen, E. Hartmann, H. Langguth, B. Marquardt, R. Mehnert *Macro. Mat. Eng.* **287**, 546 (2002)
5. Y. Q. Li, S. Y. Fu, Y. W. Mai *Polymer* **47**, 2127 (2006)
6. J.G. Balfour *JOCCA-Surface Coatings International* **12**, 478 (1990)
7. U. Gesenhues *Double Liaison: Physique, Chimie et Economie des Peintures et Adhesifs* **479** (1996)
8. J. H. Braun *Prog. Org. Coat.* **15**, 249 (1987)
9. G.A. George *Materials Forum* **19**, 145 (1995)
10. J. H. Colling, J. Dunderdale *Prog. Org. Coat.* **9**, 47 (1981)
11. U. S. Environmental Protection Agency, National Volatile Organic Compound Emission Standards for Architectural Coatings, 63 FR 48848
12. P. J. Flory Principles of Polymer Chemistry, Cornell University Press, Ithaca, NY 1953
13. R. F. G. Brown, C. Carr, M. E. Taylor *Prog. Org. Coat.* **30**, 195 (1997)
14. E. Kostansek *JCT Research* **3**, 165 (2006)
15. L. H. Princen *J. of Amer. Oil Chemists* **40** 131, (1963)
16. Y. Ishikawa, N. Aoki, H. Oshima, *Coll. and Surf. B – Biointerfaces* **45**, 35 (2005)
17. M. R. VanLandingham, N.-K. Chang, P.L. Drzal, C. C. White, S. H. Chang *J. of Poly. Sci. B: Poly. Phys.* **43** 1794 (2005)
18. S. A. S. Asif, K. J. Wahl, R. J. Colton *Rev. Sci. Inst.* **70**, 2408 (1999)
19. A. C. Fischer-Cripps *J. Mater. Res.* **19**, 2981 (2004)
20. G. Huang, B. Wang, H. Lu *Mech. Time-Dep. Mat.* **8**, 345 (2004)

21. E. H. Lee, J. R. M. Radok *Transactions of the ASME* 438 (1960)
22. T. C. T. Ting, *J. of Appl. Mech.* 845 (1966)
23. C.C. White, M. R. VanLandingham, P.L. Drzal, N. K. Chang, S. H. Chang *J. of Poly. Sci. B: Poly. Phys* **43** 1812 (2005)
24. M. L. Oyen, R. F. Cook *J. Mater. Res.* **18**, 139 (2003)
25. E. W. Flick, Water-Based Paint Formulations **4**, Noyes Publication, Westwood, NJ, 1994 p. 34
26. H. Hertz *J. Reine Angew. Math.* **92**, 156 (1881)
27. I. N. Sneddon *Int. J. Eng. Sci.* **3** 47 (1965)
28. W. C. Oliver, G. M. Pharr *J. Mater. Res.* **7** 1564 (1992)
29. M. F. Doerner, W. D. Nix *J. Mater. Res.* **1** 601 (1986)
30. D. Tabor The Hardness of Metals, Clarendon Press, Oxford, 1951
31. M. R. VanLandingham *J. Res. Natl. Inst. Stand. Technol.* **108** 249 (2003)
32. R. Saha, W. D. Nix *Acta Materialia* **50** 23 (2002)
33. D. E. Kramer, A. A. Volinsky, N. R. Moody, W. W. Gerberich *J. Mater. Res.* **16** 3150 (2002)
34. A. J. Crosby, K. R. Shull *J. of Poly. Sci. B: Poly. Phys.* **37** 3455 (1999)
35. K. L. Johnson, Contact Mechanics, Cambridge University Press, New York, 1985.
36. J. Sun, L. F. Francis, W. W. Gerberich *Poly. Eng. Sci.* **45** 207 (2005)
37. G. Kourtesis, G. M. Renwick, A. C. Fischer-Cripps, M. V. Swain *J. Mat. Sci.* **32** 4493 (1997)
38. M. R. VanLandingham, J. S. Villarrubia, W. F. Gutherie, G. F. Meyers *Macromol. Symp.,* **167**, 15 (2001)
39. B.J. Briscoe and K.S. Sebastian *Proc. R. Soc. Lond. A,* **452**, 439 (1996).
40. D. Y. Perera *Prog. Org. Coat.* **50** 247 (2004)
41. L. F. Nielson, R. F. Landel Mechanical Properties of Polymers and Composites, 2nd ed., Marcel Dekker, Inc. New York, 1994
42. A. Einstein *Ann. Phys.* **17** 549 (1905)
43. A. Einstein *Ann. Phys.* **19** 289 (1906)
44. E. Guth *J. of Appl. Phys.* **16** 20 (1945)
45. E. Guth, O. Gold *Phys. Rev.* **53** 322 (1938)
46. T. B. Lewis, L. E. Nielson *J. Appl. Poly. Sci.* **14** 1449 (1970)
47. E. H. Kerner *Proc. Phys. Soc.* **B69** 808 (1956)
48. J.-P. Boisvert, J. Persello, A. Guyard *J. of Poly. Sci. B: Poly. Phys.* **41** 3127 (2003)

Chapter 15

Nanoscale Characterization of Nanostructured Polymer Films and Coatings

Louis T. Germinario[1], Emmett P. O'Brien[1], John W. Gilmer[2], and Shriram Bagrodia[3]

[1]Eastman Chemical Company, Lincoln Street, B–150B, Kingsport, TN 37662–5150
[2]King College, 1350 King College Road, Bristol, TN 37620
[3]CEREPLAST, Inc., 3411–3421 West El Segundo Boulevard, Hawthorne, CA 90250

The manipulation of matter on the nanometer scale has led to the development and commercialization of polymeric materials in which individual molecules are integrated into larger structural hierarchies in part by self organization of building blocks.(1) Continued development of such structures and the ability to control their morphology at the molecular level requires the use of a multidisciplinary approach for materials characterization for establishing structure-property-relation-ships. Advanced characterization methods and protocols developed for analysis of surfaces and interfaces will be reviewed with an emphasis on examples drawn from industrial problem-solving. Examples include different classes of polymeric materials that employ either silica colloids, surfactants or homopolymers and copolymers of polyesters, polycarbonates, polyolefins, epoxies or acrylates. These materials as a result of new structuring achieve improved performance characteristics such as adhesion, hardness, scuff and scratch resistance and barrier properties.

292   © 2009 American Chemical Society

Introduction

The analytical problem posed by characterization of nanostructured materials include, spatial localization of points and regions of interest (resolution), elemental and molecular identification of components (detectability), and determination of the concentration of detected molecular species (sensitivity). Analytical techniques found to be most suitable for characterization of nanostructured materials include atomic force microscopy (AFM), nanoindentation, Nano-Thermal analysis, scanning electron microscopy (SEM) and transmission electron microscopy (TEM). Other analytical tools such as Infrared spectroscopy and dynamic mechanical analysis (DMA) were also employed for identification of organic moieties and measurement of viscoelastic and rheological properties. Molecular modeling tools were also used to generate low energy molecular 3D structures that were optimized in MOPAC using PM3 parameters. MOPAC (Molecular Orbital PACkage) is a popular computer program designed to implement semi-empirical quantum chemistry algorithms, such as PM3 (Parameterized Model number 3). As a result, PM3 provides a semi-empirical method for the quantum calculation of molecular electronic structures. Computed structures were used to compare structures and geometries measured experimentally by AFM.

Molecular Self-assembly and Ordering of Alkyl-polyglycosides for Improved Adhesion in Paper Coatings

Cellulose is the most abundant polymer found in nature and in some forms is used as heat sealable paper for medical packaging where it acts as a filter to particulates and microorganisms while at the same time permitting free passage of gas and water vapor during sterilization. This paper must also be heat sealable over plastic trays that contain medical instrumentation. The bond of the paper to the plastic must also be sufficiently strong, but at the same time, pealable from the plastic tray as needed. The additive that was found to be suitable as an adhesion promoter was alkylpolyglycoside (APG) which also has commercial utility as a nonionic surfactant (Figure 1).(2)

APG as a paper additive has been used as a softener for tissue paper.(3) As a coating for paper, APG has been used in combination with petroleum wax as a barrier coating.(4) For heat sealable paper, the initial hypothesis was, upon application of APG to Cellulose Acetate (CA) containing paper, APG would anchor itself in the cellulosic matrix, act as a plasticizer for CA, and present a hydrophobic surface to one side of the paper.(5)

In order to define the role and possible interactions of APG within the paper structure, AFM was used as a principal tool to localize APG on APG-treated paper surfaces. AFM has been widely used for the direct imaging of Langmuir-
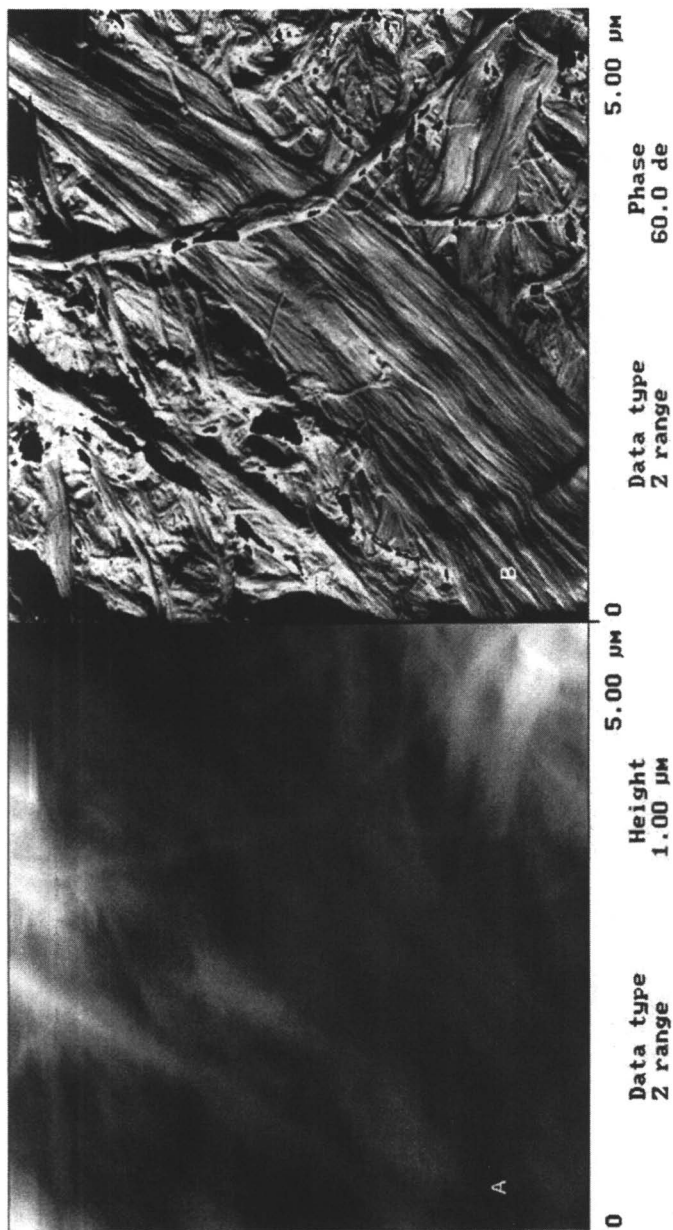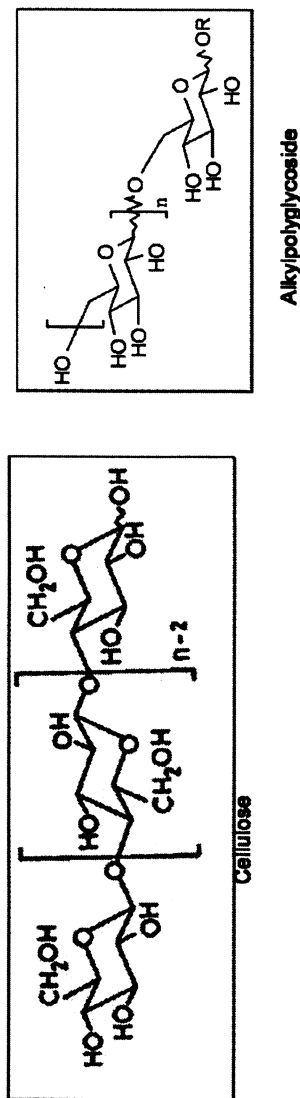
Figure 1. AFM of paper containing 25% cellulose acetate, coated with a 3% solution of APG (DP = 1.5, R= average alkyl chain length = 9.9). (A) is the height image, while (B) is a phase image. A drawing is also shown of the cellulose structure and the corresponding structure of APG and an R-group corresponding to a 10 residue alkyl chain.

Blodgett (LB) films, without the need for making replicas.(6) Characterization of self-assembly and structuring of APG on paper fiber surfaces proved to be somewhat challenging. In this account, paper containing 25% cellulose acetate was coated with a 3% solution of APG, (degree of polymerization (DP = 1.5, R= average alkyl chain length = 9.9). Large cellulose fibers are seen to traverse across the field of view (Figure 1A and 1B). Figure 1A is a height image which provides topographic information while Figure 1B is a phase image whose contrast correlates with viscoelasticity. The molecular drawing is a structure of cellulose and APG with an R-group corresponding to a 10 residue alkyl chain. The surface of this coated paper and the corresponding uncoated paper was further examined by AFM. Figure 2 provides a top-view of a coated cellulose fiber. In the left image (Figure 2A), the bright patches correspond to high points on the fiber surface while the dark regions are valleys. The corresponding right image (Figure 2B) is a phase image of the same fiber area in which the darker regions are indicative of soft domains, while the lighter areas are representative of hard domains. Three-dimensional views of fiber surfaces from coated versus uncoated paper (Figure 3) show the presence of surface patches that are not present in the corresponding areas of uncoated paper. Collectively, this data is interpreted as indicating that the soft patches correspond to APG-rich areas.

AFM-based bearing analysis was used to obtain information on the molecular dimensions of APG by measuring the thickness of the coating from height data (Figure 3). Bearing analysis generates a histogram of surface feature heights and provides a method for analyzing and plotting the distribution of surface heights. The boxed regions drawn in images in Figure 3 were taken from two different fiber areas. As can be seen, bearing analysis from these regions depict surface features with average heights of 3.6 nm, while uncoated fibers display an average surface height of <1 nm.

In order to measure the layer thickness of APG monolayers, LB techniques were employed. Formation of films using a LB trough is an established method to study monolayer self-assembly and for forming two-dimensional ordered arrays of amphiphilic molecules, such as APG, at an air-water interface.(7,8) Monolayers can be physically transferred to a variety of substrates, such as mica, for subsequent characterization. Mica is a particularly attractive substrate for use in the present study as the mica provides an atomically flat surface and offers a direct means for measuring APG layer thickness.

An LB trough was used to cast APG film monolayers that were subsequently deposited onto freshly cleaved mica surfaces. Figure 4 is an example of representative AFM images of APG monolayers on the mica substrate. The appearance of discontinuous holes in films is likely due to the lack of applied compression force when films were formed in LB troughs. Bearing analysis was also used to measure the step height between the background mica substrate and the APG film layer. The result is a measured film thickness of 3.0 nm.

Since amphiphilic molecules will preferentially orientation at an air/water interface with the hydrophilic portion buried in the water phase and the
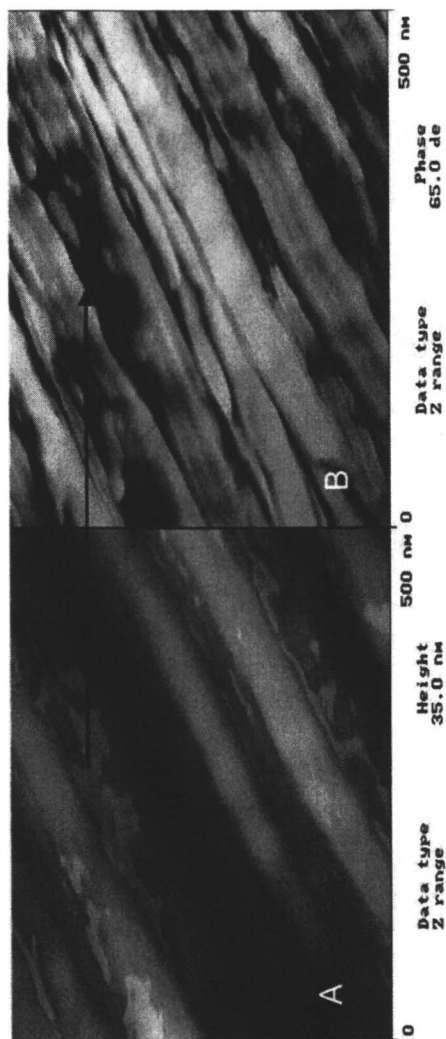
Figure 2. Magnified view of cellulose fiber reveal bright patches in height images (A) which correspond to dark, 'soft' phases in phase images (B).
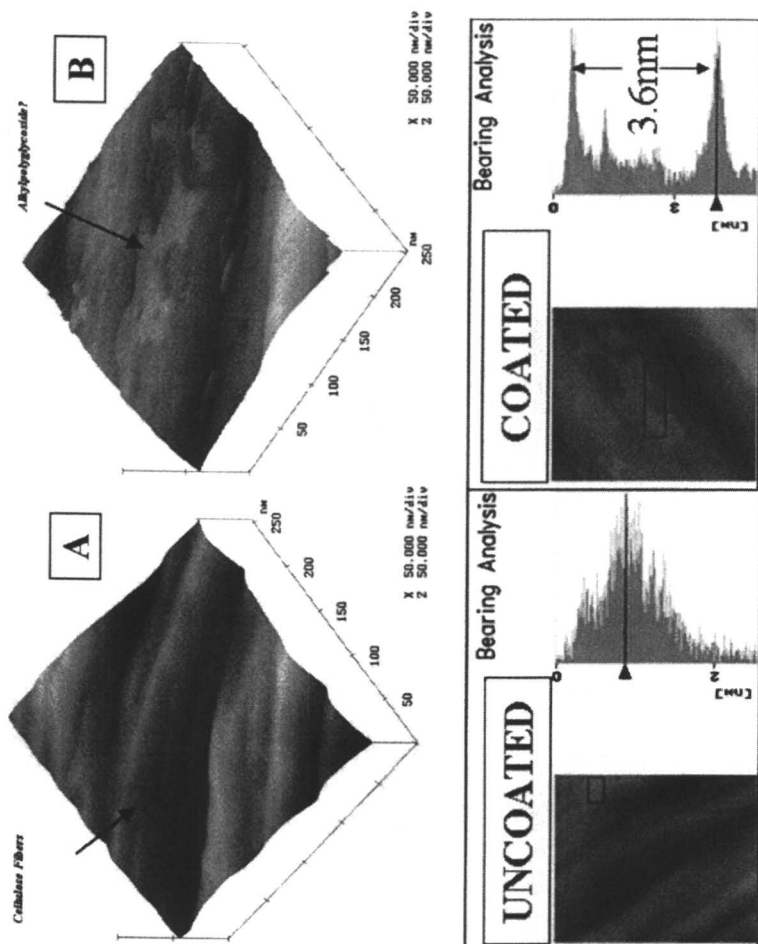
Figure 3. AFM, 3-Dimensional views reveal distinct patches of self-assembled Alkylpolyglycosides (APG) on cellulose fibers (B). Bearing analysis was used to measure the APG patch thickness.
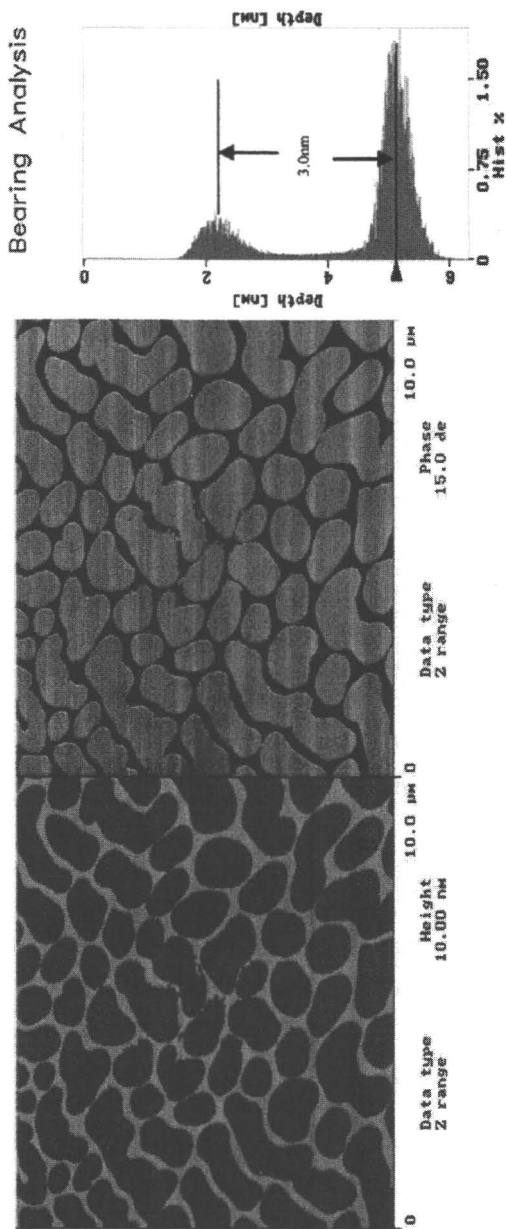
Figure 4. APG film was deposited from the air side onto freshly cleaved mica surface from a Langmuir-Blodgett trough. Since films were not compressed on the water surface they are not continuous and appear to have holes. Bearing analysis provided a measure of film thickness, 3.0 nm.

hydrophobic tail pointing out into the air, APG films were deposited on mica substrates so that the aliphatic and glucoside-rich surfaces could be analyzed. The hydrophobic, aliphatic-rich surface of the APG film is shown in Figure 5. Films were deposited on mica sheet by moving the mica through the water sub-phase so that the aliphatic chains were oriented up. Molecular modeling tools (CAChe) were next applied to generate low energy APG structures optimized in MOPAC using PM3 parameters. Average film thickness as measured by bearing analysis is 3.4 nm. The insert in Figure 5 is a magnified view of the phase image with arrows pointing to regions where shear forces induced by the tip-surface interaction removed material and exposed evidence of APG ordering from packing of aliphatic chains. When films were picked up from the air-water interface, APG films were deposited on mica substrates with the hydrophilic side facing up. (Figure 6) Regardless of the direction of pick up, all films were discontinuous. Bearing analysis measures of APG monolayers from image regions measuring 5 X 5 microns and 1 X 1 microns provided measured thicknesses 3.0 nm and 3.1nm, respectively. Since measured thickness of APG films cast as LB layers are very similar to measured film thickness of deposits on coated fibers, these data provide strong evidence for the presence of APG films on coated fibers.

Molecular modeling was next used to draw and minimize the structure of one APG molecule. Figure 7 provides a view of how molecular modeling can be use to synthesize molecular structures. The APG molecule was constructed by linking one or two D-glucose residues onto a C10 alkyl chain. The molecule was then refined by energy minimization. The measured length of one APG molecule is 1.7 nm. This molecular length is approximately half the measured heights of LB-formed APG films as measured on cellulose fibers. These data suggest that APG films are deposited as bilayers on LB-troughs and on fiber surfaces. Figure 8 compares the thickness of a bilayed APG structure. The computed bilayer thickness compares very favorably with the measured thickness of patches on cellulose fibers. The boxed region drawn in the image depicts surface features with average heights of 3.6 nm. Molecular modeling tools provided supporting evidence for the ordering of the APG adhesion promoter as a bilayer structure.

Adhesion of Nanometer-thick Scratch Resistant Coatings

Hybrid organic-inorganic coatings have evolved as the materials of choice for coatings, particularly in optics where non-reflecting, anti-abrasion, or scratch and mar resistant surfaces are desirable.(9) Typically, such coatings are fabricated by the sol-gel process and can be based on poly-caprolactone/silica organic-inorganic hybrids.(10) Since these hybrid coatings are generally applied as thin films, their chemical heterogeneity often leads to poor adhesion to substrates due to process-induced shrinkage stresses.(11) Geometrical effects
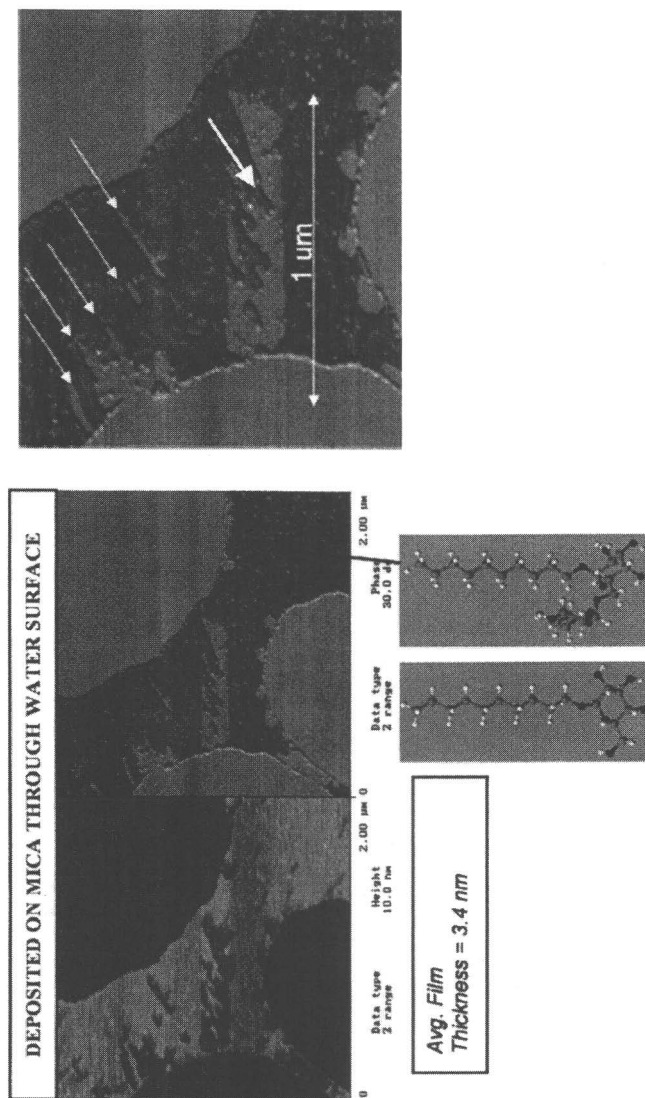
Figure 5. APG films deposited on mica sheets by moving the mica through the water sub-phase so that the hydrophobic portion of the APG is oriented away from the mica surface. Molecular modeling tools (CAChe) was used to generate low energy APG structures that were optimized in MOPAC using PM3 parameters. APG structures with both one and two glycosidic residues were computed. Average film thickness as measured by bearing analysis is 3.4 nm. Insert is a magnified view of the phase image with arrows pointing to regions where shear forces by the tip-surface interaction exposed evidence of ordering from packing of aliphatic chains.
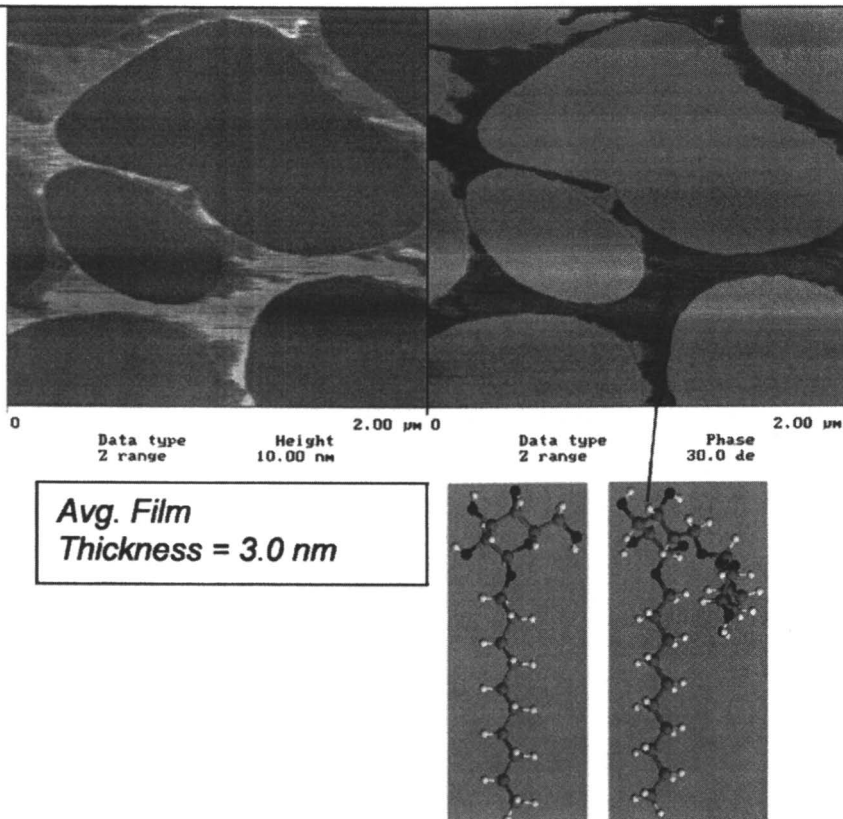
Figure 6. APG films deposited on mica sheets from the air-water interface. In this case the glycosidic residue is exposed to the air surface and analyzed by AFM. APG structures are also drawn showing the glucose moiety on the film surface.

due to the presence of non-planar surfaces can also contribute to increased interfacial shear stresses after curing.

In order to explore the influence of residual stresses on a coating's performance, instrumented indentation was employed. An instrumented indentation test consists in simultaneously measuring indentation load (P) and indentation depth (h) during the penetration of an indenter into a sample (Figure 9). During indentation a diamond tip whose geometry is either pyramidal or parabaloid of revolution is indented into the surface of a material at a controlled
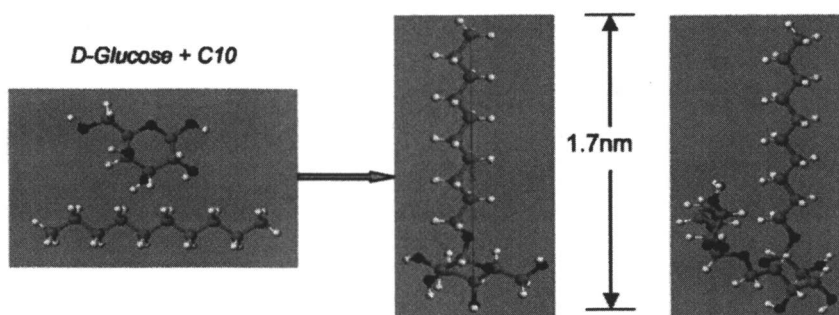
Figure 7. The APG structure was computed by linking one or two D-glucose residues to a C10 alkyl chain. The molecule was then refined by energy minimization. The measured length of one APG molecule is 1.7 nm.

loading rate and to a maximum load or displacement. The load (P) and displacement (h) are precisely measured as a function of loading history.(12) Instrumented indentation allows measuring the depth of penetration and the applied load continuously during the test. The tip is unloaded from the material after achieving the maximum load. This makes possible measurement of the elastic modulus and hardness without the need to measure the residual impression and, consequently, extending the applicability of this technique to the nanometer scale.

A modification of the instrumented indentation method was found to provide a technique for detection and mapping residual stress fields associated with nanometer thick coatings. When an array of indentations are made on a polymer surface, the residual imprints left by the indenter on the surface can be distorted and elongated due to residual stresses in the film. Furthermore, if one forms an array of indentations with increasing loads (P), the corresponding array of indents are formed with correspondingly larger pits. Figure 10 displays an indentation pattern (10x4 pattern) in which 10 indentations are made with increasing force and replicated four times. Section analysis of a row shows the formation of increasingly deeper pits. Figure 10 provides a schematic representation of a stress-strain curve which displays the characteristic linear relationship, at low stress levels, of an elastic region in the stress-strain curve where the material is deforming elastically. This deformation in the linear-elastic region is essentially recoverable on unloading. At some point beyond this stress level the polymer yields and the deformation ceases to be entirely elastic and the material starts to deform plastically. AFM-based imaging of the surface pattern after indentation also provides a qualitative measure of the onset force required for yielding (Figure 10).
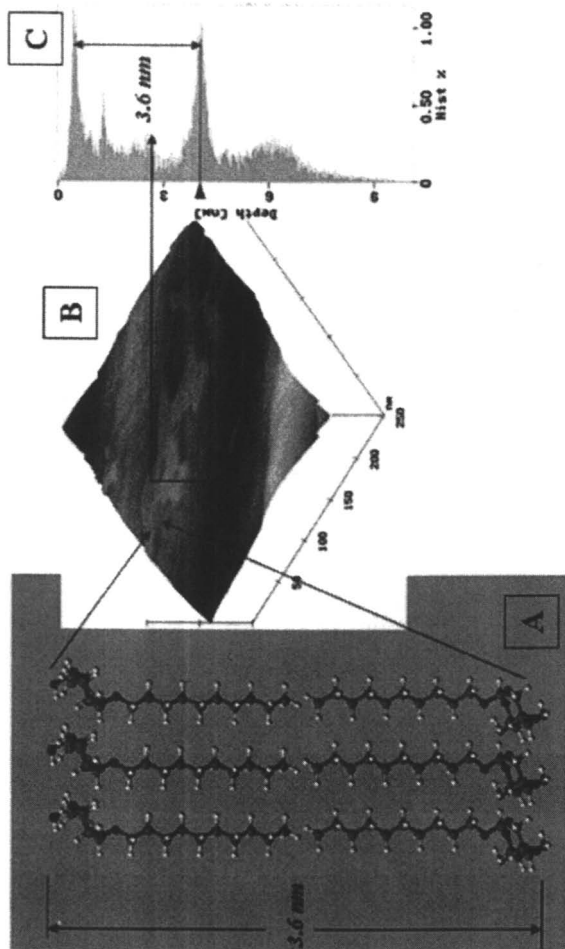
Figure 8. Comparison of the thickness of a bilayer of APG structure minimized using CAChe. The computed bilayer thickness compares very favorably to the measured thickness of patches on cellulose fibers.

This method was used to investigate abrasion resistance of coated sunglasses (Figure 11). The series A and C are representative of uncoated and coated lense surfaces with an indentation pattern (10x4 pattern) in which 10 indentations are made with increasing force and replicated four times. The shape of the indentation appears distorted for both coated and uncoated lense surfaces (A,C). Distortion of the indentation imprint is likely due to the presence of residual stresses in the curved polymer surfaces. The corresponding surfaces of plaques show indents that are triangular and undistorted (B,D). Since plaques have flat surfaces, one would not expect the presence of residual stresses on surfaces.

The formation of severe distortions in the indentation pattern of coated lenses (C) with poor scuff-resistance, suggest the presence of high residual stresses in these coatings and provide a possible mechanism for reduced performance. The extent of alignment of the indentation pattern can also be used to map surface stress fields (thick arrow). Moreover, the localization of the lowest force indentation pattern can be used to identify the yield point and provide a qualitative measure of a coating's hardness.

Pressure-sensitive Adhesives

Pressure-sensitive adhesives (PSAs) are a class of soft polymeric materials that adhere to surfaces under light contact pressure and short contact times and without chemical reaction or solvent evaporation.(13) In addition, these materials display significant debonding resistance after adhering to the surface. The characteristic properties of PSAs are due to their softness (low modulus at the application temperature) and viscoelastic properties. These materials are highly viscoelastic because the T_g lies slightly below the application temperature(14,15) and because of the adhesive morphology.(16) Under small applied loads, the material behaves like a liquid and readily deforms and wets the surface, permitting the attractive intermolecular forces between the adhesive and substrate surfaces to form a bond. The debonding resistance and capability to support significant load is attributed to viscous dissipation (cavitation and fibrillation) and to an increase in adhesive modulus as the strain rate or debond velocity increases.(16)

Styrenic block copolymers (SBCs) are an important class of high performance polymers used in the PSA tape industry which are typically composed of two styrene end blocks connected by a diene mid-block.(17) SBCs have useful properties due to their two-phase structure consisting of hard a glassy styrene phase and a soft rubbery diene phase; they can form either a spherical, cylindrical or lamellar microstructure(17). The glassy domains are
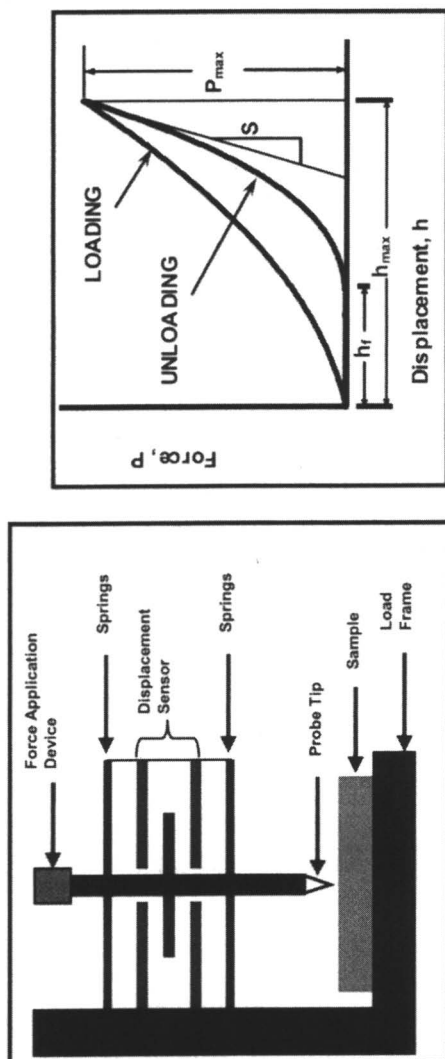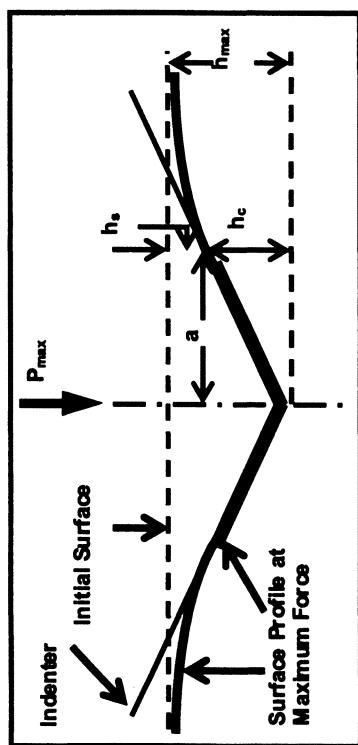
Figure 9. Instrumented indentation is often used to characterize the mechanical behavior of small length scales. Elastic modulus, E, and hardness, H, h_{max} = maximum displacement, h_f = final depth.
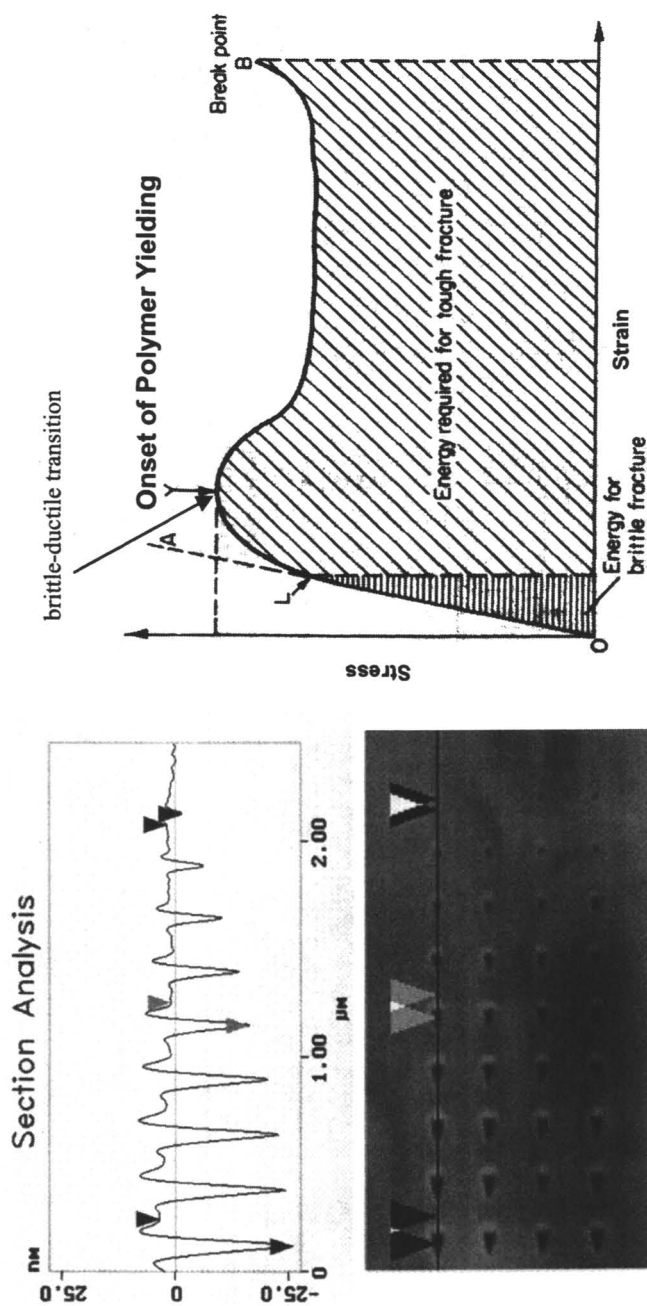
Figure 10. Surface stress analysis by indentation of a planar surface by a 10 X 4 pattern in which 10 indentations are made with increasing force and replicated four times. Scanning of the surface indentation pattern provides a qualitative measure of the onset force required for yielding. Section analysis of one of the force series was used to identify the onset of yielding.
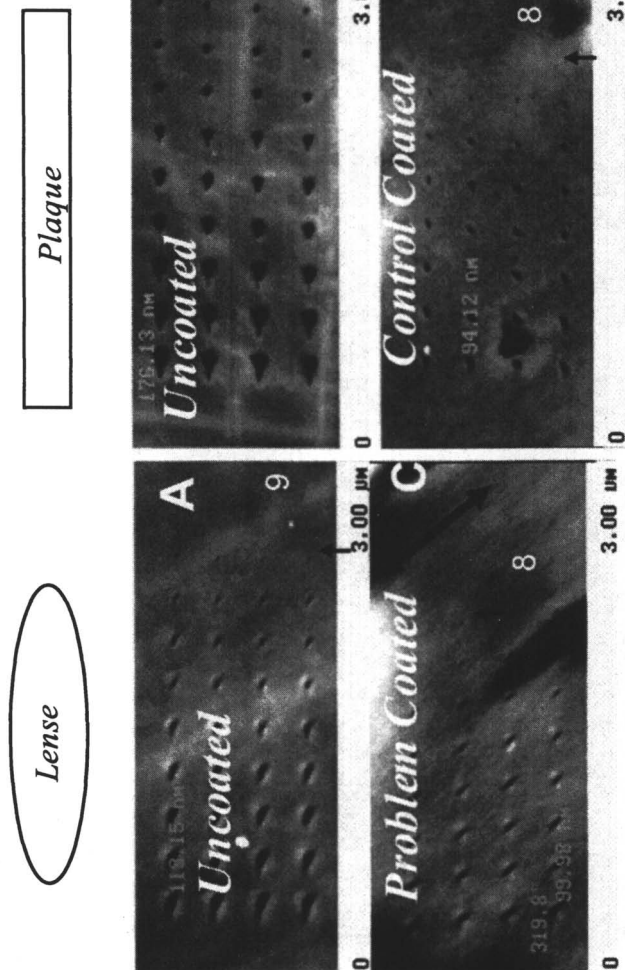
Figure 11. Surface stress analysis of problem lenses by indentation. The series A and C are representative of uncoated and coated lense surfaces with an indentation pattern (10 X 4 pattern) made with increasing force. The shape of the indentations appears distorted for both coated and uncoated lense surfaces (A,C). The corresponding surfaces of plaques have indents that are triangular and undistorted (B,D).The distorted indentation pattern(C) suggests the presence of residual stresses in coatings. The ordering and alignment of the indentation pattern can be used to map surface stress field (thick arrow). The yield point identifies the lowest force required to produce an indentation and can also provide a spatially resolved map of a coating's hardness.

connected to one another via the rubbery mid-block. As a consequence, the styrene domains form physical crosslinks between the rubbery mid-block domains. An important advantage of these materials is that above the glass transition temperature of styrene, the SBC loses cohesive strength and can be melt processed but below this temperature, the styrenic domains greatly increase the cohesion of the system.

The effect of tackifier chemistry on adhesive performance of styrene block copolymer based pressure sensitive adhesive tapes was investigated. In particular, the effect of varying the tackifier aromaticity on adhesive performance in a SBC-based pressure-sensitive adhesive tape (PSAT) is further investigated. Aromaticity strongly affects the compatibility between the tackifying resin and base polymer and is defined as the relative number of protons attached to an aromatic ring. Five tackifiers were tested listed in order of increasing aromaticity: 1) Piccotac® 1095, 2) Piccotac® 9095, 3) Piccotac® 8095, 4) Piccotac® 7590-C and 5) Piccotac® 6095-E. Each tackifier was formulated with KRATON D1161, a styrene-isoprene-styrene (SIS) triblock copolymer, and Calsol 5550 oil. Dynamic mechanical analysis, peel resistance, tack, shear resistance, and Atomic Force Microscopy (AFM) were utilized to detect changes in adhesive performance and morphology due to resin aromaticity.

Figure 12 shows the storage modulus, G' and loss tangent, tan δ as a function of temperature for the formulations each with a different tackifier. Two molecular relaxations are observed below ambient temperature which suggests that there are three phases. Near 40 °C is a shoulder in the tan δ that is a relaxation of an isoprene rich phase. Near 0 °C is a peak in tan δ which is likely the relaxation of a tackifier rich isoprene phase. The third phase is styrene. AFM-based phase imaging provided confirmation of the tri-phase structure, with the styrene phase easily detected as the hard, bright phase, which forms close packed structures, while the softer isoprene and tackifier rich phases form the continuous microdomain. (Figure 13)

The results indicate that increasing the aromaticity of the tackifying resin enhanced the compatibility between the tackifier and styrene domains. As a consequence, the high temperature cohesive performance decreased due to plasticization of the end block by the more aromatic resins (Table 1). This behavior is reflected in the dynamic mechanical results which shows that as the aromaticity of the resin increases, the high temperature where the adhesive loses stiffness and begins to flow decreases. This temperature corresponds to the temperature where the styrene domains that act as physical crosslinks melt. The reduction in high temperature performance with increasing resin aromaticity is due to plasticization of the end block by the resin as the compatibility between the resin and styrene increases. The increase in compatibility was also reflected in the AFM results which showed that size of the styrene domains increased with resin aromaticity (Figure 14). Note that other properties of interest such as the

(▲) 6095-E   (□) 7590-C   (△) 8095   (■) 9095   (◇) 1095
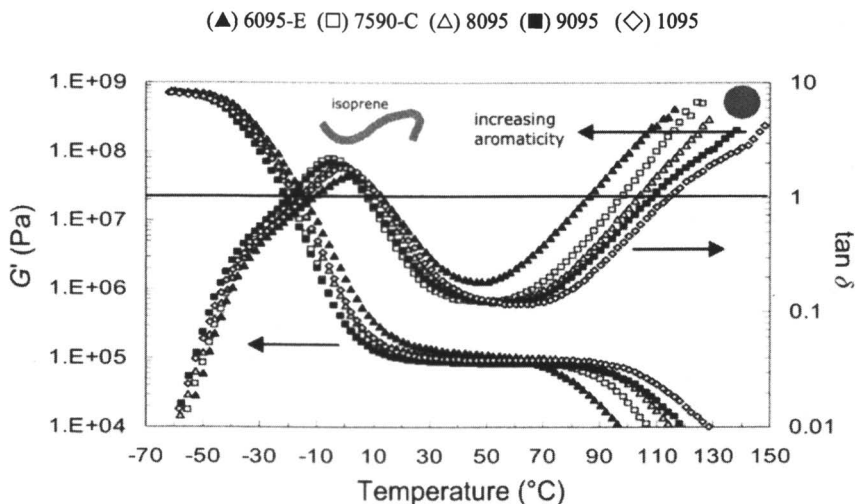
Figure 12. Dynamic Mechanical Analysis (DMA) provides a measure of the viscoelastic behavior of SIS-based tape formulation. The polystyrene domains are plasticized by resins with increasing aromaticity, while the Tg of the rubbery isoprene phase is within experimental error.

glass transition of the rubbery matrix, tack, peel resistance and holding power were less affected by the resin aromaticity(18).

Measuring Thermal Properties of Polymers at the Nanoscale

Organic polymeric materials are widely used as coatings in a variety of applications primarily to improve surface properties, appearance and performance. Coatings serve as a barrier with the hostile environment and allows for protection against corrosion or other chemical or photochemical degradation.

Chemically crosslinked coatings have evolved as the materials of choice and are commonly employed as automotive clearcoats to protect against environmental influences and provide scratch, mar and chip resistance, as well as corrosion and solvent resistance, while still maintaining a high gloss and appearance(19) The addition of chemical additives to improve photostability, coupled with variable crosslinking reactions, often produce heterogeneities ranging in size from nanometers to microns that are more susceptible to degradation(20,21). Atomic Force Microscopy (AFM) has proven to be invaluable for not only imaging polymeric systems,(22) but for probing
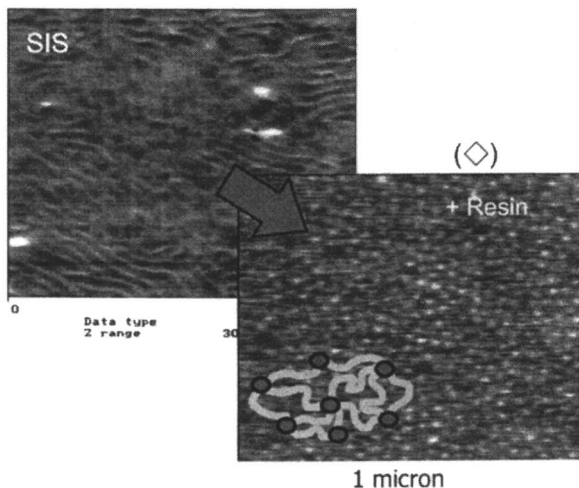
Figure 13. AFM phase imaging provides a view of the nanoscale structural transformation of styrene-isoprene-styrene (SIS) polymer phase structure with resin addition.

Table 1. Effect of resin Aromaticity on PSA performance.

Resin	% Aromaticity (NMR)	MMAP Cloud Point (°C)	DACP Cloud Point (°C)	RBSP (°C)	M$_z$ (kDa)	M$_w$ (kDa)	M$_n$ (kDa)	PDI*
Piccotac® 1095	0.5	94	47	99	33	1.7	0.82	2.1
Piccotac® 9095	2.0	88	47	95	4.0	1.9	0.93	2.0
Piccotac® 8095	5.2	76	38	95	5.7	2.2	0.94	2.3
Piccotac® 7590-C	7.5	65	27	93	3.2	1.6	0.82	1.9
Piccotac® 6095-E	14.8	35	-10	96	5.0	1.6	0.67	2.4

(Methylcyclohexane - aniline (MMAP); Diacetone alcohol - xylene (DACP))

Aromaticity of resin and rubber will effect where resin partitions.
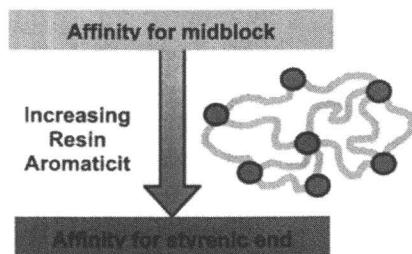
SOURCE: Reproduced with permission from J. Therm. Anal. Calorimetry. **2008,** *99 (1),* 207-211. Copyright 2008 Springer.)
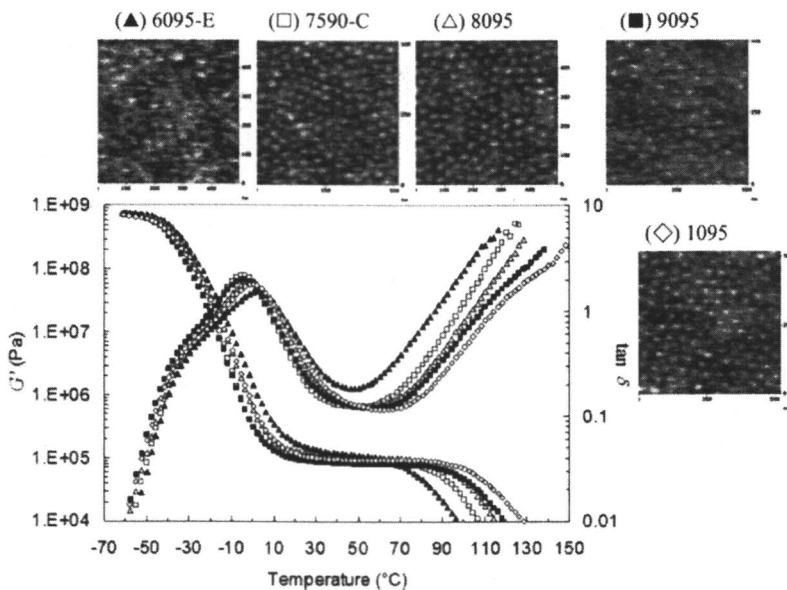
Figure 14. G' and tan δ as a function of temperature for each adhesive formulations. The legends is as follows: (▲) 6095-E; (□) 7590-C; (△) 8095; (■) 9095; (◇) 1095.

tip/sample interactions, (as in phase imaging) for mapping mechanical (elasticity, hardness) and chemical properties(23,24).

Recent breakthroughs have enabled the fabrication of thermal probes with end radii of ~20nm(25) which enable the AFM to probe local thermal properties at a sub-100nm size scale. The addition of a thermal tip to a conventional AFM adds a new and valuable capability of spatially resolved thermal analysis to the AFM. It is particularly useful for thin films since it enables the measurement of transition temperatures (melting or glass) on selected spots of the sample aiding in the identification and characterization of the phases at the nanoscale(26).

This article covers the preliminary work on the application of sub-100nm thermal analysis on crosslinked polymer coatings. Examples include the monitoring of the softening point of automotive clearcoat systems, as a function of cure time and cure temperature and characterization of degradation and embrittlement of weathered acrylic-polyurethane coatings. Comparison of nano thermal analysis with bulk DSC (Differential Scanning Calorimetry) and MDSC (Modulated DSC) is also discussed.

Experiments were performed using a Veeco Dimension 3000 AFM equipped with an Anasys Instruments (AI) nano-TA module and AI nanoscale thermal probes. The nano-TA probes are supplied attached to the standard

Dimension 3000 AFM probe mount with wires connected to each leg of the nano-TA probe for facile connection to the nano-TA controllers. The nano-TA probes directly mount onto the base of the standard piezoelectric tube shown schematically in Figure 15b. As a result, experiments can be conducted using the standard segmented photodiode detector system supplied by the AFM microscope. The flow of current through the cantilever results in heat generation at the highly resistive heater region at the tip, while little heating occurs in the highly conductive legs. Each probe is calibrated by using it to identify the onset of known sharp melting points of various polymer standards (polycaprolactone, high density polyethylene and polyethylene-terephthalate). The heating rate used for this analysis was 2 °C/s (though the nano-TA allows the probe heating rate to be controllably varied up to 10,000 °C/second). All images were recorded using tapping mode AFM.

Sample surfaces are first scanned at ambient temperature to generate an image that is used to localize and define features of interest. The probe is next moved to select areas or features and the temperature of the stationary tip is then ramped up linearly with time. This mode of analysis is referred to as local thermal analysis (LTA). As the probe is heated, the tip typically shows an increase in deflection due to local thermal expansion of the material beneath the tip (Figure 15B). As the thermal transition is reached (glass transition temperature (T_g), softening point or crystalline melting point (T_m), the material softens beneath the tip and the probe forms an indentation as it penetrates the sample (Figure 15A). This provides the nanoscale equivalent of a bulk thermo-mechanical analysis experiment. In order to confirm the tested points of interest, images are routinely recorded after performing the temperature ramp.

The nano-TA probes used in this study are the type more typically used for contact mode, and thus their resonance frequency was ~20 kHz, while the typical resonant frequency for tapping mode tips would be around 60 kHz. The probes were still capable of achieving height and phase images with sufficiently high spatial resolution to resolve polymer lamellar structures. Height images (Figure 15A) often show the presence of mounds of material associated with indentations. This deposit is most likely polymeric material that collects and solidifies around the tip after performing a LTA experiment. This buildup of polymer at the tip effectively increases the tip's diameter and leads to a loss in image resolution (Figure 16). An example of this effect is displayed in the height and phase images in Figure 16A. Surface features with sharp boundaries and interfaces are easily recognized on surface of a polyester film recorded at room temperature. Images recorded from the same region displayed in Figure 16A, after performing a LTA experiment produced images (Figure 16B) with a significant loss in resolution, as the images lack the sharp features observable in Figure 16A. Repeated imaging with nano-thermal tips after performing a LTA experiment eventually restored the tip's original image resolution. This process
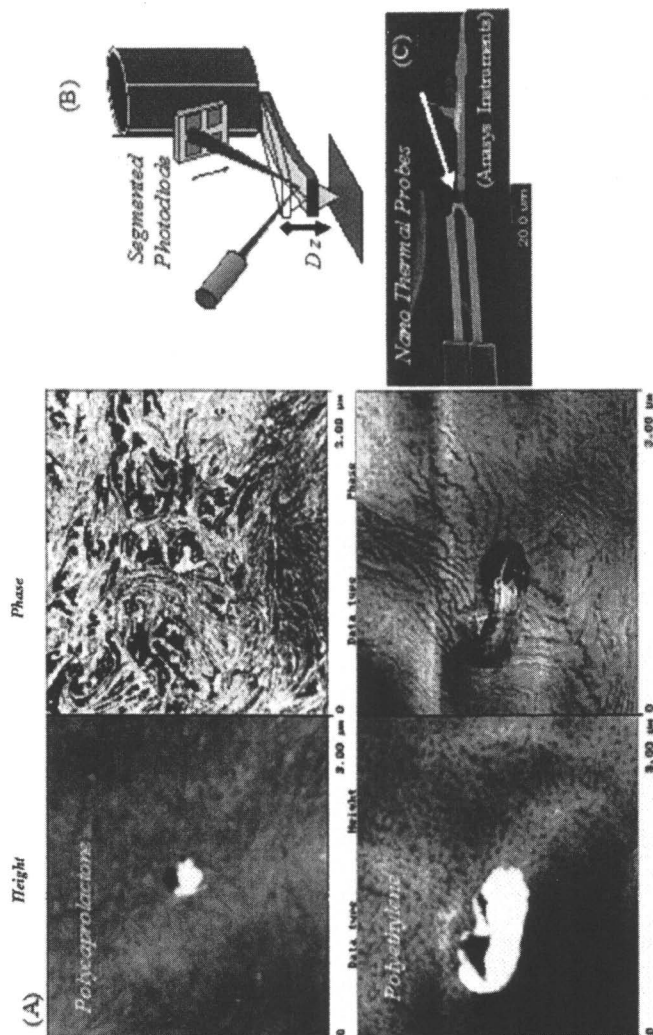
Figure 15. Example of test polymer film samples (polycaprolactone and polyethylene) used for calibration of nanothermal probes. (A) Height (left) and phase (right) images provide evidence of crystalline lamellar structure and spatial resolution comparable to standard AFM probes. Nano thermal probes (C) mount directly onto the Dimension head (B). (Reproduced with permission from J. Therm. Anal. Calorimetry. **2008**, 99 (1), 207-211. Copyright 2008 Springer.)
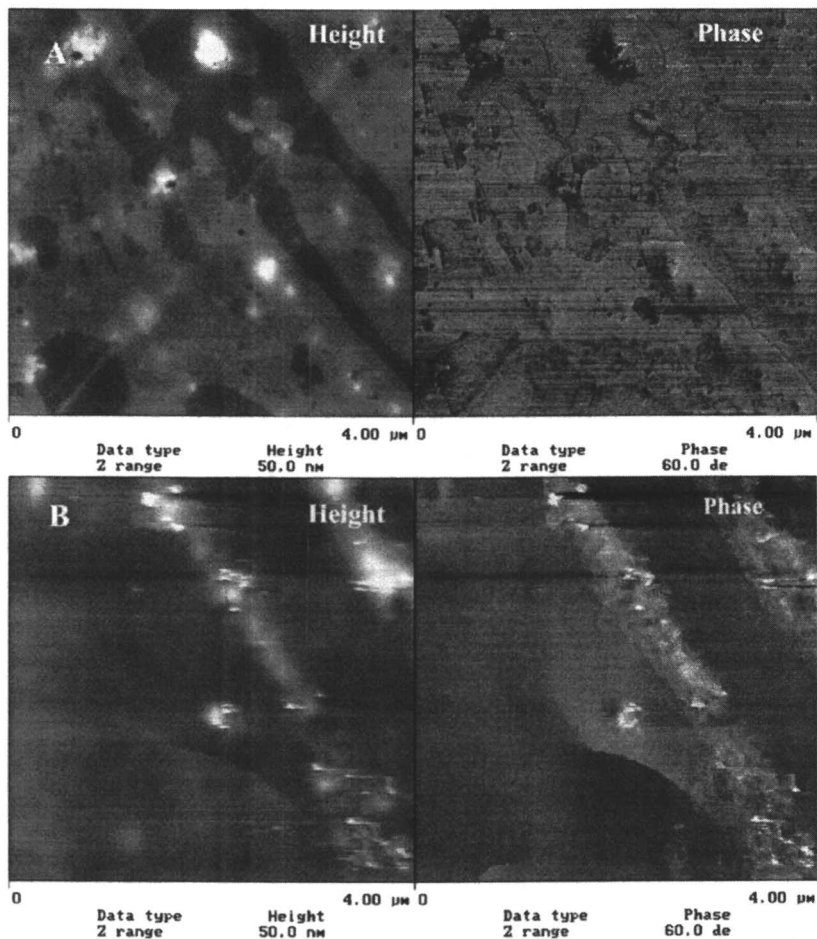
*Figure 16. Example of resolution loss in images due to tip contamination most likely due to adhesion of molten polymer onto the nano-TA tip surface after conducting a LTA experiment. (A) before LTA scan and (B) after LTA scan. (Reproduced with permission from J. Therm. Anal. Calorimetry. **2008**, 99 (1), 207-211. Copyright 2008 Springer.)*

of imaging regions after performing local thermal analysis was found to be useful for both examining the condition of the probe and for cleaning probes.

Two types of coatings were studied, (A) commercial acrylic polyol crosslinked with diisocyanate resin, catalyzed with di-butyl-tin-di-laurate (DBTDL) and cured 30 minutes at 60 °C ; and (B) weathered acrylic-polyurethane (AU) coatings. The weathered AU coatings consist of styrene-

acrylic polymer crosslinked with polymeric 1, 6 hexamethylene diisocyanate and containing two types of TiO_2 particles, TiO_2 Pigment A, (average particle size $\approx$ 20 nm; uncoated and high photoactivity) and TiO_2 Pigment B, (average particle size $\approx$ 250 nm; coated with Al_2O_3 (6%).

A cross-sectional view of a typical commercial automotive coating (Figure 17.) shows the complex, multi-functional nature of these coating systems. Due to the fact that the clearcoat is the first line of defense against environmental influences, understanding surface, near-surface chemical and mechanical property development as a function of composition, cure time and environmental exposure is fundamental to improving their performance. Furthermore, the increased demand for low volatile organic compounds (VOC) systems in automotive refinish industry places greater demands for attaining fast cure at ambient temperature in order to reduce the investment in drying equipment and the time of repair.

Figure 15 show the ambient temperature tapping mode images of polyethylene and polycaprolactone films with the thermal probes and the resolution is clearly comparable to regular non-thermal AFM probes. The thermal response of the probes was next investigated using acrylic-urethane coatings. Coatings that were a few weeks old were tested by LTA in order to measure the coating's response to a thermal scan and determine the indentation morphology and depth (Figure 18).

The residual indentation produced by the thermal probe after measurement of softening point of an acrylic clearcoat film is shown in Figure 18. Section analysis of the height image in Figure 18 was performed in order to measure the indentation depth (~350 nm) and depression made by the nano-TA tip after the LTA experiment. The measured indentation depth provides an estimation of the sampling depth using LTA analysis and can serve as a basis for comparison of softening points (T_g) from the same coatings with bulk film measurements by MDSC.

The dependence of the glass transition temperature on heating and cooling rates is well known and shown to be a kinetic effect that is due to a temperature dependence of structural relaxation rates. This temperature dependence also influences the shape of the heat capacity (C_p) near the T_g(27). In particular, experimental measurements showed T_g to depend linearly with the logarithm of the heating rate. In order to test the ability of LTA to measure a heating rate dependence of softening temperature using thermal probes, experiments were conducted on acrylic clearcoat films (Figure 19A). The three scan rates tested, (6, 10 and 120 °C/min) by LTA clearly show an increase in softening temperature with increased heated rates and a linear logarithmic rate dependence (RSquare = 0.999), similar to that shown by the bulk DSC measurement (Figure 19B).

We next explore use of LTA for measuring cure rates from softening temperature. A coating's softening point is a good measure of crosslink density(28). The formation of three-dimensional networks due to chemical
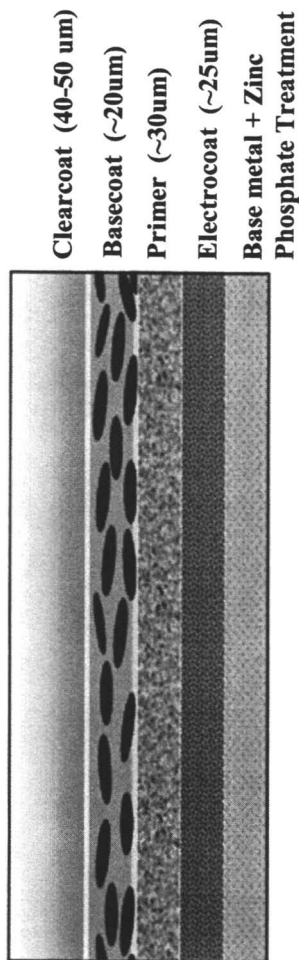
Figure 17. Schematic cross-sectional view of typical automotive coating.

Clearcoat (40-50 um)

Basecoat (~20um)

Primer (~30um)

Electrocoat (~25um)

Base metal + Zinc
Phosphate Treatment
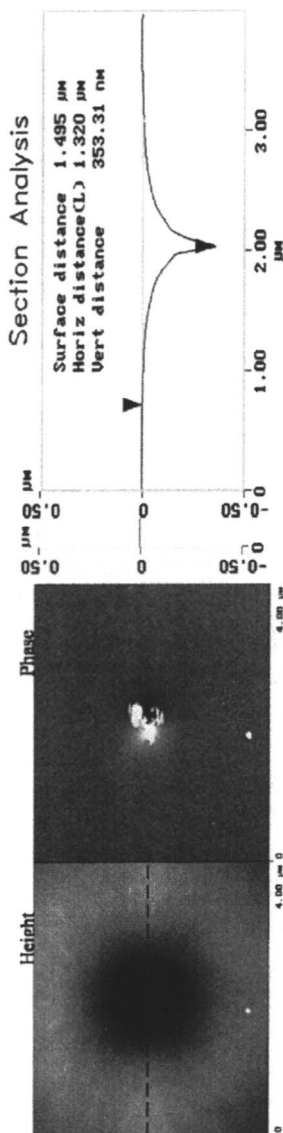
Figure 18. Topview images of the acrylic coating after LTA testing shows the formation of a residual indent ~350 nm deep when analyzed performing a section analysis (dotted line). (Figures 17 and 18 reproduced with permission from J. Therm. Anal. Calorimetry. 2008, 99 (1), 207-211. Copyright 2008 Springer.)
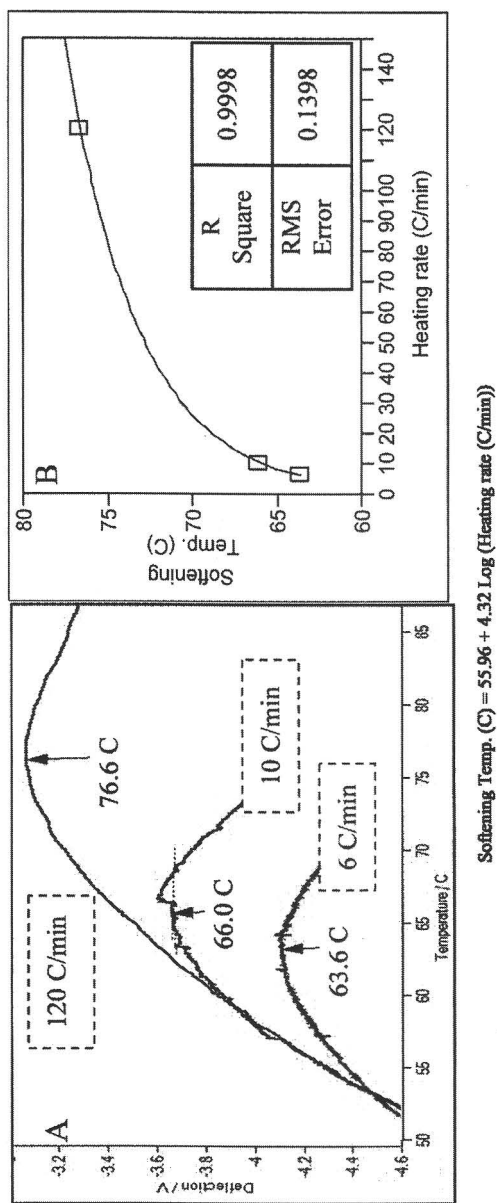
Figure 19. Dependence of (acrylic) film softening point on tip heating rate (A). In particular, softening point onset temperature shows a linear dependence on the logarithm of the tip heating rate (B). (Reproduced with permission from J. Therm. Anal. Calorimetry. 2008, 99 (1), 207-211. Copyright 2008 Springer.)

reactions is widely accepted as a means of improving a coating's properties. It has been shown on a variety of clearcoat systems (1K and 2K solvent-borne clearcoat, and 1K and 2K waterborne clearcoat) cured at different times, at different temperatures, all displayed an increase in T_g, with increasing crosslink density(29). In addition, mechanical properties of coatings also depend on the extent of crosslinks as expressed by the inverse relationship between molecular weight between crosslinks (M_x) and tensile storage modulus (E')

$$E' = 3nRT/M_x \qquad (1)$$

Where n is the density, R the gas constant and T the absolute temperature.

In order to test the utility of LTA for measuring cure (crosslinking) rates, softening points of commercial acrylic coatings cured for 30 minutes at 60 °C, were tested from 2 hrs to 72 hrs, after the 30 min. bake at 60 °C. Figure 20 shows a gradual increase in measured softening temperature with time. A plot of cure time versus softening temperature shows a linear relationship over the cure times measured. The slope of this line is a measure of cure or crosslinking rates.

We next proceeded to use LTA to follow the increase in softening temperature (and crosslink density) as a function of time, 24 and 48 hrs, for select acrylic coatings after their 30 minute bake at 60 °C (Table 2). Pooling of the measured standard deviations of softening points, made in triplicate, from eight coating systems provided a good measure of the LTA test reproducibility. The calculated standard deviation for these coating is 0.26 C (Table 2A).

Photo-degraded Acrylic-polyurethane (AU) coatings

Coatings were exposed, 20 weeks and 41 weeks to UV-A and UV-B. They consist of styrene-acrylic polymer crosslinked with 1,6 hexamethylene diisocyanate and contain two types of TiO_2 particles, TiO_2 pigment A (P-A) (average particle size $\approx$ 20 nm; uncoated and highly photoactive) and TiO_2 pigment B (P-B) (average particle size $\approx$ 250 nm; coated with Al_2O_3 (6%). Figure 21 summarizes and compares softening temperatures measured by LTA (Figure 21A), in comparison with T_g from MDSC, (Figure 21B). Scanning electron micrographs (SEM) are included to show the surface pitting and topography that develops as a result of photodegradation and volatilization of the acrylic-polyurethane coating. This spatial information is lost by the MDSC experiments as these methods can only measure an averaged response and cannot differentiate chemical inhomogeneities on or within the coating.

These data clearly show the surface sensitivity of LTA, as compared to the bulk T_g measurement using MDSC. A considerable body of knowledge has accumulated on the surface sensitivity of photodegradation processes.(30) It is therefore not surprising that LTA provides a sensitive measure of photooxidative effects of UV exposure for clear and TiO_2 filled coatings and displays an
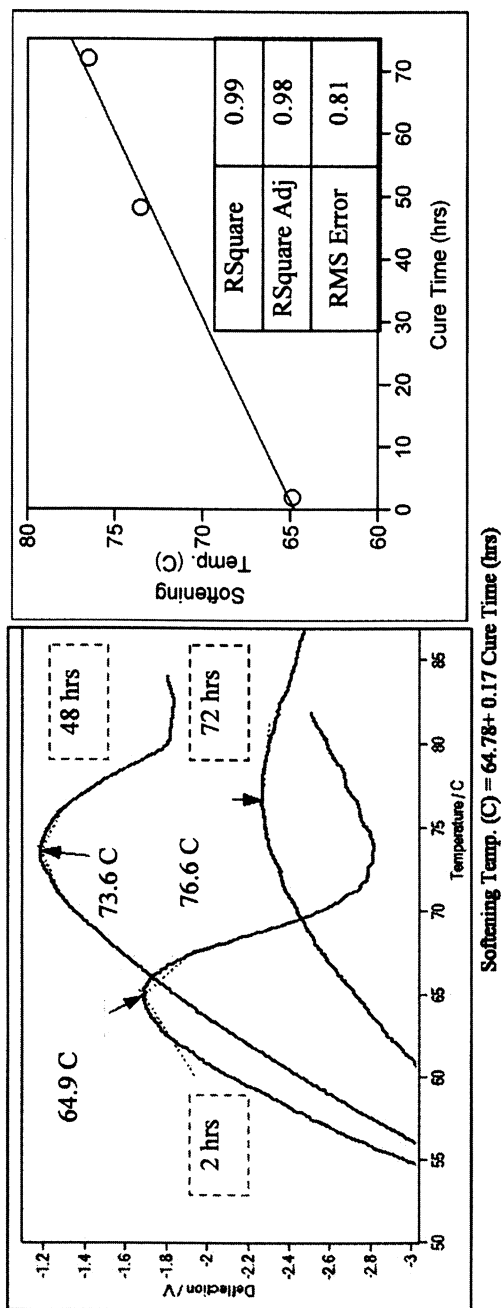
Figure 20. Effect of curing (crosslinking) time at ambient temperature of acrylic clearcoat on softening temperature (A). The softening temperature displays a linear relationship over the cure times measured (B). (Reproduced with permission from J. Therm. Anal. Calorimetry. 2008, 99 (1), 207-211. Copyright 2008 Springer.)

Table 2. Increase in softening temperatures as a function of time, 24 and 48 hrs, for select acrylic coatings (A). Bar plot (B).

(A)

	Acrylic Control	Acrylic + A	Control B	Control B + A
Tested: (24 hrs)				
Nano-Thermal AFM:	57.6	60.3	63.7	64.8
Onset Softening Temp. C.	58.1	59.8	63.8	64.7
	58.0	59.4	63.8	64.9
Avg.	57.9	59.9	63.8	64.8
Std. Dev.	0.3	0.4	0.0	0.2
Tested: (48 hrs)				
Nano-Thermal AFM:	68.2	68.9	73.0	73.8
Onset Softening Temp. C.	67.9	68.8	73.1	73.9
	67.5	69.1	73.5	74.0
Avg.	67.9	68.9	73.2	73.9
Std. Dev.	0.4	0.2	0.2	0.1
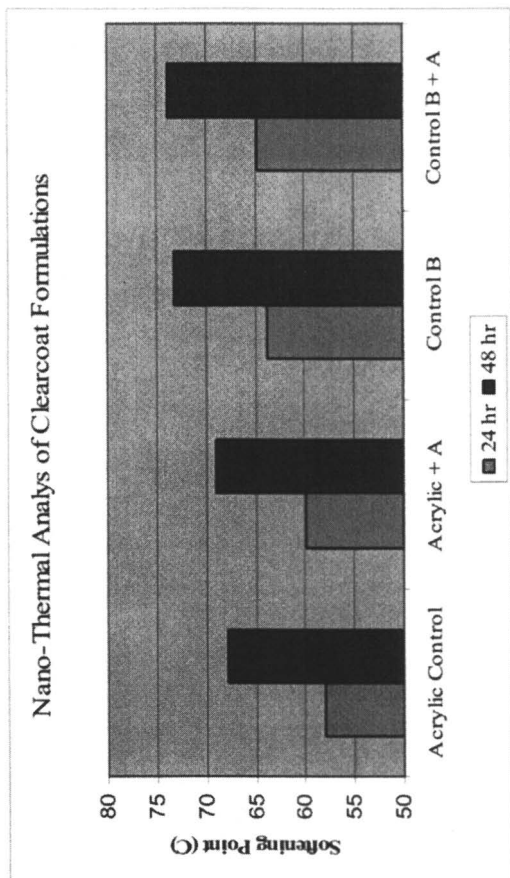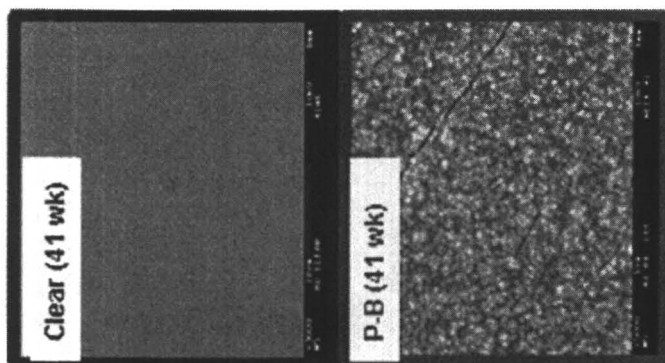
Nano-Thermal Analys of Clearcoat Formulations

(B)

(A)
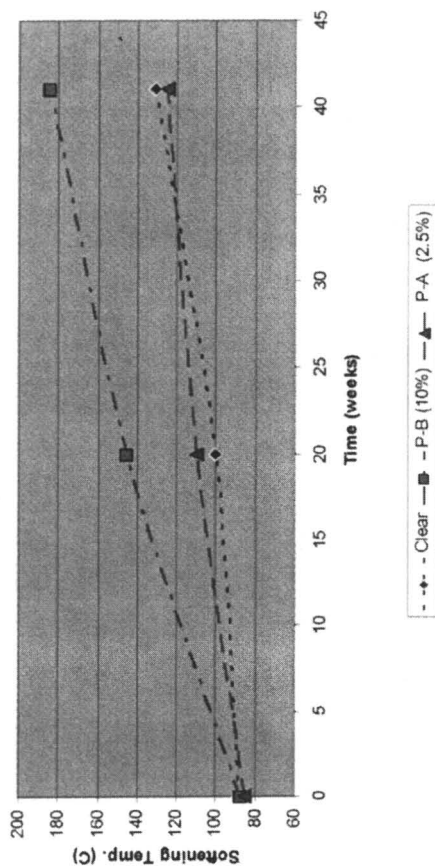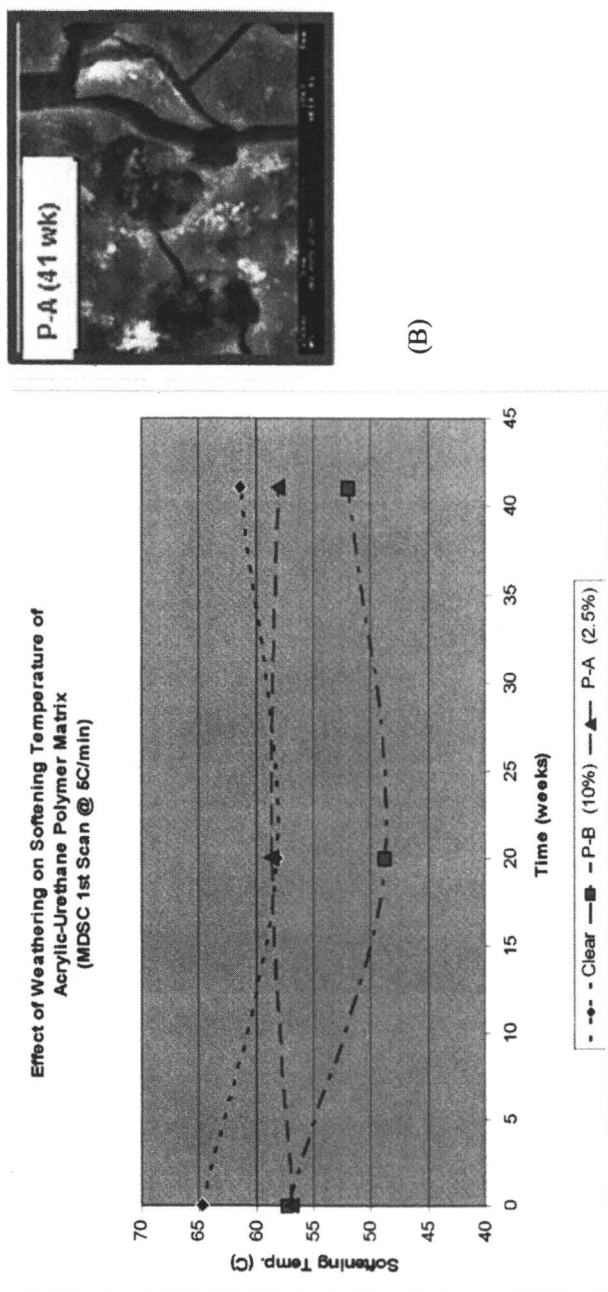
Figure 21. Comparison of softening temperatures measured for UV-exposed (0, 20 and 41 wk) clear and TiO2 filled (P-A and P-B) acrylic urethane coatings using nano thermal analysis (A) and MDSC (B). Surface morphology was also analyzed by scanning electron microscopy. (Reproduced with permission from J. Therm. Anal. Calorimetry. 2008, 99 (1), 207-211. Copyright 2008 Springer.)

increase in softening temperature (i.e. crosslink density) with increased UV exposure times. In comparison, the MDSC characterization of the bulk thin film is not capable of differentiating surface effects from bulk and cannot detect the surface chemical and structural degradation suffered by coatings as shown by the scanning electron micrographs from 41 week exposed coatings (Figure 21).

Conclusions

Nanotechnology is playing an increasing role in the advancement of new materials which are lighter, harder, tougher, smarter and safer. New products and new nano-businesses are emerging with an expanding array of products and applications. Investigations on structure-property relationships at the nanoscale are leading to the development of new nano-tools useful in both characterizing and fabricating nanostructures.

Acknowledgements

References

1. S. Forster, T. Plantenberg, *Angew. Chem. Int. Ed.* **2002**, *41*, *688*.
2. J. Steber, W. Guhl, N. Stelter, F. R. Schroeder, *Tenside Surf. Det.* **1995**, *32*, 515.
3. W.U. Spendel, *US Patent*, 4,959,125 (1990)
4. G.P. Touey, *US Patent* 3,053,677 (1962)
5. C. M. Buchanan and M. D. Wood, *Polymer Preprints* (ACS) (1998) 84.
6. A.Weisenhorn, L., M. Egger, F. Ohnesorge, S. A. C. Gould, S. P. Heyn, H. G. Hansma, R. L. Sinsheimer, H. E. Gaub, and P. K. Hansma, *Langmuir*, **1991**, *7*, 8.
7. W. C. Bigelow, D. L. Pickett and W. A. Zisman, *J. Colloid Sci.*, **1946**, *1*, 513.
8. L. T. Germinario, P. C. Gillette, *Ultramicroscopy*, **1982**, *9(3)*, 225.
9. P. Etienne, J. Phalippou, R. Sempere, *J. Mater. Sci.*, **1998**, *33*, 3999.
10. M. Messori, M. Toselli, F. Pilati, E. Fabbri, P. Fabbri, S. Busoli, L. Pasquali, S. Nannarone, *Polymer*, **2003**, *44*, 4463.
11. J. Bouchet, A.A. Roche, P. Hamelin, *Thin Solid Films*, **1999**, *270*, 355-356
12. W.C. Oliver and G.M. Pharr, *J. Mater. Res.*, **1992**, *7(6)*, 1564

13. S. H. Moon, A. Chiche, A. M. Forster, W. H. Zhang and C. M. Stafford, *Review Scientific Instruments*, **2005**, *76*, Art. No. 062210

14. D. Satas in: *Handbook of Pressure Sensitive Adhesive Technology*, D. Satas (Ed). Van Nostrand, New York (1989)

15. C. Creton in: *Materials Science of Pressure-Sensitive Adhesives*. Processing of Polymers, H.E.H. Meijer (Ed) p. 707, VCH, Weinheim (1997)

16. K. Brown, J. C. Hooker and C. Creton, *Macromol. Mater. Eng.*, **2002**, *287*, 163

17. P. Bahadur, *Current Sci.*, **2001**, *80*, 1002

18. E. P. O'Brien, L. T. Germinario, G. R. Robe, T. Williams, D. G. Atkins, D. A. Moroney, and M. A. Peters, *J. Ad. Sci. and Tech.*, **2007**, *21*, 637

19. E. V. Schmidt, *Exterior Durability of Organic Coatings*. FMJ Intern. Publ., Redhill Surrex, 1988.

20. H. Corti, R. Fernández-Prini and D. Gómez, *Prog. Org. Coat*, **1982**, *10*, 5.

21. C. –I. Wu, X. –J. Zhou and Y. –J. Tan, *Prog. Org. Coat*, **1995**, *25*, 379.

22. S. N. Magonov, V. Elings and M. -H. Whangbo, *Surf. Sci.*, **1997**, *375*, L385

23. N. Magonov, J. Cleveland, V. Elings, D. Denley and M. -H. Whangbo, *Surf. Sci.*, **1997**, *389*, 201.

24. G. Haugstad and R. R. Jones, *Ultramicroscopy*, **1999**, *76*, 77.

25. W.P King, T. Kenny, K. Goodson, G. Cross, M. Despont, U. Durig, H. Rothuizen, G. Binning, P. Vettiger, *Appl. Phys. Lett.*, **2001**, *78*, 1300.

26. B. A. Nelson and W. P. King, *Rev. Sci. Instr.*, **2007**, 78.

27. G. S. Grest and M. H. Cohen, *Phys. Rev. B.* **1980**, *21*, 4113.

28. D. J. Skrovanek and C. K. Schoff, *Prog. Org. Coat.*, **1988**, *16*, 135.

29. W. Schlesing, M. Buhk, M. Osterhold, *Prog. Org. Coat*, **2004**, *49*, 197.

30. D. R. Fagerburg, "Weathering of Polyester and Copolyester Sheeting" Atlas School of Natural and Accelerated Weathering, Miami, FL; April 28, 1999.

Chapter 16

Relating Gloss Loss to Nanoscale–Microscale Topographical Change for a Polymer Coating Exposed to UV Radiation

Xiaohong Gu[1], Li-Piin Sung[1], Bouchra Kidah[1], Mounira Oudina[1], David Martin[1], Aziz Rezig[1], Debbie Stanley[1], Jerry Y. C. Jean[2], Tinh Nguyen[1], and Jonathan W. Martin[1]

[1]Materials and Construction Research Division, National Institute of Standards and Technology, Gaithersburg, MD 20899
[2]University of Missouri at Kansas City, Kansas City, MO 64110

Surface topography and gloss are two important and highly related properties affecting the appearance of a coated surface. Upon exposure to ultraviolet (UV) radiation, the surface roughness generally increases and, correspondingly, its gloss decreases. However, the surface factors affecting gloss are difficult to ascertain. In this paper, atomic force microscopy (AFM) and laser scanning confocal microscopy (LSCM) measurements of a polymer coating exposed to UV radiation have been performed, and the relationship between changes in surface roughness and gloss has been analyzed. The root mean square (RMS) roughness of the coating is related to nanoscale and microscale morphological changes in the surface of a coating as well as to gloss retention. A near-linear dependence of RMS roughness with the measurement length scale (L) is found on a double logarithmic scale, i.e., RMS ~ Lf. The scaling factor, f, decreases with exposure time. A general relationship between surface topography, on nano- to micro-scales, and gloss loss is observed. Future work on using optical scattering technique for appearance measurement will be discussed.

Introduction

Polymeric coatings are commonly used to improve the appearance of buildings, bridges, aircraft and automobiles. The service life of a polymeric coating is largely controlled by how its appearance is affected by ultra-violet (UV) radiation, humidity, temperature and other aggressive weathering factors. Generally, polymeric materials degrade through photooxidation processes, such as chain scission, crosslinking, and the formation of oxidized products.(1) With prolonged exposure, these photochemical processes lead to physical and mechanical changes in a coating.(2,3) In the physical properties, the change in surface topography and gloss are two highly related parameters affecting the appearance of a coated system.

The surface topography of a coating is typically measured through profiling techniques such as contact stylus instruments, phase-measuring interferometers, laser scanning confocal microscopes (LSCM) and scanning probe microscopes.(4) Contact stylus profilers are not an optimal way of measuring surface topography because they apply a force that may deform or damage the surface of the coating. Interference microscopes and confocal microscopes are non-contact measurements and, thus, they are more suitable for monitoring the coating physical changes. The capabilities of these optical microscopic techniques depend on the surface reflectivity of the coating as well as the resolution limits of the microscopes.(5) Atomic force microscopy (AFM) has become a powerful tool for quantifying the surface topography of polymeric coatings because of its 3D nanoscale resolution and the ultra low interaction force between the probe and the sample. However, AFM has limitations with respect to its maximum scanning area (usually up to 100 µm x100 µm) and the maximum measurable peak-to-valley height (usually up to 6 µm). Since surface roughness measurements strongly depend on the scanned area, we have combined AFM and LSCM to study the surface topography of a coating as a function of UV exposure. The roughness of a coating is characterized here in terms of a root mean square (RMS) roughness.

Gloss is the ratio of the intensity of the light scattered by a test surface at the angle of specular reflection compared to that from a standard specular reflecting surface under the same conditions. It is affected by both the topography of a surface and its refractive index.(5) Considerable research has been conducted to identify the relationship between RMS surface roughness and gloss.(6,7) Recent results have indicated that surface height correlations affect gloss.(8,9) The in-plane distribution of undulations on the surface of a material having correlation lengths comparable to the wavelength of the incident light must also be taken into account.(5) It is well known from optical reflectance modeling and measurements that light scattering changes from predominately specular to predominately diffusive (off-specular) with an increase in RMS roughness.(10)

Off-specular reflectances, however, are not commonly measured by commercial handheld glossmeters.

The objectives of this paper are (1) to study nanoscale-to-microscale morphological changes occurring in a UV-exposed epoxy coating, and (2) to understand the relationship between these topographic changes and the gloss loss. The topographic changes of an amine-cured epoxy are monitored by AFM and LSCM during exposure to an outdoor environmental chamber. The gloss measurement is performed using a handheld commercial glossmeter at incident angles of both 20° and 60°. The relationship between surface roughness on different length scales and the gloss loss is discussed.

Experimental[*]

Materials and Specimen Preparation

The amine-cured epoxy used in this study was a mixture of a diglycidyl ether of bisphenol A and 1,3-bis(aminomethyl)-cyclohexane (1,3 BAC) at the stoichiometric ratio. Small amounts of toluene were added to the mixture of epoxy resin and amine curing agent and the resulting mixture was stirred mechanically. After degassing in a vacuum oven to remove bubbles, the mixture of epoxy, amine and solvent was applied onto substrates in a CO_2-free, dry air glove box. Films having a thickness of approximately 150 μm were obtained by casting the mixture onto silicon wafers using a drawdown technique. All samples were cured at room temperature for 24 h in the glove box, followed by heating at 130 °C for 2 h in an air-circulating oven.

Outdoor UV Exposure

Outdoor exposures were conducted on the roof of a NIST research laboratory located in Gaithersburg, Maryland, from October 2003 through September 2004. Specimens were loaded in the multiple-window exposure cells and placed in an outdoor environmental chamber at 5° from the horizontal plane facing south. The bottom of the chamber was made of black-anodized

---

* Instruments and materials are identified in this paper to describe the experiments. In no case does such identification imply recommendation or endorsement by the National Institute of Standards and Technology (NIST).

aluminium, the top of the chamber was covered with "borofloat" glass; all four sides of the chamber were perforated and these perforations were covered with a non-moisture absorbing fabric material that acted as a filter to prevent dust particles from entering the chamber. The exposure cells were equipped with thermocouples and relative humidity (RH) sensors, and the temperature and the RH in the chamber were recorded at one minute intervals throughout the day.

Sample exposures were begun in the middle of the month in four different months. The rates of degradation for the epoxy films exposed at each starting date differed; hence, the exposure durations required to achieve the same amount of degradation depended on the starting date. The starting months were March, July, September, and October and the exposures for each starting date are referred to in this paper as the March Group, the July Group, the September Group, and the October Group.

Laser scanning confocal microscopy (LSCM)

A reflection laser scanning confocal microscope (LSCM) was employed to characterize the surface morphology (topographic profile) of the specimens. A detailed description of the LSCM measurements can be found elsewhere. 3,11 The laser wavelength was 543 nm. The LSCM images are 2D intensity projections with 512 pixels by 512 pixels. The 2D intensity projection image is effectively the sum of all the light scattered by different planar layers of the coating. The pixel intensity level represents the amount of light scattered into the microscope objective. Darker areas represent regions that scatter less light than lighter colored regions do.

The root mean square (RMS) surface roughness S_q is calculated using a surface tilt correlation, i.e., automatic plane fit without a numerical filter, according to the following formula:

$$S_q = \sqrt{\frac{1}{N_x \cdot N_v} \cdot \sum_{i=1}^{N_x} \sum_{j=1}^{N_v} \cdot \left[z(x_i, y_j) - S_c \right]^2} \tag{1}$$

$$S_c = \frac{1}{N_x \cdot N_y} \cdot \sum_{i=1}^{N_x} \sum_{j=1}^{N_v} \cdot z(x_i, y_j) \tag{2}$$

where z (xi,yj) is the surface height at position (xi,yj), and Nx and Ny are the number of pixels in the X- and Y-directions, respectively.

The estimated uncertainties in the roughness data presented in this paper are plus and minus one standard deviation from the mean measurements. Roughness measurements were made at 5 different locations on each sample. All uncertainties are indicated in the figures as well as in the table. Successive LSCM measurements were performed at almost the same location on a specimen to facilitate the study of morphological changes occurring in the films as a function of UV exposure.

Atomic Force Microscopy (AFM)

A Dimension 3100 AFM (Veeco Metrology) was used to image the morphology and the microstructure of the amine-cured epoxy coatings. The AFM was operated in the tapping mode using commercial silicon probes (TESP 70, Veeco Metrology). A resonance frequency of approximately 300 kHz and a free-oscillation amplitude of 62 nm ± 2 nm were used. The set-point ratio (the ratio of set point amplitude to the free amplitude) ranged from 0.60 to 0.80. Similar to LSCM measurements, successive AFM measurements were performed at essentially the same location on a specimen to facilitate the study of morphological changes occurring in the films as a function of UV exposure.

Gloss Measurement

Gloss measurements were conducted using a handheld commercial glossmeter. The samples, which were 36 mm in diameter, were periodically removed from the exposure cells for measurement. Once removed from the exposure cell, the sample was cleaned with a dry nitrogen spray, and then 20° and 60° gloss measurements were performed. The reflection areas for 20° and 60° gloss measurements were 9 mm × 9 mm and 9 mm × 18 mm, respectively. The collection angle was ± 0.9° from the specular angle. Each sample was rotated about 45° after each measurement. A total of 8 to 10 measurements were made on each specimen at each inspection. The data presented are the average of the measurements.

Results and Discussion

Surface topography characterization with AFM and LSCM

AFM topographic images of the epoxy coating after outdoor exposure in an environmental chamber located in Gaithersburg, Maryland, for a March Group

specimen are shown in Figure 1. From left to right, the exposure times are (6, 38, 69, 77, and 84) d, respectively. For each row, starting from the top to the bottom, the scanning areas are 80 μm × 80 μm, 50 μm × 50 μm, 25 μm × 25 μm, 10 μm × 10 μm and 5 μm × 5 μm, respectively. Figure 2 shows the 3D AFM topographic images corresponding to the 5 μm × 5 μm scan area. Approximately the same region of the sample was scanned in successive images at each scan size. General micro-scale morphological changes during degradation can be observed in the 80 μm length scan, while nanoscale structural changes are more easily observed at higher magnifications. For the first 6 d of exposure, the surface appears to be similar to that of the unexposed samples. The small protuberances (bright spots) in these micrographs were most likely created during sample preparation. After 38 d, a few circular features are apparent, which can be seen clearly in the 10 μm or smaller scan sizes. The 3D images show that these circular features are protuberances of various sizes. After 69 d of exposure, a pronounced structure appears on the surface, surrounded by many new circular features. At higher magnifications and 3D presentation (Figure 2C), these features are identified as being pits having elevated edges and an average diameter of 0.3 μm. These pits grow in number and size such that after 77 d of exposure the entire scanned area of the specimen is covered with pits. The perimeters of these late term pits are not circular, but instead, are circularly distorted. These large pits appear to be created through the coalescence of smaller pits. The dimensions and the depth of the pits continue to increase with time such that, after 84 d of exposure, coalesced and deep pits dominate the surface topography. The elevated edges of those pits are still obvious from the micrographs. Chemical degradation processes such as oxidation, chain scission, and mass loss, are likely the major origins of these morphological changes.

Practically, the maximum scanning area for most current AFMs is approximately 100 μm x100 μm. The estimated RMS surface roughness, however, often strongly depends on the area measured.(12) If the scanned area is too small, then the contribution that larger surface features make on the estimated RMS surface roughness is disregarded, and vice versa, i.e., if the scanning area is too large, then the contribution that small defects have on the RMS roughness may be downplayed. To circumvent this problem, the same specimens were scanned with both AFM and LCMS, and the RMS values were estimated over the range of length scales covered by these two microscopic techniques.

Figure 3 shows LSCM (top two rows) and AFM images (bottom three rows) for the same July Group specimen. As expected, in Figure 3, some sub-microscale features revealed by AFM are not visible in LSCM images while the growth and the distribution of cracks, the pit density, and the large scale surface roughness that can be easily observed in the LSCM images can not be observed in the AFM. Therefore, by combining the LSCM technique with the AFM, one
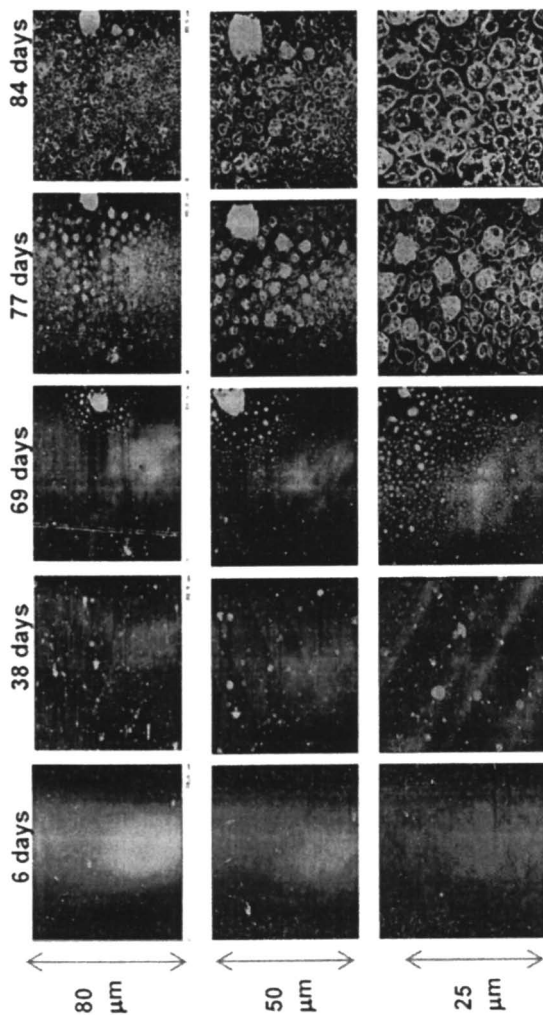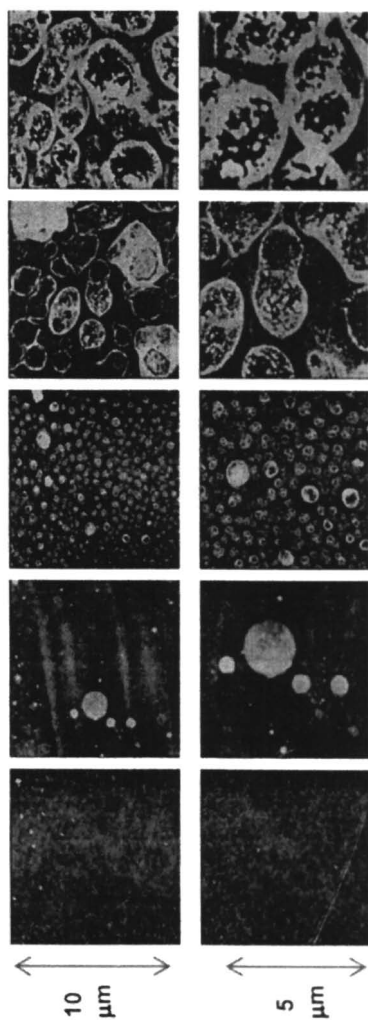
Figure 1. AFM topographic images of a March Group epoxy coating after outdoor exposure in Gaithersburg, Maryland, for (from left to right) 6, 38, 69, 77 and 84 d, respectively. Lateral dimensions for each row of images (from top to bottom) are 80 μm, 50 μm, 25 μm, 10 μm and 5 μm, in which the height scales are 75 nm, 40 nm, 30 nm and 25 nm, respectively.
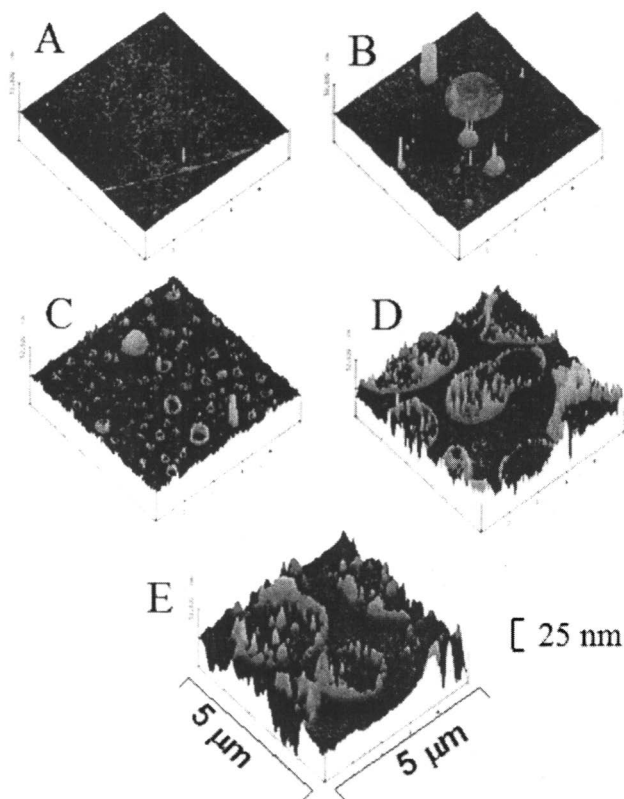
*Figure 2. 3-D AFM topographic images of a March Group epoxy coating after
outdoor exposure for (A) 6 d, (B) 38 d, (C) 69 d, (D) 77 d, (E) 84 d, respectively.
Lateral dimensions for the images are 5 μm × 5 μm. The height scale is 25 nm.*

can obtain a global topographic perspective of the information available over a range of length scales between approximately 2 mm and a few nanometers.

Surface roughness and scaling factor

Further insight into topographic changes is provided by an analysis of the surface roughness. Figure 4A shows the RMS roughness as a function of exposure time for four groups exposed in the different months. These roughness values, based on 460 μm × 460 μm LSCM images, were calculated using a surface tilt correlation (automatic plane fit) without a long wavelength cutoff filter. It can be seen that the RMS roughness for all four groups increases with exposure time, though the rate of change is highly dependent on the starting month. The increasing rate of the July Group samples is the fastest, and the rate of the October Group is lowest. Differences in the power distribution of solar spectra, temperature and humidity probably lead to these differences in the roughness change rates. The effect of measurement area on the RMS roughness is shown in Figure 4B. The length scales are (10, 25 and 50) μm for the AFM measurements, and (184 and 460) μm for the LSCM measurements. A marked dependence of surface roughness on the measurement scale is observed. For a quantitative evaluation of the measurement scale with regard to the structure characteristics of the surface, the RMS roughness values are plotted against scan sizes on a double logarithmic scale for different exposure times, as shown in Figure 5. The length scales of the measured sizes range from 2.5 μm to 460 μm. Specimens from the March and September Groups were selected for the analysis. A near-linear dependence of the RMS roughness with the measurement length scale (L) is found for the same sample in a double logarithmic scale, i.e., $RMS \sim L^f$. The scaling factor, f, can be obtained from the slope of the straight line. For both groups, the correlation coefficient (R^2) for the linear fitting varies between 0.903 and 0.972. Generally, a shorter exposure time corresponds to a higher R^2 value, while a longer exposure corresponds to a lower R^2 value. The scaling factor decreases with increasing exposure times for all groups, however, the trend of the scaling factor against exposure time varies with different groups. For example, a steeper decrease of scaling factor is found for the specimens in the March Group than for the September Group (Figure 6). These results are consistent with those reported for both fluoro-based[13] and polyurethane coatings.[14] The diminish of the scaling factor with exposure time is due to the increase in the roughness for a longer UV exposure. The lower scaling factors generally correspond to the rougher surfaces.

A linear relationship between the log of the RMS roughness and the log of the measured size has been described as a characteristic feature of a surface that has a fractal dimension.[15,16] We believe that more sophisticated analyses, e.g., multi-scale analysis[17], power spectral density and wavelet-based
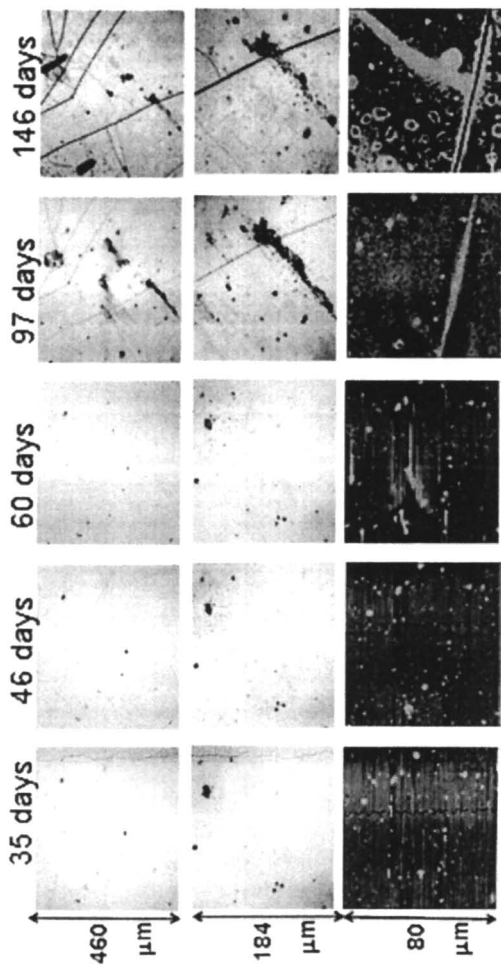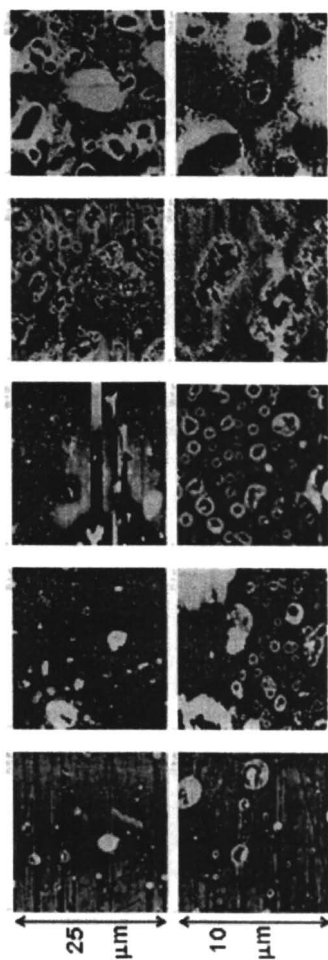
Figure 3. LSCM (top two rows) and AFM (bottom three rows) topographic images of a July Group epoxy coating after outdoor exposure in Gaithersburg, Maryland, for (from left to right) 35 d, 46 d, 60 d, 97d, 146 d and for lateral dimensions (from top to bottom) of 460 μm, 184 μm, 80 μm, 25 μm, and 10 μm, respectively. The height scales for AFM images are 100 nm, 50 nm, and 25 nm for scan sizes of 80 μm, 25 μm, and 10 μm, respectively.

method(18), need to be performed before any conclusions on the fractal character of these surfaces can be made.

Gloss Retention and Its Relationship to Surface Roughness

Gloss retention is defined as the percentage change in the gloss of a specimen relative to its initial gloss value. Figures 7A and 7B show the 20° and 60° gloss retention versus the exposure time for the four exposure groups. Different groups display different gloss change behaviors, indicating that the solar power distribution, temperature, and humidity of the different seasons may play a central role in the gloss loss of coating surfaces. It appears that the October Group has the longest plateau before the gloss significantly drops, while the July Group has the shortest one. Examination of the chemical changes by Fourier transform infrared spectroscopy (not shown) indicate that the photo-oxidation and chain scission between the different groups have a similar trend to the physical changes, i.e., the July group changes fastest while the October group changes slowest.

Figure 8 shows the correlation between roughness and gloss retention in the early stages of the degradation of the September Group for two scan sizes: (A) 50 μm × 50 μm by AFM, and (B) 460 μm × 460 μm by LSCM. For both length scales, the estimated correlation coefficient between the gloss retention and RMS roughness is slightly higher for 60° gloss than 20° gloss measurements (R^2=0.82 vs R^2=0.78 for the 50 μm scan size, and R^2=0.93 vs. R^2=0.87 for the 460 μm scan size, where R is the correlation coefficient). As discussed previously, gloss measurement by a commercial handheld glossmeter only collects a narrow angular range of light scattered around the specular direction. With the increase of RMS roughness, the proportion of the specular scattering in the total light scattering profile decreases.(9) For rougher surfaces, the 60° gloss measurement provides a higher signal to noise than the 20° gloss measurement due to a higher reflectance values for incident angle of 60° than that of 20°.(9) Additionally, the correlation coefficient between the gloss retention and RMS roughness is slightly higher for the RMS obtained from the 460 μm × 460 μm scan area than those from the 50 μm × 50 μm scan area (0.93 vs. 0.82 for 60° and 0.87 vs. 0.78 for 20°). Similar results have been reported from other AFM and LSCM studies on the weathering of polymeric coatings.(13,19,20) These observations indicate that while higher magnification images are very important for visualizing physical changes occurring in the very early stage of coating degradation(18,21), the longer wavelength surface roughness may be more directly related to the gloss measurement. It is likely that surface features that are larger or have a large periodicity could be overlooked if the size of the measured area is too small. More quantitative analysis can be provided by mathematical models.(8)
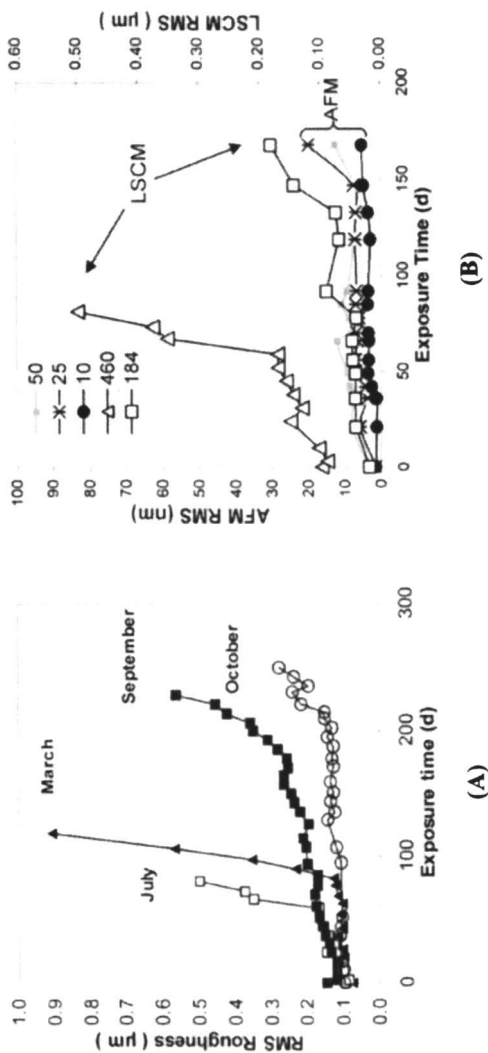
Figure 4. (A) RMS roughness (LSCM) vs. exposure time for four groups with exposure starting dates in October, March, July and September. The LSCM length scale is 460 μm. The RMS data presented in each group is averaged from at least two samples; 5 different locations were measured on each sample. (B) RMS roughness vs. exposure time for different scanned sizes (July Group). The RMS roughness was obtained from the same sample using two different techniques – LSCM and AFM as indicated in the figures. The length scales are 522.1 μm, 208.84 μm, 90.8 μm, 28.375 μm, and 11.35 μm, respectively. Each LSCM roughness data is the average of the measurements on 5 different locations, and the AFM data is the average of 3 different locations of the same sample. Uncertainties for all data points are less than 10 %.
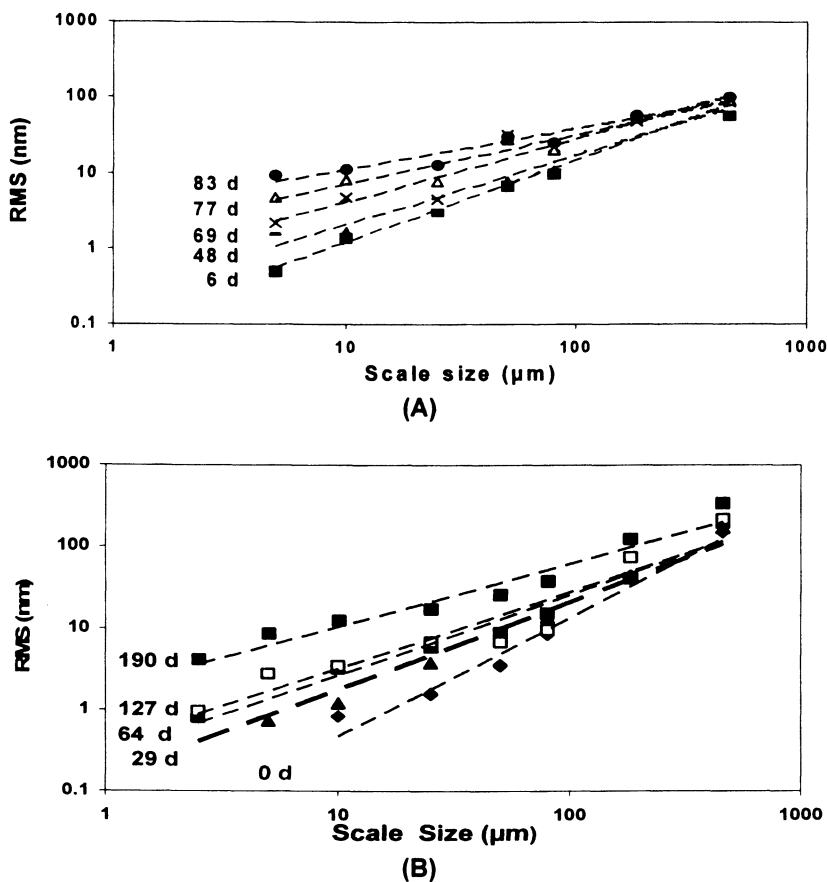
Figure 5. RMS roughness vs. scan sizes on a double logarithmic scale at different exposure times. The lateral dimensions are (2.83, 5.66, 11.32, 28.3, 56.6, and 90.56) µm for AFM and (208.88 and 520.72) µm for LSCM. (A) and (B) represent the March group and September group, respectively. The exposure times are shown in the figures. Each LSCM roughness data is the average of the measurements on 5 different locations, and the AFM data is the average on 3 different locations of the same sample. Uncertainties for all data points are less than 10 %.
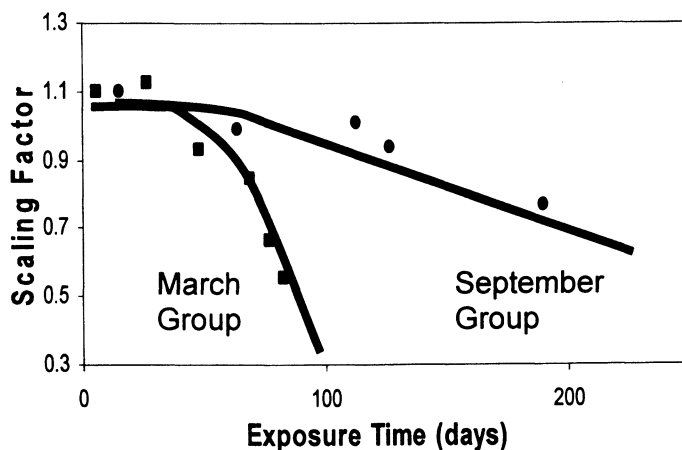
Figure 6. Scaling factor as a function of exposure time for March and September Group specimens. A faster decrease of scaling factor was found for the specimens in the March Group than for the September Group. Uncertainties for all data points are less than 10 %. Lines represent the general trend of the data.

As mentioned previously, the selected four groups exhibit an increase in the RMS roughness (Figure 3) and a corresponding decrease in the gloss retention (Figure 7) with longer outdoor exposure. To further establish the relationship between gloss and the roughness, 60° gloss retention of these four groups is plotted against the RMS roughness obtained from 460 μm × 460 μm measured areas (Figure 9). It appears that the gloss data from these four groups scatter around but still follow a straight line with the increase in surface roughness, indicating that, within the measurement range, a general relationship between microscale topographical changes and macroscale appearance could be established regardless of the seasons of outdoor exposure.

From the plots of Figure 9, however, groups having similar RMS values can have obvious different gloss retentions. This represents a shortcoming in the use of RMS alone to represent the roughness of a surface. Since the RMS roughness does not take the distance between surface features into account, a surface with a few distantly spaced high-amplitude features may have the same RMS value as one with many closely spaced low-lying features(5), which is suggested by the images in Figure 10. Future research will measure the specular and off-specular reflectance of the specimens using angle-resolved light scattering technique. By applying an optical scattering model(22) to the AFM and LSCM profile data coupled with the glossmeter geometry, the correlation between the nano-
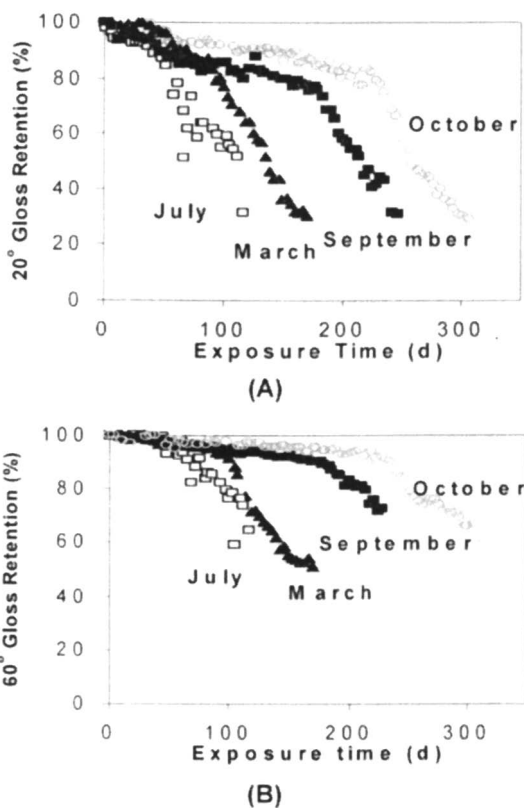
Figure 7. (A) 20° and (B) 60° gloss retention vs. exposure time for four groups, which were exposed starting in October, March, July and September, respectively. 60° gloss retention changes tend to lag behind the 20° gloss retention changes. The gloss data is the average of 8 to 10 measurements on each specimen. Variations for all data points are less than 10 %.
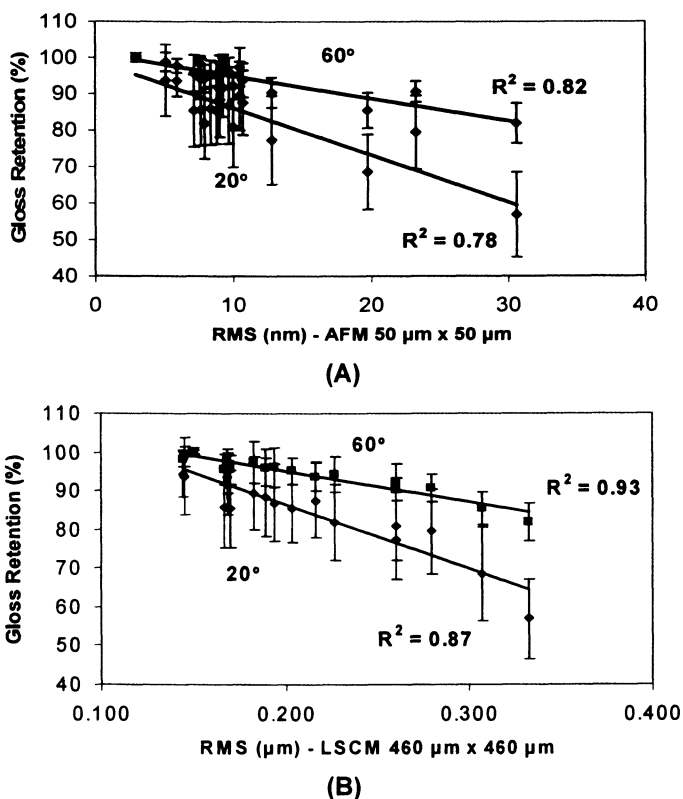
Figure 8. Correlation between roughness and gloss retention for two scan areas for September Group: (A) 50 μm × 50 μm by AFM, and (B) 460 μm × 460 μm by LSCM. R is the correlation coefficient. The uncertainty bars represent one-standard deviation.
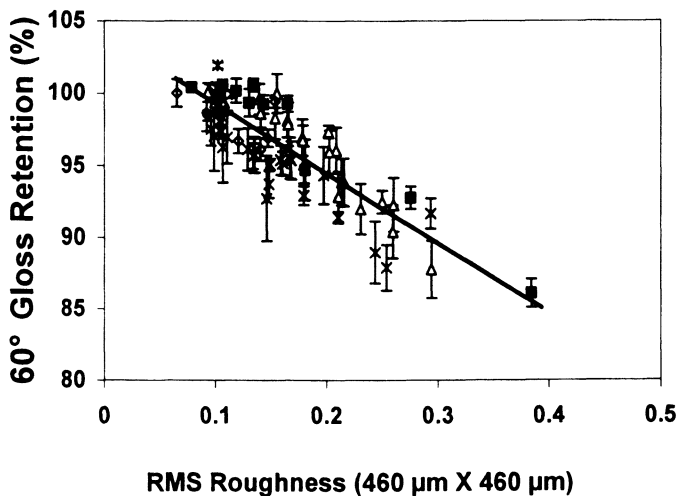
Figure 9. 60° Gloss retention vs. RMS roughness for four groups, which were exposed starting in October, March, July and September, respectively. The black solid line represents the general trend of the data within the measurement range. The uncertainty bars represent one-standard deviation.
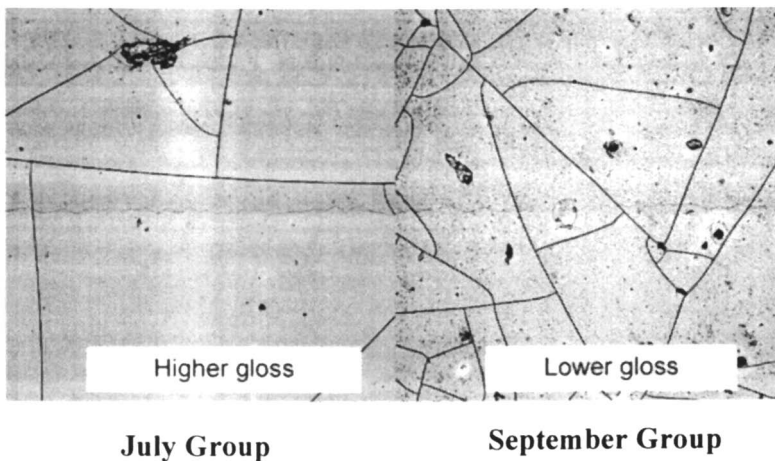
Figure 10. LSCM images of two exposed samples with the same roughness value but different gloss retention values. (RMS=0.385 μm, and gloss retention values are 88 % for the July Group and 80 % for the September Group).

scale/microscale topographical changes and macroscale appearance can be predicted.

Conclusions

AFM and LSCM techniques have been used to characterize the nanoscale and microscale topographical changes of an amine-cured epoxy coating exposed to outdoors at different starting times, and the relationship between surfaceroughness changes and gloss loss has been analyzed. The RMS roughness was observed to increase with exposure time, and the rate of change was highly dependent on the exposure starting month. The result shows a near-linear dependence of RMS with the measurement length scale on a double logarithmic scale. Further, the coefficient of correlation between gloss retention and RMS roughness is slightly higher for the 60° gloss than for the 20° gloss, and gloss of both angles appear to relate better with the roughness obtained by LSCM than that measured by AFM. By applying an optical scattering model to the AFM and LSCM profile data coupled with the glossmeter geometry, the correlation between the surface morphology of the polymeric coatings and the macroscale appearance could be better predicted.

References

1. Rabek, J. F. In Polymer Photodegradation – Mechanisms and Experimental Methods; Chapman &Hall, New York, 1995, p 4.
2. VanLandingham, M.R.; Nguyen, T.; Byrd, W.E.; Martin, J.W., *J Coat Technol* **2001**, *73*, 43.
3. Sung, L.; Jasmin, J.; Gu, X.; Nguyen, T.; Martin, J. W., *J. Coat Technol. Research* **2004**, *1* (4), 267.
4. Vorburger, T.V.; Dagata, J.A.; Wilkening, G.; Iizuka, K. In Beam Effects, Surface Topography, and Depth Profiling in Surface Analysis; Czanderna et al. Eds.; Plenum Press, New York, 1998.
5. Assender, H.; Bliznyuk, V.; Porfyrakis, K., *Science* **2002**, *297*, 973.
6. Davies, H. In Proc. Inst. Electr. Eng. Part IV, 1954, V. 101, p. 209.
7. Beckmann, P.; Spizzichino, A. In The Scattering of Electromagnetic Waves from Rough Surfaces; Pergamon Press Ltd., London, 1987.
8. Alexander-Katz, R.; Barrera, R.G.. *J Polym Sci Part B: Polym Phys* **1998**, *36*, 1321.
9. McKnight, M. E.; Marx, E.; Nadal, M.; Vorburger, T. V.; Barnes, P. Y.; Galler, M. A., *Appl Optics* **2001**, *40(13)*, 2159.
10. Bennett, J.M.; Mattsson, L. In Introduction to Surface Roughness and Scattering; Opt. Soc. Am., Washington, D.C., 1989.

11. Corle, T.R.; Kino, G.S. In Confocal Scanning Optical Microscopy and Related Imaging Systems; Academic Press, 1996, pp 37-39
12. Sayles, R.S.; Thomas, T.R., *Nature*, **1978**, *271*, 431.
13. J. Faucheu, L.P. Sung, J.W. Martin, K.A. Wood, "Relating Gloss Loss to Topographical Features of A PVDF Coating", FSCT·ICE 2004 Proceedings of the 82th Annual Meeting Technical Program, McCormick Place North, Chicago, IL, October 27-29, 2004.
14. Johnson, M.A.; Cote, P.J., *J Coat Technol* **2003**, *75*, 51.
15. Bliznyuk, V.N.; Burlakov, V.M.; Assender, H.E.; Briggs, G.A.D.; Tsukahara, Y., *Macromol Symp* **2001**, *167*, 89.
16. Mandelbrot, B.B. In The Fractal Geometry of Nature; Freeman, New York, 1982.
17. Bigerelle, M.; Gorp, A.V.; Lost, A. In Proceedings of 10th International Conference Metrology and Properties of Engineering Surfaces, 2005, pp. 69-80.
18. Jiang, X.; Blunt, L., *Wear*, **2004**, *25*, 1235.
19. Gu, X.; Nguyen, T.; Ho, D.L.; Oudina, M.; Martin, D.; Kidah, B.; Jasmin, J.; Rezig, A.; Sung, L.; Byrd, E.; Jean, Y.C.; Martin, J. W., *J Coat Technol Research*, **2005**, *1*, 547-556.
20. Biggs, S.; Lukey, C.A.; Spinks, G.M.; Yau, S.T., *Prog Organic Coat* **2001**, *42*, 49.
21. Gu, X.; Nguyen, T.; Sung, L.; VanLandingham, M.R.; Nguyen, D.; Fasolka, M.J.; Chang, N.; Wu, T.; Jean, Y.C.; Martin, J.W., *J Coat Technol Research*, **2004**, *1(3)*, 191.
22. Hunt, F. Y.; Marx, E.; Meyer, G. W.; Vorburger, T. V.; Walker, P. A.; Westlund, H. B. In *Service Life Prediction: Methodology and Metrologies*; Martin, J. W.; Bauer, D. R., Eds., ACS Symposium Series 805, American Chemical Society: Washington, DC, 2002.

Chapter 17

Assesment of Spectrophotometric Assay Methods on Nanostructured Pigments

Stephanie S. Watson, Amanda Forster, I-Hsiang Tseng, and Li-Piin Sung

Polymeric Materials Group, Building and Fire Research Laboratory, National Institute of Standards and Technology, 100 Bureau Drive, Gaithersburg, MD 20899

Titanium dioxide (TiO_2) is used in building and construction applications as a pigment or filler for polymeric products to improve their appearance and mechanical properties. TiO_2 pigments exhibit a wide range of photoreactivity including reactivities that would be detrimental to the service life of polymeric materials. The lack of a simple, inexpensive metrology for measuring photoreactivity has hindered innovation and acceptance of new pigments, especially nanostructured pigments. Spectrophotometric assays, which monitor specific reactions within the photoreactivity mechanism, show promise as a reliable diagnostic method for ranking pigment reactivity and for understanding variations in the photoreactivity mechanisms in TiO_2. In this study, spectrophotometric assays were investigated on an array of TiO_2 pigments of different crystal phases, particle sizes, and metal oxide encapsulants as a function of assay experimental parameters, such as buffer composition and buffer pH. Assays include the reduction of methyl viologen, in which electron production from the TiO_2 particles is measured, and the oxidation of leuco-crystal violet with horseradish peroxidase to measure the production of peroxide, a common reaction product in the photoreactivity mechanism. Light scattering measurements were used to follow TiO_2 particle flocculation in the assays upon changing experimental conditions of assay matrix to determine pigment cluster size and to ascertain the contribution that pigment clusters have on pigment photoreactivity.

© 2009 American Chemical Society

349

Introduction

Large quantities of titanium dioxide (TiO_2) are used in coatings, sealants, plastics and paper products for opacification and other pigmentary purposes. TiO_2 is the most effective pigment for hiding or opacity due to its high refractive index and excellent ultraviolet (UV) absorption properties.(1) However, TiO_2 is also a photoreactive material in that absorption of UV radiation promotes electrons from the valence band into the conduction band, leaving behind a positively charged species, or hole, in the valence band. These electron-hole pairs are extremely reactive and are capable of participating directly in oxidation-reduction reactions with organic materials and/or undergoing interfacial charge transfer with surface or adsorbed species to form reactive radical species.(2)   Within the last decade, the ability of TiO_2 to decompose organic compounds has been exploited in applications such as air cleaning, water purification and self-cleaning/self-disinfecting surfaces.(3,4) Photostable, nano-particle TiO_2, on the other hand, appears to improve the long-term performance and initial mechanical and durability properties of coatings without affecting appearance.(5,6)

Commercial TiO_2 materials exhibit a wide range of photoreactivities, depending on crystal phase, manufacturing method, and post-processing steps employed.(7) Presently, no standardized, quantitative measurement techniques exist for assessing the photoreactivity of pigments. Instead, qualitative or product-based tests are used, which often do not provide fundamental information about the underlying mechanisms.(8-10) Observing the performance of a pigment or catalyst in the final product, while a necessary part of any product development cycle, does not provide insight into the mechanistic processes involved.

This paper evaluates spectrophotometric assay methods for measuring photoreactivity of TiO_2 nanostructures. Spectrophotometric assays quantitatively measure the concentration of holes and electrons generated during band gap irradiation or of products arising from the reactions of holes and electrons with a surrounding matrix, such as hydrogen peroxide. A number of chemical assays for assessing the photoreactivity of TiO_2 exist and are documented in the technical and patent literature.(11-13) As yet, these assays have not been used for testing photoreactivity of nanoparticle materials. TiO_2 pigments of different crystal phases, particle sizes, and metal oxide encapsulants were studied using these assays. Buffer composition, buffer pH, and pigment loading effects were also investigated. Light scattering measurements were used to follow TiO_2 particle flocculation in the assays to determine cluster size and to ascertain the contribution that clusters have on pigment photoreactivity.

Experimental[†]

Methyl Viologen Assay

A 1.5 g/L suspension of TiO_2 with 2.5 x 10^{-3} mol/L in methyl viologen dichloride and 3.0 x 10^{-2} mol/L in disodium ethylenediaminetetraacetic acid (EDTA), buffered to pH = 6.0 with a 0.2 mol/L phosphate buffer, was prepared. In later methyl viologen assay experiments, a buffer using potassium hydrogen phthalate (KHP) was used for examining results with no phosphates present. The suspension was purged with argon (Ar) in a sealed sparging reactor for 20 min, and then irradiated with UV radiation with a 100 W mercury (Hg) lamp for 2 h. During the UV irradiation period, the TiO_2 suspension was mixed with a magnetic stir bar. In an Ar-purged glove bag, 3 mL of the irradiated suspension was transferred into a cuvette for UV-visible (UV-VIS) spectroscopy using a syringe equipped with a 0.2 μm filter. The absorbance of the methyl viologen cation radical at 602 nm was measured on a UV-VIS spectrometer with a diode array detector. Dilutions of dye solutions with absorbance values greater than 2.0 AU were sequentially diluted to determine linearity with dye concentration. All solutions exhibited linear behavior with dilution. Absorbance values are reported as absolute values without normalization. The standard uncertainty associated with UV-VIS spectroscopy absorbance measurements is typically ±2%.

Hydrogen Peroxide Assay with Leuco-Crystal Violet

250 mg of TiO_2 pigment was mixed with 25 mL of 1 mol/L acetate buffer (pH = 4.4) and irradiated with UV radiation with a 100 W Hg lamp for 2 h. During the UV irradiation period, the TiO_2 suspension was mixed with a magnetic stir bar. The irradiated pigment suspension was then filtered and 8.5 mL of the filtrate was mixed with 0.5 mg/mL horseradish peroxidase and 1 mL leuco-crystal violet (LCV) solution (100 mg LCV dye in 200 mL of 0.5 % by volume hydrochloric acid). A solution of 0.3 % by volume solution of hydrogen peroxide was used as a standard for calibration. The absorbance of the leuco-crystal violet solution at 596 nm was immediately measured using UV-VIS

[†] Certain trade names and company products are mentioned in the text or identified in an illustration in order to adequately specify the experimental procedure and equipment used. In no case does such an identification imply recommendation or endorsement by the National Institute of Standards and Technology, nor does it imply that the products are necessarily the best available for the purpose.

spectroscopy with a diode array detector. Absorbance values are reported as absolute values without normalization. The standard uncertainty associated with UV-VIS spectroscopy absorbance measurements is typically ± 2 %.

Isopropyl Alcohol Test

TiO$_2$ suspensions were prepared from dried TiO$_2$ (120 °C for 2 h) and 20 mL isopropanol and purged with compressed air (500 mL/min) for 1 min prior to UV irradiation. Pigment loadings were varied and were based on the pigment surface treatment: 1 g for alumina (Al$_2$O$_3$)-treated pigments and 4 g for silica (SiO$_2$)-treated pigments. A jacketed beaker, containing the TiO$_2$ suspension, was illuminated from the top with UV light from a 100 W Hg lamp. Suspensions were stirred with a magnetic stirrer to maintain the suspension of the pigment. After 2 h of UV exposure, the suspension was filtered and the acetone content of the filtrate was determined by gas chromatography with flame ionization detection. A blank measurement was also performed using isopropanol without pigment to establish the initial amount of acetone present in the isopropanol reagent.

Light Scattering Measurements

Light scattering measurements were carried out using a variable angle light scattering instrument. The instrument was calibrated with National Institute of Standards and Technology (NIST) traceable polymer sphere standards ranging in diameter from 90 nm to 304 nm. In this study, dynamic light scattering (DLS) data was analyzed to estimate the particle/cluster size of TiO$_2$ in the various assays. The wavelength of laser used in this study was 532 nm. Scattering angles of 15° and 30° were used for the measurements. Suspensions consisted of TiO$_2$ and the spectrophotometric assay components as described in the above sections. Suspensions were mixed for 3 min by shaking followed by sonication for 30 min. 2 mL aliquots of the assay suspension were transferred into a 15 mm diameter DLS vial. The assay suspension was measured at 15° for 50 min followed by measurements at 30° for 90 min. The assay suspensions remained stable after 50 min, but some pigment settled after 90 min. Thus, all data was measured for 50 min. Some of the assay suspensions were diluted from 90 % to 10 % by volume of their original TiO$_2$ concentration with their corresponding buffer solutions.

Dynamic fluctuations of the scattered light from the particles in the assay matrix were measured. The time dependence of the scattered light at a particular scattering angle (θ) was analyzed by an autocorrelation function of the scattered light. The normalized time autocorrelation function of the intensity of the scattered light, $g_2(\tau)$, for a time, τ, is given by(14):

$$g_2(\tau) = \frac{\{I(t)I(t+\tau)\}}{\{I(t)\}^2} \tag{1}$$

where I (t) and I (t + τ) are the intensities of the scattered light at times t and t + τ, respectively. The intensity-intensity time autocorrelation function, g_2 (τ), may be expressed as

$$g_2(\tau) = 1 + \beta[g_1(\tau)]^2 \tag{2}$$

where

$$g_1(\tau) = \frac{\{E(t)E^*(t+\tau)\}}{\{E(t)E^*(t)\}} \tag{3}$$

is the time autocorrelation function of the electric field of the scattered light. E (t) and E (t + τ) are the scattered electric fields at times t and t + τ, respectively, and * denotes complex conjugates. β is a factor that depends on the experimental geometry. For monodisperse particles in solution, the correlation function is characterized by an exponential decay

$$g_1 \ (\tau) = \exp \ [\ -\Gamma\tau] \tag{4}$$

with a decay rate, $\Gamma = D q^2$, where q is the magnitude of the scattering wave vector and D is the diffusion coefficient. For Eqn 4 the intensity-intensity time autocorrelation data provides information about diffusion in the sample. The Stokes-Einstein relation

$$D = \frac{k_B T}{6\pi\eta R_h} \tag{5}$$

relates the diffusion coefficient to the hydrodynamic radius, R_h, of the particles, where k_B is Boltzmann's constant, T is the absolute temperature in degrees Kelvin, and η is the dynamic viscosity for the solvent of the suspension. For dilute suspensions used in this study, η was similar to solvent viscosity. For a polydisperse sample, g_1 (τ) no longer has a simple exponential function. The effect of a distribution of decay rates on g_1 (τ) is given by

$$g_1(\tau) = \int_0^\infty G(\Gamma) \exp[-\Gamma\tau] d\Gamma \tag{6}$$

where G (Γ) is the function describing the distribution of decay rates. In this study, non-linear least squares regression analysis was used to fit the experimental autocorrelation functions to determine the hydrodynamic radius of particles in the TiO_2 suspensions based on these expressions.

Results

Table 1 lists the TiO_2 pigments used in this investigation. A range of surface treatments on the pigments and particle sizes was examined.

Photoreactivity Results using Standard Experimental Conditions

For the methyl viologen (MV) assay, the colorimetric assay is based on the reaction of methyl viologen, an electron acceptor, with conduction band electrons. The methyl viologen ion, a colorless compound, is easily reduced to its relatively stable cation radical form, which is deeply blue in color and has a strong absorption at 602 nm.(11) Methyl viologen cation radicals also react with holes to regenerate the original methyl viologen cation in a competing reaction. EDTA reacts with the photogenerated holes to limit the contribution of this competing reaction.(7)

UV-VIS spectroscopy analysis of the TiO_2 slurries assayed with methyl viologen showed an intense absorption at 602 nm for a variety of TiO_2 samples (Figure 1). A lower range of absorption values were observed for some of the surface treated TiO_2 pigments (Figure 2). These MV results are indicative of the greater net production of free electrons by catalytic TiO_2 relative to coated TiO_2. The MV results also reveal that uncoated, nanosized, anatase TiO_2 pigments are more photoreactive than the rutile TiO_2 pigments.

The amount of hydrogen peroxide produced from reactions of TiO_2 electrons and holes with particle surface species was measured using a leuco-crystal violet / horseradish peroxidase (LCV) assay. The intensity of the absorption peak at 596 nm (Figure 3) for the TiO_2 specimens resulted in a different photoreactivity compared to the methyl viologen assay as shown in Figure 4. A 3 % by volume hydrogen peroxide solution is also shown as a standard sample in the figure. Pigments without surface treatments showed a greater peroxide production in the LCV assay. However, among the uncoated TiO_2 pigments, the larger particle size, anatase pigment showed the greatest peroxide concentration as compared to the nanosized, anatase pigment in the MV assay.

Both MV and LCV assay results were also compared to a conventional industrial method used to measure photoreactivity, the isopropyl alcohol conversion to acetone test (Figure 5). The isopropyl alcohol conversion test is another measure of conduction band electrons from the TiO_2 particles and so should be closest to the MV assay results. Again, the photoreactivity ranking differed, but the anatase pigments were still the most photoreactive as observed in the MV assay. This is a possible indication that the product mechanism for each assay provides a different measure of photoreactivity or it could be due to the different assay matrix (buffer composition, pH, and solvent) causing the

**Table 1. TiO₂ pigments (values were provided by manufacturer).
All percentages are based on mass.**

Label	Crystal Phase	Particle Size (nm)	Surface Treatment*
A	anatase (70 %), rutile (30 %)	20	none
B	anatase	7-8	none
C	anatase	35-40	Al_2O_3/SiO_2 (25 %)
D	rutile	10-30	Al_2O_3 (9 % to 14 %), SiO_2 (1 % to 7 %)
E	rutile	250	Al_2O_3 (6 %)
F	rutile	250	Al_2O_3/SiO_2 (12 %)
G	anatase	400	none
H	rutile	>400	none

*represents a hydrous metal oxide coating on the surface of the pigment particles.
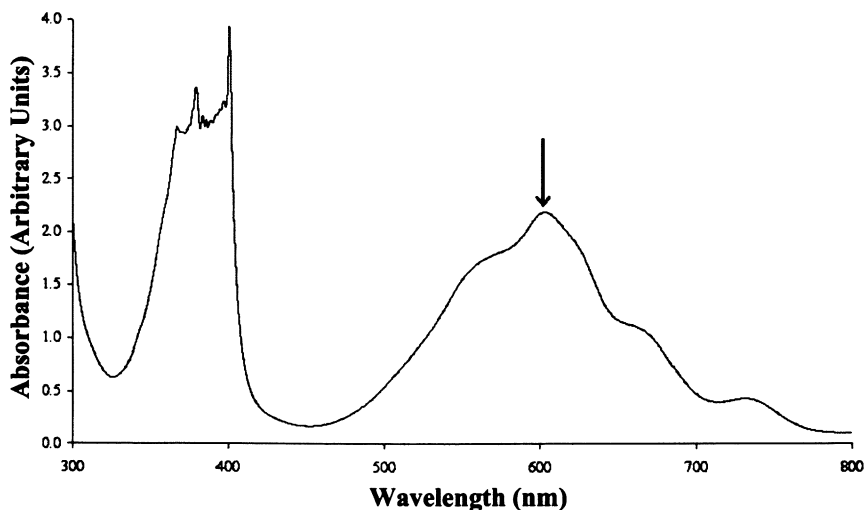
Figure 1. Absorbance spectrum for a methyl viologen assay with TiO₂ pigment A. The methyl viologen radical maximum absorbance is found at 602 nm (arrow).
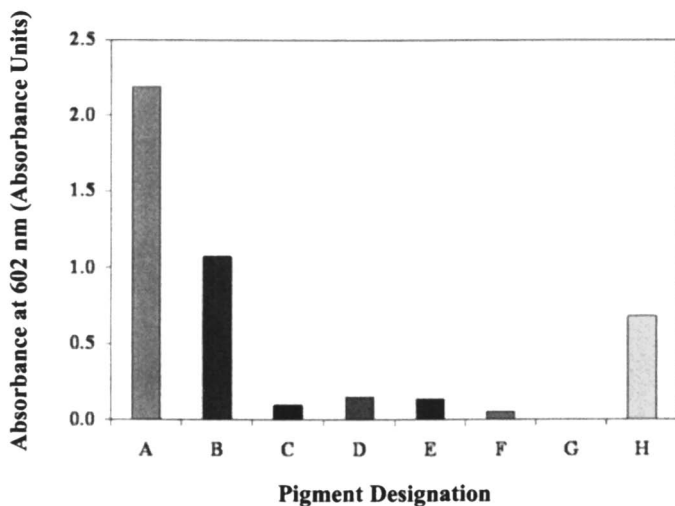
*Figure 2. Photoreactivity comparison of absorbance values obtained using
the methyl viologen assay with TiO₂ pigments. Standard uncertainty in the
absorbance values is ± 2 %.*
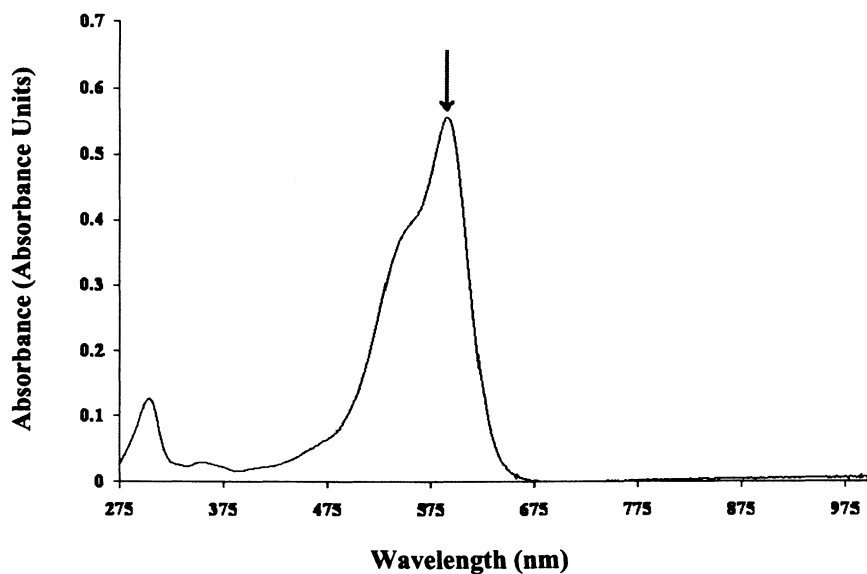
*Figure 3. Absorbance spectrum for a leuco crystal violet assay for peroxide
with TiO₂ pigment A. The leuco crystal violet maximum absorbance is found at
596 nm (arrow).*

nanoparticles to flocculate and form different-sized particle clusters. In turn, larger clusters may shield inner nanoparticles from UV irradiation and produce a lower photoreactivity value. Therefore, the number of TiO_2 particles available for UV light absorption would be lower. That being said, a simple UV light transmission test for each assay / pigment suspension was used to examine the pigment concentration regime under the various assay conditions. Regardless of assay matrix or pigment concentration, no significant difference in the absorbance spectrum was observed. Hence, this UV transmission light test indicates that the presence of flocs does not alter the amount of UV light absorbed by the TiO_2 in the assay suspensions. Dynamic light scattering will be used to examine the pigment flocs.

Photoreactivity Results after Altering Experimental Conditions

Each assay examined in this study used a different solvent, buffer pH, and pigment loading. To more accurately compare the photoreactivity results from the assays, the experimental conditions of the MV assay and the LCV assay were changed such that the experimental conditions were the same for both assays. The same pH (4.4 versus 6.0) and the same pigment loading, 1 mg/mL (MV assay) and 10 mg/mL (LCV assay), were used. Buffer composition was also
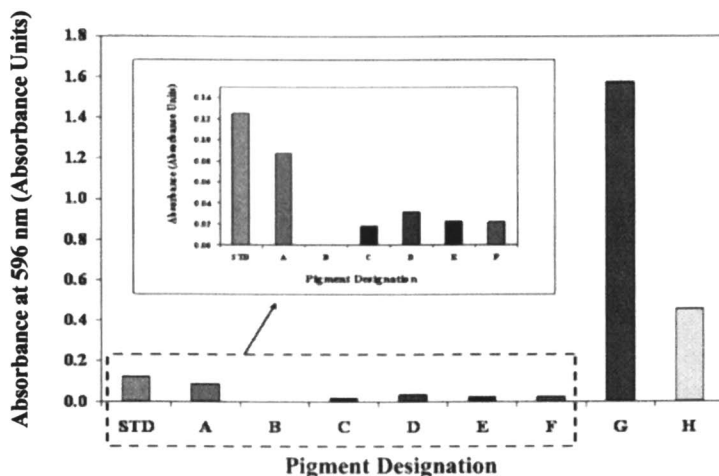
Figure 4. Photoreactivity comparison based on peroxide concentration using absorbance from the leuco crystal violet assay with TiO_2 pigments. The standard sample (STD) is a 0.3 % by volume hydrogen peroxide solution. The inset figure is a magnified version of the original graph to view the lower concentrations (specimens A-F). Standard uncertainty in the absorbance values is ± 2 %.
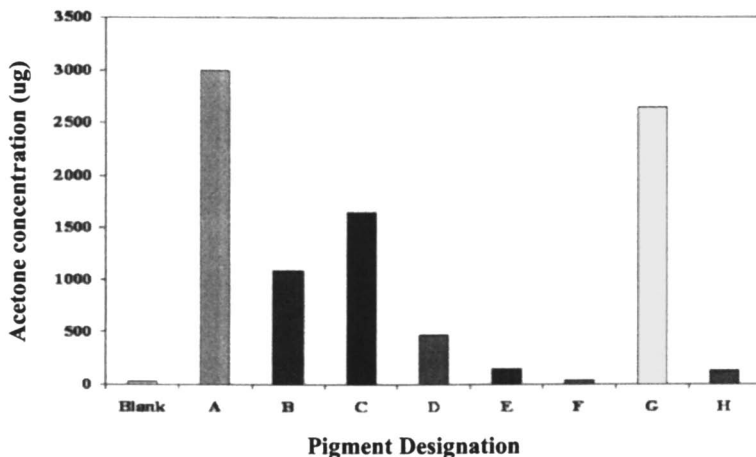
Figure 5. Isopropyl alcohol conversion results for the series of TiO$_2$ specimens. The blank sample is a measure of acetone present initially in the isopropanol. Standard uncertainty in the acetone values is ±2 %.

examined in the case of the MV assay. A phosphate buffer is the standard buffer used in the MV assay. However, phosphate addition has been reported to negatively influence the reactivity of titanium dioxide.(15-16) Phosphates are known to modify alumina, a common surface treatment on pigments and nanoparticle catalysts.(17-19) This study used potassium hydrogen phthalate (KHP) as the non-phosphate buffer. At the time of publication, the investigation was limited to pigments A, E, and F. The results for the entire set of pigments will be reported in a future publication.

Experiments with the MV assay revealed that experimental conditions influenced the absorbance response for the pigments investigated. Figure 6 shows the results of the MV assay with phosphate buffer and a change in buffer pH from the standard pH 6.0 to pH 4.4. The results indicate that pH 6.0 is the optimum condition, producing the highest response, especially for pigment A. The buffer composition in the MV assay was investigated in Figure 7 switching phosphate buffer to KHP buffer. KHP buffer experiments were run at pH 6.0, the optimum revealed in Figure 6. KHP buffer results for the MV assay reveal that KHP buffer produces a higher response for all pigments, especially for pigment E, an alumina surface treated pigment.

This result indicates that the phosphate groups may be exchanging with the hydrous alumina surface treatment on the pigment and forming aluminum phosphate under standard phosphate conditions in the MV assay and reduce the photoreactivity response. Figure 8 examines the effects of pigment loading on the MV assay response. The results show that increasing the pigment loading

increases the MV assay response for all investigated pigments, except pigment F. The response for pigment F was very low for both pigment concentrations. The solutions with greater pigment loading for pigment A resulted in a deeply colored solution, which was off the absorbance scale for the UV- VIS instrument. Dilutions with deionized water were necessary to keep the absorbance readings onscale.
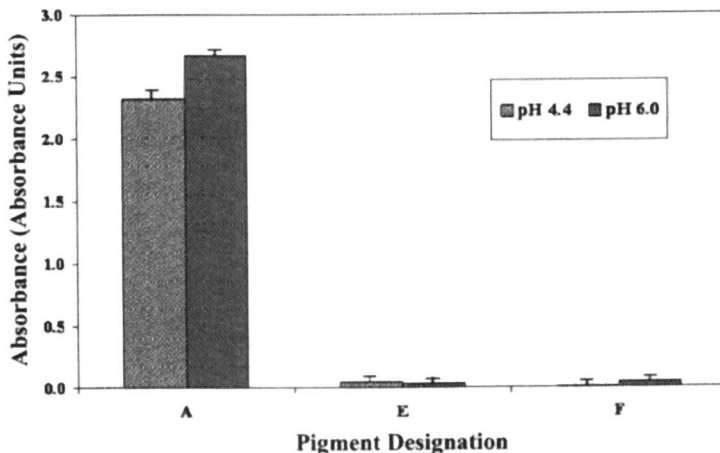
Figure 6. Methyl viologen assay absorbance results for phosphate buffer using a pH 4.4 (light gray) and 6.0 (dark gray). Error bars represent one standard uncertainty.

Results from the LCV assay revealed that assay matrix experimental conditions more strongly influenced the absorbances measured for the pigments investigated. It has been reported that the effectiveness of horseradish peroxidase is dependent upon buffer pH and composition.(20) In addition, dissolution of the leuco crystal violet dye is also very sensitive to pH.(21) Figure 9 shows the results of the experiments with the LCV assay using acetate buffer. pH 5.8 was the highest pH possible with acetate buffer and so an exact match for pH 6.0 was not possible in this system. Regardless, the assay results showed that increasing the pH from 4.4 to 5.8 increased the response for pigment A at 1 mg/mL was different from that obtained under similar conditions for the surface treated pigments. For pigment A, the absorbance obtained after the standard assay condition of 2 h UV irradiation exposure time was slightly greater than that obtained for an overnight run. Furthermore, both responses obtained for pigment A at the different UV irradiation exposure times at the lower pigment loading were significantly greater than that obtained for the 10 mg/mL pigment loading.
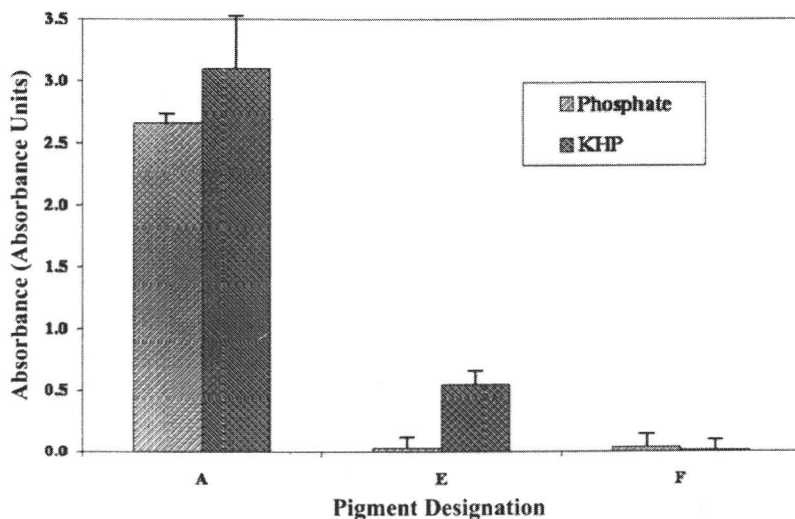
Figure 7. Methyl viologen assay absorbance results using phosphate buffer (light gray) and KHP buffer (dark gray) at pH 6.0. Error bars represent one standard uncertainty.
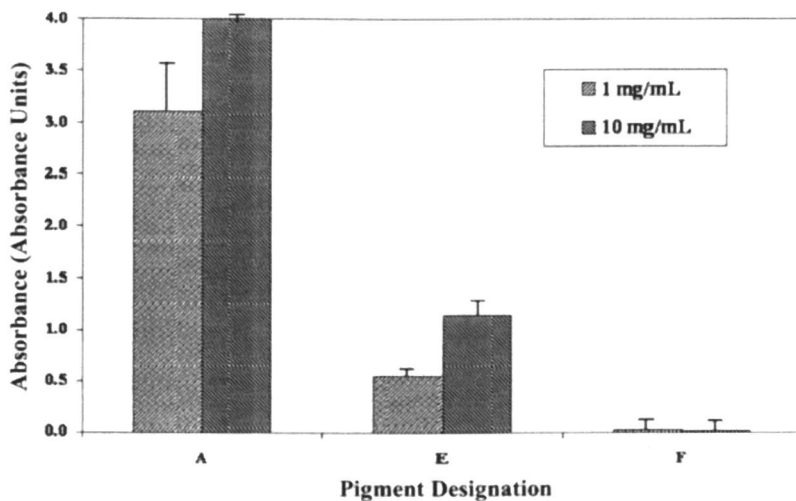
Figure 8. Methyl viologen assay absorbance results with KHP buffer at pH 6.0 and using two pigment loadings, 1 mg/mL (light gray) and 10 mg/mL (dark gray). Error bars represent one standard uncertainty.
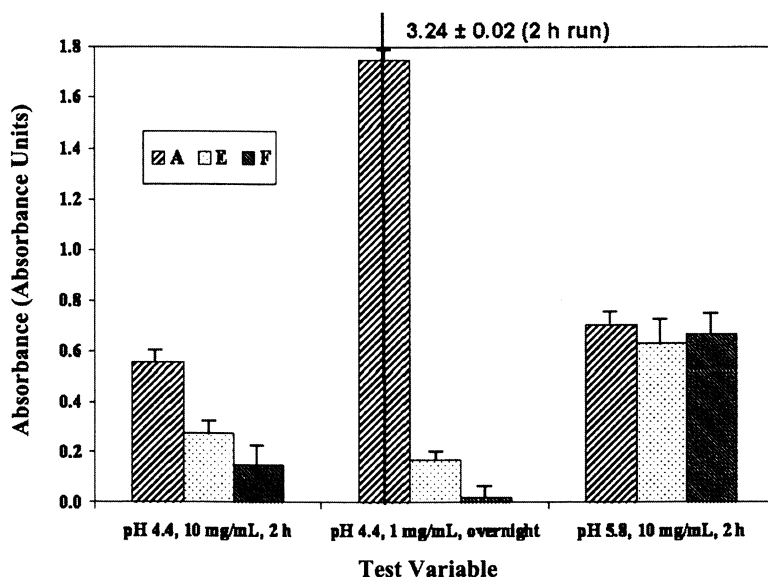
*Figure 9. Leuco crystal violet assay absorbance results with acetone buffer
using pH of 4.4 and 5.8 with 10 mg/mL run for 2 h and at pH 4.4 with 1 mg/mL
as noted. Pigments are shown as: A (horizontal-up), E (dots), and F
(horizontal-down). The line in the pH 4.4, 1 mg/mL pigment loading
experiments presents pigment A run for the standard 2 h UV irradiation
exposure time. Error bars represent one standard uncertainty.*

Dynamic light scattering (DLS) measurements were performed to measure
particle cluster size of the pigments A, E, and F in the various assays. The
results for the entire set of pigments will be reported in a future publication. In
this paper, a particle cluster represents a floc, which is a loose structure formed
by primary particles, aggregates, and agglomerates from the pigments.(22)
Aggregates are considered to be primary particles joined at their faces with a
specific surface area that is significantly less than the sum of the area of the
constituents. Aggregates are very difficult to separate. Agglomerates are a
collection of primary particles or aggregates joined at their edges or corners,
with a specific surface area not markedly different from the sum of the areas of
the constituents. Agglomerates can be separated into their primary particles.
For the DLS measurements in this study, a limited number of scattering angles
were chosen to measure pigment clustering and so the entire shape of the cluster
has not been determined. Particle cluster shape can be assessed by using
additional scattering angles in the DLS measurements. It is also possible to
determine the cluster or floc composition, the distribution of aggregates,
agglomerates, and primary particles, from multi-angle static light scattering

measurements and/or by introducing shear to the assay suspension during the light scattering measurement.

Normalized autocorrelation function, $g_1(\tau)$, versus lag time, τ (s), curves were calculated from the DLS data and were used to derive particle cluster size from the measured hydrodynamic radius (Eqn 4). Figure 10 shows typical shapes of curves from normalized correlation functions for monodisperse and polydisperse particle suspensions. Curves from monodisperse suspensions show a sharp exponential decrease or turnover as a result of the concentration of similarly sized particles. The figure also illustrates the complexity of autocorrelation function curves for polydisperse suspensions. Because there is a distribution of various particle sizes in a polydisperse suspension, the sharpness of the turnover in the curve as observed in monodisperse suspensions is lessened due to the scattering of the various sized particles resulting in a broader curve at longer lag times.
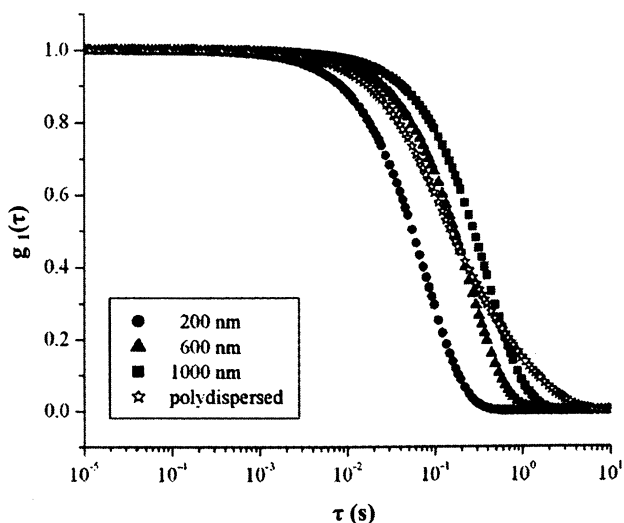
Figure 10. Theoretically calculated normalized autocorrelation functions, $g_1(\tau)$, versus lag time, τ (s), for sphere suspensions with particle diameters of: 200 nm (circle), 600 nm, (triangle), 1000 nm (square), and a polydisperse suspension (star) from DLS measurements at a 15° scattering angle.

For the MV assays, the DLS data revealed that experimental conditions of the assay influenced the particle cluster size of the pigments. Figure 11 shows the DLS data for the MV assay using phosphate buffer at pH (6.0 and 4.4). The shapes of all curves are most similar to the shape of polydisperse suspensions
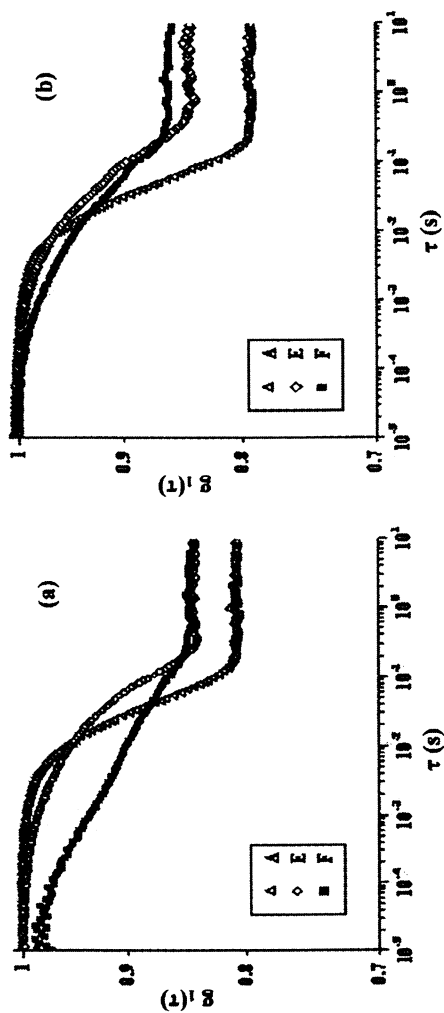
Figure 11. Normalized autocorrelation functions, $g_1(\tau)$, versus lag time, τ (s), from DLS measurements at a scattering angle of 15° for the MV assay in phosphate buffer: a) pH = 6.0 and b) pH = 4.4. Pigment loading for both pHs was 1 mg/mL. Standard uncertainty in the autocorrelation function values is ± 5 %.

shown in Figure 10. Furthermore, the curves for pigments E and F are most visibly different between the two pHs. Table 2 summarizes the measured hydrodynamic diameter or particle cluster results obtained from a non-linear least squares regression analysis on the autocorrelation functions for the MV assay. The measured pigment cluster sizes do not agree with the pigment particle size based on crystallite size reported by the manufacturer. These results indicate that nano- and pigmentary-sized particles have a strong tendency to form clusters in the MV assay matrix. The largest change was observed for pigment E, whose cluster size nearly doubles from pH (6.0 to 4.4). The opposite trend was observed for the cluster size of pigments A and F, which decreased with decreasing pH. However, the large measured cluster size for pigment F at pH 6.0 was a result of very large clusters that produced an unstable suspension and therefore, unstable intensity during the DLS measurements. Buffer composition also affects the cluster size for MV assays as shown in Figure 12. The shapes of the curves differ in the sharpness of the turnover for each pigment between the two buffers. There is also a new feature at longer lag times in the curves for the KHP buffer results. This peak may represent a secondary, larger-sized, pigment cluster set. Interpretation of the data is continuing. Pigment loading has the greatest effect for pigment A in the MV assay as shown in Figure 13. The curve for pigment A at higher pigment loading shows an increase in amplitude, an indication of increased organization of the clusters. The shapes of the curves for the surface treated pigments do not change with increasing pigment loading. Table 3 summarizes the measured hydrodynamic diameter or particle cluster results obtained from non-linear least squares regression analysis of the autocorrelation functions for the MV assay after changing buffer

Table 2. Measured hydrodynamic diameter values for MV assay in phosphate buffer versus pH. Standard uncertainty in the particle diameter values is ± 5 %.

Measured Hydrodynamic Diameter (nm)		
	pH	
Pigment	4.4	6.0
A	206	360
E	1270	676
F	1204	mm[♦]

♦ denotes unstable suspensions in terms of intensity resulting from large clusters
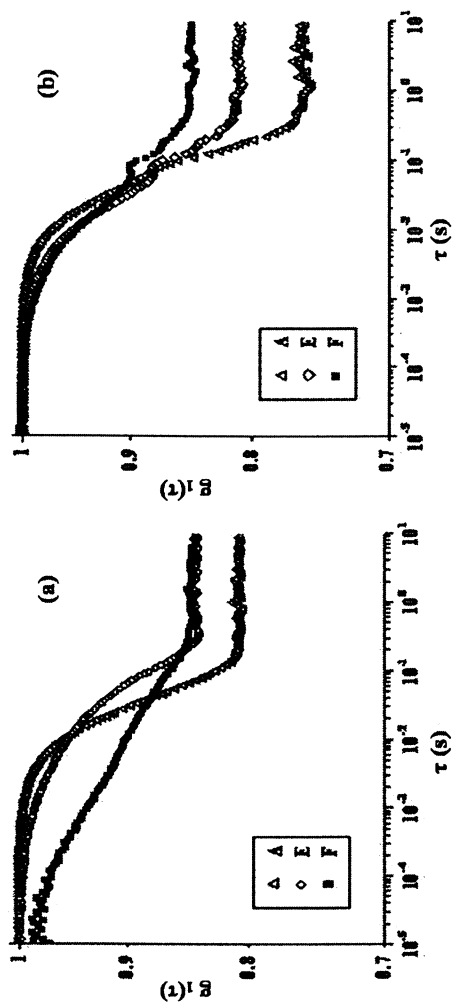
Figure 12. Normalized autocorrelation functions, $g_1(\tau)$, versus lag time, τ (s), from DLS measurements at a scattering angle of 15° for the MV assay at pH 6.0 and 1 mg/mL pigment loading: a) phosphate buffer and b) KHP buffer. Standard uncertainty in the autocorrelation function values is ±5 %.

composition and pigment loading. In general, all pigments more than double in cluster size with a change in buffer from phosphate to KHP. No large clusters were observed for the KHP buffer for any pigments as was observed for pigment F in the phosphate buffer. For the KHP buffer all pigments had similar cluster size, regardless of surface treatment and initial particle size. Decreasing pigment concentration in KHP buffer did not affect the surface coated pigments.
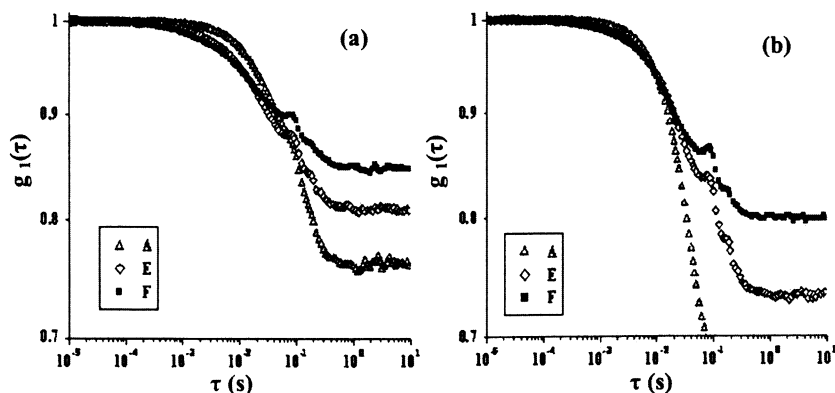
Figure 13. Normalized autocorrelation functions, g $_1$ (τ), versus lag time, τ (s), from DLS measurements at a scattering angle of 15° for the MV assay in KHP buffer at pH 6.0 and pigment loadings of: a) 1 mg/mL and b) 10 mg/mL. Standard uncertainty in the autocorrelation function values is ±5 %.

Table 3. Measured hydrodynamic diameter values for MV assay at pH 6.0 for phosphate and KHP buffers and as a function of pigment loading for KHP Buffer. Standard uncertainty in the particle diameter values is ±5 %.

	Measured Hydrodynamic Diameter (nm)			
	Buffer at 1 mg/mL Pigment Loading		Pigment Loading in KHP	
Pigment	Phosphate	KHP	1 mg/mL	10 mg/mL
A	360	962	962	1118
E	676	1140	1140	1130
F	mm*	1210	1210	1030

* denotes unstable suspensions in terms of intensity resulting from large particle clusters

For the LCV assays, the DLS data revealed that the experimental conditions of the assay also influence the cluster size of the pigments. Figure 14 shows the

DLS data for the LCV assay upon changing pH of buffer and pigment loading. Upon increasing the pH value to 5.8 at 10 mg/mL pigment loading for the LCV assay, the curves for the surface treated pigments become more polydisperse. The curves for surface treated pigments E and F at pH 5.8 and 10 mg/mL pigment loading, again, show new peaks at longer lag times, an indication of a possible secondary, larger-sized, cluster set. However, pigment A remains close to a monodisperse shape despite the pH and there is an amplitude increase in the curve at pH 5.8 at 10 mg/mL pigment loading. This increase in amplitude of the curve is an indication of increased organization of the clusters. Lowering the pigment loading in the LCV assay produces curves that are similarly shaped for all pigments regardless of pigment surface treatment. Table 4 summarizes the summarizes the measured hydrodynamic diameter or particle cluster results obtained from non-linear least squares regression analysis of the autocorrelation
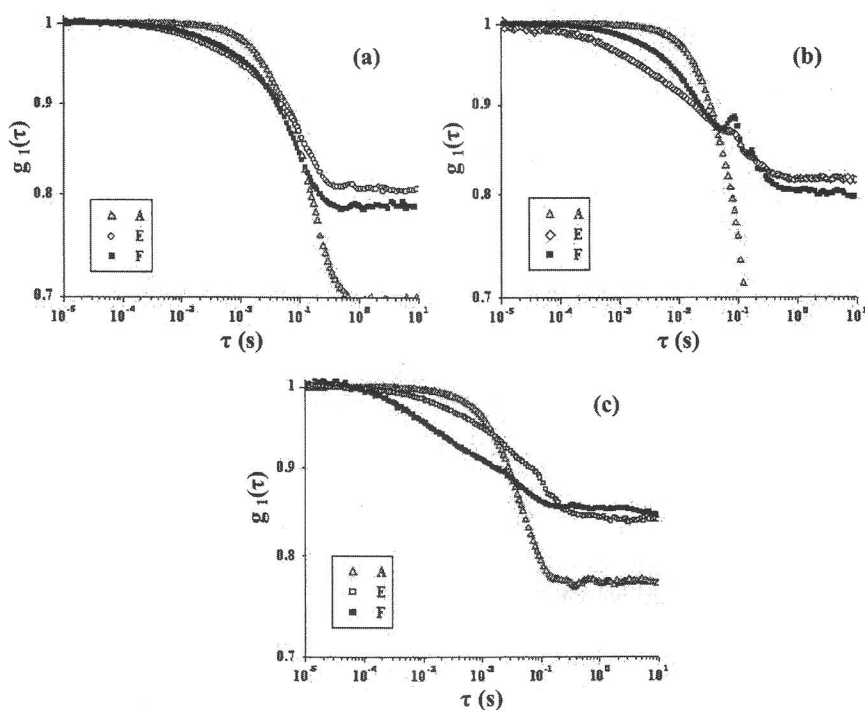
Figure 14. Normalized autocorrelation functions, $g_1(\tau)$, versus lag time, τ (s), from DLS measurements at a scattering angle of 15° for the LCV assay in acetate buffer at a) pH 4.4 for 10 mg/mL pigment loading, b) pH 5.8 for 10 mg/mL pigment loading, and c) pH 4.4 for 1 mg/mL pigment loading. Standard uncertainty in the autocorrelation function values is ±5%.

functions for the LCV assay after a change in buffer pH and pigment loading. In general, pigments E and F show similar trends in cluster size. The cluster size for pigments E and F increased with increasing pH. The cluster size of pigment A slightly decreases with increasing pH. Decreasing the pigment loading markedly increased the cluster size of the surface treated pigments, E and F. The large calculated cluster size for pigments E and F at 1 mg/mL was a result of very large clusters that produced an unstable suspension and therefore unstable intensity during the DLS measurements. The lower pigment loading had the opposite effect on pigment A such that the cluster size decreased by a factor of 3.

Table 4. Measured hydrodynamic diameter values for LCV assay in acetate buffer at pH 4.4 as a function of pH and pigment loading. Standard uncertainty in the particle diameter values is ± 5 %.

Measured Hydrodynamic Diameter (nm)				
	Buffer pH at 10 mg/mL Pigment Loading		Pigment Loading at pH 4.4	
Pigment	4.4	5.8	1 mg/mL	10 mg/mL
A	1206	934	386	1206
E	862	1158	mm*	862
F	676	1558	mm*	676

* denotes unstable suspensions in terms of intensity resulting from large particle clusters

Discussion

This study showed that the photoreactivity response from TiO_2 analyzed in the spectrophotometric assays changed with experimental conditions. Light scattering measurements were performed to examine the effects of assay experimental conditions on the pigment cluster size to test the hypothesis that cluster size is one variable that can affect the photoreactivity response for the various assays. For example, the surface treatment on pigments affect the measured zeta potential of the base pigment, which in turn affect the electrostatic interactions of the pigments in solution and therefore, the pigment cluster size. For the three pigments examined in this study the zeta potential values were 4.3 for pigment A, 6.5 for pigment E, and 7.0 for pigment F. Interpretations of pigment zeta potential and DLS measurements are ongoing. Many factors (particle size, crystal phase, and surface treatment) influence pigment photo-reactivity. This study attempted to examine the effect of pigment cluster size on the photoreactivity response. It was hypothesized that larger clusters shield inner nanoparticles from UV irradiation and produce a lower photoreactivity value.

Smaller cluster sizes result in a higher pigment surface area for UV interaction. Evidence from DLS measurements was presented that cluster size changed with different experimental conditions and was dependent on the pigment examined and the type of assay used (MV versus LCV).

For the MV assay, changes in the photoreactivity response can be largely attributed to pigment cluster size. Figure 15 illustrates the trends of pigment cluster size with photoreactivity from the MV assay under the various experimental conditions. In general, there is no clear trend of increasing photoreactivity with decreasing pigment cluster size for all pigments. However, trends are observed for individual pigments. Pigment surface treatment and crystal phase also influence pigment photoreactivity. When the pH was changed from pH (6.0 to 4.4), DLS data showed that the particle cluster sizes for
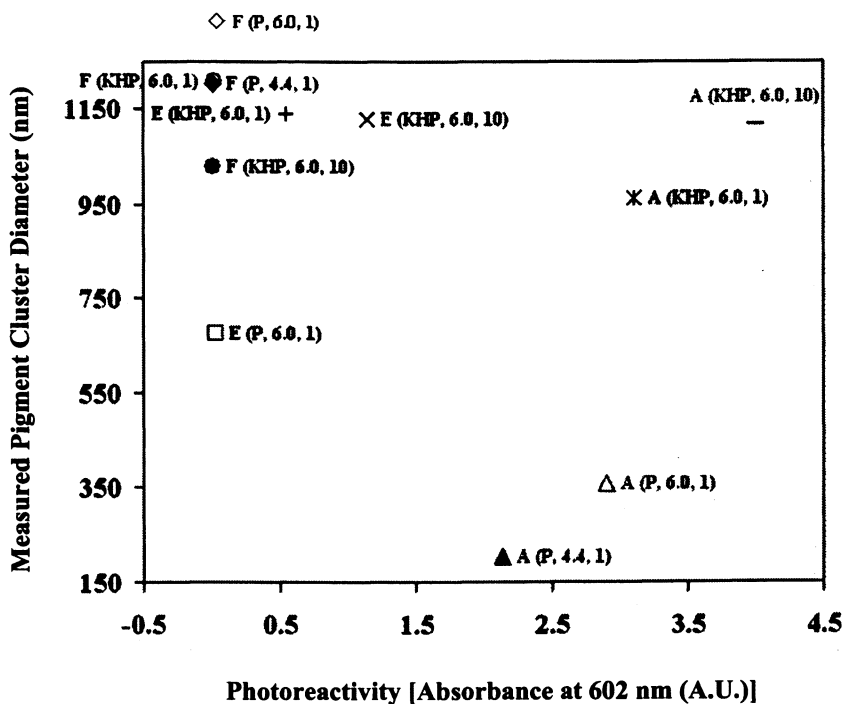
Figure 15. A plot of pigment cluster size as a function of photoreactivity for the methyl viologen assay for TiO_2 pigments under the various experimental conditions (buffer composition, pH, pigment loading). Pigment F using phosphate buffer at pH 6.0 (open, blue diamond) was offscale with a pigment cluster size of 10^6 nm. Standard uncertainty in the particle diameter and photoreactivity values is ±5 %.

pigments E and F increased, while that of pigment A decreased. The MV assay photoreactivity response did not change for pigments E and F, an indication that the larger cluster size did not affect the photoreactivity response. The smaller cluster size for pigment A did not result in a greater photoreactivity response. Upon changing buffer composition from phosphate to KHP, the particle cluster size increased for all pigments. However, there was an increase in the photoreactivity response for pigments, especially pigment E. It appears that phosphate buffer may have a chemical interaction with the pigments that reduces the photoreactivity response. This chemical interaction may depend on the type of surface treatment as the alumina surface treated pigment showed the largest increase in photoreactivity response. Upon increasing pigment loading for the MV assay, DLS measurements showed that the cluster size of the pigments did not change significantly. However, the photoreactivity response did increase most significantly for pigment A. In fact, the assay solution had to be diluted to obtain a UV-VIS measurement. The increase in the photoreactivity response for pigment A upon increasing pigment loading indicates that something more than pigment cluster size affects the assay response. For the case of pigment A, a catalytic TiO_2, the physical properties of the pigment (smaller particle size, lack of surface treatment, lower zeta potential, and anatase phase) may more greatly influence the electron population upon irradiation.

The results for the LCV assay reveal that experimental conditions of the assay influence the photoreactivity response more than the pigment cluster size. Figure 16 shows the trends of pigment cluster size with photoreactivity from the LCV assay under the various experimental conditions. There is a better trend of increasing photoreactivity with decreasing pigment cluster size for all pigments, especially pigment A. DLS measurements showed that after increasing the pH from pH (4.4 to 5.8), the cluster size increases for the surface treated pigments, E and F, but decreased for pigment A. Experiments with the LCV assays revealed that the leuco crystal violet dye caused a clouding of the solution, which caused a false increase in the UV-VIS measurement. There was no visible increase in the purple color of the solution upon increase the pH. Decreasing pigment loading from 10 mg/mL to 1 mg/mL caused the cluster size for the surface treated pigments, E and F, to increase. The cluster size of pigment A decreased by a factor of 3. The photoreactivity response for the LCV assay did not change for the surface coated pigments, but increased greatly for the pigment A. The results indicate that the smaller cluster size of pigment A caused an increase in the photoreactivity response for the LCV assay.

Conclusions

In principle, spectophotometric assay methods appear to be useful for measuring and ranking TiO_2 pigment photoreactivity. The reaction mechanism

F (4.4, 1) OC E (4.4, 1)
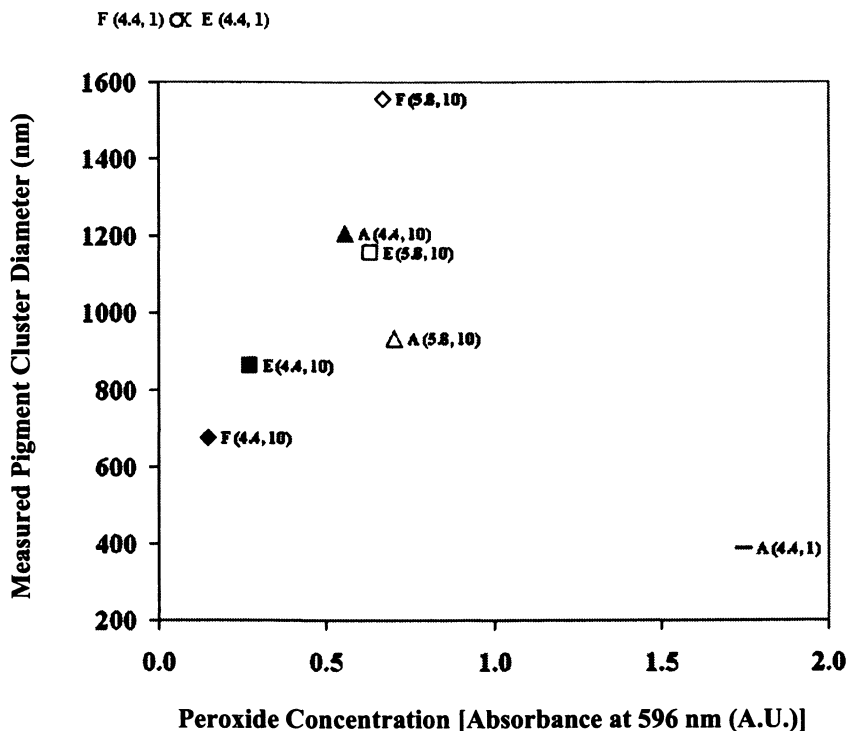
Figure 16. A plot of pigment cluster size as a function of photoreactivity for the leuco crystal violet assay for TiO₂ pigments under the various experimental conditions (buffer composition, pH, pigment loading). Pigments E (red x) and F (open blue circle) at pH 4.4 and 1 mg/mL pigment loading were offscale with a pigment cluster size of 10^6 nm. Standard uncertainty in the particle diameter and photoreactivity values is ±5 %.

of the assay must be taken into account to accurately rank the pigments for photoreactivity. However, the current assay results are highly susceptible due to a large number of variables that have historically neither been controlled nor measured. The assay matrix appears to affect nanoparticle cluster size, which in turn may influence photoreactivity values. In particular, the pH of an assay system can affect nanoparticle cluster formation. In addition to cluster size of pigments, other variables also affect photoreactivity. For example, the composition of a buffer system can influence assay mechanisms by controlling the nature of chemical complexes formed from species present on the pigment and in the assay matrix. From a practical standpoint, until measurement and control metrologies and protocols are imposed, the results from such analyses

are suspect. The results from this study will be used to optimize the standard assay protocol to account for the interactions of pigments with the assay matrix.

References

1. Solomon, D.; Hawthorne, D. in "Chemistry of Pigments and Fillers"; Krieger Publishing Company: Malabar, 1991.
2. Diebold, M., *Surf. Coatings Intern.* **1995**, *6*, 250-256.
3. Hoffman, M.; Martin, S.; Choi, W.; Bahnemann, D., *Chem. Rev.* **1995**, *95*, 69-96.
4. Blake, D.; Maness, P.-C.; Huang, Z.; Wolfrum, E.; Huang, J.; Jacoby, W., *Separation and Purification Methods* **1999**, *28*, 1-50.
5. Pilotek, S.; Tabellion, F., *European J. Coatings* **2005**, April, 170-176.
6. Fernando, R., *J. Coatings Tech.* **2004**, May, 32-38.
7. Sciafani, A.; Palmisano, L.; Schiavello, M., *J. Phys. Chem.* **1990**, *94*, 829-832.
8. Brand, J., *Plastics Compounding* **1985**, 27-29.
9. Diebold, M.; Kwoka, R.; Mehr, S.; Vargas, R. Proc. 81st Annual Meeting of the FSCT, 2003.
10. FB Stieg, J., *J. Paint Tech.* **1966**, *38*, 29-36.
11. Maruszewski, K.; Jasiorski, M.; Hreniak, D.; Strek, W., *J. Molec. Structure,* **2001**, *597*, 273-277.
12. Degani, Y.; Heller, A.; AT&T Bell Labs: USA, 1990.
13 Pappas, S.; Fischer, R., *J. Paint Tech.* **1974**, *46*, 65-72.
14 Berne, B.J.; Pecora, R. "Dynamic Light Scattering with Applications to Chemistry, Biology, and Physics", Dover Publications, Inc., New York, 2000.
15 Hidaka, H.; Zhao, J.; Satoh, Y.; Nohara, K.; Pelizzetti, E.; Serpone, N., *J. Molec. Catal.* **1994**, *88*, 239-248.
16. Ortiz-Islas, E.; Lopez, T.; Gomez, R.; Navarrete, J., *J. Sol-Gel Sci. Techn.* **2006**, *37*, 165-168.
17. Parida, K.M.; Acharya, M.; Samantaray, S.K.; Mishra, T., *J. Colloid Interface Sci.* **1999**, *217*, 388-394.
18. Li, W. Li, S.; Zhang, M.; Tao. K., *Colloids Surf. A: Physicochem. Eng. Aspects* **2006**, *272*, 189-193.
19. Ramis, G.; Rossi, P.F.; Busca, G.; Lorenzelli, V.; La Ginestra, A.; Patrono, P., *Langmuir* **1989**, *5*, 917-923.
20. Worthington, V. ""Worthington Enzyme Manual: Enzymes and Related Biochemicals", The Worthington Biochemical Corporation, NJ, 1993, pp. 293-299.
21. Mottola, H.A.; Simpson, B.E.; Gorin, G., *Anal. Chem.* **1970**, *42*, 410-411.
22. Ross, S.; Morrison, I.D. "Colloidal Systems and Interfaces", John Wiley & Sons, NY, 1988.

Chapter 18

Size Determination of Nanoparticles Used in Coatings

S. Kim R. Williams[1], Leonardo Cinque[1], and Paul M. Shiundu[2]

[1]**Department of Chemistry and Geochemistry, Colorado School of Mines, Golden, CO 80401**
[2]**Department of Chemistry, University of Nairobi, Nairobi, Kenya**

This chapter begins with a description of some commonly used particle sizing techniques, their applicability to nanoparticles, and their advantages and disadvantages. A special emphasis is given to fractionation techniques and their ability to simultaneously characterize nanoparticles and isolate monodispersed fractions from polydispersed samples. The latter part of this chapter provides an in-depth discussion of sedimentation field-flow fractionation (SdFFF) size analysis of nanoparticles used in coatings.

Introduction

Particle size and size distributions are important parameters in raw materials used in coating technologies, and as we approach the nanometer realm, size increasingly becomes the leading variable in the chemical and physical behavior of matter. For example, the ability for pigments to scatter light, i.e., their hiding power, undergoes a maximum at a diameter that is roughly equal to half the wavelength of the dominant light. Consequently, organic pigments are usually between 100 nm and 500 nm in size and the larger inorganic pigments, such as titanium dioxide, are reduced to approximately 250 nm in size(*1,2*). However, if

© 2009 American Chemical Society 373

we consider titanium dioxide particles in the size range of 20-50 nm, the light scattering behavior changes radically to the extent that they can form highly optically transparent layers. Such coatings have greatly improved mechanical properties and have applications for optical lenses. While organic pigments give the best results above the 100 nm size, modern inkjet photo printers give the brightest colors with nanoparticles dyes smaller than 50 nm.

Thin film coatings of silica nanoparticles are also used to create super hydrophobic surfaces(3,4) and similar coatings have been demonstrated to substantially improve the efficiency of solar panels(5). The same solar panels exploit nanocrystals or 'quantum dots' that are several nanometers in size to convert light to electric energy. Changing the size of these nanocrystals causes the wavelength of maximum absorption of light to change, thereby making it possible to design solar panels that offer the best performance in different situations(6-8).
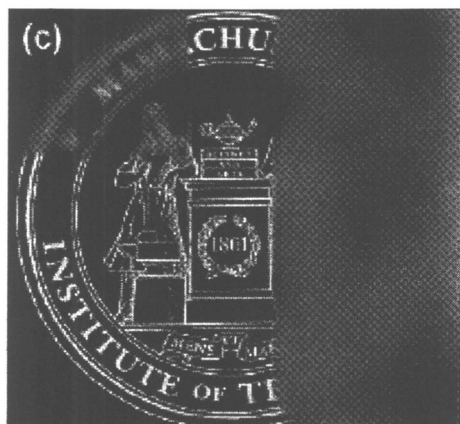
Figure 1. image demonstrating the antifogging properties of multilayer coated glass (left) compared to that of an untreated glass substrate (right)(4). [Reprinted with permission from American Chemical Society.]

Many other nanoparticles are of interest for coating processes. In recent years, gold nanoparticles and carbon nanotubes have been the subject of great attention in the scientific community and industry. The former exhibits vastly different properties than those observed in bulk or in micron sized particles. The optical properties of gold nanoparticles depend on their size and shape(9,10). Spherical gold nanoparticles demonstrate a red shift as the size increases. Gold nanorods, on the other hand, show a wider absorption range than their spherical counterpart with the color dependent on the length and aspect ratio(11). For a

fixed aspect ratio, a red shift characterizes a length increase. Greater understanding of the impact of nanoparticle size and shape is one of the important steps towards designing coatings with desired properties.

Nanoparticle Size Analysis

This section introduces some commonly used particle sizing methods. For more in-depth treatments, readers are referred to textbooks devoted to this subject(*12,13*). Instruments for measuring particle size distribution can be divided into the categories of fractionation and nonfractionation methods (see Table 1).

Table 1. Some commercially available particle size analysis techniques

Fractionation methods	*Nonfractionation methods*
Sieving (SIV)	Microscopy (optical, electron)
Particle electrophoresis (PE). Capillary Zone Electrophoresis (CZE)	Electrozone sensing (Coulter)
Disc centrifugation (DCF)	Electroacoustic
Size Exclusion Chromatography (SEC).	Light scattering (classical, turbidimetric, Fraunhofer, photon correlation, etc.)
Capillary hydrodynamic fractionation (CHDF)	
Field-flow fractionation (FFF): sedimentation, flow, thermal, electrical, etc.	

Fractionation-based methods yield high resolution and detailed information about the various particle populations present in a sample. Non-fractionation methods are generally easy to use but are ensemble methods that provide an average diameter of the sample mixture (ensemble average). Some of the techniques used for particles characterization, like microscopy, field-flow fractionation (FFF) and light scattering, are family of techniques, each having different capabilities.

Non-Fractionation Methods

Imaging

Imaging is the most direct and intuitive way to characterize particles. Microscopy is the only particle sizing technique capable of directly providing

detailed shape information. Optical transmission microscopy has a lower size limit of about 500 nm. The theoretical lower limit is at a size comparable with half the wavelength of the light used for the observation, due to the diffraction limit theorized by Ernst Abbe in 1873(*14*). However, many methods have recently been devised to overcome this limitation and optical microscopy has been used to observe sizes as low as 10 nm. Examples of these techniques include Far Field Optical Microscopy, Near Field Optical Microscopy, and Stimulated Emission Depletion microscopy(*15-18*). Other microscopy techniques used to image nanoparticles and nanostructures are electron, transmission, tunneling, confocal, and atomic force microscopy, many of which are done under vacuum.

Hybrid techniques based on imaging and light scattering have also been developed for nanoparticle analyses giving rise to Nanoparticle Tracking Analysis (NTA) for nanoparticles characterization in the 1-1000 nm range(*19*) and Scanning Mobility Particle Sizer (SMPS) Spectrometry(*20*).

While the task of measuring particle size has been made less tedious, faster and more accurate by the use of image analysis software, the number of particles sampled is lower than that of many other size analysis techniques, and the sampling may not be representative. In addition, differentiating true particle aggregates from overlapped particles remains a difficult process. Microscopy provides a number average diameter.

Electrozone Sensing

Electrozone sensing, also known as Coulter counting(*21,22*), measures changes in the potential between two electrodes placed on either side of a small aperture in an insulating wall. A particle drawn into the aperture or sensing zone will displace a quantity of electrolyte proportional to its volume. This event will cause a change in resistance and lead to a voltage pulse. Each voltage pulse is counted as an event while the amplitude of the pulse is proportional to the volume of the particle. The diameter is calculated assuming a spherical shape for the particle. This counting method yields a number distribution of volume equivalent diameter. General characteristics of Coulter counters include low sample volumes and counting efficiencies. Smaller apparent diameters will be reported for conductive and porous particles unless special techniques are employed.

The nominal applicable size range of commercial instruments is typically 300 nm to 1500 µm. To cover this entire range, different size apertures have to be used (the aperture is the cylindrical orifices which hosts the sensing zone). A complete size distribution is obtained by blending the data from each aperture.

Many attempts to apply this powerful technique to nanoparticles have been published. A 1970 paper reported the measurement of 90 nm polystyrene particles(*23*) using a 450-nm diameter channel fabricated by track etching of a

polycarbonate membrane(24). The Coulter Counter principle has also been adapted to a microchip format for use in the analysis of particles with diameters as low as 87 nm(25). The latest advancements in this technique are the simultaneous use of multiple apertures instead of sequential single apertures of different sizes(26) and carbon nanotubes-based Coulter Counter(24).

Light Scattering

A number of particle sizing techniques are based on light scattering. Fraunhofer diffraction(27) is widely employed because of its apparent ease of use. Size information is obtained from the diffraction pattern generated by deflection of a light beam. Spherical particles of different, but distinct, diameters will generate a series of concentric light rings. A sample containing a range of sizes (polydispersed) will yield a diffraction pattern that is difficult to analyze. In general, it is useful for micron-sized particles. However, Fraunhofer diffraction has been combined with Mie scattering theory to produce a combined instrument capable of characterizing nanometer-size particles. Instrument manufacturers list an applicable size range from 50 to 1500 nm, but this is not attainable for all types of particles. Refractive index values must be known for the different wavelengths that are used.

Photon correlation spectroscopy (PCS) is also known as dynamic light scattering, quasi-elastic light scattering, autocorrelation spectroscopy, and intensity fluctuation spectroscopy. PCS uses a laser beam to illuminate a sample suspension(28-30). Particles undergoing Brownian motion within this illuminated area will cause fluctuations in signal intensity. Small particles cause rapid fluctuations compared to large slow moving particles. The time dependency of these random fluctuations gives rise to an autocorrelation function that is used to calculate size and size distribution. PCS is widely used to characterize nanoparticles ranging in size from ~1 to 1000 nm. Above 1000 nm, Brownian motion is slow, the diffusion rate is difficult to accurately measure, and particle sedimentation may be significant. The main advantage of PCS is its ease of use, and hence, it is well suited for quality control applications. PCS results are usually fitted to a Gaussian or log normal curve and the mean size and polydispersity are calculated. The assumption is that the sample distribution can indeed be described by one of these two functions and that the sample is a single population. Bimodal populations must have a 2-3x size difference in order for PCS to report the presence of both populations rather than a single population with a single average diameter. PCS can be performed in the batch mode or flow-through mode coupled to a separation device like field-flow fractionation or size exclusion chromatography. This coupling of separation and light scattering methods offer the best of both worlds(31,32).

Multiangle light scattering (MALS) utilizes an array of detectors set at various angles(33-35). The total intensity of scattered light as a function of

scattering angles is used to calculate a root mean square radius that is then transformed to a hydrodynamic diameter. (The transformation is more complicated for nonspherical particles.) For polydisperse samples, MALS is coupled on-line with a separation method such as FFF so that light scattering measurements can be made on 'monodisperse' sample plugs. As with flow-through PCS, the MALS detector yields independent diameter values that can be compared with values obtained from FFF theory. Consequently, these detectors allow for small experimental errors and nonidealities in FFF such as sample overloading and fluctuations in flowrate. MALS sizing has a lower limit of about 10 nm(*36*).

When the particle size approaches 1 nm, the magnitude of the scattering ray vector (q) becomes too small for accurate sizing by visible light scattering. The value of q is inversely related to the light wavelength and thus using shorter wavelengths allow for scattering of smaller particles to be detected. Small Angle X-ray Scattering and Small Angle Neutron Scattering exploit the very short wavelength of X-rays (~ 0.1 nm) and neutrons (~ 0.5 nm, calculated by the deBroglie relation) which enables the measurement of particles or structures at the nanometer level(*37*).

Ultrasonic or Electroacoustic Measurements

Ultrasonic or electroacoustic measurements are based on two physical effects(*38- 41*). The first involves application of an ultrasound wave to an electrolyte solution to induce alternating potentials possessing the same frequency as sound waves(*38*). Ions or charged colloids of different masses will yield alternating potentials with different displacement amplitudes and phases. This effect is called the colloid (or ultrasonic) vibration potential (CVP or UVP). The second physical effect, discovered in 1985, is the electronic sonic amplitude (ESA)(*39*) and is the reverse of CVP. An applied electric field causes particles to vibrate, thus generating sound waves. For the sound wave to be transmitted and measured, there must be a significant difference between the particle and medium densities. The ESA effect is easier to measure than CVP and easier to interpret because it is independent of the complex conductivity of the suspension. Manufacturers of electroacoustic instruments state an applicable size range of a few nanometers to tens of microns. The recognized advantage of this technique is the ability to handle highly concentrated suspensions and the automated features (which translate to ease of use). However, it is necessary to understand the basic theory and assumptions made by the instrument manufacturers. For instance, when dealing with TiO_2, the particle permittivity must be known in order to obtain accurate diameter results(*40*). Some of the algorithms used by manufacturers may not take this into account. The measured dynamic mobility is proportional to two properties of the sample – zeta potential (potential at the shear plane) and diameter. The former must be measured in

order to calculate diameter. The reproducible measurement of zeta potential can be tricky and requires the development of a protocol that is then strictly followed for every sample. Polydispersity will also affect the final results. An empirically determined correction factor is introduced when dealing with a polydisperse suspension to relate dynamic and static mobilities and enable calculation of diameter. For TiO_2, the best results are obtained at pH values below the isoelectric point where flocculation is minimized(*41*).

Fractionation Methods

Resolution or discriminating power is important for any technique, fractionation or nonfractionation, so that details of size distributions can be revealed. In general, nonfractionation methods tend to be rapid and of low resolution. Fractionation methods tend to be more complicated and time consuming but are capable of providing detailed size information. This attribute is important when the critical component of a polydisperse sample is present in small amounts or if the particle population undergoes changes over time. A comparison of fractionation techniques is given below with respect to four intrinsic features. Elution is important because monodisperse fractions can be collected for further analysis and testing. Exact theory is useful because it means that particle fractions can be characterized without calibration. Flexibility is desirable because particle characterization needs are so diverse.

Table 2. Comparison of fractionation-based particle size analysis methods

	Resolution	*Elution*	*Exact theory*	*Flexibility*	*Size range*
SIV	Low	No	No	Low	>1 μm
PE	High	Yes	No	Medium	>10 nm
DCF	High	No	Yes	Medium	10 nm–50 μm
SEC	Medium/Low	Yes	No	Low	-
CHDF	Medium	Yes	No	Medium	10 nm -3 μm
FFF	High	Yes	Yes	High	2 nm - 50 μm

Sieving (SIV) is a low resolution technique that is often used as a preparation step prior to performing size analysis with one of the other techniques(*42,43*). Particle electrophoresis has been used to separate a variety of materials from latex beads 20-50 nm size to cells(*44-46*). Preparative gel electrophoresis has been used to separate gold nanoparticles by size and shape(*47*). Capillary Zone Electrophoresis was recently applied to separate fullerenes(*48*), polymers, polystyrene latex beads (20 to 300 nm) and gold

nanoparticles (5 and 20 nm)(*49*). Although it is possible to use electrophoresis for nanoparticles separation, it is complicated to relate the retention to particle size, since it would require the use of standards having identical electrophoretic mobility as the sample. Electrophoresis techniques suffer from various surface phenomena, e.g., electroosmosis and phase wall wetting, which adversely affect precision and accuracy. Consequently, they have not been extensively used to separate and characterize particles despite their potential usefulness. Many studies have been conducted to better understand and thus control these surface phenomena(*50-52*).

Size Exclusion Chromatography (SEC)(*53*) is traditionally used to separate polymers and proteins but its application has been extended to gold nanoparticles(*54*). As the nanoparticles are displaced through the SEC column, different sizes are retained to different extents depending on their residence time in the pores of the column packing material. Gold nanoparticles with sizes ranging between 5 and 38 nm have been separated using an SEC column with 100 nm pores(*55*). Recycle SEC, where separated fractions were sent back through the column, could separate an original polydisperse 2.6 nm gold nanoparticles into 0.9, 1.5, and 2.7 nm size fractions after 8 cycles(*56*). Microchannel SEC has been recently utilized to separate 20 and 100 nm polystyrene latex nanoparticles(*57*). The size range for SEC is not listed in Table 2 as this depends on the pore size of the packing material in the SEC column. Interactions between the SEC column packing material and nanoparticles can lead to nonquantitative sample recovery and subsequent column plugging. Different strategies, such as the use of surfactants, have been employed to ensure high nanoparticles recovery.

Sedimentation methods, such as disk centrifugation (DCF), are high resolution sizing techniques(*58,59*). The nominal applicable size range is 10 nm to 50 μm(*60*). DCF can be performed in a number of different ways. The highest resolution is obtained using a line start with a fixed detector. With a line start, the sample suspension (~0.25 mL) is injected into the spinning centrifuge cavity near the axis of the rotor. From a common starting position and time, different mass particles are forced out radially at different speeds and will cross the detection zone at different times. The hydrodynamic sizes are calculated using Stokes' Law for centrifugation and the time between injection and arrival at the detector. (Density has to be known.) Since the sedimentation velocity is also dependent on friction coefficient, particle shape will have an effect on the results. The analysis can be speeded up by using a homogeneous start and a scanning detector head. In this case, a large volume of sample (10-20 mL) is injected into the disk cavity. Upon centrifugation, the initially homogeneous sample fluid experiences changes in particle concentration as a function of time. This change is registered by a scanning detector head and translated back to a particle mass. Since data can be obtained without the formation of distinct mass bands, analysis time is reduced. Resolution is lower than that obtained with the line start. Two types of detectors are usually used with DCF- light and X-ray.

Light scattering corrections are not needed for the latter detector. DCF is not an elution technique, which means that fractionated samples are not easily collected for further analyses or studies.

Capillary hydrodynamic fractionation (CHDF) and field-flow fractionation (FFF) are similar techniques in that separations are carried out in narrow conduits under conditions of laminar flow(61-69). Figure 2 shows the parabolic flow profile that is established in CHDF and FFF channels. The flow velocity is highest at the center of the channel and decreases towards the walls. Particle separation occurs as a result of different average residence times in the different regions across the conduit. In CHDF, particles continuously diffuse across the entire thickness of the conduit. Since large particles are excluded from regions near the wall where the flow velocity is slowest, they will elute prior to small particles. The main difference between CHDF and FFF is that in the latter a field is applied perpendicular to the separation axis. The field induces transport of nanoparticles to one wall (termed the accumulation wall) as shown in Figure 3b. However, the nanoparticles also undergo diffusion away from the wall to regions of lower concentration. The net result is that at equilibrium, these two opposing transport mechanisms are balanced and each nanoparticle component forms a compact steady state layer with a unique thickness distributed across the parabolic flow profile. Smaller or faster diffusing nanoparticles will form thicker layers with average distances further from the accumulation wall and will be swept out of the FFF channel faster. Hence, the order of elution in this normal mode of FFF is from small to large.

The use of a field opens up tremendous analytical possibilities for the FFF family of techniques that are not achievable using CHDF. In addition to particle size, it is also possible to monitor minute (10^{-16}-10^{-18}g) changes in mass due to adsorption of proteins and polymers onto colloidal particles, measure charge and density, obtain shell thickness and composition of core-shell structures, study aggregation-deaggregation processes, etc.(68,70-73). The use of different fields that interact with different particle properties to affect their retention times allows insight into these physicochemical properties. The field also allows much higher resolution to be achieved by FFF. However, the absence of a field makes CHDF a simpler technique to use than FFF. CHDF is applicable to particles in the size range of ~15 nm - 1 μm whereas FFF has a range of ~2 nm − 1 μm for normal mode. There is an additional FFF separation mechanism, called steric mode, which applies to micron sized particles(74). A common misconception is that two different channels are needed to perform normal mode and steric mode analyses. The modes refer to the separation mechanism, which can both be achieved using the same FFF channel.

There is one major problem encountered by all sizing techniques that utilize light based detection. Light scattering corrections must be performed on all results obtained using a turbidity detector in order to obtain the correct scaling on the y-axis of the particle size distribution[75-78]. This includes disk centrifugation with an optical detector, CHDF, and FFF with UV detectors. The
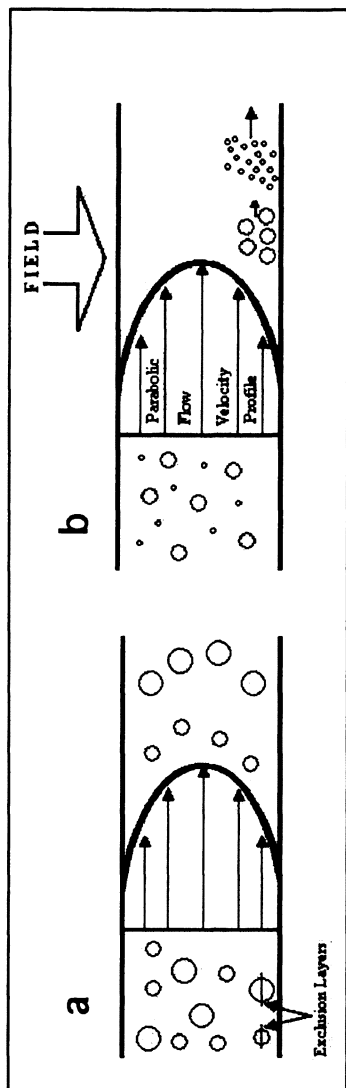
Figure 2. Separation mechanism for a.) CHDF and b.) FFF. The use of an external field applied perpendicular to the separation axis gives FFF its high resolution and particle characterization capabilities.
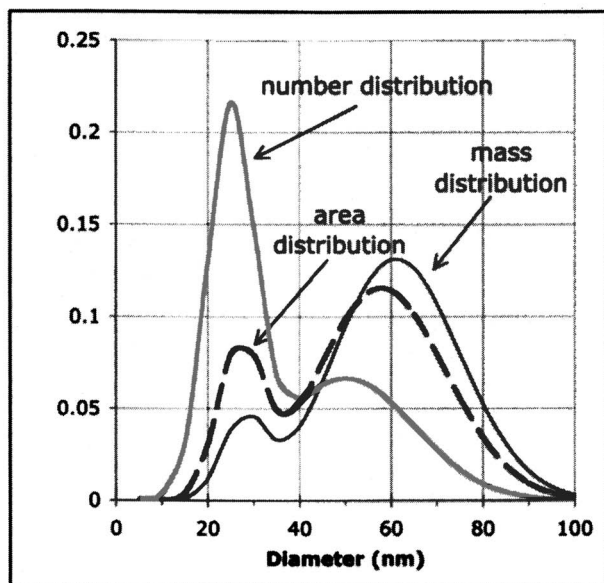
*Figure 3. Different types of size distribution curves for TiO₂ nanoparticles.
(Calculations based on equal numbers of 25 ± 5 nm and 50 ± 15 nm particles
and a density of 3.2 g/mL)*

particles' optical properties (refractive index and molar absorptivity) must be known in order to implement these corrections. These optical properties are not readily available even for many pure samples. They are also needed when light scattering techniques are used. The problem is particularly severe for complex samples where a single refractive index and molar absorptivity value is not valid. Light scattering corrections become simpler for micron size particles because the extinction efficiency reaches a constant value. In this size region, the detector signal is proportional to the cross sectional area of the particle. Figure 3 illustrates the importance of performing light scattering corrections and knowing the type of size distribution that is being displayed. Number and volume average diameters can produce widely different average particle diameters and size distributions.

Sedimentation Field-Flow Fractionation Characterization of Pigments

Different types of 'fields' are used to effect an FFF separation. Fields that have been used include gravity, centrifugal, electric, dielectrophoretic, magnetic,

temperature gradient, and a crossflow of fluid. Crossflow or flow FFF, the most commonly used technique of the FFF family, uses a fluid flow to transport nanoparticles to a semipermeable accumulation wall. The separation is based solely on diffusion coefficients, which in turn, are related to hydrodynamic diameter through the Stokes-Einstein equation. Flow FFF is applicable to nanoparticles as small as ~2 nm and as large as ~50 μm particles(68). Nanoparticle applications include colloidal silicas(79) magnetic beads(80), quantum dots(81) and gold nanorods(82).

Sedimentation FFF (SdFFF), the highest resolution technique of the FFF family, is discussed in detail in this latter half of the chapter. The theory, method development for titanium dioxide and inorganic pigments, and data analysis are described. The use of a centrifugal field gives rise to the technique of sedimentation FFF. The retention ratio R or time t_r of the nanoparticles is related to its effective mass m_{eff} or diameter d as represented in equation (1).

$$R = \frac{t_o}{t_r} = \frac{36kT}{\pi m_{eff}Gw} = \frac{36kT}{\pi d^3 \Delta\rho Gw} \tag{1}$$

The term $\Delta\rho$ isthe difference in density between the particle and carrier liquid, G is gravitational acceleration, w is channel thickness, t_0 is the void time, k is the Boltzmann constant, and T is temperature. The advantage that SdFFF offers over other particle analysis techniques arises from t_r being proportional to d^3. In other words, a 10x difference in diameter yields a 1000x difference in retention time. This ability to spatially spread out different particle sizes over a wide range of retention times gives SdFFF its characteristic high resolution and sensitivity to subtle size or mass differences.

SdFFF has a lower size limit that is determined by $d^3\Delta\rho$ and the instrumental design. The commercially available SdFFF instrument has a maximum rpm of ~2500 and a rotor radius of 15.1 cm(83). Figure 4 shows a plot of minimum diameter d_{min} as a function of $\Delta\rho$ at two retention ratios. For R = 0.1, the minimum diameter for SdFFF of polystyrene latex beads ($\Delta\rho$ =0.05 g/mL) is 152 nm and rutile TiO_2 ($\Delta\rho$ ~3.28 g/mL) is 38 nm.

Field strength programming is used routinely in SdFFF when the sample is polydisperse. A decrease in rpm with respect to retention time will cause highly retained particles to elute earlier and thus decrease the overall analysis time. The decrease in field strength can follow different mathematical functions, e.g., linear, step, exponential, power, etc. The power program is the function currently used by the instrument manufacturers because it gives a constant fractionating power over a wide diameter interval(84). The power program equation states that the field strength at any given time, $S(t)$, is equal to the initial field strength, S_0, multiplied by a continuously decreasing ratio of times raised to the power p.
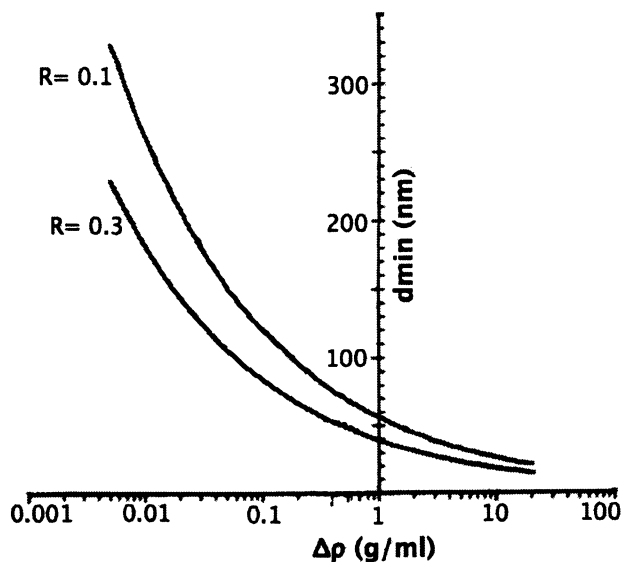
*Figure 4. Minimum diameter that can be analyzed by SdFFF. A retention ratio
R = 0.1 means the particle is retained 10 channel volumes. R = 0.3 means the
particle is retained 3 channel volumes (less retaintion). Experimental conditions
used in these calculations were 2500 rpm, 0.0254 cm thickness, 15 cm rotor
radius, and 298 K. The R~6λ approximation was used.*

$$S(t) = S_0 \left(\frac{t_1 - t_a}{t - t_a} \right)^p \qquad (2)$$

The parameter t_1 is the delay time between sample injection and start of field
strength programming and t_a is the asymptotic time.

Experimental Conditions

The experimental conditions for SdFFF of titanium dioxide and iron oxides
were chosen based on the desired retention times of the expected minimum and
maximum diameters. For example, the programmed field conditions needed to
elute TiO_2 particles with an estimated size distribution of 0.08 μm to 0.80 μm
within 60 mins were: initial field strength S_0 of 828 rpm, a final field strength of

100 rpm, t_l = 6.2 min, t_a = -49.6 min, and p = 8. The estimated $\Delta\rho$ value for rutile TiO_2 used in the calculations is 3.28 g/mL and the flowrate was 4.0 mL/min. The SdFFF channel's void volume is 3.41 mL and thickness is 0.0254 cm. The retention time calculations for red and yellow iron oxides utilized Δp values of ~4.0 and 3.1 g/mL, respectively. The experimental conditions used for iron oxides analyses were: S_0 = 1159 rpm, a final field strength of 20 rpm, t_l = 3.16 min, t_a = -25.3 min, and p = 8. The flowrate was 2.06 mL/min. These optimum conditions were calculated using a program developed by P. Stephen Williams (Cleveland Clinic Lerner Institute, Cleveland, Ohio). The SdFFF instrument is similar to that offered by PostNova Analytics (Salt Lake City, Utah).

The aqueous carrier liquid used in the TiO_2 separation contained 0.1% (v/v) FL-70 (Fisher Scientific, Fair Lawn, New Jersey) and 0.02% (w/v) sodium azide. Two TiO_2 samples were analyzed. Sample A is used in plastics and has a small amount of phosphate from the first treatment and ~1.7 wt% alumina from the second treatment. Sample B is a pigment for architectural use and has ~1.5 wt% silica as the first treatment and 3 wt% alumina as the second treatment(*85*). A 0.01 (w/v)% TiO_2 sample was prepared by weighing out TiO_2, adding carrier liquid, and sonicating the suspension for three mins at 60W and 40% duty cycle.

The carrier liquid used for the analysis of the iron oxide pigments was 0.5% (v/v) Tamol 731 and 0.1% $(NaPO_3)_6$. Sodium hexametaphosphate and Tamol (Rohm and Haas) are good dispersants for mineral pigments(*86*).

Results and Discussion

Example analyses using SdFFF are given in this section. Figure 5 is a demonstration of the high resolution separation obtained as a result of the retention time being proportional to the third power of diameter. The nominal 230 nm polymethylmethacrylate particle suspension is composed of more than one size as suggested by the multiple peaks in the fractogram shown in Figure 5.

Since FFF is an elution technique, each peak can be collected and further analyzed by scanning electron microscopy (SEM). The micrographs clearly show that each peak corresponds to a different degree of aggregation - from singlets to octuplets. The regular spacing between each peak is due to the addition of one particle mass unit with successive aggregates (t_r is proportional to effective mass). SdFFF has also been used to monitor changes in the size of particle populations through different stages of sonication(*72*), to separate fused doublets from 2-particle aggregates(*73*), and as a microbalance to quantify adsorption(*70,87*).

Fractograms of two TiO_2 samples obtained using programmed field SdFFF are shown superimposed in Figure 6. The retention time axis is transformed to a size axis using Equation 1. These results suggest the presence of a bimodal
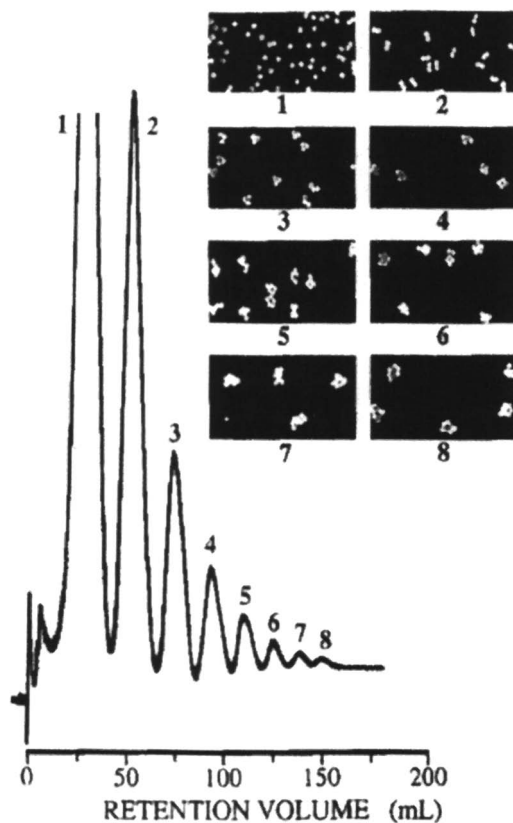
Figure 5. SdFFF fractogram and scanning electron microscopy images of 230 nm PMMA beads and their aggregates(72). [Reprinted with permission from American Chemical Society.]
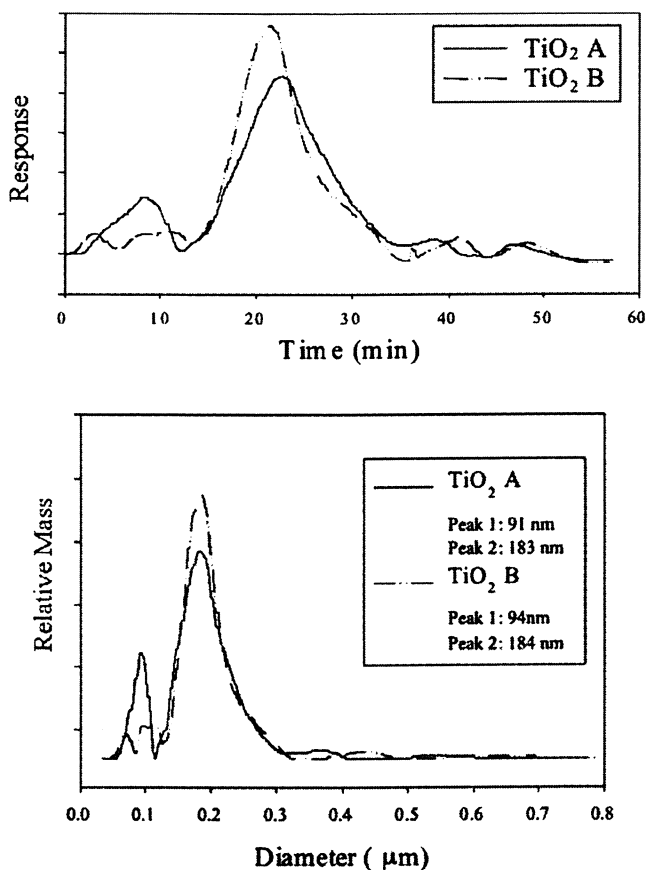
*Figure 6. SdFFF fractogram and size distribution of TiO₂. The carrier liquid
was 0.1% FL-70 and 0.02% NaN3. The densities used to calculate these
particle size distributions were based on their nominal compositions.
(Sample A: Dr = 3.20 g/mL, Sample B: Dr = 3.16 g/mL)*

population. The major peak has a maximum diameter at approximately 184 nm.
This is close to the calculated optimal diameter (relative to binder) of rutile TiO_2
of 190 nm(*13*).

The fractograms and size distributions of yellow and red iron oxides and
TiO_2 are shown superimposed in Figure 7. In this case, the TiO_2 $\Delta\rho$ was
experimentally determined using a combination of photon correlation
spectroscopy (PCS) and SdFFF. The average diameter obtained by PCS was

substituted into Equation 1 to obtain $\Delta\rho = 3.28$ g/mL. This value is comparable to that calculated using the nominal wt% composition of TiO_2 particles.

Nanoparticle Shape

Finally, particle shape is an important parameter for many nanoparticles used for coatings. However, among the commercially available techniques, microscopy is the only one able to provide detailed shape information. The capability to indirectly obtain estimates of shape factors have been mentioned for some techniques. Since flow and sedimentation FFF separate on the basis of hydrodynamic diameter and effective mass, nonspherical particles will give different size distribution curves(88). The difference between the two FFF results is an indication of the shape of the particles. Sedimentation FFF has also been combined with electron microscopy to obtain the thickness of platey particles(89). Sedimentation FFF and light scattering measurements were used to determine the 'platyness' of kaolin particles(90). Flow FFF and light scattering have also been used to obtain a shape factor (ratio of root mean square radius to hydrodynamic diameter) for nonspherical particles(91). Electrozone sensing measures the volume of fluid that is displaced by the particle. The duration of the electrozone pulse is related to the length of the particle. Calculation of shape factors using Fraunhofer diffraction (particles > 1 µm) has been investigated(92). The application of principal component analysis to particle shape has been addressed(93).

Nanoparticles in Coatings

The main focus of this chapter is the characterization of nanoparticles in suspension. However, the behavior of these nanoparticles when applied to coatings is also very important. Nanoparticles dispersion (aggregation) and alignment within a film will influence the appearance, and optical and mechanical properties of coated materials.

The use of coherent anti-Stokes Raman scattering polarized microscopy for non-invasive three-dimensional imaging of director patterns in multi-component heterogeneous systems such as liquid crystals, anisotropic polymers, and nanoparticle-LC composite materials was recently demonstrated(94).

The characterization of thin film coatings requires an extreme spatial resolution. In this situation, the techniques based on imaging or light scattering might not suffice. Small angle X-ray scattering (SAXS) and Small Angle Neutron Scattering (SANS), capable of nanometer resolution, are powerful tools for surface analysis applicable to thin film characterization(37,95,96). A synchrotron source of coherent X-rays must be used to obtain the highest
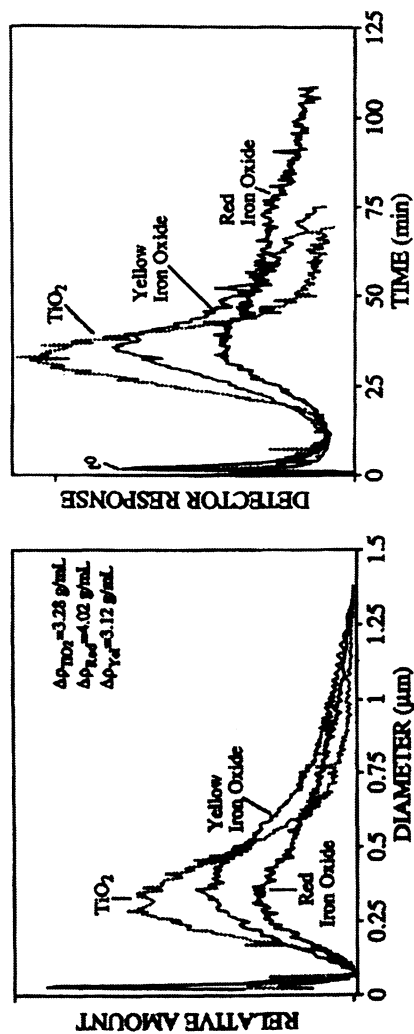
Figure 7. SdFFF fractogram and size distribution of iron oxides and TiO$_2$. The carrier liquid is 0.5% Tamol and 0.1% (NaPO3)6. The void peak is marked as t0.

resolution with X-ray scattering. Synchrotron and neutron sources are costly and not easily available and as a consequence, commercial SAXS and SANS instruments are not feasible. However, recent developments in X-ray beam focusing may overcome this limitation for SAXS(95). Even though neutron and X-ray scattering techniques are not easily accessible, they are unique tools for investigating materials at the nanometer scale.

Conclusions

Particle characterization has long been a marginal branch of analytical chemistry. The recent development of nanotechnology focused an unprecedented interest on this topic. It is now clear that such a complex task requires a well articulated approach.

New technologies developed by and previously confined to the academic environment have found their way to the market. A remarkable example is the FFF family of techniques. Thermal, flow and sedimentation FFF are now commercially available. This family of techniques is able to cover the needs for particles characterization in the entire range from macromolecules to micronsize particles. The new demands for nanoparticles characterization stimulated innovations in imaging(15-18) and light scattering and led to the realization of hybrid(19-20) and hyphenated techniques. Complex and polydisperse nanoparticle mixtures have been shown to benefit from the coupling of a separation device to other sizing techniques such as light scattering detector and microscopy(33-35).

Nanofabrication technologies are being tested for the construction of nanofluidic separative device and to improve the performance of established techniques (i.e., the etching of homogeneous size pores for SEC columns)(97).

New analytical technologies and approaches are expected to emerge as challenges specific to nanoparticle analyses are met. One recent development that presents intriguing analytical capabilities is nanoparticle mass spectrometry. Matrix laser desorption ionization time-of-flight mass spectrometry has been used to monitor the size of ZnS nanocrystals as a function of annealing times. Differences between ~1.4 nm and ~2.1 nm could be discerned as was the evolution of singly charged ZnS clusters into nanocrystals(98).

Acknowledgements

References

1. Lambourne, R., Strivens, T.A., Eds., Paint and Surface Coatings: Theory and Practice, William Andrews, Inc., (1999).
2. Buxbaum, G., Pfaff, G., Eds., Industrial Inorganic Pigments, 3rd Ed., Wiley-VCH Verlag GmbH, Weinham (2005).
3. Zhai, L., Cebeci, F.C., Cohen, R.E., and Rubner, M.F., *Nano Lett.* **2004**, *4*, 1349-1353.
4. Lee, D., Rubner, M.F., Cohen, R.E., *Nano Lett.*, **2006**, *6(10)*, 2305-2312.
5. Stupca, M., Alsalhi, M., Al Saud, T., Almuhanna, A., and Nayfeh, M. H., *Appl. Phys. Lett.,* **2007**, *91*, 063107.
6. Chikan, V. and Kelle, D. F., *Nano Lett.*, **2002**, *2(2)*, 141-145.
7. Tu, H., Yang, S., Chikan, V., and Kelley, D. F., *J. Phys. Chem. B*, **2004**, *108(15)*, 4701-4710.
8. Chikan, V. and Kelley, D. F., *J. Phys. Chem. B*, **2002**, *106(15)*, 3794 -3804.
9. Daniel, M. C., Astruc, D., *Chem. Rev.*, **2004**, 104, 293-346.
10. Jain, P. K., Huang, X., El-Sayed, I. H., and El-Sayed, M. A., *Plasmonics*, **2007**, *2*, 107-118.
11. Link, S., Mohammed, M. B., and El-Sayed, M. A., *J. Phys. Chem. B*, **1999**, *103*, 3073-3077.
12. Allen, T., Particle Size Measurement, 5th Ed., Kluwer, Dordrecht, 1997.
13. Xu, X. R., Particle Characterization: Light Scattering Methods, Kluwer Academic Publishers, 2002.
14. Volkmann, H., *Applied Optics*, **1966**, *5*, 11.
15. Hell, S. W., *Science*, **2007**, *316 (5828)*,1153-1158.
16. Hell, S. W, Dyba, M. and Jakobs, S., *Curr. Opin. Neurobiol.*, **2004**, *14*, 599-609.
17. Gerton, J. M., Wade, L. A., Lessard, G. A., Ma, Z., *Phys. Rev. Lett.*, **2004**, *93*, 18.
18. Ünlü, M. S., Goldberg, B. B., and Ippolito, S. B., Proceedings of the 7th International Symposium on Advanced Physical Fields, November 2001.
19. Malloy, A., Carr, B., *Part. Part. Sys. Char.,* **2006**, *23*, 2, 197-204.
20. Hsu, L.; Chein, H., *J. Nanopart. Res.*, **2007**, *1*, 157-163.
21. Coulter, W. H., *Proc. Natl. Electron. Conference*, **1956**, *12*, 1034.
22. Bayley, H. and Martin, C. R., *Chem. Rev.*, **2000**, *100*, 2575-2594.
23. DeBlois, R. W. and Bean, C. P., Rev. Sci., *Instrum.,* **1970**, *41*, 909.
24. Ito, T., Sun, L., and Crooks, R. M., *Anal. Chem.*, **2003**, *75*, 2399-2406.
25. Saleh, O.A. and Sohn, L. L., *Rev. Sci. Instrum.*, **2001**, *72*, 4449-4451.
26. Jagtiani, A. V., Zhe, J., Hu, J., and Carletta, J., *Meas. Sci. Technol.*, **2006**, *17*, 1706-1714.
27. Felton, P., in Liquid Particle Size Measurement Techniques: 2nd Volume ASTM STP 1083, E.D. Hirleman, W.D. Bachalo, and P.G. Felton, Eds., American Society for Testing ad Materials, Philadelphia, pp 47-59, 1990.

28. Phillies, G. D. J., in Measurement of Suspended Particles by Quasi-Elastic Light Scattering, B. E. Dahneke, Ed., Wiley, New York, pp. 291–326, 1985.
29. Pecora, R., Dynamic Light Scattering: Applications of Photon Correlation Spectroscopy, Springer, 1985.
30. "Monitoring Pigment Milling Processes Using Dynamic Light Scattering", Malvern Instruments Application Note, 2007. http://www.malvern.com
31. Filella, M., Zhang, J., Newman, M.E., and Buffle, *J., Coll. Surf. Physicochem. Eng. Aspects*, **1997**, *120*, 27.
32. Clogston, J. D., Zheng, J., McNeil, S. E. and Patri, A. K., Symposium FF: Engineered Nanoscale Materials for the Diagnosis and Treatment of Disease, Materials Research Society Spring Meeting, 2007.
33. Wyatt, P. J., *J. Coll. Interf. Sci.*, **1998**, *197*, 9.
34. Shortt, D. W., Roessner, D., and Wyatt, P. J., *Am. Lab.*, **1996**, *Nov.*, 21.
35. White, R. J., *Polym. Int.*, **1997**, *43*, 373.
36. Wittgren, B., Wahlund, K. G., *J. Chromatogr. A*, **1997**, *760*, 205-218.
37. Chu, B. and Liu, T., *J. Nanopart. Res.*, **2000**, *2*, 29-41.
38. Debye, P., *J. Chem. Phys.*, **1933**, 1, 13.
39. Oja, T., Peterson, G., and Cannon, D.A., US Patent 4,497,207 (1985).
40. Bayer, T. S. B., *Colloids Surf. A: Physicochem. Eng. Aspects*, **1993**, *11*, 39.
41. O'Brien, R. W., Midmore, B. R., Lamb, A., and Hunter, R. J., *Faraday Discuss. Chem. Soc.*, **1990**, *90*, 301.
42. Allen, T., Particle Size Measurement. London, Chapman & Hall, 1968.
43. Beuselinck, L., Govers, G., Poesen, J., Degraer, G. and Froyen, L., *CATENA*, **1998**, *32 (3-4)*, 193-208.
44. Ebersole, R. C. and McCormick, R. M., *Bio/Technology*, **1993**, *11*, 1278.
45. Petersen, S. L. and Ballou, N. E., *Anal. Chem.*, **1992**, 64, 1676.
46. Orbán, L., Tietz, D., Chrambach, A., *Gel. Electrophoresis*, **2005**, *8*, 10.
47. Xu, X., Caswell, K. K., Tucker, E., Kabisatpathy, S., Brodhacker, K. L. and Scrivens, W. A., *J. Chromatogr. A*, **2007**, *1167*, 1, 35-41.
48. Chan, K. C., Patri, A. K., Veenstra, T. D., McNeil, S. E., Issaq, H. J., *Electrophoresis*, **2007**, *28*, 10.
49. Hwang, W.-M., Lee, C.-Y., Boo, D. W. and Choi, J.-G., *Bull. Korean Chem. Soc.,* **2003**, *24*, 5.
50. Towns, J. K. and Regnier, F. E., *Anal. Chem.*, **1992**, *64*, 2473-2478.
51. Zhao, Z., Malik, A. and Lee, M. L., *Anal. Chem.*, **1999**, *65*, 2747-2752.
52. Knox, R. J., Burns, N. L., van Alstine, J. M., Harris, J. M. and Seaman, G. V. F., *Anal. Chem.*, **1998**, *70*, 2268-2279.
53. Wu, C.-S., Handbook of Size Exclusion Chromatography. Science 1995.
54. Wei, G.-T., Liu, F.-K. and Wang, C. R. C., *Anal. Chem.*, **1999**, *71*, 2085-2091.
55. Wei, G.-T., Liu, F-K., *J. Chromatogr.*, **1999**, 836, 253-260.
56. Al-Somali, A. M., Krueger, K. M., Falkner, J. C., Colvin, V. L., *Gold. Anal. Chem.,* **2004**, *76*, 5903-5910.
57. Yamaguchi, T., Okuyama, K., *Part. Part. Sys. Char*, **2007**, *24*, 424-430.

394

58. Holsworth, R. M., Provder, T. and Stansbrey, J. J., In Particle Size Distribution, Provder, T., Ed., ACS Symp. Ser. 332, American Chemical Society, Washington, D.C., 1987. Chapter 13.
59. Koehler, M. E. and Provder, T., In Particle Size Distribution, Provder, T. Ed., ACS Symp. Ser. 332, American Chemical Society, Washington, D.C., 1987. Chapter 16.
60. Kissa, E., "Dispersions: Characterization, Testing, and Measurements, Marcel Dekker, New York, 1999, p. 386.
61. Small, H., *Adv. in Chromatogr.*, **1997**, *15*, 113.
62. Miller, C. M., Sudol, E. D., Silebi, C.A., and El-Aasser, M. S., *J. Colloid Interf. Sci.*, **1995**, *172*, 249.
63. Dos Ramos, J. G. and Sileb, C.A., *Polym. Int.*, **1993**, *30*, 445.
64. Blom, M. T., Chmela, E., Oosterbroek, R. E., Tijssen, R. and van den Berg, A., *Anal. Chem.*, **2003**, *75*, 6761-6768.
65. Giddings, J.C., *Sep. Sci.*, **1966**, *1*, 123.
66. Giddings, J. C., *Science*, **1993**, *260*, 1456.
67. Schimpf, M. E., Caldwell, K.D. and Giddings, J.C., Eds., FFF Handbook, Wiley Science (2000).
68. Ratanathanawongs, S.K., Giddings, J.C., In Particle Size Distribution II: Assessment and Characterization, Provder, T., Ed., ACS Symp. Ser. 472, American Chemical Society, Washington, D.C., Chapter 15, 229-246 (1991).
69. Williams, S.K.R. and Li, D., *J. Sep. Sci.*, **2006**, *29*, 1720-1732.
70. Beckett, R., Ho, J., Jiang, Y., Giddings, J.C., *Langmuir*, **1991**, *7*, 2040-2047.
71. Ratanathanawongs, S. K., Shiundu, P. M. and Giddings, J. C., *Colloid Surface A*, **1995**, *105*, 243-250.
72. Barman, B.N. and Gidding, J.C. In Chromatography of Polymers: Characterization by SEC and FFF, Provder, T., Ed., ACS Symp. Ser. 521, 1993, p. 30.
73. Barman, B.N. and Giddings, J.C., *Langmuir*, **1992**, *8*, 51-58.
74. Ratanathanawongs, S. K. and Giddings, J. C., *Chromatographia*, **1994**, *38*, 545-554.
75. Weiner, B. B., Fairhurst, D. and Tscharnute, W. W., In Particle Size Distribution, Provder, T., Ed., ACS Symp. Ser. 472, American Chemical Society, Washington, D.C., 1991. Chapter 12.
76. Van de Hulst, H. C., Light Scattering by Small Particles, Dover Publications, New York, 1981.
77. Bohren, C. F. and Huffman, D. R., Absorption and Scattering of Light by Small Particles, Wiley-Interscience, New York, 1983.
78. Kerker, M., The Scattering of Light and Other Electromagnetic Radiation, Academic Press, New York, 1969.
79. Ratanathanawongs S. K. and Giddings, J. C., In Chromatography of Polymers: Characterization by SEC and FFF (ACS Symp. Ser.. 521), pp.

13-29, Provder, T., Ed., American Chemical Society, Washington D.C., 1993.

80. Williams, S. K. R., Lee, H. K. and Turner, M. M., *J. Magn. Magn. Mate*, **1999**, *194*, 248-53.

81. Rameshwar, T., Samal, S., Lee, S., Kim, S., Cho, J., and Kim, I. S., *J Nanosci. Nanotechnol.*, **2006**, *6*, 2461-2467.

82. Runyon, J.R., Goering, A., Williams, S.K.R., Yong, K.-T., and Prasad, P.N., *Anal. Chem.*, in preparation.

83. PostNova Analytics, S101 Product Information, Salt Lake City, Utah.

84. Williams, P.S. and Giddings, J.C., *Anal. Chem.*, **1987**, *59*, 2038.

85. Williams, S.K.R., Butler-Veytia, B., Lee, H., In Service Life Prediction: Methodology and Metrologies, J.W. Martin and D.R. Bauer, Eds., ACS Symp. Ser. 805, American Chemical Society, Washington, D.C., 2002. Chapter 14.

86. Bernhardt, C., *Adv. Coll. Interf. Sci.*, **1988**, *29*, 79-139.

87. Bohner, M., Ring, T.A., Rapoport, N. and Caldwel, K.D., *J. Biomat. Sci.-Polym. E.*, **2002**, *13*, 733-746.

88. Giddings, J. C., Ratanathanawongs, S. K., Barman, B. N., Moon, M. H., Liu, G., Tjelta, B. L. and Hansen, M. E.. In Colloid Chemistry of Silica, Bergna, H., Ed., Adv. Chem. Ser. 234, ACS, Washington, D.C., p. 332.

89. Beckett, R., Murphy, D., Tadjiki, S., Chittleborough, D. J. and Giddings, J. C., *Colloid Surface A*, **1997**, *120*, 17.

90. Slepetys, R. A. and Cleland, A., *J. Clay Miner.*, **1993**, *28*, 495.

91. Kammer, F. v.d., Baborowski, M., Friese, K., *Anal. Chim. Acta*, **2005**, *552*, 166-174.

92. Brown, D. J., *Powder Technol.*, **1986**, 49, 71.

93. Whiteman, M. and Ridgeway, K., *Spec. Publ.-R. Soc. Chem., Part. Size Anal.*, **1992**, *102*, 340.

94. Kachynski, V., Kuzmin, A. N., Prasad, P. N., Smalyukh, I. I., *Appl. Phys. Lett.*, **2007**, *91*, 151905.

95. Tanner, B. K., Hase, T. P. A., Clarke, J., Pape, I., Li-Bassi, A. and Fulthorpe, B. D., *Appl. Surf. Sci.*, **2001**, *182*, 3, 202-208.

96. Grosso, D., F. Babonneau, Albouy, P., Amenitsch, H., Balkenende, A. R., Brunet-Bruneau, A., and Rivory, J., *Chem. Mater.,* **2002**, *14*, 931-939.

97. Abgrall, P. and Nguyen, N. T., *Anal. Chem.* Articles ASAP:Web Released March 6 (2008).

98. Kuzuya, T., Tai, Y., Yamamuro, S., Sumiyama, K., *Chem. Phys. Lett.*, **2005**, *407*, 460-463.

Author Index

399

Subject Index

401

constant load scratch width for
  unfilled coating and coatings
  with Filler A, B, and C, 252*f*
dividing scratch profiles, 253
experimental, 233–235
Filler A system, 237, 240
Filler B system, 241, 243–244
Filler C system, 248
full scratch width, peak-to-peak
  scratch width vs. scratch force
  of unfilled and Filler B systems,
  246*f*
glass transition temperature and
  pendulum hardness vs. particle
  concentration for coatings with
  Filler A, B, and C, 238*f*
initial and residual penetration
  depth from progressive scratch
  (P-scratch) profiles of Filler A
  systems, 242*f*
initial and residual penetration
  depth from P-scratch profiles of
  Filler B systems, 245*f*
laser scanning confocal microscope
  (LSCM) method, 235
LSCM images of profiles from P-
  scratch of unfilled coating and
  coatings with Filler A, B, and C,
  251*f*
LSCM images of progressive
  scratch profiles and residual
  scratch depth for unfilled and
  Filler C coatings, 250*f*
LSCM images of P-scratch profiles
  from progressive load-scratch on
  unfilled and coating with Filler
  B, 244*f*
LSCM images of P-scratch profiles
  on unfilled and coating with
  Filler A, 240*f*
LSCM images of P-scratch with
  Filler B systems, 247*f*
LSCM images of scratch, 239*f*
mechanical measurements,
  234

peak-to-peak scratch width, full
  scratch depth, and ratio for Filler
  A system, 241*t*
peak-to-peak scratch width, full
  scratch depth, and ratio for Filler
  B system, 248*t*
penetration curves from P-scratch
  on unfilled PU, 239*f*
percentage of recovery from P-
  scratch test, 252*f*
progressive-load scratch testing,
  237, 239*f*
scratch morphology
  characterization, 234–235
scratch profiles of 1 and 2.5 wt%
  Filler A systems, 243*f*
scratch testing, 234–235
surface elastic modulus and
  hardness vs. nanoparticle
  concentration of coatings with
  Filler A, B, and C, 236*f*
surface mechanical measurements,
  235–236
Scratch resistance
  acrylate films with organoclay,
  267, 270*t*, 271
  adhesion of nanometer-thick,
  coatings, 300, 302–303, 305
  gloss retention of polyurethane
  coatings with alumina
  nanoparticles, 221*t*
  gloss values of coatings before
  scratching, 217*t*
  mechanisms, 225, 229
  percentage gloss retention after
  scratch test, 220*f*
  results for coatings with
  nanoparticles, 218, 221
  solvent-free coatings, 225, 228*f*
  testing, 213–215
  understanding mechanisms, 211–
  212
  See also Polyurethane coatings;
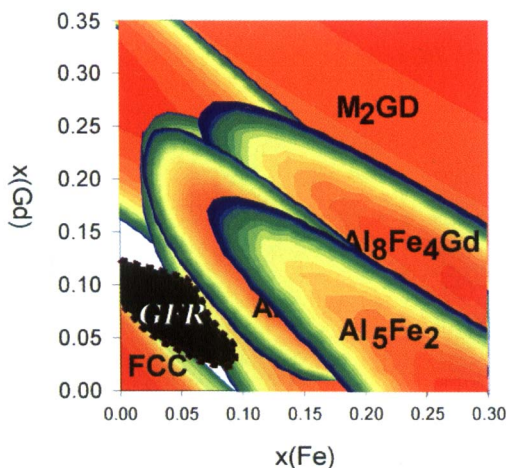 Scratch behavior of
  polyurethane coating

Figure 8.3. The experimental GFR for Al-Fe-Gd superimposed on calculated plot for crystallinity. Note the overlap of GFR with region predicted not to be kinetically favored for crystallization.
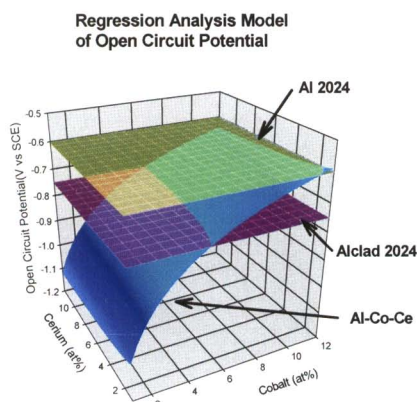

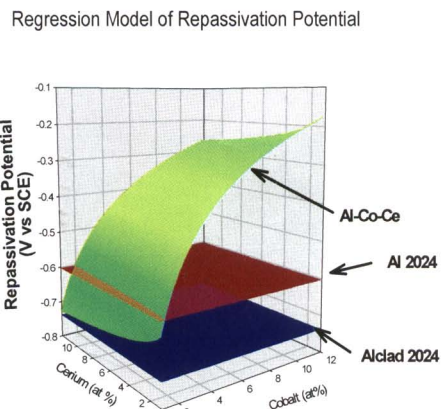*Figure 8.4. The open circuit potential of the Al-Co-Ce system as compared to AA2024 and Alclad^{TM} 2024.*

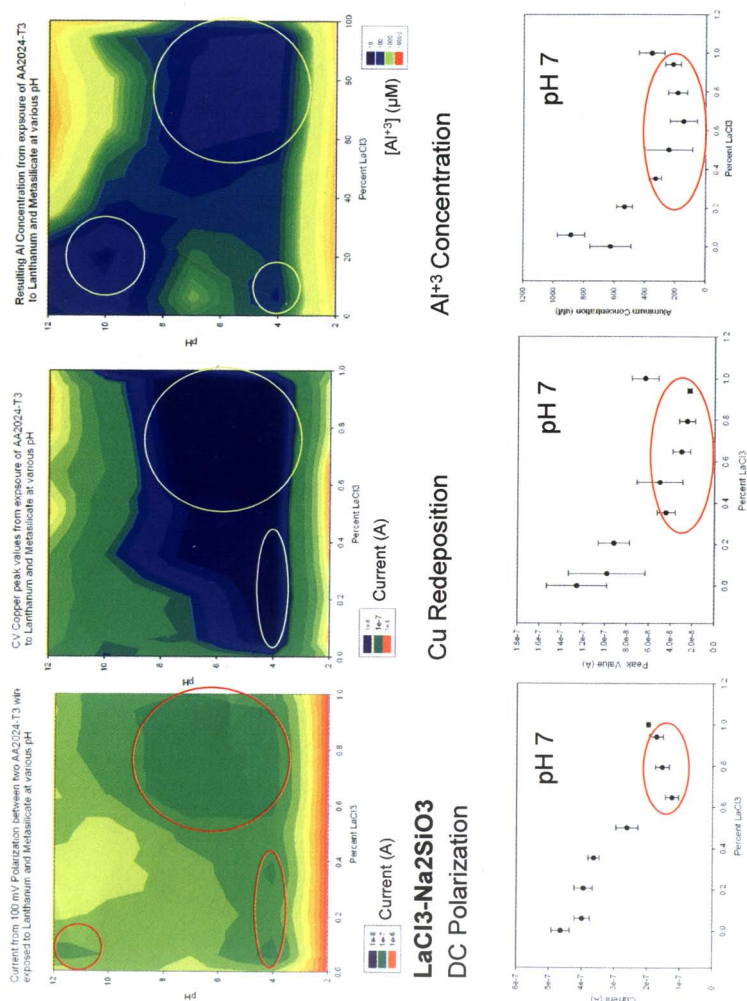*Figure 8.5. The repassivation potential of the same Al-Co-Ce system shown in Figure 4*

Figure 8.8. Inhibitor performance results for lanthanum chloride and sodium metasilicate using DC polarization (left), Cu redeposition (center) and fluorometric detection of Al^{3+} The regions showing synergy have been circled 66.
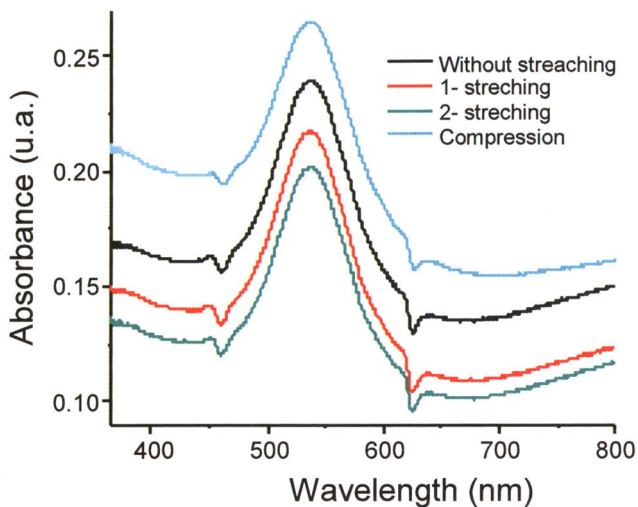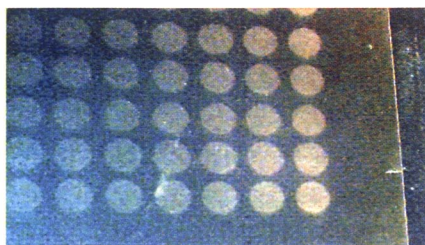
Figure 8.15. Plasmon adsorption spectra from a colloidal gold lattice as discussed in the text. The different curves demonstrate the strain sensitivity of the structure. Zero deformation: black, Compression: blue, tension: red and green. The film used to obtain the spectra is shown on the right.

Figure 9.2. 12.7 mm diameter, 2 μm thick E. coli latex ink patches printed on polyester sheet. Epson 640 printer, 26μm aperture (44).
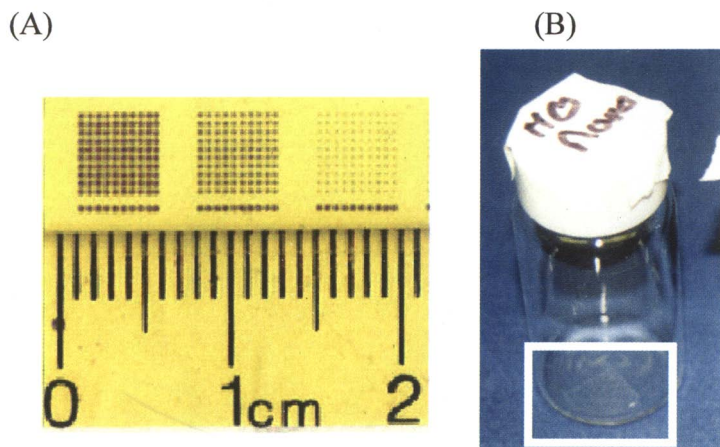
(A)

(B)

Figure 9.6. Latex microbial ink dot arrays. A. Printed on WSP using a 50 μm aperture tip, 0.5 mm pitch, ~0.5 nl droplets; 10 x 10 arrays of 5, 3, and 1 droplet per dot respectively left to right. B. E. coli dot array printed on polyester, excised and placed in a scintillation vial for measurement of bioluminescence reactivity by mercury induction.
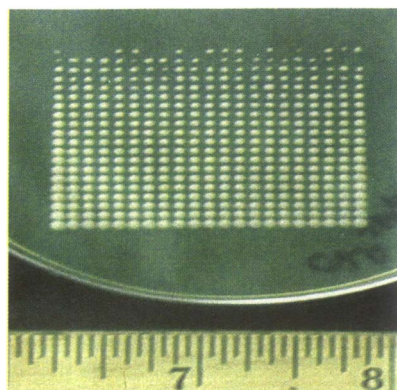

Figure 9.10. Ink-jet printed K. fragilis micro colony array printed onto YEPD agar plate to determine the viability following piezoelectric deposition through a 50 μm diameter aperture tip. Plate incubated for 48 hours, 30°C. Array printed from left to right starting at the lower left hand corner and then upward.
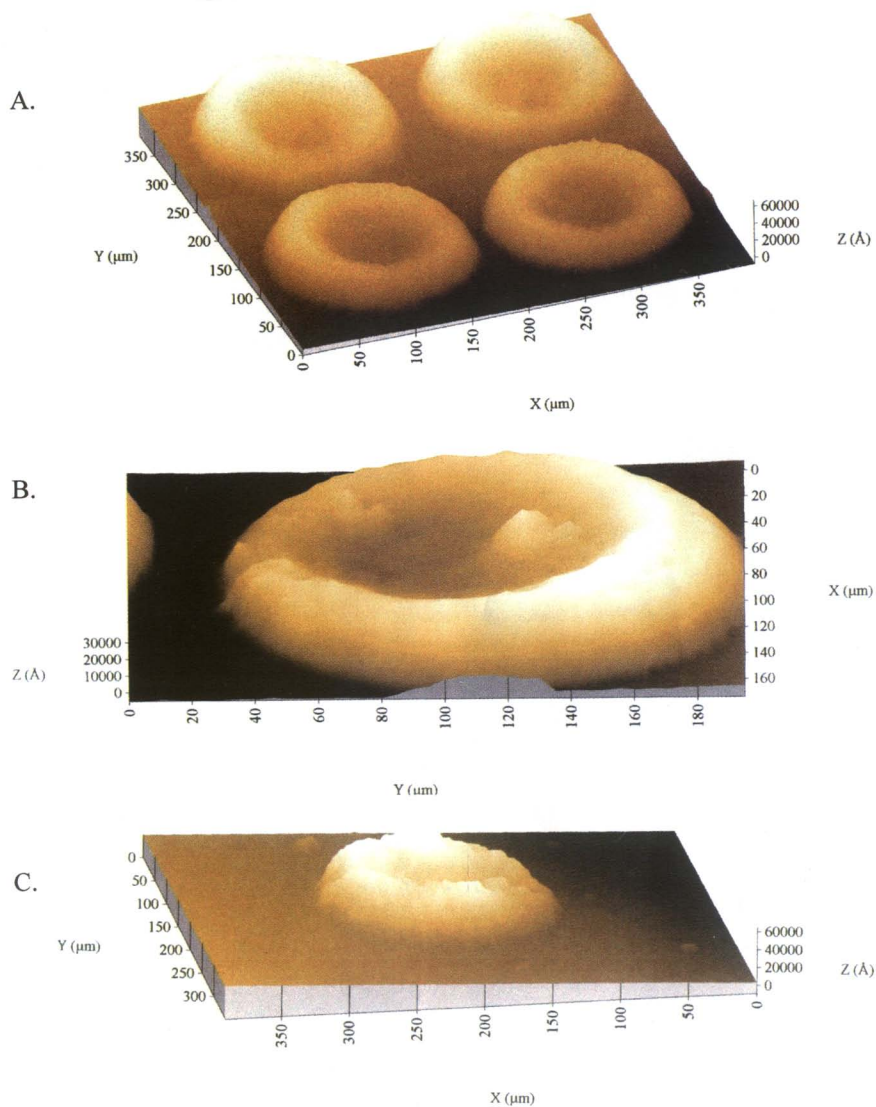
Figure 9.8. Profilometer images of E. coli pRB28 latex ink dots printed using formulation IV with a piezoelectric DOD nano-plotter. A. 50 μm aperture tip. B. Higher magnification, 50 μm aperture tip. C. 25 μm aperture tip.